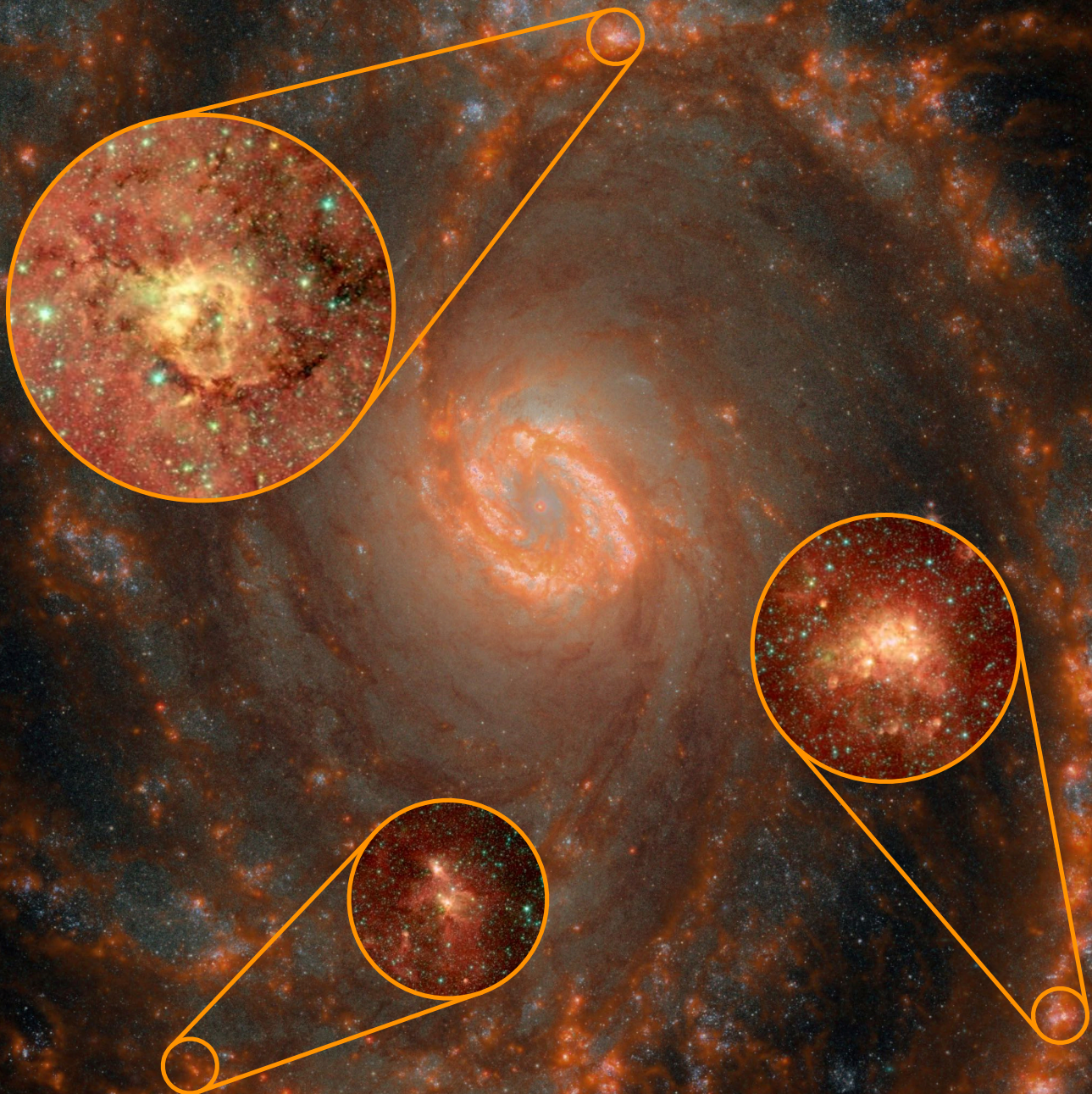


Dense Gas and Star Formation from the Milky Way to Nearby Galaxies



Lukas Neumann

Dense Gas and Star Formation from the Milky Way to Nearby Galaxies

Dissertation
zur
Erlangung des Doktorgrades (Dr. rer. nat.)
der
Mathematisch-Naturwissenschaftlichen Fakultät
der
Rheinischen Friedrich-Wilhelms-Universität Bonn

vorgelegt von
Lukas Neumann
aus
Bielefeld, Nordrhein-Westfalen, Deutschland

Bonn, 10.09.2024

Angefertigt mit Genehmigung der Mathematisch-Naturwissenschaftlichen Fakultät
der Rheinischen Friedrich-Wilhelms-Universität Bonn

Gutachter/Betreuer: Prof. Dr. Frank Bigiel
Gutachter: Prof. Dr. Karl M. Menten
Tag der Promotion: 06.05.2025
Erscheinungsjahr: 2025

To all humans, animals, and whatever form of life in the universe.

Abstract

Galaxies are the building blocks of the universe, which come in different sizes and shapes. Driven by dark matter, galaxies can interact and merge to form bigger galaxies across cosmic time. Across the cosmos, there are billions of galaxies that can be divided into two main classes – ellipticals and spirals. Spiral galaxies contain large gas reservoirs and show active star formation, while ellipticals are often depleted of gas and quenched in star formation. Galaxies contain hundreds of millions of stars that light up the universe. Everything between the stars is called the interstellar medium – a complex, turbulent subject containing various components and phases. One of the most interesting component are molecular clouds, which are the sites of star formation.

Star formation is at the heart of many astrophysical processes from planet formation to galaxy evolution that is intimately connected to the cycle of matter in galaxies, dominating its energy budget and chemical composition. At the same time, star formation is one of the most complex processes in the universe and hence only poorly understood. One of the key science questions is whether star formation proceeds in a universal way across the universe or if it varies across galaxies. Gaining a deeper understanding of the process of star formation requires the study of molecular gas in galaxies, which is the fuel for star formation. While it is known that stars form in the densest parts of giant molecular clouds, it is not very well understood how fast and efficiently gas is converted into stars and if and how star formation varies between and within galaxies.

Answering these questions requires observations of the densest parts of giant molecular clouds in a representative sample of star-forming galaxies. While hardly observable at optical wavelength, the interstellar medium shines at radio wavelength in molecular line emission. Only recently, radio observatories such as ALMA and the IRAM facilities have opened up a golden age of radio astronomy, allowing the detailed study of the interstellar medium in galaxies. This thesis makes use of the novel capabilities of ALMA to present the largest sample of dense gas observations across the local universe paired with multi-wavelength observations from state-of-the-art telescopes such as the VLT and JWST, allowing the most detailed view of dense gas and star formation in nearby galaxies.

In this thesis, we connect dense molecular gas, star formation, galactic environment and molecular cloud properties in a comprehensive way using new observations of nearby, star-forming galaxies. We find that the efficiency of converting dense gas into stars is not the same across galaxies, but varies with galactic environment and dynamical properties of molecular clouds in agreement with turbulent clouds models. On the one hand, these findings suggest that more extreme, dense, high-pressure, turbulent environments, typically found towards galaxy centres, might convert dense gas less efficiently into stars compared to the discs where clouds tend to decouple from the environment and show higher star formation efficiencies. On the other hand, these results also indicate that the tracers used to infer the mass of dense gas might become less trustworthy in these extremer environments. Therefore, we test the

capabilities and limitations of these dense gas tracers, using new radio observations of molecular clouds in the Milky Way that provide a robust, high-resolution view of the physical conditions of molecular clouds and their associated line emission. We find that typical extragalactic dense gas tracers can also trace lower-density gas, questioning their utilisation as robust tracers of dense gas. Nevertheless, we show that these tracers are still sensitive to density and hence powerful extragalactic tools.

Zusammenfassung

Galaxien sind die Bausteine des Universums, die in verschiedenen Größen und Formen vorkommen. Beeinflusst von dunkler Materie können Galaxien interagieren und verschmelzen, um im Laufe der kosmischen Zeit größere Galaxien zu bilden. Im gesamten Kosmos gibt es Milliarden von Galaxien, die in zwei Hauptklassen unterteilt werden können – elliptische und spiralförmige Galaxien. Spiralgalaxien enthalten große Gasreservoirs und zeigen aktive Sternentstehung, während elliptische Galaxien oft gasarm und in der Sternentstehung erloschen sind. Galaxien enthalten Hunderte Millionen von Sternen, die das Universum erleuchten. Alles zwischen den Sternen wird als interstellares Medium bezeichnet – eine komplexe, turbulente Substanz, die verschiedene Komponenten und Phasen enthält. Eine der interessantesten Komponenten sind molekulare Wolken, in welchen Sternentstehung passiert.

Die Sternentstehung steht im Zentrum vieler astrophysikalischer Prozesse von der Planetenbildung bis zur Galaxienentwicklung, die eng mit dem Materiekreislauf in Galaxien verbunden ist und das Energiebudget und die chemische Zusammensetzung dominiert. Gleichzeitig ist die Sternentstehung einer der komplexesten Prozesse im Universum und daher nur unzureichend verstanden. Eine der wichtigsten wissenschaftlichen Fragen ist, ob die Sternentstehung im gesamten Universum auf eine universelle Weise abläuft oder ob sie von Galaxie zu Galaxie variiert. Ein tieferes Verständnis des Prozesses der Sternentstehung erfordert das Studium von molekularem Gas in Galaxien, das den Treibstoff für die Sternentstehung liefert. Während bekannt ist, dass Sterne in den dichtesten Teilen von riesigen Molekülwolken entstehen, ist es noch nicht gut verstanden, wie schnell und effizient Gas in Sterne umgewandelt wird und ob und wie sich die Sternentstehung zwischen und innerhalb von Galaxien unterscheidet.

Um diese Fragen zu beantworten, sind Beobachtungen des dichten Gases von Molekülwolken in einer repräsentativen Stichprobe von sternbildenden Galaxien erforderlich. Im optischen Wellenlängenbereich kaum beobachtbar, leuchtet das interstellare Medium im Radiowellenbereich in Form von molekularer Linienemission. Erst kürzlich haben Radioobservatorien wie ALMA und die IRAM-Observatorien ein goldenes Zeitalter der Radioastronomie eingeläutet, das die detaillierte Untersuchung des interstellaren Mediums in Galaxien ermöglicht. Diese Arbeit nutzt die revolutionären Fähigkeiten von ALMA, um die größte Stichprobe von Beobachtungen des dichten Gases im lokalen Universum zu präsentieren. Kombiniert mit Beobachtungen von hochmodernen Teleskopen wie dem VLT und JWST, bildet diese Studie eines der detailliertesten Blicke auf dichtes Gas und Sternentstehung in nahegelegenen Galaxien.

In dieser Arbeit werden dichtes molekulares Gas, Sternentstehung, galaktische Umgebung und die Eigenschaften von Molekülwolken auf umfassende Weise verknüpft. Dabei werden neue Beobachtungen von nahegelegenen, sternbildenden Galaxien verwendet. Wir finden, dass die Effizienz der Umwandlung von dichtem Gas in Sterne nicht in allen Galaxien gleich ist, sondern mit der galaktischen Umgebung und den dynamischen Eigenschaften von Molekülwolken in Übereinstimmung mit Modellen turbulenter

Wolken variiert. Einerseits deuten diese Ergebnisse darauf hin, dass in extremen, dichten, turbulenten Umgebungen mit hohem Druck, die typischerweise in Galaxienzentren zu finden sind, dichtes Gas weniger effizient in Sterne umgewandelt wird als in Galaxienscheiben, in denen sich die Molekülwolken von der Umgebung entkoppeln und höhere Sternentstehungseffizienzen zeigen. Andererseits weisen diese Ergebnisse auch darauf hin, dass die Indikatoren, die verwendet werden, um die Masse von dichtem Gas abzuleiten, in diesen extremeren Umgebungen weniger zuverlässig sein könnten. Daher testen wir die Fähigkeiten und Einschränkungen dieser Indikatoren für dichtes Gas unter Verwendung neuer Radiobeobachtungen von Molekülwolken in der Milchstraße, die einen robusten, hochauflösenden Blick auf die physikalischen Bedingungen von Molekülwolken und deren zugehörige Linienemission bieten. Wir stellen fest, dass typische extragalaktische Indikatoren für dichtes Gas auch Gas mit niedrigerer Dichte nachweisen können, was ihre Verwendung als robuste Indikatoren für dichtes Gas in Frage stellt. Nichtsdestotrotz zeigen wir, dass diese Indikatoren dennoch empfindlich auf Dichte reagieren und somit mächtige extragalaktische Werkzeuge sind.

Acknowledgements

“Strange is our situation here on earth. Each of us comes for a short visit, not knowing why, yet sometimes seeming to a divine purpose. From the standpoint of daily life, however, there is one thing we do know: we are here for the sake of others.”

Albert Einstein – 20th century physicist

I would like to thank Frank Bigiel for offering me a PhD position in his group and giving me the opportunity to independently work on a fascinating project. The past five years in your group, including the internship, Master and PhD thesis, have been a magnificent, fulfilling journey and made me realise that being an astrophysicist is the best job in the world. I have enjoyed every single day of my work that I would never even consider work. I love what I do, and I hope I can continue in academia to live my passion. You might not be the best day-to-day supervisor, mental support, responsive or punctual person, that many PhD students wish in a supervisor. But for me, I could not image a better group to pursue my PhD thesis and supervisor to promote my academic career. You opened up the world of science to me, connecting me to big collaborations like PHANGS or LEGO, and supported me in any way possible to interact and flourish in the minefield of academia. When I look back to the beginning of my Master’s in Bonn, I could have never imagined how much I would learn as a scientist and grow as a person, so right now I am in the position to continue my academic journey in one of the best places possible. Thank you for your scientific, personal, and career advice and for every single beer we had together whenever you were around. The late-night chats in Harmonie or Fiddlers were probably one of the most important career talks of my life. I hope our paths will cross in the future and I wish you all the best for your group in Bonn, your wife and the two kids. But I do not doubt that you will make the right decisions to win the grants, hire the best people and balance family life and work.

I thank Karl Menten for investing his time to examine my thesis and being one of the kindest persons I ever met, and Simon Stellmer as well as Dennis Lehmkuhl for agreeing to complement the PhD examination committee as externals. I am thankful to Ash, Jakob, and Mallory for providing comments and feedback on the thesis manuscript.

I have to, I need to, I want to thank you, Ash! I cannot put into words how grateful I am to have you as a supervisor, mentor, colleague, and friend. I would not be standing here, finishing my PhD thesis with ease and having a PostDoc position in my pocket without you. I cannot thank you enough for supporting me from the very first day of my PhD till today, despite you are not even part of the group any more. You showed me how to think as a scientist, optimise my programming skills, make better plots and write proposals. But in the first instance, you are on the highest level helpful, unselfish, and supportive.

You were always there when I needed advice, and even read my whole PhD thesis during your wedding preparations. Thank you for introducing me to new people at my first conference in Nice, thank you for sharing a room with me in Gothenburg, thank you for accommodating me at ESO, and thank you for having the first whiskey of my life with you. See you soon!

Much of the skills I have acquired over the past five years have been due to you, Jakob. Thank you for supervising me as an intern and during my Master's thesis, where I have learned most of my programming and data visualisation skills that I am using on a daily basis. You probably make some of the prettiest scientific plots that exist, giving me amazement and inspiration. Much of this thesis also bears your signature. However, you do not only stand out by presenting your work, but in particular shine with your relentless drive to master all the dirty details leading to fantastic scientific results.

I would like to thank the whole PHANGS collaboration for welcoming me as a colleague and allowing me to work and collaborate with probably the best group of people a PhD student can imagine. I have to thank everybody in PHANGS because there is no person, about whom I could say a negative thing. However, I would like to express my gratitude to some individual PHANGS colleagues in the following.

Adam and Antonio – I express my deepest thankfulness to you for accompanying, motivating, supporting, and supervising my PhD project from start to finish. Much of my knowledge about molecular gas, dense gas, star formation, and cloud models is thanks to the countless chats and discussions I could have with you. Thank you, Adam, for showing me (basically everything, but in particular) how to write better scientific papers. Thank you, Antonio, for sharing your expertise on statistics and cloud models. Thank you, Molly, for passing on your projects and data sets that form the foundation of this thesis, Erik, for always waking up early to make it to the Europe-friendly calls, and for your incredibly high-quality feedback on statistical and technical issues, Eva, for sponsoring and supporting my journey in PHANGS, Jiayi, for your extensive support with data processing, analysis and, in general, proving data products in a blink of a second, Maria, for your immense expertise and support to help interpret scientific results, Sophia, for your infectious enthusiasm, and for sharing the PhD time with me, Miguel, for providing environmental masks of NGC 4321 and for sharing your expertise on dense gas studies, Francesco, for helping out with MUSE data products, Ralf and Simon, for your detailed comments and fruitful discussions about molecular cloud models, Danny, for your kind, motivating words that every young scientist desired, and everyone who supported my projects and provided feedback on my paper drafts.

In particular, I want to thank members of the ALMA data reduction and molecular ISM working groups. Thank you, Andrea, Annie, Antoine, Chris, Daizhong, Elias, Elizabeth, Eric K., Jerome, Jonny, Lise, Melanie, Rowan, Ryan, Sumit, Tom, Yixian.

Moreover, I would like to thank Jens for providing science-ready LEGO data and Eric M. for sharing VLA data of NGC 4321.

Scientific research has no value without exchange with others. I would like to thank Daniel and Steffi for inviting me to Cologne and giving me the opportunity to present my work. Thank you, Eva, Sophia, and Kathryn, for having me at MPIfR and ARI, where I spent a wonderful week. Many thanks to Jackie for inviting me to Leiden Observatory to promote my work.

I am very thankful for the amazing people that have accompanied me during my time in Bonn. It is not the science but the people that make a PhD project enjoyable. Thank you, Johannes, Ivana, Cosima, Dario, Mallory, Ina, Zein, Niklas, and Hao.

During my PhD, I had the pleasure to co-supervise plenty of students, which has been one of the most enjoyable parts of my work. Thank you, Michele, Marius, Malena, Lars, Wajdee, Patrick, Selina, Niklas, Sabrina, and Minou.

Seeing this long list of people who have accompanied me over the past years during my PhD makes

me realise how much of a team effort science is. Most of this work would not have been possible without the people listed above, and I apologise to everyone who is missing from this list but should have been included.

Last but not least, I would like to thank the people who enabled me to study and attempt a PhD in the first place, that is, my family. I am extremely grateful to have such great, caring, pushing, but never over-demanding parents. I think, some of the success in my career and private life is due to my effort, but none of the accomplishments would have been possible without the excellent starting conditions that you have provided. I could always explore whatever I wanted and you always supported me, both mentally and financially, even at the point when I decided to pursue a second Master's because I followed my passion to become an astrophysicist. I know that the past few years have been tough, especially since Johanna is asking a lot about your physical condition and mental composure. I hope you can forgive me for not being a better son, for not being around for family events, for helping so little with Johanna, and for putting my career and passions too high to be healthy at some points.

Finally, I would like to thank my second family and I can very well say that you, Valerie, the love of my life, and your parents, grandparents, siblings, cousins, uncles and aunts have become my second family. I know that I am not always the best partner, especially at times when I am immersed in my work and forget everything around me. Thank you for always supporting me, no matter what. You may think that my work or sports is what makes me happy, but the only thing I need to be happy is you.

List of Publications

The list below presents the first-author publications relevant to this PhD thesis project, specifically highlighting the author's contribution to each individual publication. This thesis is written in a cumulative form and culminates three peer-reviewed publications, whereof two are published, one in *Monthly Notices of the Royal Astronomical Society* (MNRAS) and three in *Astronomy and Astrophysics* (A&A). In addition, one manuscript is in preparation to be submitted to A&A.

1. **Neumann, L.**, Gallagher, M. J., Bigiel, F., Leroy, A. K., Barnes, A. T., Usero, A., den Brok, J. S., Belfiore, F., Bešlić, I., Cao, Y., Chevance, M., Dale, D. A., Eibensteiner, C., Glover, S. C. O., Grasha, K., Henshaw, J. D., Jiménez-Donaire, M. J., Klessen, R. S., Kruijssen, J. M. D., Liu, D., Meidt, S., Pety, J., Puschig, J., Querejeta, M., Rosolowsky, E., Schinnerer, E., Schrubba, A., Sormani, M. C., Sun, J., Teng, Y.-H., Williams, T. G., *The ALMOND survey: molecular cloud properties and gas density tracers across 25 nearby spiral galaxies with ALMA*, *Monthly Notices of the Royal Astronomical Society*, **521**, 3348, DOI: [10.1093/mnras/stad424](https://doi.org/10.1093/mnras/stad424).

Author's Contribution: L.N. performed the scientific analysis and wrote the manuscripts under the supervision of F.B., A.K.L., A.T.B., A.U., and the PHANGS molecular ISM working group. An early version of the data analysis was performed by M.G., which however was not used in the final publication. A substantial part of the data analysis, including some of the key results of the work, has been done during L.N.'s Master thesis, performed under the supervision of F.B. The ALMA observations have been led by A.K.L and A.U. (PIs). The data reduction was performed in the ALMA data reduction (ADR) working group of PHANGS led by A.T.B., where L.N. helped with the quality assessment. The publication process, including the writing of the manuscript as well as performing additional, critical data analysis was done as part of this PhD thesis project. The other co-authors helped with the scientific interpretation of the results and provided comments to improve the final manuscript.

2. **Neumann, L.**, den Brok, J. S., Bigiel, F., Leroy, A. K., Usero, A., Barnes, A. T., Bešlić, I., Eibensteiner, C., Held, M., Jiménez-Donaire, M. J., Pety, J., Rosolowsky, E. W., Schinnerer, E., Williams, T. G., *Spectral stacking of radio-interferometric data*, *Astronomy and Astrophysics*, **675**, A104, DOI: [10.1051/0004-6361/202346129](https://doi.org/10.1051/0004-6361/202346129).

Author's Contribution: L.N. performed the scientific analysis and wrote the manuscript under the supervision of F.B., A.K.L., A.U., J.P., E.R., A.T.B., and the PHANGS ADR working group. The python code published along with the paper was developed by J.S.B. with significant contributions from L.N. L.N. processed and analysed the simulated ALMA observations, which have been

provided by the PHANGS team, employing aforementioned code. The co-authors provided useful feedback on the data analysis and edits on the draft, that helped to interpret the results and improve the final version of the manuscript.

3. **Neumann, L.**, Bigiel, F., Barnes, A. T., Gallagher, M. J., Leroy, A. K., Usero, A., Rosolowsky, E., Bešlić, I., Boquien, M., Cao, Y., Chevance, M., Colombo, D., Dale, D. A., Eibensteiner, C., Grasha, K., Henshaw, J. D., Jiménez-Donaire, M. J., Meidt, S., Menon, S. H., Murphy, E. J., Pan, H.-A., Querejeta, M., Saito, T., Schinnerer, E., Stuber, S. K., Teng, Y.-H., Williams, T. G., *A 260 pc resolution ALMA map of HCN(1-0) in the galaxy NGC 4321*, *Astronomy and Astrophysics*, **691**, A121, DOI: [10.1051/0004-6361/202449496](https://doi.org/10.1051/0004-6361/202449496).

Author's Contribution: L.N. performed the scientific analysis and wrote the manuscript under the supervision of F.B., A.T.B., A.K.L., A.U., E.R. and the PHANGS molecular ISM working group. The ALMA observations have been led by M.J.G. (PI). The data reduction was performed in the ADR working group of PHANGS led by A.T.B.. L.N. assisted with the quality assessment of the reduced data and performed all further analysis steps. The co-authors provided useful feedback on the data analysis and edits on the draft, that helped to interpret the results and improve the final version of the manuscript.

4. **Neumann, L.**, Jiménez-Donaire, M. J., Bigiel, F., Leroy, A. K., Barnes, A. T., Usero, A., Rosolowsky, E., Sun, J., Schinnerer, E., Querejeta, M., Stuber, S. K., Bešlić, I., and the PHANGS team, *Dense gas scaling relations at kiloparsec scales across nearby galaxies with the ALMA ALMOND and IRAM 30 m EMPIRE surveys*, *Astronomy and Astrophysics*, **693**, L13, DOI: [10.1051/0004-6361/202453208](https://doi.org/10.1051/0004-6361/202453208).

Author's Contribution: L.N. performed the scientific analysis and wrote the major part of the manuscript under the supervision of M.J.J.D., F.B., A.K.L., A.T.B., A.U. and the molecular ISM working group of the PHANGS collaboration. M.J.J.D. contributed parts of the text and provided key and ancillary datasets. L.N. included the data provided by M.J.J.D. and performed all further analysis steps. The co-authors provided useful feedback on the data analysis and edits on the draft, that helped to interpret the results and improve the final version of the manuscript.

5. **Neumann, L.**, Bigiel, F., Barnes, A. T., Schuchmann, M., Steinrötter, M., Kauffmann, J., and the LEGO team, *LEGO III: Dense gas tracers across massive star-forming regions*, to be submitted to *Astronomy and Astrophysics*.

Author's Contribution: L.N. performed the scientific analysis and wrote the manuscript under the supervision of F.B., A.T.B., and the LEGO team. The IRAM observations have been led and reduced by J.K. (PI). L.N. and A.T.B. assisted with the quality assessment of the reduced data. Some of the results presented in this work were included in the Bachelor theses of M. Schuchmann and M. Steinrötter. L.N. repeated these and additional analysis steps.

The following list displays co-author publication that are relevant to this work.

1. den Brok, J. S., Chatzigiannakis, D., Bigiel, F., Puschig, J., Barnes, A. T., Leroy, A. K., Jiménez-Donaire, M. J., Usero, A., Schinnerer, E., Rosolowsky, E., Faesi, C. M., Grasha, K., Hughes, A., Kruijssen, J. M. D., Liu, D., **Neumann, L.**, Pety, J., Querejeta, M., Saito, T., Schruha, A., Stuber, S., *New constraints on the $^{12}\text{CO}(2-1)/(1-0)$ line ratio across nearby disc galaxies*, *Monthly Notices of the Royal Astronomical Society*, 504, 3221, DOI: [10.1093/mnras/stab859](https://doi.org/10.1093/mnras/stab859).

Author's Contribution: L.N. provided comments and edits on the draft that helped to improve the manuscript.

2. den Brok, J. S., Bigiel, F., Sliwa, K., Saito, T., Usero, A., Schinnerer, E., Leroy, A. K., Jiménez-Donaire, M. J., Rosolowsky, E., Barnes, A. T., Puschig, J., Pety, J., Schruha, A., Bešlić, I., Cao, Y., Eibensteiner, C., Glover, S. C. O., Klessen, R. S., Kruijssen, J. M. D., Meidt, S. E., **Neumann, L.**, Tomičić, N., Pan, H.-A., Querejeta, M., Watkins, E., Williams, T. G., Wilner, D., *A CO isotopologue Line Atlas within the Whirlpool galaxy Survey (CLAWS)*, *Astronomy and Astrophysics*, 662, A89, DOI: [10.1051/0004-6361/202142247](https://doi.org/10.1051/0004-6361/202142247).

Author's Contribution: L.N. performed a small part of the data analysis and provided comments/edits on the draft that helped to improve the manuscript.

3. Belfiore, F., Leroy, A. K., Sun, J., Barnes, A. T., Boquien, M., Cao, Y., Congiu, E., Dale, D. A., Egorov, O. V., Eibensteiner, C., Glover, S. C. O., Grasha, K., Groves, B., Klessen, R. S., Kreckel, K., **Neumann, L.**, Querejeta, M., Sanchez-Blazquez, P., Schinnerer, E., Williams, T. G., *Calibration of hybrid resolved star formation rate recipes based on PHANGS-MUSE $H\alpha$ and $H\beta$ maps*, *Astronomy and Astrophysics*, 670, A67, DOI: [10.1051/0004-6361/202244863](https://doi.org/10.1051/0004-6361/202244863).

Author's Contribution: L.N. provided comments and edits on the draft that helped to improve the manuscript.

4. Sun, J., Leroy, A. K., Ostriker, E. C., Meidt, S., Rosolowsky, E., Schinnerer, E., Wilson, C. D., Utomo, D., Belfiore, F., Blanc, G. A., Emsellem, E., Faesi, C., Groves, B., Hughes, A., Koch, E. W., Kreckel, K., Liu, D., Pan, H.-A., Pety, J., Querejeta, M., Razza, A., Saito, T., Sardone, A., Usero, A., Williams, T. G., Bigiel, F., Bolatto, A. D., Chevance, M., Dale, D. A., Gensior, J., Glover, S. C. O., Grasha, K., Henshaw, J. D., Jiménez-Donaire, M. J., Klessen, R. S., Kruijssen, J. M. D., Murphy, E. J., **Neumann, L.**, Teng, Y.-H., Thilker, D. A., *Star Formation Laws and Efficiencies across 80 Nearby Galaxies*, *The Astrophysical Journal*, 945, L19, DOI: [10.3847/2041-8213/acbd9c](https://doi.org/10.3847/2041-8213/acbd9c).

Author's Contribution: L.N. provided comments and edits on the draft that helped to improve the manuscript.

5. Teng, Y.-H., Sandstrom, K. M., Sun, J., Gong, M., Bolatto, A. D., Chiang, I.-D., Leroy, A. K., Usero, A., Glover, S. C. O., Klessen, R. S., Liu, D., Querejeta, M., Schinnerer, E., Bigiel, F., Cao, Y., Chevance, M., Eibensteiner, C., Grasha, K., Israel, F. P., Murphy, E. J., **Neumann, L.**, Pan, H.-A., Pinna, F., Sormani, M. C., Smith, J. D., Walter, F., Williams, T. G., *The Physical Drivers and Observational Tracers of CO-to- H_2 Conversion Factor Variations in Nearby Barred Galaxy Centers*, *The Astrophysical Journal*, 950, 119, DOI: [10.3847/1538-4357/accb86](https://doi.org/10.3847/1538-4357/accb86).

Author's Contribution: L.N. provided comments and edits on the draft that helped to improve the manuscript.

6. Jiménez-Donaire, M. J., Usero, A., Bešlić, I., Tafalla, M., Chacón-Tanarro, A., Salomé, Q., Eibensteiner, C., García-Rodríguez, A., Hacar, A., Barnes, A. T., Bigiel, F., Chevance, M., Colombo, D., Dale, D. A., Davis, T. A., Glover, S. C. O., Kauffmann, J., Klessen, R. S., Leroy, A. K., **Neumann, L.**, Pan, H., Pety, J., Querejeta, M., Saito, T., Schinnerer, E., Stuber, S., Williams, T. G., *A constant N_2H^+ (1-0)-to-HCN (1-0) ratio on kiloparsec scales*, [Astronomy and Astrophysics](#), **676**, L11, DOI: [10.1051/0004-6361/202347050](#).

Author's Contribution: L.N. provided comments and edits on the draft that helped to improve the manuscript.

7. Panessa, M., Seifried, D., Walch, S., Gaches, B., Barnes, A. T., Bigiel, F., **Neumann, L.**, *The evolution of HCO^+ in molecular clouds using a novel chemical post-processing algorithm*, [Monthly Notices of the Royal Astronomical Society](#), **523**, 6138, DOI: [10.1093/mnras/stad1741](#).

Author's Contribution: L.N. provided observational data to be compared with the simulated results and gave comments and edits on the draft that helped to improve the manuscript.

8. Belfiore, F., Leroy, A. K., Williams, T. G., Barnes, A. T., Bigiel, F., Boquien, M., Cao, Y., Chastenet, J., Congiu, E., Dale, D. A., Egorov, O. V., Eibensteiner, C., Emsellem, E., Glover, S. C. O., Groves, B., Hassani, H., Klessen, R. S., Kreckel, K., **Neumann, L.**, Neumann, J., Querejeta, M., Rosolowsky, E., Sanchez-Blazquez, P., Sandstrom, K., Schinnerer, E., Sun, J., Sutter, J., Watkins, E. J., *Calibrating mid-infrared emission as a tracer of obscured star formation on H II-region scales in the era of JWST*, [Astronomy and Astrophysics](#), **678**, A129, DOI: [10.1051/0004-6361/202347175](#).

Author's Contribution: L.N. provided comments and edits on the draft that helped to improve the manuscript.

9. Stuber, S. K., Pety, J., Schinnerer, E., Bigiel, F., Usero, A., Bešlić, I., Querejeta, M., Jiménez-Donaire, M. J., Leroy, A., den Brok, J., **Neumann, L.**, Eibensteiner, C., Teng, Y.-H., Barnes, A., Chevance, M., Colombo, D., Dale, D. A., Glover, S. C. O., Liu, D., Pan, H.-A., *Surveying the Whirlpool at Arcseconds with NOEMA (SWAN). I. Mapping the HCN and N_2H^+ 3mm lines*, [Astronomy and Astrophysics](#), **680**, L20, DOI: [10.1051/0004-6361/202348205](#).

Author's Contribution: L.N. assisted S.K.S. with the data analysis and provided comments/edits on the draft that helped to improve the manuscript.

10. Beslic, I., Barnes, A. T., Bigiel, F., Jimenez-Donaire, M. J., Usero, A., Henshaw, J. D., Faesi, C., Leroy, A. K., Rosolowsky, E., den Brok, J. S., Chevance, M., Eibensteiner, C., Grasha, K., Klessen, R. S., Kruijssen, J. M. D., Liu, D., Meidt, S., Neumann, J., **Neumann, L.**, Pan, H.-A., Puschnig, J., Querejeta, M., Schinnerer, E., Williams, T. G., *The properties and kinematics of HCN emission across the closest starburst galaxy NGC 253 observed with ALMA*, [arXiv e-prints](#), DOI: [10.48550/arXiv.2403.13751](#).

Author's Contribution: L.N. shared data for a literature comparison and provided comments/edits on the draft that helped to improve the manuscript.

11. Querejeta, M., Leroy, A. K., Meidt, S. E., Schinnerer, E., Belfiore, F., Emsellem, E., Klessen, R. S., Sun, J., Sormani, M., Bešlić, I., Cao, Y., Chevance, M., Colombo, D., Dale, D. A., García-Burillo, S., Glover, S. C. O., Grasha, K., Groves, B., Koch, E. W., **Neumann, L.**, Pan, H.-A., Pessa, I., Pety, J., Pinna, F., Ramambason, L., Razza, A., Romanelli, A., Rosolowsky, E., Ruiz-García, M., Sánchez-Blázquez, P., Smith, R., Stuber, S., Ubeda, L., Usero, A., Williams, T. G., *Do spiral arms enhance star formation efficiency?*, *Astronomy and Astrophysics*, 687, A293, DOI: [10.1051/0004-6361/202449733](https://doi.org/10.1051/0004-6361/202449733).

Author's Contribution: L.N. provided comments and edits on the draft that helped to improve the manuscript.

12. Williams, T. G., Lee, J. C., Larson, K. L., Leroy, A. K., Sandstrom, K., Schinnerer, E., Thilker, D. A., Belfiore, F., Egorov, O. V., Rosolowsky, E., Sutter, J., DePasquale, J., Pagan, A., Berger, T. A., Anand, G. S., Barnes, A. T., Bigiel, F., Boquien, M., Cao, Y., Chastenet, J., Chevance, M., Chown, R., Dale, D. A., Deger, S., Eibensteiner, C., Emsellem, E., Faesi, C. M., Glover, S. C. O., Grasha, K., Hannon, S., Hassani, H., Henshaw, J. D., Jiménez-Donaire, M. J., Kim, J., Klessen, R. S., Koch, E. W., Li, J., Liu, D., Meidt, S. E., Méndez-Delgado, J. E., Murphy, E. J., Neumann, J., **Neumann, L.**, Neumayer, N., Oakes, E. K., Pathak, D., Pety, J., Pinna, F., Querejeta, M., Ramambason, L., Romanelli, A., Sormani, M. C., Stuber, S. K., Sun, J., Teng, Y.-H., Usero, A., Watkins, E. J., Weinbeck, T. D., *PHANGS-JWST: Data-processing Pipeline and First Full Public Data Release*, *The Astrophysical Journal Supplement Series*, 273, 13, DOI: [10.3847/1538-4365/ad4be5](https://doi.org/10.3847/1538-4365/ad4be5).

Author's Contribution: L.N. provided feedback on the quality of the data products and gave comments and edits on the draft that helped to improve the JWST data reduction pipeline and the manuscript.

Contents

1	Introduction	1
1.1	The big picture	1
1.1.1	Star formation	1
1.1.2	Galaxies	1
1.2	The interstellar medium	3
1.2.1	Constituents and phases of the ISM	3
1.2.2	The baryon lifecycle and galaxy evolution	4
1.3	Observing the cold ISM	6
1.3.1	The problem of molecular hydrogen	6
1.3.2	Dust as a tracer of gas	6
1.3.3	Molecular line emission	7
1.4	Tracing star formation	11
1.4.1	Counting young stellar objects (YSOs)	12
1.4.2	Ultraviolet emission from young stars	12
1.4.3	Infrared emission from heated dust	12
1.4.4	Recombination lines from ionised gas	13
1.4.5	Free-free emission	14
1.4.6	Combined calibrators	14
1.5	Empirical star formation scaling relations	15
1.5.1	Kennicutt-Schmidt relation	16
1.5.2	Gao-Solomon relation	18
1.5.3	Dense gas scaling relation	19
1.6	Science goals and outline of this thesis	21
2	Observations	26
2.1	Fundamentals of radio astronomy	26
2.1.1	Radio antennas	26
2.1.2	Brightness temperature	27
2.1.3	Radiometer noise	28
2.1.4	Doppler velocity	29
2.1.5	Radio interferometers	29
2.2	Relevant radio and mm telescopes	32
2.2.1	IRAM 30m	32
2.2.2	Atacama Large Millimeter/sub-mm Array (ALMA)	33

2.2.3	Other relevant telescopes	34
2.3	Surveys	37
2.3.1	Physics at High Angular resolution in Nearby Galaxies (PHANGS)	37
2.3.2	Line Emission as a Tool for Galaxy Observations (LEGO)	42
3	Analysis Techniques	44
3.1	PyStructure	44
3.1.1	FITS format	46
3.1.2	Convolution	46
3.1.3	Reprojection	48
3.1.4	Products and moment maps	49
3.2	PyStacker	54
3.2.1	Velocity alignment	55
3.2.2	Spectral line stacking	56
3.2.3	Data binning	56
3.3	Measurement uncertainties	57
3.3.1	Uncertainties and upper limits	57
3.3.2	Sigma clipping and bias	58
3.4	Linear regression	59
3.4.1	Classical fitting	60
3.4.2	Advanced fitting	60
3.4.3	LinMix - Bayesian fitting	61
4	Spectral stacking of radio-interferometric data	68
4.1	Simulated ALMA observations	69
4.2	Spectral line stacking	70
4.3	Recovery of integrated intensities	71
4.4	Interferometric filtering	72
4.5	Conclusions	73
5	Dense gas scaling relations	75
5.1	EMPIRE and ALMOND surveys	76
5.2	Gao-Solomon relation	77
5.3	Dense gas fraction	81
5.4	Environmental variations in nearby galaxies	83
5.5	Dense gas and star formation in galaxy centres	85
5.6	Conclusions	86
6	The missing link between dense gas, star formation and molecular cloud properties	88
6.1	The ALMOND survey	89
6.2	Model expectations	90
6.3	Linking star formation to cloud properties	92
6.4	Conclusions	93

7	A spatially resolved view on dense gas in the galaxy NGC 4321	94
7.1	NGC 4321 – the ideal target to study dense gas at resolved scales	95
7.2	Dense gas properties across morphological regions	96
7.3	Spatially resolved scaling relations	98
7.4	Low star formation efficiency in the bar	99
7.5	HCN/CO as a density-sensitive line ratio	101
7.6	Conclusions	101
8	Linking dense gas tracers from the Milky Way to external galaxies	103
8.1	LEGO observations of massive star-forming regions	105
8.2	Molecular line scaling relations	107
8.3	Dense gas tracers	110
8.4	Density-sensitive line ratios	112
8.5	Conclusions	114
9	Conclusions	115
10	Outlook and Open Questions	119
A	Stacking paper	125
B	ALMOND paper	135
C	NGC 4321 paper	184
D	Supplementary material	211
D.1	ALMOND: additional figures/tables	211
D.2	LEGO: additional figures/tables	216
	Bibliography	229
	List of Figures	238
	List of Tables	240

Introduction

“For what could be more beautiful than the heavens which contain all beautiful things.”

Nicolaus Copernicus – 16th century astronomer

Across this chapter, the main sources of information have been taken from the book *Physics of the Interstellar and Intergalactic Medium* by Bruce Draine (Draine, 2011), the lecture book *Notes on Star Formation* by Mark Krumholz (Krumholz, 2015), and the annual review article *Star Formation in the Milky Way and Nearby Galaxies* by Robert C. Kennicutt, Jr., and Neil J. Evans II (R. C. Kennicutt and N. J. Evans, 2012).

1.1 The big picture

1.1.1 Star formation

Star formation (SF) is one of the most fundamental processes in astrophysics affecting physics on all scales and timescales. Stars completely dominate the energy output in the universe and hence most physical processes are connected to star formation. In the early universe, the first stars initiated the epoch of reionisation making the universe transparent and observable. Once gravity took over, stars accumulated in the first galaxies, where they regulate the baryon lifecycle and evolution of their host galaxies. Inside galaxies, stars are created from the cold gas via gravitational collapse. Along with the protostar, the conservation of angular momentum yields the creation of planetary discs around the star from which planets can form. Stars are also the birthplaces of new elements and hence fundamentally affect the elemental composition of the interstellar medium (ISM). Eventually, all of the heavier elements beyond helium have been produced inside stars via nuclear fusion and supernova explosions, making stars the fundamental factories of the universe, facilitating the formation of complex molecules and essential to the creation of life.

1.1.2 Galaxies

In the early universe, after the formation of the first stars, dark matter dominated the formation of larger structures, eventually leading to the formation of the first galaxies and galaxy clusters. Galaxies are the

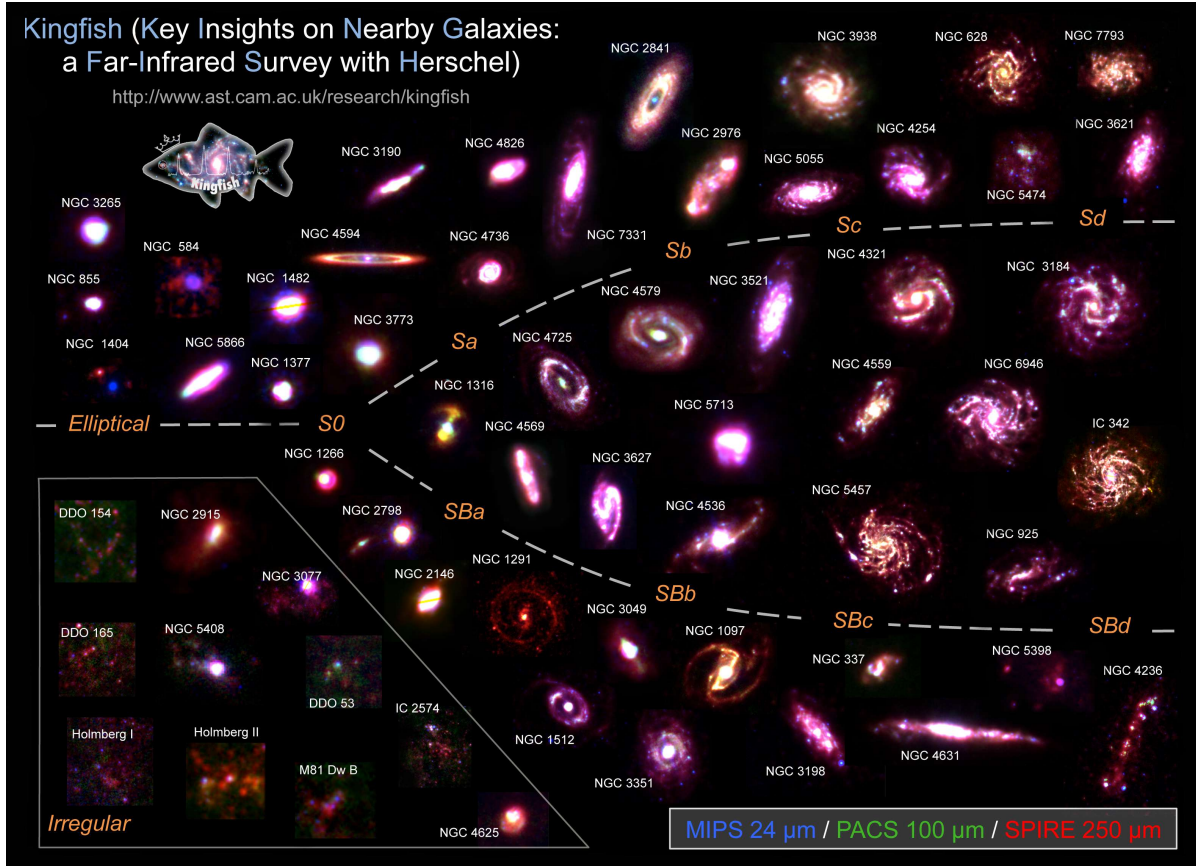


Figure 1.1: **Hubble tuning fork.** Hubble classification of galaxies visualised with multi-colour *Herschel* maps of nearby galaxies from the KINGFISH survey. Galaxy types are separated into elliptical, spiral (S) and irregular galaxies, where spiral galaxies split up into two branches according to the presence of a stellar bar (B). Image Credit: <https://research.ast.cam.ac.uk/kingfish>.

building blocks of the universe that come in different shapes and sizes. There are two main classes of galaxies – ellipticals and spirals. Elliptical galaxies are basically a big accumulation of older stars in a smooth disc and a big spherical bulge in the centre of the galaxy. Ellipticals are gas-poor, have little star formation and their old stellar populations let them appear reddish. Spiral galaxies are dominated by the ordered motion of stars around their galactic centre and show morphological features like bars and spiral arms. Spirals are typically gas-rich and the places of active star formation, giving them a much bluer appearance than ellipticals. According to the Hubble classification, the morphology of spiral galaxies can be separated into barred (SBa-d) and non-barred (Sa-d) galaxies, where the small letter indicates the winding degree of the spiral arms, increasing from a to d (Figure 1.1). There is also a revised, more detailed version of the Hubble classification, where galaxies with a straight bar are denoted with SAa-d and galaxies with a small or faint bar (i.e. intermediate spirals) are labelled with SABa-d. Moreover, elliptical galaxies can be split up into E0-7, where the number indicates the ellipticity of the galaxy.

The current cosmological model (i.e. Λ CDM) predicts that dark matter halos and hence galaxies merge progressively to form ever bigger galaxies. However, there is relatively little known about the formation of the first galaxies and recent James Webb Space Telescope (JWST) observations of apparently massive

Table 1.1: Phases of the interstellar medium

Phase	T_K [K]	n [cm ⁻³]	f_V	Tracers
HIM (hot ionised medium)	$\gtrsim 10^5$	~ 0.004	~ 0.5	UV, x-ray, radio synchrotron
HII regions	10^4	0.3 to 10^4	0.1	optical lines, radio free-free
WNM (warm neutral medium)	$\sim 5 \times 10^3$	0.6	0.4	HI 21-cm line, absorption lines
CNM (cold neutral medium)	~ 100	30	0.01	HI 21-cm line, absorption lines
Molecular clouds (H ₂)	10 to 50	10^2 to 10^6	0.001	CO, dust FIR, molecular lines

Notes – Conditions of the (galactic) ISM phases along with their temperature (T_K), hydrogen number density (n), volume filling factor (f_V) and how to observe them. Note that the list of tracers is by no means complete.

galaxies at redshifts $z > 10$ have challenged the current picture of a bottom-up scenario of galaxy growth. We know that galaxies at cosmic noon ($z \sim 2$) already show morphological features like spiral arms and bars that are comparable to the morphological types found in the nearby universe. Cosmic noon is also the time in the universe when the star formation rate density is the highest. However, it is not yet understood if star formation proceeds universally across the universe and across cosmic time.

Understanding the universe as a whole as well as in detail is certainly bound to understanding the formation and evolution of galaxies and their components. Molecular line studies show that gas accumulates in spiral arms, bars and centres and ultraviolet or infrared observations find that these are also the sites of active star formation. These are the first indications that star formation is tightly linked to the presence of gas in galaxies and understanding star formation requires the investigation of spiral, star-forming galaxies. In this thesis, we focus on studying gas and star formation in the Milky Way and nearby galaxies, which are the only accessible objects to investigate star formation at scales of molecular clouds.

1.2 The interstellar medium

1.2.1 Constituents and phases of the ISM

We refer to the ISM as everything between the stars in a galaxy, including dust, gas, magnetic fields, and cosmic rays. All of these components are well-mixed and interact with each other via various physical processes across a wide range of sizes and timescales, making the ISM extremely complex to study and analyse. A remarkable observation is that all of the constituents of the ISM have roughly the same energy density, demonstrating that physical processes are well-connected in galaxies. Nevertheless, the ISM comprises a wide range of physical conditions, spanning densities and kinetic temperatures from $n < 0.01 \text{ cm}^{-3}$ to $> 10^6 \text{ cm}^{-3}$ and $T_K \sim 10 \text{ K}$ to $> 10^5 \text{ K}$, respectively (Table 1.1).

In the MW, most of the volume is filled by a combination of the hot ionised medium (HIM) and warm neutral medium (WNM), which are hottest ($T_K \gtrsim 5 \times 10^3 \text{ K}$) and most diffuse ($n \lesssim 1 \text{ cm}^{-3}$) phases of the ISM. The neutral medium can be separated into two phases, likely the result of a thermal instability (Field et al., 1969) creating either warm gas around $T_K \sim 5 \times 10^3 \text{ K}$ (WNM) or cold gas around $T_K \sim 100 \text{ K}$, which is called the cold neutral medium (CNM). The coldest, densest phase of the ISM is in the form of molecular gas, often accumulated in molecular cloud (MC), with $n > 30 \text{ cm}^{-3}$ and



Figure 1.2: **Interstellar medium in the Carina nebula.** The above image shows the edge of a nearby, young, star-forming region (NGC 3324) in the Carina Nebula, observed by the JWST at near-infrared wavelength. Dust and gas (orange colours) are pushed away by the strong stellar radiation of the hot, massive, young stars at the top of the image and ionise the surrounding region (bluish glow). The image is a colour-composite produced from NIRCcam filters (red: F444W, orange: F335M, yellow: F470N, green: F200W, cyan: F187N, blue: F090W). Credit: NASA, ESA, CSA, STScI.

$T_K < 100$ K. Molecular clouds are of major concern for this thesis since they are the only plausible sites of star formation.

Figure 1.2 shows a nearby star-forming region in the Carina Nebula taken by the JWST, illustrating how molecular clouds are shaped by stellar feedback. In Section 1.3 we describe approaches of observing and characterising MCs in galaxies. When massive, young stars form in MCs, they ionise the surrounding medium, creating HII regions that are hot ($T_K \approx 10^4$ K) and span a wide range of densities ($n \sim 0.3$ to 10^4 cm $^{-3}$). These HII regions are physically connected to the sites of star formation and their bright optical recombination lines or free-free emission can be used to infer the star formation rate associated with the created HII region. In Section 1.4, we review the most common ways of measuring the star formation rate in the MW and nearby galaxies.

1.2.2 The baryon lifecycle and galaxy evolution

The lifecycle of matter in galaxies is mainly driven by radiation, gravity and magnetic fields, creating an ecosystem of mutual interactions. First and foremost, galaxies are not isolated objects but interact with the intergalactic medium, which can feed galaxies with new gas to trigger star formation, but also strip away gas, for example via close galaxy interactions or mergers, to stop star formation. Inside galaxies hot, diffuse gas can cool down via various cooling lines (e.g. [CI]) to form the CNM observable via H I 21 cm line emission at radio wavelength. Further cooling and condensation eventually lead to

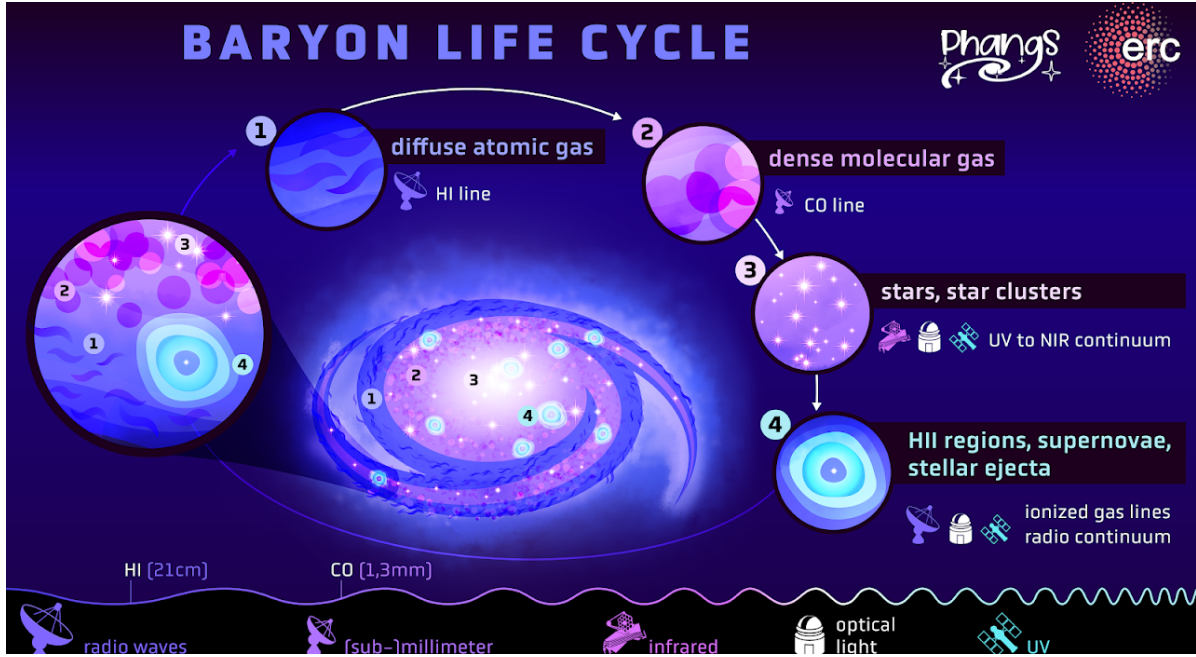


Figure 1.3: **Baryon lifecycle in galaxies.** The schematic illustrates the matter cycle in galaxies focusing on the CNM (1), which cools down to form dense molecular gas (2) from which stars form (3) that create HII regions and inject energy and matter back into the ISM (4) closing the baryon lifecycle. Image Credit: PHANGS/D. Leitner.

the formation of molecular clouds at the densest parts of the CNM, which can be traced via CO line emission at millimetre wavelength. Inside molecular clouds, gravitational collapse leads to the formation of dense clumps from which stars and stellar clusters can form. Recent star formation is observable at various wavelengths from ultraviolet (UV) to infrared (IR) wavelength. The newly formed young, massive stars inject high energy radiation into the ISM and ionise their surroundings creating HII regions, which shine at optical wavelength via hydrogen recombination lines as well as in radio continuum via free-free emission. After several 100 million years the massive stars undergo core-collapse supernovae and inject new elements and metals into the ISM, from which the next generation stars can be formed, hence restarting the cycle of barons.

After all, the baryon lifecycle sketched above is not everlasting since gas is converted into stars at a rate of a few solar masses per year for normal, spiral galaxies such as our own galaxy, the Milky Way. Eventually, gas is completely consumed and converted into stars if gas cannot be replenished at a high enough rate. Therefore, galaxies will eventually stop to form stars and become so-called quenched galaxies. The quenching of star formation might also be induced by other mechanisms such as active galactic nucleus (AGN) feedback (internal) or galaxy interactions (external). There is the idea that galaxies eventually start as star-forming galaxies, building up stellar mass till they eventually undergo a quenching phase to become quiescent galaxies that are rich in stars but do not form new stars any more. However, there is still limited knowledge of galaxy evolution. In particular, there key drivers of star formation quenching are poorly understood. To understand galaxy evolution and eventually solve the mystery of star formation quenching, we first have to understand how star formation works fundamentally in normal spiral galaxies. In this thesis, we focus on understanding how molecular gas, and in particular dense molecular gas, is converted into stars.

1.3 Observing the cold ISM

1.3.1 The problem of molecular hydrogen

The by far most abundant element in the universe is hydrogen, making up $\approx 75\%$ by mass. Helium, the second most abundant element makes up $\approx 25\%$ of the mass and all other species combined account for less than 1% . Hence, inferring the properties of the phases of the ISM comes down to measuring the properties of hydrogen in ionised (HIM), atomic (CNM), or molecular (MCs) form. In this work, we are mostly interested in studying the cold ISM. The CNM is relatively straightforward to observe via the H I 21 cm hyperfine transition¹. The 21 cm line is the result of a spin-flip of the hydrogen's electron, yielding a photon at 1.4 GHz frequency or 21 cm wavelength, observable with ground-based radio telescopes.

One might think that observing molecular gas is similarly straightforward by the most abundant molecule, that is, molecular hydrogen, H_2 . However, the problem of H_2 is that it is basically invisible at typical molecular cloud conditions. This is because even the lowest energetic transitions, (i.e. the rotational transition $J = 2 \rightarrow 0$) lie 510 K above the ground state. Hence, for typical MC gas temperatures of $T_K \sim 10$ to 50 K, this state is only exited for one in 10^{22} H_2 molecules (Krumholz, 2015). The reason for the high excitation temperature of the rotational transitions of H_2 is on the one hand, the symmetry of the molecule, which prohibits the lower energy $J = 1 \rightarrow 0$ transitions, and on the other hand, the low mass of H_2 molecule since the level spacing of a quantum rotor scales with reduced mass as $m^{-1/2}$. Therefore, even if H_2 was antisymmetric, the $J = 1$ state would lie at 175 K.

The invisibility of H_2 makes it necessary to find other ways to investigate the molecular gas. One approach is to observe other, abundant molecules that are easily excited in MCs, such as CO, the second most abundant molecule in the ISM (Section 1.3.3). Another possibility is to observe dust emission or absorption as an indicator of the molecular gas (Section 1.3.2).

1.3.2 Dust as a tracer of gas

Interstellar dust is always mixed with gas and thus provides a conceptually straightforward proxy of the gas mass. In fact, molecules can only efficiently form in the presence of dust, since they form on the surface of dust grains. In the ISM, dust is heated by the interstellar radiation field created by stars and re-emits thermal emission at infrared wavelength. This is the reason, why large parts of the MW disc are dark at optical wavelengths. The thermal dust emission can approximately be described as a blackbody radiator (with some modifications) with a temperature of $T_{\text{dust}} \sim 10$ to 50 K, such that most of dust emission can be observed at far-infrared (FIR) wavelength, requiring space observatories (Section 2.2.3).

Dust emission is an excellent tracer of the dust column density, since essentially all dust emission along the line of sight is observed, such that the total dust emission reflects the dust mass along the line of sight column. Note that this approximation is not fulfilled for many molecular lines, such as CO or HCN lines, which are often optically thick. In order to estimate the molecular gas column density (N_{mol}) from the dust mass (N_{dust}), we have to account for the dust-to-gas ratio (DGR):

$$\text{DGR} = \frac{N_{\text{dust}}}{N_{\text{mol}}} \quad (1.1)$$

¹ Interestingly, the H I 21 cm line is a forbidden line following the selection rules for energy transitions postulated by quantum mechanics. Therefore, the probability of spontaneous emission is extremely low. So low that it could never be observed in a laboratory within human timescales. Nevertheless, there are so many hydrogen atoms in the ISM and the excitation energy is so low that the H I 21 cm line is one of the brightest lines in the universe

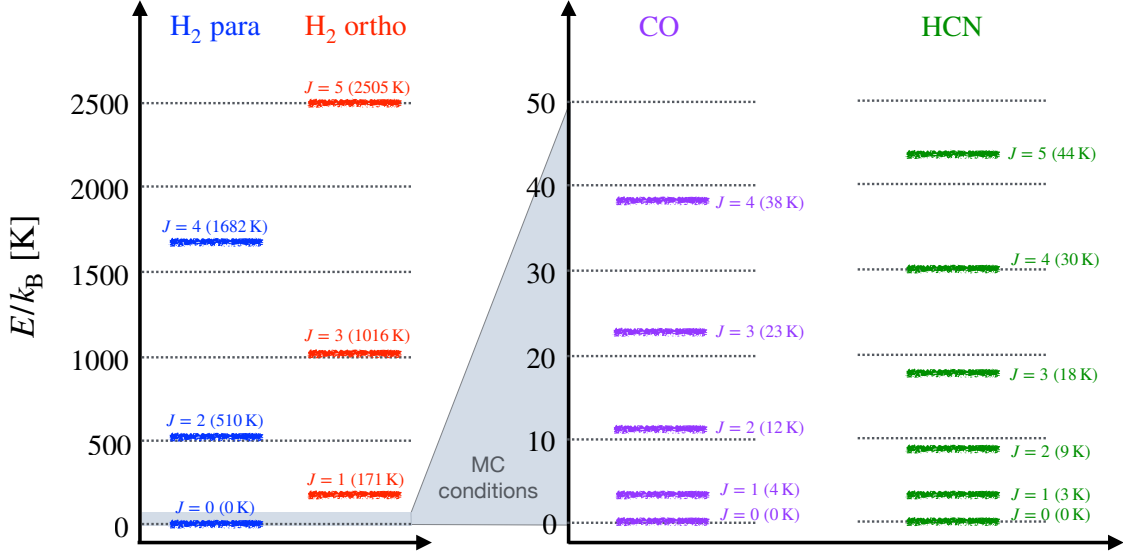


Figure 1.4: **Rotational transition diagram.** *Left:* Molecular hydrogen energy levels, separated between para- and ortho-rotational states. For a symmetric molecular like H₂, only transitions between mutual para- or ortho-states, respectively, are allowed. Therefore, the lowest energy transition of H₂ the $J = 2 \rightarrow 0$ transition at 510 K, which is basically never excited at typical molecular cloud conditions, where $T_K \lesssim 50$ K. *Right:* Rotational energy diagrams of CO and HCN, which lie at much lower energies compared to H₂. CO and HCN are asymmetric molecules. Therefore, transitions between all states are possible and the lowest energy transitions are at 3.8 K (CO ($1 - 0$)) and 3.0 K (HCN ($1 - 0$)). Values are taken from the Leiden Atomic and Molecular Database (LAMDA; Schöier et al., 2005).

which is typically on the order of 1-to-100 in the MW (Draine et al., 2007), but varies across and within galaxies². For instance, the DGR varies with metallicity and increases with the distance to the galactic centre, spanning $\gtrsim 1$ dex (Giannetti et al., 2017). Therefore, DGR variations are the main source of uncertainty in utilising dust as a tracer of molecular gas.

1.3.3 Molecular line emission

Most of our knowledge regarding ISM conditions and star formation arises from studying molecular line emission. Molecular lines are such powerful tools because they provide a wealth of information. Molecular lines are intimately connected to the physical conditions of the gas, such as density or temperature, but also trace the kinematics and chemistry. While being powerful tools in theory, molecular lines are often difficult to interpret in reality. Therefore, one of the key aims of ISM studies is to (a) better understand how molecular line emission is driven by the physical conditions, and (b) develop sophisticated recipes to convert the observed line emission into physical quantities.

First of all, we need to understand the basics of molecular line emission. A molecule can have three types of excitations: electronic, vibrational and rotational. All of these transitions have in common that the emitted photon of any given transition has an intrinsic, fixed energy and hence frequency (f) or

² There is some confusion across the literature, whether N_{mol} refers to the all molecular gas or just the hydrogen content, which differ by a factor of 1.4 (accounting for helium). Across this work, we consistently use the subscript “mol” to refer to all molecular gas and “H₂” to denote only molecular hydrogen, so that $N_{\text{mol}} = 1.4 N_{\text{H}_2}$ and similarly for all other measures concerning molecular gas.

wavelength (λ), which corresponds to the energy spacing between the upper and lower states: $E_{ul} = hf$, where h is the Planck constant. Electronic excitations are highest in energy ($\sim 1 \text{ eV} \sim 10^4 \text{ K} \sim 1 \mu\text{m}$). They arise from transitions of electrons within the molecule (or atom), which yields photons at optical wavelengths. Optical recombination lines (e.g. the Balmer lines of hydrogen, $H\alpha$, $H\beta$) are an example of electronic transitions (Section 1.4.4). Next are vibrational states, which are connected to vibrations between the atoms in the molecule, that can have different harmonic states, typically on the order of $\sim 10^{-1} \text{ eV} \sim 1000 \text{ K} \sim 10 \mu\text{m}$, thus emitting at infrared wavelengths. The lowest energy transitions are rotational transitions, which arise from rotational states of the molecule, commonly labelled with the quantum number J , so that the $J = 1 \rightarrow 0$ transition denotes a rotational transition from the first excited to the ground state. These transitions are key to studying the cold ISM since they are lowest in energy ($\sim 10^{-3} \text{ eV} \sim 10 \text{ K} \sim 1 \text{ mm}$) and hence easy to excite in typical CNM and MC environments. Molecular rotation lines mostly lie at radio and (sub)-millimetre wavelengths, which can be observed by ground-based telescopes (Section 2.2).

Though molecular lines, and emission lines in general, emit at a given frequency intrinsic to the transition, we do not observe line emission solely at its rest frequency. One reason is that the relative motion between the source and the observer results in a Doppler shift of the line's frequency (see Section 2.1.4). Moreover, the line profile is not simply a sharp peak but has a certain line shape driven by the intrinsic, natural line width and line broadening effects. The natural line width is a direct consequence of Heisenberg's uncertainty principle, which manifests in the energy uncertainties of the upper and lower energy states. Its line profile can be well approximated by a Lorentz profile. For this work, the natural line profile is never observed. Instead, line broadening effects dominate the line width, in particular Doppler broadening due to the turbulent motion of the gas. If the gas motion is purely thermal (i.e. the velocity distribution can be described by a Maxwell-Boltzmann distribution), the velocity dispersion of the gas is directly linked to the kinetic temperature of the gas as $\sigma_v \propto T^{1/2}$, where σ_v is the standard deviation of a Gaussian. Hence, under local thermodynamic equilibrium (LTE)³ conditions, the Doppler profile follows a Gaussian. Therefore, for most applications throughout this thesis, molecular lines can be well approximated by a Gaussian, or a superposition of a few Gaussians, reflecting multiple molecular clouds along the line of sight.

Critical density

Among the most commonly employed molecular lines are the low- J rotational transitions (i.e., $J = 1 \rightarrow 0$ and $J = 2 \rightarrow 1$) of the molecule carbon monoxide (CO). CO (hereafter we refer to the molecular species as a synonym of its transition) is the brightest molecular lines because (a) it is the second most abundant molecule after H_2 , (b) it has a low excitation temperature $\sim 10 \text{ K}$, and (c) it has a low critical density. The low critical density is a critical requirement that CO is observable at low gas densities $n \sim 10^3 \text{ cm}^{-3}$, making it the ideal tracer of the bulk of the molecular gas.

The critical density describes the threshold density of the gas that is needed to populate the upper energy level of a given transition. It is fundamentally connected to the rate for spontaneous emission, A_{ul} , and the collisional rates among collision partners (i.e. molecules, primary H_2 , in the molecular gas phase). Note that the excitation of rotational transitions in the ISM is completely dominated by collisions between molecules, as opposed to radiative excitation. We can easily derive the critical density for a

³ LTE implies that all physical processes are in thermodynamic equilibrium. In particular, this means that the kinetic and excitation temperatures are equal, which is only fulfilled at sufficiently high gas densities.

two-level system. In LTE, the level population is given by the Maxwell-Boltzmann distribution:

$$\frac{n_u}{n_l} = e^{-\frac{E_{ul}}{k_B T_{\text{ex}}}}, \quad (1.2)$$

where T_{ex} is the excitation temperature of the transition. In this example, we assume LTE so that $T_{\text{ex}} = T_K$, but in general excitation and kinetic temperature can be different. For astronomical observations, the most relevant process is the spontaneous radiative transition from the upper to the lower state. Taking into account the rate for spontaneous emission, collisional excitation and de-excitation, we can derive a formula for the equilibrium case, where $dn_u/dt = 0$:

$$\frac{dn_u}{dt} = -A_{ul}n_u + C_{lu}n_l n - C_{ul}n_u n = 0 \quad (1.3)$$

The above equation yields:

$$\frac{n_u}{n_l} = \frac{C_{lu}n}{A_{ul} + C_{ul}n} = \frac{e^{-\frac{E_{ul}}{k_B T_{\text{ex}}}}}{1 + A_{ul}/(C_{ul}n)}. \quad (1.4)$$

The second step assumes that collisions occur frequently (i.e. collisions dominate over spontaneous emission) such that C_{lu} and C_{ul} are related via the Boltzmann factor (right-hand-side of Equation (1.2)).

Equation (1.4) has a few interesting implications for the level population of the two-level system. If collisions dominate over spontaneous emission ($A_{ul} \ll C_{ul}n$), the level population is simply given by the Maxwell-Boltzmann distribution (Equation (1.2)). On the contrary, if collisions are rare compared to spontaneous emission ($A_{ul} \gg C_{ul}n$), the level population approaches zero: $n_u/n_l \rightarrow 0$. This means, that at low gas densities collisions can not sufficiently populate the upper energy level, while at high gas densities, the level population is completely in equilibrium with the gas and collisions dominate the de-excitation making spontaneous emission less emission. The threshold density between the two extremes, where both processes occur at the same rate, is defined as the critical density:

$$n_{\text{crit}} = \frac{A_{ul}}{C_{ul}} \quad (1.5)$$

For gas densities around n_{crit} , collisions are sufficiently frequent to populate the upper energy level and allow efficient emission via spontaneous emission. Practically, this means that emission from a certain molecular transition can only be observed if the gas density is close to or exceeds the critical density of that transition. We can leverage this intrinsic property of molecular lines to trace gas at different gas densities by observing molecular lines with different critical densities.

Table D.2 lists properties of some relevant molecular lines in the 3 mm window, including the energy of the upper state (E_u), the Einstein coefficient for spontaneous emission (A_{ul}), the collisional de-excitation rate (C_{ul}), and critical density (n_{crit}). We can see CO has a low critical density of $n_{\text{crit}} = 5.7 \times 10^2 \text{ cm}^{-3}$ and HCN has a much higher critical density of $n_{\text{crit}} = 3.0 \times 10^5 \text{ cm}^{-3}$. This suggests that CO can be used to trace the bulk molecular gas while HCN is a tracer of denser gas, which is exactly how these lines have been utilised in ISM studies. However, in practice, it is not that simple. On the one hand, converting line intensities of CO or HCN into physical quantities, such as molecular gas masses, is far from trivial. Moreover, the theoretical critical density derived above is only a rough indication of the actual, effective critical density of a given line, that can be impacted by various effects, including gas

temperature, astrochemistry, optical depth, or radiative trapping.

Therefore, I. Evans N. J. (1999) proposed an alternative definition of an empirically based critical density, called the effective excitation density (n_{eff}). It is defined as the density where a line reaches an intensity of 1 K km s^{-1} and hence naturally includes effects such as optical depth and radiative trapping. We listed the effective excitation densities, n_{eff} , for some of the lines in Table D.2, based on the study by Shirley (2015), who particular investigated the effective excitation densities of dense gas tracers. They show that HCN most likely traces lower gas densities ($n_{\text{eff}} = 4.5 \times 10^3 \text{ cm}^{-3}$) as previously assumed based on n_{crit} . However, it is still not well understood how physical conditions drive the excitation of certain dense gas tracers. The in-depth investigation of the emissivity of dense gas tracers such as HCN or HCO^+ is one of the key aims of this thesis (Section 1.6).

Conversion factors

In Section 1.3.3, we have introduced the concept of the critical density and the effective excitation density, suggesting that certain emission lines should be suitable tracers of gas above their critical or effective excitation densities. For instance, CO is proposed as a tracer of the bulk molecular gas due to its low critical density. However, molecular lines can be optically thick, so that not all emitted photons can be observed as for optically thin emission. This raises the question of how reliably CO and other molecular lines can be used to measure physical quantities of the molecular gas, such as the surface density or mass of molecular clouds. For optically thick lines, such as CO, only emission from the surface of the cloud can be observed.

In other words: How can we tell anything about the depth of a building by only observing its wall? The answer is twofold and has to do with the physical properties of molecular clouds as well as the richness of information contained in molecular line emission. Molecular clouds can approximately be described as virialised objects, meaning that their kinetic energy is linked to the gravitational energy, or in other words, the velocity dispersion of the gas scales with the mass of the cloud. Therefore, more massive clouds typically show higher velocity dispersion. Fortunately, molecular line emission does not only reflect the peak intensity, but also the velocity dispersion via the Doppler broadening of the line and hence the total emission of the line is a solid measure of the total mass of the cloud. It can be shown that for virialised clouds the integrated intensity of a molecular line is proportional to the surface density of molecular gas, motivation a simple CO-to- H_2 conversion factor:

$$\alpha_{\text{CO}} = \frac{\Sigma_{\text{mol}}}{W_{\text{CO}}} = \frac{M_{\text{mol}}}{L_{\text{CO}}} . \quad (1.6)$$

The basic idea of α_{CO} is that all of the radiative transfer effects are merged into one factor that is calibrated from observations. Galactic measurements of gamma rays and dust infrared emission have been employed to calibrate α_{CO} yielding a MW-average consistent with $\alpha_{\text{CO}} = 4.35 M_{\odot} \text{ pc}^{-2} (\text{K km s}^{-1})^{-1}$ within a factor of two (Bolatto et al., 2013). However, these values only apply to MW conditions and α_{CO} is not constant but varies by at least 1 dex within and between galaxies. For instance, starburst galaxies have a factor of ~ 3 lower α_{CO} than normal spiral galaxies. Within galaxies α_{CO} varies with metallicity (Z) and total surface density (Σ_{tot}), such that α_{CO} decreases with metallicity and total surface density (review by Bolatto et al., 2013). Locally, α_{CO} shows variations with the gas temperature and molecular cloud surface density (Σ_{mol}). Teng, Sandstrom, Sun, Gong et al. (2023) measured α_{CO} in normal spiral galaxies finding a tight relation between α_{CO} and the optical depth of CO as well as the velocity dispersion of

CO at ~ 100 pc scales (i.e. GMCs scales), suggesting that α_{CO} is lower in clouds with larger velocity dispersion as a consequence of increased optical depth of the CO line. As a rule of thumb, for normal spiral galaxies, α_{CO} decreases towards the centres of galaxies, where it is typically a factor of 3 to 10 lower compared to the discs. We will discuss the effect of α_{CO} variations on the interpretation of our results in the respective dense gas projects (Sections 5, 6, 7).

Similar to α_{CO} , we can define a HCN-to-dense gas conversion factor, assuming that HCN traces gas above a certain density (e.g. $n_{\text{H}_2}^{\text{dense}} \approx 10^4 \text{ cm}^{-3}$):

$$\alpha_{\text{HCN}} = \frac{\Sigma_{\text{dense}}}{W_{\text{HCN}}} = \frac{M_{\text{dense}}}{L_{\text{HCN}}} \quad (1.7)$$

On whole galaxy scales, (Gao and Solomon, 2004) proposed a value of $\alpha_{\text{HCN}} = 10 M_{\odot} \text{ pc}^{-2} (\text{K km s}^{-1})^{-1}$, which has been established as the fiducial value across the dense gas literature over the past 20 years. In a theoretical work, Onus et al. (2018) predicted a slightly higher $\alpha_{\text{HCN}} = 14 M_{\odot} \text{ pc}^{-2} (\text{K km s}^{-1})^{-1}$, assuming that HCN traces gas above a density of $n_{\text{H}_2}^{\text{dense}} = 10^4 \text{ cm}^{-3}$. Galactic measurements usually yield higher values ($\alpha_{\text{HCN}} > 20 M_{\odot} \text{ pc}^{-2} (\text{K km s}^{-1})^{-1}$), which indicates that HCN is not only emitted in the dense clumps of molecular clouds (e.g. I. Evans N. J., K.-T. Kim et al., 2020). Studies of the HCN emissivity in MW clouds indicate that HCN is not a robust tracer of dense gas alone, but can also be efficiently emitted at lower gas densities ($n < 10^4 \text{ cm}^{-3}$) and that α_{HCN} can vary from $\alpha_{\text{HCN}} = 0.3$ to $300 M_{\odot} \text{ pc}^{-2} (\text{K km s}^{-1})^{-1}$ from kiloparsec-scale extragalactic to parsec-scale galactic studies (García-Burillo et al., 2012; Pety et al., 2017; Kauffmann, Goldsmith et al., 2017; Shimajiri et al., 2017; Nguyen-Luong et al., 2020; I. Evans N. J., K.-T. Kim et al., 2020; Barnes, Kauffmann et al., 2020). The current status of the literature does not allow a clear statement of how well HCN can be used to measure a dense gas mass, especially if a constant α_{HCN} is assumed. Certainly, α_{HCN} variations with local conditions are much less investigated and understood as the CO analogue. On the one hand, this motivates further studies of α_{HCN} variations across the MW and other galaxies to develop more sophisticated conversion recipes. On the other hand, currently, a reasonable approach is to use a constant α_{HCN} while pointing out and discussing the caveats of a constant α_{HCN} . Recently, Schinnerer and A. K. Leroy (2024) used a value of $\alpha_{\text{HCN}} = 15 M_{\odot} \text{ pc}^{-2} (\text{K km s}^{-1})^{-1}$ in nearby galaxy studies as an empirical average across the aforementioned literature, which is the value adopted in one of the projects of this thesis.

1.4 Tracing star formation

One of the central aims of this thesis is the investigation of star formation in galaxies, where the key physical quantity is the star formation rate (SFR). Therefore, inferring the SFR from observations is one of the fundamental methods of this work. As stars form and evolve on timescales much longer than human lifespans, we have to be clever to derive the SFR from observations that are just snapshots of stellar evolution. The basic idea is to observe young stars, this means, stars that have formed over the past ~ 100 Myr. Fortunately, the lifetime of stars depends strongly on their mass ($\tau_{\star} \propto M_{\star}^{-2}$), so that massive stars ($M_{\star} \gtrsim 10 M_{\odot}$) are always short-lived ($\tau_{\star} \lesssim 100$ Myr). Massive stars can be observed directly (via counting stars or measuring ultraviolet emission) or indirectly. Observations of massive stars provide a measure of the SFR of massive stars, which is however only a small fraction of the total SFR since massive stars only make up $\lesssim 1\%$ of the total stellar mass. This means, we have to extrapolate

from the massive stars to all stars adopting an initial mass function (IMF), which accounts for the mass distribution of newly formed stars. There exist several, empirical IMF versions (e.g. Salpeter, 1955; Kroupa, 2001; Chabrier, 2003), that yield similar results. The basic approach of all SFR calibrations is to observe young, massive stars, which are then converted into a SFR assuming a physical mechanism that links the tracer to young stars, often supported by theoretical models (e.g. Starburst99, Leitherer et al., 1999), and a preferred IMF. All calibrations listed below are based on a Kroupa IMF and the Starburst99 model following R. C. Kennicutt and N. J. Evans (2012). The crucial thing to keep in mind is that we can only expect to measure the SFR as long as we believe it to be constant on timescales that are long compared to the timescales of the observed tracers.

1.4.1 Counting young stellar objects (YSOs)

The most straightforward way of observing young, massive stars is simply to count young stellar objects (YSOs). Assuming that the YSOs sample the IMF reasonably well, the SFR can be inferred from the average mass of the YSOs and their IR excess duration. The big drawback with this approach is that it can only be applied for very nearby regions ($\lesssim 1$ kpc) since counting stars requires resolving individual stars. Therefore, this method only applies to the nearby regions in the MW but is irrelevant for extragalactic studies. For more distant targets, we rely on unresolved observations of young stars and their direct (UV) or processed (lines, free-free, IR) emission.

1.4.2 Ultraviolet emission from young stars

Stars emit as almost perfect blackbody radiators so that their spectra are well described by the Planck function, whose shape is determined by the (surface) temperature of the star. The surface temperature (T_{eff}) of (main-sequence) stars approximately depends on their mass as $T_{\text{eff}} \propto M_{\star}^{0.6}$. This means that UV emission can only be emitted by young, massive, hot stars, such that $> 99\%$ of the UV luminosity will be dominated by stars with $M_{\star} > 10 M_{\odot}$. Therefore, observing UV emission directly traces young stars with lifetimes less than, hence providing an excellent direct tracer of the SFR.

A technical downside of utilising UV emission is the need for space observatories since Earth's atmosphere is opaque at UV wavelength. This challenge has been overcome by the *GALEX* spacecraft (C. L. Martin, 2005, also see Section 2.2.3), which surveyed the whole sky at far-UV (FUV; 155 nm) and near-UV (NUV; 230 nm) bands, yielding a census of star formation across the nearby galaxy population. The FUV band is sensitive to stars younger than 100 Myr with an average age of 10 Myr. It can be converted into a SFR via a linear relations (Murphy et al., 2011; Hao et al., 2011):

$$\left(\frac{\text{SFR}}{M_{\odot} \text{ yr}^{-1}} \right) = 4.42 \times 10^{-44} \left(\frac{L_{\text{FUV}}}{\text{erg s}^{-1}} \right). \quad (1.8)$$

The biggest disadvantage of a UV-based SFR calibrator is its significant sensitivity to dust attenuation. This becomes particularly severe for dusty galaxies or towards galaxy centres, where UV emission can be almost completely absorbed by interstellar dust.

1.4.3 Infrared emission from heated dust

The absorption of stellar light by dust leads to heating of the dust grains, which will re-emit thermal emission at IR wavelength. The dust-processed starlight traces similar stellar ages (i.e. < 100 Myr) than

at FUV wavelength. This is because the dust heating is dominated by very massive, young stars so that the IR emission is approximately proportional to the UV emission and hence the SFR (Murphy et al., 2011; Hao et al., 2011):

$$\left(\frac{\text{SFR}}{M_{\odot} \text{ yr}^{-1}} \right) = 3.88 \times 10^{-44} \left(\frac{L_{\text{IR}}}{\text{erg s}^{-1}} \right). \quad (1.9)$$

The above equation assumes that the infrared luminosity (L_{IR}) includes all emission between $3 \mu\text{m}$ and $100 \mu\text{m}$, which has the advantage of covering the whole dust-enshrouded stellar population. However, this wavelength coverage is not available for most galaxies. Instead, IR space observatories like *Spitzer*, *Herschel*, *WISE*, and *JWST* observe in certain IR bands, e.g. at $\sim 20 \mu\text{m}$. Therefore, special SFR calibrations that are specific to the IR bands of certain instruments have been developed (e.g. A. K. Leroy, Sandstrom et al., 2019; Belfiore, A. K. Leroy, Williams et al., 2023). In this thesis, we utilise $24 \mu\text{m}$ emission (WISE4) from *WISE* and $21 \mu\text{m}$ emission (F2100W) from *JWST* as tracers of the SFR.

One of the big caveats of IR-based SFR calibrations is that only embedded star formation is traced, while unobscured star formation is not detected. Moreover, dust emission can be contaminated by sources that are not associated with recent star formation, for example AGN in galaxy centres. Furthermore, it has been found that shorter IR wavelengths trace more compact sources associated with HII regions, while longer IR wavelengths trace the more diffuse part of the dust.

1.4.4 Recombination lines from ionised gas

The most applicable way of observing star formation with ground-based telescopes is via optical recombination lines. Young stars ionise their surrounding environment creating HII regions, where hydrogen is completely ionised. In these regions, hydrogen eventually recombines and produces recombination lines. Some of the brightest recombination lines are visible at optical wavelength, in particular the $\text{H}\alpha$ line at 656.3 nm which is the brightest line of the Balmer series. Since the ionisation of hydrogen atoms and the subsequent recombination line luminosity is approximately proportional to the luminosity of young stars, we can employ the $\text{H}\alpha$ luminosity to infer the (Murphy et al., 2011; Hao et al., 2011):

$$\left(\frac{\text{SFR}}{M_{\odot} \text{ yr}^{-1}} \right) = 5.37 \times 10^{-42} \left(\frac{L_{\text{H}\alpha}}{\text{erg s}^{-1}} \right). \quad (1.10)$$

One of the key differences to the aforementioned tracers (UV and IR) is that $\text{H}\alpha$ traces significantly younger stars with ages $< 10 \text{ Myr}$ and 3 Myr on average.

Similar to UV wavelength, dust also absorbs optical wavelength and hence $\text{H}\alpha$ emission can be highly obscured in dense, dusty regions, which is one of the biggest caveats of $\text{H}\alpha$ as a tracer. However, there are ways to correct for the dust extinction by utilising the $\text{H}\beta$ line at 486.1 nm . Since extinction is wavelength dependent, $\text{H}\alpha$ and $\text{H}\beta$ are differently affected by extinction, which can be used to measure and correct for the extinction via the Balmer-decrement. This way, the corrected $\text{H}\alpha$ luminosity should trace the even in dust-obscured regions. Note, however, that the Balmer-decrement is, on the one hand, limited to the significance of the less bright $\text{H}\beta$ line, and, on the other hand, known to break down in extremely dusty regions, for example, the MW plane or galaxy centres. The big advantage with optical recombination lines is the high angular resolution of ground-based optical telescopes such as the

VLT, providing the highest angular resolution view on star formation. In this work, we make use of the high angular resolution $H\alpha$ observation from VLT–MUSE, to trace star formation in the nearby galaxy NGC 4321.

1.4.5 Free-free emission

The free electrons in HII regions do not only recombine with hydrogen ions but also scatter off ions, hence producing free-free emission (or Bremsstrahlung) that is observable as radio continuum emission. We expect that the free-free emission is proportional to the rate of ionising photons, which is again proportional to the SFR . Murphy et al. (2011) presented a $L_{1.4\text{ GHz}}$ -calibration using the 1.4 GHz radio continuum:

$$\left(\frac{SFR}{M_{\odot} \text{ yr}^{-1}} \right) = 6.35 \times 10^{-29} \left(\frac{L_{1.4\text{ GHz}}}{\text{erg s}^{-1} \text{ Hz}^{-1}} \right) \quad (1.11)$$

by benchmarking against IR calibration shown in Equation (1.9). However, the radio continuum is not only composed of (thermal) free-free emission but also contains (non-thermal) synchrotron emission associated with supernovae. Therefore, Murphy et al. (2011) also derive more refined recipes to derive the SFR from the radio continuum.

Similar to optical recombination lines or UV emission, the radio continuum is also subject to dust extinction, though not as strongly affected as optical or UV wavelength. In this work, we employ this refined prescription to measure the SFR in the centre of NGC 4321 using 33 GHz from the VLA and compare it with $H\alpha$ - and IR-based estimates.

1.4.6 Combined calibrators

The above listed tracers show that star formation is linked to various physical processes and emission across almost the full electromagnetic spectrum. However, the tracers are not identical, can trace different timescales and have different caveats. For example, IR tracers require dust in the vicinity of newly formed stars, while other tracers (e.g. UV or $H\alpha$) are absorbed by dust. Therefore, it can be useful to combine different tracers to mitigate the drawbacks of each individual tracer. For instance, A. K. Leroy, Sandstrom et al. (2019) use a linear combination of FUV and IR bands:

$$SFR = C_{UV} L_{UV} + C_{IR} L_{IR} \quad (1.12)$$

This combined estimation leverages the ability of FUV to trace unobscured and IR to trace obscured star formation, and has become a standard recipe for maps of nearby galaxies. The constants C_{UV} and C_{IR} are dependent on the exact wavelength bands and can vary per galaxy. We adopt the methodology of A. K. Leroy, Sandstrom et al. (2019) in two of the projects of this thesis to measure the SFR across nearby galaxies at kiloparsec scales. We note that there are other possible combinations, such as combining $H\alpha$ and IR, which provides the advantage of higher angular resolution with current optical (e.g. VLT) and new IR (JWST) observatories (Belfiore, A. K. Leroy, Sun et al., 2023).

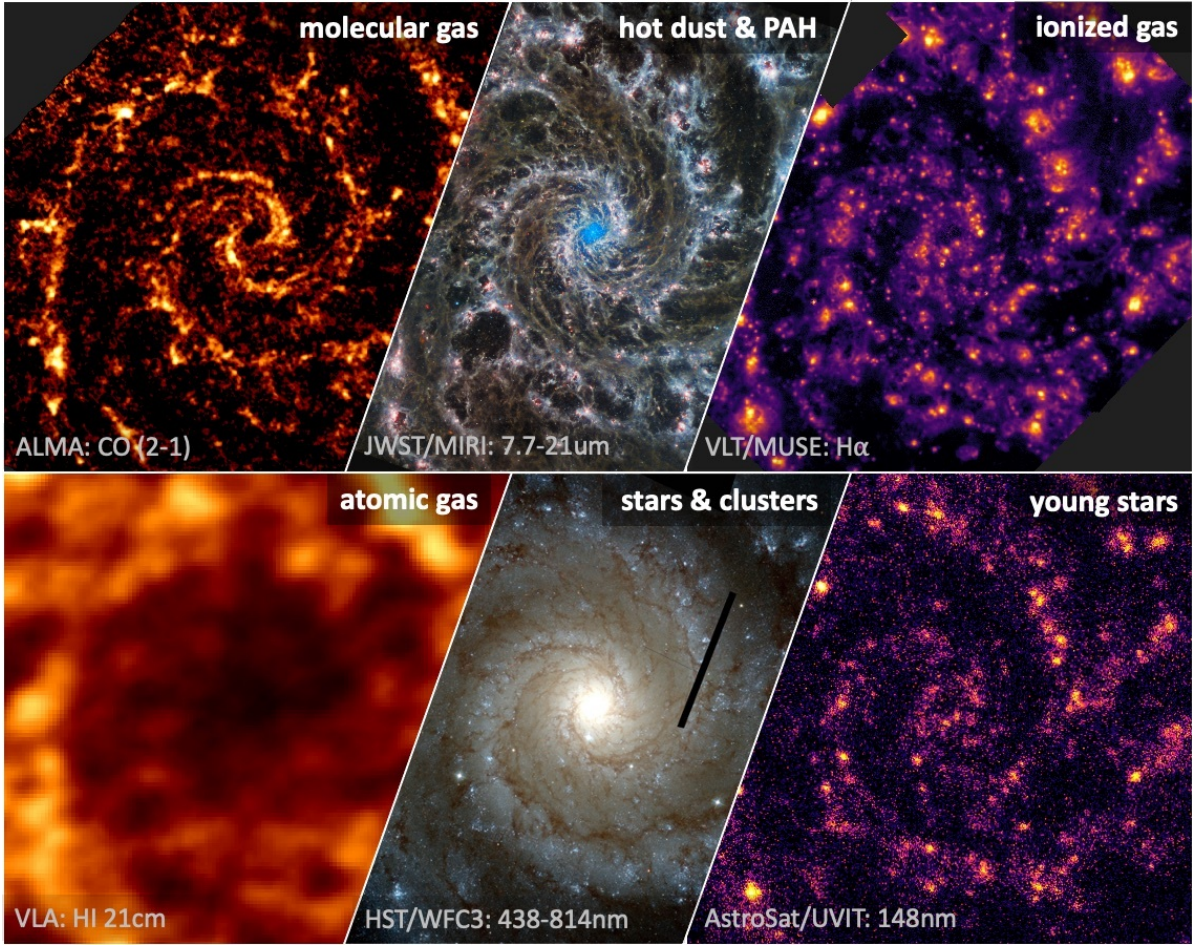


Figure 1.5: **NGC 628 across the electromagnetic spectrum.** Images of the galaxy NGC 628/M74 showing, from top left to bottom right, the molecular gas traced by CO (2 – 1) (PHANGS–ALMA; A. K. Leroy, Schinnerer et al., 2021), hot dust and PAH traced by MIRI 7.7 to 21 μm (PHANGS–JWST; Lee, Sandstrom et al., 2023), ionised gas, an indicator of star formation, traced by $\text{H}\alpha$ line emission (PHANGS–MUSE; Emsellem et al., 2022), atomic gas traced by HI 21 cm line emission (THINGS; Walter et al., 2008), stars and stellar clusters traced by optical wideband filter emission (PHANGS–HST; Lee, Whitmore et al., 2022), and young, massive stars traced by far-UV emission (PHANGS–AstroSat; Hassani et al., 2024). Image Credit: PHANGS/J. Sun.

1.5 Empirical star formation scaling relations

Figure 1.5 shows a multi-wavelength view of the nearby spiral galaxy NGC 628. The different wavelengths trace different physical processes and phases of the ISM, such as the atomic, molecular and ionised gas, dust as well as star formation. Comparing the different images it becomes obvious that the SFR (traced by $\text{H}\alpha$ emission) is spatially well correlated with the presence of molecular gas (traced by CO emission). This excellent correlation between molecular gas and star formation is not only seen for this specific galaxy but across the whole population of star-forming galaxies from entire galaxy measurements to resolved observations within galaxies. These findings proposed that the presence of gas is a good predictor of the star formation rate in galaxies, which raises the fundamental science question of whether there is a universal star formation law in the universe.

1.5.1 Kennicutt-Schmidt relation

Empirically, the relation between gas surface density and tracers of SFR has been well studied over the past few decades from the local to the high redshift universe, finding a tight relation between the surface density of gas and SFR. The basic idea that gas is the key ingredient to regulate SFR goes back to 1959, when Schmidt (1959) proposed a super-linear power law behaviour between the SFR and gas surface density:

$$\Sigma_{\text{gas}} \propto \Sigma_{\text{SFR}}^N \quad (1.13)$$

Four decades later, integrated galaxy observations by J. Kennicutt R. C. (1998) supported the super-linear power law relation, finding a power law index of $N = 1.4$ and coining Equation (1.13) the Kennicutt-Schmidt (KS) relation (sometimes also called KS law, Figure 1.6). The seminal works by Schmidt (1959) and J. Kennicutt R. C. (1998) motivated a whole field of radio astronomy to better understand the physical connection between gas and star formation across the universe, making use of the technological advances to observe the molecular ISM with new radio telescopes such as the Institut de Radioastronomie Millimétrique (IRAM) 30 m telescope or the Atacama Large Millimeter/submillimeter Array (ALMA) (Section 2.2).

The original relation compared the SFR surface density (Σ_{SFR}) with the total gas surface density (Σ_{gas}), which includes both the atomic (Σ_{atom}) and the molecular gas phase (Σ_{mol}). Bigiel, A. Leroy et al. (2008) took a novel step to separate these two gas phases using resolved measurements from nearby galaxies to show that only the molecular gas is tightly correlated with SFR, while the atomic gas surface density appears almost uncorrelated with SFR (Figure 1.6, right panel). They find that in their sample of normal spiral galaxies, Σ_{SFR} is linearly related with Σ_{mol} (i.e. $N \approx 1$ in Equation (1.13)), indicating that molecular gas might be the key ingredient to regulate star formation in galaxies with a fixed $\Sigma_{\text{SFR}}/\Sigma_{\text{mol}}$ ratio.

The inverse ratio (i.e. $\Sigma_{\text{mol}}/\Sigma_{\text{SFR}}$) is often referred to as the (molecular gas) depletion time:

$$\tau_{\text{dep}}^{\text{mol}} = \frac{M_{\text{mol}}}{\text{SFR}}, \quad (1.14)$$

and describes how long it would take to consume the molecular gas reservoir given the current SFR, where timescales obtained from the KS relation yield $\tau_{\text{dep}}^{\text{mol}} \sim 2 \text{ Gyr}$, which is more than 10 % of the age of the universe. In empirical studies, the star formation efficiency of molecular gas is often defined as:

$$\text{SFE}_{\text{mol}} = \frac{\text{SFR}}{M_{\text{mol}}}, \quad (1.15)$$

so that $\text{SFE}_{\text{mol}} = 1/\tau_{\text{dep}}^{\text{mol}}$. In words, SFE_{mol} measures how many stars are formed per unit time per unit molecular gas mass. Assuming that the observed SFR and M_{mol} are physically related, SFE_{mol} describes the efficiency with which molecular gas is converted into stars. However, SFE_{mol} does not measure the star formation efficiency in the sense of the fraction of gas that is converted into stars. This is because SFE_{mol} does not take into account the timescale of the star formation process, i.e the time it takes to turn molecular gas into stars, which also manifests in the fact that SFE_{mol} has dimensions of yr^{-1} . Assuming that stars form from self-gravitating gas that collapses under its own gravity, this timescale is given by

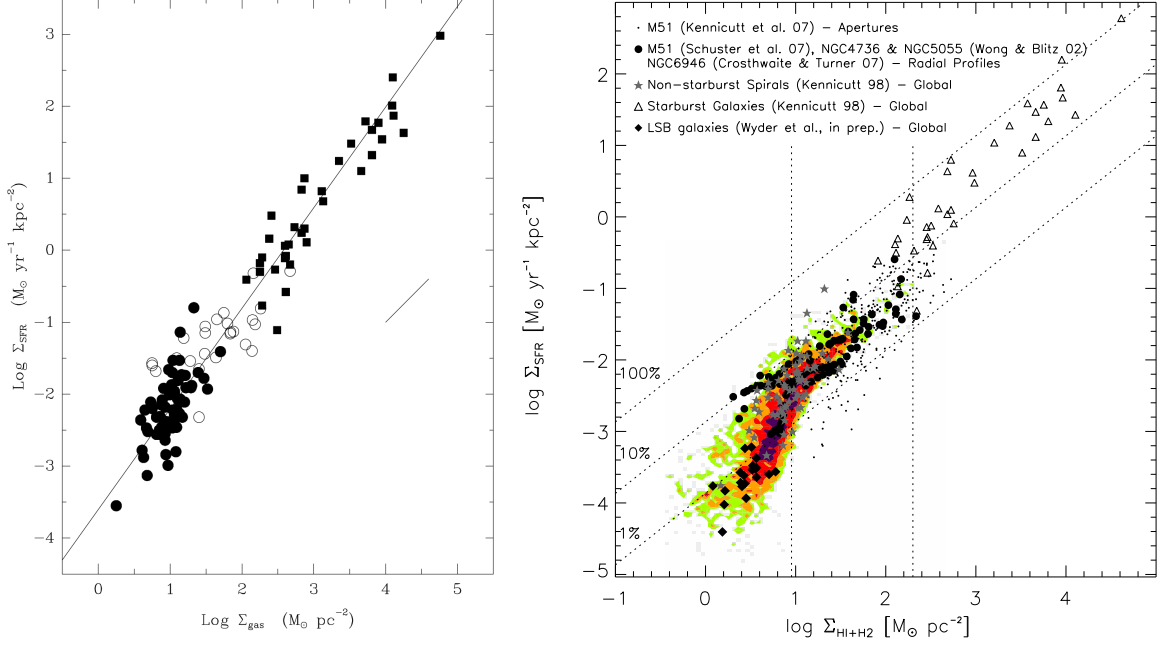


Figure 1.6: **Kennicutt-Schmidt relation.** *Left:* SFR surface density (Σ_{SFR}) against total gas surface density (Σ_{gas}) of global measurements across 61 normal spiral (circles) and 36 starburst galaxies (squares). The black line is a fit to the data with slope 1.4. The figure is reproduced from J. Kennicutt R. C. (1998). *Right:* The same relation as in the left panel, but additionally showing resolved, sub-kiloparsec scale measurements from M51 (small points) and 18 nearby galaxies (coloured contours). The dotted diagonal lines indicate constant gas star formation efficiencies. The dotted vertical lines at $\Sigma_{\text{gas}} = 9 M_{\odot} \text{pc}^{-2}$ and $\Sigma_{\text{gas}} = 200 M_{\odot} \text{pc}^{-2}$ mark different regimes (see text). The figure is reproduced from Bigiel, A. Leroy et al. (2008).

the free-fall time:

$$t_{\text{ff}} = \sqrt{\frac{3\pi}{32G\rho}} = 4.4 \left(\frac{n}{100 \text{ cm}^{-3}} \right)^{-0.5} \text{ Myr} \quad (1.16)$$

where G is the gravitational constant, ρ is the gas density, and n is the H_2 number density. For molecular gas with average density $n \sim 10^2 \text{ cm}^{-3}$, the mass-weighted free-fall time is on the order of $t_{\text{ff}}^{\text{mol}} \sim 10 \text{ Myr}$. The resulting star formation efficiency per free-fall time is defined as:

$$\epsilon_{\text{ff}}^{\text{mol}} = \text{SFE}_{\text{mol}} \cdot t_{\text{ff}}^{\text{mol}}, \quad (1.17)$$

and measures how much of the molecular gas is converted into stars per free-fall time, giving a dimensionless quantity. For normal spiral galaxies, $\epsilon_{\text{ff}}^{\text{mol}}$ is on the order of $\sim 0.5 \%$, demonstrating that molecular clouds are very inefficiently producing stars. The low star formation efficiency was one of the big mysteries of astronomy, which has nowadays been solved, also thanks to theoretical works (e.g. Krumholz and McKee, 2005), proposing that molecular clouds are extremely turbulent objects that are possibly driven by stellar feedback, regulating star formation and causing low star formation efficiencies.

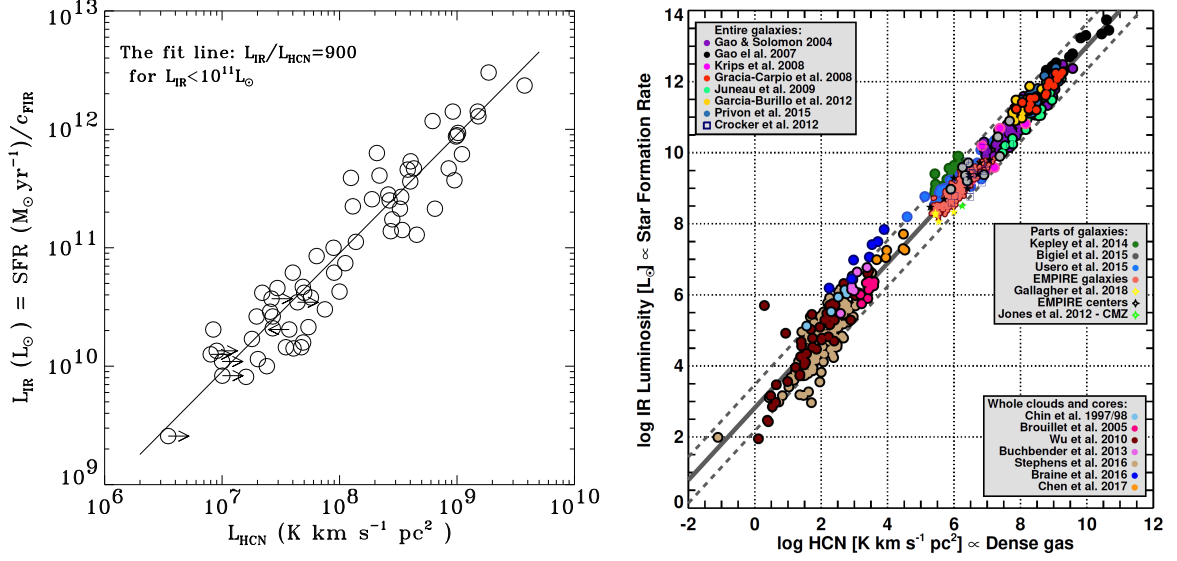


Figure 1.7: **Gao-Solomon relation.** *Left:* IR luminosity, a proxy of SFR, against the HCN (1 – 0) luminosity, a proxy of the dense gas mass across global measurements of 34 normal spiral and 22 luminous infrared galaxies (LIRGs). The figure is taken from Gao and Solomon (2004). *Right:* Literature compilation of HCN studies including local MW clouds, resolved measurements in nearby galaxies and integrated entire galaxy observations. The figure is reproduced from Jiménez-Donaire, Bigiel, A. K. Leroy, Usero et al. (2019).

1.5.2 Gao-Solomon relation

The molecular gas works presented in Section 1.5.1 suggest that molecular gas is tightly connected to the star formation rate. However, there is a wide range of star formation efficiencies, especially between normal spiral and starburst galaxies. This means that molecular gas might be the initial fuel for star formation, but it is not intimately connected to the overdense parts of molecular gas that collapse to form stars. Following the basic picture of the molecular clouds’ lifecycle laid out in Section 1.2.2), the SFR should be more tightly connected to the dense molecular gas.

Therefore, in a seminal work, Gao and Solomon (2004) observed a large sample of normal and starburst galaxies in HCN (1 – 0) line emission to trace the dense gas mass. They found that the HCN luminosity is linearly related to the SFR as traced via the total IR luminosity, where the relation with CO yield a super-linear relation (Figure 1.7, left panel). These findings supported the picture that HCN emission traces the dense molecular gas (M_{dense}) which is ultimately regulating the star formation rate:

$$M_{\text{dense}} \propto \text{SFR} . \quad (1.18)$$

Over the past 20 years, many more surveys aimed at mapping HCN (1 – 0) emission on small scales (MW clouds), within resolved regions in nearby galaxies to the high-redshift universe. Remarkably, all studies find a roughly fixed HCN-to-IR luminosity ratio spanning more than ten orders of magnitude in HCN and IR luminosity (Figure 1.7, right panel), manifesting one of the tightest empirical relations in astronomy, which has recently been coined the Gao-Solomon (GS) relation (Schinnerer and A. K. Leroy, 2024).

Adopting the same logic as in Section 1.5.1, the star formation efficiency of dense molecular gas can

be defined as:

$$\text{SFE}_{\text{dense}} = \frac{\text{SFR}}{M_{\text{dense}}}, \quad (1.19)$$

where M_{dense} is the dense gas mass traced via HCN. Similarly, the inverse ratio (i.e. $M_{\text{dense}}/\text{SFR}$) is usually defined as the dense gas depletion time ($\tau_{\text{dep}}^{\text{dense}}$)

$$\tau_{\text{dep}}^{\text{dense}} = \frac{M_{\text{dense}}}{\text{SFR}}, \quad (1.20)$$

which comes out to be ~ 150 Myr and hence more than a factor of 10 shorter than $\tau_{\text{dep}}^{\text{mol}}$. Thus, dense molecular gas is much faster converted into stars than bulk molecular gas. However, the star formation efficiency per free-fall time associated with the dense gas:

$$\epsilon_{\text{ff}}^{\text{dense}} = \text{SFE}_{\text{dense}} \cdot \tau_{\text{dep}}^{\text{dense}}, \quad (1.21)$$

is on the order of $\sim 0.3\%$ and hence similarly low as for the bulk molecular gas.

The linear GS relation implies a constant $\text{SFE}_{\text{dense}}$ from clump to whole galaxy scales. The interpretation could be that HCN traces the dense, overdense clumps of molecular clouds which are converted into stars at a fixed efficiency so that larger scale observations (e.g. kiloparsec or global galaxy scales) just average over a large number of these clumps, which all have the same $\text{SFE}_{\text{dense}}$. The conclusion would be that dense gas is converted into stars at a constant $\text{SFE}_{\text{dense}}$ – or in other words, there is a universal star formation law in the universe.

1.5.3 Dense gas scaling relation

The tight relation between dense gas and SFR might suggest that there is a universal $\text{SFE}_{\text{dense}}$ in the universe. However, although the GS relation appears tight when viewed across 10 orders of magnitude, there is an almost 1 dex scatter at smaller scales. This is an indication that there might be other factors at play that affect $\text{SFE}_{\text{dense}}$ on a cloud-to-cloud basis. Moreover, turbulent models of star formation (e.g. Krumholz and McKee, 2005) predict that the properties of molecular clouds should affect the formation of dense gas and its star formation efficiency.

In recent years, resolved measurements of dense gas tracers in nearby galaxies (e.g. Usero et al., 2015; Bigiel, A. K. Leroy, Jiménez-Donaire et al., 2016; Gallagher, A. K. Leroy, Bigiel, Cormier, Jiménez-Donaire, E. Ostriker et al., 2018; Gallagher, A. K. Leroy, Bigiel, Cormier, Jiménez-Donaire, Hughes et al., 2018; Jiménez-Donaire, Bigiel, A. K. Leroy, Usero et al., 2019) enabled new possibilities to study environmental variations of $\text{SFE}_{\text{dense}}$ and the dense gas fraction:

$$f_{\text{dense}} = \frac{M_{\text{dense}}}{M_{\text{mol}}}. \quad (1.22)$$

The dense gas fraction (f_{dense}) measures the fraction of gas that is dense and can be traced via the HCN-to-CO line ratio (hereafter HCN/CO).

The expectation from molecular cloud models is that f_{dense} increases while $\text{SFE}_{\text{dense}}$ decreases in dense, turbulent environments. This hypothesis motivated a series of resolved dense gas studies in nearby galaxies to test whether f_{dense} and $\text{SFE}_{\text{dense}}$ vary systematically with the physical environment. Usero

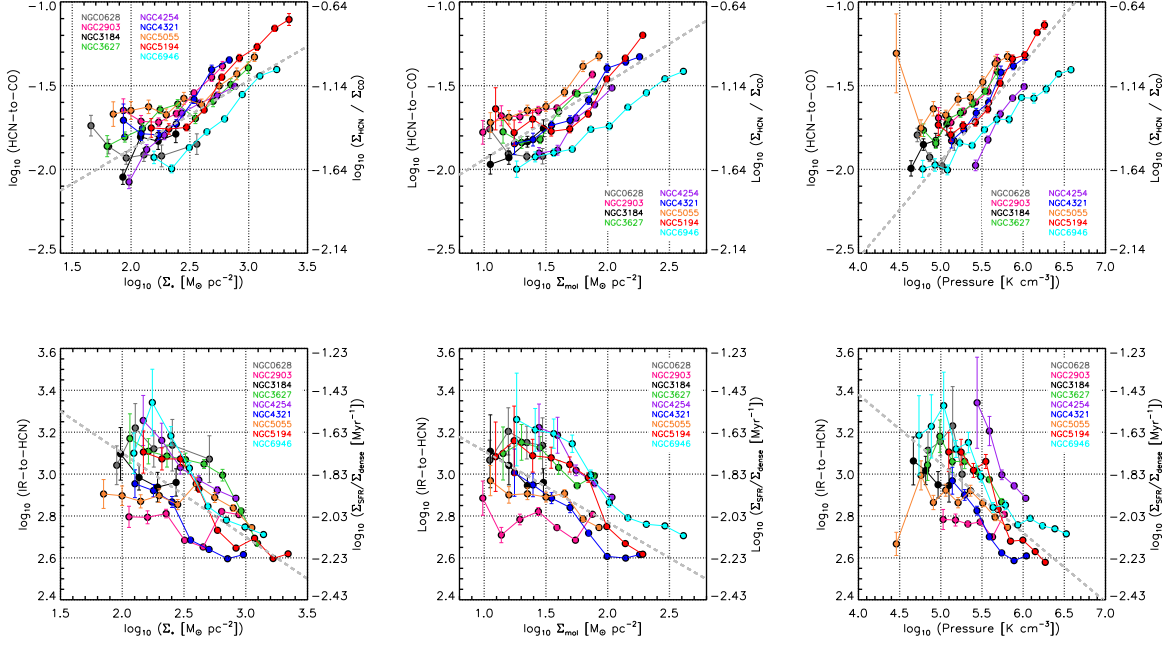


Figure 1.8: **Dense gas scaling relations.** *Top:* HCN/CO, a proxy for the dense gas fraction, against the stellar mass surface density (Σ_\star), molecular gas surface density (Σ_{mol}), and dynamical equilibrium pressure (P_{DE}) across kiloparsec scale resolved measurements in nine nearby spiral galaxies from the EMPIRE survey. *Bottom:* Similar as the top panels, but plotting IR/HCN, a proxy for the dense gas star formation efficiency, against Σ_\star , Σ_{mol} , and P_{DE} across the same galaxies. The figure is reproduced from Jiménez-Donaire, Bigiel, A. K. Leroy, Usero et al. (2019).

et al. (2015) presented HCN (1 – 0) observations across several nearby galaxies at kiloparsec resolution finding trends between f_{dense} and $\text{SFE}_{\text{dense}}$ in agreement with turbulent cloud models. In a pilot study of the EMPIRE survey, Bigiel, A. K. Leroy, Jiménez-Donaire et al. (2016) showed that there are systematic variations between these f_{dense} and $\text{SFE}_{\text{dense}}$ (in the literature sometimes referred to as spectroscopic ratios being traced by HCN/CO and IR/HCN) and the kiloparsec scale environments in the spiral galaxy M51. The analysis has been extended to a larger sample of nine galaxies (EMPIRE; Jiménez-Donaire, Bigiel, A. K. Leroy, Usero et al., 2019), yielding the systematic variations between the spectroscopic ratios and the kiloparsec scale stellar mass surface density (Σ_\star), molecular gas surface density (Σ_{mol}), and dynamical equilibrium pressure (P_{DE} ; Figure 1.8).

The results from EMPIRE show that f_{dense} increases, while $\text{SFE}_{\text{dense}}$ decreases in high-density, high-pressure environments. Gallagher, A. K. Leroy, Bigiel, Cormier, Jiménez-Donaire, E. Ostriker et al. (2018) confirmed the results from EMPIRE at sub-kiloparsec scale using ALMA observations of HCN from nearby galaxies. In a second paper, Gallagher, A. K. Leroy, Bigiel, Cormier, Jiménez-Donaire, Hughes et al. (2018) compared the spectroscopic ratios with the properties of molecular clouds, measured at ~ 100 pc scale via CO (2 – 1) from PHANGS–ALMA (A. K. Leroy, Schinnerer et al., 2021). They find that, across a small sample of five nearby galaxies, f_{dense} depends on the properties of the cloud-scale gas supporting the predictions from molecular clouds models that the average density and turbulence of molecular clouds drive variations in the dense gas ratios.

In addition, molecular cloud studies using PHANGS–ALMA data demonstrate that GMC properties

vary with the kiloparsec scale environment (Sun, A. K. Leroy, Schinnerer et al., 2020). Overall, the above-summarised findings suggest that there are connections between kiloparsec scale environmental conditions, molecular cloud properties and spectroscopic dense gas ratio (also see review by Schinnerer and A. K. Leroy, 2024, which already includes results from this thesis).

1.6 Science goals and outline of this thesis

“Recognizing the problem is more important than recognizing the solution, because the exact description of the problem leads to the solution.””

Albert Einstein – 20th century physicist

Star formation is at the heart of many astrophysical processes from planet formation to galaxy evolution. Yet, the process of star formation is not very well understood. Some of the key questions are: Is star formation a universal process in the universe? How is dense gas formed in galaxies? How efficiently is (dense) molecular gas converted into stars in galaxies? Does the star formation efficiency vary within and between galaxies? What is driving the star formation efficiency?

In Section 1.5, we presented the current state of the literature which tried to answer the above science questions by studying (dense) molecular gas in galaxies manifesting two star formation relations – the Kennicutt-Schmidt and Gao-Solomon relations. These empirical relations demonstrate that molecular gas is the fuel for star formation and that stars predominantly form in the dense parts of GMCs. Recent studies also show that the star formation efficiency of the dense gas is not constant but varies systematically within galaxies. The connections between dense gas spectroscopic ratios, kiloparsec scale environment, and GMC properties are visualised in Figure 1.9.

This thesis is composed of five projects (P1 to P5), which focus on studying dense molecular gas from the MW (P5) to nearby galaxies (P1, P2, P3). The aim is (a) to gain a deeper understanding of how dense gas forms and produces stars in galaxies by linking dense gas and star formation with environmental (P2, P4) and GMC properties (P3), and (b) making sense of dense gas tracers by studying the emissivity of extragalactic dense gas tracers in the MW (P5). Project P1 introduces the spectral stacking technique used to recover dense gas tracers in order to measure dense gas scaling relations with higher significance. In project P2, we will address the connection between dense gas spectroscopic ratios and kiloparsec scale environment, putting new constraints on dense gas scaling relations. Project P3 aims to find the missing link between the spectroscopic ratios and molecular cloud properties. In project P4, we go beyond spectral stacking and study dense gas at sub-kiloparsec scale, differentiating different morphological environments that have been blurred together at kiloparsec scales. Project P5 investigates the ability of HCN as a dense gas tracer, linking galactic studies of molecular clouds to extragalactic works.

(P1) PyStacker: Recovering faint line emission via spectral stacking

The first project of this thesis is a technical work, which presents the spectral stacking tool **PyStacker**. This tool has been developed in the group of Frank Bigiel to recover faint line emission from radio astronomical observations and has been excessively used throughout these thesis’ works (P2, P3, P4). One of the big challenges in extragalactic astronomy is the detection of emission lines fainter than the low-J CO transitions. Even with state-of-the-art radio observatories like the IRAM 30 m, NOEMA, or

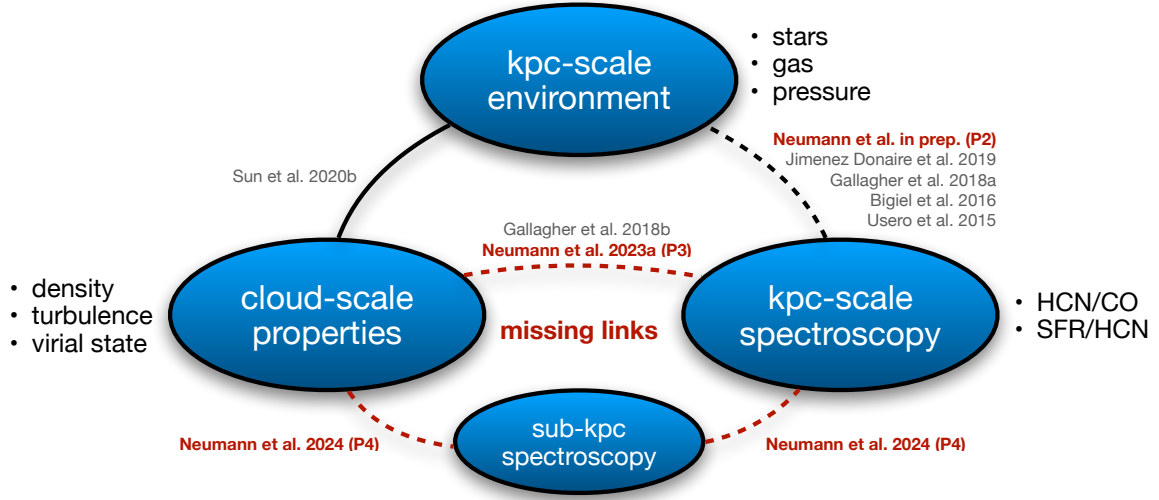


Figure 1.9: **Dense gas-environment-GMC connections.** The empirical connections between the kiloparsec scale environment, cloud properties and dense gas spectroscopy in galaxies. Sun, A. K. Leroy, Schinnerer et al. (2020) show that molecular clouds couple to the local environment in galaxies using data from PHANGS-ALMA (A. K. Leroy, Schinnerer et al., 2021). Dense gas studies in nearby galaxies (Usero et al., 2015; Bigiel, A. K. Leroy, Jiménez-Donaire et al., 2016; Gallagher, A. K. Leroy, Bigiel, Cormier, Jiménez-Donaire, E. Ostriker et al., 2018; Jiménez-Donaire, Bigiel, A. K. Leroy, Usero et al., 2019) find that kiloparsec scale spectroscopic ratios (HCN/CO, SFR/HCN, proxies for the dense gas fraction and dense star formation efficiency) also depend on the environmental conditions (stellar mass surface density, gas surface density, pressure). This connection is further investigated with the ALMOND survey (Neumann, Gallagher et al., 2023) presented in this thesis (P2). Motivated by Gallagher, A. K. Leroy, Bigiel, Cormier, Jiménez-Donaire, Hughes et al. (2018) and theoretical predictions (e.g. Krumholz and McKee, 2005), (P3) aims at finding the missing link between cloud-scale gas properties and kiloparsec scale spectroscopic ratios using the ALMOND data. With (P4), we go to higher spatial resolution bridging the gap between kiloparsec and cloud scales using new ALMA data of NGC 4321 (Neumann, Bigiel et al., 2024).

ALMA, mapping of dense gas tracers such as HCN or HCO^+ are expensive and only feasible within reasonable telescope times for small samples of galaxies at coarse resolution or dedicated single-target projects. Therefore, sophisticated analysis tools that extract emission hidden in the noise are crucial to exploit the full potential of dense gas tracer observations.

In this project, we apply the PyStacker tool to simulated ALMA observation to test the capabilities of the spectral stacking technique to recover faint emission lines. Some of the key questions addressed by this work are: Can spectral stacking recover faint line emission otherwise hidden in the noise? Does spectral stacking yield reasonable uncertainty estimates? Can PyStacker induce biases on stacked measurements? What are the limitations of spectral stacking? How important is the choice/availability of a prior (i.e. bright line) to define the velocity field? Do purely spectroscopic observations filter out extended emission and if so how much flux is missing for typical ALMA observations?

(P2) ALMOND: Dense gas relations at kiloparsec scales

In this thesis, we present new observations of dense gas tracers across 25 nearby galaxies taken with ALMA. This survey called ACA Large-sample Mapping Of Nearby galaxies in Dense gas (ALMOND), comprises the largest sample of dense gas maps at kiloparsec scales. In this project, we combine the ALMOND data set with the EMIR Multiline Probe of the ISM Regulating Galaxy Evolution (EMPIRE) survey to form a large, homogeneous sample of dense gas observations at kiloparsec scale (31 galaxies).

Building on the works of EMPIRE, we use this larger data set to study kiloparsec scale dense gas relations across 31 nearby galaxies. In the first step, we combine these observations with a large set of literature observations to study the Gao-Solomon relation, addressing the following science questions: What is the average star formation efficiency of dense gas ($\text{SFE}_{\text{dense}}$) across the largest sample of HCN observations from the MW to high-redshift galaxies? Are there other factors at play that affect the star formation rate than the dense gas mass? Are $\text{SFE}_{\text{dense}}$ variations larger at smaller scales within the MW or at larger scales across the diverse galaxy population? In other words: Are cloud-to-cloud variations (local) larger than galaxy-to-galaxy variations (global)?

In the next step, we use the combined EMPIRE + ALMOND data set to investigate dense gas relations with kiloparsec scale environment to tackle the following questions: How do $\text{SFE}_{\text{dense}}$ and f_{dense} vary with the kiloparsec scale environment across nearby spiral galaxies? How strong and significant are these relations based on the largest sample of resolved measurements and state-of-the-art methodology? How large is the scatter in these relations? Are there significant galaxy-to-galaxy variations? Are these relations driven by galaxy centres or also observed across the discs? How do methodological choices affect the scaling relations? While these relations have already been studied with EMPIRE (Jiménez-Donaire, Bigiel, A. K. Leroy, Usero et al., 2019), ALMOND provides a much larger sample to constrain the kiloparsec scaling relations with much higher significance. Moreover, putting the ALMOND sample into the context of the current literature sets the groundwork for the next project.

(P3) ALMOND: Dense gas relations with GMC properties

Past studies (Usero et al., 2015; Bigiel, A. K. Leroy, Jiménez-Donaire et al., 2016; Gallagher, A. K. Leroy, Bigiel, Cormier, Jiménez-Donaire, E. Ostriker et al., 2018; Jiménez-Donaire, Bigiel, A. K. Leroy, Usero et al., 2019) have shown that SFR/HCN , a proxy of the dense gas star formation efficiency, and HCN/CO , a proxy of the dense gas fraction, vary systematically with kiloparsec scale environmental conditions such as the stellar mass surface density, molecular gas surface density, or pressure. These studies conclude that SFR/HCN is lower, while HCN/CO is higher in high-density, high-pressure environments, but do not provide a physical explanation of the observed relations.

Gallagher, A. K. Leroy, Bigiel, Cormier, Jiménez-Donaire, E. Ostriker et al. (2018) lays out that variations of these dense gas ratios should be driven by changes in the molecular cloud properties as expected by turbulent cloud models finding systematic trends between HCN/CO and the molecular cloud gas density. If expectations of turbulent cloud models were believed, there should be systematic trends of SFR/HCN and HCN/CO with the properties of molecular clouds, raising the following science questions: Are dense gas and star formation linked to the properties of molecular clouds? Are expectations about dense gas scaling relations from turbulent cloud models supported by observations? Is there a comprehensive picture connecting dense gas tracers, star formation and molecular cloud properties?

Addressing these science questions requires a set of dense gas observations at $\lesssim 1$ kpc scales, tracing SFR/HCN and HCN/CO , paired with molecular gas observations at $\lesssim 100$ pc, tracing molecular cloud properties. However, these observations do not exist for a significantly large sample of galaxies hence motivating the ALMOND survey. With ALMOND we can finally make the connection between dense gas, star formation and cloud properties, testing predictions of cloud models and possibly gaining a deeper understanding of star formation in galaxies.

(P4) NGC 4321: Dense gas relations at sub-kiloparsec scales

The kiloparsec dense gas surveys EMPIRE and ALMOND address some of the key questions of whether dense gas and star formation are connected to the larger scale environment, and the cloud-scale gas physics in galaxies. However, these surveys were optimised to detect dense gas tracers, in particular HCN, across a large sample of galaxies yielding mostly detections towards galaxy centres and very few detections across the discs. Therefore, stacking was needed to recover the low-significant emission in low-density, low-pressure regions at the cost of spatial information. Hence, these kiloparsec scale studies only display average trends and do not represent the true sub-kiloparsec scale scatter. Moreover, at kiloparsec resolution, individual morphological environments, such as centres, bars, bar ends, spiral arms, and interarm regions are not resolved.

We do not know: How do dense gas fraction (HCN/CO) and star formation efficiency (SFR/HCN) vary at \sim cloud scale across the disc of a spiral galaxy? How do SFR/HCN and HCN/CO vary within the centres of galaxies and in different morphological environments? Are spiral arms more efficiently producing stars than interarm regions? How do gas dynamics, such as gas flows, and shear, typically present in galactic bars, affect star formation? Do cloud-cloud-collisions in bar ends boost or suppress star formation?

To address these science questions, the galaxy NGC 4321 has been observed with ALMA to create one of the deepest, 260 pc resolution, full galaxy maps of a nearby spiral galaxy in dense gas tracers. These observations detect HCN emission out to galactocentric radii of ~ 10 kpc without the need for stacking, producing many individual sightline detections across different morphological environments.

Besides, these observations probe for the first time the low-pressure environment comparable to the conditions found in the solar neighbourhood. Previous works (including EMPIRE and ALMOND studies) suggest that clouds couple to the local environment in the inner parts of galaxies. However, there are theoretical works (e.g. Elmegreen, 2018), which predict a decoupling in the low-pressure environments, asking the questions: Do molecular clouds decouple from the environment in low-pressure environments? Is there a pressure threshold for star formation? These questions can be addressed for the first time with the new ALMA observation presented in this thesis.

(P5) LEGO: Making sense of dense gas tracers

Recent galactic works (Pety et al., 2017; Kauffmann, Goldsmith et al., 2017) have challenged the role of HCN as a tracer of dense molecular gas, finding that HCN ($1 - 0$) is also efficiently emitting at intermediate gas densities and hence not only tracing the dense gas that is associated with the immediate star-forming gas. Instead, these studies suggest N_2H^+ as the gold standard tracer of cold, dense gas. However, N_2H^+ ($1 - 0$) is much fainter than HCN ($1 - 0$) and hence not feasible to map in other galaxies. Therefore, efficiently mapping dense gas tracers with current telescopes is limited to brighter dense gas tracers such as HNC ($1 - 0$), HCO^+ ($1 - 0$) or HNC ($1 - 0$). Since many of the extragalactic studies use HCN to trace dense gas, including the famous GS relation, these recent MW findings raise some important questions such as: Is HCN a robust tracer of dense gas in star-forming regions? How does the emissivity of HCN vary with the physical conditions of the gas? Are there other factors, besides gas density, at play that affect the HCN emission? If so, can these secondary effects be mitigated/corrected? Are there alternative dense gas tracers that could potentially replace HCN as a dense gas tracer in extragalactic studies?

Overall, a better understanding of the emissivity of dense gas tracers is needed to make sense of

extragalactic observations and draw meaningful conclusions. These science questions motivated the Line Emission as a tool for Galaxy Observations (LEGO) survey which is designed to investigate typical extragalactic dense gas tracers across a wide range of environments in the MW. In this project, we focus on the three massive star-forming regions of the sample to make the most reasonable comparison with extragalactic studies of spiral, star-forming galaxies.

Observations

“Remember to look up at the stars and not down at your feet. Try to make sense of what you see and wonder about what makes the universe exist. Be curious.”

Stephen Hawking – 20th century astrophysicist

2.1 Fundamentals of radio astronomy

The main sources of information for this Section 2.1 are taken from books and lecture notes. The fundamentals of single-dish radio astronomy (Sections 2.1.1 to 2.1.3) are based on the book *Tools of Radio Astronomy* by Thomas L. Wilson, Kristen Rohlfs, and Susanne Hüttemeister (Wilson et al., 2013) and the lecture notes *Essential Radio Astronomy* by James J. Condon and Scott M. Ransom, which are based on a lecture series taught at the University of Virginia, Charlottesville, US (Condon and Ransom, 2016). Section 2.1.5 additionally uses material from the lecture notes *Radio Interferometry* by Uli Klein, which are based on a Master’s course Prof. Klein taught at the University of Bonn.

2.1.1 Radio antennas

For a typical single-dish radio telescope, the response of the antenna when observing a point source will look like the beam pattern shown in Figure 2.1. The central feature is called the antenna’s main beam, and the additional peaks left and right of the main beam are called side lobes. Through the design of the telescope, we aim to minimize the amplitude of the side lobes to ensure the observed signal is not contaminated by other sources on the sky.

The main beam of the antenna (Ω_{MB}) is defined as the region within the first zeros of the beam response function. It also defines the resolution of the instrument. For an axisymmetric Gaussian beam, the angular resolution (θ) of the telescope, defined as the full width at half maximum (FWHM) of the Gaussian, can be approximated using:

$$\theta \approx 1.2 \frac{\lambda}{D}, \quad (2.1)$$

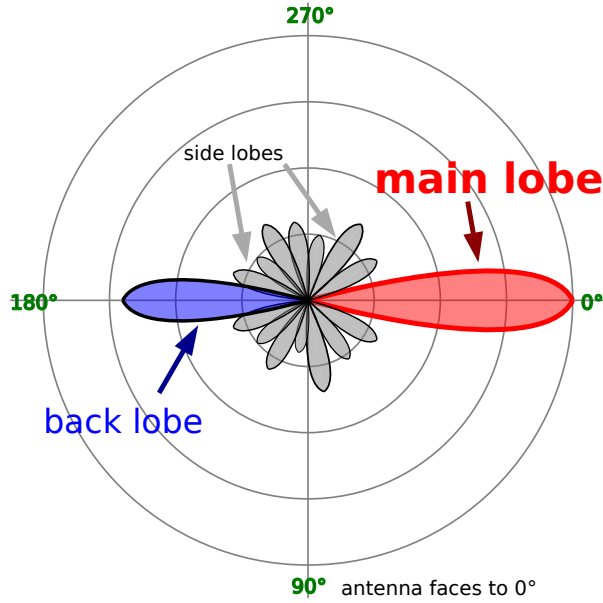


Figure 2.1: **Antenna beam pattern.** Visualisation of the beam intensity distribution of a typical radio single-dish telescope. The red pattern shows the main beam lobe pointing towards in the direction of the telescope’s optical axis. The grey features are side lobes that originate from diffraction effects and contamination. The blue peak illustrates the back lobe, which created by the receiver itself. The drawn circles show intensity levels on a logarithmic scale. Image Credit: Timothy Truckle.

where λ is the wavelength of the detected radiation and D is the aperture (or diameter) of the antenna. This means, at a fixed wavelength the resolution of a telescope scales proportional to its diameter ($\theta^{-1} \propto D$)¹. Likewise, for a given telescope, the resolution increases proportional to the frequency ($\theta^{-1} \propto 1/\lambda \propto f$) of the radiation.

To quantify the measured signal, meaning the power per unit frequency that is collected by the antenna, it is convenient to define the antenna temperature, T_A . The antenna temperature has nothing to do with the actual physical temperature of the antenna but describes the equivalent power output per unit frequency P_ν of a resistor with temperature T_A , such that $T_A = P_\nu/k_B$. This definition is convenient because also the receiver noise is characterised in terms of a temperature and many radio telescopes can be calibrated by hot and cold loads of a given temperature which is connected to the receiver output.

2.1.2 Brightness temperature

In Section 2.1.1, the concept of antenna temperature (T_A) was introduced as the temperature of a matched resistor whose power equals that measure by the antenna – but how does this relate to the actual intensity (or flux density) of the source? The reason that we express the flux in terms of a temperature is a) that at radio wavelength the intensity of a source can be expressed in units of K and b) that this so-called brightness temperature is related to the antenna temperature.

The intensity of a blackbody is described by the Planck law², which simplifies to the Rayleigh-Jeans

¹ Note that smaller θ means higher resolution, since smaller angular scales can be resolved.

² The Planck law is one of the most fundamental laws in physics and essential to all fields of astronomy. It describes the intensity of an ideal blackbody with temperature T , given as $B_\nu(\nu, T) = 2h\nu^3/(c^2(\exp(h\nu/(k_B T)) - 1))$, where c is the speed of light and k_B is the Boltzmann constant.

approximation at long wavelengths (i.e. $h\nu \ll k_B T$, typically satisfied at radio wavelengths³):

$$T_b = \frac{c^2}{2k_B \nu^2} I_\nu \quad (2.2)$$

so that the brightness temperature is directly proportional to its equivalent blackbody intensity. The convention in radio astronomy is to define the brightness temperature via Equation (2.2) even if the source is not a blackbody, so that, in general, T_b is frequency dependent. It must be noted that the brightness temperature has little to do with the physical temperature of the source, especially if the emission is non-thermal (e.g. for line emission), it is just another way to quantify the spectral brightness of a celestial object in units of K.

It can be shown that for extended sources, $T_A = T_b$, this means, the antenna temperature of an extended source equals the source brightness temperature. For the case that the beam solid angle of the antenna (Ω_A) is smaller than the source extent (Ω_s), the above relation changes to:

$$T_A = \frac{\Omega_s}{\Omega_A} T_b, \quad (2.3)$$

where the ratio, Ω_s/Ω_A , is called beam filling factor. The antenna beam solid angle (Ω_A) is related to the main beam solid angle (Ω_{MB}) via the beam efficiency: $\eta_B = \Omega_{MB}/\Omega_A$.

2.1.3 Radiometer noise

A receiver that detects radio emission is called a radiometer. The radio emission detected by the radiometer is not exclusively originating from the astrophysical object of interest, but a superposition of signal from various sources including the Earth's atmosphere, spillover emission from the ground or noise from the receiver electronics. It is convenient to describe all of these contributions in units of temperature combined into the system temperature T_s . Usually, it is a good assumption that the fluctuations of the system temperature can be described as Gaussian rms noise, σ_T . For Gaussian noise, the rms scales with the integration time (τ) of the observations and the bandwidth ($\Delta\nu$) of the receiver, such that:

$$\sigma_T = \frac{T_s}{\sqrt{\Delta\nu \tau}}. \quad (2.4)$$

Above equation implies that the Signal-to-Noise Ratio (S/N) improves with increasing bandwidth ($S/N \propto \Delta\nu$) at the cost of spectral resolution or integration time ($S/N \propto \sqrt{\tau}$) at the cost of telescope time.

It is important to note that the astronomical signal is typically orders of magnitude weaker than the total system temperature. Therefore, in addition to optimising the integration, it is necessary to mitigate all contaminating radio sources via sophisticated calibration steps. One typical approach is to perform so-called on-off calibrations, where the telescope is iteratively pointed at the source and an empty patch of the sky with no astrophysical emission (called the off-position), such that the difference between both integrations is the signal of the source of interest.

³ Note that at millimetre wavelengths, the condition $h\nu \ll k_B T$ is not strictly satisfied any more, so that the relation between T_b and I_ν will slightly deviated from the proportional form presented in Equation (2.2)

2.1.4 Doppler velocity

Emission lines emit at a specific frequency (or wavelength), given by the energy difference of the transition (see Section 1.3.3). This frequency is commonly referred to as rest frequency (f_{rest}). However, this is not necessarily the frequency at which the line is observed due to the so-called Doppler effect. The Doppler effect, named after the physicist Christian Andreas Doppler, states that the emission of an emitter with rest frequency f_{rest} that moves with a velocity Δv relative to the observer, will be observed at a different frequency:

$$f_{\text{obs}} = \left(1 - \frac{\Delta v}{c}\right) f_{\text{rest}}, \quad (2.5)$$

where $c = 299\,792\,458 \text{ m s}^{-1}$ is the speed of light. This implies that the observed frequency is shifted compared to the rest frequency by:

$$\Delta f = f_{\text{obs}} - f_{\text{rest}} = -\frac{\Delta v}{c} f_{\text{rest}}. \quad (2.6)$$

Quantitatively, this means that the observed frequency of sources moving away from the observer ($\Delta v > 0$) are shifted to lower frequencies ($f_{\text{obs}} < f_{\text{rest}}$; red-shifted) and emission of sources approaching the observer ($\Delta v < 0$) are shifted to higher frequencies ($f_{\text{obs}} > f_{\text{rest}}$; blue-shifted). Given that f_{rest} of a targeted line is usually known, the observed frequency of the line can be used to compute the relative line of sight velocity of the source from which the emission originates by rearranging Equation (2.5) via Δv . This is, for example, routinely applied to infer redshifts of galaxies, but also useful to study the kinematics of interstellar gas. Relevant to this work is the latter application, such that the observed frequency of molecular line emission can directly be related to the mean velocity of the molecular gas.

Actually, in radio/mm astronomy it has become conventional to directly convert the frequency axis of an observed spectrum into a (Doppler-shifted) velocity axis via Equation (2.6), which puts the velocity axis origin ($\Delta v = 0$) at the rest frequency of the respective line⁴. This also means that every molecular line has its own f_{rest} -specific velocity axis. The advantage for astronomers working with velocity units instead of frequencies is that the relative motion of the gas can directly be read off. Given that intensities are usually measured in units of K (Section 2.1.2) and frequencies in units of m s^{-1} , this means that integrated line intensities are commonly measured in K km s^{-1} , which appears like a very unusual unit to non-radio astronomers.

2.1.5 Radio interferometers

Based on Equation (2.1), it becomes apparent that single-dish radio telescopes lack angular resolution compared to telescopes operating at shorter wavelengths such as infrared or optical telescopes. For example, reaching the same resolution as a small 1 m optical telescope at wavelengths of $\sim 1 \text{ mm}$ requires a 2 km diameter radio dish. Since building radio telescopes reaches its technical limitations at sizes of around hundreds of metres, there is no way to build radio telescopes as large as needed to reach angular resolutions of arcseconds.

⁴ The astronomy python package `astropy` offers build-in functions to perform the conversion from frequency to velocity units (`astropy.units.equivalencies.doppler_radio`) as well as intensity to brightness temperature units (`astropy.units.equivalencies.brightness_temperature`).

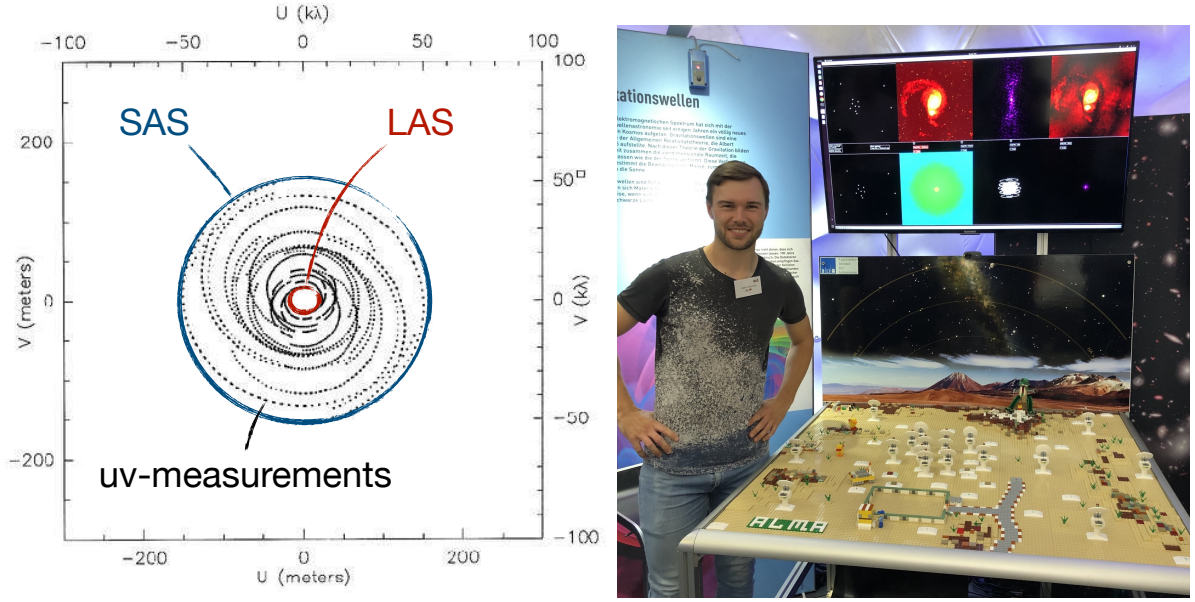


Figure 2.2: **UV-plane and ALMA LEGO model.** *Left:* Visualisation of the $u - v$ sampling of a typical observation with the Plateau de Bure Interferometer (PdBI, the precursor of NOEMA) consisting of six antennas (Credit: U. Klein). Each black point denotes a visibility measurement. The maximum extent in $u - v$ space defines the smallest angular scale (SAS) that can be recovered and hence the angular resolution of the interferometer. The minimal baselines (hole in $u - v$ space) specify the largest angular scale (LAS), which means that large-scale emission will be filtered out and single dish (total power) observation is needed to recover the full flux. *Right:* A model of the ALMA radio interferometer built out of LEGO bricks presented by me at the public outreach event “Universe on Tour” at Bonner Hofgarten in August 2023. The model has built-in functionalities so that the effect of changing the antenna configuration on the observed image can be explored in real-time.

Fortunately, there is a mathematical trick that allows one to artificially imitate a large telescope by connecting many smaller telescopes distributed over a wider area – a so-called interferometer. Technical challenges aside, the bottom line is that the resolution of an interferometer is determined by the maximum separation (B , called baseline) between the telescopes:

$$\theta \approx \frac{\lambda}{B_{\max}} . \quad (2.7)$$

Radio interferometers such as the VLA, MeerKAT, SMA, NOEMA, or ALMA initiated a golden age of radio astronomy offering even higher angular resolutions than state-of-the-art optical telescopes (e.g. ALMA can reach 10 milliarcsecond resolution at 1 mm). The diameters of the antennas (D) of an interferometer define the primary beam (PB):

$$\text{PB} \approx \frac{\lambda}{D} , \quad (2.8)$$

and hence the FOV of the interferometer for a single pointing, but not the resolution. It is important to note that although interferometers can achieve resolutions of synthetic kilometre-sized telescopes, they can not reach the same sensitivity, which is given by the effective, combined surfaces of the individual dishes.

The interferometry technique relies on the mathematical principle of the Fourier transformation An

interferometer does not observe the real sky brightness, $S(\xi, \eta)$, directly, but instead we measure a correlated signal pair-wise between all antennas. The correlated signals corresponds to the Fourier transform of the sky, which is called the visibility:

$$V(u, v) = \iint S(\xi, \eta) e^{-i2\pi(u\xi + v\eta)} d\xi d\eta, \quad (2.9)$$

where ξ, η are the real sky coordinates (right ascension, declination), and u, v are the coordinates in Fourier space, which can be understood as spatial frequencies in units of metre. In aperture synthesis, the goal is to measure the visibilities and then reconstruct the true sky brightness by essentially inverting Equation (2.9).

Each antenna pair of an interferometer measures the visibility (amplitude and phase) at the coordinate tuple u, v . The projected distance of the antennas relative to the source (i.e. the projected baseline) defines the absolute value of the spatial frequency. Hence, longer baselines recover higher spatial frequencies and smaller scales, while shorter baselines measure small spatial frequencies corresponding to larger scales. A single pair of antennas will only measure a single coordinate (actually two, since $V(u, v) = V(-u, -v)$) in Fourier space. However, to properly recover $S(\xi, \eta)$, the $u - v$ space must be sufficiently well sampled. Therefore, interferometers typically consist of many antennas that are configured in a clever way spanning a range of baselines and orientations. We can improve the sampling of the $u - v$ plane by using more antennas, or if we observe for a longer period of time, the rotation of the Earth also helps to achieve a more complete sampling.

Figure 2.2 visualises the $u - v$ coverage of a typical observation with the . The arc-like tracks indicate measurements of a single baseline taken over 8 hours of integration time. The maximum angular resolution can be easily inferred from the largest $d(u, v) = \sqrt{u^2 + v^2}$ values. Besides, one can notice a “hole” around the origin of the $u - v$ space. This is because smaller baselines than the size of the individual antenna dishes are not possible. Thus, the smallest baseline of an interferometer defines the LAS that can be recovered:

$$\text{LAS} \approx \frac{\lambda}{B_{\min}}. \quad (2.10)$$

Emission that is more extended than the LAS will simply be filtered out by the interferometer. Therefore, purely interferometric observations are often combined with single-dish observations to essentially fill the hole in $u - v$ space.

Inverting Equation (2.9) to crate a sky image from the visibilities may appear like a simple mathematical operation. However, the $u - v$ space is never perfectly sampled, so that there is no analytical solution to the inverse Fourier transform. Moreover, the beam of an interferometer is usually extremely complex. Therefore, imaging radio interferometric observations is almost an own field of science and many methods and tools have been developed to perform the so-called deconvolution. One of the most naive approaches is the CLEAN algorithm, which iteratively extracts peaks from the dirty image (i.e. the raw, uncleaned image) until the residual image can be well described by pure noise, and then convolves the image of point sources with the clean beam to reconstruct the sky brightness. For the interferometric data in this thesis, the imaging has been performed with Common Astronomy Software Applications (CASA), which is the default data analysis tool for ALMA observations, and employing its CLEAN method.



Figure 2.3: **IRAM 30 m and ALMA.** The left image shows the IRAM 30 m radio telescope on Pico Veleta, Spain, at an altitude of 2850 m (Image credit: IRAM/K. Zacher). The right image shows the interferometre ALMA, consisting of 66 antennas with 7 m or 12 m diameter. ALMA is located in the Atacama desert in Chile at an altitude of 5000 m (Image credit: ESO/C. Malin).

2.2 Relevant radio and mm telescopes

Radio/millimetre astronomical observations from the IRAM 30 m and ALMA telescopes form the foundation of this thesis as tracers of the molecular ISM, which is linked to star formation and the baryon life cycle in galaxies. In the following subsections (Sections 2.2.1 and 2.2.2), we will introduce these two state-of-the-art instruments and explain how they have been used in this work. In addition, we will briefly discuss other relevant telescopes used to probe different physical processes in galaxies (Section 2.2.3).

2.2.1 IRAM 30m

The IRAM 30 m telescope is one of the largest, most sensitive millimetre telescopes in operation since the 1980s by the IRAM. It is located on Pico Veleta in the Sierra Nevada close to Granada, Spain at an altitude of 2850 m (Figure 2.3). The telescope is designed to work at millimetre wavelengths covering 3 to 0.8 millimetres, which relates to frequencies of 80 to 370 GHz.

The unique feature of the IRAM 30 m telescope is its cutting edge receivers, which provide excellent sensitivity as well as large bandwidth ideally suited to perform multi-line surveys at millimetre wavelength. For comparison, the bandwidth of the Eight Mixing Receiver (EMIR) receiver (16 GHz) of the IRAM 30 m has two times the bandwidth of ALMA (8 GHz), which enables detecting many molecular lines (e.g. $\text{HCN} (1 - 0)$ and $\text{N}_2\text{H}^+ (1 - 0)$) simultaneously, where ALMA would need two spectra setups hence doubling its observing time.

The IRAM 30 m produced major contributions to the field of ISM studies and SF in galaxies by mapping bulk molecular gas and dense molecular gas tracers across nearby galaxies with HERA CO Line Extragalactic Survey (HERACLES; A. K. Leroy, Walter et al., 2009) and EMIR Multiline Probe of

the ISM Regulating Galaxy Evolution (EMPIRE; Jiménez-Donaire, Bigiel, A. K. Leroy, Usero et al., 2019) as well as focused multi-line, multi-transition studies of the Whirlpool Galaxy, M51 with CO isotopologue Line Atlas within the Whirlpool galaxy Survey (CLAWS; den Brok, Bigiel, Sliwa et al., 2022). Moreover, the 30 m has proven its exclusive capabilities of efficiently mapping a suite of molecular lines across galactic star-forming regions over a wide spectral bandwidth with LEGO (Kauffmann, Goldsmith et al., 2017; Barnes, Kauffmann et al., 2020). In this work, we present new observations from the LEGO project focussing on three massive star-forming regions in the Milky Way (Chapter 8).

Besides the 30 m telescope, IRAM also operates an interferometer called NOthern Extended Millimeter Array (NOEMA), which is located on the Plateau de Bure (hence its former name Plateau de Bure Interferometer (PdBI)) in the French Alps. Although not used in this work, NOEMA is one of the most advanced radio interferometers and has, for example, been used to follow up molecular gas surveys of nearby galaxies such as M51 at higher angular resolution (e.g., PdBI Arcsecond Whirlpool Survey (PAWS); Schinnerer, Meidt et al., 2013, or Surveying the Whirlpool at Arcseconds with NOEMA (SWAN); Stuber et al., 2023).

2.2.2 Atacama Large Millimeter/sub-mm Array (ALMA)

The ALMA is the most advanced radio interferometer ever built, consisting of 66 antennas with baselines of up to 16 km at an altitude of around 5000 m, combining the highest sensitivity and angular resolution at (sub-)millimetre wavelength with one of the best possible observing sites on Earth, located in the Atacama desert in Chile. ALMA is an international endeavour funded by institutions from Northern America (NSF, NRC), Europe (ESO) and Asia (NSC, NINS, AS) and operated by the NRAO (US), ESO (Europe), and NAOJ (Asia).

Since its first observing cycle in 2013, ALMA has indubitably revolutionised the field of (sub-)millimetre astronomy from uncovering the first images of planetary discs, over efficiently mapping entire galaxies in the local universe, to investigating the ISM in high-redshift galaxies providing unprecedented resolution and sensitivity at millimetre/sub-millimetre wavelength. ALMA operates at 30 to 950 GHz (3 to 0.1 mm), where the shorter wavelengths can only be observed due to the excellent observing site of ALMA, providing precipitable water vapour (pwv) values mostly below 2 mm.

One of the peculiar features of ALMA is its antenna configurations, along with the Submillimeter Array (SMA) and Combined Array for Research in Millimeter-Wave Astronomy (CARMA). In contrast to many other interferometers (e.g. the VLA or NOEMA), which align their antennas on linear tracks for easier transportation, the antenna positions of ALMA are chosen to optimally cover the $u-v$ space, naturally yielding circular beams to simplify the scientific analysis of the images. The main array of ALMA consists of 50 antennas, each 12 m in diameter, using the full extent of the ALMA site to reach high angular resolutions. In addition, ALMA contains a sub-array, called the Atacama Compact Array (ACA), which consists of four 12 m and twelve 7 m dishes. As the name tells, the ACA is more compact offering shorter baselines (up to m) and hence lower angular resolution, but at the same time larger FOVs due to the smaller, 7 m antennas as well as single dish total power (TP) observations needed to detect extended emission. For ISM studies, it is often necessary to combine 12 m main array observations with the ACA (7 m + TP) to cover all spatial scales and avoid filtering out extended emission.

In the field of ISM studies in nearby galaxies, ALMA has established itself as the workhorse telescope to efficiently map galaxies in molecular line emission at 3 mm, 1 mm or even shorter wavelength. One of the seminal surveys of nearby galaxies is the PHANGS–ALMA survey (A. K. Leroy, Schinnerer et al., 2021), which observed 90 galaxies in CO (2 – 1) line emission at $\sim 1''$ resolution to map the molecular

gas content (more details in Section 2.3.1). All of the extragalactic projects in this thesis are based on, or use PHANGS–ALMA data, such as project P1 (Chapter 4), where the capabilities of recovering faint emission via spectral stacking of interferometric ALMA data are tested. Moreover, PHANGS–ALMA CO data is utilised in projects P2 (Chapter 5), P3 (Chapter 6) and P4 (Chapter 7). Besides just tracing the bulk molecular gas via low-J CO lines, ALMA is excellently suited to map nearby galaxies in fainter, higher critical density lines, such as HCN ($1 - 0$), which is one of the central higher density gas tracers of this thesis. In projects P3 and P4, we present new ALMA observations of dense gas tracers that go beyond CO to actually map the dense molecular gas that is tightly linked to SF. While ALMOND was a large survey of 25 galaxies at lower angular resolution ($20''$) using the ACA (more details in Section 2.3.1), the observations of NGC 4321 focused on one target to reach high angular resolutions ($3.7''$). These observations are at the forefront of dense gas studies of nearby galaxies to allow the first systematic investigation of dense gas conditions and their ability to form stars in nearby galaxies.

2.2.3 Other relevant telescopes

In the following, we briefly list and describe additional telescopes and surveys that are relevant to this work, and span a large range of the electromagnetic spectrum from UV to radio wavelength. Figure 2.4 illustrates the transmission of electromagnetic radiation through Earth’s atmosphere. We can see that there are two main atmospheric windows at optical and radio wavelength, respectively. Therefore, at these wavelength, we can operate ground-based telescope to observe space. For millimetre wavelength, the atmosphere at sea level is almost completely opaque. However, at high altitudes and in dry regions, millimetre and even sub-millimetre wavelength can be detected from ground. For other wavelength ranges, for instance, gamma rays, x-rays, UV, and IR (except for some near-IR windows) we need space observatories. The overview below is biased towards the science field of this thesis, highlighting important contributions to the field of star formation and ISM studies of the MW and nearby galaxies.

VLA

The Karl G. Jansky Very Large Array (VLA), named after 20th century radio astronomer Karl Guthe Jansky, is one of the largest radio interferometers, and located in Socorro, New Mexico, at an altitude of 2100 m. It is operated by the NRAO and consists of 27 antennas, each 25 m in diameter, mounted on a Y-shaped track to facilitate baselines of up to 36 km. The VLA is particularly designed to work at centimetre wavelength, where it has made big contributions to mapping nearby galaxies in H I 21 cm line with the The HI Nearby Galaxy Survey (THINGS; Walter et al., 2008). At 21 cm ~ 1.4 GHz the most extended configuration provides an angular resolution of $\approx 1.5''$, which relates to ~ 100 pc physical scales in nearby galaxies ($d \sim 10$ Mpc). However, to optimise surface brightness, most nearby galaxy surveys were performed at configurations with $\approx 10''$. In this thesis, we adopt H I 21 cm emission from THINGS (and some supplemental VLA observations) to trace the atomic gas content in nearby galaxies, which is taken into account to estimate the pressure in the ISM disc in galaxies. We note that the new MeerKAT telescope in South Africa has recently been used to map nearby galaxies in H I 21 cm emission at $\sim 10''$ resolution but much higher sensitivity (de Blok et al., 2024; Eibensteiner, Sun et al., 2024). However, these observations have not been used in this work.

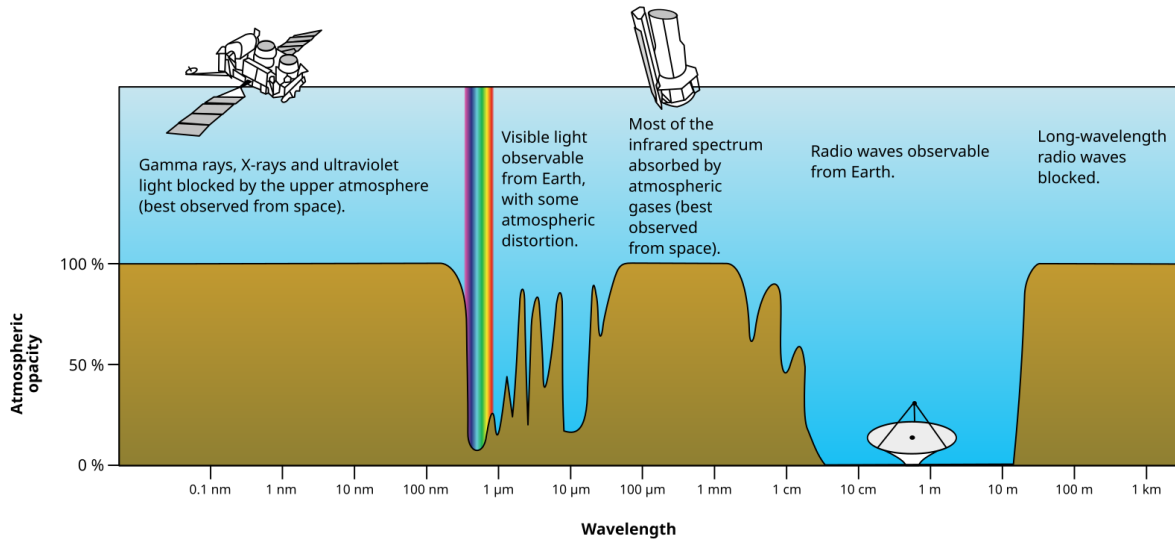


Figure 2.4: **Atmospheric electromagnetic transmission.** The brownish area indicates the opacity of Earth’s atmosphere across the electromagnetic spectrum. An opacity of 100 % means that no radiation from space will reach the ground, while an opacity of 0 % implies complete transmission of radiation. There are two big atmospheric windows (opacity ≤ 10 percent) at optical and radio wavelengths. Across the rest of the spectrum the atmosphere blocks most of the radiation from space. Note that the opacity depends on the location on Earth, that is, it decreases with altitude and is affected by the amount of water vapour along the line of sight. Image Credit: NASA.

Herschel

The *Herschel* telescope (Pilbratt et al., 2010), named after 18th century astronomers William and Caroline Herschel, was an infrared space observatory operated by ESA between 2007 and 2013 and designed to work at FIR to submillimetre wavelengths. Due to the opacity of Earth’s atmosphere at IR wavelength, space satellites are necessary to get access to this part of the spectrum, which is essential to study stars, dust and star formation in the universe. With its 3.5 m mirror, *Herschel* was the largest IR space telescope ever built until the launch of JWST. The three instruments onboard the spacecraft (PACS, SPIRE, HIFI) cover a wavelength range of 55 – 671 μm ideally suited to observe dust emission at angular resolutions of $\sim 10''$. For example with the Key Insights on Nearby Galaxies: a Far-Infrared Survey with Herschel survey (KINGFISH; R. C. Kennicutt, Calzetti et al., 2011), *Herschel* made major contributions to studying dust, gas and star formation in nearby galaxies. Moreover, *Herschel* produced widespread maps of FIR emission across the MW, such as the Herschel infrared Galactic Plane Survey (Hi-Gal; Molinari, Swinyard, Bally, Barlow, Bernard, P. Martin, Moore, Noriega-Crespo, Plume, Testi, Zavagno, Abergel, Ali, André et al., 2010), which is utilised in this thesis to estimate the physical conditions of the molecular ISM, such as the density and temperature.

Spitzer

The *Spitzer* Space Telescope (Werner et al., 2004), named after 20th century astrophysicist Lyman Spitzer, was an IR instrument operated by NASA. It was launched in 2003 and decommissioned in 2020, exceeding its predicted lifetime by more than eleven years. *Spitzer* employs an 85 cm mirror with imaging and spectroscopy instruments, designed to operate at 3 – 180 μm wavelengths via its MIPS

(Rieke et al., 2004) and IRAC (Fazio et al., 2004) instruments, where it reaches angular resolutions from $\sim 1''$ to 30° . With the Spitzer Infrared Nearby Galaxies Survey (SINGS; J. Kennicutt R. C. et al., 2003), *Spitzer* laid out the infrared science of nearby galaxies for years to come. In this work, we adopt *Spitzer* $3.6\ \mu\text{m}$ observations of nearby galaxies from the S⁴G survey (Sheth et al., 2010) to trace old stars, which can be used to infer the stellar mass distribution in galaxies.

WISE

One of the main drawbacks of *Spitzer* for surveying large parts of the sky is its limited field of view. To overcome this limitation at IR wavelength, NASA launched the Wide-field Infrared Survey Explorer (WISE; Wright et al., 2010) in 2009, with the purpose of creating an all-sky survey in the IR regime, which was completed in 2011. WISE has a 40 cm mirror and observed in four IR wavelength bands ($3.4\ \mu\text{m}$, $4.6\ \mu\text{m}$, $12\ \mu\text{m}$, $22\ \mu\text{m}$) referred to as WISE1, WISE2, WISE3, WISE4, or simply W1, W2, W3, W4, respectively, at angular resolutions $\lesssim 7.5''$. At these wavelengths, WISE detected, for example, emission of warm dust from galaxies, which can be utilised as an indirect probe of star formation. In this thesis, we utilise $22\ \mu\text{m}$ (W4) images of nearby galaxies to measure the star formation rate in nearby galaxies, adopting the maps from the $z = 0$ Multiwavelength Galaxy Synthesis study (z0MGS A. K. Leroy, Sandstrom et al., 2019).

JWST

Since the decommissioning of *Spitzer*, *Herschel*, and other infrared telescope (e.g. SOFIA), the IR universe has become inaccessible for astronomers for several years until the JWST opened up a whole new window of high resolution, high sensitivity IR astronomy. The JWST, named after former NASA administrator James Edwin Webb, is the biggest space telescope ever built, holding a 6 m mirror to observe near-to-mid-IR wavelengths at unprecedented resolution and depth. Operated by CSA, ESA, and NASA, the James Webb Space Telescope has been one of the biggest achievements of science and engineering. JWST harbours a whole suite of instruments for imaging and spectroscopy at IR wavelengths. The telescope is designed to operate at $0.6 - 28\ \mu\text{m}$ covering mostly emission of old stellar populations and hot dust in the local universe. With its revolutionising sensitivity, even exceeding the Hubble Space Telescope, it is the first telescope to detect galaxies at redshift beyond 10. Furthermore, JWST produces ground-breaking science in nearby galaxies, in particular with the PHANGS–JWST survey (Lee, Sandstrom et al., 2023), which mapped dust emission across a large sample of galaxies at $\sim 0.1''$ resolution (more details in Section 2.3.1).

VLT–MUSE

The Very Large Telescope (VLT) is an optical-to-near-IR telescope operated by ESO. In its extend, it consists of four 8 m telescopes, which can be correlated to work as an interferometer at near-IR wavelength to reach extremely high angular resolutions of order milliarcseconds, able to, for example, map the motion of stars around the centre of the MW. Besides, one of the VLT telescopes is equipped with an integral field spectrograph unit (IFU) called Multi Unit Spectroscopic Explorer (MUSE), which is capable of simultaneously detecting spectra while imaging a source. The PHANGS–MUSE survey (Emsellem et al., 2022) exploited the groundbreaking capabilities of MUSE to map optical spectra across the nearby galaxy population (more details in Section 2.3.1). At these optical wavelengths

(465 – 930 nm), VLT–MUSE can observe strong recombination lines such as $H\alpha$, $H\beta$, or $[OIII]$, which originate from the ionised gas phase. These lines can not only be used to study the physical conditions and kinematics of the ionised gas but also to, for example, observe indirect traces of star formation and to study the chemical composition of the ISM.

GALEX

The Galaxy Evolution Explorer (GALEX; C. L. Martin, 2005) was an ultraviolet space telescope operated by NASA. It was active from 2003 (launch) until 2013. The main purpose of GALEX has been to map UV emission across a large sample of galaxies to gain a deeper understanding of how galaxies are formed and evolve. The spacecraft’s instruments detected near- and far-UV emission collected via a 50 cm mirror to reach angular resolutions of $< 1''$. GALEX conducted an all-sky survey and dedicated deeper observations of 200 nearby galaxies. The FUV emission is tightly linked to the presence of young, massive stars and serves as an excellent tracer of the . Combined with IR 22 μm data from WISE, A. K. Leroy, Sandstrom et al. (2019) created extremely robust maps across the local galaxy population, which are adopted in this thesis.

2.3 Surveys

The backbone of this thesis are radio astronomical observations of nearby galaxies and galactic clouds, which are complemented with multi-wavelength observations (e.g. optical and infrared) at matched scales to physical processes and conditions of the multi-phase ISM. Four of the projects in this thesis (P1 to P4) have been carried out as part of the PHANGS collaboration (Section 2.3.1) and make extensive use of PHANGS observations and data products to supplement new ALMA observations presented in this thesis, such as the ALMOND survey (Section 2.3.1). The last project of this thesis (P5) investigates star-forming regions in the MW as part of IRAM 30 m large program LEGO (Section 2.3.2).

2.3.1 Physics at High Angular resolution in Nearby Galaxies (PHANGS)

The Physics at High Angular resolution in Nearby Galaxies (PHANGS) project aims to “understand the interplay of the small-scale physics of gas and star formation with galactic structure and galaxy evolution. [PHANGS utilises] observations of nearby galaxies [...] to understand how physics at or near the “cloud” scale are affected by galaxy-scale conditions, how they affect still smaller scale processes, and how these influence the evolution of whole galaxies”⁵. PHANGS was founded in 2016 as an international endeavour to bring together institutions from all over the world such that today the collaboration has more than 100 members. The collaboration is structured in working groups that focus on specialised topics which can be data or science-driven. As an affiliate member (since 2024 full member) of PHANGS via Prof. Frank Bigiel, I have actively contributed to the working groups “ALMA data reduction”, where I will take over a leading role from November 2024, and “Molecular ISM”, where most of the PHANGS projects presented in this thesis have been tracked and supported by the team. The base of the PHANGS sample comprises around 90 galaxies observed with ALMA so that PHANGS mainly uses southern hemisphere telescopes to build up a multi-wavelength data set of nearby galaxies. However, there are also plans to extend the sample to the northern hemisphere with the IRAM facilities. In the following,

⁵ www.phangs.org

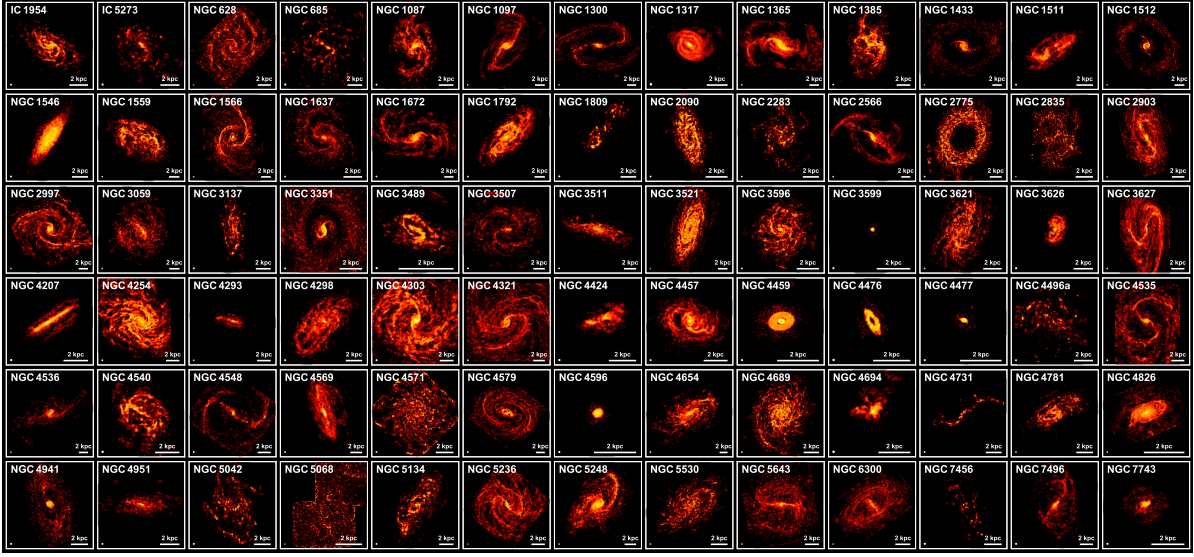


Figure 2.5: **The PHANGS–ALMA survey.** Shown are integrated intensity maps of CO (2 – 1) across 78 galaxies from PHANGS–ALMA. The colour map has an arcsinh strength and ranges from 0 to the maximum intensity of each individual galaxy.

we will briefly introduce and showcase some of the key PHANGS surveys, including legacy programs from ALMA (Section 2.3.1), VLT–MUSE (Section 2.3.1), and JWST (Section 2.3.1), which are relevant to this thesis. We note that the below-presented surveys are by far not complete to represent the rich coverage of nearby galaxies with PHANGS. There are, for example, additional surveys covering radio (with MeerKAT), optical (with HST), UV (with AstroSat), and x-ray wavelengths (with Chandra), as well as dedicated, detailed multi-transitions, multi-line sub-mm observations of individual targets (e.g. NGC 4321).

PHANGS-ALMA

The large program PHANGS–ALMA (A. K. Leroy, Schinnerer et al., 2021) utilised the groundbreaking capabilities of ALMA to produce the first survey of CO emission at $1'' \sim 100$ pc scales across 90 nearby galaxies. With only 1 – 2 hours of on-source observing time, ALMA can map CO (2 – 1) emission across a $\sim 2' \times 2'$ FOV with a sensitivity to detect individual GMCs with $M_{\text{mol}} > 10^5 M_{\odot}$. In order to gain a deeper understanding of the physical conditions of the ISM, star formation, the baryon cycle in galaxies, and galaxy evolution, it is crucial to study the distribution and kinematics of molecular gas in galaxies. Therefore, PHANGS–ALMA represents one of the most important milestones to understanding star-forming galaxies by mapping a representative sample of 90 nearby spiral galaxies. The sample was selected to represent the main sequence of star-forming galaxies in the current universe targeting a representative sample of galaxies that are nearby ($d \lesssim 20$ Mpc, so that $1 \leq 100$ pc), relatively face-on ($i \lesssim 75^\circ$ to distinguish gas clouds), visible to ALMA ($-75^\circ < \text{Dec.} < 25^\circ$), relatively massive ($\log_{10} M_{\star} \gtrsim 9.75 M_{\odot}$), and actively star-forming ($\text{SFR}/M_{\star} > 10^{-11} \text{ yr}^{-1}$, i.e. galaxies on the star-forming main sequence). The assembled sample spans over two orders of magnitude in stellar mass, star formation rate, and specific star formation rate across a wide range of galaxy morphologies from flocculent, over grand-design spiral, to strongly barred galaxies.

PHANGS–ALMA made use of the full capabilities of ALMA with its 66 antennas (12 m + 7 m + TP) to map the full molecular gas discs of 90 galaxies at $\sim 1''$ angular, 2.5 km s^{-1} spectral resolution at a sensitivity of 2 K per channel over only a few observing cycles (the core of 58 galaxies in Cycle 5). The PHANGS team developed an imaging pipeline (A. K. Leroy, Hughes et al., 2021) to create science-ready data products from the observations employing the data reduction software CASA. Along the position-position-velocity (ppv) cubes of CO (2 – 1) line emission, the pipeline produced additional data products, including moments (mom-0, mom-1, mom-2), peak intensity and line width maps (see Section 3.1.4 for more details on data products), all of which have been made publicly available⁶.

Figure 2.5 presents a compilation of CO (2 – 1) integrated intensity maps from the latest data release (DR4) to showcase the PHANGS–ALMA survey. In this thesis, we will make extensive use of PHANGS–ALMA data to trace the properties of the bulk molecular gas. Moreover, being typically the most significantly detected line, we employ the line emission of CO (2 – 1) as a prior to mask and uncover emission of fainter lines such as, for example, HCN (1 – 0) via velocity-masking or stacking (see Section 3.1.4 and Section 3.2.2).

PHANGS-MUSE

PHANGS–MUSE (Emsellem et al., 2022) used the integral field spectrograph MUSE at the VLT to map 19 of the PHANGS–ALMA galaxies in optical emission lines. In contrast to common optical observations, which use either narrow or wideband filters, the integral field spectrograph onboard the VLT enables mapping of spectra across optical wavelength comparable to radio observations. PHANGS–MUSE detected 15×10^6 spectra, including optical emission lines like H α , H β , [SII], or [OIII] and provides the first integral field spectrograph view of SF across external galaxies. The optical emission line gives access to studying the ionised phase of the ISM, which is tightly linked to energetic processes in galaxies such as star formation.

Figure 2.6 (left panel) shows three-colour images across the observed galaxies from PHANGS–MUSE. The goal of PHANGS is to extend this sample to eventually cover the full 90 galaxies of the PHANGS–ALMA sample, which is however challenging due to the immense over-subscription rate of the MUSE instrument. Here, we will not go into the detailed science applications of PHANGS–MUSE, which include the characterisation of H₂ regions, stellar kinematics and SF history. In this work, we adopt the Balmer-decrement corrected H α maps, produced by the PHANGS–MUSE team, as a tracer of the at high angular resolution ($1'' \sim 100 \text{ pc}$), which, until JWST (Section 2.3.1), no other tracers (e.g. IR or UV) could provide.

PHANGS-JWST

The JWST opened up a completely new window into studying the multi-phase ISM in nearby galaxies at cloud scales, perfectly matched to the goals of the PHANGS collaboration. Hence, PHANGS took a big attempt towards mapping their galaxy sample with the JWST and got granted a large treasury program to map 19 galaxies (matching the MUSE sample) in Cycle 1 using the Near Infrared Camera (NIRCam) and Mid-Infrared Instrument (MIRI) instruments (Lee, Sandstrom et al., 2023). These instruments cover a wavelength range from 3 to 21 μm , where the SED is dominated by emission from hot dust and polycyclic aromatic hydrocarbons (PAH), which are linked to various physical processes in the ISM including star formation. In addition, dust is well mixed with gas so that the distribution and properties of dust can

⁶ <https://www.canfar.net/storage/list/phangs/RELEASES/PHANGS-ALMA>

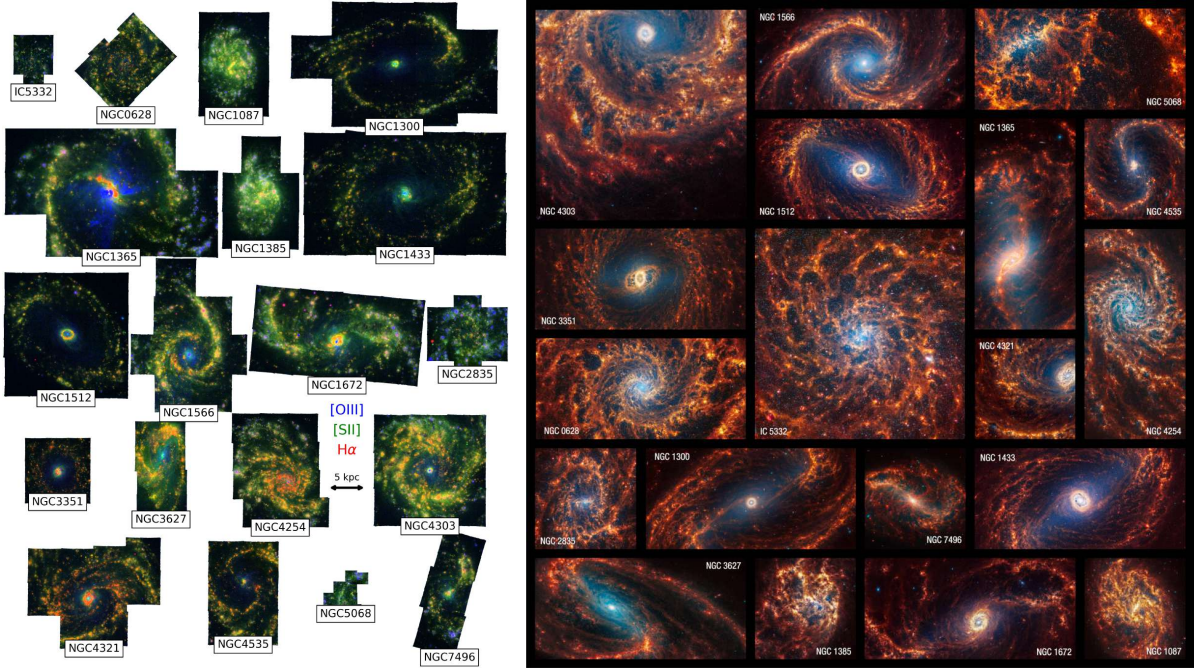


Figure 2.6: **The PHANGS-MUSE and PHANGS-JWST surveys.** *Left:* Three-colour composite images of 19 galaxies from PHANGS-MUSE. Red, green and blue represent emission from the optical recombination lines H α , [SII] (ionised sulfur), and [OIII] (ionised oxygen), respectively. The maps are scaled to the same linear scale. The figure is reproduced from Emsellem et al. (2022). *Right:* Shown are colour-composite images of the 19 first galaxies that have been mapped by JWST in the Cycle 1 treasury program. Red colours represent MIRI filters and blue colours are composed of NIRCAM data. This figure was adopted from Williams et al. (2024).

be used to study the structure of ISM and link to the gas conditions inferred from PHANGS-ALMA. Compared to PHANGS-ALMA, the JWST have the big advantage that they have a \sim factor 10 higher resolution and sensitivity so that smaller structures of the ISM can be detected and studied.

The beautiful PHANGS-JWST images (Figure 2.6, right panel) have created widespread response in the press, showing an incredible amount of detail. In this thesis, we adopt the MIRI 21 μ m observations of NGC 4321 (Chapter 7) as a secondary probe of the (in addition to H α from MUSE). These data have been processed through the PHANGS-JWST pipeline (Williams et al., 2024) and provide a $< 1'' \sim 100$ pc view on star formation via dust-processes emission from massive stars.

ACA Large-sample Mapping Of Nearby galaxies in Dense gas (ALMOND)

PHANGS-ALMA laid out the ground for studying the molecular ISM in a large sample of nearby galaxies. However, CO (2 – 1) only traces the bulk molecular gas ($n \approx 1 \times 10^2 \text{ cm}^{-3}$) and not the dense molecular gas ($n \gtrsim 1 \times 10^4 \text{ cm}^{-3}$) which is more tightly linked to star formation. Thus, in order to gain a deeper understanding of the SF process in galaxies, higher-density gas tracers are needed, such as HCN (1 – 0), HCO $^+$ (1 – 0), or CS (2 – 1). Until 2017, not much more than a handful of nearby galaxies have been mapped in dense gas tracers such as HCN (1 – 0). The EMPIRE survey (Jiménez-Donaire, Bigiel, A. K. Leroy, Usero et al., 2019) was the first larger survey of nearby galaxies in dense gas, using the IRAM 30 m telescope to map nine northern hemisphere galaxies in HCN, HCO $^+$ and HNC at

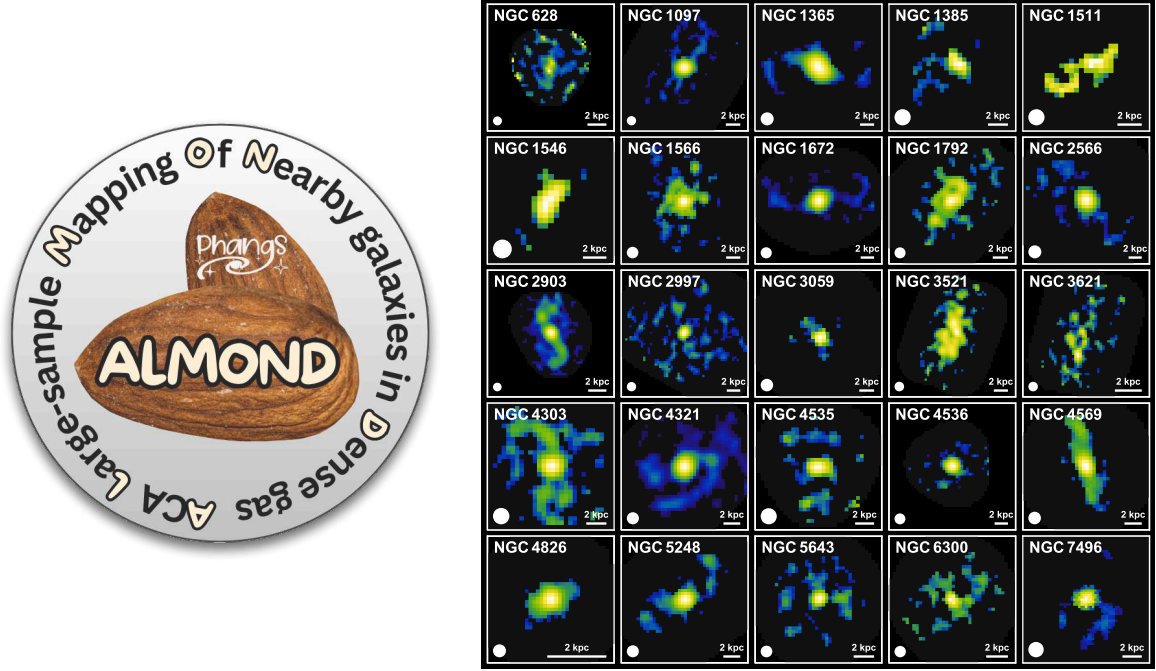


Figure 2.7: **The ALMOND survey.** Shown are integrated intensity maps of HCN ($1 - 0$) across the 25 galaxies from the ALMOND survey. The colour map has an arcsinh strength scaled for each galaxy individually. Line intensity maps of HCO^+ , CS and ancillary CO ($2 - 1$) are presented in the Appendix Appendix D.1.

$\sim 30'' \sim 2$ kpc resolution. However, the EMPIRE sample has only a small overlap of three galaxies with the PHANGS sample. Therefore, Gallagher, A. K. Leroy, Bigiel, Cormier, Jiménez-Donaire, E. Ostriker et al. (2018) mapped five PHANGS galaxies in dense gas tracers using the ALMA-ACA.

Certainly, the existing observations covered only a few galaxies, especially when compared to the PHANGS sample, such that new observations were necessary to conduct a statistically significant study of dense gas conditions and star formation laws in nearby galaxies. Therefore, PHANGS achieved a large sample dense gas campaign to map 25 nearby galaxies with ALMA in HCN ($1 - 0$), HCO^+ ($1 - 0$), CS ($2 - 1$), divided over three observing cycles from 2017 to 2019 using more than 300 hours of ALMA time. The observations were optimised to map a large number of galaxies, while still detecting dense gas tracers across most of the molecular gas discs, using the ACA with a resolution of $\sim 20'' \sim 1$ kpc. The survey has been coined ALMOND (Neumann, Gallagher et al., 2023) and is one of the key data sets of this thesis. This survey has extended the current sample of kiloparsec scale dense gas maps by more than a factor of two and is accompanied by excellent ancillary data from ALMA, MUSE, and JWST (among others) providing the richest nearby galaxies dense gas survey to date. The ALMOND survey paper was first led by Molly Gallagher (a former student of Adam Leroy) but transferred to me during the time of my Master’s thesis (in the group of Frank Bigiel). The imaging was carried out with the PHANGS–ALMA pipeline (A. K. Leroy, Hughes et al., 2021), led by Ashley Barnes, after which we received the science-ready data cubes, from which we performed all further analysis steps. Figure 2.7 shows HCN ($1 - 0$) integrated intensity maps of the 25 ALMOND galaxies.

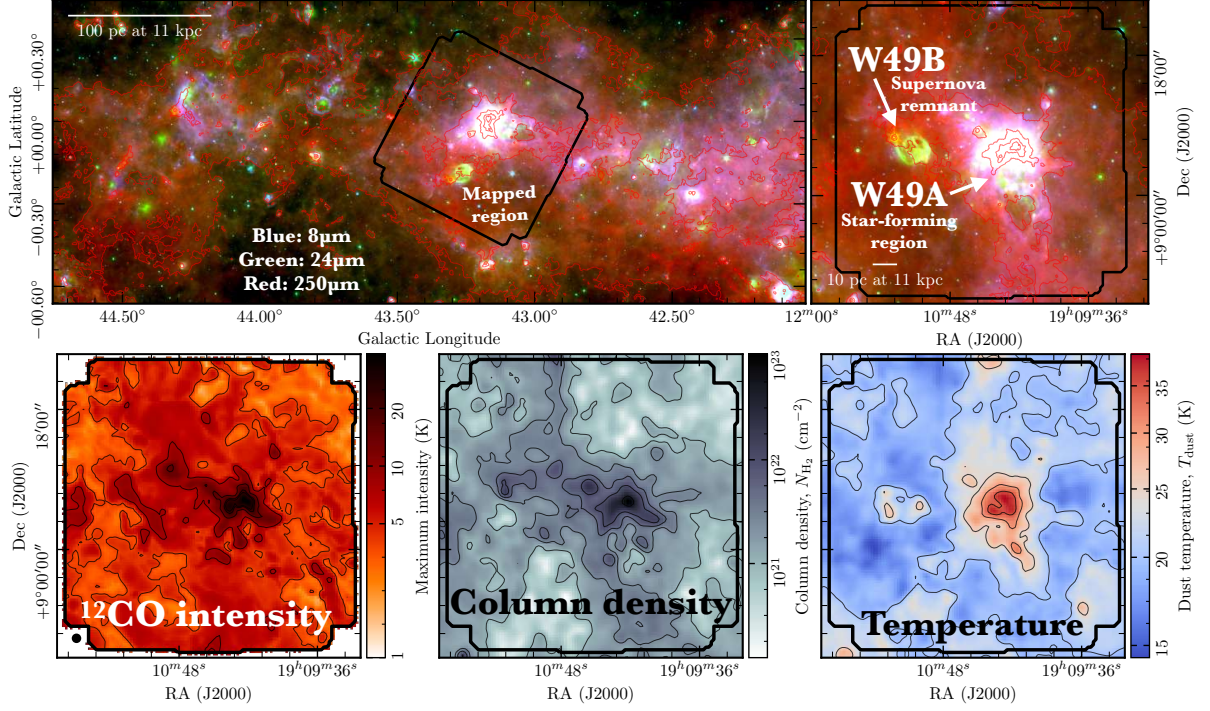


Figure 2.8: **LEGO: Massive star-forming region W49.** The top panels show a colour-composite image showing infrared emission from *Spitzer* and *Herschel* to highlight the dust and hence gas distribution. The black contours denote the FOV of the LEGO observations. The bottom panels show the ^{12}CO (1 – 0) peak intensity, dust-inferred column density and dust temperature, pointing out the potential of the data set to study the line emission of more than 20 lines in the column density-temperature plane. The figure is adopted from Barnes, Kauffmann et al. (2020).

2.3.2 Line Emission as a Tool for Galaxy Observations (LEGO)

Over many decades (going back to Kwan and Scoville, 1975), the use of HCN (1 – 0) emission (among other lines), despite its nominal high critical density ($n_{\text{crit}} = 1 \times 10^6 \text{ cm}^{-3}$), has been questioned as a tracer of dense molecular gas due to its theoretically predicted and observationally supported lower effective excitation density, $n_{\text{eff}} = 1 \times 10^3 \text{ cm}^{-3}$ (e.g. Shirley, 2015). While extragalactic studies have continued using these lines to study dense gas in galaxies (e.g. Gao and Solomon, 2004), Galactic works have concentrated on either different tracers (e.g. N_2H^+ (1 – 0)) or observing only the very dense clumps of clouds, making a sophisticated comparison to extragalactic studies impossible. Therefore, the LEGO survey (PI: Jens Kauffmann) requested more than 400 hours of IRAM 30 m time to observe a representative sample of 14 molecular cloud regions (Table D.1) in the MW in the 1 mm wavelength range (including more than 20 detected lines; Table D.2) typically used to probe molecular gas conditions in galaxies. The novel approach of LEGO is that the sources are selected across environments from the inner to the outer galaxies and include the most massive star-forming region in the galaxy, which would dominate the emission if the MW would be viewed as an extragalactic target. Moreover, LEGO mapped large FOVs ($0.5^\circ \times 0.5^\circ$) to capture the full extent of the molecular cloud. This is crucial since a large fraction of the HCN emission might arise from low-to-intermediate density gas, which is inevitably included in extragalactic observations that average over whole clouds due to the coarse physical resolution.

In a first letter, Kauffmann, Goldsmith et al. (2017) presented new LEGO observations of Orion B, which studies the capabilities of extragalactic dense gas tracers, finding that HCN ($1 - 0$) is also emitting from intermediate-density gas in contrast to N_2H^+ ($1 - 0$) which is only efficiently emitting in the cold, dense gas. The second LEGO paper (Barnes, Kauffmann et al., 2020) focuses on the W49, one of the most massive star-forming regions in the MW, and showcases the richness of the observations, presenting spectra, maps and scaling relations of all detected lines, as well as studying their emission properties in the density-temperature plane. These first science highlights show the impact of LEGO to better interpret molecular line observations of galaxies. In this thesis, we specifically focus on the massive star-forming regions of the LEGO sample, which provide the most direct comparison to extragalactic studies of nearby, star-forming galaxies from PHANGS.

Analysis Techniques

“Science is magic that works.”

Kurt Vonnegut – 20th century writer

3.1 PyStructure

Studies of the ISM often deal with multi-instrument, multi-wavelength, multi-temporal observations of the same astrophysical objects, e.g. molecular clouds or galaxies. However, observations from different instruments across the electromagnetic spectrum typically come at different angular (and spectral) resolutions and are sampled on different coordinate grids. Therefore, these data sets must be spatially and spectrally homogenised and reprojected onto the same coordinate system. The group of Prof. Frank Bigiel has developed a python package called `PyStructure`, which automates the above steps, allowing easy and quick data processing and analysis of multi-observation data sets of the same or a large sample of targets in a homogeneous way. The basis of the `PyStructure` code goes back to the methodology introduced by Rosolowsky and A. Leroy (2006) to create homogenised data sets and multi-line data products. In its original form, the code was written in IDL, mainly maintained and improved by Maria J. Jimenez-Donaire until it was translated to python by Jakob S. den Brok in 2019 and further refined by Ivana Bešlić and Jakob S. den Brok during their time as PhD students in the group of F. Bigiel. Since joining the group in October 2020, I have continuously helped improve and extend the code’s functionality. In October 2023, Jakob S. den Brok and we facilitated a first public release of the code via `GitHub`¹ along with a quick start documentation². The code has been utilised in several extragalactic studies, including large programs such as EMPIRE (Jiménez-Donaire, Bigiel, A. K. Leroy, Usero et al., 2019), CLAWS (den Brok, Bigiel, Sliwa et al., 2022), ALMOND (Neumann, Gallagher et al., 2023), and SWAN (Stuber et al., 2023), as well as various spectroscopic studies of nearby galaxies supported by the PHANGS collaboration (Bešlić et al., 2021; den Brok, Chatzigiannakis et al., 2021; Eibensteiner, Barnes et al., 2022; Eibensteiner, Bigiel et al., 2023; den Brok, Bigiel, Chastenet et al., 2023; den Brok, A. K. Leroy et al., 2023; Neumann, Bigiel et al., 2024).

The basic idea behind the `PyStructure` package is to assemble a set of homogenised observations into one big database and to create simple data products, such as moment maps. Figure 3.1 illustrates

¹ <https://github.com/jdenbrok/PyStructure>

² <https://pystructure.readthedocs.io>

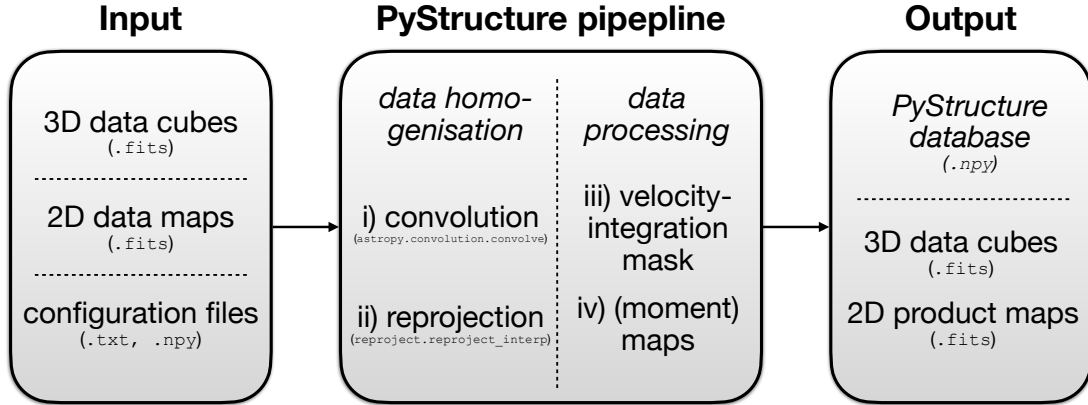


Figure 3.1: **PyStructure workflow.** *Left:* Input files: three-dimensional position-position-velocity cubes (usually radio line emission cubes, e.g., CO (2 – 1)), two-dimensional maps (e.g. infrared emission to trace the star formation), and configuration files, which define the parameters of the pipeline, e.g. the location of the files, the definition of the so-called “overlay” file to define the coordinate system and common resolution, or the selection of priors used to create velocity-integration mask. *Middle:* PyStructure pipeline: There are two main steps: 1) data homogenisation, where all input data files are convolved to the same resolution (Section 3.1.2) and reprojected onto a common grid (Section 3.1.3) and 2) computation of data products, where a velocity-integration mask is created to select the voxels of significant line emission in order to compute moment maps and other data products (Section 3.1.4). *Right:* Output: The pipeline returns a single database per source as a `numpy` dictionary, which contains the homogenised and processed data from all input files. The convolved data cubes and produced images (data products) can optionally be saved as FITS files.

a schematic of the PyStructure workflow. For any given source, e.g. a galaxy or a molecular cloud region, the PyStructure code takes a set of observations (stored as FITS files; Section 3.1.1) that share a similar spatial region on the sky. Those observations can be position-position-velocity (ppv) cubes, i.e. three-dimensional, or position-position maps, i.e. two-dimensional, and do not need to be at the same angular resolution or coordinate grid. The PyStructure pipeline will homogenise the data sets and produce moment maps from the ppv cubes. The data homogenisation involves two main steps: 1) convolution to a common resolution (Section 3.1.2) and 2) reprojection onto the same pixel grid (Section 3.1.3). After homogenisation, the pipeline further processes the data from the cubes to produce moment maps (Section 3.1.4). The final homogenised data sets and products are stored in a single file (per source) as a `python` dictionary, which is basically a table where each row corresponds to one spaxel³ and each column specifies the value of any given quantity. The big advantage of such a database is that it allows straightforward comparison on a pixel-by-pixel (or spaxel-by-spaxel) basis of multi-wavelength, multi-instrument observations without further data reduction steps. Moreover, the data processing is specifically optimised to deal with multi-line, spectroscopic data in the (sub-)mm/radio regime. It allows building a velocity-integration mask based on a high-significant prior (e.g. CO) that is applied to the fainter lines (e.g. HCN) to potentially recover more emission. The following subsection (Sections 3.1.2 to 3.1.4) gives a detailed description of the key data processing steps executed by the PyStructure pipeline. Moreover, Section 3.1.1 briefly introduces the FITS formation, which is the default file format for astronomical data.

³ The elements of a 2D image are called pixels. For 3D position-position-velocity cubes, we can differentiate between spatial pixels, called spaxels, and velocity pixels, called voxels.

3.1.1 FITS format

The most widely used format to store astronomical data is the so-called FITS format⁴. FITS stands for Flexible Image Transport System and is designed to store scientific multidimensional arrays (images or cubes) and tables. A FITS file consists of Header/Data Units (HDUs), which can be one-dimensional (spectrum), two-dimensional (image), or three-dimensional (cube). These HDUs contain a primary array, which can be followed by an arbitrary number of additional extensions, such that a single FITS file can also contain a whole suite of data sets. The header unit comprises a list of keywords in ASCII format, which contain metadata about the observations as well as information about the coordinate system in order to link the spaxel coordinates to real positions on the sky and spectral channels to real frequency or velocity values. The data unit comprises the scientific data as 1D, 2D or 3D arrays, in 8-, 16- (only for integers), and 32-, 64-bit representation.

There exist common FITS viewers, which can load and visualise FITS files, such as SAOImageDS9⁵ or Carta⁶. Moreover, widely used programming languages in astrophysics, predominantly python, provide easy-to-use routines to load, manipulate and save FITS files. The main programming language used for the data analysis of this thesis is python, which comes with plenty of user-friendly libraries to manipulate data arrays using numpy (Harris et al., 2020), run mathematical operations and algorithms via scipy (Virtanen et al., 2020), plot and visualise data with matplotlib (J. D. Hunter, 2007), as well as processing astronomical data using astropy (Astropy Collaboration, Robitaille et al., 2013; Astropy Collaboration, Price-Whelan, Sipőcz et al., 2018; Astropy Collaboration, Price-Whelan, Lim et al., 2022).

3.1.2 Convolution

To spatially homogenise the data, the PyStructure pipeline performs a spatial, two-dimensional (2D) convolution with a 2D Gaussian kernel to the angular resolution of a reference file, or any given angular resolution, which can be specified in the configuration settings. This procedure assumes that the beam of the respective loaded data sets is well approximated by a two-dimensional Gaussian function, which is typically fulfilled for many science-ready maps or cubes. The convolution smooths the intensity distribution, such that it artificially mimics observing the source at a lower resolution. In the pipeline, all operations are performed in pixel units and hence all physical units are converted into pixel units.

To convolve from a higher, original resolution θ_{original} to a lower, target resolution θ_{target} , a two-dimensional Gaussian kernel of the form

$$\Omega_{\text{kernel}}(x, y; \sigma) = \frac{1}{2\pi\sigma^2} \exp\left(-\frac{x^2 + y^2}{2\sigma^2}\right) \quad (3.1)$$

is generated using the astropy function `convolution.Gaussian2DKernel`, where x, y are the pixel coordinates and σ is the standard deviation of the Gaussian⁷. The resolution (θ) is usually expressed as

⁴ <https://fits.gsfc.nasa.gov>

⁵ <https://sites.google.com/cfa.harvard.edu/saoimageds9>

⁶ <https://cartavis.org>

⁷ Note that most single-dish telescope beams are axisymmetric and can be well described by a symmetric 2D-Gaussian function. However, interferometers often yield asymmetric beams due to asymmetric sampling of the uv -plane. Therefore, PyStructure can also deal with asymmetric beams as long as the geometry of the beam (minor axis, major axis and orientation) is provided.

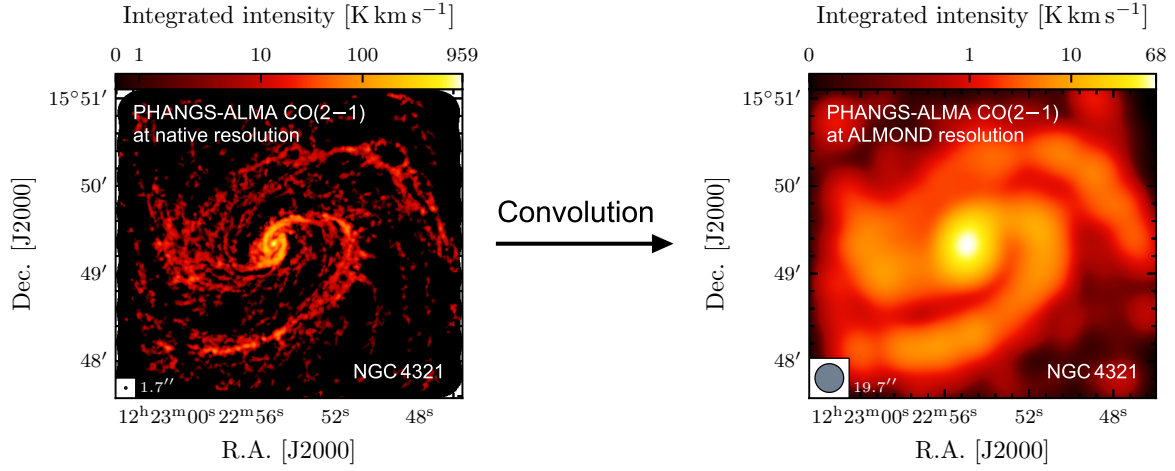


Figure 3.2: **Convolution to a common spatial resolution.** The left panel shows the CO (2 – 1) integrated intensity map of NGC 4321 from the PHANGS–ALMA survey (A. K. Leroy, Schinnerer et al., 2021) at its native angular resolution of $1.7''$. The right panel presents the same map convolved to an angular resolution of $19.7''$, i.e. the resolution of the HCN (1 – 0) data from the ALMOND survey (Neumann, Gallagher et al., 2023). The convolution is performed via the `astropy` function `convolution.convolve`, using a Gaussian kernel. Note that the PyStructure pipeline runs the convolution on the ppv cubes for each respective channel and not on the integrated intensity maps, which are here only shown for illustration purposes.

the full width at half maximum (FWHM) of the beam. For a Gaussian beam, the FWHM is related to the standard deviation via $\theta = 2\sqrt{2 \ln 2} \sigma \approx 2.355 \sigma$. The above-generated kernel is then applied to the map:

$$F(x, y; \theta_{\text{target}}) = F(x, y; \theta_{\text{original}}) \otimes \Omega_{\text{kernel}}(x, y), \quad (3.2)$$

where $F(x, y; \theta)$ describes the value of any arbitrary quantity, e.g. the intensity of CO (1 – 0), at spaxel position x, y , at resolution θ , and \otimes denotes the convolution operation. The convolution is numerically implemented via the `convolution.convolve` function from the `astropy` package⁸. For 3-dimensional cubes, the convolution is run for each spectral (or velocity) channel, or in other words for each spatial layer within the cubes, utilising the fast Fourier transform method `convolution.convolve_fft` from `astropy`, which is generally faster for large arrays. Figure 3.2 illustrates the convolution of a suit of observations to a common best resolution⁹.

Spectral smoothing

Position-position-velocity data cubes have, in addition to their two spatial axes, a spectral or Doppler shift-related velocity axis with a given resolution. The native velocity resolution is related to the channel width of the receiver, but can be adjusted to a coarser resolution in the imaging step of the data reduction (e.g. in CASA) to gain higher S/N per channel. Note that the channel width is not identical to spectral resolution, but can be much smaller than the actual velocity resolution, similar to an oversampled pixel

⁸ The convolution function is specifically designed to work on astrophysical data and can interpolate regions containing nan values, which is the key difference to other `python` convolution functions, such as the `signal.convolve` function from the `scipy` package.

⁹ The data shown in Figure 3.2 have entered the work presented in Chapter 7

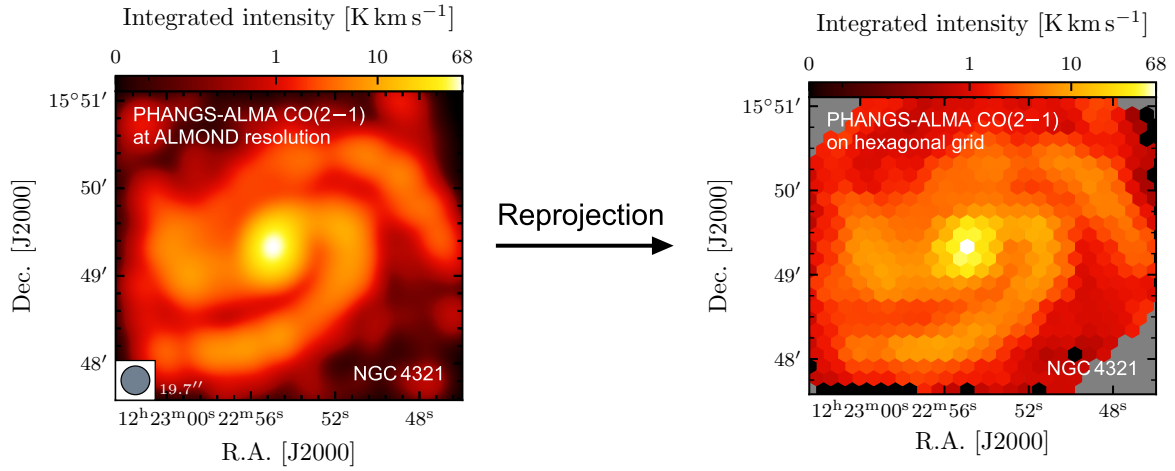


Figure 3.3: **Reprojection onto a common, hexagonal spaxel grid.** The left image shows the convolved CO (2 – 1) integrated intensity map of NGC 4321 (right panel of Figure 3.2). The PyStructure code creates a hexagonal spaxel grid centred on the central position of the source. The separation of the hexagonal spaxels is (by default) half of the beam size in both coordinate axes. We note that the reprojection step is flux conserving, i.e. the total flux in the reprojected image equals the total flux of the previous image.

image. Typically multi-line data cubes originating from the same survey and processed through the same data reduction pipeline have matched velocity resolution. In general, data cubes from different surveys can have different velocity resolutions and PyStacker can smooth the velocity axis of higher-spectral resolution cubes to obtain matched velocity resolution. Naively, one could think that the spectral axis can be smoothed using a one-dimensional Gaussian kernel. However, this will create a channel-to-channel correlation, which yields biased-low root mean square (rms) noise estimates and hence biased-high estimates of the S/N of integrated intensities of molecular lines. The most robust approach to smoothing the spectral axis is to bin adjacent channels together, which is the default spectral smoothing setting implemented by PyStacker if spectral smoothing is needed. This approach has the downside of allowing only smoothing to integer multiples of the current channel width but guarantees proper noise propagation. In general, the recommended way of matching the spectral resolution is to adjust the channel width during the data reduction process.

3.1.3 Reprojection

The convolution step described in Section 3.1.2 has been done on the original coordinate grids of each respective input data. Producing a unified database requires resampling all maps and cubes onto the same spatial and spectral pixel grid. The spatial and spectral reprojection onto a common ppv cube is shown in Figure 3.3. PyStructure takes the “overlay file” as a reference to create the unified ppv coordinate grid.

The spatial reprojection can conveniently be performed using the package `reprojection`, which is based on `astropy`. However, PyStructure has a unique approach and resamples onto a newly generated hexagonal spaxel grid, which has the key advantage that every spaxel has the same distance to its neighbouring spaxels, such that statistics involving spaxel-by-spaxel correlations (e.g. when computing propagated uncertainties) are well-defined. With the default settings, a hexagonal spaxel grid

is created, where the distance between two neighbouring spaxels is exactly half the beam size hence fulfilling the Nyquist–Shannon sampling theorem¹⁰. This sampling yields an oversampling factor of about four, i.e. the area of the beam encloses four spaxels. We note that the settings can be modified to create any arbitrary spaxel spacing. For instance, in projects P3 (Chapter 6) and P4 (Chapter 7), we adopt a beam size spaxel spacing, i.e. each spaxel has the same size as the beam, such that all spaxels are independent measurements. Similarly to the spatial reprojection, PyStructure resamples the spectral data onto a common velocity axis taking two spectral samples per velocity resolution, again fulfilling the Nyquist–Shannon sampling theorem.

3.1.4 Products and moment maps

After the above steps (convolution and reprojection) the input data sets have successfully been homogenised, i.e. all cubes and maps are at the same spatial and spectral resolution and on a common coordinate grid. Line cubes contain a wealth of information due to the spectral axis in addition to the two spatial axis. In the following, we will describe the creation of so-called “moment maps”, which are produced by the PyStructure pipeline from the convolved, reprojected line cubes. The idea of moment maps is to collapse the information of each spectrum, i.e. along each line of sight, into a single value. Mathematically, this is achieved via integration of a function that depends on velocity v , e.g. the brightness temperature $T_B(v)$ along the velocity axis. Sections 3.1.4 to 3.1.4 summarise the most important moments (moments 0 to 2) used in this work, which physically quantify the integrated intensity of the line, as well as the mean velocity and velocity dispersion of the gas from which the line is originating.

Velocity-integration mask

In order to compute the moments across the velocity range where emission is expected, PyStructure builds a mask to identify this velocity range. The velocity-integration mask is created using one or several “priors”, i.e. typically the most significantly detected lines across the cube. The mask is built employing the following procedure on a spaxel-by-spaxel basis, i.e. for each sightline individually:

1. **rms estimation:** The noise level within each spectrum is estimated from the median absolute deviation (MAD) of the intensities via the `scipy.stats` function `median_abs_deviation`, which is a measure of the standard deviation of a distribution that is more robust against outliers, i.e. the MAD is less driven by the emission line. Then, all intensities above three times the MAD¹¹ are cut and the computation of the MAD is repeated in order to estimate the rms from the emission-free channels, hereafter referred to as σ_T .
2. **Low-S/N and high-S/N mask:** There are two initial masks that are built based on the above-estimated rms, a) a low-S/N mask, which considers all voxels above $2\sigma_T$, and b) a high S/N-mask,

¹⁰ The Nyquist–Shannon sampling theorem states that there are at least two samples, i.e. data points, per (spectral or spatial) wavelength necessary to reconstruct the true information of the signal (spectral) or image (spatial). This means that a spectrum has to be sampled with at least twice the frequency as the frequency of the signal. For an image, the Nyquist–Shannon sampling theorem implies that at least two samples per beam size per spatial axis are needed to retain the full spatial information.

¹¹ Actually, for a Gaussian distribution the MAD is approximately 0.67 times the standard deviation. Hence, we multiply the MAD by 1.48 to get robust measure of the standard deviation.

which selects voxels above $4\sigma_T$ (the mentioned σ_T -threshold values are the default parameters that work sufficiently well in most cases, but can be modified in the pipeline configurations).

3. **Master mask:** Afterwards, the high-S/N mask is expanded into the low-S/N mask, so that only voxels above $2\sigma_T$ that contain a $\geq 4\sigma_T$ peak end up in the final mask.
4. **Combined mask:** If more than one line is used to define the mask, those masks are combined via a logical OR operation, so that the velocity range detected by either of these lines is included in the integration.

The final combined mask (the grey shaded area in Figure 3.4) is applied to all lines to compute the moment maps. In the formulas below it is labelled as $\delta(x, y, v)$, which is a three-dimensional array of the same dimensions as the ppv cube and contains ones for emission voxels and zeros for emission-free voxels. Hence, multiplying a quantity in the ppv cube, e.g. the brightness temperature $T_B(x, y, v)$, with $\delta(x, y, v)$ sets all values in emission-free voxels to zero. The inverse (zeros for emission voxels and ones for emission-free voxels) mask is referred to as $\tilde{\delta}(x, y, v)$ and consequently selects only the emission-free voxels, which is utilised to study the noise properties of the cube. This step assumes that all lines share the same velocity field, which is typically a good assumption for observations of molecular lines from galaxies. However, for high-spectral resolution observations of Galactic clouds, this assumption is not necessarily valid anymore, since the fine structure of the molecular lines can be resolved. Therefore, in project P5 (Chapter 8), where the fine structure of many lines can be resolved, we comment on some modifications of the velocity masking.

Moments

The mathematical definition of moments is given in the following way:

$$M_0 = \int F(s) ds \quad (3.3)$$

$$M_1 = \frac{1}{M_0} \int F(s) s ds \quad (3.4)$$

$$M_n = \frac{1}{M_0} \int F(s) (s - M_1)^n ds, \quad (3.5)$$

where $F(s)$ is a function depending on the variable s and M_n is the n th moment, i.e. M_0 is the 0th moment, M_1 the 1st moment, etc. Applied to radio astronomical data, i.e. ppv cubes containing brightness temperatures T_B as a function of the spatial coordinates x, y and the spectral/velocity coordinate v , the moments computed along the velocity axis are given as:

$$M_0(x, y) = \int T_B(x, y, v) dv \quad (3.6)$$

$$M_1(x, y) = \frac{1}{M_0} \int T_B(x, y, v) v dv \quad (3.7)$$

$$M_n(x, y) = \frac{1}{M_0} \int T_B(x, y, v) (v - M_1)^n dv, \quad (3.8)$$

where the integral is taken over the velocity axis in each spatial position x, y , respectively. In the

following sections, we will discuss the first three moments, explain how they are computed in the PyStructure pipeline, and comment on their physical interpretation.

Integrated intensity (moment-0)

The moment-0 (in short, mom-0; $M_0(x, y)$) is the most simple map that can be created from a cube, which is simply the integration of the intensity or brightness temperatures $T_B(x, y, v)$ along the velocity axis v :

$$W(x, y) \equiv M_0(x, y) = \int_{\text{mask}} T_B(x, y, v) dv = \sum_i T_B(x, y, v_i) \delta(x, y, v_i) \Delta v_{\text{ch}} \quad (3.9)$$

Therefore, it is also commonly referred to as the “integrated intensity” or “line intensity” map ($W(x, y)$), which is often used to estimate the gas column density or gas mass assuming a certain line traces the amount of molecular gas above a certain density threshold (Section 1.3.3). For instance, in projects P3 (Chapter 6) and P4 (Chapter 7), we employ the integrated intensity of the rotational transitions of CO and HCN to trace the total molecular gas and dense molecular gas surface densities, respectively. For a Gaussian emission line, the mom-0 is equivalent to the area of the Gaussian, i.e. $W = \sqrt{2\pi} T_{\text{peak}} \sigma$, where T_{peak} and σ are the peak and standard deviation of the Gaussian. The uncertainty of the integrated intensity is computed from the noise in the emission free-channels, i.e. the standard deviation of the pure-noise intensities ($\sigma_T(x, y) = \text{std}[T_B(x, y, v_i) \delta(x, y, v_i)]$), the square root of the number of channels within the velocity-integration mask ($\sqrt{\sum_i \delta(x, y, v_i)}$), and the channel width (Δv_{ch}):

$$\sigma_W(x, y) = \sigma_T(x, y) \left(\sum_i \delta(x, y, v_i) \right)^{1/2} \Delta v_{\text{ch}} \quad (3.10)$$

The uncertainty estimation assumes that the noise of the brightness temperature is propagated to the integrated intensity via Gaussian error propagation. Above Equations 3.9 and 3.10 imply that if a line is detected ($T_B/\sigma_T \geq 3$) in 10 consecutive voxels the signal-to-noise ratio of the integrated intensity (W/σ_W) is at least $3 \cdot \sqrt{10} \approx 9$. Therefore, integrated intensities typically yield higher S/N maps than individual channel maps. Moreover, spectra of faint emission lines (e.g. HCN in extragalactic observations) that are not detected in individual channels, might be detected in the mom-0 map, if a high-significant prior is used to select the velocity range, where emission from fainter lines is expected. The recovery of faint emission lines is further discussed in Section 3.2, where a high-significant prior is not only used to build the velocity-integration mask but also to stack several spectra in order to recover even fainter lines.

Mean velocity (moment-1)

The first moment (moment-1, or short mom-1) is given by:

$$\bar{v}(x, y) \equiv M_1(x, y) = \frac{1}{M_0(x, y)} \int_{\text{mask}} T_B(x, y, v) v dv \quad (3.11)$$

$$= \frac{1}{W(x, y)} \sum_i T_B(x, y, v_i) \delta(x, y, v_i) v_i \Delta v_{\text{ch}}, \quad (3.12)$$

Table 3.1: PyStructure products.

Map	Expression & Uncertainty	Unit
Integrated intensity (mom-0)	$W(x, y) = \sum_i T_B(x, y, v_i) \delta(x, y, v_i) \Delta v_{\text{ch}}$ $\sigma_W(x, y) = \sigma_T(x, y) \left(\sum_i \delta(x, y, v_i) \right)^{1/2} \Delta v_{\text{ch}}$	K km s^{-1}
Peak intensity	$T_{\text{peak}}(x, y) = \max_{v_i} [T_B(x, y, v_i) \delta(x, y, v_i)]$ $\sigma_T(x, y) = \text{std}_{v_i} [T_B(x, y, v_i) \delta(x, y, v_i)]$	K
Mean velocity (mom-1)	$\bar{v}(x, y) = \frac{1}{W(x, y)} \sum_i T_B(x, y, v_i) \delta(x, y, v_i) v_i \Delta v_{\text{ch}}$ $\sigma_{\bar{v}}(x, y) = \frac{\sigma_T(x, y)}{W(x, y)} \left[\sum_i \delta(x, y, v_i) [v_i - \bar{v}(x, y)]^2 \right]^{1/2} \Delta v_{\text{ch}}$	km s^{-1}
Velocity dispersion (mom-2)	$\sigma_v(x, y) = \left[\frac{1}{W(x, y)} \sum_i T_B(x, y, v_i) \delta(x, y, v_i) [v_i - \bar{v}(x, y)]^2 \Delta v_{\text{ch}} \right]^{1/2}$ $\sigma_{\sigma_v}(x, y) = \frac{1}{2} \left(\frac{\sigma_T(x, y)}{W(x, y) \sigma_v(x, y)} \right)^2 \left[\sum_i \delta(x, y, v_i) [v_i - \bar{v}(x, y)]^2 - \sigma_v(x, y)^2 \right]^{1/4} \Delta v_{\text{ch}}$	km s^{-1}
Equivalent/effective width	$\text{EW}(x, y) = \left W(x, y) / \left[\sqrt{2\pi} T_{\text{peak}}(x, y) \right] \right $ $\sigma_{\text{EW}}(x, y) = \text{EW}(x, y) \left[\left(\frac{\sigma_W(x, y)}{W(x, y)} \right)^2 + \left(\frac{\sigma_T(x, y)}{T_{\text{peak}}(x, y)} \right)^2 \right]^{1/2}$	km s^{-1}

Notes – All data products are computed from the ppv line cubes, respectively, containing the brightness temperatures $T_B(x, y, v)$ of the respective lines. A more detailed description of the individual data products is given in Section 3.1.4. $\delta(x, y, v)$ denotes the velocity-integration mask described in Section 3.1.4. “max” and “std” are the maximum and standard deviation computed over the data within the brackets along the velocity axis.

and describes the intensity-weighted velocity, or in other words, the mean velocity (\bar{v}) of the emission line. For a Gaussian emission line, the mom-1 is the mean of the Gaussian, i.e. the velocity of the peak emission. The uncertainty of the mom-1 can be computed as follows via Gaussian error propagation:

$$\sigma_{\bar{v}}(x, y) = \frac{\sigma_T(x, y)}{W(x, y)} \left[\sum_i \delta(x, y, v_i) [v_i - \bar{v}(x, y)]^2 \right]^{1/2} \Delta v_{\text{ch}}. \quad (3.13)$$

Thus, $\sigma_{\bar{v}}(x, y)$ scales with the rms noise (σ_T) and a term that depends on the line width ($(v_i - \bar{v})^2$). The mean velocity, or velocity field, is a useful physical quantity from radio astronomical observations to study the kinematics of the gas from which the tracer line is originating. Within the galaxy, the velocity information of molecular clouds can be used to infer their (kinematic) distance assuming a rotation model of the Milky Way. In external galaxies, the velocity field tracks the rotation of the galaxy if the galaxy is tilted towards us, i.e. the inclination angle is significantly different from zero. The velocity fields of galaxies can thus be used to estimate the rotation curves of galaxies, which in turn are robust probes of the total mass inside galaxies.

RMS line width (moment-2)

The second moment (moment-2, or short, mom-2) describes the velocity variance (Var_v) of the emission around the mean velocity, i.e. the width of the line. Physically, the line width is connected to the velocity dispersion of the gas, since the relative motion of the gas with respect to the observer will shift and, in a turbulent medium, broaden the line (Doppler broadening). It is common to quantify the velocity dispersion as the rms line width, i.e. the standard deviation of the line, which is the square root of the

variance ($\sigma_v = (\text{Var}_v)^{1/2}$). Hence, the rms line width is given as:

$$\sigma_v(x, y) \equiv [M_2(x, y)]^{1/2} = \left[\frac{1}{M_0(x, y)} \int_{\text{mask}} T_B(x, y, v) (v - M_1)^2 dv \right]^{1/2} \quad (3.14)$$

$$= \left[\frac{1}{W(x, y)} \sum_i T_B(x, y, v_i) \delta(x, y, v_i) [v_i - \bar{v}(x, y)]^2 \Delta v_{\text{ch}} \right]^{1/2}, \quad (3.15)$$

The resulting Gaussian error-propagated uncertainty is:

$$\sigma_{\sigma_v}(x, y) = \frac{1}{2} \left(\frac{\sigma_T(x, y)}{W(x, y) \sigma_v(x, y)} \right)^2 \left[\sum_i \left(\delta(x, y, v_i) [v_i - \bar{v}(x, y)]^2 - \sigma_v(x, y)^2 \right)^2 \right]^{1/4} \Delta v_{\text{ch}}. \quad (3.16)$$

The rms line width, or velocity dispersion is a valuable probe of the physical conditions of the gas from which the line is originating. This is because the line width depends on the velocity dispersion of the gas, which, for an isolated cloud, is a good proxy for the kinetic temperature of the gas. If individual clouds can not be resolved (scales larger than 100 pc), the velocity dispersion is also driven by the inter-cloud motion or, at kpc-scales, the main contribution to the velocity dispersion can be galactic rotation, or streaming motions within the galaxy, especially towards the centres of galaxies. The various possible drivers of the velocity dispersion illustrate how challenging it can be to properly interpret the mom-2 in galaxies. The aforementioned discussion of mom-1 and mom-2 maps makes it obvious why radio astronomers prefer to translate frequency units into Doppler-shifted velocity units (Section 2.1.4) since the velocity units directly relate to physical velocities, which allow studying the kinematics of the gas in galaxies.

Peak intensity

Along with the moment maps described above there are a few additional, commonly used quantities that can directly be computed from the processed data cubes. One of these quantities is the peak brightness temperature, or peak intensity ($T_{\text{peak}}(x, y)$), which is the maximum brightness temperature of the line in each respective spaxel or sightline:

$$T_{\text{peak}}(x, y) = \max_{v_i} [T_B(x, y, v_i) \delta(x, y, v_i)], \quad (3.17)$$

where \max_{v_i} computes the maximum along the velocity axis v_i , considering only channels within the velocity-integration mask $\delta(x, y, v_i)$. The uncertainty of T_{peak} is given by the rms noise in the respective spectrum, computed from the emission-free channels:

$$\sigma_T(x, y) = \text{std}_{v_i} [T_B(x, y, v_i) \tilde{\delta}(x, y, v_i)]. \quad (3.18)$$

Equivalent width

One of the drawbacks of the mom-2 as a tracer of the line width is its sensitivity to noise. This means, that for noisy spectra (low-S/N), the mom-2 can significantly be driven by the noise since noise peaks at large velocity offsets from the mean velocity can yield an apparently wide line. Therefore, it is often preferred to use the so-called equivalent, or effective width (short EW), from the less noise-affected

mom-0 and peak intensity, assuming a Gaussian line profile:

$$EW(x, y) = \left| \frac{W(x, y)}{\sqrt{2\pi} T_{\text{peak}}(x, y)} \right|. \quad (3.19)$$

The uncertainty of the equivalent width:

$$\sigma_{EW}(x, y) = EW(x, y) \left[\left(\frac{\sigma_W(x, y)}{W(x, y)} \right)^2 + \left(\frac{\sigma_T(x, y)}{T_{\text{peak}}(x, y)} \right)^2 \right]^{1/2} \quad (3.20)$$

scales with the S/N of the line peak and integrated intensity. Hence, EW is always significantly measured if a line is detected. In most extragalactic works, the line width can be well-approximated by a Gaussian function, such that the above approach yields reasonable line-width estimates. Therefore, throughout the extragalactic projects of this thesis, we adopt the more robust equivalent width to measure the velocity dispersion of molecular gas at cloud scales (see Chapter 6 and Chapter 7). However, we note that especially towards galaxy centres, molecular line spectra consist of multiple ($\sim 2 - 3$) Gaussian components so that the assumption of a single Gaussian function is not fulfilled in these environments (PHANGS internal discussion; Henshaw et al. in prep.).

3.2 PyStacker

Recovering faint emission lines is one of the key challenges in (radio) astronomy, in particular from extragalactic targets that are typically much fainter than sources within the Milky Way. Therefore, astronomers have developed clever tools and techniques to recover faint emission hidden in the noise of their observations. One of these tools is called “spectral line stacking”, which is an advanced way of averaging emission in order to increase the signal-to-noise ratio of an emission line. The basic idea is to correct for Doppler-shifted velocity offset of the emission utilising a known velocity field and then stack the emission across a larger region, i.e. over many spaxels. The backbone of the spectral stacking method is the availability and selection of a proper “prior”, which is used to define the velocity field and, in addition, to potentially create the velocity-integration mask for the stacked spectra.

When dealing with molecular emission lines, like in this work, typically the most significant line is a good choice for a prior, i.e. typically the low-J CO transitions (CO (1 – 0) or CO (2 – 1)). At cloud-average scales or above, it is a robust assumption that molecular lines tracing the colder ISM originate from the same kinematics and location in ppv space, i.e., in particular, they share the same mean velocity. Hence, it is expected that emission from fainter emission lines, e.g. HCN (1 – 0), HCO⁺ (1 – 0), or N₂H⁺ (1 – 0), shares the same line profile and mean velocity as the brighter lines, which can be utilised to cleverly stack faint emission. Moreover, even if the lines are well detected, spectral stacking allows robust computation of average spectra and subsequent products (e.g. moments) to recover unbiased mean trends, e.g. the trend of the CO (1 – 0) line emission with galactocentric radius. In contrast to naive binning, i.e. averaging of integrated values (e.g. moments), spectral stacking has the advantage of retrieving an average spectrum thus conserving the kinematic information of the spectral line data.

During this PhD work, we have helped to develop a python package that performs spectral stacking of emission lines. The tool is called PyStacker and builds upon the PyStructure package introduced

in Section 3.1. The original code goes back to an IDL package written by María J. Jiménez-Donaire (Jiménez-Donaire, Cormier et al., 2017; Jiménez-Donaire, Bigiel, A. K. Leroy, Cormier et al., 2017; Jiménez-Donaire, Bigiel, A. K. Leroy, Usero et al., 2019), and was translated into python3 by Jakob S. den Brok in 2019. The python code has been excessively used in the research group of Prof. Frank Bigiel to recover emission from CO isotopologues (e.g., ^{13}CO , or C^{18}O) and dense gas tracers (e.g., HCN, or HCO^+), which have entered numerous works, including undergraduate theses and publications (Bešlić et al., 2021; den Brok, Chatzigiannakis et al., 2021; den Brok, Bigiel, Sliwa et al., 2022; den Brok, Bigiel, Chastenet et al., 2023; den Brok, A. K. Leroy et al., 2023; Eibensteiner, Bigiel et al., 2023). Personally, we made extensive use of PyStacker in our extragalactic works (Neumann, Gallagher et al., 2023; Neumann, den Brok et al., 2023; Neumann, Bigiel et al., 2024) and have been actively involved in developing and improving the tool since 2022. In 2023, the PyStacker package has been made public¹² as part of the publication Neumann, den Brok et al. (2023) (Chapter 4), which tests the capabilities of the tool when applied to radio interferometric data from ALMA – a project I led within the PHANGS–ALMA data reduction working group. In the following, we describe the functioning principle of spectral stacking of (extragalactic, radio) emission lines as embodied in the PyStacker python package.

3.2.1 Velocity alignment

The relative motion of a source with respect to the observer leads to the Doppler shift of an emission line originating from the source (Section 2.1.4). For radio-line observations of the ISM, this implies that the same emission, even though emitted at its fixed, intrinsic rest frequency, can be shifted to lower or higher frequencies depending on the relative velocity of the source. Therefore, naive averaging of emission over larger regions most certainly yields a broader line profile that reflects the velocity dispersion of the gas across that region but does not produce more significant line detection if the velocity dispersion of the source’s medium is large. However, if the line spectra of the individual sightline measurements across a certain spatial region are first spectrally aligned, i.e. their Doppler-shift is corrected, the spectra can successfully be stacked to yield more significant (higher S/N) average spectra. This is the fundamental principle of the spectral line stacking method.

Figure 3.6 illustrates the velocity alignment of CO (2 – 1) spectra across a nearby spiral galaxy. Due to the galactic rotation of the disc, line emission from one side of the galaxy is red-shifted (shifted to higher frequencies/velocities) while the other side is blue-shifted (shifted to lower frequencies/velocities) if the galaxies are viewed from an angle, which is the case for NGC 4321 (inclination angle of 38.5; Lang et al. (2020)). In this case, which is representative of many of the nearby galaxies investigated in this work, the relative motion between the two ends of the molecular gas disc is more than 200 km s^{-1} , which is much larger than the typical line width in the disc ($\text{FWHM} \sim 20 \text{ km s}^{-1}$). Therefore, spectral stacking requires proper velocity alignment on a spaxel-by-spaxel basis.

The most straightforward approach to align the spectra is to use the velocities of the line peaks and subtract these velocities from the spectra. This practice works well if the emission lines are significantly detected across a large fraction of the spaxels across the regions used for stacking. However, it fails if the line that is stacked is only poorly detected in individual spaxels. In this case, the velocity field (mean velocities of the spectra) has to come from other tracers, e.g. more significant emission lines, a lower-resolution velocity field, or a model. A very common procedure to recover faint emission lines

¹² <https://github.com/PhangsTeam/PyStacker>

(e.g. dense gas tracers) is to use brighter lines (e.g. bulk molecular gas tracers) as a prior `PyStacker` allows to input either a ready-to-use velocity field or reconstructs the velocity field from a ppv cube prior, using the locations of the peak emission¹³.

3.2.2 Spectral line stacking

After aligning the spectra, the final step is to stack the spectra and (optionally) to compute integrated quantities of the stacked spectra. In principle, the stacking of aligned spectra is easy to do – we just compute the arithmetic mean over all spectra inside a given region/bin, as illustrated in Figure 3.7. The stacked spectra will then represent the average emission line over the given region. For the naive assumption that we stack n individual spectra, which have the same S/N of X , the stacked spectrum will yield a S/N of $\sqrt{n} \times X$, since the signal (amplitude) will remain the same, but the noise drops proportionally to \sqrt{n} . For instance, this means that, under the above assumptions, stacking 25 spectra leads to a five times better S/N of the stacked spectrum. In other words, an otherwise undetected line might be detected only via stacking, which is a very powerful tool to analyse faint emission lines.

However, there are a few things to consider: 1) Do the individual spectra that enter the stacking have similar line shapes? 2) How complete is the average stack, i.e. how many spaxels of the given region enter the stacked spectra, or in turn, how many spaxels are disregarded for the stack? The first point affects the analysis of the kinematics of the gas from the stacked spectra related to the line shape, for instance, the velocity dispersion of the gas. Often, coarser extragalactic observations naturally include several velocity components within the beam, so that the observed line is not Gaussian. Especially towards galaxy centres, spectra can significantly differ from Gaussian shapes, for example, via outflows, leading to strong line wings. The latter remark becomes relevant when stacked spectra are interpreted as representative population means over the stacking region. For example, if we compute the integrated intensity of stacked spectra that was computed from a large region in the outskirts of a spiral galaxy, where less than 10 % of the sightlines contribute to the stack, then our stacked spectrum is most certainly biased towards the over-luminous regions and our integrated intensity will be biased high. Therefore, `PyStacker` by default sets spaxels to zero if no velocity information is available but the spaxels lie within the stacking region. Therefore, `PyStacker` by default corrects for the bias to high intensity. Note that the above de-biasing can also overcorrect the bias since there might be a substantial fraction of the emission in the spaxels that are artificially set to zero. However, this can be accounted for in the uncertainties of the stacked spectrum and is actually implemented in the `PyStacker` tool by measuring the noise in these spectra and propagating it into the uncertainty of the integrated quantities computed from the stacked spectra. For further discussion, we refer to project P1 (Chapter 4), where the effect of completeness on the stacked spectra is analysed based on a model galaxy. Finally, the stacked spectra can be utilised to compute integrated quantities like the integrated intensity or rms line width, similar to the data products computed from spectra in individual sightlines (see Section 3.1.4).

3.2.3 Data binning

An alternative approach to stacking emission lines is the binning of integrated quantities. This means instead of stacking spectra over a spaxel region and computing the integrated quantity, we compute the

¹³ There are plans to improve the stacking tool such that it optionally determines the velocity field via the mean velocity of a Gaussian fit to the spectra, or via “Fourier-shuffling”, i.e. obtaining the peak positions in Fourier space. These options are currently in a test phase but did not enter the data analysis of this thesis.

integrated quantities on a spaxel-by-spaxel basis (e.g. moment maps; Section 3.1.4) and compute the average of the integrated quantities over the same spaxel region. The advantage of binning is that it is typically easier to perform since it does not require to correct for the velocity field of the line, i.e. a spectral stacking tool like `PyStacker`. Besides, previous studies (e.g., Gallagher, A. K. Leroy, Bigiel, Cormier, Jiménez-Donaire, Hughes et al., 2018) report that spectra stacking and data binning yield the same results within $\sim 10\%$, suggesting that stacking is not always needed to recover faint emission lines and to measure unbiased average trends. However, similar to spectral stacking, also binning is critically limited by the choice and sensitivity of the prior used to compute the integrated quantities. In addition, averaging integrated quantities has the drawback of losing the line shape information, which is conserved with spectral stacking.

In our works, we applied both approaches, for example, project P3 (Chapter 6) uses bin averages to infer the average HCN/CO trends, while projects P2 (Chapter 5) and P4 (Chapter 7) use spectral stacks to study similar line ratio trends. In our dedicated stacking project (Chapter 4), we show that both methods yield similar results ($\sim 10\%$) when recovering radial trends of integrated intensities of molecular lines at various sensitivity levels thus supporting the comparability of both approaches. However, in the latter two projects (P4 and P5), we found that stacking does slightly better in recovering very faint emission thus extending the dynamic range in some relations by a few per cent. Therefore, we recommend spectral stacking over data binning, if feasible.

3.3 Measurement uncertainties

3.3.1 Uncertainties and upper limits

Statistics is at the heart of most sciences, in particular in a field like astrophysics, where measurements are typically affected by many sources of uncertainties, assumptions and biases. A key difference between astrophysics and most other sciences is that the parameters of the experiment are essentially set by nature, i.e. we can not tweak the initial conditions of our astrophysical experiments to our liking and study the outcome – there is only one universe that we can observe. This fact introduces some fundamental limits to statistical inference about the properties of the universe, embodied in the so-called cosmic variance¹⁴. Thus, we can only study this one universe from our position on Earth (at the time of this thesis; who knows if humankind eventually sets sail to explore other stars and galaxies) only thing we can control is what we observe and how we observe. Simply put, this means, we select a part of the sky that we want to observe and point our favourite telescope at the targeted area. Hence, it is clear that, in astrophysics, the design of the observations is key to making reasonable inferences about general hypotheses on physical laws and mechanisms in the universe (further discussed in Chapter 2). In addition, testing hypotheses usually requires two steps: 1) extracting the emission of the source from the raw observations and 2) converting the observed quantities, i.e. line intensities, into physical quantities, e.g. the mass of a cloud. Both steps inevitably introduce measurement and potentially systematic uncertainties.

Measurement uncertainties or noise, can usually be well characterised, in particular if the measured quantity approximately follows a Gaussian distribution, which is a good assumption for radio emission lines. In this case, if calibration uncertainties are neglected, the noise can be measured from the scatter

¹⁴ Cosmic variance denotes the finite sampling of a parent distribution due to the fact that there is only one universe that we can observe. This principle poses a fundamental limit to large-scale studies of the universe. we note that cosmic variance is not relevant to the objectives of this PhD thesis.

(rms or standard deviation) in the emission-free part of the spectra (as described in Section 3.1.4; $\sigma_T(x, y) = \text{std}_{v_i} [T_B(x, y, v_i) \tilde{\delta}(x, y, v_i)]$). We describe in Section 3.1.4, how this uncertainty propagates to the uncertainty of integrated quantities that are computed from the spectra. Thereby, the uncertainty is computed as

$$\sigma_F(x_i) = \left[\sum_i \left(\frac{\partial F(x_i)}{\partial x_i} \sigma_i \right)^2 \right]^{1/2} \quad (3.21)$$

via Gaussian error propagation, where $F(x_i)$ is a function that is differentiable by each variable x_i with uncertainties σ_i . In general, above Equation (3.21) is applied whenever measurement uncertainties are propagated to a quantity that is a function of the measurements. Throughout this thesis, we often investigate line ratios as tracers of physical quantities, i.e. the HCN-to-CO line ratio can be utilised as a proxy of the dense gas fraction (see, e.g., Chapter 6 for more details). Hence, the uncertainty of the intensity ratio R_{21} of two lines, W_1 and W_2 , with uncertainties σ_{W_1} and σ_{W_2} is given by:

$$\sigma_{R_{21}} = R_{21} \left[\left(\frac{\sigma_{W_1}}{W_1} \right)^2 + \left(\frac{\sigma_{W_2}}{W_2} \right)^2 \right]^{1/2} \quad (3.22)$$

Astronomical observations usually do not significantly detect emission across the full targeted field of view (FOV). This means, some parts of the FOV, or maybe even the entire field are dominated by noise. A common way of identifying significant emission is to select data above a certain noise level, e.g. all data about three times the rms ($S/N \geq 3$). Assuming Gaussian noise, this would mean that there is only a 0.13 % probability that the emission peak arises from pure noise thus making it very likely that the emission peak indicates a real signal. In the contrary, emission below the 3σ threshold ($S/N < 3$) is usually referred to as non-detection. However, a non-detection also contains information. On the one hand, there might be true emission hidden in $< 3\sigma$ pixel that can be recovered by stacking emission across several pixels (see Section 3.2). On the other hand, we can indicate non-detections, or censored data as so-called upper limits. This means we can assign upper limits (UL) of $3 \cdot \sigma$ to the $S/N < 3$ pixels, which indicate that the true values are very likely (99.87 %) below the upper limit value:

$$\text{UL}_W = 3 \cdot \sigma_W \quad (3.23)$$

For ratios of emission line ($R_{21} = W_1/W_2$; see above), an upper limit can be defined if the line in the denominator (W_2) is detected while the line in the numerator (W_1) is not detected, and the inverse case yields a lower limit (LL):

$$\text{UL}_{R_{21}} = \frac{3 \cdot \sigma_{W_1}}{W_2}, \quad \text{LL}_{R_{21}} = \frac{W_1}{3 \cdot \sigma_{W_2}}. \quad (3.24)$$

3.3.2 Sigma clipping and bias

Systematic uncertainties or bias quantifies the accuracy of a measurement, and are usually more challenging to address. Often, biases are not properly identified and thus remain untreated. Here, we want to specifically highlight a bias connected to neglecting censored data, which can yield systematically wrong population averages and hence conclusions on trends and scaling relations (e.g., discussed in

Section 4.5 of the P4 paper; Appendix C). When studying scaling relations, i.e. the correlation and functional form between two quantities x and y , these two quantities must not have the same significance. Actually, in most cases, one of the quantities will be more significantly detected than the other. Say, y depends linearly on x and x is completely detected over the full dynamic range, for example, across the full FOV of the observations, but y is only well detected at high x and becomes less completely detected at lower x due to the sensitivity of the measurement. In this case, selecting data above a certain noise level, so-called “sigma clipping”, for example, by imposing $S/N \geq 3$, will create a biased representation of the true relation.

Figure 3.9 demonstrates the effect of sigma clipping on the radial trend of CO (2 – 1) line emission across a modelled galaxy taken from project P1 (Chapter 4). In this example, the true intensities are known (model input) and the simulated data (black and grey markers) mimic realistic observing conditions with PHANGS–ALMA-like sensitivity. The detected sightlines (black markers) illustrate the bias created by sigma clipping towards the outer parts of the disc. This can be explained via the dramatic change in completeness (detection fraction) of sightlines in each radial bin. In the centre of the galaxy, almost all sightlines are detected thus recovering the true, unbiased trend. With increasing radius the completeness drops from 96 % to 2 %. At the same time, the bias of the sigma-clipped averages increases from 0.02 dex to 1.6 dex. This is because at low completeness the sigma-clipped data are not representative of the true sample population, but are biased high by construction. This phenomenon is extremely relevant to the trends and scaling relations studied in this work.

Fortunately, there is a way to remove this bias by considering non-detections instead of throwing these data away. Binning or spectral stacking naturally includes all data within a certain region and thus can recover the true values. The blue markers in Figure 3.9 show the stacked values which are very close to the true trend, demonstrating that: 1) considering non-detections is crucial to obtain true population averages and 2) stacking can recover the true population averages. Therefore, across this thesis, stacking is one of the key methods to recover unbiased, or at least less biased, average measurements in order to constrain scaling relations. Nor at least less biasedote that even when non-detections are accounted for in binned or stacked averages, the resulting measurement can yield a non-detection. Nevertheless, even these data can be considered to constrain scaling relations using sophisticated linear regression tools that take into account non-detections, like e.g. `LinMix`, as is discussed in the following Section 3.4.

3.4 Linear regression

Linear regression is very common in astrophysics. This is because most scaling relations can, to first order, be described by a power-law, which, in turn, produces a linear relation if the quantities are displayed in logarithmic space. Thus it is crucial to determine the regression parameters with no or little bias and to report statistically trustworthy uncertainties. In the literature, it is often not properly justified why the chosen linear regression tool is particularly suitable to best recover the true regression parameters based on the statistical properties of the data. Beyond that, it is seldom addressed if the regression can be biased and how large the bias is expected to be, even though this is usually inevitable by converting the data from linear to logarithmic scale, especially if upper limits on the data are not incorporated into the regression routine.

In the following, we will give a brief summary of a few linear regression tools commonly used in astronomy, starting from simple ordinary least square (OLS) fitting, over more advanced methods, like Bivariate Correlated Errors and intrinsic Scatter (BCES), Akritas-Thiel-Sen (ATS), and “ASURV”, to

Table 3.2: Linear Regression Tools

	OLS	BCES	ASURV	ATS	LinMix
Uncertainties	y	x and y	No	No	x and y
Censored Data	No	No	Yes (upper & lower limits in both variables)	Yes (upper & lower limits in both variables)	Yes (upper lower limits in one variable)
Intrinsic Scatter	No	Yes	No	No	Yes
Unc. Covariance	No	Yes	No	No	Yes
Parameter Unc. (trustworthy)	Yes (No)	Yes (Yes)	Yes	No (Yes)	Yes (Yes)
Pros	– can be generalised to arbitrary fitting function	– y x, y x, bisector and orthogonal regression	– can handle all combinations of censored data	– can handle all combinations of censored dat – more robust than ASURV	– statistical approach
Cons	– cannot handle censored data – poor unc. estiamtes	– cannot handle censored data	– arbitrary bins	– no uncertainty estimates	– assumes Gaussian distr. in x and y – slow

Notes – Summary of the capabilities, pros and cons of the linear regression methods described in Section 3.3. It is listed if the methods can account for uncertainties in the data, censored data, intrinsic scatter in the linear relation and correlation of the data uncertainties. Moreover, it is specified if the methods provide uncertainty estimates on the regression parameters and if they are statistically trustworthy. In addition, brief notes on the advantages and caveats of each tool are displayed.

the Bayesian statistics based **LinMix** package, which is the preferred tool throughout this thesis. The comparison below highlights why OLS fits are usually biased and do not yield reasonable uncertainties for the scaling relations studied in this thesis and why **LinMix** is the most suitable tool for our purposes. Be warned that this comparison is neither adequate to all data demands, nor does it claim to be complete. There exist many more linear regression tools, which might suit one’s specific data properties better than any method presented here. We have tested these methods on simulated data and compared the regression results in terms of their bias and precision. A summary of the capabilities of the linear regression tools is shown in Table 3.2.

3.4.1 Classical fitting

OLS fitting is the standard approach to fitting a curve (here a line) to data by minimising the χ^2 , i.e. minimising the residuals in the dependent variable. The OLS approach is powerful in the sense that it is simple and can be applied to any arbitrary fitting function. However it can (in its basic formulation) only handle detections and uncertainties in the dependent variable. The `scipy.curve_fit` function offers an easy-to-use implementation of OLS fitting within `python`.

3.4.2 Advanced fitting

The BCES tool is a generalisation of the OLS method developed by Akritas and Bershady (1996). It has several advantages over the default OLS method in handling the uncertainties, i.e. it can handle uncertainties on both coordinates and take the correlation between the uncertainties into account. Furthermore, it takes into account an intrinsic scatter about the regression relation and yields four different regression lines, such as the bisector or the orthogonal regression. The orthogonal regression is particularly interesting if neither of the variables can be considered as the independent variable. We use

the `python` implementation by R. Nemmen¹⁵ to perform orthogonal BCES fits in project P2 (Chapter 5).

ASURV is a survival analysis software based on the Kaplan-Meier estimator and uses the Schmitt binning method (Schmitt (1985)). It was developed for astronomy by E. Feigelson of Penn State University¹⁶ and is designed to account for left- and right-censored data (i.e. upper and lower limits) in both coordinates. Here, we adopt the `python` implementation of the ASURV tool¹⁷.

Similarly to ASURV, the ATS method can handle censored data in both axes, but is not subject to the arbitrary binning of the Schmitt method hence being more robust for the basic user. Its implementation is only available in the programming language R as part of the statistics package NADA (Nondetects And Data Analysis: Statistics for Censored Environmental Data¹⁸). However, it can be interfaced from `python` using RPy.

3.4.3 LinMix - Bayesian fitting

The `LinMix` package is based on Kelly (2007) and has a line-by-line `python` implementation that has been utilised throughout this work¹⁹. `LinMix` exploits Bayesian statistics to find the best linear regression fit. This means that it builds a likelihood function for the linear regression model and performs a Markov chain Monte Carlo (MCMC) simulation to explore the posterior distribution of the regression parameters where it uses the Gibbs sampler to take an MCMC step. It is designed to account for heteroscedastic measurement errors (i.e. uncertainties with different magnitudes) in both coordinate axes, correlation in the uncertainties, and intrinsic scatter in the regression relationship. Moreover, it can handle censored data (upper limits) in the dependent variable (y -axis data). Due to its statistical MCMC approach, `LinMix` naturally provides trustworthy constraints on the regression parameters as well as credibility areas for the regression line, which is one of the key advantages of this tool.

Figure 3.10 shows a simulated scaling relation of the form $y = b \cdot x^m$, or equivalently $\log_{10} y = b + m \cdot \log_{10} x$ in log-log scale, where $b = 1$ and $m = 2$ are the intercept and slope of the relation.. The initial relation was created as a perfect power-law with additional intrinsic Gaussian scatter. Then, Gaussian noise was added to the y -axis quantity in linear scale, mimicking noise of brightness or integrated intensities. The nature of the relation is such that the sensitivity and hence the completeness of the measurements on the y -axis depends on the x -axis so that the lower x -values regime is dominated by low-sensitive data, i.e. upper limits. The resulting data is fitted using the aforementioned introduced `LinMix` fitting routine, which takes into account the detected data as well as the upper limits to compute the best-fit line with robust uncertainties.

¹⁵ <https://github.com/rsnemmen/bces>

¹⁶ <https://www.astrostatistics.psu.edu/statcodes>

¹⁷ <http://python-asurv.sourceforge.net>

¹⁸ <https://cran.r-project.org/web/packages/NADA/index.html>

¹⁹ <https://github.com/jmeyers314/linmix>

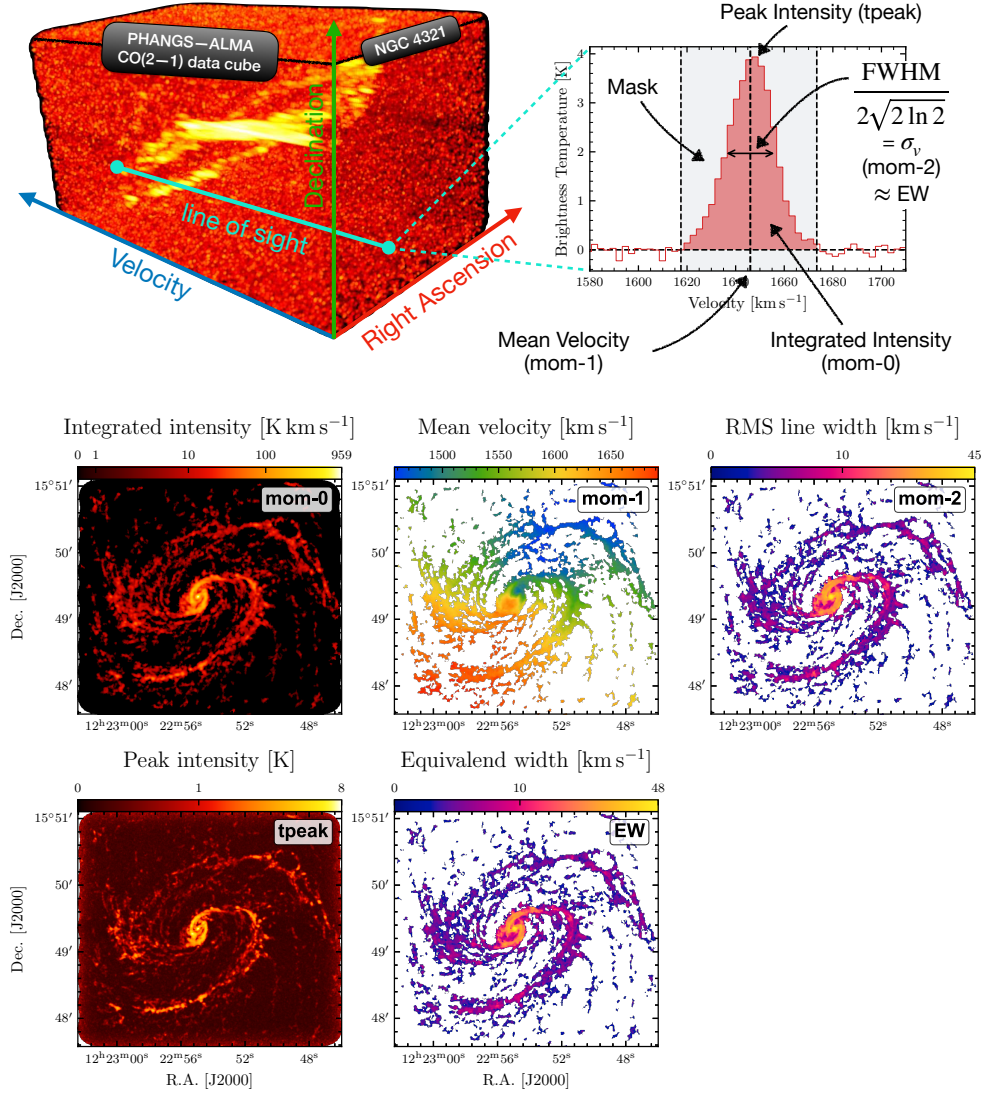


Figure 3.4: **Computation of data products from a ppv data cube.** The top left presents the CO (2 – 1) ppv data cube of NGC 4321 visualised using `glnemo2`. The data is taken from the PHANGS-ALMA survey (A. K. Leroy, Schinnerer et al., 2021). The spectrum on the right shows the CO emission line across a single sightline (cyan line). For each sightline, the PyStructure pipeline computes the products shown as images in the lower five panels, i.e. the integrated intensity (mom-0), the peak intensity (tpeak), the mean velocity (mom-1), the rms line width (mom-2), and the equivalent width (EW). The mom-2 and EW are related to the full-width half maximum (FWHM) of the line via a factor of $2\sqrt{2 \ln 2}$.

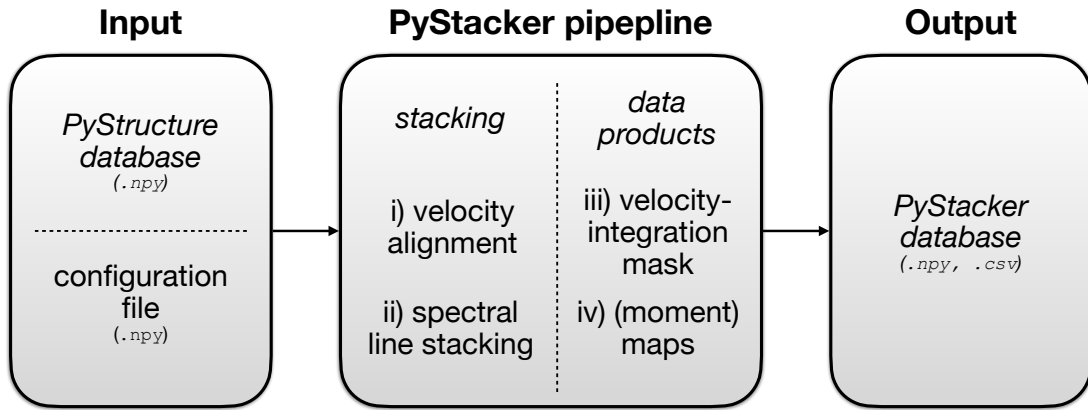


Figure 3.5: **PyStacker workflow.** *Left:* Input files: A database produced using the PyStructure pipeline (Section 3.1), which contains a homogenised data set with data products including the velocity field of the emission lines. The configuration file defines the parameters of the PyStacker pipeline, e.g. the selection of priors for the velocity field and velocity masking, or the quantity and bins used to select the regions over which to stack (a detailed description of the setup parameters is given in the README on the PyStacker webpage). *Middle:* Main pipeline: There are two main steps, 1) the spectral line stacking, which uses the velocity field of the prior to align the spectra of all molecular lines, and 2) the computation of data products, which is following the same procedure as the PyStructure pipeline. *Right:* Output files: The pipeline returns a single numpy dictionary, which contains the stacked spectra and the data products.

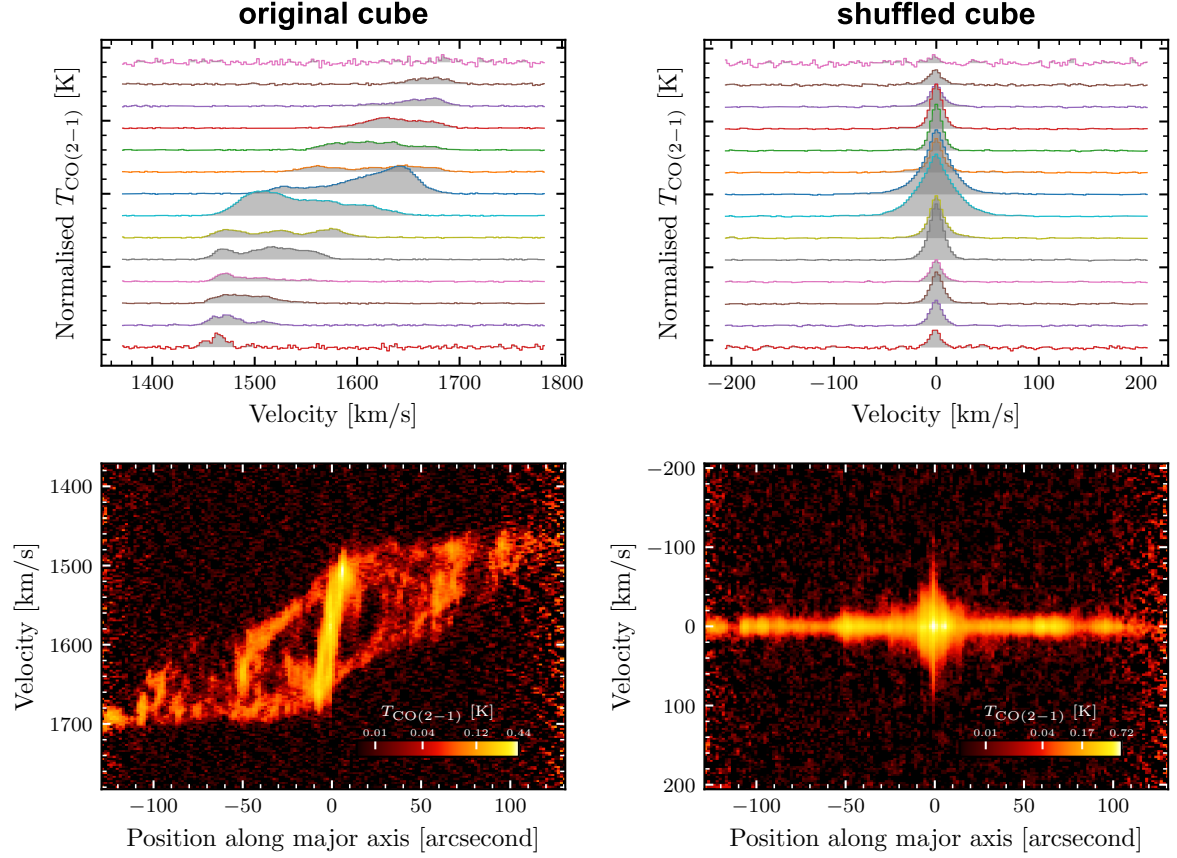


Figure 3.6: **Velocity alignment of CO (2 – 1) spectra across the galaxy NGC 4321.** *Top:* CO (2 – 1) spectra along the major axis of the galaxy, averaged in steps of $20''$, yielding 10 increments. The mean velocity of the spectra represents the Doppler motion of the galaxy due to its rotation. Left and right panels indicate the spectra before and after shuffling, demonstrating the alignment of the spectra after successful shuffling of the spectra. *Bottom:* Position-velocity (pv) diagram of the same data along the major axis of the galaxy. The left and right panels show the pv-diagram before and after velocity alignment, respectively. The colourmap indicates the brightness of the CO emission at each pv-pixel. Pv-diagrams directly visualise the motion of structures and are thus powerful tools to study the kinematics of the ISM in galaxies.

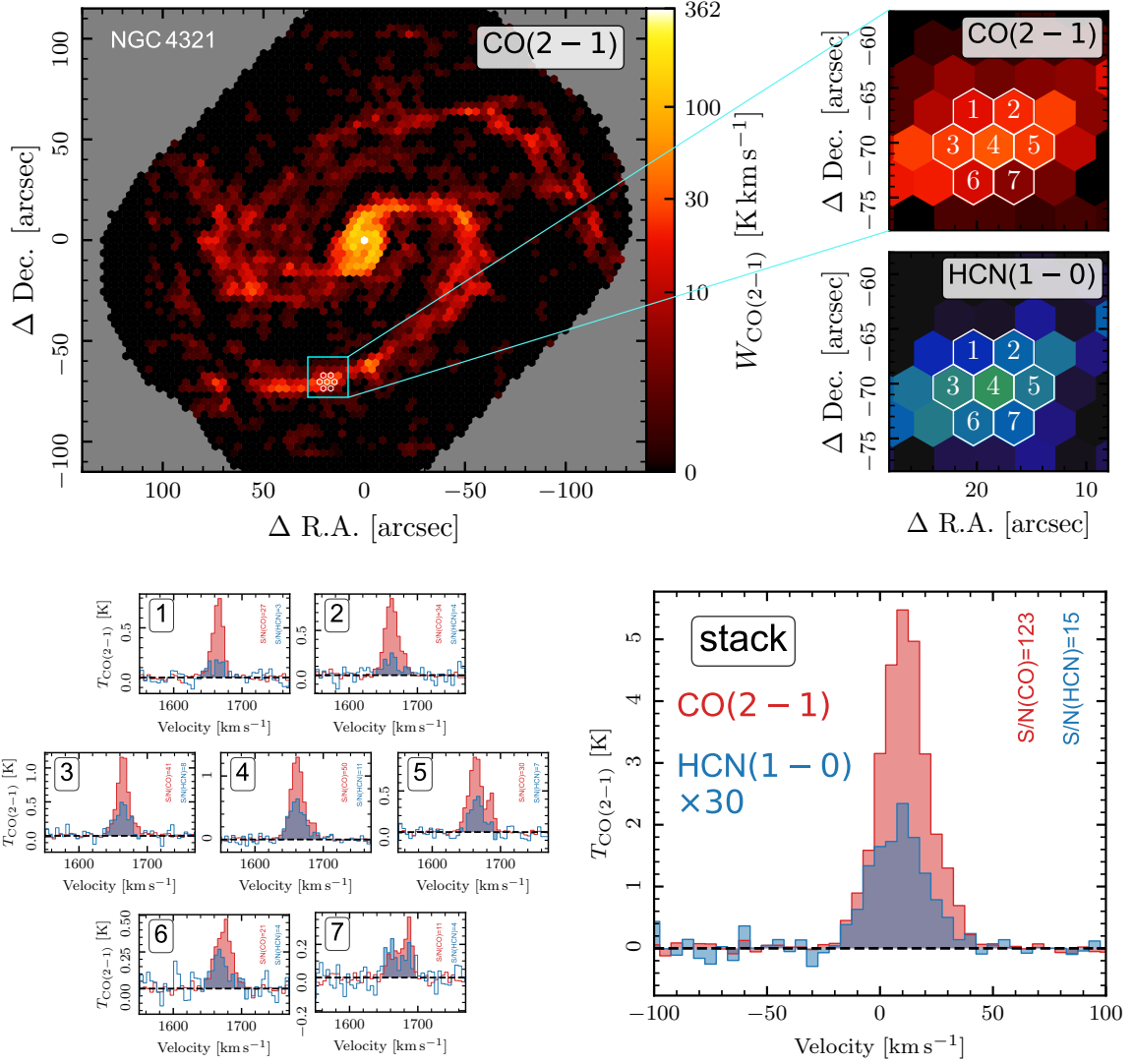


Figure 3.7: Functioning principle of spectral line stacking. *Top left:* CO (2 – 1) integrated intensity map of NGC 4321. *Top right:* The upper panel shows a zoom-in of the cyan rectangular plotted in the full map. The lower panel shows the same cutout but for the integrated intensity of HCN (1 – 0). The sightlines to be stacked are marked with white contours and labelled with numbers from 1 to 7. *Bottom left:* CO (2 – 1) and HCN (1 – 0) spectra of the selected spaxels. HCN (1 – 0) is multiplied by a factor of 30. *Bottom right:* Stacked spectrum of the seven spectra shown on the left. The stacking is performed according to the procedure described in Section 3.2.1 and Section 3.2.2, using the CO line as a prior for shuffling. Before stacking the S/N of the sightline CO (2 – 1) and HCN (1 – 0) intensities range from 11 to 50, and 3 to 15, respectively. The stacked spectra have S/N of 123 and 15 for CO (2 – 1) and HCN (1 – 0), respectively.

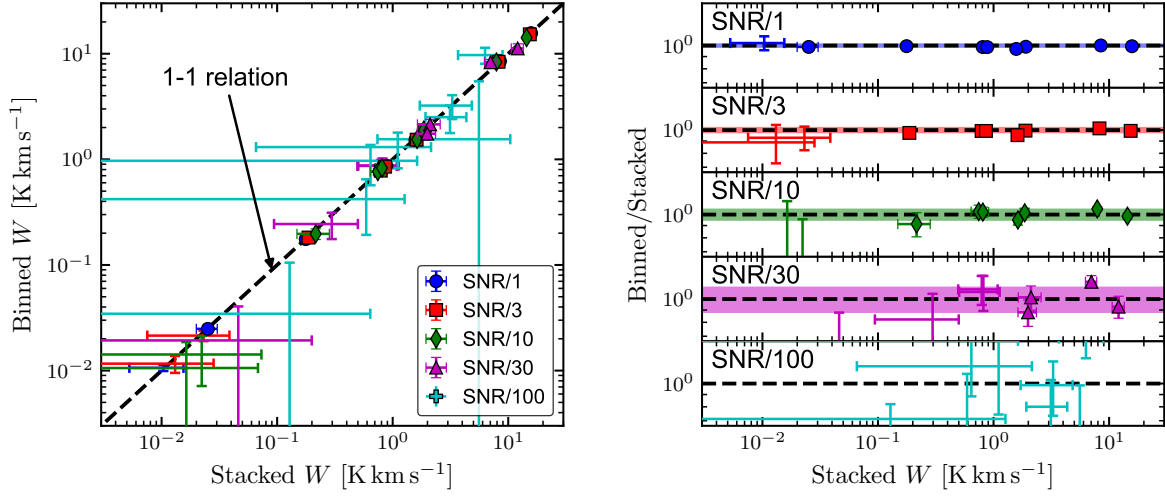


Figure 3.8: **Comparison between line stacking and data binning.** Shown are the integrated intensities obtained via spectral line stacking vs binning as a function of galactocentric radius in the model lookalike-NGC 3059 galaxy. *Left:* Binned vs stacked integrated intensities for data at different signal-to-noise ratio levels (see Chapter 4 for more details on the data). *Right:* The plotted data are identical to those in Figure 7 from Neumann, den Brok et al. (2023).

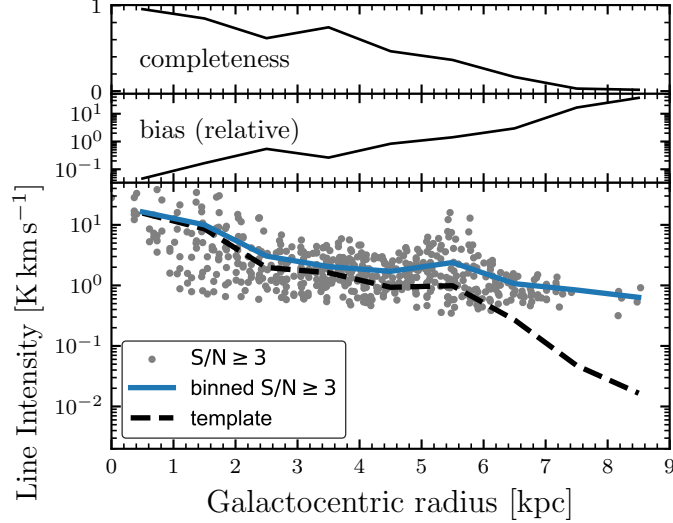


Figure 3.9: **Bias of sigma-clipped trends in the presence of incomplete data.** The lower panel shows the radial trend of CO (2 – 1)-like integrated intensities across the the NGC 3059-lookalike template galaxy. The dashed line denotes the average trend of the true intensities. The grey markers indicate the detected ($S/N \geq 3$) CO (2 – 1) measurements, from which the average trend is obtained (blue line). The upper two panels show the completeness (number of detected sightlines with respect to the total number of pixel at the specific radius) and the relative bias (difference between the sigma-clipped trend and the true values).

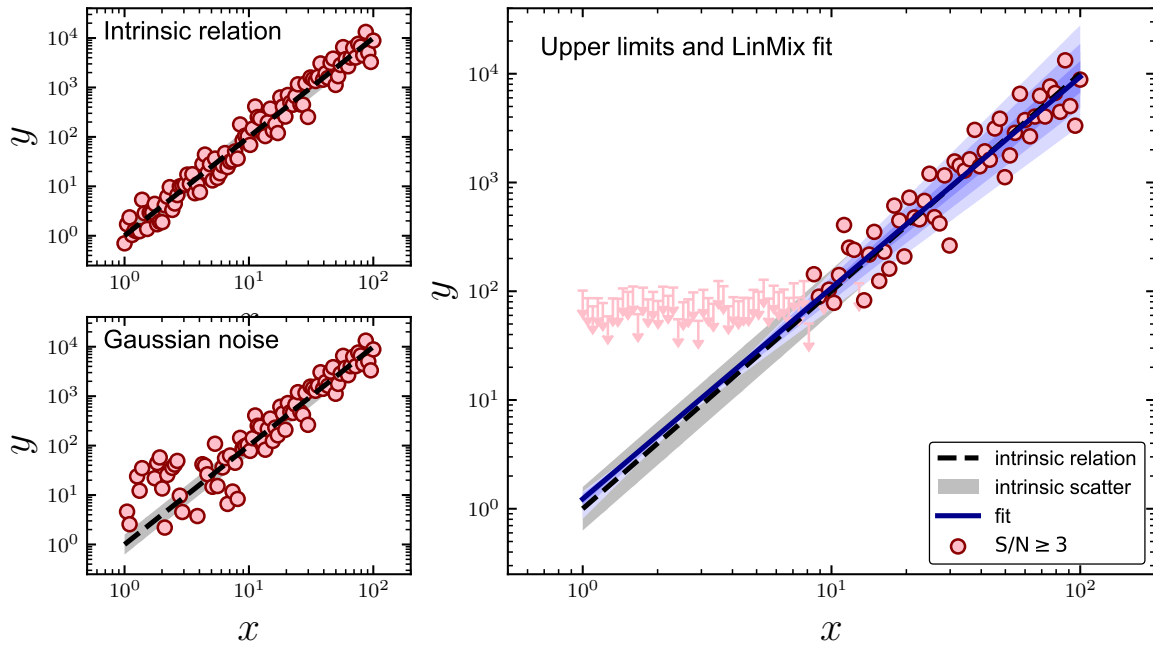


Figure 3.10: **Linear regression of simulated data.** The left two panels illustrate the creation of the simulated data. The top left panel shows the intrinsic relation of the form $y = x^2$, plotted in log-log scale, with intrinsic Gaussian scatter of 0.2 dex (grey area). In the bottom left panel, Gaussian noise with an amplitude of ~ 3 was added. The right panel shows the same data, but instead of showing all data, markers indicate data with $S/N \geq 3$ and downward pointing arrows denote upper limits. The blue line presents the LinMix best-fit line and the blue-shaded areas show the 1-, 2-, and 3-sigma credibility intervals. The fitting tool yields a slope of $m_{\text{fit}} = 1.98 \pm 0.08$ in good agreement with the intrinsic relation ($m = 2$)

Spectral stacking of radio-interferometric data

Spectral stacking of radio-interferometric data

*L. Neumann, J. S. den Brok, F. Bigiel, A. Leroy, A. Usero, A. T. Barnes,
I. Bešlić, C. Eibensteiner, M. Held, M. J. Jiménez-Donaire, J. Pety,
E. W. Rosolowsky, E. Schinnerer, and T. G. Williams*

2023, A&A, 675, A104, 9 pp. (DOI: [10.1051/0004-6361/202346129](https://doi.org/10.1051/0004-6361/202346129))

Overview

Observing molecular line emission from external, nearby galaxies beyond the low-J CO transition is observationally expensive even with state-of-the-art radio interferometers like ALMA. Therefore, the development of techniques that can recover these fainter molecular lines is key to understanding the physical conditions of the ISM in galaxies. One such technique is the so-called “spectral stacking”, where faint molecular lines (e.g., HCN or HCO⁺) are averaged over larger spatial areas using a bright, high S/N prior (e.g., CO or H₂ 1 cm emission). The resulting stacked spectra often detect faint lines otherwise hidden in the noise. In the work presented in this chapter, the spectral stacking technique has been applied to simulated observations to test the capabilities and limitations of recovering emission a factor of 3 – 100 fainter than CO from ALMA-like radio-interferometric observations.

This work was published in *Astronomy and Astrophysics* (A&A) in July 2023. The paper Neumann, den Brok et al. (2023) is provided in its entirety in Appendix A. The following sections summarise the key findings of this work, specifically highlighting my exclusive contributions to the paper. The simulated ALMA observations (Section 4.1) have been produced as part of the PHANGS–ALMA pipeline paper (A. K. Leroy, Hughes et al., 2021) and were generously provided by the PHANGS collaboration. We adopted these data to test the capabilities of spectral stacking of radio-interferometric data. The basic technique of stacking spectral lines is presented in Section 3.2.2 along with its python package `PyStacker`, where we have been one of the major developers together with Jakob S. den Brok. Here, we are commenting on the specific application of this tool on the simulated ALMA observations (Section 4.2) and its capability of recovering unbiased integrated intensities (Section 4.3). We are also quantifying and discussing the filtering out of emission when using interferometric observations without

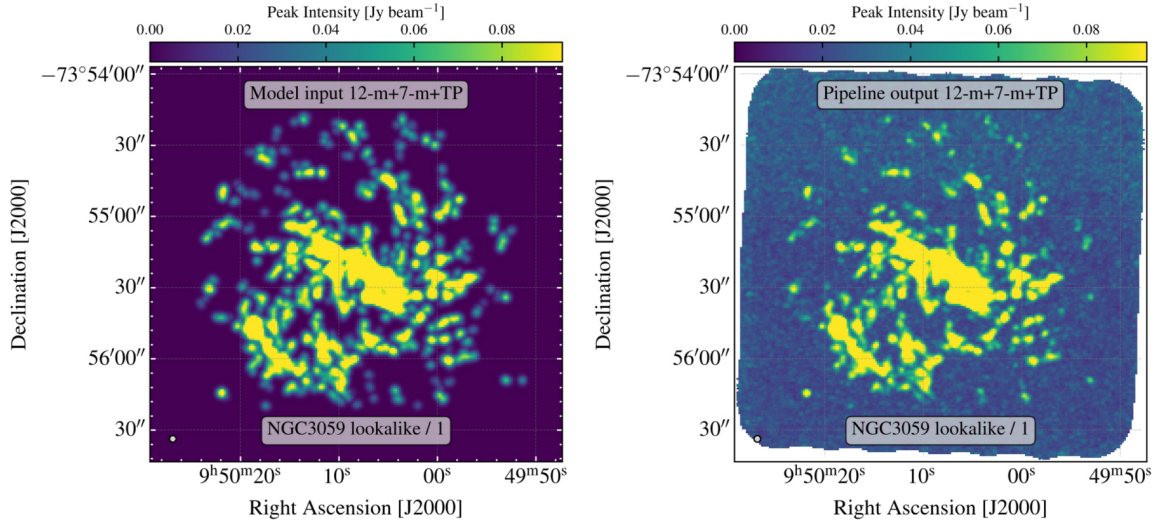


Figure 4.1: **Peak intensity maps of the template galaxy NGC 3059.** The template data is taken from A. K. Leroy, Hughes et al. (2021). *Left:* Lookalike model of NGC 3059 before running it through the pipeline to perform simulated observations and imaging. *Right:* Peak intensity map of NGC 3059 after executing the pipeline, i.e. including realistic noise comparable to PHANGS–ALMA CO (2 – 1) observations.

accounting for shorter baselines (Section 4.4). The whole data analysis presented in Neumann, den Brok et al. (2023) has been performed by myself.

4.1 Simulated ALMA observations

The simulated ALMA observations have been produced as part of the PHANGS–ALMA survey to test the performance of the pipeline used to produce combined single dish total power (TP) and interferometric (12 m and 7 m) data. In this work, we adopted the final simulated cubes to test the performance of spectral line stacking using PyStacker on ALMA-like observations of molecular line fainter than CO. The crucial advantage of simulated observations is that we know the true intensities so that we can compare the recovered intensities yielded by the stacking pipeline with the expected, true values. In the following, we will briefly describe how the simulated observations have been produced.

The production of the simulated observations was performed using CASA’s `simobserve` task and is described in detail in the PHANGS–ALMA pipeline paper (A. K. Leroy, Hughes et al., 2021). Two example galaxies (NGC 1097 and NGC 3059) have been selected as templates to perform simulated observations adopting the ALMA Cycle5 configuration from the PHANGS–ALMA survey at normal observing conditions (observations around transit; added thermal noise; 1 mm of precipitable water vapour). The templates, i.e. simulated CO (2 – 1) intensity distributions mimicking those of the respective galaxies, were produced using CASA’s `simdata` task, with some modifications to the orientations and distances of the galaxies to create templates that span the intensity distribution variability across the PHANGS–ALMA sample. Figure 4.1 shows peak intensity maps of the template galaxy NGC 3059 (left: template, right: template processed through imaging pipeline).

It was simulated to observe each galaxy for 1.5 hr with the ACA (7 m+TP) and for 6 hr using the large 12 m array in its most compact configuration (C43-1). To create a set of observations with different S/N,

the intensity distribution of the respective template galaxies has been divided by factors of 3, 10, 30, and 100 while keeping the integration time and thus the noise fixed. Given that the fiducial simulated data are mimicking PHANGS–ALMA CO (2 – 1) observations, the lower S/N versions approximately correspond to the amplitudes of ^{13}CO (1 – 0) (S/N divided by 10), HCN (1 – 0) or HCO^+ (1 – 0) (S/N divided by 30), and N_2H^+ (1 – 0) (S/N divided by 100). The simulated observations have then been run through the PHANGS pipeline with the same settings as for the real PHANGS–ALMA observations to produce combined interferometric and total power data cubes (12 m+7 m+TP). In addition, the pipeline provides imaging of various combinations of ALMA arrays, i.e. 12 m+7 m, 7 m, and 7 m+TP. We will also utilise these products to test the spatial filtering of interferometric observations propagated through the stacking pipeline.

4.2 Spectral line stacking

The spectral line stacking technique has been applied to the simulated ALMA observations of the template galaxies NGC 1097 and NGC 3059 described in Section 4.1. In this work, we produce spectral stacks in radial bins for the full set of observations at different S/N and test if the true radial trend can be recovered within the expected uncertainties. To define the velocity field, we use the simulated observations with the highest S/N, which mimic the line brightness of CO (2 – 1). To compare the line intensities of the different S/N observations among each other and with the true template values, we rescale the amplitudes to match the template intensities by multiplying the intensities by the respective factors of 3, 10, 30, and 100. In turn, this results in five observations at the same amplitude but different S/N values. We will refer to these as SNR/1, SNR/3, SNR/10, SNR/30, SNR/100, where SNR/1 is the fiducial PHANGS–ALMA CO (2 – 1) S/N level and SNR/3 is the version having a factor of 3 lower S/N, etc.

The analysis presented in Neumann, den Brok et al. (2023) focuses on one of the template galaxies, i.e. NGC 3059, which is the fainter target and, therefore, more challenging to recover faint lines. The idea is that if flux recovery of faint lines is successfully achieved for this galaxy, it is expected to work for brighter galaxies as well. To support that statement we repeated the analysis for NGC 1097 as well, yielding even better results, i.e. for this target we could recover line emission fainter by a factor of 3 compared to NGC 3059.

In Figure 4.2, we present the radially stacked spectra of all S/N observations across NGC 3059 in bins of 1 kpc width, spanning the full molecular gas disc, i.e. out to the maximum radius ($r_{\text{gal}} = 9$ kpc) where emission can be expected given the template data. The stacked spectra show that the true line shape can be well recovered out to 9 kpc for the two brightest lines (SNR/1, SNR/3) and out to 6 kpc for the two fainter lines (SNR/10, SNR/30). However, at larger radii ($r_{\text{gal}} > 6$ kpc), even for the brightest lines, the peak of the stacked spectra is significantly lower than the true line peak. The reason is the low detection fraction of the prior at larger radii, which is further discussed in Section 4.3. The SNR/100 observations are close to a pure noise cube and even stacking fails to recover significant emission for this target. Nevertheless, stacking can provide better constraints on upper limits, and if the stacks are cleverly weighted, e.g. via the CO intensity, stacks might yield some detections even for very faint lines (for more details we refer to Section 3.3 in Neumann, den Brok et al., 2023).

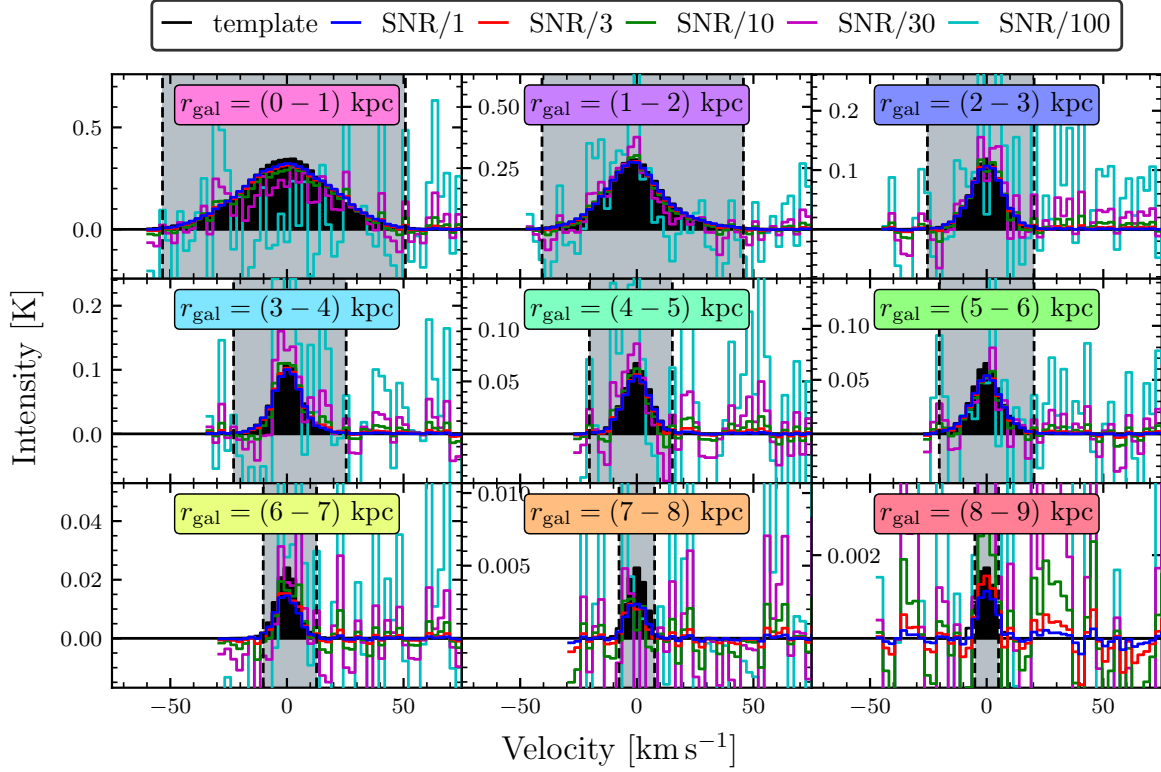


Figure 4.2: **Stacked spectra of the NGC 3059-lookalike at different S/N levels.** Shown are the stacked spectra computed over radial bins of 1 kpc width. The template line refers to the true spectra obtained from the input model. The coloured lines show the stacked spectra of the simulated observations of different S/N. The grey-shaded area denotes the velocity-integration window to compute the integrated intensities of the stacked spectra.

4.3 Recovery of integrated intensities

We use the radially stacked spectra shown in Figure 4.2 to compute the integrated intensities of the stacked spectra of the respective line cubes. The velocity-integration mask (grey shaded area in Figure 4.2) used to define the velocity window over which the stacked spectra are integrated is obtained via the procedure explained in Section 3.2.2 and implemented in PyStacker. In addition, the stacking tool yields uncertainties of the stacked line intensities by measuring the rms in the emission-free channels (see Section 3.2.2) for more details). The recovered radial trends for the different S/N versions are presented in the left panel of Figure 4.3. In addition, the right panel of Figure 4.3 shows the ratio between the integrated intensities from the stacks and the true values, clipped at different, measured S/N levels. We find that, for the NGC 3059-lookalike, the obtained stacked integrated intensities recover the true trend at 3σ significance within $r_{\text{gal}} = 0 - 4$ kpc for lines up to 30 times fainter than CO (2 – 1). At larger radii ($r_{\text{gal}} > 4$ kpc), the stacks yield biased-low values despite being apparent 3σ , 5σ , or 10σ detections. The reason is that at larger galactocentric radius the adopted prior, i.e. here SNR/1 mimicking CO (2 – 1) intensities, is much less complete within the respective radial bins, thus missing the accumulated flux over these pixels, which can only be recovered if the true velocity field is known. Within $r_{\text{gal}} < 4$ kpc, CO is detected in 62 % to 96 % of the pixels in the four radial bins. From $r_{\text{gal}} = 4$ kpc to 6 kpc, the

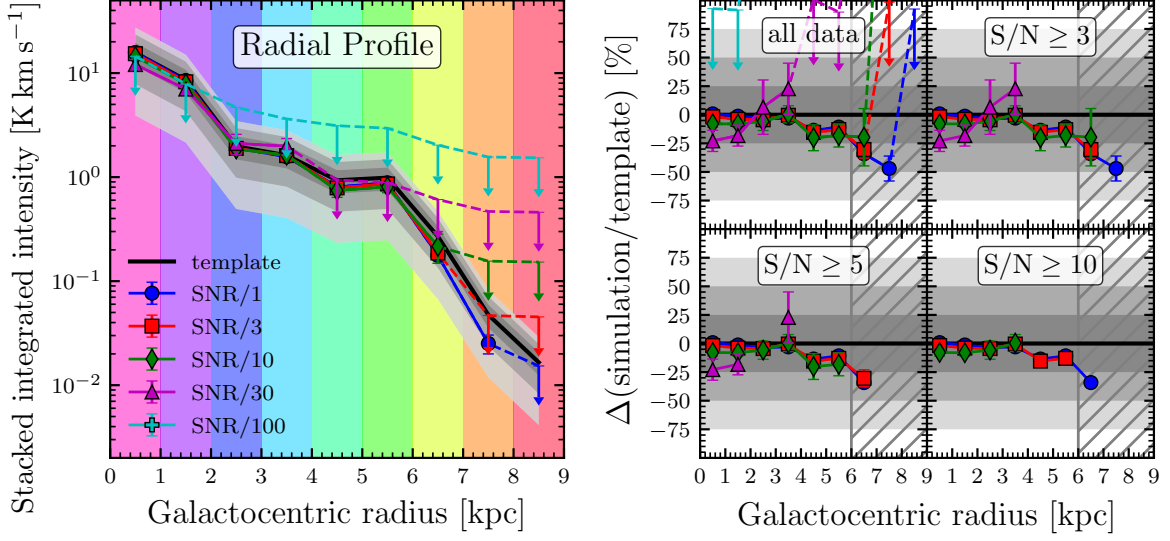


Figure 4.3: **Radial profile of the NGC 3059-lookalike galaxy obtained via spectral stacking.** *Left:* Stacked integrated intensities as a function of galactocentric radius. The black line indicates the true radial trend of the input template. The coloured lines show the integrated intensities of the stacked spectra from the simulated observations at different S/N corresponding to Figure 4.2. Downward-pointing arrows denote 3σ upper limits. The grey shaded areas show deviations from the true trend of $\pm(25, 50, 75)\%$ at decreasing opacity. *Right:* The same radial trends but shown as the ratio of the stacked integrated intensities from the simulated data and the template data. The top left panel shows all data. The other panels show only data above a S/N of 3, 5, and 10.

detection fraction is between 36 % and 47 %, yielding up to 20 % biased-low intensity values. At radii above 6 kpc (detection fraction < 16 %) the bias increases to up to 50 %. This means that it can only be expected to obtain robust stacked intensities within the uncertainty limits if the detection fraction of the prior across the stacking region is at least $\sim 50\%$.

4.4 Interferometric filtering

In Section 2.1.5, we explain that interferometers can only recover a certain range of spatial scales defined via the minimum and maximum baseline between two antennas. While the spatial resolution of the telescopes depends on the maximum baseline, the minimum baseline determines the largest angular scale (LAS) that can be recovered. Therefore, interferometers are spatial filters that will miss extended emission larger than the LAS and are often combined with single-dish observations to obtain full flux recovery. ALMA (Section 2.2.2, one of the most powerful sub-mm interferometers, is no exception to this fundamental limits and thus offers total power observations to combine with the interferometric observations if needed. Our simulated data provide the ideal test case to study the effect of flux filtering using different typical ALMA telescope array configurations similar to the PHANGS–ALMA observations. We take the simulated observations from A. K. Leroy, Hughes et al. (2021), who produced pipeline-imaged line cubes at different array configurations, including observations that consider only interferometric data (7 m, 12 m, 7 m+12 m) and those combined with total power observations from the ACA (7 m+TP, 12 m+7 m+TP). We note that the main analysis was done using the 12 m+7 m+TP

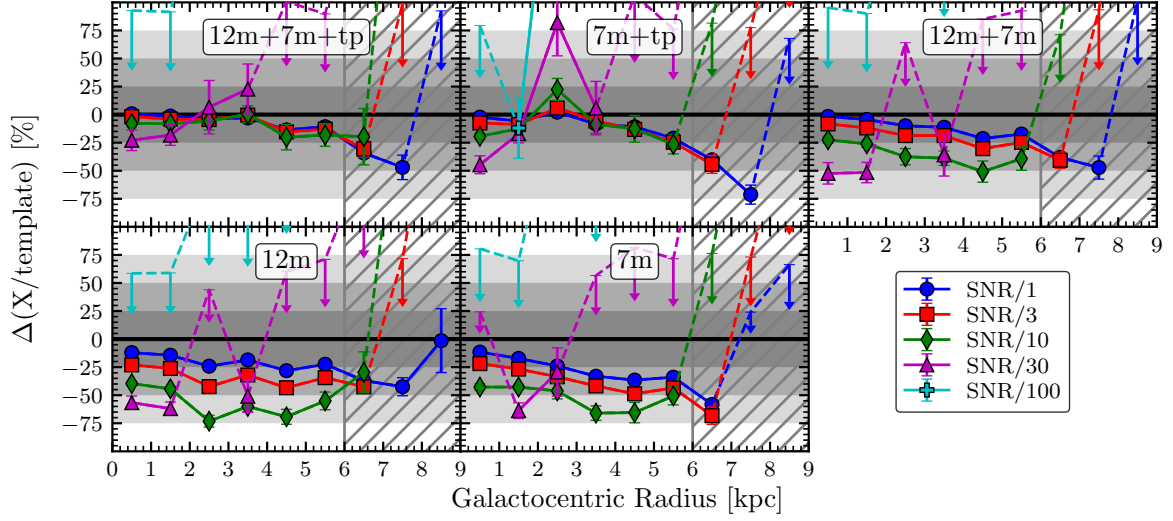


Figure 4.4: **Radial stacks for different antenna configurations.** Similar to the right panels of Figure 4.3, but showing the stacking results computed from different ALMA antenna configurations. In particular, the top right and middle panels include single dish total power observations (TP), while the other panels present radial stacks from interferometric-only observations from the 12 m array, the 7 m dishes of the ACA or the combinations (12 m+7 m).

configuration. Figure 4.4 shows the resulting radial stacks with respect to the true values of the different array configurations and at different S/N levels of the line cubes. We find that for bins within 4 kpc, where the velocity field has a completeness of more than 50 %, the interferometric observations without TP correction of the CO (2 – 1) S/N level (SNR/1) miss up to 25 % of the flux, which agrees with the results from A. K. Leroy, Hughes et al. (2021). Interestingly, we find a trend with S/N, i.e. interferometric observations of fainter lines miss more relative flux the fainter the line if TP data is not used. On the contrary, if TP observations are combined with the interferometric data, all S/N levels recover the same flux within their uncertainties.

4.5 Conclusions

In this work, we present the capabilities and limitations of spectral stacking applied to radio-interferometric data. Within our research group, we developed the spectral stacking tool `PyStacker` with major contributions from myself. The `PyStacker` code has been facilitated as a `python` package, which is publicly available via `GitHub`. We applied this tool to a set of simulated ALMA observations of two template galaxies at five different S/N levels. The goal was to compare the measured results from the spectral stacking with the true template values to quantify the performance of `PyStacker` in a realistic scenario mimicking typical molecular line observations of nearby galaxies with ALMA. The key result of this work is that spectral stacking can successfully recover the true integrated intensities of the radial trend of a relatively faint nearby galaxy like NGC 3059 out to $r_{\text{gal}} = 4$ kpc for lines up to 30 times fainter than CO (2 – 1), e.g. HCN (1 – 0) or HCO⁺ (1 – 0). Therefore, this work strongly supports the robustness of recovering faint molecular lines via spectra stacking of typical ALMA observations (see e.g., Jiménez-Donaire, Bigiel, A. K. Leroy, Usero et al., 2019; Bešlić et al., 2021; den Brok,

Chatzigiannakis et al., 2021; den Brok, Bigiel, Sliwa et al., 2022; Neumann, Gallagher et al., 2023). However, unbiased stacks are only obtained if the velocity field is known for at least $\sim 50\%$ of the spaxels in the respective stacking region. Moreover, for typical molecular line observations of nearby galaxies with ALMA, total power observations are crucial to recover the full flux.

Dense gas scaling relations

Dense gas relations at kiloparsec scale across nearby galaxies with EMPIRE and ALMOND

*L. Neumann, M. J. Jiménez-Donaire, F. Bigiel, A. Leroy, A. Usero,
and the PHANGS collaboration*

in preparation

Overview

Star formation happens in the dense parts of giant molecular clouds. Over the last two decades, the $J = 1 - 0$ rotational transition of hydrogen cyanide, HCN, has successfully been utilised as a probe of the dense molecular gas in external galaxies (e.g., Neumann, Gallagher et al., 2023). HCN has a higher critical density than the low- J transitions of CO and is thus typically tracing denser gas that is more tightly linked to sites of star formation. The immediate link between HCN luminosity, a proxy for the amount of dense gas, and the star formation rate has observationally been studied from nearby clouds within the Milky Way, over nearby galaxies, to the distant universe, resulting in the so-called Gao–Solomon relation. This tight and linear relation between HCN and SFR suggests that the rate at which stars form is ultimately regulated by the amount of dense molecular gas, i.e. the immediate fuel for star formation. In other words, the Gao–Solomon relation might indicate a constant dense gas star formation efficiency ($\text{SFE}_{\text{dense}} = \text{SFR}/M_{\text{dense}}$) across the universe. However, until ten years ago, dense gas tracers have only been mapped in Milky Way clouds (pc scales), or across entire galaxies (10 kpc scales), i.e. extragalactic studies could not resolve any morphological structures and thus environmental variations within galaxies. Only recently, due to the rise of ALMA and dedicated large programs with the IRAM facilities, it has become possible to efficiently map nearby galaxies in dense gas tracers like HCN, making it possible to study dense gas and star formation at 100 pc to kpc scales. These studies show that $\text{SFE}_{\text{dense}}$, although roughly constant at integrated-galaxy scales, does systematically vary within galaxies as a function of \sim kpc-scale environment (e.g., Usero et al., 2015; Bigiel, A. K. Leroy, Blitz et al., 2015; Gallagher, A. K. Leroy, Bigiel, Cormier, Jiménez-Donaire, E. Ostriker et al., 2018; Jiménez-Donaire, Bigiel, A. K. Leroy, Usero et al., 2019) and molecular cloud properties (Gallagher, A. K. Leroy, Bigiel, Cormier, Jiménez-Donaire, Hughes et al., 2018; Neumann, Gallagher et al., 2023). In particular, EMPIRE (Jiménez-Donaire, Bigiel, A. K. Leroy, Usero et al., 2019) and ALMOND

(Neumann, Gallagher et al., 2023), the two largest dense gas surveys of nearby galaxies to date, produced major contributions to improving our understanding of dense gas variations within nearby, star-forming galaxies.

The paper (in preparation) presented in this chapter will be submitted to A&A in 2024. This work has been led by me and conducted with significant contributions from María J. Jiménez-Donaire and the PHANGS collaboration. M. J. Jiménez-Donaire provided the spectral stacks of the EMPIRE data. The rest of the data analysis and all figures have been produced by myself. Some of the results presented in this work have also entered the review paper by Schinnerer and A. K. Leroy (2024) (their section 3). In the following sections, we elaborate on the findings of the paper. In this work, we merge the two surveys (EMPIRE – northern sky with IRAM 30 m, ALMOND – southern sky with ALMA), to create the largest sample of dense gas maps across nearby galaxies, i.e. 31 galaxies, at a matched, \sim kpc physical resolution. In combination with numerous, resolved HCN surveys conducted in nearby galaxies, we compile the most updated dataset of HCN emission across the universe to study dense gas star formation relations across various scales. In particular, this data allows us to fill the gap between the Milky Way and external galaxy measurements in the Gao–Solomon relation, which was only poorly studied until very recently (Section 5.2). In the next step, we investigate how HCN/CO, a proxy for the dense gas fraction (f_{dense}), affects the star formation efficiency of the molecular gas (SFE_{mol}), traces via glssfrco , and the dense molecular gas ($\text{SFE}_{\text{dense}}$), traces via SFR/HCN (Section 5.3). The main goal of this paper is to constrain systematic variations of HCN/CO and SFR/HCN as a function of the \sim kpc-scale environment on the largest, homogeneous sample of nearby spiral galaxies to date (Section 5.4).

5.1 EMPIRE and ALMOND surveys

The key results of this work are based on the two largest, resolved dense gas tracer mapping campaigns of nearby galaxies, i.e. the “EMIR Multiline Probe of the ISM Regulating Galaxy Evolution” survey (EMPIRE; Jiménez-Donaire, Bigiel, A. K. Leroy, Usero et al., 2019) and the “ACA Large-sample Mapping Of Nearby galaxies in Dense gas” survey (ALMOND; Neumann, Gallagher et al., 2023). Both surveys covered several dense gas tracers, including HCN (1 – 0), HCO^+ (1 – 0), HNC (1 – 0) (only EMPIRE), and CS (2 – 1) (only ALMOND). In this work, we focus on HCN (1 – 0) as the primary dense gas tracer since it is the brightest of these lines, which has extensively been studied extragalactically to study dense gas. EMPIRE observed nine galaxies in the northern hemisphere with the IRAM 30 m telescope at a common best resolution of $33''$ corresponding to ~ 2 kpc linear scale. ALMOND utilised ALMA-ACA to map 25 galaxies in the southern hemisphere at the common best resolution of ~ 2 kpc. The galaxy sample is presented in Table 5.1 along with their coordinates and global properties. Note that three galaxies (NGC 628, NGC 2903, NGC 4321) are covered by both surveys. We have checked that the cubes and maps of both surveys are consistent with each other and select the ALMOND observations for further analysis due to better sensitivity. The merged sample includes 31 galaxies and forms the largest, homogeneous sample of HCN maps of nearby galaxies at ~ 2 kpc resolution.

EMPIRE also observed CO (1 – 0) emission at a matched resolution to trace the bulk molecular gas. In this work, we adopt a constant CO-to- H_2 conversion factor of $\alpha_{\text{CO}} = 4.35 M_{\odot} \text{ pc}^{-2} (\text{K km s}^{-1})^{-1}$ (Bolatto et al., 2013) to relate the CO (1 – 0) emission to a molecular gas mass:

$$M_{\text{mol}} = \alpha_{\text{CO}} \cdot L_{\text{CO}} \implies \left(\frac{M_{\text{mol}}}{M_{\odot}} \right) = 4.35 \left(\frac{L_{\text{CO}}}{\text{K km s}^{-1} \text{ pc}^2} \right). \quad (5.1)$$

ALMOND only has corresponding CO (2 – 1) maps for the full sample from the PHANGS–ALMA survey (A. K. Leroy, Schinnerer et al., 2021). To form a homogeneous sample, we convert the CO (2 – 1) intensities of the ALMOND galaxies into CO (1 – 0) intensities. Since the CO (2 – 1)-to-CO (1 – 0) systematically varies within galaxies as a function of the star formation rate surface density (Σ_{SFR}), we adopt the calibration from Schinnerer and A. K. Leroy (2024):

$$R_{21} = \frac{W_{\text{CO}(2-1)}}{W_{\text{CO}(1-0)}} = 0.65 \left(\frac{\Sigma_{\text{SFR}}}{1.8 \times 10^{-2} M_{\odot} \text{ yr}^{-1} \text{ kpc}^{-2}} \right)^{0.125} \quad (5.2)$$

to correct for these systematic variations, where R_{21} is set to within the boundaries of [0.35, 1].

The star formation rates are taken from the ALMOND survey paper (Neumann, Gallagher et al., 2023), and use a combined calibration based on 22 μm FIR from WISE (Wright et al., 2010) and 154 nm FUV from GALEX (C. L. Martin, 2005) adopting the methodology from z0MGS ($z = 0$ Multiwavelength Galaxy Synthesis; A. K. Leroy, Sandstrom et al., 2019, also see Section 1.4). In comparison, EMPIRE uses an infrared-based SFR calibration Equation (5.4) based on *Herschel* observations at various infrared wavelengths to measure the total infrared luminosity (L_{IR}).

5.2 Gao-Solomon relation

Two decades ago, Gao and Solomon (2004) found that HCN emission is tightly linked to the infrared luminosity in galaxies, proposing that HCN traces the dense gas that is intimately connected to the rate at which stars form, as opposed to the bulk molecular gas traced by CO. Wu et al. (2010), Lada et al. (2012) and many others (see references in Figure 5.1) found a remarkably similar relation between HCN and IR luminosity within dense clumps of molecular clouds in the Milky Way, supporting a fundamental connection between dense molecular gas and star formation from sub-parsec to integrated-galaxy scales. Over the last twenty years, many more surveys aimed at mapping HCN (1 – 0) in the local group and more recently across nearby galaxies at arcsecond relation, where ALMA has been a key player in efficiently mapping and resolving HCN in external galaxies at unprecedented resolution (references are listed in the text below). Today, we have an almost complete sampling of the HCN-IR plane from Milky Way clouds to distant galaxies (redshift ≤ 3) spanning more than ten orders of magnitude.

In Figure 5.1 (top panels), we present the Gao–Solomon relation with one of the most complete and up-to-date compilations of HCN surveys with corresponding IR measurements¹. Cloud- and clump-scale measurements are taken from observations within the Milky Way (Wu et al., 2010; Lada et al., 2012; I. Evans N. J., Heiderman et al., 2014; Stephens et al., 2016), the CMZ (Jones et al., 2012; Barnes, Longmore et al., 2017) and the local group, i.e. LMC/SMC (Chin, Henkel, Whiteoak et al., 1997; Chin, Henkel, Millar et al., 1998), M31 (Brouillet et al., 2005), M33 (Buchbender et al., 2013), low-metallicity local group galaxies (Braine et al., 2017), and M51 (Chen et al., 2017). Resolved galaxy observations, typically from nearby galaxies at 100 pc to 2 kpc scales, include M82 (Kepley et al., 2014), M51 (Usero et al., 2015; Querejeta et al., 2019), NGC 4038/39 (Bigiel, A. K. Leroy, Blitz et al., 2015), NGC 3351, NGC 3627, NGC 4254, NGC 4321, NGC 5194 (Gallagher, A. K. Leroy, Bigiel, Cormier, Jiménez-Donaire, E. Ostriker et al., 2018), NGC 3627 (Bešlić et al., 2021), NGC 1068 (Sánchez-García et al., 2022), NGC 6946 (Eibensteiner, Barnes et al., 2022), NGC 4321 (Neumann, Bigiel et al., 2024),

¹ Note that some of the resolved HCN observations in nearby galaxies lack associated IR observations at a matched resolution (e.g., Neumann, Bigiel et al., 2024) so that in these cases we rely on extinction-corrected H α observations to trace SFR.

Table 5.1: Galaxy sample (EMPIRE + ALMOND)

Galaxy	R.A. (J2000)	Dec. (J2000)	d (Mpc)	i ($^{\circ}$)	M_{\star} ($10^9 M_{\odot}$)	M_{H_2} ($10^9 M_{\odot}$)	SFR ($M_{\odot} \text{ yr}^{-1}$)	SFR/ M_{\star} (10^{-10} yr^{-1})	Resolution ($''$)	Resolution (kpc)	Survey
(1)	(2)	(3)	(4)	(5)	(6)	(7)	(8)	(9)	(10)	(11)	(12)
NGC 0628	1 ^h 36 ^m 41.7 ^s	15 [°] 47'1.1''	9.8	8.9	21.94	2.70	1.75	0.80	18.6	0.89	ALMOND (EMPIRE)
NGC 1097	2 ^h 46 ^m 18.9 ^s	−30 [°] 16'28.8''	13.6	48.6	57.48	5.52	4.74	0.83	19.4	1.28	ALMOND
NGC 1365	3 ^h 33 ^m 36.4 ^s	−36 [°] 8'25.5''	19.6	55.4	97.77	18.07	16.90	1.73	20.6	1.96	ALMOND
NGC 1385	3 ^h 37 ^m 28.6 ^s	−24 [°] 30'4.2''	17.2	44.0	9.53	1.68	2.09	2.19	19.9	1.67	ALMOND
NGC 1511	3 ^h 59 ^m 36.6 ^s	−67 [°] 38'2.1''	15.3	72.7	8.09	1.47	2.27	2.80	17.6	1.30	ALMOND
NGC 1546	4 ^h 14 ^m 36.3 ^s	−56 [°] 3'39.2''	17.7	70.3	22.39	1.94	0.83	0.37	19.0	1.63	ALMOND
NGC 1566	4 ^h 20 ^m 0.4 ^s	−54 [°] 56'16.8''	17.7	29.5	60.85	5.05	4.54	0.75	19.8	1.69	ALMOND
NGC 1672	4 ^h 45 ^m 42.5 ^s	−59 [°] 14'50.1''	19.4	42.6	53.61	7.24	7.60	1.42	17.7	1.67	ALMOND
NGC 1792	5 ^h 5 ^m 14.3 ^s	−37 [°] 58'50.0''	16.2	65.1	40.96	6.64	3.70	0.90	18.8	1.47	ALMOND
NGC 2566	8 ^h 18 ^m 45.6 ^s	−25 [°] 29'58.3''	23.4	48.5	51.21	7.17	8.72	1.70	18.6	2.11	ALMOND
NGC 2903	9 ^h 32 ^m 10.1 ^s	21 [°] 30'3.0''	10.0	66.8	43.02	3.74	3.08	0.71	18.4	0.89	ALMOND (EMPIRE)
NGC 2997	9 ^h 45 ^m 38.8 ^s	−31 [°] 11'27.9''	14.1	33.0	54.06	6.79	4.37	0.81	20.4	1.39	ALMOND
NGC 3059	9 ^h 50 ^m 8.2 ^s	−73 [°] 55'19.9''	20.2	29.4	23.87	2.43	2.38	1.00	16.8	1.64	ALMOND
NGC 3184	10 ^h 18 ^m 17.0 ^s	41 [°] 25'28''	13.0	16					33	2.07	EMPIRE
NGC 3521	11 ^h 5 ^m 48.6 ^s	0 [°] 2'9.4''	13.2	68.8	105.21	5.90	3.72	0.35	21.2	1.36	ALMOND
NGC 3621	11 ^h 18 ^m 16.3 ^s	−32 [°] 48'45.4''	7.1	65.8	11.38	1.15	0.99	0.87	18.9	0.65	ALMOND
NGC 3627	11 ^h 20 ^m 15.0 ^s	12 [°] 59'30''	9.4	62					33	1.50	EMPIRE
NGC 4254	12 ^h 18 ^m 50.0 ^s	14 [°] 24'59''	16.8	32					33	2.68	EMPIRE
NGC 4303	12 ^h 21 ^m 54.9 ^s	4 [°] 28'25.5''	17.0	23.5	33.39	8.12	5.33	1.60	20.3	1.67	ALMOND
NGC 4321	12 ^h 22 ^m 54.9 ^s	15 [°] 49'20.3''	15.2	38.5	55.61	7.77	3.56	0.64	19.7	1.45	ALMOND (EMPIRE)
NGC 4535	12 ^h 34 ^m 20.3 ^s	8 [°] 11'52.7''	15.8	44.7	33.96	3.99	2.16	0.64	22.9	1.75	ALMOND
NGC 4536	12 ^h 34 ^m 27.1 ^s	2 [°] 11'17.7''	16.2	66.0	25.07	2.62	3.45	1.37	21.6	1.70	ALMOND
NGC 4569	12 ^h 36 ^m 49.8 ^s	13 [°] 9'46.4''	15.8	70.0	64.04	4.55	1.32	0.21	19.3	1.47	ALMOND
NGC 4826	12 ^h 56 ^m 43.6 ^s	21 [°] 40'59.1''	4.4	59.1	17.40	0.41	0.20	0.12	18.8	0.40	ALMOND
NGC 5055	13 ^h 15 ^m 49.2 ^s	42 [°] 1'45''	8.9	59					33	1.42	EMPIRE
NGC 5194	13 ^h 29 ^m 52.7 ^s	47 [°] 11'43''	8.4	20					33	1.34	EMPIRE
NGC 5248	13 ^h 37 ^m 32.0 ^s	8 [°] 53'6.7''	14.9	47.4	25.49	4.54	2.29	0.90	19.9	1.44	ALMOND
NGC 5643	14 ^h 32 ^m 40.8 ^s	−44 [°] 10'28.6''	12.7	29.9	21.69	2.66	2.59	1.20	18.1	1.11	ALMOND
NGC 6300	17 ^h 16 ^m 59.5 ^s	−62 [°] 49'14.0''	11.6	49.6	29.45	1.90	1.89	0.64	17.7	1.00	ALMOND
NGC 6946	20 ^h 34 ^m 52.2 ^s	60 [°] 9'14''	7.0	33					33	1.12	EMPIRE
NGC 7496	23 ^h 9 ^m 47.3 ^s	−43 [°] 25'40.3''	18.7	35.9	9.92	1.81	2.26	2.28	17.9	1.63	ALMOND

Notes – (2) Right ascension, (3) declination, (4) distance (NASA Extragalactic Database (NED), or Anand et al., 2021), (5) inclination angle (Makarov et al., 2014; Lang et al., 2020). Integrated galaxy properties, (6) global stellar mass, (7) global H_2 mass and (8) global star formation rate are taken from A. K. Leroy, Schinnerer et al. (2021). (10) native angular resolution, (11) corresponding linear resolution, given the distance d . (12) survey coverage.

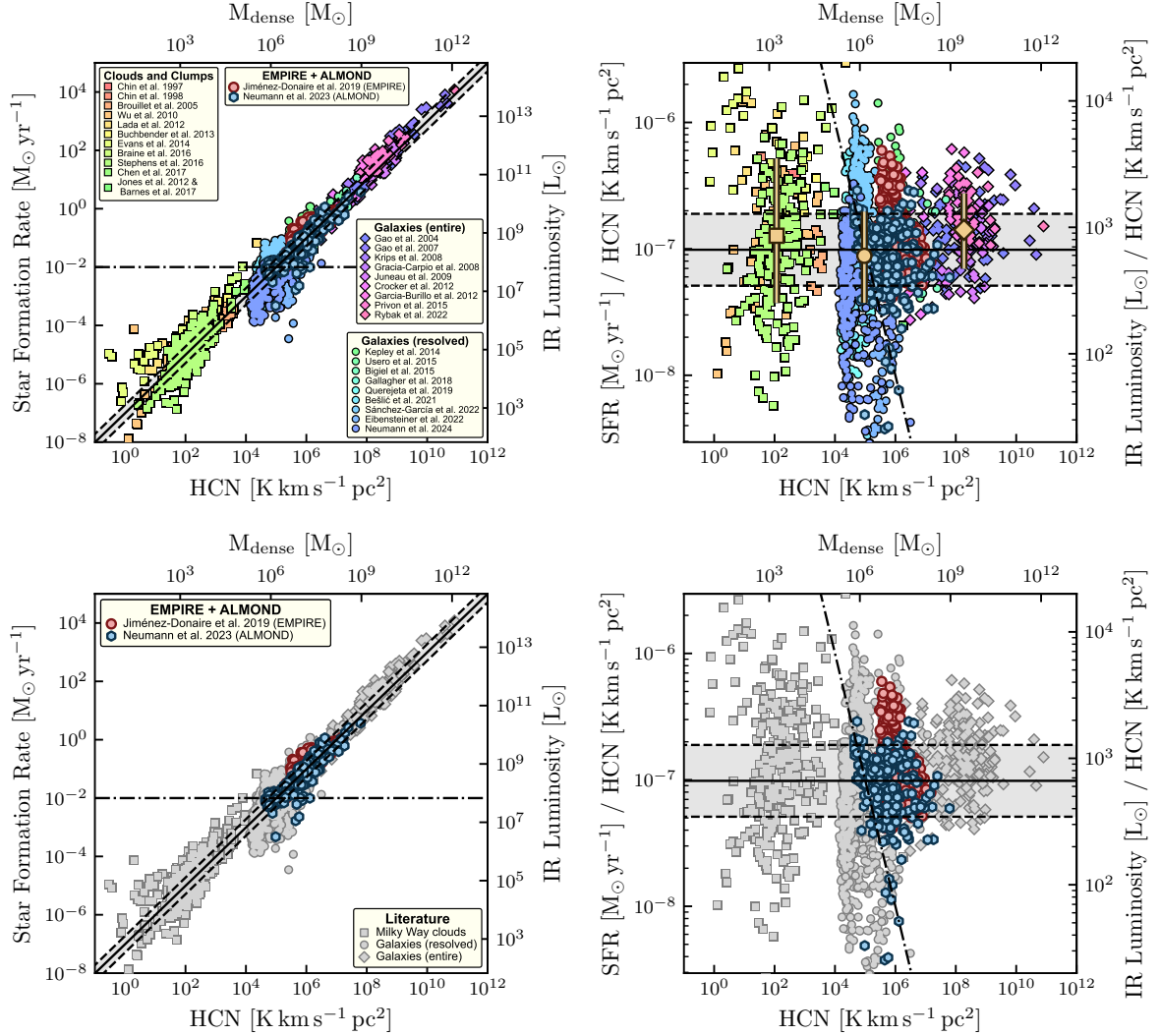


Figure 5.1: **Gao–Solomon relation – a literature compilation.** *Top:* Total infrared luminosity, a tracer of the star formation rate, against the HCN (1 – 0) luminosity, a proxy for the dense gas mass, across 31 HCN surveys from the Milky Way to the high-redshift universe. The HCN surveys cover observations of molecular clouds within the Milky Way and the local group, spatially resolved measurements within galaxies and integrated intensity data, spanning scales from the Solar neighbourhood to the distant, high-redshift universe (more details on the respective sources are given in the text; Section 5.2). The solid line denotes the average SFR/HCN of $1 \times 10^{-7} M_{\odot} \text{ yr}^{-1} (\text{K km s}^{-1} \text{ pc}^2)^{-1}$ and the dashed lines indicate the ± 1 -sigma scatter. The wheat-coloured markers (square, circle, diamond) and bars show the respective average and scatter for the different regimes (clouds, resolved and entire galaxies). The dash-dotted line at $\text{SFR} = 10^{-2} M_{\odot} \text{ yr}^{-1}$ indicates the threshold below which SFR values have to be interpreted with certain caveats since at these scales one might not average over large enough regions and hence timescales to yield robust SFR estimates. *Bottom:* Similar to the top panels, but highlighting (EMPIRE; Jiménez-Donaire, Bigiel, A. K. Leroy, Usero et al., 2019, red circles) and (ALMOND; Neumann, Gallagher et al., 2023, blue hexagons) in contrast to the literature data (grey markers). The two large HCN mapping campaigns of nearby galaxies encompass 9 and 25 galaxies, respectively for EMPIRE and ALMOND, mapped at $\sim \text{kpc}$ resolution.

and the two larger-sample surveys EMPIRE (nine galaxies; Jiménez-Donaire, Bigiel, A. K. Leroy, Usero et al., 2019) and ALMOND (25 galaxies; Neumann, Gallagher et al., 2023). Integrated-galaxy data

Table 5.2: Gao–Solomon relation

	SFR/HCN $M_{\odot} \text{ yr}^{-1} (\text{K km s}^{-1} \text{ pc}^2)^{-1}$	IR/HCN $L_{\odot} (\text{K km s}^{-1} \text{ pc}^2)^{-1}$	σ dex	$\tau_{\text{dep}}^{\text{dense}}$ yr	$\epsilon_{\text{ff}}^{\text{dense}}$
clouds/clumps	−6.90	2.93	0.69	8.07	−2.43
resolved galaxies	−6.99	2.84	0.37	8.17	−2.52
entire galaxies	−6.85	2.98	0.27	8.03	−2.38
combined	−6.98	2.85	0.40	8.15	−2.51

Notes – Average dense gas scaling relation values across the combined literature sample presented in Figure 5.1 and for respective sub-samples, i.e. clouds/clumps, resolved and integrated galaxy surveys. All values are displayed on a logarithmic scale. Columns 2 and 3 list the average SFR/HCN and SFR/IR, using $\alpha_{\text{HCN}} = 15 M_{\odot} \text{ pc}^{-2} (\text{K km s}^{-1})^{-1}$. Column 4 shows the 1-sigma scatter (σ) of the detected data around the average value. Columns 5 and 6 display the dense gas depletion time ($\tau_{\text{dep}}^{\text{dense}}$) and the dense gas star formation efficiency per free-fall time ($\epsilon_{\text{ff}}^{\text{dense}}$).

cover LIRGs/ULIRGs and AGN galaxies (Krips et al., 2008; Graciá-Carpio et al., 2008; Juneau et al., 2009; García-Burillo et al., 2012; Privon et al., 2015), early-type galaxies (A. Crocker et al., 2012), and high-redshift galaxies (Gao, Carilli et al., 2007; Rybak et al., 2022).

On the x - and y -axes, we indicate on the one hand the observed luminosities (HCN and IR) and on the other hand the inferred physical quantities (M_{dense} and SFR), assuming linear conversions of the form:

$$M_{\text{dense}} = \alpha_{\text{HCN}} \cdot L_{\text{HCN}} \implies \left(\frac{M_{\text{dense}}}{M_{\odot}} \right) = 15 \left(\frac{L_{\text{HCN}}}{\text{K km s}^{-1} \text{ pc}^2} \right) \quad (5.3)$$

$$\text{SFR} = C_{\text{IR}} \cdot L_{\text{IR}} \implies \left(\frac{\text{SFR}}{M_{\odot} \text{ yr}^{-1}} \right) = 1.48 \times 10^{-10} \left(\frac{L_{\text{IR}}}{L_{\odot}} \right) \quad (5.4)$$

using the conversion factors $\alpha_{\text{HCN}} = 15 M_{\odot} \text{ pc}^{-2} (\text{K km s}^{-1})^{-1}$ from Schinnerer and A. K. Leroy (2024) and $C_{\text{IR}} = 1.48 \times 10^{-10} M_{\odot} \text{ yr}^{-1} L_{\odot}^{-1} = 3.88 \times 10^{-44} M_{\odot} \text{ yr}^{-1} (\text{erg s}^{-1})^{-1}$ from Murphy et al. (2011). In the top right panel of Figure 5.1, the y -axis displays the ratio between SFR and L_{HCN} (left axis) to highlight relative changes to a constant SFR/HCN. The secondary y -axis shows the L_{IR} -to- L_{HCN} ratio, which is proportional to SFR/HCN via the C_{IR} conversion factor from above (5.4). In Sections 5.3 and 5.4, we also display the associated $\text{SFE}_{\text{dense}}$ following the above conversion factors and (5.10).

The black solid line in Figure 5.1 indicates the average SFR/HCN across the full literature sample and the grey shaded area represents the 1-sigma scatter of 0.40 dex. We also compute the respective average $\text{SFE}_{\text{dense}}$ values and scatter ranges for the individual sample regimes, i.e. clouds (square), resolved galaxy observations (circle), and entire galaxies (diamond). The values are listed in Table 5.2. Overall, the literature compilation demonstrates that the HCN luminosity is, to zeroth order, an excellent predictor of the star formation rate from cloud to galaxy scale, with consistent average $\text{SFE}_{\text{dense}}$ across 10 orders of magnitude. However, the scatter increases from large ($\sigma = 0.27$ dex) to small scales ($\sigma = 0.69$ dex), indicating that variations within galaxies are larger than galaxy-to-galaxy variations. This is already a first hint that there are systematic variations of $\text{SFE}_{\text{dense}}$ within galaxies (discussed in Section 5.4) that average out at integrated galaxy scales and that there might be other factors at play that affect $\text{SFE}_{\text{dense}}$ at kpc to cloud scales.

In the bottom panels of Figure 5.1, we show the same relations, but specifically highlighting

Table 5.3: Spectroscopic ratio relations

$\log_{10}(Y)$	$\log_{10}(X)$	m (unc.)	b (unc.)	σ	Corr. (p)	Reference
SFR/CO	HCN/CO	1.30 (0.05)	-6.47 (0.08)	0.16	0.30 (4.7×10^{-9})	Jiménez-Donaire, Bigiel, A. K. Leroy, Usero et al. (2019)
		1.02 (0.05)	-7.03 (0.08)	0.18	0.44 (5.2×10^{-12})	Neumann, Gallagher et al. (2023)
		1.23 (0.90)	-6.06 (1.10)	0.14	0.25 (2.3×10^{-1})	Kepley et al. (2014)
		1.37 (0.09)	-6.73 (0.12)	0.21	0.38 (4.2×10^{-10})	Querejeta et al. (2019)
		1.83 (0.13)	-6.11 (0.19)	0.21	0.40 (5.1×10^{-12})	Neumann, Bigiel et al. (2024)
SFR/HCN	HCN/CO	-1.33 (0.05)	-9.02 (0.08)	0.16	-0.33 (6.9×10^{-11})	Jiménez-Donaire, Bigiel, A. K. Leroy, Usero et al. (2019)
		-1.06 (0.06)	-8.69 (0.10)	0.17	-0.51 (2.0×10^{-16})	Neumann, Gallagher et al. (2023)
		-1.04 (1.02)	-7.61 (1.23)	0.15	-0.24 (2.5×10^{-1})	Kepley et al. (2014)
		-1.23 (0.07)	-8.83 (0.09)	0.23	-0.26 (2.6×10^{-3})	Querejeta et al. (2019)
		-0.54 (0.96)	-8.10 (1.39)	0.37	-0.04 (5.3×10^{-1})	Neumann, Bigiel et al. (2024)

Notes – Fit parameters obtained via linear regression with LinMix to the data shown in Figure 5.2. m , b and σ are the slope, intercept and scatter of the relation. Corr. (p) denotes the Pearson correlation coefficient with corresponding p -value.

data from EMPIRE (red) and ALMOND (blue), which are the two kpc-scale resolved surveys of nearby galaxies featured in this work. Both surveys roughly cover the same parameter space between $L_{\text{HCN}} = 10^4 \text{ K km s}^{-1} \text{ pc}^2$ and $10^8 \text{ K km s}^{-1} \text{ pc}^2$, since they mapped the same type of spiral, star-forming galaxies at similar physical scales of $\sim \text{kpc}$. It is shown that both data sets follow the Gao–Solomon relation and have comparable scatter, consistent with the full literature sample. The resolution of $\sim \text{kpc}$ is on the one hand high enough to resolve morphological structures like centres, bars and spiral arms and is on the other hand coarse enough to average over large enough regions to yield robust SFR measurements. Therefore, this combined data set is the ideal sample to study resolved environmental trends of dense gas and star formation across nearby, star-forming galaxies.

The $\text{SFE}_{\text{dense}}$ tells us how many stars are forming per unit time per dense gas mass. Assuming that the current amount of dense gas is causally linked to the currently measured SFR, $\text{SFE}_{\text{dense}}$ can be interpreted as the efficiency of converting dense molecular gas into stars. In turn, assuming the current SFR stays constant for the next few 100 million years, the inverse of $\text{SFE}_{\text{dense}}$, i.e. the depletion time $\tau_{\text{dep}}^{\text{dense}} = \text{HCN}/\text{SFR}$ tells us how long it takes until the dense gas reservoir is completely converted into stars. In this work, we find an average dense gas depletion time of $\langle \tau_{\text{dep}}^{\text{dense}} \rangle = 140 \text{ Myr}$. One issue with $\text{SFE}_{\text{dense}}$ as an efficiency measure is that it has units of yr^{-1} and does not take into account how fast the gas collapses under its own gravity. This shortcoming is addressed by the star formation efficiency per free-fall time, which is given as $\epsilon_{\text{ff}}^{\text{dense}} = \text{SFE}_{\text{dense}}/t_{\text{ff}}^{\text{dense}}$, where the free-fall time of the dense molecular gas can be computed assuming that HCN traces gas above a density of $n_{\text{H}_2}^{\text{dense}} \approx 10^4 \text{ cm}^{-3}$, yielding $t_{\text{ff}}^{\text{dense}} \sim 1 \text{ Myr}$, following Equation (1.16). Across the full literature sample, we obtain an average $\epsilon_{\text{ff}}^{\text{dense}} = 0.3 \%$, which suggests that only 0.3 % of the dense molecular gas is converted into stars. This demonstrates that even in the dense, immediate star-forming gas, star formation appears to be an extremely inefficient process, which is consistent with turbulent cloud models, that predict $\epsilon_{\text{ff}}^{\text{mol}} \sim \epsilon_{\text{ff}}^{\text{dense}}$ (McKee and E. C. Ostriker, 2007).

5.3 Dense gas fraction

The measured SFR/HCN yields consistently low dense gas star formation efficiencies across all surveys and scales. However, there is a significant scatter of $\text{SFE}_{\text{dense}}$ about the mean relation. In Figure 5.2, we present how SFE_{mol} , traced by glssfrco, and $\text{SFE}_{\text{dense}}$, traced by SFR/HCN, vary with f_{dense} , traced by

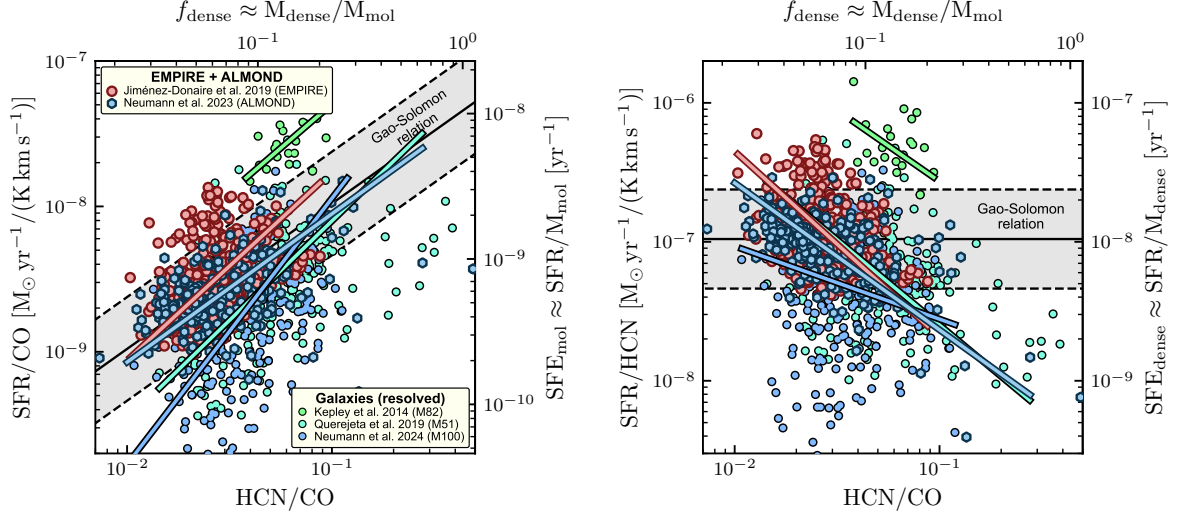


Figure 5.2: **Dense gas fraction scaling relations.** *Left:* glssfrco , a proxy of the star formation efficiency of bulk molecular gas (SFE_{mol}), against the HCN/CO , a proxy of the dense gas fraction (f_{dense}). *Right:* Analogously for SFR/HCN , a proxy of the star formation efficiency of dense molecular gas ($\text{SFE}_{\text{dense}}$). Shown is significant data from a selection of resolved galaxy observations at ~ 100 pc scales with M51 (Querejeta et al., 2019) and NGC 4321 (Neumann, Bigiel et al., 2024), as well as kpc-scale measurements from M82 (Kepley et al., 2014), EMPIRE and ALMOND. The solid black line and attached grey area indicate the Gao–Solomon relation from Figure 5.1. The coloured lines show the best-fit lines from BCES orthogonal linear regression (the fitting tool is described in Section 3.4.2). The fit parameters are listed in Table 5.3.

HCN/CO , across the EMPIRE and ALMOND galaxies, as well as within M51, M82 and NGC 4321. In each panel, we show the more observationally based ratios (HCN/CO , glssfrco , SFR/HCN) on the primary x - and y -axes, and the inferred physical quantities (f_{dense} , SFE_{mol} , $\text{SFE}_{\text{dense}}$) on the secondary axes. The physical quantities are computed assuming constant conversion factors, consistent with the values in Section 5.2. The dense gas fraction, f_{dense} , is assumed to be proportional to the HCN-to-CO line ratio:

$$f_{\text{dense}} = \frac{M_{\text{dense}}}{M_{\text{mol}}} = \frac{\alpha_{\text{HCN}} L_{\text{HCN}}}{\alpha_{\text{CO}} L_{\text{CO}}} \quad (5.5)$$

$$\Rightarrow f_{\text{dense}} = 3.45 \left(\frac{L_{\text{HCN}}}{\text{K km s}^{-1} \text{ pc}^2} \right) \left(\frac{L_{\text{CO}}}{\text{K km s}^{-1} \text{ pc}^2} \right)^{-1}. \quad (5.6)$$

The star formation efficiency of the molecular gas, SFE_{mol} , is traced via SFR-to-CO ratio:

$$\text{SFE}_{\text{mol}} = \frac{\text{SFR}}{M_{\text{mol}}} = \frac{\text{SFR}}{\alpha_{\text{CO}} L_{\text{CO}}} \quad (5.7)$$

$$\Rightarrow \left(\frac{\text{SFE}_{\text{mol}}}{\text{yr}^{-1}} \right) = 2.30 \times 10^{-1} \left(\frac{\text{SFR}}{M_{\odot} \text{ yr}^{-1}} \right) \left(\frac{L_{\text{CO}}}{\text{K km s}^{-1} \text{ pc}^2} \right)^{-1}. \quad (5.8)$$

Similarly, the SFR-to-HCN ratio is assumed to be proportional to the star formation efficiency of the dense gas:

$$\text{SFE}_{\text{dense}} = \frac{\text{SFR}}{M_{\text{dense}}} = \frac{\text{SFR}}{\alpha_{\text{HCN}} L_{\text{HCN}}} \quad (5.9)$$

$$\Rightarrow \left(\frac{\text{SFE}_{\text{dense}}}{\text{yr}^{-1}} \right) = 6.67 \times 10^{-2} \left(\frac{\text{SFR}}{M_{\odot} \text{ yr}^{-1}} \right) \left(\frac{L_{\text{HCN}}}{\text{K km s}^{-1} \text{ pc}^2} \right)^{-1}. \quad (5.10)$$

In agreement with previous works (e.g. Jiménez-Donaire, Bigiel, A. K. Leroy, Usero et al., 2019), we find that glssfrco increases, while SFR/HCN decreases with HCN/CO across all surveys shown in Figure 5.2. EMPIRE and ALMOND yield very similar relations that are also consistent with the higher resolution studies from M51 (at 100 pc) and NGC 4321 (at 260 pc). The starburst galaxy M82 shows significantly higher (factor of 3) SFR/CO and SFR/HCN at the same HCN/CO , indicating that starburst galaxies might be more efficiently producing stars. This is in contrast to a scenario where starbursts create more stars due to an excess of gas available. Using the BCES fitting tool (Section 3.4.2), we obtain slopes between $m = 1.0$ (ALMOND) and $m = 1.8$ (NGC 4321), where the kpc-scale data (EMPIRE and ALMOND) yield slopes roughly consistent with a fixed SFR/HCN , i.e. the Gao–Solomon relation with a slope of 1 (black line in Figure 5.2). In other words, the positive correlation between glssfrco and HCN/CO suggests that clouds with a higher fraction of dense gas form stars more efficiently from the reservoir of bulk molecular gas, which is consistent with the picture that dense gas is the key ingredient to control star formation. However, we also find that SFR/HCN systematically decreases with HCN/CO , finding slopes between $m = -0.53$ and $m = -1.33$ in contradiction to a constant SFR/HCN . If the physical quantities (f_{dense} and $\text{SFE}_{\text{dense}}$) were taken at face value this would imply that denser clouds convert dense gas less efficiently into stars than less dense clouds. An alternative interpretation put forward by e.g., Gallagher, A. K. Leroy, Bigiel, Cormier, Jiménez-Donaire, Hughes et al. (2018) and Neumann, Gallagher et al. (2023) is that at high HCN/CO , the molecular cloud density distribution is shifted to higher densities such that HCN is tracing more of the bulk molecular gas and not just the overdense gas, which is collapsing to eventually form stars.

5.4 Environmental variations in nearby galaxies

Many previous works have found that HCN/CO and SFR/HCN are not constant within galaxies, but vary systematically with environmental properties. Usero et al. (2015) and Gallagher, A. K. Leroy, Bigiel, Cormier, Jiménez-Donaire, E. Ostriker et al. (2018) show that HCN/CO systematically varies with the \sim kpc-scale, such as stellar surface density (Σ_{\star}), molecular gas surface density (Σ_{mol}), and environmental pressure (P_{DE}). Jiménez-Donaire, Bigiel, A. K. Leroy, Usero et al. (2019) find similar positive correlations between HCN/CO and Σ_{\star} , Σ_{mol} , P_{DE} and also report negative correlations between SFR/HCN and the aforementioned environmental conditions using the EMPIRE data. Here, we present the best constraints on these scaling relations using the combined EMPIRE and ALMOND data (Figure 5.3). The physical quantities (Σ_{\star} , Σ_{mol} , P_{DE}) are estimated following Jiménez-Donaire, Bigiel, A. K. Leroy, Usero et al. (2019). The stellar mass is inferred from *Spitzer* 3.6 μm observations. The molecular gas surface density is computed from the CO (1 – 0) intensity as in Equation (5.1). The dynamical equilibrium pressure is estimated from the weight of atomic (traced by H I 21 cm line emission), molecular (traced by CO line emission) and stellar mass (traced by 3.6 μm emission) and the velocity

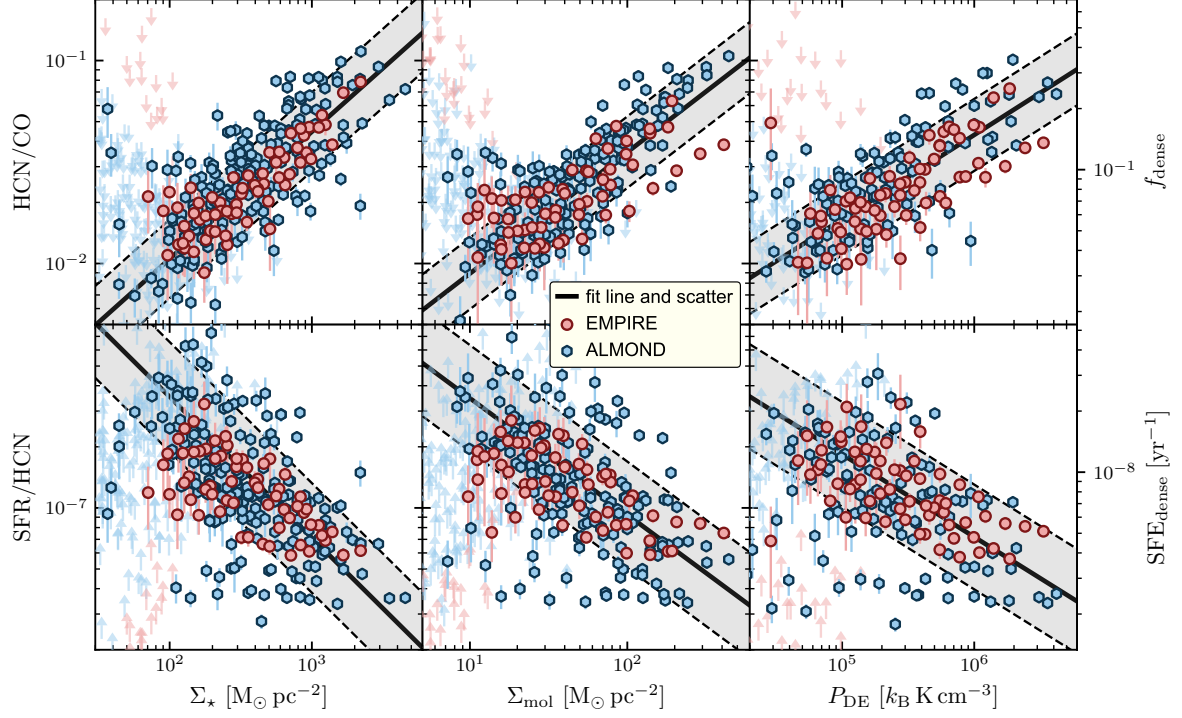


Figure 5.3: **Dense gas scaling relations with kpc-scale environment.** HCN/CO (*top*), a proxy of f_{dense} , and SFR/HCN (*bottom*), a proxy of $\text{SFE}_{\text{dense}}$, as a function of stellar mass surface density (Σ_{\star}), molecular gas surface density (Σ_{mol}), and dynamical equilibrium pressure (P_{DE}) across 31 galaxies from EMPIRE (red) and ALMOND (blue). The markers denote significant ($S/N \geq 3$) stacked measurements and the downward and upward pointing arrows indicate upper (HCN/CO) and lower limits (SFR/HCN). All relations have been fitted with LinMix taking into account measurement uncertainties and upper/lower limits (parameters in Table 5.4). The black solid line shows the best fit line and the grey-shaded area indicates the 1-sigma scatter of the detected data.

dispersion of the atomic and molecular gas, assuming an isothermal ISM disc with a fixed vertical profile, such that P_{DE} balances the weights of the individual components (see e.g., Gallagher, A. K. Leroy, Bigiel, Cormier, Jiménez-Donaire, E. Ostriker et al., 2018; Jiménez-Donaire, Bigiel, A. K. Leroy, Usero et al., 2019; Neumann, Gallagher et al., 2023; Neumann, Bigiel et al., 2024, for more details). The HCN (1 – 0) and CO (1 – 0) lines are spectrally stacked via PyStacker (see Section 3.2.2 for details on the methodology) via Σ_{\star} , Σ_{mol} and P_{DE} for each galaxy individually using the CO (1 – 0) line as a prior. For non-detected stacks, we provide upper (for HCN/CO) and lower limits (for SFR/HCN) as described in Section 3.3. The relations are fitted to a linear function of the form:

$$\log_{10} Y = b + m \cdot \log_{10} X, \quad (5.11)$$

where b and m are the intercept and slope, and $Y = \{\text{HCN/CO}, \text{SFR/HCN}\}$ and $X = \{\Sigma_{\star}, \Sigma_{\text{mol}}, P_{\text{DE}}\}$. The fitting is performed with the linear regression tool LinMix, which takes into account measurement uncertainties and censored data (the functioning principle of LinMix is described in Section 3.4.3). The fit parameters are presented in Table 5.4.

We find very similar scaling relations as reported by Jiménez-Donaire, Bigiel, A. K. Leroy, Usero

Table 5.4: Dense gas scaling relations with \sim kpc-scale environment

$\log_{10}(Y)$	$\log_{10}(X)$	m (unc.)	b (unc.)	σ	Corr. (p)
HCN/CO	Σ_{\star}	0.63 (0.03)	-3.23 (0.07)	0.19	0.85 (6.7×10^{-120})
	Σ_{mol}	0.60 (0.03)	-2.65 (0.05)	0.18	0.87 (9.7×10^{-142})
	P_{DE}	0.42 (0.02)	-3.86 (0.13)	0.18	0.83 (6.9×10^{-75})
SFR/HCN	Σ_{\star}	-0.70 (0.04)	0.94 (0.10)	0.27	-0.76 (7.4×10^{-84})
	Σ_{mol}	-0.57 (0.04)	0.11 (0.07)	0.26	-0.75 (9.1×10^{-82})
	P_{DE}	-0.41 (0.04)	1.30 (0.19)	0.26	-0.68 (3.2×10^{-41})

Notes – Fit parameters obtained via linear regression with LinMix to the data shown in Figure 5.3. m , b and σ are the slope, intercept and scatter of the relation. Corr. (p) denotes the Pearson correlation coefficient with corresponding p -value. Σ_{\star} and Σ_{mol} are given in units of $M_{\odot} \text{ pc}^{-2}$; and P_{DE} in $k_{\text{B}} \text{ K cm}^{-3}$.

et al. (2019) but across a larger sample of galaxies and morphologies. This means, HCN/CO increases, while SFR/HCN decreases with Σ_{\star} , Σ_{mol} , P_{DE} . However, there are some small differences compared to previous studies. On the one hand, we find more significant fit relations due to the larger sample of galaxies, making the results reported in this work more robust. On the other hand, we observe a larger scatter across the full sample of 31 galaxies compared to the EMPIRE galaxies alone, pointing towards galaxy-to-galaxy variations in the scaling relations. The enhanced HCN/CO in high-surface density, high-pressure environments, which could indicate that deeper gravitational potentials and higher external pressure exerted on molecular clouds leads to the formation of denser gas. At the same time this denser molecular gas is less efficiently converted into stars since only the overdense part is expected to collapse and form stars (based on turbulent cloud models, e.g., Krumholz and McKee, 2005). Overall, these results support the picture that there are consistent, systematic variations of HCN/CO and SFR/HCN with the \sim kpc-scale environment, suggesting that molecular clouds couple to the environment in which they are embedded.

5.5 Dense gas and star formation in galaxy centres

High-density, high-pressure regimes are typically found in centres of galaxies, hence one might expect systematically high HCN/CO and low SFR/HCN in galaxy centres compared to the discs. In Figure 5.4, we separately show the centre measurements in contrast with the disc data in the Gao–Solomon relation. For EMPIRE and ALMOND, the centres are simply a single sightline measurement from the centre of each galaxy and all remaining spaxels are denoted as disc environment. To first order, we find that both environments (centres and discs) follow the Gao–Solomon relation with similar mean and scatter if purely based on detected measurement. However, while the centre measurements are complete the disc data has a large fraction ($\sim 80\%$) of non-detections (we refer to Section 3.3.2 for background information on the effect of non-detections on population statistics). To account for the non-completeness, we also compute the median SFR/HCN across the disc sightlines taking into account censored data, which yields $\text{SFR/HCN} = 2.1 \times 10^{-7} M_{\odot} \text{ yr}^{-1} (\text{K km s}^{-1} \text{ pc}^2)^{-1}$, a factor of 2 – 3 lower than the median across the centres ($\text{SFR/HCN} = 9.4 \times 10^{-8} M_{\odot} \text{ yr}^{-1} (\text{K km s}^{-1} \text{ pc}^2)^{-1}$). Hence, the typically higher density and pressure in galaxy centres appear to yield lower SFR/HCN. If taken at face value, this would imply that galaxy centres are typically less efficiently forming stars per unit dense gas mass, which could be

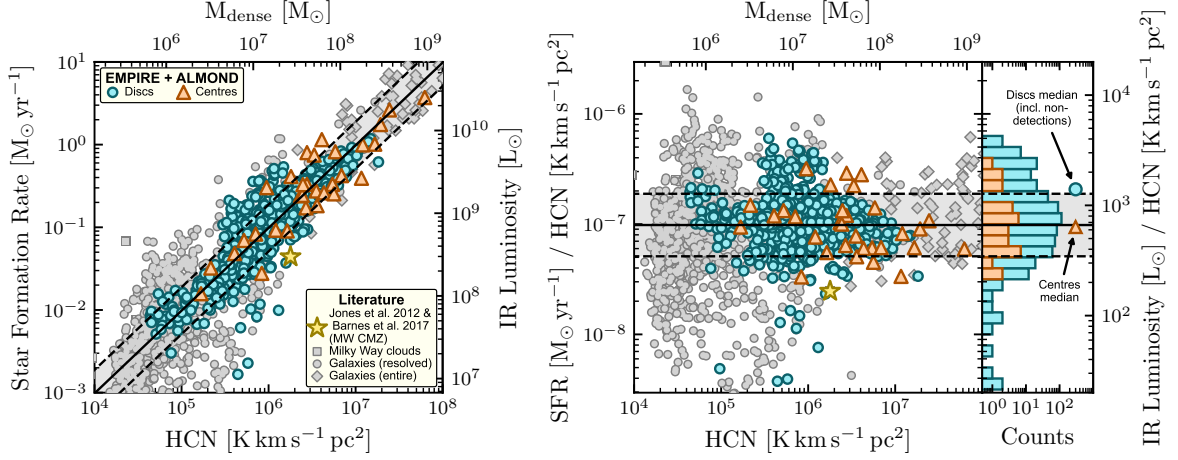


Figure 5.4: **Gao–Solomon relation – centres vs discs.** *Left:* Similar to the left panels of Figure 5.1, but contrasting centres (orange triangles) and disc (cyan circles) measurements across the 31 galaxies from EMPIRE and ALMOND. *Right:* Similar to the right panels of Figure 5.1 for centres and disc, and additionally showing histograms of the detected centre (orange) and disc (cyan) data. The markers (circle and triangle) in the histogram panel denote median SFR/HCN across the centres and discs, where also non-detections have to be taken into account.

explained by higher gas turbulence in these environments acting against gravitational collapse. However, we emphasise that interpretation of physical quantities like M_{dense} and $\text{SFE}_{\text{dense}}$ in galaxy centres are tentative, since we might expect the strongest α_{HCN} variations in centres of galaxies.

We also measure a low SFR/HCN in the central molecular zone (CMZ) of the Milky Way. Even more so, the MW-CMZ shows a lower SFR/HCN compared to all 31 external galaxies. However, we note that the value of the MW-CMZ has been measured at ~ 100 pc scale, while the centre measurements of this study have physical scales of ~ 1 kpc, hence smearing out CMZ trends. Therefore, the MW-CMZ might be consistent with ~ 100 pc measurements in external galaxies.

Dynamically, galaxy centres are fed by gas falling along the bar, which should increase their dense gas fraction, though, not smoothly as this gas inflow happens intermittently, so that gas can overshoot the CMZ and fall back later, yielding a delayed boost of star formation. These effects could raise or lower the observed SFR and HCN stochastically, but also gives some evolutionary variability to the CMZ that could be highly CMZ-by-CMZ dependent and linked to the host galaxy properties (e.g., Loose et al., 1982; Kruijssen and Longmore, 2014; Krumholz and Kruijssen, 2015; Krumholz, Kruijssen and R. M. Crocker, 2017; Torrey et al., 2017; Armillotta et al., 2019; Sormani, Tress et al., 2020; Tress et al., 2020; Moon et al., 2021; Moon et al., 2022; Moon et al., 2023).

5.6 Conclusions

To summarise, this work studies \sim kpc-scale dense gas scaling relation using the newly acquired ALMOND dense gas survey from Neumann, Gallagher et al. (2023), which is supplemented by data from EMPIRE to form the largest resolved data set of dense gas maps from the nearby spiral galaxy population. We find that the combined data set follows the well-established Gao–Solomon relation between SFR and HCN, demonstrating that, to zeroth order, HCN is linearly correlated with SFR over more than ten

orders of magnitude, ranging from local clouds to the high-redshift universe, hence forming one of the most remarkable scaling relations in astronomy. However, SFR/HCN (and HCN/CO) is not constant but varies systematically within galaxies as a function of environmental conditions measured on $\sim \text{kpc}$ scales. In this work, we provide the most robust constraints on these scaling relations using sensitive, stacked measurements across 31 galaxies, which show that HCN/CO increases and SFR/HCN decreases with stellar mass density, gas density, and external pressure.

In conclusion, this work shows that HCN/CO and SFR/HCN depend on $\sim \text{kpc}$ -scale environment and Neumann, Gallagher et al. (2023) find that these ratios also systematically vary with cloud-scale molecular gas properties. Moreover, Sun, A. K. Leroy, E. C. Ostriker et al. (2020) and Sun, A. K. Leroy, Schinnerer et al. (2020) find that (using a similar sample of galaxies from PHANGS–ALMA) the properties of molecular clouds (surface density, velocity dispersion) are affected by the $\sim \text{kpc}$ -scale environment. Linking these three findings, there is the emerging picture that the $\sim \text{kpc}$ -scale environment controls the local conditions of molecular clouds, which in turn regulate the formation of dense gas and its subsequent conversion into stars.

The missing link between dense gas, star formation and molecular cloud properties

The ALMOND survey: molecular cloud properties and gas density tracers across 25 nearby spiral galaxies with ALMA

L. Neumann, M. J. Gallagher, F. Bigiel, A. K. Leroy, A. T. Barnes, A. Usero, J. S. den Brok, F. Belfiore, I. Bešlić, Y. Cao, M. Chevance, D. A. Dale, C. Eibensteiner, S. C. O. Glover, K. Grasha, J. D. Henshaw, M. J. Jiménez-Donaire, R. S. Klessen, J. M. D. Kruijssen, D. Liu, S. Meidt, J. Pety, J. Puschignig, M. Querejeta, E. Rosolowsky, E. Schinnerer, A. Schruba, M. C. Sormani, J. Sun, Y.-H. Teng, and T. G. Williams

2023, MNRAS, 521, 3348, 36 pp. (DOI: [10.1093/mnras/stad424](https://doi.org/10.1093/mnras/stad424))

Overview

The tight relation between M_{dense} , traced by HCN, and SFR, traced by IR suggests that dense gas is the key ingredient for star formation (e.g. Gao and Solomon, 2004). However, dense gas alone is not enough to set the star formation rate. Over the last decade several studies pointed out systematic variations of SFR/HCN, a proxy of $\text{SFE}_{\text{dense}} = \text{SFR}/M_{\text{dense}}$, as a function of kiloparsec scale physical conditions across nearby, star-forming galaxies (e.g. Jiménez-Donaire, Bigiel, A. K. Leroy, Usero et al., 2019, also see Chapter 5). Gallagher, A. K. Leroy, Bigiel, Cormier, Jiménez-Donaire, Hughes et al. (2018) argued that these relations are a manifestation of following the theoretical picture laid out by Krumholz and Thompson (2007). However, Gallagher, A. K. Leroy, Bigiel, Cormier, Jiménez-Donaire, Hughes et al. (2018) only looked at the link between HCN/CO, a tracer of f_{dense} , as a function of molecular cloud properties in a small sample of five galaxies. Therefore, PHANGS designed a dense gas survey across 25 nearby galaxies with existing cloud-scale CO (2 – 1) measurements to investigate the missing link between dense gas spectroscopic ratios (HCN/CO, SFR/HCN) and molecular cloud properties.

This work was published in MNRAS in May 2023. The paper Neumann, Gallagher et al. (2023) is provided in its entirety in Appendix B. The following sections provide a commentary on the study’s key results, focusing on the link between dense gas, star formation and molecular cloud properties. At first, we introduce the new ALMA observations of the ALMOND survey, that are presented along with the

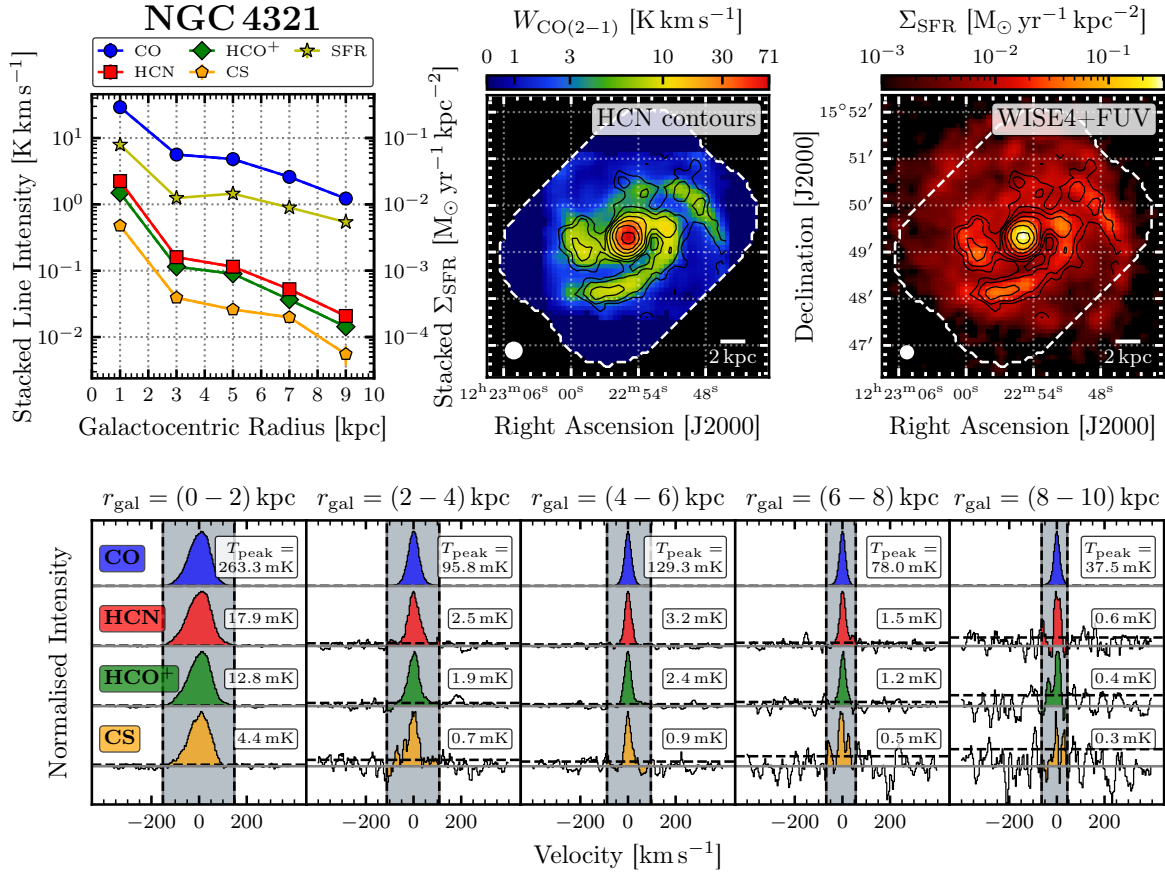


Figure 6.1: **ALMOND radial stacks across NGC 4321.** The map shows CO (2 – 1) integrated intensity (top middle), and the SFR surface density (top right), overlaid with the HCN (1 – 0) contours. The top left panel presents radial trends resulting from the radial stacks in the bottom panel.

paper (Section 6.1). Next, we lay out expectations about the studied scaling relations as inferred from turbulent cloud models (Section 6.2). Then, we summarise the key results of the paper, linking dense gas spectroscopic ratios to molecular cloud properties (Section 6.3). Finally, these results are put into the context of dense gas scaling relations, yielding a consistent picture across recent extragalactic dense gas studies (Section 6.4).

6.1 The ALMOND survey

The ALMOND survey is one of the largest surveys of dense gas tracers across nearby, star-forming galaxies (also see Section 2.3.1). It was performed using the ALMA telescope (Section 2.2.2), which is the most efficient instrument to map a large number of galaxies in molecular line emission. The survey covered the classical extragalactic dense gas tracers HCN (1 – 0), HCO⁺ (1 – 0), and CS (2 – 1), which were mapped at $\sim 20'' \sim 1 - 2 \text{ kpc}$ resolution. The main motivation for the ALMOND survey was to study the relation between dense gas properties and the properties of GMCs. The PHANGS–ALMA survey (Section 2.3.1) set the ground for studying molecular gas at cloud scales across nearby galaxies.

However, there was only a small overlap between the PHANGS–ALMA sample and existing dense gas surveys (e.g. Jiménez-Donaire, Bigiel, A. K. Leroy, Usero et al., 2019) hence motivating the Section 2.3.1 survey, which targeted the brightest, gas-rich galaxies from PHANGS–ALMA.

Appendix D.1 presents integrated intensity maps of the dense gas tracers from ALMOND. For this study, we focus on HCN (1 – 0) as the primary tracer of dense gas. HCN is detected across the centres of all galaxies, and the detection fraction decreases towards larger distances from the centre. HCN is mostly detected in the centres and spiral arms structures, which contain the highest amounts of molecular gas. Across the discs especially at larger galactocentric radii, the detection fraction is much lower, requiring spectral stacking to recover more emission. One of the most significantly detected sources is NGC 4321, which has additional observations yielding better, combined sensitivity. In NGC 4321, we can detect all dense gas tracers out to galactocentric radii of 10 kpc. However, in some other galaxies, HCN is only detected in the central 2 kpc, even with the help of stacking (see Chapter 6).

6.2 Model expectations

The idea of this section is to give an intuitive physical picture of how molecular cloud properties can affect line emission and star formation, neglecting many details that may be important to make quantitatively sophisticated statements. Here, the approach is simply to support the observed relations with a physical picture. Following Krumholz and McKee (2005), molecular clouds can be described by an analytical model, which assumes a spherically symmetric, self-gravitating object of supersonic, isothermal gas. In this prescription, the density distribution can be described by a log-normal probability distribution function (PDF), which is a function of the mean density (n_0) and the Mach number (\mathcal{M}), where the latter is directly related to the velocity dispersion of the gas (σ_{mol}). Hence, the density PDF of a (simplified) molecular cloud can be described by only two parameters: mean density and Mach number (for more details, we refer to section 2 of the original publication; Appendix B).

In the upper panels of Figure 6.2, we plot the log-normal PDF for different cloud parameters, (left) keeping n_0 fixed and varying \mathcal{M} , (right) keeping \mathcal{M} and varying n_0 . We can see that increasing the mean density shifts the PDF to higher densities, without affecting the shape of the PDF. On the contrary, changing the Mach number affects the width of the PDF but keeps the mean density constant (note that the centre of the PDF is not equivalent to the mean density). In this model, we can tweak n_0 , \mathcal{M} and study their effect on the PDF as well as the resulting line emission and SFR. To infer the luminosity of a certain line, we assume the line traces gas above its (effective) critical density (n_{eff} , Section 1.3.3), such that its luminosity scales with the total gas mass above n_{eff} . Here, we adopt $n_{\text{eff}}(\text{CO}) = 3 \times 10^2 \text{ cm}^{-3}$ and $n_{\text{eff}}(\text{HCN}) = 5 \times 10^3$ to $5 \times 10^4 \text{ cm}^{-3}$ (Shirley, 2015), where the range for HCN (solid and dashed lines in Figure 6.2) reflects the observational uncertainties of the critical density of HCN. Similarly, the SFR can be inferred through the Jeans criterion for gravitational collapse, assuming virialised clouds (i.e. a fixed ratio, $\alpha_{\text{vir}} \approx 1.3$, between gravitational and kinetic energy, which is supported by observations, e.g. Sun, A. K. Leroy, Schinnerer et al. (2020)), such that the critical density for gravitational collapse $n_{\text{SF}} \propto n_0 \mathcal{M}^2$. Hence, in our model, all gas mass above n_{SF} is converted into stars within a free-fall time $\tau_{\text{ff}} \propto n_0^{-1/2}$. This means gas at higher densities collapses faster, yielding higher SFR.

Putting it all together, the above model can estimate the star formation rate and the line luminosities of HCN (1 – 0) and CO (2 – 1) as a function of the cloud parameters n_0 and \mathcal{M} . The resulting relations of HCN/CO and SFR/HCN against n_0 and \mathcal{M} are shown in the bottom panels of Figure 6.2. We observe an increase of HCN/CO with increasing n_0 or \mathcal{M} . This is because increasing either the mean density or the

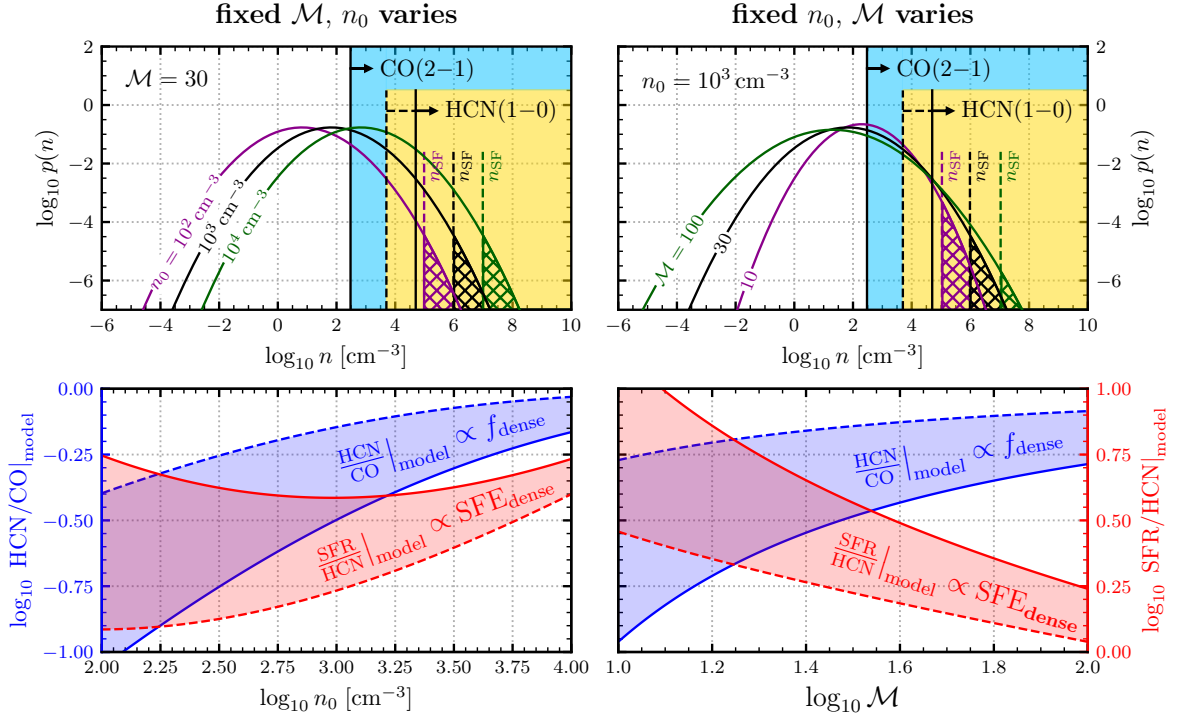


Figure 6.2: **Expectations from cloud models.** The model prescription is based on Krumholz and McKee (2005), where the density PDF is described by a log-normal distribution. The top panels show the density PDFs for varying mean density (left) and varying Mach number (right). The blue and yellow areas indicate the density regimes traced by CO (2 – 1) and HCN (1 – 0) line emission. The hatched regions above n_{SF} denote the regime for gravitational collapse according to the Jeans criterion. The bottom panels show the estimated HCN/CO and SFR/HCN as a function of the varying cloud properties corresponding to the upper panel PDFs. The range enclosed by the solid and dashed lines corresponds to the range in critical densities assumed for HCN as indicated in the upper panels.

Mach number yields larger fractions of gas at high densities. Moreover, we find that SFR/HCN decreases with increasing \mathcal{M} . This can be intuitively understood as gas turbulence affecting the density threshold for gravitational collapse such more turbulent gas is producing lower SFR, while HCN is tracing larger fractions of the gas PDF, hence SFR decreases and HCN increases. The relation between SFR/HCN and n_0 is less clear. This is because, on the one hand, increasing n_0 yields higher HCN luminosity, but, on the other hand, the overdense gas at higher densities is collapsing faster hence increasing SFR. Therefore, in our model, SFR/HCN decreases at low densities, since the change in HCN luminosities dominates, and then increases since for higher densities the behaviour of $\text{SFR} \propto n_0^{1/2}$ becomes dominant.

We note that the above picture is very simplistic and neglects that observations support a correlation between n_0 and \mathcal{M} , which manifests in a roughly constant α_{vir} . Therefore, in the paper, we take this correlation into account and use the observations to infer n_0 from the surface density (Σ_{mol}) and \mathcal{M} from the line width (Σ_{mol}) on a pixel-by-pixel basis (see figure 2 of the original paper, B). This modification creates more realistic predictions of the relations between HCN/CO, SFR/HCN and cloud-scale molecular gas surface density (Σ_{mol}), and velocity dispersion (σ_{mol}). These expectations break the ambiguity of the SFR/HCN against n_0 relation, predicting a clear negative correlation. This is because clouds with higher n_0 typically also have higher \mathcal{M} , which is driving a decrease of SFR.

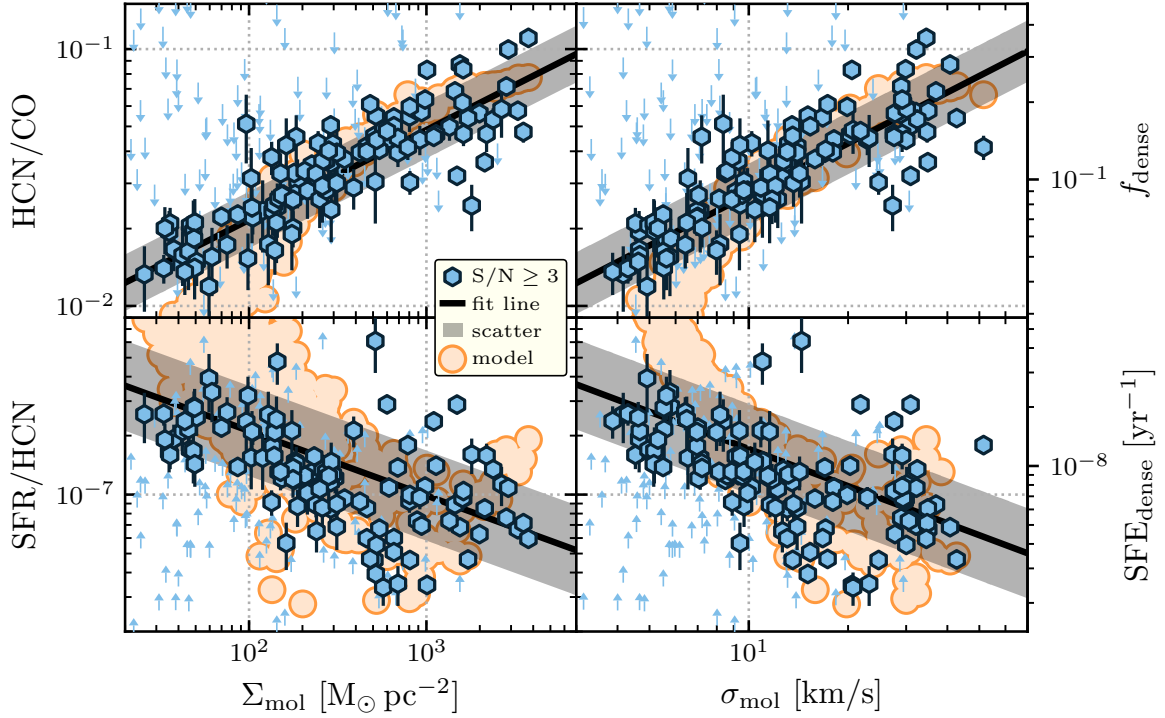


Figure 6.3: **Dense gas relations with cloud properties.** HCN/CO (top), a proxy for f_{dense} , and SFR/HCN, a proxy for $\text{SFE}_{\text{dense}}$, measured at 2.1 kpc scale against molecular cloud properties (Σ_{mol} , σ_{mol}) computed at 150 pc scale. The markers show significant data ($S/N \geq 3$) across all 25 galaxies from the ALMOND survey, and the arrows indicate upper (HCN/CO) and lower limits (SFR/HCN). The black solid line shows the best fit line and the grey-shaded area is the 1-sigma scatter of the detections about the fit line. The orange circles in the background indicate the model predictions. This figure is a simplified version of Figure 6 in the full paper.

6.3 Linking star formation to cloud properties

The above section laid out the physical connections between molecular cloud properties, density-sensitive lines ratios (e.g. HCN/CO), and star formation efficiency proxies (e.g. SFR/HCN), prediction systematic variations between the density and turbulence of molecular clouds and these spectroscopic ratios. In the following, we investigate these relations using observational data across the ALMOND survey. Here, we focus on the relation between SFR/HCN and HCN/CO against the cloud-scale Σ_{mol} and σ_{mol} (Figure 6.3). The cloud properties on the x -axis are computed from PHANGS–ALMA CO (2 – 1) data at a homogeneous physical resolution of 150 pc. The molecular gas surface density (Σ_{mol}) is computed from the integrated line intensity assuming constant $\alpha_{\text{CO}} = 4.35 M_{\odot} \text{pc}^{-2} (\text{K km s}^{-1})^{-1}$ (Bolatto et al., 2013) and $R_{21} = 0.65$ (den Brok, Chatzigiannakis et al., 2021; A. K. Leroy, Rosolowsky et al., 2022) conversion factors. The velocity dispersion (σ_{mol}) is inferred from the effective line width, assuming a Gaussian line profile (see full paper for more details). The HCN observations across the 25 galaxies have a common best resolution of 2100 pc. For y -axis measurements, we homogenise the HCN (1 – 0), CO (2 – 1) and SFR datasets to a resolution of 2.1 kpc. The SFR maps are taken from the zOMGS survey, which uses a combination of FIR and far ultraviolet (FUV) (A. K. Leroy, Sandstrom et al., 2019). The HCN line intensity is associated with dense gas mass using a constant $\alpha_{\text{HCN}} = 14 M_{\odot} \text{pc}^{-2} (\text{K km s}^{-1})^{-1}$

(Onus et al., 2018). In order to compute the x -axis (150 pc scale) with the y -axis (2.1 kpc scale) data on a pixel-by-pixel basis, we compute intensity-weighted averages of the 150 pc measurements by performing a CO (2 – 1) intensity-weighted convolution to a target resolution of 2.1 kpc. This formalism allows proper comparison between the cloud properties and the kiloparsec scale measurements by preserving the high-resolution information of the cloud scale measurements.

We then stack the y -axis measurements (HCN/CO, SFR/HCN), individually for each galaxy, to obtain more significant measurements, especially in the low Σ_{mol} regime, which significantly increases the dynamic range that is probed in the scaling relations. The resulting stacks are then fitted across all 25 galaxies by employing the linear regression tool LinMix (Section 3.4.3), which includes upper (HCN/CO) and lower limits (SFR/HCN). We also compute Pearson correlation coefficients to quantify the strength of the correlations, finding a very strong positive correlation between HCN/CO and the surface density ($\rho = 0.88$) as well as the velocity dispersion of the cloud-scale molecular gas ($\rho = 0.85$). Furthermore, we find a strong negative correlation between SFR/HCN and Σ_{mol} ($\rho = -0.63$) and σ_{mol} ($\rho = -0.60$). These findings are consistent with the expectation from turbulent cloud models laid out in Section 6.2 and suggest that cloud properties are key drivers of HCN/CO and SFR/HCN variations.

6.4 Conclusions

The ALMOND observations compile the largest survey of resolved dense gas observations across nearby, spiral galaxies. These observations are paired with robust SFR maps and cloud-scale measurements of the molecular gas thus allowing the first sophisticated investigation of the link between dense gas, star formation and GMC properties. In this first ALMOND paper, we focus on HCN (1 – 0) as the primary dense gas tracer and study the relation between HCN/CO, a proxy of f_{dense} , and SFR/HCN, a proxy of $\text{SFE}_{\text{dense}}$, with the surface density and velocity dispersion of the cloud scale molecular gas. These results suggest that denser, more turbulent clouds typically contain higher fractions of dense gas, but the dense gas is less efficiently converted into stars. In other words, at high mean densities or velocity dispersion, dense gas tracers such as HCN trace more of the bulk of the gas instead of purely the overdense part of GMCs that is collapsing to form stars.

These results link dense gas and star formation to the properties of molecular clouds, in agreement with expectations from turbulent cloud models. By finding this missing link, these findings yield a consistent picture of galactic environment conditions, cloud properties and their ability to form dense gas and stars. The emerging picture is that the kiloparsec scale galactic environment affects the properties of GMCs, which in turn, regulates the formation of dense gas and its conversion into stars (see also the review by Schinnerer and A. K. Leroy, 2024). Certainly, these connections describe only first-order, average relations and there are most likely other factors at play that regulate f_{dense} and $\text{SFE}_{\text{dense}}$. In particular, the large scatter of $\text{SFE}_{\text{dense}}$ about the average relations indicates that other physical mechanisms might affect the star formation efficiency. These cloud-to-cloud variations can only be studied at sub-kiloparsec scales, requiring deep, high-resolution dense gas observations, hence motivating the study of NGC 4321 presented in the following Chapter 7.

A spatially resolved view on dense gas in the galaxy NGC 4321

A 260 pc resolution ALMA map of HCN(1–0) in the galaxy NGC 4321

L. Neumann, F. Bigiel, A. T. Barnes, M. J. Gallagher, A. K. Leroy, A. Usero, E. Rosolowsky, I. Bešlić, M. Boquien, Y. Cao, M. Chevance, D. Colombo, D. A. Dale, C. Eibensteiner, K. Grasha, S. H. Menon, E. Schinnerer, J. D. Henshaw, M. J. Jiménez-Donaire, S. Meidt, E. J. Murphy, H. Pan, M. Querejeta, T. Saito, S. K. Stuber, Y. Teng, and T. G. Williams

2024, A&A, 691, A121, 26 pp. (DOI: [10.1051/0004-6361/202449496](https://doi.org/10.1051/0004-6361/202449496))

Overview

Star formation happens in the dense parts of giant molecular clouds (GMCs), and hence dense gas is the key ingredient to regulate star formation. Thus, understanding the process of star formation requires investigation of dense gas at scales comparable to the size of individual GMCs or at least for ensembles of a few GMCs. While these scales can easily be reached in the MW, our galaxy does not provide a universal view of star formation across a large range of environments and physical conditions. Moreover, in the MW, we have to deal with line of sight confusion, and assumptions of distance and source geometry, which induce large caveats relative to external galaxies. Therefore, it is crucial to study dense gas in external galaxies that provide a larger parameter space and enable a face-on view of the galaxy discs. However, past studies of dense gas in galaxies were often limited to kiloparsec-scale resolution (like EMPIRE or ALMOND), or sub-kiloparsec-scale observations in small regions. This means deep, sub-kiloparsec-scale, full-galaxy maps of dense gas tracers are basically non-existent, motivating the proposed observations of this work. In this work, we present new ALMA observations of HCN (1 – 0) across the full disc of the nearby, spiral galaxy NGC 4321 (a.k.a. M100) at 260 pc resolution. These data sets allowed us to take the novel step of studying dense gas and star formation at 260 pc scales across the full disc of a spiral galaxy, detecting HCN emission in 275 independent sightlines and resolving different morphological environments, to study the spatial and environmental variations of f_{dense} and $\text{SFE}_{\text{dense}}$ at unprecedented detail.

This work has been accepted on June 13, 2024, to be published in Astronomy and Astrophysics (A&A).

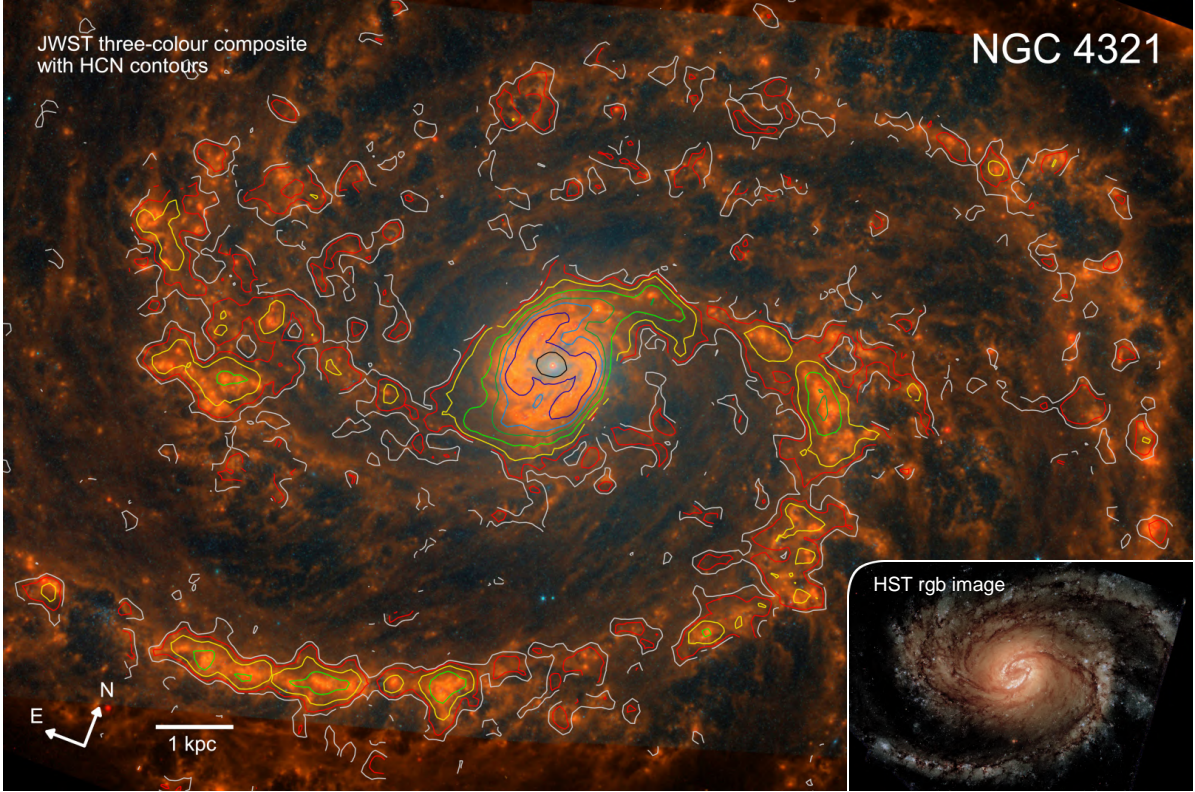


Figure 7.1: **Infrared and optical images of NGC 4321** The background shows a three-colour composite image from PHANGS–JWST (Lee, Sandstrom et al., 2023), where the reddish colours highlight mid-infrared wavelength emitted by hot dust related to recent star formation. The overlaid contours denote signal-to-noise level loci of the new ALMA HCN (1 – 0) observations at values of (2, 3, 5, 10, 20, 30, 50, 100). The bottom right image show an optical rgb image from PHANGS–HST (Lee, Whitmore et al., 2022).

The paper is provided in its entirety in Appendix C. In the following sections, we summarise the key findings of the paper and highlight my exclusive contributions to the paper. This work has been a major effort within the PHANGS collaboration, such that we could build our analysis on already observed and reduced ALMA observations. The newly acquired ALMA observations of NGC 4321 have been led by Molly J. Gallagher and reduced via Ashley T. Barnes (using the PHANGS–ALMA pipeline). In Section 7.1 will explain why this specific galaxy has been selected as the ideal target to study dense gas tracers at high-spatial resolutions and what ancillary data products were used to address the science questions laid out above. We will then highlight the key results of this work (Sections 7.2 to 7.5) and comment on how this work has helped to better understand molecular gas conditions and the process of star formation in galaxies (Section 7.6).

7.1 NGC 4321 – the ideal target to study dense gas at resolved scales

NGC 4321, also called M100, is a barred, spiral galaxy (SAB(s)bs), with a large molecular gas reservoir ($M_{\text{H}_2} = 7.8 \times 10^9 M_{\odot}$; A. K. Leroy, Schinnerer et al. (2021)) and active star formation ($\text{SFR} =$

$3.6 M_{\odot} \text{ yr}^{-1}$). The main global properties of NGC 4321 are listed in Table 7.1. As part of the Virgo galaxy cluster, NGC 4321 is relatively nearby ($d \approx 15 \text{ Mpc}$), such that $\sim 1''$ angular scales relate to $\sim 100 \text{ pc}$ physical scales.

From the PHANGS sample of galaxies, NGC 4321 is one of the brightest targets in (dense) molecular gas tracers (i.e. CO, HCN, etc.), with a large molecular gas disc, that is at the ideal distance to be efficiently mapped with ALMA, while allowing access to cloud-scales. Moreover, NGC 4321 shows large gradients in physical conditions (e.g. stellar surface density, molecular gas surface density, pressure), and various morphological environments (centre, bar, bar ends, spiral arms, interarm regions) without being affected by an AGN, hence making NGC 4321 the ideal target to study trends of dense gas properties in a local spiral galaxy.

Figure 7.1 shows an optical rgb image from the HST (bottom right) and a colour-composite image from the JWST overlaid with HCN contours from new ALMA observations. The bright orange hue traces regions of active star formation, which are spatially well correlated with the emission of HCN. Figure 7.2 presents the full set of arcsecond-scale observations of NGC 4321 used in this study, including CO (2 – 1), a tracer of molecular gas, at $1.7''$ resolution from PHANGS–ALMA (A. K.

Leroy, Schinnerer et al., 2021), $H\alpha$, a tracer of the SFR, at $1.2''$ resolution from PHANGS–MUSE (Emsellem et al., 2022), $21 \mu\text{m}$ wideband emission, an alternative tracer of the SFR, at $0.7''$ resolution from PHANGS–JWST (Lee, Sandstrom et al., 2023), and new ALMA observations of HCN (1 – 0), a proxy for dense molecular gas, at $3.7''$ resolution. The spectral setup of the new ALMA observations also covers alternative dense gas tracers, including HCO^+ (1 – 0) and CS (2 – 1). However, for this first work, we focus on HCN (1 – 0) as the primary tracer of dense molecular gas. More details on the observational setup, array configurations, pointings, and sensitivity can be found in Appendix C. The imaging has been carried out with the PHANGS pipeline along with quality assurance within the PHANGS collaboration. For the following analysis, we convolve all observations to the common best resolution of $3.7'' \sim 260 \text{ pc}$ and resample to a matching grid using PyStacker (Section 3.2).

Table 7.1: Properties of NGC 4321.

Property	Value
Alternative Name	M100
Right Ascension (J2000) ^(a)	$12^{\text{h}}21^{\text{m}}54.9^{\text{s}}$
Declination (J2000) ^(a)	$4^{\circ}28'25.5''$
Inclination, $i^{(b)}$	$(38.5 \pm 2.4)^{\circ}$
Position Angle ^(b)	$(156.2 \pm 1.7)^{\circ}$
Radius, $r_{25}^{(d)}$	$(182.9 \pm 47.3)''$
Systemic Velocity, $V_{\text{LSR}}^{(b)}$	$(1572 \pm 5) \text{ km s}^{-1}$
Distance, $d^{(a)}$	$(15.21 \pm 0.49) \text{ Mpc}$
Linear Scale	$73.5 \text{ pc}''$
Matched Beam Size	$3.7'' \sim 260 \text{ pc}$
Morphology ^(e)	SAB(s)bc
SFR ^(c)	$(3.56 \pm 0.92) M_{\odot} \text{ yr}^{-1}$
$\log_{10}(M_{\star}/M_{\odot})^{(c)}$	10.75 ± 0.11

Notes –

(a) Anand et al. (2021);

(b) Lang et al. (2020);

(c) A. K. Leroy, Sandstrom et al. (2019);

(d) HyperLeda database (Makarov et al., 2014);

(e) NASA Extragalactic Database (NED).

7.2 Dense gas properties across morphological regions

The high spatial resolution of 260 pc paired with excellent sensitivity of these data allows us to detect many independent sightlines (~ 300) and resolve morphological environments to study dense gas spectroscopic ratios (HCN/CO, SFR/HCN) across these environments. We note that such a study has never been at these scales and sensitivity across the full molecular gas of a nearby spiral galaxy outside of the local group. Building on our previous works (*Dense Gas Letter* and *ALMOND*; Sections 5 and 6),

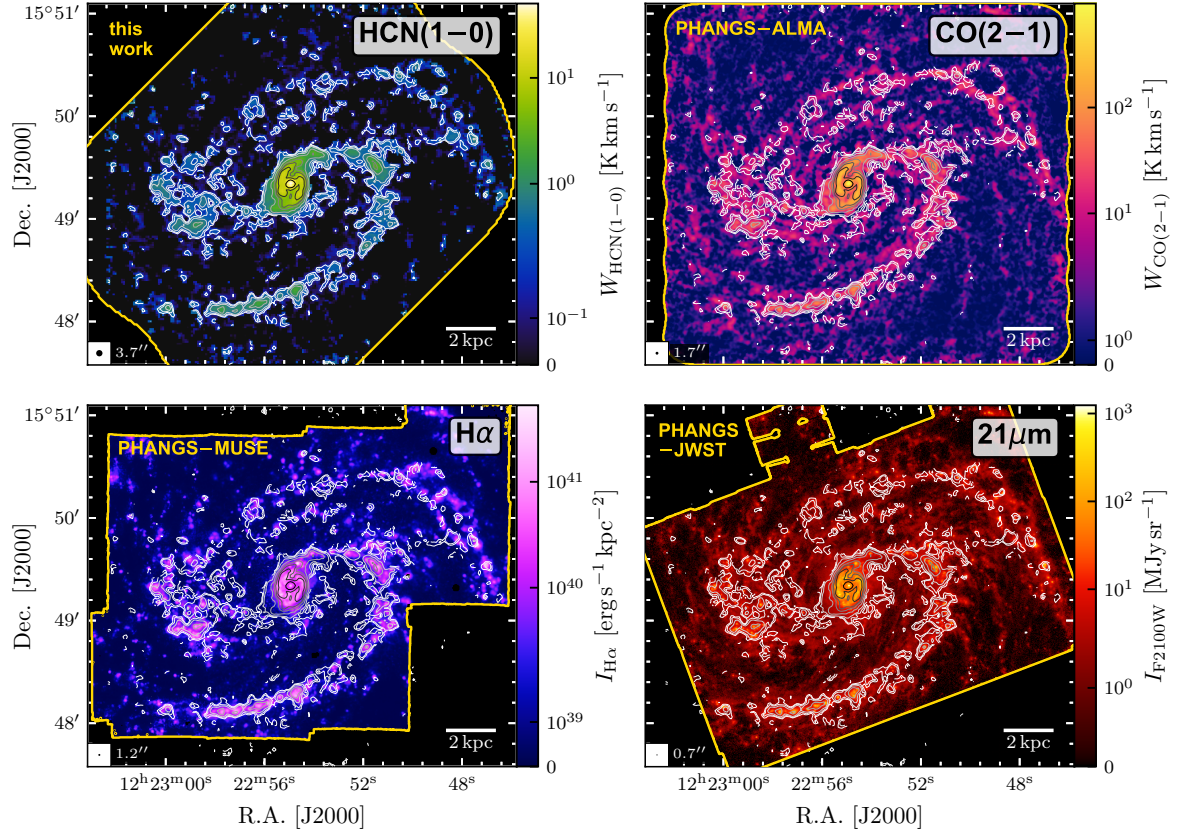


Figure 7.2: **Maps of NGC 4321.** *Top left:* HCN (1 – 0) integrated intensity map from new ALMA observations of NGC 4321 at $3.7'' \sim 260$ pc resolution. *Top right:* CO (2 – 1) integrated intensity maps from PHANGS–ALMA (A. K. Leroy, Schinnerer et al., 2021). *Bottom left:* $H\alpha$ map from PHANGS–MUSE (Emsellem et al., 2022) and corrected for dust-extinction via the Balmer decrement. *Bottom right:* $21\mu\text{m}$ wide-band intensity from PHANGS–JWST (Lee, Sandstrom et al., 2023). All maps are shown at the native resolutions of the respective observations, where the golden outline indicates their covered footprints. The beam size is shown as the black circle in the lower left corner of each panel and the scale bar denotes a physical scale of 2 kpc at a distance of 15.2 Mpc.

we use the HCN-to-CO line ratio to trace the dense gas fraction (f_{dense}) and SFR/HCN as a proxy of the dense gas star formation efficiency. Here, we use attenuation-corrected $H\alpha$ observations as the primary tracer of the SFR, referred to as $\text{SFR}_{H\alpha}$. In the paper (Appendix C), we comment on the robustness of tracing the SFR via $H\alpha$, especially towards the centre of the galaxy and compare with alternative SFR tracers ($21\mu\text{m}$ from the JWST and 33 GHz from the VLA). We show that $H\alpha$ and $21\mu\text{m}$ yield similar SFR values across the disc, but differ in the centre, where $H\alpha$ (corrected using the Balmer decrement) produces more robust estimates of the SFR if benchmarked against 33 GHz. Hence, we consider $\text{SFR}_{H\alpha}$ the best available tracer of the SFR across the full molecular gas disc of NGC 4321.

Figure 7.3 plots the distributions of HCN/CO and SFR/HCN across the full galaxy (grey) and the different morphological environments. We find that HCN/CO is systematically higher by a factor of two to three compared to the disc, while SFR/HCN is lower in the centre by the same factor compared to the disc. Interestingly, significant data of HCN/CO and SFR/HCN have similar distributions in the bar ends, spiral arms and interarm regions, which could indicate that molecular clouds and the efficiency of

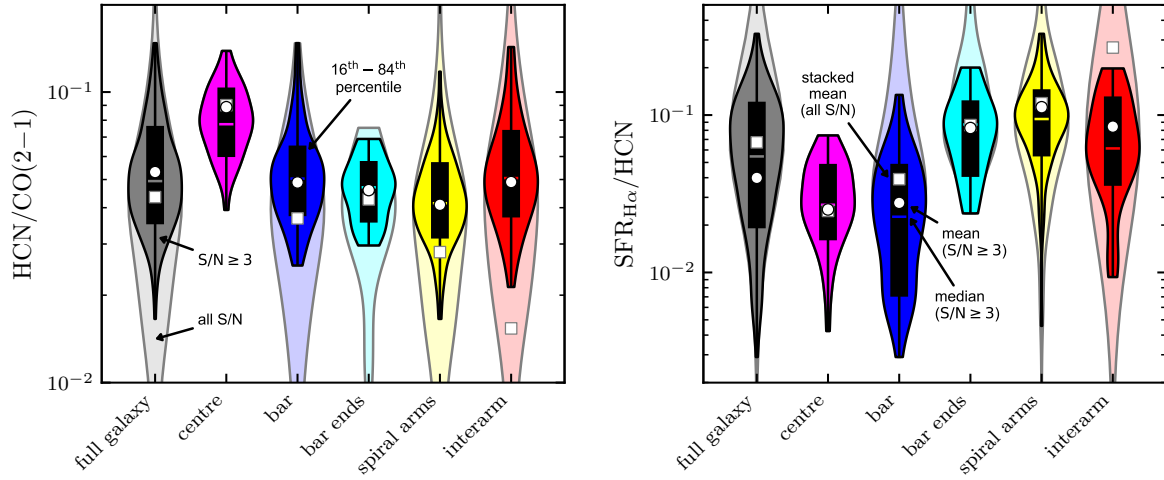


Figure 7.3: **Dense gas ratios across morphological regions in NGC 4321.** *Left:* Violin distribution plots of the HCN (1 – 0)/CO (2 – 1) line ratio across the different morphological regions (coloured) and for the whole galaxy (grey). The filled violins in the foreground indicate detected data ($S/N \geq 3$) and the transparent violins in the background show low-significant measurements. The black bars denote the 16th to 84th percentile range, the coloured line the median and the white circle the arithmetic mean (of detections). The stacked mean across all sightlines, i.e. including non-detections, is indicated by the white square. *Right:* Similar to the left panel, but for the $\text{SFR}_{\text{H}\alpha}/\text{HCN}$ ratio.

star formation are comparable in spiral arms and the interarm regions, which would agree with results from the Milky Way (Urquhart et al., 2021). However, if we include the non-detections, the interarm regions yield a lower HCN/CO and higher SFR/HCN (by a factor of two) than the spiral arms. If taken at face value, these results indicate that the dense gas fraction is higher, while the star formation is lower in the spiral arms than in the interarm regions. However, we want to highlight that the apparently low HCN/CO and high SFR/HCN in the interarm regions are driven by many non-detected sightlines in the outer disc and that in the inner ~ 7 kpc interarm regions and spiral arms yield similar mean HCN/CO and SFR/HCN.

7.3 Spatially resolved scaling relations

In the previous section, we pointed out that the spectroscopic ratios have the strongest variations towards the centre of NGC 4321. In Figure 7.4 (left panels), we show the radial trend of HCN/CO and SFR/HCN. We find that in the inner $\sim 2 - 3$ kpc, HCN/CO systematically increases, while SFR/HCN decreases by almost one order of magnitude towards the centre of the galaxy, while these ratios stay roughly constant across the disc. In addition, the right panels of Figure 7.4 present the scaling relations of HCN/CO and SFR/HCN with the dynamical equilibrium pressure, P_{DE} , which is a measure of the external pressure in the ISM disc, taking into account the gravitation potential of stars and gas, as well as the cloud-scale self-gravity of the molecular gas. In agreement with previous kiloparsec-scale studies (see project P2; Chapter 5), HCN/CO increases, while SFR/HCN decreases with P_{DE} . The high spatial resolution of the HCN observations across the full molecular gas disc allows us to study these scaling relations over more than three orders of magnitude in P_{DE} . While previous works (e.g. Gallagher, A. K. Leroy, Bigiel, Cormier, Jiménez-Donaire, E. Ostriker et al., 2018; Jiménez-Donaire, Bigiel, A. K. Leroy, Usero et al.,

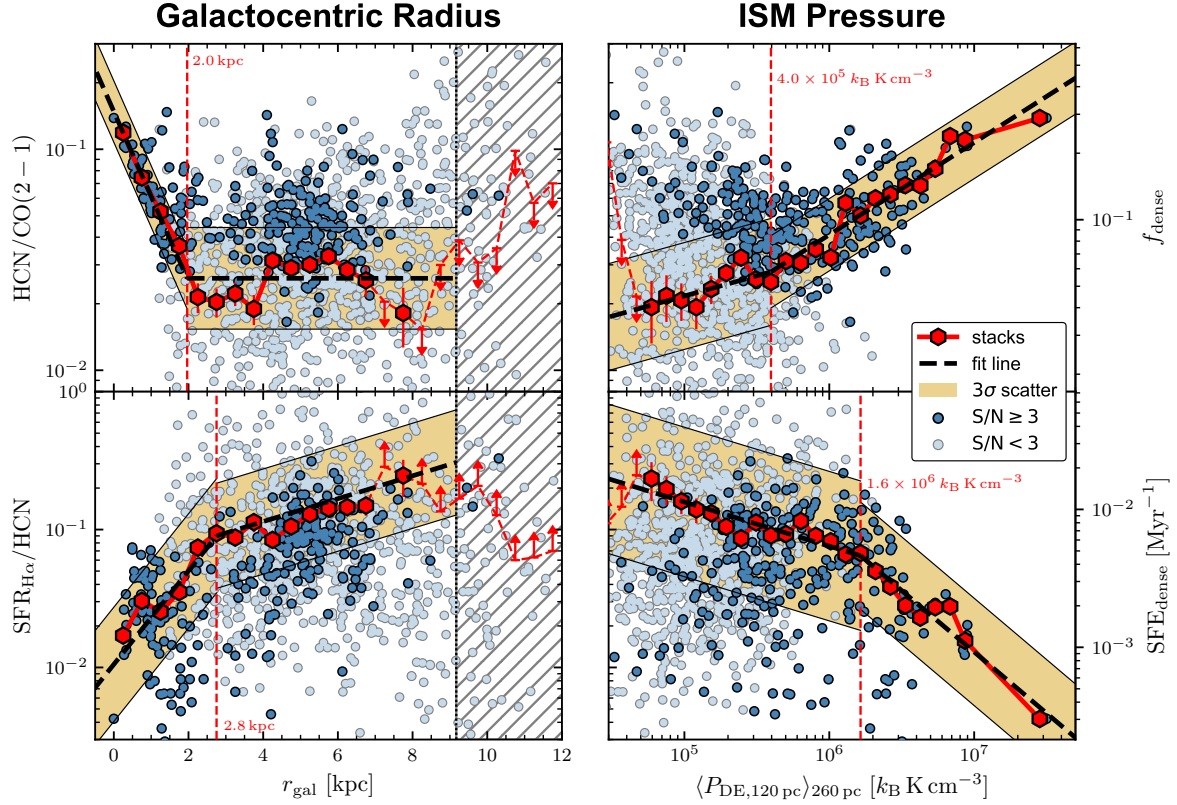


Figure 7.4: **Dense gas scaling relations at 260 pc in NGC 4321.** *Left:* HCN/CO (*top*) and SFR/HCN (*bottom*) against the galactocentric radius (r_{gal}). Dark blue markers indicate detected ($S/N \geq 3$) sightlines and light blue markers denote low significant ($S/N < 3$) data. Red hexagons show stacked measurements in 500 pc increments that take into account non-detections. The black dashed line is a piecewise fit to the binned data. The hatched region ($r_{\text{gal}} > 9.17$ kpc) indicates the data range where radial bins are not complete. *Right:* Similar to the left panels, but against the dynamical equilibrium pressure (P_{DE}). The stacked measurements are computed in 0.1 dex wide bins.

2019) only had access to measurements in high-pressure environments (centres and spiral arms), these new data allow to study trends in the low-pressure (interarm regions; $P_{\text{DE}} \approx 1 \times 10^5 k_B \text{ K cm}^{-3}$) as well. We find that the scaling relations with pressure become significantly flatter (slopes change by a factor of two) in the low-pressure regime ($P_{\text{DE}} \lesssim 1 \times 10^6 k_B \text{ K cm}^{-3}$). This means that while being strongly dependent on pressure in the high-pressure environments, HCN/CO and SFR/HCN become less dependent on pressure in the low-pressure environments, typically found at larger radii in the disc of the galaxy. Assuming, that HCN/CO and SFR/HCN are robust tracers of f_{dense} and $\text{SFE}_{\text{dense}}$, this could indicate that molecular clouds are strongly coupled to the local environment in high-pressure environments, but tend to decouple from the environment in low-pressure regions.

7.4 Low star formation efficiency in the bar

In the paper, we present the above scaling relations (with radius and pressure) for each morphological environment individually. Most of the environments either populate distinct regimes in these relations,

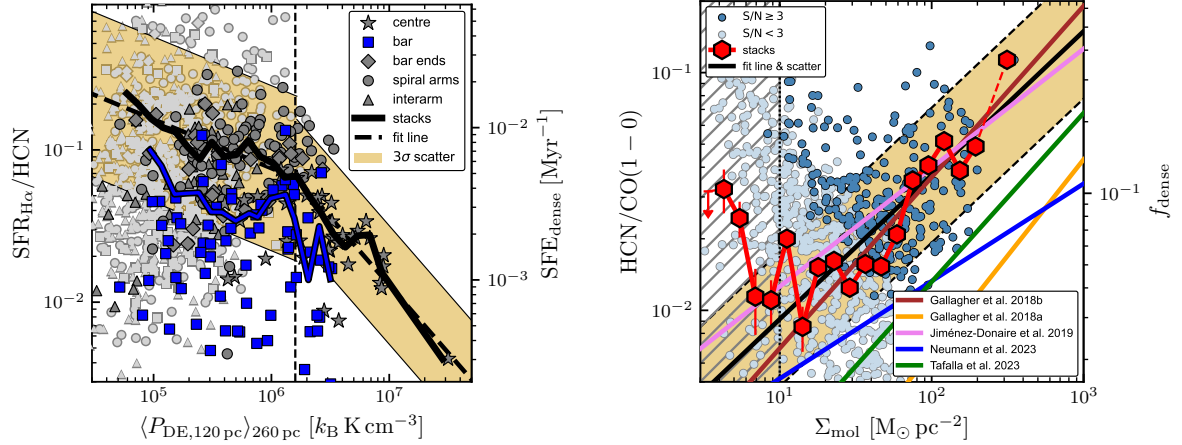


Figure 7.5: $\text{SFE}_{\text{dense}}$ in the bar of NGC 4321 and HCN/CO as a tracer of molecular gas density. *Left*: SFR/HCN against dynamical equilibrium pressure, P_{DE} , similar to Figure 7.4 (lower right), but highlighting the bar environment. The blue markers show significant ($S/N \geq 3$) measurements in the bar, and the blue solid line indicates the bin average trend. The dark grey markers show significant measurements across the other morphological environments, and the light grey markers present non-significant data. The solid black line shows the stacked trend over all environments (same as in Figure 7.4) with corresponding 3-sigma scatter. *Right*: HCN/CO against molecular gas surface density, Σ_{mol} . The blue markers show the significant data across the full galaxy, while the light blue markers indicate low-significant data. The red hexagons show the stacked integrated values, which are fitted by a line using LinMix (black solid line). The hatched region indicates the regime where non-detections dominate and the stacked values are potentially biased high. These data are therefore excluded from the fit. The coloured solid lines show scaling relations from various studies spanning sub-parsec (Tafalla et al., 2023) to kiloparsec scales (e.g. Jiménez-Donaire, Bigiel, A. K. Leroy, Usero et al., 2019).

for example, the centre or follow the same relation (e.g. spiral arms and interarm), which indicates that the pressure plays a key role in regulating gas conditions and star formation in galaxies. However, there is one exception, that is the bar environment. In the bar, HCN/CO behave similarly to the other environments (see Fig. 8 in Chapter 7), while SFR/HCN is lower by a factor of two across the full pressure range (right panel of Figure 7.5). Assuming that HCN is robustly tracing dense gas in the bar regions, this could mean that the bar contains a substantial amount of dense molecular gas which is compressed under pressure but the gas is less efficiently converted into stars compared to other environments. Low star formation efficiencies have already been found in bars of other galaxies by studying the molecular gas traced by CO (Maeda et al., 2023) and can be explained by the strong shear (e.g. Federrath et al., 2016) and streaming motions (e.g. Sormani, Treß et al., 2018; Wallace et al., 2022) or fast cloud-cloud collisions (Fujimoto et al., 2020) in bars, which are known to distort and disrupt molecular star clouds moving along the bar, hence potentially preventing their gravitational collapse yielding lower star formation efficiencies. An alternative explanation is that timescales and evolutionary effects play a much bigger role in the bar compared to other environments. This means that either the fast streaming motions lead to a spatial displacement of the sites of young stars and the locations of dense molecular gas or NGC 4321 might be in an evolutionary phase where the observed SFR in the bar is low (Verwilghen et al., 2024). Investigation of the latter hypothesis would require a similar analysis across a larger sample of barred galaxies.

7.5 HCN/CO as a density-sensitive line ratio

Several galactic works (e.g. Kauffmann, Goldsmith et al., 2017; Pety et al., 2017) have challenged the use of HCN (1 – 0) as a robust tracer of dense molecular gas, showing that HCN can also be efficiently emitted at moderate gas densities. Nevertheless, extragalactic studies (e.g. Gallagher, A. K. Leroy, Bigiel, Cormier, Jiménez-Donaire, E. Ostriker et al., 2018; Gallagher, A. K. Leroy, Bigiel, Cormier, Jiménez-Donaire, Hughes et al., 2018; Jiménez-Donaire, Bigiel, A. K. Leroy, Usero et al., 2019; Neumann, Gallagher et al., 2023) have shown that the line ratio between HCN and CO (HCN/CO) is sensitive to density variations at kiloparsec scales, indicating that HCN, despite being also emitted from lower density gas, is robustly tracing denser gas than CO. Recently, Tafalla et al. (2023) inspected the relation between HCN/CO and Σ_{mol} in galactic clouds in the solar neighbourhood at physical scales of ~ 0.1 pc and found remarkably similar scaling relations as in the aforementioned extragalactic works.

In this work, using the HCN observations of NGC 4321, we study the HCN/CO versus Σ_{mol} scaling relation for the first time at 260 pc resolution across the full disc of a nearby galaxy, where Σ_{mol} spans two orders of magnitude (Figure 7.5, right panel). We find that the scatter in the individual sightline measurements is significantly larger (0.28 dex) across NGC 4321 as at larger kiloparsec-scales across a sample of 30 galaxies (0.18 dex), pointing towards additional drivers of HCN/CO at smaller scales than just the gas density. However, the average trend yields a slope of 0.61, which agrees well with previous literature results (slopes ranging from 0.41 to 0.81; see Tab. 5 in Chapter 7 for a literature comparison). Some apparent offsets and discrepancies between the different studies are associated with varying methodologies (e.g. beam-scale versus beam-average measurements, or CO-to-H₂ conversion factor prescriptions) and are discussed in the paper in more detail. Overall, these results show that HCN/CO is a good predictor of the average gas density above $\Sigma_{\text{mol}} = 10 M_{\odot} \text{ pc}^{-2}$ and thus sensitive to changes in gas density across galaxies from sub-parsec to kiloparsec scales. However, we point out that this might not be true in extreme environments (e.g. AGN-dominated centres) or UV-illuminated, low-density regions (e.g. Santa-Maria et al., 2023).

7.6 Conclusions

In this work, we use new ALMA observations of HCN from the spiral galaxy NGC 4321 to study dense gas and star formation at 260 pc scales, resolving individual morphological environments. The novelty of this study is the access to high physical resolution paired with high sensitivity to detect many independent sightlines of HCN emission across the full molecular gas disc of a nearby galaxy. We find that HCN/CO, a proxy of f_{dense} , and SFR/HCN, a proxy of $\text{SFE}_{\text{dense}}$, show the strongest variations in the inner 2 – 3 kpc. Towards the centre, HCN/CO increases, while SFR/HCN decreases by ~ 1 dex. At larger galactocentric radii ($r_{\text{gal}} \gtrsim 3$ kpc), HCN/CO and SFR/HCN stay roughly flat, consistently across bar ends, spiral arms and interarm regions for $3 \text{ kpc} < r_{\text{gal}} < 7 \text{ kpc}$. This indicates that outside of galaxy centres, and in particular spiral arms and interarm regions are similarly efficiently forming stars from the dense molecular gas phase. This hypothesis is consistent with the pressure threshold at $P_{\text{DE}} \approx 1 \times 10^6 k_{\text{B}} \text{ K cm}^{-3}$ constraint from the HCN/CO and SFR/HCN against P_{DE} scaling relations, suggesting that molecular clouds tend to decouple from the surrounding environment across the disc of galaxies, where the pressure is much lower than in the centres of galaxies, where properties of GMCs are much more affected by the environmental conditions. Furthermore, we identified the bar region as a special morphological environment, where SF appears to be suppressed given the amount of dense

molecular gas and pressure conditions, potentially linked to the strong dynamical effects in bars or the results of evolutionary phases of the bar. Finally, we make use of this data set to test how HCN/CO traces the molecular gas density at 260 pc and compare it with literature results from sub-parsec to kiloparsec scales. Overall, there is a consistent picture that HCN/CO scales with Σ_{mol} with a slope of 0.61 (in log-log scale), demonstrating that HCN/CO is a powerful extragalactic tool to trace density variations.

Linking dense gas tracers from the Milky Way to external galaxies

LEGO III: Dense gas tracers across massive star-forming regions

*L. Neumann, F. Bigiel, A. T. Barnes, M. Schuchmann, M. Steinrötter, J. Kauffmann
and the LEGO collaboration*

in preparation

Overview

The Gao-Solomon relation (Section 1.5.2; Gao and Solomon, 2004) and many other studies of the ISM and SF in galaxies are fundamentally based on adopting HCN ($1 - 0$) as a tracer of dense molecular gas. However, recent works within the MW (in particular within Orion, Pety et al., 2017; Kauffmann, Goldsmith et al., 2017; Santa-Maria et al., 2023) have shown that HCN is not always a robust tracer of dense gas. It has been found that HCN ($1 - 0$) can be efficiently emitted at intermediate gas densities due to its substantial dependence on the ISRF and electron excitation, yielding high HCN luminosities at gas densities much below its nominal critical density. In contrast, N_2H^+ ($1 - 0$) has been identified as the gold-standard tracer of dense molecular in these observations, since N_2H^+ can only be efficiently excited in the cold, dense gas. These results have questioned the use of HCN as a dense gas tracer in extragalactic works. Hence, it is unclear whether HCN should still be used to infer properties of the dense gas in extragalactic studies, or if alternative tracers (e.g., N_2H^+ , N_2D^+ , H_2D^+), which are more challenging to detect, need to be considered for future studies. Therefore, we need a better understanding of how a variety of (dense) molecular gas tracers vary and depend on the physical conditions of the ISM across a wide range of environments.

The LEGO project specifically addresses this scientific question of studying probes of molecular gas across representative environmental variations within the MW. LEGO observed 14 molecular cloud regions in the MW with the IRAM 30 m telescope (Section 2.2.1), mapping large $0.5^\circ \times 0.5^\circ \sim 50 \text{ pc} \times 50 \text{ pc}$ areas to capture the whole molecular cloud as in extragalactic observations (more details on the survey are in Section 2.3.2).

In this work, we study the massive star-forming regions (W49, W43, G45.1+0.1; for simplicity, we will

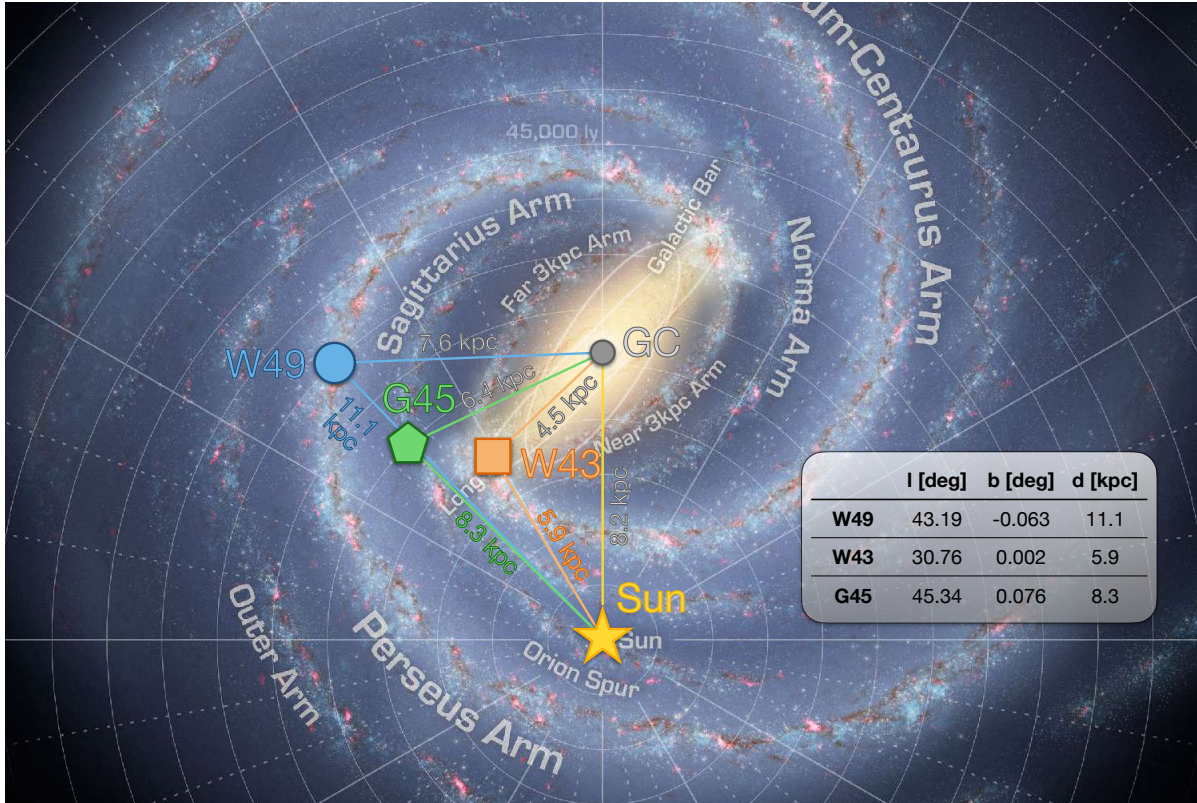


Figure 8.1: **Artistic view of the MW with LEGO cloud locations.** Face-on, artist's impression of the galaxy overlaid with galactic coordinates, the location of the Sun (yellow star), and spiral arm labels (R. Hurt: NASA/JPL-Caltech/SSC). The positions of the three massive star-forming clouds from LEGO are shown as coloured circles (W49, blue; W43, orange; G45.1+0.1, green). Their positions have been determined using the BESSEL kinematic distance estimator from https://www3.mpi-fr-bonn.mpg.de/staff/abrunthaler/bessel_calc2.0/ based on Reid et al. (2009).

refer to G45.1+0.1 as G45) of the LEGO sample, which is the third paper of the LEGO project and builds on previous works by Kauffmann, Goldsmith et al. (2017) and Barnes, Kauffmann et al. (2020), who studied Orion-A and W49. We present new IRAM 30 m observations of the regions W43 and G45.1+0.1, and include the data of W49 from Barnes, Kauffmann et al. (2020). The goal of this work is to study the emission properties of typical extragalactic tracers of dense gas in comparison with N_2H^+ (1 – 0), using ancillary dust observations to quantify the physical conditions of the gas (i.e. density and temperature). Hence, for this study, we focus on a set of five to ten selected molecular lines. A more complete list of detected molecular lines covered by the LEGO spectral setup is shown in Table D.2. The reduced data cubes and dust data products have been provided by Jens Kauffmann (PI of LEGO) and present a homogeneous data set. Some of this work was included in Bachelor theses by Michele Steinrötter (W43) and Marius Schuchmach (G45) supervised by Frank Bigiel and co-supervised by myself. All of the analysis steps and figures presented here have been performed by me, including the computation of data products, and more advanced analysis plots discussed in the following sections. This work is planned to be submitted to A&A by the end of the fourth quartile of 2024. In the following, we will give a comprehensive overview of the key results of the paper, which focus on the emission efficiency of dense gas tracers across the LEGO regions (Section 8.3). Furthermore, we link these results to extragalactic

Table 8.1: Source properties.

Source	R.A. [J2000]	Dec. [J2000]	d [kpc]	v_{sys} [km s ⁻¹]	Velocity Range [km s ⁻¹]	N_{H_2} [cm ⁻²]	T_{dust} [K]	Resolution	Location
W49	19 ^h 10 ^m 15.376 ^s	9°4′30.922″	11.1 ^(a)	11	[-5, 80]	$[0.2, 2.1, 66] \times 10^{21}$	[14.7, 20.4, 37.8]	60″ ~ 3.2 pc	Perseus arm
W43	18 ^h 47 ^m 44.502 ^s	-1°51′12.606″	5.9 ^(b)	93	[0, 125]	$[0.6, 6.3, 79] \times 10^{21}$	[15.8, 23.5, 38.0]	60″ ~ 1.7 pc	Bar end (near)
G45.1+0.1	19 ^h 13 ^m 27.326 ^s	10°53′10.909″	8.3 ^(c)	59	[0, 80]	$[0.2, 1.7, 23] \times 10^{21}$	[15.2, 21.0, 36.2]	60″ ~ 2.4 pc	Sagittarius arm

Notes – Source name, coordinates, most-probable associated location, distance, systemic velocity, velocity range of all emission, resolution, molecular hydrogen column density (minimum, mean, maximum), and dust temperature (minimum, mean, maximum) across the three massive star-forming regions.

References are: (a) Zhang et al. (2013), (b) Nguyen Luong et al. (2011), (c) Kraemer et al. (2003)

scaling relations (Section 8.4).

8.1 LEGO observations of massive star-forming regions

The LEGO observations have been carried out with the IRAM 30 m telescope in on-the-fly (OTF) mapping mode, which is the most time-efficient approach to map large regions on the sky. The drawback is that with fast scanning, speed such as employed for these observations, the effective beam is smeared out in the scanning direction. Therefore, the actual resolution is moderately smaller than the native beam size of $\sim 25''$ at ~ 100 GHz. To mitigate the beam smearing effect, we smooth all line cubes and dust maps to a common resolution of $60''$, similarly to the procedure described in Barnes, Kauffmann et al. (2020), but using the PyStructure pipeline (Section 3.1), which automatically produces molecular line products. The resulting cubes have an angular resolution of $60''$ and a spectral resolution of 0.6 km s^{-1} .

Figure 8.2 presents maps of the $^{12}\text{CO} (1-0)$ peak intensity (T_{peak}), the dust-based H_2 column density (N_{H_2}) and the dust temperature (T_{dust}). The dust data is taken from *Herschel* IR observations (Herschel infrared Galactic Plane Survey (Hi-Gal); Molinari, Swinyard, Bally, Barlow, Bernard, P. Martin, Moore, Noriega-Crespo, Plume, Testi, Zavagno, Abergel, Ali, André et al., 2010; Molinari, Swinyard, Bally, Barlow, Bernard, P. Martin, Moore, Noriega-Crespo, Plume, Testi, Zavagno, Abergel, Ali, Anderson et al., 2010), which have been fitted by a modified blackbody spectrum on a pixel-by-pixel basis (Guzmán et al., 2015), to infer the dust column density and temperature. We then assume a fixed dust-to-gas ratio of 100 to convert the dust column density into a H_2 column density, adopting a mean molecular weight of $\mu_{\text{H}_2} = 2.8$ (Kauffmann, Bertoldi et al., 2008), assuming that all gas is in molecular phase.

The clouds exhibit a range of physical conditions, spanning column densities from $N_{\text{H}_2} = 2 \times 10^{19} \text{ cm}^{-2}$ to $8 \times 10^{22} \text{ cm}^{-2}$ and dust temperatures from $T_{\text{dust}} = 15 \text{ K}$ to 38 K (Table 8.1). The core of W49 (i.e. W49A) is located in the Perseus spiral arm near the solar circle at a distance of $d \approx 11.1 \text{ kpc}$ (Zhang et al., 2013). The molecular line emission of W49 is very much concentrated in the centre of W49A, where densities and temperatures are high. G45.1+0.1 is likely positioned in the Sagittarius arm at a distance of $d \approx 9.7 \text{ kpc}$ (T. R. Hunter et al., 1997), and consists of several smaller clumps, referred to as G45.07+0.1, G45.12+0.1 in the south, and G45.45+0.1, G45.47+0.1 in the south (Kraemer et al., 2003) that are connected via a 30 pc-long filament. In contrast, W43 is located in the bar end of the MW, where the Scutum-Centaurus arm originates from the galactic bar at a distance of $d \approx 5.9 \text{ kpc}$ (Nguyen Luong et al., 2011). In this turbulent environment, W43’s morphology appears scattered and structured, likely the result of recent cloud-cloud collisions.

Figure 8.3 shows the average spectra of several selected lines across the three regions. We identify

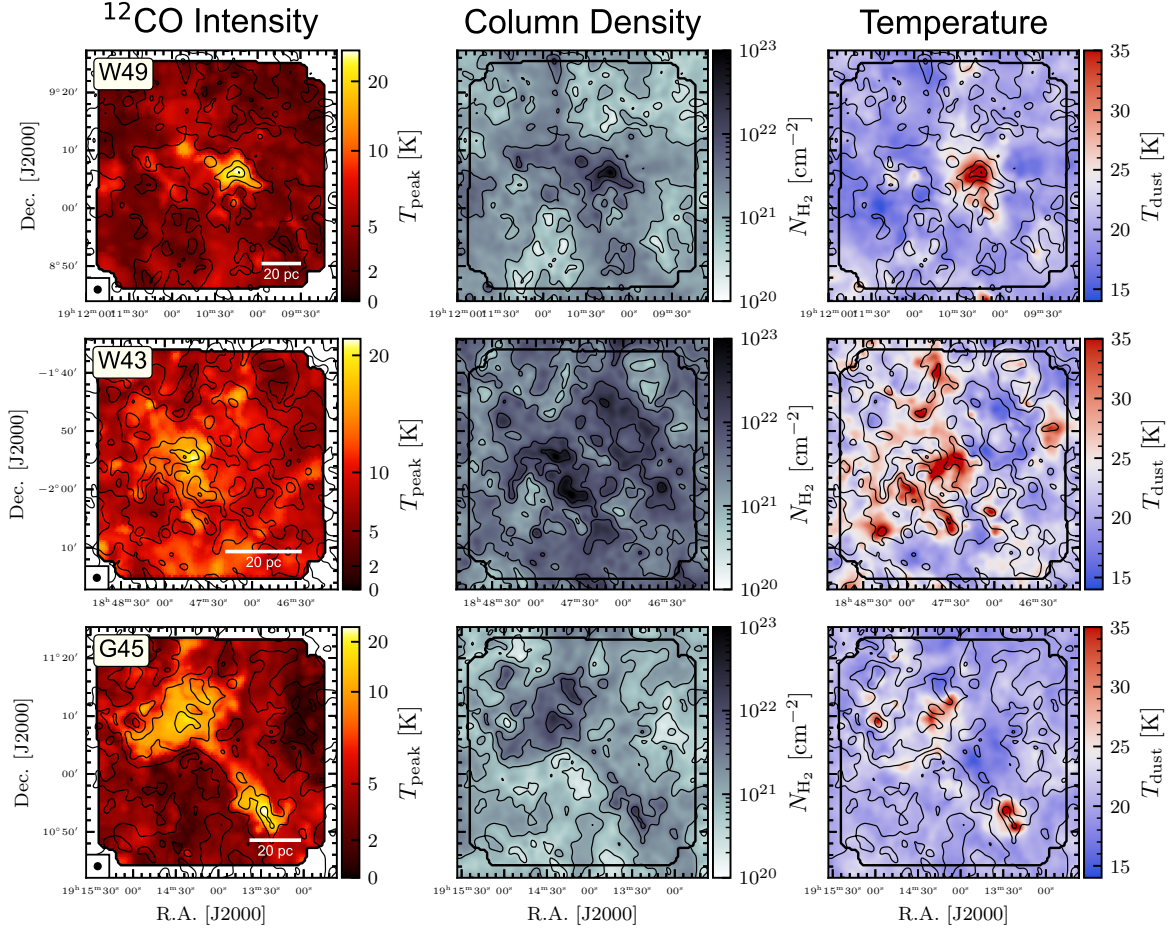


Figure 8.2: **LEGO massive star-forming regions.** ^{12}CO (1 – 0) peak temperature (*left*), dust-based H_2 column density (*middle*), and dust temperature (*right*) across the three LEGO massive star-forming regions W49, W43, and G45.1+0.1 from top to bottom. The beam size of the CO observations (i.e. $60''$) is indicated by the black circle in the lower left corner, and represents the common spatial resolution of all molecular lines across all LEGO clouds. The black contours show seven column density levels from $N_{\text{H}_2} = 10^{20}$ to 10^{23} cm^{-2} in 0.5 dex steps for each respective cloud. The rectangular-shaped outline indicates the FOV of the LEGO IRAM 30 m observations, covering about $0.5^\circ \times 0.5^\circ$.

the systemic velocities of the clouds via the velocity of the peak ^{12}CO (1 – 0) emission as 10 km s^{-1} , 10 km s^{-1} , and 10 km s^{-1} for W49, W43, and G45.1+0.1, respectively. For all clouds, there are several velocity components along the line of sight, e.g., at $v_{\text{LSR}} = 40 \text{ km s}^{-1}$ and 60 km s^{-1} for W49, $v_{\text{LSR}} = 40 \text{ km s}^{-1}$ for W43, and $v_{\text{LSR}} = 25 \text{ km s}^{-1}$ for G45.1+0.1. For simplicity and to make the observations comparable to the dust maps, we consider all emission along the LOS and integrate over all velocity components. This approach also makes the results more comparable to extragalactic studies which typically average over ensembles of molecular clouds due to the coarser resolution. We used the two most significantly detected lines (i.e. ^{13}CO (1 – 0) and ^{12}CO (1 – 0)) as priors to create a master velocity-integrations mask. Furthermore, we dealt with hyperfine transitions (e.g., of N_2H^+ (1 – 0)) by shifting the integration mask to the corresponding hyperfine velocities in order to integrate over all hyperfine transitions for a given molecular line transition.

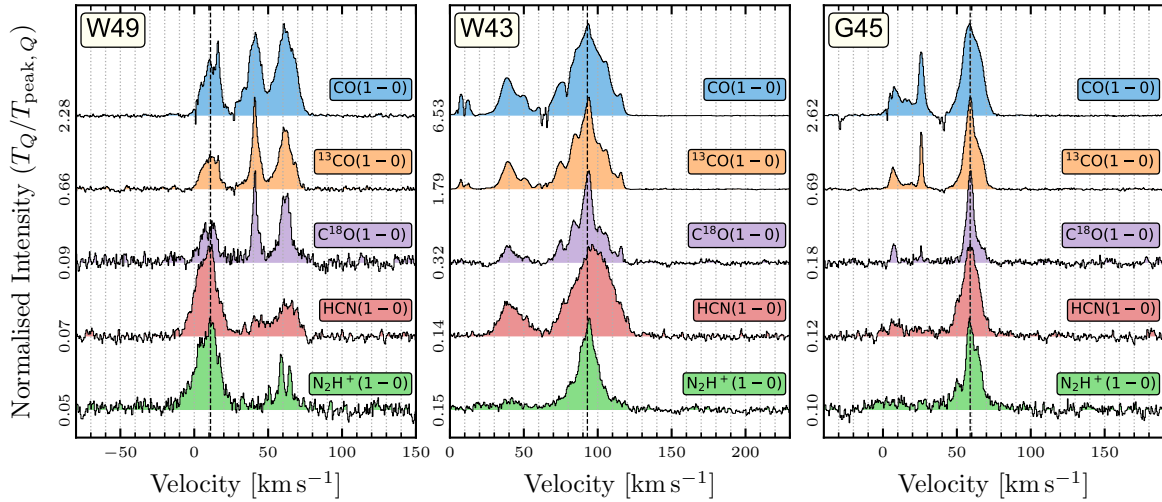


Figure 8.3: **Cloud-average spectra across massive star-forming regions from LEGO.** Cloud-average spectra of five selected lines across the LEGO massive star-forming regions. The average spectra are computed from sightline measurements with $S/N \geq 5$ of each respective line. The spectra are normalised by their respective peak intensities, T_{peak} , in units of kelvin (K), which are shown on the left of each spectrum. The vertical dashed line denotes the systemic velocities (11 km s^{-1} for W49, 93 km s^{-1} for W43, and 59 km s^{-1} for G45.1+0.1) of the main clouds within each field, respectively. Further line peaks indicate additional velocity components within the FOV. Spectra of all molecular lines covered by LEGO are presented in Figure D.5.

Figure 8.4 presents the integrated intensity maps (mom-0) of the same selected lines as in Figure 8.3. The maps are overlaid with column density contours in order to visually inspect the spatial correlation between the line intensities and the column densities. In general, we observe that CO and ^{13}CO are well detected across almost the full FOV and trace the bulk molecular gas, as well as the, to first order, the column density. In contrast, C^{18}O , HCN, and N_2H^+ originate from more constrained regions, typically tracing higher column densities than the other CO lines. However, there are significant differences between these lines. While N_2H^+ seems to only originate from the very dense clumps, C^{18}O and HCN are also emitted at intermediate gas densities, especially in W43, which is extremely bright in these two lines even at column densities below $N_{\text{H}_2} = 10^{21} \text{ cm}^{-2}$. Moreover, C^{18}O and HCN do not synchronously trace the same dense clumps, for example, HCN reaches its maximum intensity in the northern dense clump of W43, while C^{18}O peaks in the southern clump. In the following section (Section 8.2), the emissivity of these lines as a function of the column density is discussed in a more quantitative way.

8.2 Molecular line scaling relations

From basic collisional excitation theory (see Section 1.3.3) it is expected that the intensity of a molecular line scales with the density of the gas if the gas density is comparable to the critical density (n_{crit}) of the line. Furthermore, it is expected that a line becomes inefficient if the density is either much lower than n_{crit} because the upper energy level can not be populated, or much higher than n_{crit} because collisional deexcitation becomes the dominant process. Since n_{crit} is a fundamental property of any given molecular line transition, it can be utilised to trace gas at a certain density level. Thus, certain molecular lines serve

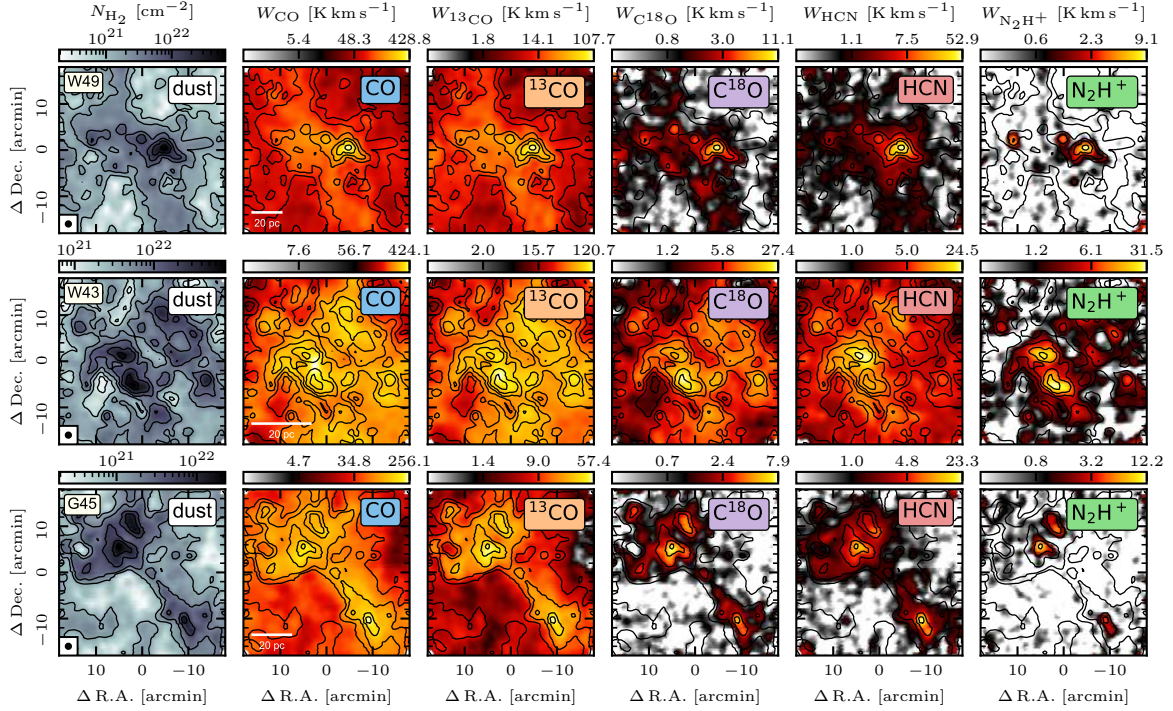


Figure 8.4: **Integrated intensity maps of selected lines.** The left column panels show dust-inferred H_2 column density across the three LEGO clouds (W49, W43, G45.1+0.1; from top to bottom), where the black circle denotes the common, homogenised spatial resolution across all maps and the white scale bar indicates a linear size of 20 pc. Further panels present the integrated intensity maps (mom-0) of ^{12}CO (1 – 0), ^{13}CO (1 – 0), C^{18}O (1 – 0), HCN (1 – 0), and N_2H^+ (1 – 0) (from left to right with increasing effective excitation density, n_{eff}) for each respective cloud. The black contours denote loci of H_2 column density at $N_{\text{H}_2} = \{1 \times 10^{21}, 2 \times 10^{21}, 5 \times 10^{21}, 1 \times 10^{22}, 2 \times 10^{22}, 5 \times 10^{22}\} \text{cm}^{-2}$. The colourmaps are scaled to show low-significant emission ($\text{S/N} < 5$) in grey tones and high-significant data ($\text{S/N} \geq 5$) in colours (from red to yellow). Moment-0 maps of all molecular lines covered by LEGO are presented in Figures D.6 to D.8.

as tracers of certain gas densities, for example, in extragalactic studies CO (1 – 0) ($n_{\text{crit}} = 5.7 \times 10^2 \text{cm}^{-3}$) is typically used as a tracer of bulk molecular gas, while HCN (1 – 0) ($n_{\text{crit}} = 3.0 \times 10^5 \text{cm}^{-3}$) is a common tracer of the dense molecular gas. We note that the above consideration neglects additional effects like abundance variations, temperature and optical depth, which all affect the observed line intensity and hence the capabilities of the given line to trace a certain density (I. Evans N. J., 1999). Therefore, Shirley (2015) introduced the concept of an effective critical density, or effective excitation density (n_{eff}), which is defined as the density where a line reaches an integrated intensity of 1K km s^{-1} , hence naturally taking into account all additional effects mentioned above. From theory, it is not trivial to estimate n_{eff} for any given molecular line transition. Therefore, observations are needed to study the emission behaviour of molecular lines as a function of the gas density, in order to benchmark their capabilities as gas density tracers.

In this work, we focus on a suite of molecular lines that are commonly used to trace dense molecular gas, this means, gas densities above $n \approx 10^4 \text{cm}^{-3}$, including HCN (1 – 0), HNC (1 – 0), HCO^+ (1 – 0), CS (2 – 1), CN (1 – 0), N_2H^+ (1 – 0). For comparison, we also present results for lower-to-intermediate-density tracers, i.e. CO (1 – 0), ^{13}CO (1 – 0), C^{18}O (1 – 0) (Figures 8.5 and 8.6). Spectra, maps, and

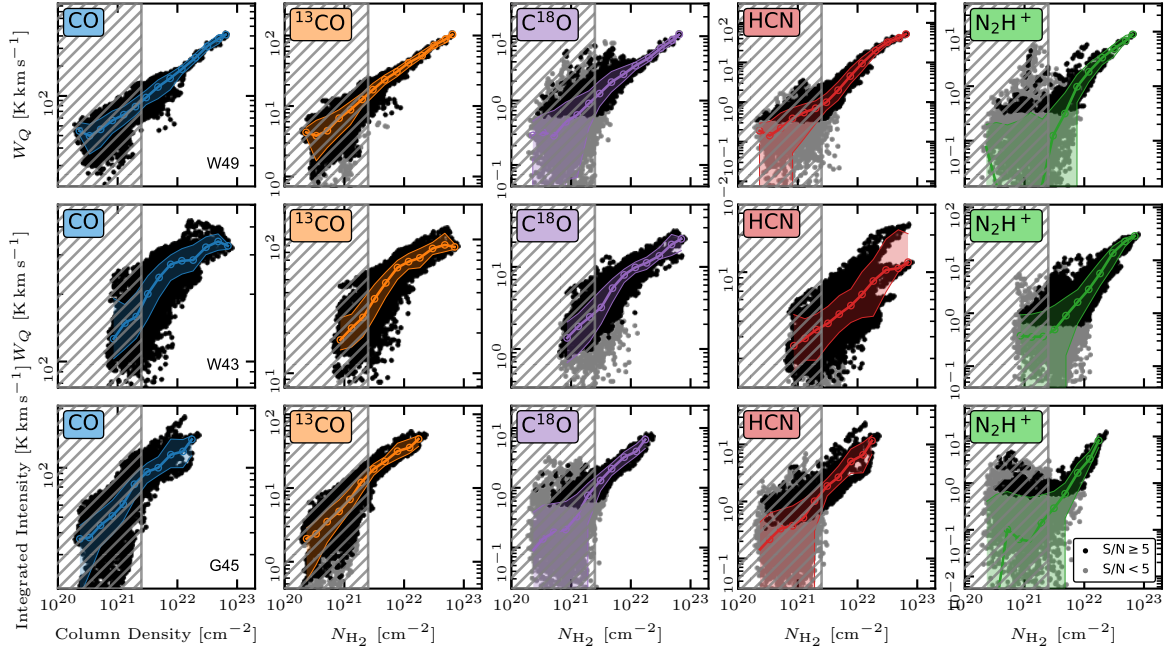


Figure 8.5: **Line intensity versus column density.** Scaling relation between ^{12}CO ($1-0$), ^{13}CO ($1-0$), C^{18}O ($1-0$), HCN ($1-0$), N_2H^+ ($1-0$) integrated intensity (from left to right) and dust-based H_2 column density (N_{H_2}) across the three regions W43, W49, G45.1+0.1 (from top to bottom). Black and grey markers denote high-significant ($S/N \geq 5$) and low-significant ($S/N < 5$) data, respectively. Coloured lines show bin averages computed in increments of 0.2 dex, where significant bin means are plotted as open circles. The hatched area indicates the column density range ($N_{\text{H}_2} < 2.5 \times 10^{21} \text{ cm}^{-2}$) where dust observations are background contaminated. Corresponding plots of other molecular lines are presented in Figures D.9 to D.11.

scaling relations for all molecular lines in the LEGO setup can be found in the Appendix Appendix D.2.

Figure 8.5 shows the integrated intensity (W_Q) of five selected molecular lines (CO , ^{13}CO , C^{18}O , HCN , N_2H^+), ordered by increasing n_{eff} against the column density (N_{H_2}). As expected, all molecular line intensities scale with density, roughly following a power law. However, there are key differences between the molecular lines and sources. CO scales with N_{H_2} in a roughly uniform way, following a single power law, over the whole data range, which is why it is an excellent tracer of molecular gas in general. Similarly, ^{13}CO and C^{18}O follow an even tighter power law, which is a good indication that those lines trace the column density even better, most likely because they are optically thin compared to CO , which is typically optically thick. In contrast to the CO lines, HCN , N_2H^+ show a steeper increase with column density, which indicates that they trace higher gas densities. While N_2H^+ follows a similar trend in all clouds, HCN shows significant scatter, especially for W43, where the scaling relation splits up into three branches at high densities.

In the next step, we analyse the emission efficiency, or emissivity of the molecular lines, which is defined as the integrated intensity of the line divided by the column density ($h_Q \equiv W_Q/N_{\text{H}_2}$). Thus, the emissivity quantifies the integrated intensity of a molecular line per unit (column) density. Figure 8.6 plots h_Q against N_{H_2} for the same molecular lines as in Figure 8.5. If the line intensity is linearly scaled with the column density, we would observe a flat, horizontal line in these plots. However, we find that the emissivity of the CO and ^{13}CO lines decreases with N_{H_2} over the whole parameter range, which indicates

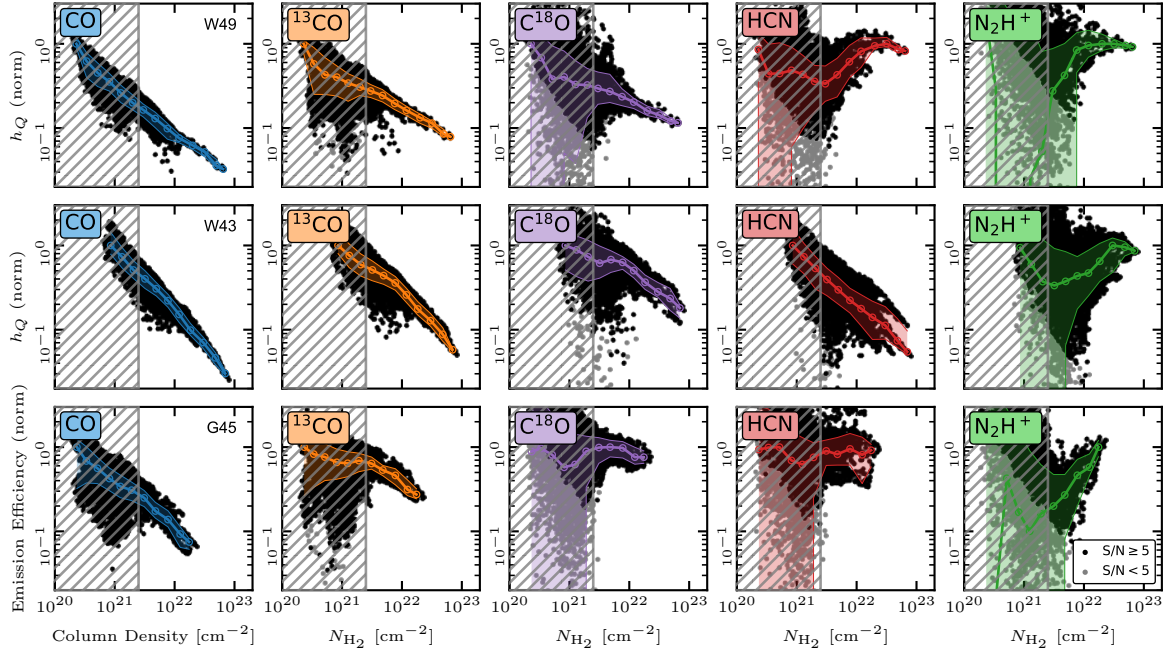


Figure 8.6: **Line efficiency scaling relations.** Similar to Figure 8.5, but showing the normalised emission efficiency $h_Q \equiv W_Q/N_{H_2}$ on the y-axis. Corresponding plots of other molecular lines are presented in Figures D.12 to D.14.

that their (effective) critical density is lower than the minimum column density probes in these fields. Therefore, CO and ^{13}CO are excellent probes of the bulk molecular gas. N_2H^+ shows the complete opposite behaviour and increases with column density over almost the full parameter range and across all clouds, demonstrating that N_2H^+ has a high (effective) critical density. The emissivity of HCN varies strongly between the molecular clouds. In W49, h_Q of HCN increases with density similarly to N_2H^+ , but in W43, it strongly decreases with N_{H_2} similarly to CO, and for G45, the HCN emissivity is roughly constant. Based on these results, it is not clear whether HCN traces

8.3 Dense gas tracers

In the previous section, we analysed the emissivity of a suite of selected lines as a function of gas column density across the three massive star-forming regions. Figure 8.7 summarised the key results by overlaying the average emissivity trends of ^{12}CO ($1-0$), HCN ($1-0$), C^{18}O ($1-0$), and N_2H^+ ($1-0$) in one panel per cloud. In addition, we show results of Orion A, another LEGO target, gratefully provided by Kauffmann, Goldsmith et al. (2017). Across all clouds, we find the coherent picture that the emissivity of N_2H^+ always peaks at high column densities around $N_{H_2} \approx 3 \times 10^{22}$ to $1 \times 10^{23} \text{ cm}^{-2}$, demonstrating that N_2H^+ is a robust tracer of dense molecular gas at $\sim 1 \text{ pc}$ scales across massive star-forming regions. In addition to its high effective critical density, N_2H^+ is chemically expected to only form in the cold, dense gas, when CO freezes out onto dust grains, strengthening its capability to trace the cold, dense medium.

In contrast, HCN, the classical proxy for dense molecular gas in extragalactic studies, can trace high

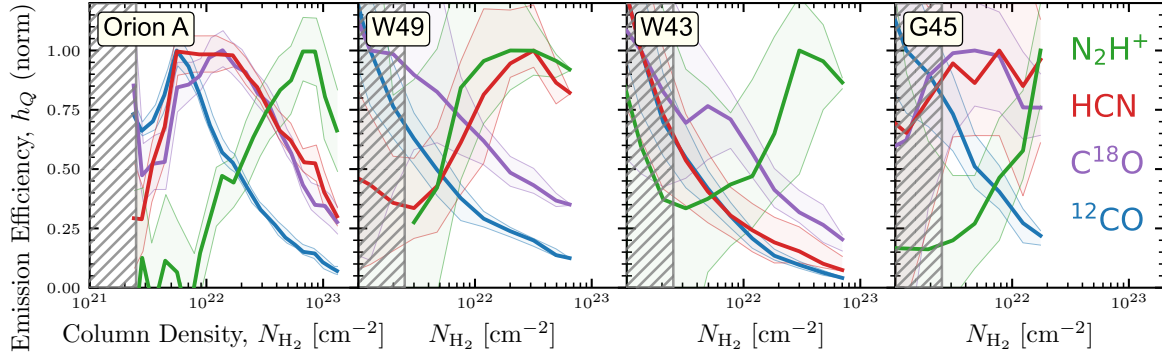


Figure 8.7: **Line efficiencies of (dense) molecular gas tracers.** Similar to Figure 8.6, but showing the average line efficiency trends of CO, $C^{18}O$, HCN, and N_2H^+ overlaid in the same panel per cloud, respectively. The left panel shows the corresponding trends of Orion A, adopted from Kauffmann, Goldsmith et al. (2017).

column densities ($N_{H_2} \approx 4 \times 10^{22} \text{ cm}^{-2}$ in W49), but also intermediate ($N_{H_2} \approx 1 \times 10^{22} \text{ cm}^{-2}$ in Orion A and G45) and low densities ($N_{H_2} < 2 \times 10^{21} \text{ cm}^{-2}$ in W43). Therefore, it can not be considered a robust tracer of dense molecular gas at $\sim 1 \text{ pc}$ scales such that converting from HCN ($1-0$) line intensities to a dense gas mass likely introduces large uncertainties and potential biases. These results are also consistent with findings from Orion B (Pety et al., 2017; Santa-Maria et al., 2023). The physical explanation underlying the poor abilities of HCN to trace only the dense gas despite its nominal high critical density is likely connected to the versatile excitation and radiative transfer mechanisms involving HCN. It has been proposed already 50 years ago that radiative trapping can effectively lower the effective critical density of a transition like HCN ($1-0$) with hyperfine structure (HFS) (e.g. Kwan and Scoville, 1975). Moreover, it has been argued that line overlap effects of HFS lines together with electron-assisted weak collisional excitation (Goicoechea et al., 2022). All of these effects should play an important role in GMCs with active star formation since free electrons are likely found in HII regions around massive star-forming regions. Observationally, it has been found that HCN can originate from low visual extinction gas (e.g. Pety et al., 2017; Shimajiri et al., 2017; Kauffmann, Goldsmith et al., 2017; I. Evans N. J., K.-T. Kim et al., 2020; Barnes, Kauffmann et al., 2020; Tafalla et al., 2021; Patra et al., 2022; Dame and Lada, 2023; Santa-Maria et al., 2023), where the HCN intensity scales with the IR luminosity and UV field, which are both tracers of active star formation and hence environments, where electron excitation might become the dominant excitation mechanism to populate the upper energy level of HCN. This can result in high HCN luminosities in low-density, but high UV field environments. Furthermore, Tafalla et al. (2023) found that the HCN intensity, while being first and foremost controlled by density, depends on the dust temperature. They propose a temperature correction of the HCN intensity, assuming that the dust temperature (T_{dust}) correlates well with the gas kinetic temperature (T_K), by benchmarking to a reference temperature of $T_{\text{dust}} = 10 \text{ K}$. They find tighter, more consistent relations between HCN intensity and N_{H_2} across the three studies clouds (California, Perseus, Orion A). For the LEGO clouds presented in this work, we tested the proposed temperature, which reduces the scatter in these scaling relations. All of these findings promote the coherent picture that HCN does not only trace density but also the UV field, which can however be partially corrected if the dust temperature is known.

Based on the caveats of HCN as a dense gas tracer, there are a few promising alternative dense gas tracers. While N_2H^+ seems to be the obvious choice to robustly trace cold, dense gas, it is five to ten

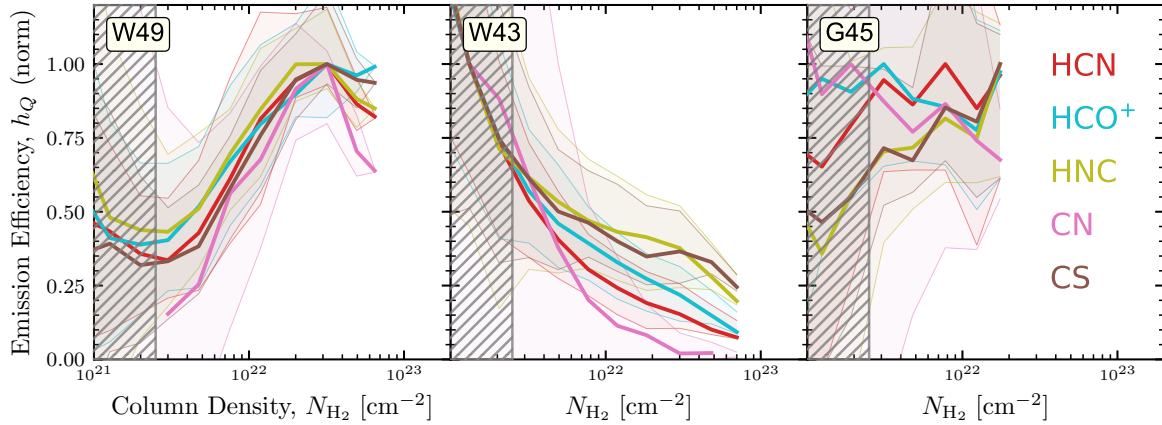


Figure 8.8: **Line efficiencies of alternative dense gas tracers.** Similar to Figure 8.7, but for different molecular lines: HCN (1 – 0), HCO⁺ (1 – 0), HNC (1 – 0), CN (1 – 0), CS (2 – 1).

times fainter than HCN and thus extremely challenging to map in external galaxies. SWAN (Stuber et al., 2023) produced the only, sensitive N₂H⁺ map of a nearby galaxy to date. All other surveys focus on specific environments or have very coarse resolution. However, there are a handful of alternative tracers (e.g., HCO⁺, CS, HNC, or CN) that are similarly bright as HCN, but possibly less affected by the effects laid out above, and additionally less dependent on metallicity (e.g., HCO⁺; Braine et al., 2017).

In Figure 8.8, we present the same emissivity relations as in Figure 8.7, but for the aforementioned alternative dense gas tracers, including HCO⁺ (1 – 0), HNC (1 – 0), CN (1 – 0), CS (2 – 1), and contrasts these lines with HCN (1 – 0) across the three LEGO clouds. We find that all lines, though showing different behaviour between clouds, yield remarkably similar results for each cloud, respectively. For W43, we observe some differences between the tracers at high column densities, pointing towards CS (2 – 1) and HNC (1 – 0) being more efficiently emitted at these densities by a factor of ~ 2 compared to HCN (1 – 0). However, overall, all lines show similar emission efficiencies for any given cloud. This suggests that for typical massive star-forming regions, all of these brighter dense gas tracers probe similar densities. However, we note that these regions can not probe extreme environments like AGN-dominated regions or metallicity variations. Nevertheless, these results show that whatever physical process (e.g., electron excitation, radiative trapping) affects the emissivity of HCN (1 – 0), can also affect the emissivity of HCO⁺ (1 – 0), HNC (1 – 0), CN (1 – 0), CS (2 – 1).

8.4 Density-sensitive line ratios

The above sections have shown that HCN is not a robust tracer of dense molecular gas, but can instead also originate from low extinction, intermediate-density gas in agreement with previous galactic studies of HCN (e.g. Pety et al., 2017; Shimajiri et al., 2017; Kauffmann, Goldsmith et al., 2017; I. Evans N. J., K.-T. Kim et al., 2020; Barnes, Kauffmann et al., 2020; Tafalla et al., 2021; Patra et al., 2022; Dame and Lada, 2023; Santa-Maria et al., 2023). However, HCN has been extensively utilised in extragalactic studies to study dense molecular gas and exhibits one of the most essential SF relations in astrophysics (Gao–Solomon relation Gao and Solomon, 2004; Jiménez-Donaire, Bigiel, A. K. Leroy, Usero et al., 2019). Moreover, A. K. Leroy, Usero et al. (2017) propose that the HCN (1 – 0)-to-CO (1 – 0) line

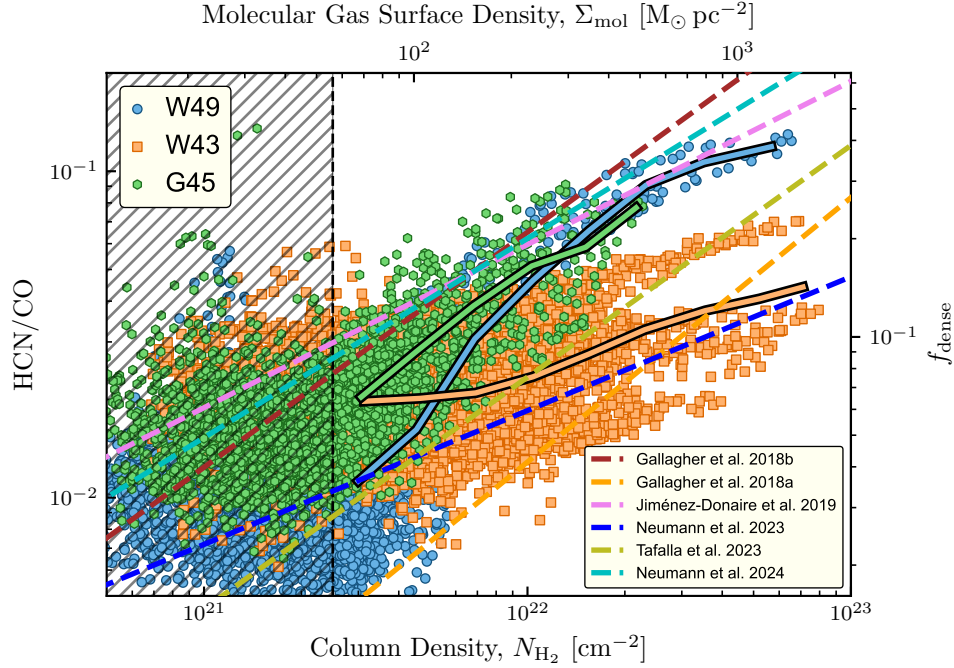


Figure 8.9: **HCN/CO as a density-sensitive line ratio.** HCN/CO against the H_2 column density across all detected pixel measurements of the three LEGO clouds (W49 in blue, W43 in orange, G45 in green). The solid coloured lines show the running average trend for each cloud, respectively. The dashed coloured lines denote relations from the literature at small (~ 0.1 pc, MW clouds; Tafalla et al., 2023) and large scales ($\sim 200 - 2$ kpc, resolved studies of external galaxies; Gallagher, A. K. Leroy, Bigiel, Cormier, Jiménez-Donaire, E. Ostriker et al., 2018; Gallagher, A. K. Leroy, Bigiel, Cormier, Jiménez-Donaire, Hughes et al., 2018; Jiménez-Donaire, Bigiel, A. K. Leroy, Usero et al., 2019; Neumann, Gallagher et al., 2023; Neumann, Bigiel et al., 2024).

ratio (HCN/CO) should be sensitive to changes in the mean gas density (n_0) and even predicts the strongest dependence of HCN/CO on n_0 , compared to alternative line ratios, involving HCO^+ ($1 - 0$), CS ($2 - 1$), or HNC ($1 - 0$). Furthermore, recent observational studies from external galaxies support the density-sensitive nature of HCN/CO, finding strong positive correlations between HCN/CO and the average \sim kiloparsec scale (Gallagher, A. K. Leroy, Bigiel, Cormier, Jiménez-Donaire, E. Ostriker et al., 2018; Jiménez-Donaire, Bigiel, A. K. Leroy, Usero et al., 2019) and ~ 100 pc scale (Gallagher, A. K. Leroy, Bigiel, Cormier, Jiménez-Donaire, Hughes et al., 2018) gas density. Recently, Tafalla et al. (2023) have shown that also in MW clouds observed at sub-parsec scales, HCN/CO positive increases with the column density of the gas.

Figure 8.9 presents the above mentioned literature results overlaid onto the ~ 3 pc scale measurements across W49, W43, and G45 from LEGO. The LEGO observations are just in the middle of scales between solar neighbourhood clouds (~ 0.1 pc) and the extragalactic data (> 200 kpc). Moreover, as the most representative star-forming regions in the MW, the LEGO targets are the ideal regions to compare with external, star-forming galaxies. We find that across all LEGO clouds, the average HCN/CO increases with N_{H_2} , even for W43, where the line efficiencies of HCN and CO scale similarly with N_{H_2} . This is a good indication that HCN, despite tracing also lower density gas, most likely traces denser gas than CO in the same region from clump (0.1 pc) to galaxy-environment (1 kpc) scales. The

literature relations that have mostly been determined from kiloparsec scale external observations are very consistent with the results from the LEGO clouds, finding similar slopes and offsets. However, the scatter in the LEGO data is large and there is cloud-to-cloud variation. We find a flatter HCN/CO versus N_{H_2} relation for W43 compared to W49 or G45 and offset between the relations, indicating that the exact relation can substantially vary between regions. Nevertheless, over large enough regions ($\gtrsim 50$ pc) these cloud-to-cloud variations might average out so that HCN/CO could be used as a good indicator of the average gas density at cloud-average scales.

8.5 Conclusions

In this work, we study three of the most massive star-forming regions (W49, W43, G45.1+0.1) in the MW from the LEGO survey, which forms the most direct comparison to extragalactic studies of molecular gas in star-forming galaxies. The three clouds have been mapped in their entirety in over 20 molecular lines at 1 mm wavelength, including the key molecular gas tracers utilised in extragalactic studies (e.g., CO and HCN). Ancillary data from *Herschel* dust observations provide column density (N_{H_2}) and dust temperature (T_{dust}) estimates in order to explore the emission properties of various molecular lines in the $N_{\text{H}_2} - T_{\text{dust}}$ plane across a wide parameter range.

In this first paper focussing on the massive star-forming regions, we studied the emissivity of dense gas tracers as a function of the column density. In agreement with recent works, we find that the emissivity of HCN ($1 - 0$), the most commonly used extragalactic tracer of dense gas, varies strongly between sources and indicates that HCN can trace dense (W49), intermediate (G45) and low gas densities (W43). On the contrary, N_2H^+ ($1 - 0$) is only efficiently emitting from the high-density gas, strengthening its role as a robust dense gas tracer. In the next step, we compared HCN with alternative, bright dense gas tracers (HCO^+ , HNC, CS, CN), which are feasible to map external galaxies and possibly challenge the role of HCN as the dense gas tracer in extragalactic studies. However, we find that all of these lines behave almost identically to HCN and thus present no critical improvement over HCN, at least in normal, spiral galaxies with little metallicity variation. Finally, we show that, despite HCN originating from lower density gas, HCN robustly traces denser gas than CO, such that HCN/CO scales with the average gas density, consistent with smaller scale (0.1 pc) and larger scale (~ 1 kpc) studies.

We conclude that N_2H^+ constitutes the only reliable tracer of cold, dense gas at sub-cloud resolution, motivating studies of N_2H^+ in external galaxies. However, HCN remains a useful tracer to efficiently map higher-density gas in other galaxies and HCN/CO provides a powerful tool to trace density variations. Certainly, this analysis should be extended to the full LEGO sample to probe a larger range of environments and conditions, especially the outer galaxy and low-metallicity environments, where abundance variations might play a crucial role. This is particularly relevant to link to extragalactic studies of low-metallicity environments (e.g., outer discs of spiral galaxies or dwarf galaxies).

Conclusions

“Equipped with his five senses, man explores the universe around him and calls the adventure Science.”

Edwin Hubble – 20th century astrophysicist

In this thesis, we aim to gain a deeper understanding of star formation, one of the most fundamental processes in the universe. We approach the investigation of the star formation process by studying the material from which stars form, that is, the dense parts of giant molecular clouds. This cold, dense phase of the ISM is accessible via molecular line emission at radio wavelength, providing a wealth of information about the physical conditions of the molecular gas. We make use of the capabilities of state-of-the-art telescopes such as ALMA and the IRAM 30 m telescope to observe molecular line emission in nearby galaxies and the MW. In particular, this thesis project focuses on the investigation of the densest parts of molecular clouds, which are intimately linked to the formation of stars. Since stars form from dense gas, a sophisticated study of dense gas and its subsequent conversion into stars is necessary across a wide range of physical conditions and environments. Our galaxy, the Milky Way, provided only a limited range of physical conditions and our positions within the disc of the MW complicate the analysis and interpretation of observations. Therefore, only external galaxies provide a wide range of conditions and hence a representative view of the physical conditions of dense molecular gas and the process of star formation.

The golden age of radio astronomy with current-day radio observatories such as ALMA make it possible to efficiently map the bulk molecular gas in nearby galaxies at scales of GMCs via the bright, low-J CO lines. On the contrary, even the brightest dense gas tracers (e.g. HCN) are at least a factor of 10 fainter than CO, making it much more challenging to observe and study dense gas in other galaxies than our own, hence motivating novel approaches to access this dense gas phase. On the one hand, this requires well-designed observations that make the most out of the valuable, expensive telescope time. On the other hand, we can develop clever tools to get the most out of the data.

One of these tools is the spectral stacking technique, which employs high-significant lines, such as the bright CO lines, to extract emission of fainter lines, such as HCN or HCO⁺, otherwise hidden in the noise. In the first project of this thesis (P1: Spectral stacking of radio-interferometric data, Chapter 4), we present spectral stacking code that has been developed in our group and apply it to simulated ALMA observations to test the capabilities and limitation of the code. Along with the publication, we also make

the code publicly available. In this technical work, we find that spectral stacking can robustly recover emission of faint emission lines in typical ALMA interferometric observations, providing a powerful tool to recover unbiased average trends within galaxies (i.e. scaling relations), which are one of the key diagnostics to relations between dense gas, star formation and physical conditions in galaxies.

In Section 1.5.2, we introduce the Gao-Solomon relation, which demonstrates the strong, tight relation between the star formation rate and the dense gas mass across the universe, which might suggest a universal dense gas star formation law in galaxies. However, recent studies show that the ratio between SFR and HCN (SFR/HCN), a proxy of the dense gas star formation efficiency ($\text{SFE}_{\text{dense}}$), is not constant within galaxies but varies systematically with the environmental conditions (Section 1.5.3). In this thesis, we want to gain a deeper understanding of the systematic variations of SFR/HCN and HCN/CO , a proxy of the dense gas fraction, in nearby spiral galaxies.

This is achieved by making use of new ALMA observations of dense gas tracers across nearby galaxies (the ALMOND survey), which enable to connect the kiloparsec scale spectroscopic ratios (i.e. SFR/HCN , HCN/CO), the kiloparsec scale environment (P2), and the cloud-scale molecular gas properties (P3). While the connection to the kiloparsec scale environment has been investigated in previous works (e.g. Jiménez-Donaire, Bigiel, A. K. Leroy, Usero et al., 2019), the new ALMOND survey provides a much larger sample and range of physical conditions, yielding the most significant constraints on these scaling relations to date. In project P2 (Dense gas scaling relations, Chapter 5), we show that HCN/CO increases, while SFR/HCN decreases with increasing stellar mass surface density, gas mass surface density and dynamical equilibrium pressure. Assuming that HCN/CO and SFR/HCN trace f_{dense} and $\text{SFE}_{\text{dense}}$ reasonably well, this implies that molecular clouds contain higher fractions of dense gas, but are less efficiently converting dense gas into stars in high-density, high-pressure environments.

In project P3 (The missing link between dense gas, star formation and molecular cloud properties, Chapter 6), we connect the spectroscopic ratios with the properties of molecular clouds, which has only become possible recently due to the efforts of the PHANGS team to map nearby galaxies in molecular gas at cloud scales. We find that the variations of HCN/CO and SFR/HCN also link to the properties of the cloud-scale molecular gas, suggesting that f_{dense} is high, while $\text{SFE}_{\text{dense}}$ is low in denser, more turbulent molecular clouds. We also demonstrate that these correlations are expected based on turbulent cloud models (e.g. Krumholz and McKee, 2005). Hence, our study provides a comprehensive physical picture that connects dense gas, star formation and molecular cloud properties.

Moreover, we present new, deep, highly-resolved dense gas observations of the galaxy NGC 4321 to study systematic variations of SFR/HCN and HCN/CO in unprecedented detail in different morphological environments (P4: A spatially resolved view on dense gas in the galaxy NGC 4321, Chapter 7). This dataset is one of the deepest, full-galaxy observations of dense gas tracers across a nearby spiral galaxy paired with cloud-scale resolution molecular gas, dust, and star formation tracers. At 260 pc resolution, we can resolve morphological environments (e.g., centre, bar, bar ends, spiral arms, and interarm regions) that have been blurred together at kiloparsec resolution in the ALMOND maps. We find that HCN/CO and SFR/HCN show the strongest systematic variations in the inner few kiloparsecs of the galaxy, where we also find the strongest variations in density and pressure. Across the disc and between spiral arms and interarm regions, HCN/CO and SFR/HCN stay relatively flat, suggesting that, despite having deeper gravitational potentials and accumulating more gas, spiral arms are not fabricating higher dense gas fraction or higher star formation efficiencies. Moreover, we find indications for a pressure threshold such that HCN/CO and SFR/HCN are less dependent on pressure in low-pressure regions. While these results are still tentative, given the low detection fraction in the low-pressure regime, these findings are indicative of a decoupling of molecular clouds from the local environment in the discs of galaxies.

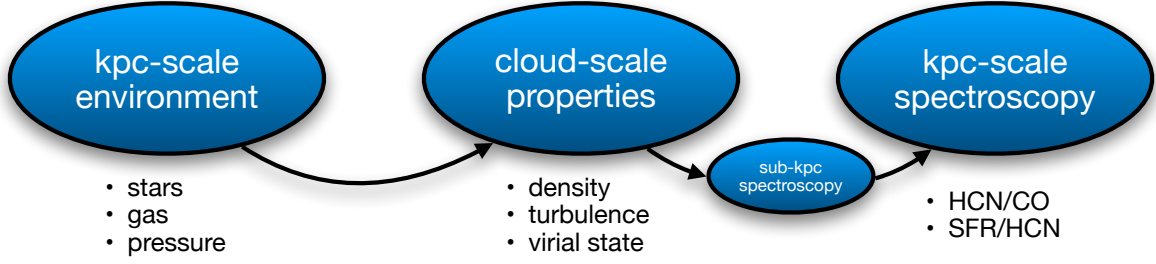


Figure 9.1: **Schematic of dense gas relations.** The diagram visualises the key connections made during this thesis project, connecting kiloparsec scale environmental conditions (Σ_{\star} , Σ_{mol} , P_{DE}) with molecular cloud properties (Σ_{mol} , σ_{mol} , α_{vir}) and dense gas spectroscopic ratios (HCN/CO, SFR/HCN, proxies of f_{dense} , $\text{SFE}_{\text{dense}}$) from 260 parsec to kiloparsec scales. These connections between dense gas, star formation, cloud properties, and local environment suggest the physical picture that the local environment affects the properties of GMCs, which then regulate the formation of dense gas and its conversion into stars.

Furthermore, we find that the bar of NGC 4321 is a unique environment, where star formation seems to proceed differently than in other environments, showing normal HCN/CO, but much lower SFR/HCN, which could point at dynamical effects such as streaming motion or shear that suppress the efficient conversion of dense gas into stars.

Recently, observations from the Orion star-forming region in the Milky Way have challenged the role of HCN ($1-0$) as a tracer of dense molecular gas, showing that it can also be efficiently emitted at intermediate gas densities (Pety et al., 2017; Kauffmann, Goldsmith et al., 2017). Motivated by these works, the LEGO survey aims at gaining a better understanding of the emissivity of classical extragalactic dense gas tracers, using the MW as a laboratory to study a representative sample of molecular clouds regions across the galaxy. In P5 (Linking dense gas tracers from the Milky Way to external galaxies, Chapter 8), we present a sub-sample of the LEGO observations consisting of three massive star-forming regions, which is the ideal sample to compare with nearby star-forming galaxies. We analyse the emissivity, meaning the line brightness of a given line per unit column density, of a suite of selected lines, including dense gas tracers such as HCN, HCO^+ , or CS, as well as N_2H^+ . We find that HCN, along with other classical dense gas tracers (HCO^+ , HNC, CS, CN), traces not only the dense gas but also intermediate gas density, especially if this gas is associated with high dust temperatures. On the contrary, N_2H^+ only emits efficiently in cold, dense regions, supporting its role as the gold standard tracer of dense gas. Despite its substantial emissivity variations between regions, we find that HCN can still be used as a proxy for dense gas. On the one hand, the second-order emissivity effects can be mitigated by correcting for the dust temperature as proposed by Tafalla et al. (2023). On the other hand, we demonstrate that line ratios between extragalactic dense gas tracers (e.g. HCN) and bulk molecular gas tracers (e.g. CO) scale with the gas column density across all three LEGO regions in agreement with extragalactic results. The sensitivity of HCN/CO to density suggests that HCN (and other dense gas tracers) robustly trace denser gas relative to CO, and that these density-sensitive line ratios likely mitigate secondary emissivity effects such as the dependence on gas temperature, making them powerful extragalactic tools.

To conclude, this thesis work presents new observations of dense gas tracers that yield new insights into dense gas conditions and star formation in galaxies and provide rich datasets far from being fully exploited. In this thesis, we connected physical processes and scales, addressing the missing link between dense gas, star formation and molecular cloud properties. On the one hand, this work demonstrates

that faint molecular lines such as dense gas tracers in extragalactic observations can successfully be recovered via spectral stacking enabling the study of star formation relations. On the other hand, our findings from MW clouds show that commonly used dense gas tracers in extragalactic studies inherit significant caveats making them less robust tracers of dense gas and promoting either alternative, though much fainter, dense gas tracers or the development of improved prescriptions to utilise these classical dense gas tracers in a less biased manner. Despite these methodical drawbacks, classical extragalactic dense gas tracers are still powerful tools to trace density variations from sub-cloud to kiloparsec scales. Some of the key results of this thesis have been summarised in the review paper “Molecular Gas and the Star Formation Process on Cloud Scales in Nearby Galaxies” (Schinnerer and A. K. Leroy, 2024) to appear in *Annual Reviews of Astronomy and Astrophysics* 2024, Vol 62. The basic emerging picture is that within star-forming galaxies, the kiloparsec scale environment affects the properties of molecular clouds, which in turn regulate how efficiently dense gas is converted into stars (Figure 9.1).

Outlook and Open Questions

“What I love about science is that as you learn, you don’t really get answers. You just get better questions.”

John Michael Green – 21th century author

In this thesis, we studied dense molecular gas from the MW to nearby galaxies, presenting new radio astronomical observations that are at the forefront of scientific advances. We connect these observations to the star formation in galaxies and study how the conditions of the gas affect the star formation process, yielding a comprehensive picture of dense gas, star formation, and the local, physical conditions of the gas in normal spiral galaxies. While these results are a step forward to understanding how dense gas forms and star formation is regulated in galaxies, there are still many unexplored and open science questions.

Dense gas and star formation

To date, dense gas spectroscopic ratios have mainly been studied at kiloparsec scale in nearby spiral galaxies and thus average over ensembles of tens to hundreds of clouds. There are good indications that these kiloparsec scale measurements are connected to the cloud-scale physics (Neumann, Gallagher et al., 2023), but variations at cloud scales remain unexplored due to the lack of cloud-scale dense gas observations. The increased scatter in the Gao-Solomon relation points towards an increased variation of the star formation efficiency of dense gas at smaller, cloud scales. However, it is not known what drives these SFR/HCN variations at cloud scales. Therefore, higher resolution observations of dense gas tracers are needed across a significant sample ($\gtrsim 10$ galaxies), much like a “dense gas PHANGS–ALMA”. A dense gas survey of this extent would require several 100 times the observing time of PHANGS–ALMA, and is hence not feasible with current observatories. However, we initiated the first pilot studies of individual galaxies in the PHANGS collaboration, so that the galaxy NGC 2903 has recently been observed at $\lesssim 100$ pc scale resolution (PI: A. T. Barnes). Furthermore, we got ALMA cycle 11 observations of the galaxies NGC 4254 approved to be observed over the next year at ~ 100 pc resolution. These observations and future efforts will allow us to study dense gas at unprecedented resolution in nearby galaxies in order to understand what drives star formation at GMC scales.

In addition, these new observations open up new possibilities for studying the properties of molecular clouds, such as density, turbulence and gravitational boundedness from the perspective of dense gas. They also enable the first constraints on the timescales of dense gas in the lifecycle of molecular clouds. Until now, statistical studies of molecular cloud timescales have only been done via the bulk molecular gas traced by CO. The works of Chevance et al. (2020), J. Kim, Chevance, Kruijssen, Schruba et al. (2021) and J. Kim, Chevance, Kruijssen, A. K. Leroy et al. (2022) show that using the cloud scale ($\lesssim 100$ pc) observations from PHANGS, the timescales of the molecular cloud lifecycle can be determined. The analysis is based on a statistical method (Kruijssen and Longmore, 2014; Kruijssen, Schruba et al., 2019), which uses the spatial decorrelation of molecular line emission (e.g. CO) and star formation tracer ($\text{H}\alpha$ or $21\ \mu\text{m}$) peaks only seen at physical scales $\lesssim 150$ pc. While the aforementioned studies measure the timescales of the molecular gas and stellar feedback phases, it is not known how fast dense gas forms, how long it takes to convert dense gas into stars and how fast stellar feedback is in resolving the dense gas phase. All of these questions can only be addressed with new cloud-scale dense gas observations.

Besides the cloud-scale observation of dense gas, another promising avenue is the study of dense gas in yet unexplored physical environments. Until now, most dense gas relations have been limited to normal, main-sequence galaxies, which are the obvious targets to study star formation and dense gas but are not representative of the whole galaxy population. Therefore, expanding the parameters space of dense gas relations certainly requires observing more exotic, extreme environments, such as starburst, elliptical and dwarf galaxies. Only by studying the full galaxy population, we will gain a complete picture of star formation and understand galaxy evolution. Moreover, current studies (e.g. Neumann, Bigiel et al., 2024) motivate a larger sample study of specific morphological environments in galaxies, such as galaxy centres, nuclear rings, bars or bar ends. There are still many open questions related to these dynamical environments, such as whether nuclear rings form stars in a “popcorn” or “pearls on a ring” scenario (Böker et al., 2008), whether galactic bars evolve to eventually quench star formation (Verwilghen et al., 2024), and whether cloud-cloud collisions in bar ends boost or suppress star formation (Takahira et al., 2014). While some of these questions have been addressed in this thesis (Neumann, Bigiel et al., 2024) via NGC 4321, this study only considers one galaxy hence prohibiting general statements and requiring a large, diversion sample of galaxies. Our works also motivate further studies of low-density, low-pressure environments, where theoretical works propose a decoupling between molecular clouds and their local environments (e.g. Elmegreen, 2018). We find some indications of a pressure threshold for the coupling between molecular clouds and the galactic environment in the low-pressure regions of discs. However, the limited sensitivity of our observations does not allow a strong statement about the existence of this pressure threshold. To probe the low-density, low-pressure regime, requires deeper observations of the outer disc of nearby galaxies, possibly employing clever observing strategies similar to the stratified random sampling techniques in Tafalla et al. (2021).

Eventually, dense gas studies have to be extended to more distant galaxies to investigate whether cosmic evolution affects the regulation of star formation, which is tightly connected to the question of how galaxies evolve over cosmic time. These next-generation observations should include the most active star-formation period of the universe (cosmic noon) at redshifts $\sim 1 - 3$ but also cover the epoch where the first galaxies have formed around redshift $\gtrsim 5$. Rybak et al. (2022) has shown that dense gas detections in dusty star-forming galaxies around $z \approx 3$ are challenging but feasible with state-of-the-art radio observatories like ALMA, motivating further studies of these targets towards a comprehensive picture of star formation laws across the universe.

Dense gas tracers

Certainly, much of the interpretation related to dense gas observations is connected to the viability of adopted tracers and the prescriptions used to infer physical quantities from measured data. This work highlights how difficult it is to interpret molecular lines as tracers of dense gas. There is still a poor understanding of these tracers and hence no reliable recipe to infer robust dense gas masses from feasible tracers in extragalactic observations. One approach to getting more robust estimates of dense gas masses is to find the best possible tracers of dense gas across galaxies and environments, while still being feasible to observe with current-day facilities. This thesis project (Chapter 8) along with other studies (e.g. Pety et al., 2017; Kauffmann, Goldsmith et al., 2017; Barnes, Kauffmann et al., 2020; Santa-Maria et al., 2023) show that N_2H^+ could be considered the gold standard tracer of dense, cold gas. Hence, despite its high observing costs, these results trigger extragalactic observations of N_2H^+ in nearby spiral galaxies. Recently, this novel, expensive approach has been undertaken by Jiménez-Donaire, Usero et al. (2023) and Stuber et al. (2023), who observed N_2H^+ along with HCN in two nearby spiral galaxies (NGC 6946, M51) finding that the N_2H^+ -to-HCN line ratio is roughly fixed at these $\gtrsim 100$ pc scales. These results may seem surprising given the significant differences between these tracers in galactic observations at smaller scales and might indicate that the HCN emitting gas is actually more fundamentally connected to the N_2H^+ emitting gas than previously assumed. While these findings could tell us something about the intrinsic structure of molecular clouds, they also strengthen the use of HCN as a dense gas tracer in extragalactic works despite the galactic works. Nevertheless, the aforementioned studies only observed a few kiloparsec-sized regions in two galaxies, motivating further extragalactic studies of N_2H^+ , which is one the efforts in PHANGS, such that recently the galaxy NGC 4321 has been mapped in N_2H^+ (PI: M. J. Jiménez-Donaire) at kiloparsec resolution, producing the first full-galaxy N_2H^+ map. In addition, several alternative dense gas tracers are similarly bright as HCN, which are worth exploring and comparing with HCN. Some of these might be better suited in extreme environments, such as starbursts or AGN-dominated centres (e.g. HCO^+ or CS), or in low-metallicity environments (HCO^+ , Braine et al. (2017)). Many of the extragalactic dense gas surveys (e.g. ALMOND) also contain these alternative tracers, which have not been explored in detail.

Another approach to improve the inference of dense gas masses is to gain a better understanding of how certain, feasible tracers depend on secondary emissivity effects, like temperature or optical depth. In other words, we need better prescriptions of the light-to-mass conversion factors (e.g. α_{HCN}) that correct these effects are yield more robust dense gas estimates from these classical dense gas tracers. As shown in this work, the MW is an excellent laboratory to calibrate conversion factors and mitigate secondary effects, such as the dependence on temperature (Chapter 8 and Tafalla et al. (2023)). However, dust temperatures are inaccessible at high angular resolution in other galaxies (there is no space observatory working FIR wavelengths that would allow proper dust temperature observations) and we rely on other tracers to infer gas or dust temperatures that have either strong caveats or are expensive to observe. Moreover, conversion factors most certainly also depend on other factors such as chemistry, metallicity, and optical depth, which have been extensively studied for the CO-to- H_2 (α_{CO}) conversion factors, yielding improved, variable α_{CO} prescription for external studies (e.g. Bolatto et al., 2013; Gong et al., 2020; Sun, A. K. Leroy, E. C. Ostriker et al., 2020; Teng, Sandstrom, Sun, A. K. Leroy et al., 2022; Teng, Sandstrom, Sun, Gong et al., 2023). However, similar, sophisticated recipes have not been developed for dense gas tracers, such that studies rely on constant conversion factors. The LEGO survey comprises an excellent dataset, including several low-metallicity, outer galaxy clouds, to explore variations of conversion factors with metallicity, and thus motivates a sophisticated study of the

HCN-to- M_{dense} conversion factor across the MW. Furthermore, the LEGO team aims to follow up their targets with 1 mm radio observations using the Atacama Pathfinder EXperiment (APEX) telescope in order to cover the higher-J transitions of the lines that have been observed by the IRAM 30 m telescope at 3 mm wavelengths. These have been observed for the massive star-forming regions W49 (PI: A. T. Barnes), W43 (PI: H. Lin), and G45 (approved for current cycle, PI: L. Neumann), and allow radiative transfer modelling to constrain optical depth variations of dense gas tracers such as HCN, HCO^+ , or N_2H^+ . This future analysis will provide new insights into the dependence of dense gas conversion factors on optical depth.

Physical conditions of the ISM

Eventually, a key goal of ISM astrophysics is the inference of the physical conditions of the gas. In project P5 (Chapter 8), we have seen that the emission of each molecular line depends differently on the physical conditions of the gas. To some extent, this is because each molecular line transition is unique and defined by fundamental atomic physics, making molecular lines extremely powerful tools to study the ISM. However, often variations of different physical conditions (e.g. temperature, density) can yield the same changes in the intensity of a single line or the ratio between two lines. For example, the change in the CO (1 – 0)-to-CO (2 – 1) line ratio can mean either a change in gas density or temperature (e.g. den Brok, Chatzigiannakis et al., 2021). Therefore, observations of many molecular lines at matched physical resolution are needed to break these degeneracies such that parameters like the density and temperature of the gas can be constrained, for instance, via radiative transfer modelling (e.g. using the radiative transfer code RADEX van der Tak et al., 2007). To date, there exist very few extragalactic datasets that allow a proper radiative transfer modelling analysis due to the need for multi-species, multi-J observations at high S/N. The ALMA Comprehensive High-resolution Extragalactic Molecular Inventory (ALCHEMI) survey (Martín et al., 2021) is one of these rare datasets detecting 78 molecular line species across the central region of the nearby starburst galaxy NGC 253. Another galaxy that has been subject to many radio line surveys is M51 (a.k.a. NGC 5194; e.g. Schinnerer, Meidt et al., 2013; den Brok, Chatzigiannakis et al., 2021; Stuber et al., 2023) and hence of the obvious candidate to employ radiative transfer modelling.

Besides employing physically motivated modelling approaches (such as RADEX), the technical advances in the field of machine learning (ML) provide also new opportunities across all fields of astrophysics. While ML techniques have already been used as object classification (Hannon et al., 2023), or structure identification tools (Colombo et al., 2016), there are many unexploited opportunities to constrain the physical conditions of the ISM. One approach could be to adapt ML image classification tools to constrain physical parameters from a suit of molecular line emission maps. The basic idea is that the ML model is trained on a set of real or simulated observations where these parameters are known such that the ML learns how certain physical conditions (e.g. gas density and temperature) correlate with the emission of various molecular lines. After the training and verification phase, the ML tool can then be applied to molecular line data in order to infer the physical conditions. The beauty of this approach is that on the one hand, these tools exist and should be easily adaptable, and on the other hand no information about the physics is needed. The biggest challenge of applying ML techniques like the one sketched above is most likely the preparation of a representative training set and the proper evaluation and interpretation of the outcome. Nevertheless, the rapid rise of ML application makes it only a matter of time until these tools find widespread application in all fields of astronomy, physics, and science in general.

A cosmic star formation law

One of the ultimate goals of astrophysics is to understand how star formation is regulated across the universe, from small to large scales, from short to long timescales, across cosmic time and throughout the evolution of galaxies. On this journey towards a comprehensive picture of star formation across the cosmos, many pieces of a big puzzle of intertwined physical processes have to be brought together. One of the key probes to gain a deeper understanding of the star formation process is the investigation of molecular, and in particular, dense molecular gas.

The next generation telescopes such the Square Kilometre Array (SKA), next generation-Karl G. Jansky Very Large Array (ngVLA), and future upgrades of ALMA (e.g. the planned wide band upgrade) and NOEMA (e.g. frequency-switching mode, higher frequency bands, and more extended baselines), as well as possibly new FIR space observatories, will revolutionise ISM and SF studies, providing pivotal improvements in resolution and sensitivity, allowing larger surveys, the detection of fainter lines and more distant objects, which will be critical to study star formation across the whole universe. In particular, the next generation (sub-)mm telescopes will enable efficient mapping of faint lines that are routinely observed in the MW (e.g. N_2H^+), providing a less biased view on dense gas and gas conditions in general across the local and more distant galaxy population.

Certainly, a comprehensive view of star formation can only be achieved if connections can be made between MW, local and high-redshift works, as well as theory, simulations and observations, which is one of the key, yet poorly explored challenges of astrophysics for the next few decades. One of the key goals of simulations is to optimise and extend chemical networks in astrochemical simulations such as the SImulating the LifeCycle of molecular Clouds (SILCC) project (Walch et al., 2015). Then, sophisticated post-processing of simulations can provide proper comparison between observations and simulations (e.g. Panessa et al., 2023). In conclusion, the future of ISM studies and radio astronomy is bright and there is ever more to explore towards a comprehensive view of one of the most complex processes in the universe – star formation.

Appendix

Stacking paper

The paper Neumann et al. 2023, A&A, 675, A104, 9 pp. (DOI: [10.1051/0004-6361/202346129](https://doi.org/10.1051/0004-6361/202346129)) is reproduced below in its original form with permission by ESO.

Spectral stacking of radio-interferometric data

Lukas Neumann¹, Jakob S. den Brok^{1,2}, Frank Bigiel¹, Adam Leroy³, Antonio Usero⁴, Ashley T. Barnes⁵,
 Ivana Bešlić^{1,6}, Cosima Eibensteiner¹, Malena Held¹, María J. Jiménez-Donaire⁴, Jérôme Pety^{6,7},
 Erik W. Rosolowsky⁸, Eva Schinnerer⁹, and Thomas G. Williams¹⁰

¹ Argelander-Institut für Astronomie, Universität Bonn, Auf dem Hügel 71, 53121 Bonn, Germany
 e-mail: lukas.neumann.astro@gmail.com

² Center for Astrophysics, Harvard & Smithsonian, 60 Garden St., 02138 Cambridge, MA, USA

³ Department of Astronomy, The Ohio State University, 140 West 18th Ave, Columbus, OH 43210, USA

⁴ Observatorio Astronómico Nacional (IGN), C/ Alfonso XII, 3, 28014 Madrid, Spain

⁵ European Southern Observatory, Karl-Schwarzschild Straße 2, 85748 Garching bei München, Germany

⁶ LERMA, Observatoire de Paris, PSL Research University, CNRS, Sorbonne Universités, 75014 Paris, France

⁷ Institut de Radioastronomie Millimétrique (IRAM), 300 rue de la Piscine, 38406 Saint Martin d'Hères, France

⁸ Dept. of Physics, University of Alberta, Edmonton, Alberta, T6G 2E1, Canada

⁹ Max Planck Institute for Astronomy, Königstuhl 17, 69117 Heidelberg, Germany

¹⁰ Sub-department of Astrophysics, Department of Physics, University of Oxford, Keble Road, Oxford OX1 3RH, UK

Received 12 February 2023 / Accepted 28 April 2023

ABSTRACT

Context. Mapping molecular line emission beyond the bright low- J CO transitions is still challenging in extragalactic studies, even with the latest generation of (sub-)millimetre interferometers, such as ALMA and NOEMA.

Aims. We summarise and test a spectral stacking method that has been used in the literature to recover low-intensity molecular line emission, such as HCN(1–0), HCO⁺(1–0), and even fainter lines in external galaxies. The goal is to study the capabilities and limitations of the stacking technique when applied to imaged interferometric observations.

Methods. The core idea of spectral stacking is to align spectra of the low S/N spectral lines to a known velocity field calculated from a higher S/N line expected to share the kinematics of the fainter line (e.g. CO(1–0) or 21 cm emission). Then these aligned spectra can be coherently averaged to produce potentially high S/N spectral stacks. Here we used imaged simulated interferometric and total power observations at different S/N levels, based on real CO observations.

Results. For the combined interferometric and total power data, we find that the spectral stacking technique is capable of recovering the integrated intensities even at low S/N levels across most of the region where the high S/N prior is detected. However, when stacking interferometer-only data for low S/N emission, the stacks can miss up to 50% of the emission from the fainter line.

Conclusions. A key result of this analysis is that the spectral stacking method is able to recover the true mean line intensities in low S/N cubes and to accurately measure the statistical significance of the recovered lines. To facilitate the application of this technique we provide a public Python package, called PYSTACKER.

Key words. methods: data analysis – techniques: interferometric – galaxies: ISM – radio lines: galaxies – radio lines: ISM

1. Introduction

Mapping extragalactic molecular line emission with high spatial resolution and sensitivity is still challenging even with the latest generation of (sub-)millimetre interferometers, such as the Atacama Large Millimeter/submillimeter Array (ALMA) and the Northern Extended Millimeter Array (NOEMA). In practice, for most nearby galaxies, only the low- J CO transitions, which are the brightest millimetre-wave lines, can be rapidly surveyed at a good resolution ($\lesssim 1''$) while also achieving widespread high-significance detections across the full disc of a typical star-forming galaxy (e.g. Leroy et al. 2021b). Recovering integrated intensities of fainter, and hence typically low signal-to-noise ratio (S/N) lines, such as HCN(1–0), HCO⁺(1–0), or N₂H⁺(1–0), is more challenging. These lines carry critical physical information on the composition, temperature, and density of the gas, but often have intensities 30 to >100 times fainter than the CO lines (e.g. Usero et al. 2015; Jiménez-Donaire et al. 2017). To measure the intensities of these other lines, ‘spectral stacking’ methods have become popular in recent years.

Stacking of astronomical data has been used for at least four decades (e.g. Cady & Bates 1980) and applied across wavelength regimes, from X-ray (e.g. Hickox et al. 2007; Chen et al. 2013) to sub-millimetre and radio wavelengths (e.g. Knudsen et al. 2005; Karim et al. 2011; Schrubba et al. 2011; Delhaize et al. 2013; Caldú-Primo et al. 2013; Bigiel et al. 2016; Lindroos et al. 2016; Jolly et al. 2020). In the past decade, spectral stacking has become a particularly important tool in millimetre studies of galaxies, allowing the recovery of otherwise undetected line emission. For example, Jiménez-Donaire et al. (2019), Bešlić et al. (2021), and Neumann et al. (2023) all use spectral stacking leveraging a CO emission prior to recover emission from faint high critical density emission lines, including HCN(1–0), HNC(1–0), or HCO⁺(1–0), across large areas in the discs of nearby galaxies. den Brok et al. (2021) and den Brok et al. (2022) used spectral stacking based on ¹²CO to obtain more significant constraints on lines tracing rarer CO isotopologues. And Schrubba et al. (2011) used 21 cm emission as a prior to construct extended, sensitive radial profiles of CO emission even in the outer parts of galaxies. These studies all demonstrate how spectral stacking

recovers more information about the distribution, composition, and physical conditions of the molecular gas in galaxies.

The basic idea of spectral stacking as often applied to nearby galaxies is to align all spectra by recentring them on the local mean velocity of the interstellar medium (ISM), which is measured using a high S/N prior (e.g. CO(1–0)) or the 21 cm line (Sect. 2). Then spectra from different parts of the galaxy can be coherently averaged with minimal contributions from noise in empty parts of the bandpass. By averaging in azimuthal rings, one can construct sensitive radial profiles. One can also average as a function of other quantities to test specific hypotheses or scaling relations (e.g. galactocentric radius, line intensity, surface density, or star formation rate). Carrying out this stacking on the spectra allows an important visual check that the averaged result indeed looks like an astrophysical spectral line (i.e. to first order a Doppler-broadened Gaussian line profile), and can even allow recovery of mean kinematic information via the width of the Gaussian.

While these techniques are simple in principle, a key uncertainty remains surrounding their application to the most powerful current millimetre-wave telescopes, ALMA and NOEMA. These facilities are interferometers, and the images they produce reflect both incomplete sampling of the $u-v$ plane and a deconvolution process that often focuses on bright emission. While $u-v$ plane stacking can alleviate both concerns in unresolved objects or those with simple geometries, stacking in the image plane remains the most practical option for extended, complex sources, such as nearby galaxies. Since stacking using these powerful telescopes represents a key way to push our knowledge of the physical state and makeup of the ISM, evaluating the accuracy of this technique when applied to recover faint low S/N lines from interferometer data is a key next step.

The goal of this work is to provide such a demonstration. For this purpose we used the Common Astronomy Software Applications (CASA; CASA Team et al. 2022) ALMA simulator to simulate interferometric and total power observations of low S/N lines based on a known input model. The resulting simulated observations were imaged using the Physics at High Angular resolution in Nearby Galaxies (PHANGS)–ALMA pipeline (Leroy et al. 2021a). Then we applied the spectral stacking method and assessed how well the stacks recover the known input. In particular, we stacked via the galactocentric radius using simulated CO(2–1) data cubes built on real observations of galaxies from the PHANGS–ALMA survey (Leroy et al. 2021b).

We also present a new public Python package, PYSTACKER that can be used to easily apply these techniques. This utility complements the tool LINESTACKER presented by Jolly et al. (2020), which is also validated against simulation. Their work focuses on spectrally stacking many distinct sources in three dimensions, while our code emphasises stacking within an individual data set in the presence of a complex prior velocity field. Another stacking package called SPECTRAL-STACK¹, relies on Fourier shifting to align the spectra to be averaged. The advantage of this approach is that the noise properties and channel-to-channel correlations are preserved. However, it deals less well with edge effects.

2. Description of the spectral stacking method

The main goal of the spectral stacking technique is the recovery of low S/N lines by shifting the spectra to a known velocity field defined by a high S/N prior (e.g. CO(1–0) or CO(2–1) or the

HI 21 cm line) and then averaging the spectra based on another parameter such as environment, star formation rate, or line intensity. Our stacking method is based on den Brok et al. (2022) and Neumann et al. (2023) and our implementation is available as a Python package, called PYSTACKER². We describe the basic steps of the code in the following.

We begin with a set of data cubes of the same target with different S/N levels of the input line emission. First, we homogenise the data bringing all data cubes to the same coordinate grid and convolving to the same spatial resolution. Then we define a prior, typically the most significantly detected line, which is used to obtain the velocity field as the velocity at the peak intensity of each spectrum³ (Koch et al. 2018). We use this velocity field to redefine the spectral axis for each individual spectrum in the cube⁴ so that the emission of all lines should be centred at a velocity of 0 km s^{−1}. The result is sometimes referred to as a ‘shuffled’ cube, in reference to the shuffle task of the Groningen Image Processing System (GIPSY; van der Hulst et al. 1992).

Figure 2 shows the basic functioning scheme of the PYSTACKER package, which allows for two input options. The first is the PyStructure database, a numpy dictionary containing all the molecular line emission data. The PyStructure database is produced by a separate pipeline and already contains the velocity alignment analogous to the velocity shuffling performed by PyStacker. In the second option (the default for most users), the input can be data cubes in the form of .fits files, where each FITS file contains the position-position-velocity information of the respective spectral line. Here the user can provide a model velocity field used to shuffle the velocity field of the lines to be stacked. In both cases, a configuration file must be specified, which sets the parameters for the stacking. If data cubes are provided, they are sampled on hexagonal gridded pixels with half-beam spacing. Next, the significant pixels of the given prior are identified and the velocity field is shuffled based on the moment-1 of the prior (if not provided by the input model). After applying the velocity offsets to the molecular line data, the spectra inside the given bins are averaged. The user can specify in the configuration file if the prior-non-detected pixels are ignored or set to zero for the bin average. Afterwards, the stacked spectra of the prior are used to build a velocity mask for each stack, which is used to compute the integrated intensities (inside the mask) and the uncertainties (rms outside the mask). The final output is a numpy dictionary containing the stacked spectra along with their integrated intensities, uncertainties, and other quantities (see the documentation for the full output content).

One can average the shuffled spectra inside bins defined by any arbitrary quantity of scientific interest (e.g. galactocentric radius, CO(1–0) line intensity, or star formation rate). For instance, in this work we stack as a function of galactocentric radius (Sect. 3). If signal is present in the stacked line within a given bin, the averaged spectrum should then appear as a clear emission line (e.g. Fig. 1 right panel). For comparison, averaging across different parts of strongly rotating discs without first adjusting to the local velocity yields a broad lower signal-to-noise profile (e.g. see Fig. 2 in Schrubba et al. 2011).

² <https://github.com/PhangsTeam/PyStacker>

³ The code also allows inputting a model velocity field.

⁴ Recentring the spectrum itself has some associated subtleties, and can be done using either Fourier techniques or via regridding and oversampling. In this paper we use re-gridding techniques, but the choice of approach can affect the channel-to-channel correlation and noise properties of the stacked spectrum.

¹ https://github.com/low-sky/spectral_stack

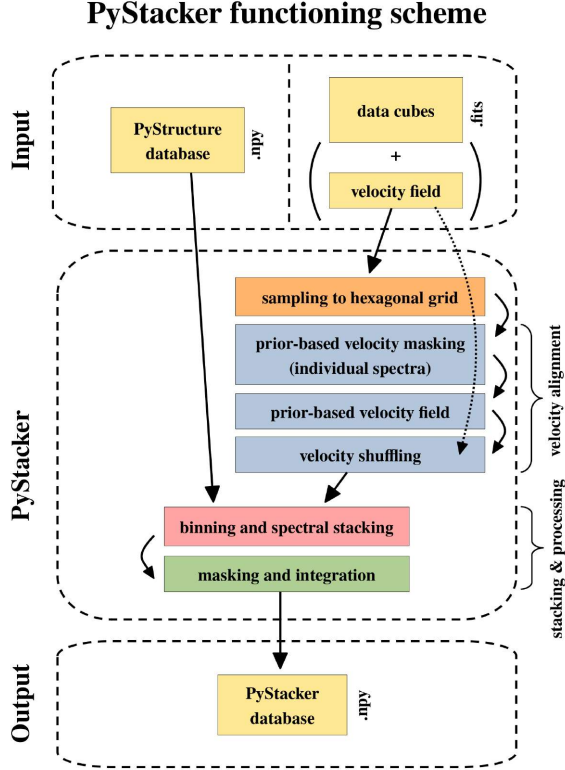


Fig. 1. Schematic of the PyStacker package functioning principle. The input can be either a so-called PyStructure database (at the moment of submission only internally used) or FITS files of data cubes containing the molecular line emission. The latter is applicable to all users. The PyStructure files does already include the re-sampled and velocity aligned data. If FITS files are provided, the PyStacker package will perform the velocity alignment given an input prior or take the input velocity field. In both cases, the spectra will be stacked according to the input stacking quantity and processed to retrieve average integrated intensities. The results are then returned as a Python dictionary, which can be read e.g. following the example script coming with the PyStacker package.

We can only reliably shuffle the spectra if the prior is actually detected in the respective spectrum. Thus, if the prior is only detected in a fraction of the spectra inside a bin, we rely on these spectra to infer the average of the bin. In this case we consider the emission in the spectra that could not be shuffled to be equal to zero, such that the average is always measured relative to all spectra inside a given bin⁵. We expect this to be a reasonable assumption when stacking a rare faint molecular line such as HCN(1–0) using CO as a prior⁶.

Within any given bin n , we measure the average spectrum

$$T_{n,\text{stack}}(v) = \frac{1}{N_{\text{tot}}(n)} \sum_{i=0}^{N_{\text{det}}(n)} T_{n,i}(v), \quad (1)$$

⁵ The alternative, i.e. averaging over the prior-detected spectra only, tends to overestimate the stacked intensity. However, PyStacker allows us to also use this option, and we show its results in Fig. A.3.

⁶ In other applications of this method, a lower resolution cube or even a model rotation curve may sometimes be used as a prior to shuffle in cases where the brighter line has patchy coverage or limited S/N.

where $N_{\text{tot}}(n)$ and $N_{\text{det}}(n)$ are the total number and the prior-detected number of spectra in bin n . To compute the integrated intensities of the stacked spectra, we built a mask based on the high-S/N reference cube. We selected the velocity range of significant emission for each spectrum as described in Bešlić et al. (2021) and integrated the intensities over mask-selected velocity channels

$$W_n = \sum_{N_{\text{mask}}} T_{n,\text{stack}}(v) \cdot \Delta v_{\text{channel}}, \quad (2)$$

where $\Delta v_{\text{channel}}$ is the channel width and N_{mask} is the number of (independent) channels inside the mask. The nominal uncertainties of the integrated intensities (σ_W , studied in Sec. 3.1) are given by

$$\sigma_W = \text{rms} \times \sqrt{\frac{N_{\text{tot}}}{N_{\text{det}}}} \times \Delta v_{\text{channel}} \times \sqrt{N_{\text{mask}}}, \quad (3)$$

where rms is the root mean square of the emission-free channels (i.e. outside the mask) in the stacked spectrum. Since the stacked spectrum is computed from the prior-detected pixels, N_{det} , but divided by the total number of pixels in that bin, N_{tot} (Eq. (1)), the measured rms of the emission-free channels is biased low if $N_{\text{det}} < N_{\text{tot}}$. Therefore, we have to correct the rms by the factor $\sqrt{N_{\text{tot}}/N_{\text{det}}} (\geq 1)$ in Eq. (3) in order not to underestimate the rms, and thus σ_W . The correction factor mimics the increase in noise when adding up N_{tot} spectra with the same noise level.

3. Recovery of integrated intensities

We apply our method to simulated data cubes with known input to test how well spectral stacking can recover the integrated intensities of molecular line emission as a function of the noise level of the observations. Specifically, we use a set of simulations of molecular line emission produced to validate the PHANGS–ALMA data reduction pipeline (Leroy et al. 2021a). As described in Leroy et al. (2021a), the simulated CO(2–1) data cubes were produced using the CASA tasks `simdata` and `simobserve` using inputs based on real PHANGS–ALMA CO(2–1) images. The simulated observations mimic interferometric observations of the galaxy NGC 3059 similar to the PHANGS–ALMA survey⁷. The simulations included the creation of a simulated total power map constructed by convolving the input model to the resolution of the ALMA TP antennas and adding Gaussian noise of the expected magnitude for a real PHANGS–ALMA TP observation.

The input intensity cube, hereafter referred to as the template, is the actual masked NGC 3059 cube from PHANGS–ALMA. We show the integrated intensity map of this template data cube in the upper left panel of Fig. 2. These ‘true’ data are used to construct simulated 12 m, 7 m, and total power observations and imaged via the PHANGS–ALMA pipeline (for more details see Leroy et al. 2021a). Then we run these through the stacking pipeline in this study. The use of real data as a model means that there will be some observational noise in the true data, but we consider that as signal, and explore how well it gets recovered, and it should have only a modest impact on the analysis.

The simulations produce images for different combinations of the ALMA main array, the ACA 7 m antennas, and the

⁷ The NGC 3059 look-alike has been rotated so that the major axis of the galaxy is aligned with the declination. However, these modifications have no effect on our analysis.

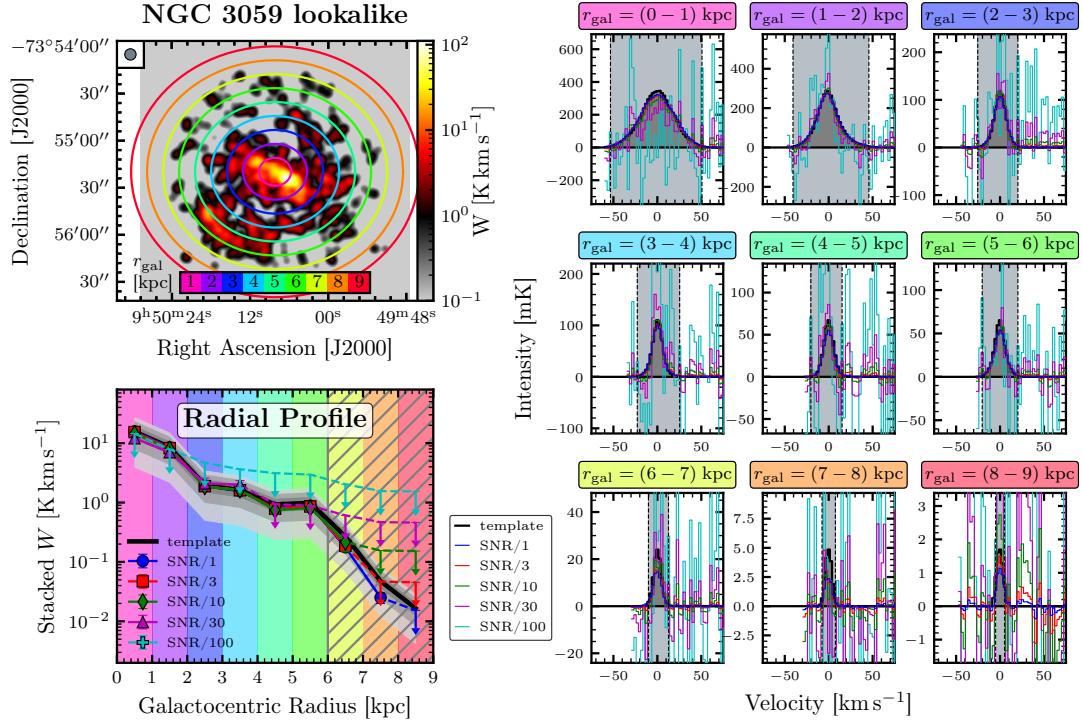


Fig. 2. Spectral stacking of the NGC 3059 template galaxy via galactocentric radius. *Top left:* moment-0 map of the true (i.e. known) simulated CO(2–1) emission mimicking the intensity distribution of NGC 3059. The data have been convolved to the common highest resolution over all array configurations (7.2'') indicated by the grey circle in the upper left. The coloured rings show the loci of the galactocentric radius. *Right panels:* stacked spectra in 1 kpc radial bins from the centre out to 9 kpc as illustrated in the top left panel. The dark grey histogram shows the true spectra (i.e. those obtained by stacking the input template). The coloured lines show the stacked spectra from the respective simulated data cubes. The grey-shaded area indicates the velocity range used to compute the integrated intensities. *Bottom left:* stacked integrated intensities corresponding to the spectra shown in the right panels plotted against galactocentric radius. The black line shows the true radial trend, and the coloured lines show the recovered trend of the simulated data cubes. Solid points indicate data above 3σ ; downward pointing arrows denote 3σ upper limits. The grey shaded areas show differences to the true trend in levels of $\pm[25, 50, 75]\%$. The hatched area denotes the regime where the prior S/N/1 is detected ($S/N \geq 3$) in less than 20% of the pixels.

total power data: 12m+7m+tp, 12m+7m, 7m+tp, 12 m and 7 m (Sect. 3.2). They also produce cubes with a range of different signal-to-noise levels, which we refer to as S/N/1, S/N/3, and so on. The S/N/1 cube mimics the sensitivity of a typical PHANGS–ALMA CO(2–1) observation, while S/N/3, S/N/10, S/N/30, and S/N/100 have a factor of 3, 10, 30, and 100 lower S/N⁸, respectively, but leave the noise the same. Here, we take these cubes and rescale them with the respective factors to obtain cubes at the same intensity but with different noise, and thus S/N levels. At the common PHANGS–ALMA sensitivity and for a brightness distribution similar to NGC 3059, S/N/10 could be representative for ¹³CO(1–0), S/N/30 for HCN(1–0) or HCO⁺ and S/N/100 for fainter lines such as N₂H⁺(1–0).

The S/N levels of the moment-0 maps resulting from the various S/N cubes range from 2.5 (minimum), 341.7 (maximum) for the S/N/1 data; over –1.9 (minimum), 32.5 (maximum) for the S/N/10 cube; and down to –3.8 (minimum), 3.7 (maximum) for the version with 100 times higher noise. This means we can

study cubes that contain significant emission across most of the field of view all the way to almost pure noise cubes.

The angular resolution of the 12m+7m+tp cube is 2.7'' and higher than that of the 7m and 7m+tp cubes at 7.2'', which correspond to a linear scales of 264 pc and 702 pc, respectively, at a distance of 20.2 Mpc. In order to compare the 12m+7m+tp results more directly with the other arrays, we convolve all cubes to a common 7.2'' resolution and focus on the 12m+7m+tp at 7.2'' resolution for most of the analysis. We note that the convolution from the native 12m resolution (2.7'') to the common best resolution (7.2'') might smear out some of the significant compact emission, and thus potentially reduce the efficiency of the stacking. However, we checked, in our case, that the recovered stacks from the native resolution cubes are consistent with the stacks from the convolved cubes.

We apply the spectral stacking method described in Sect. 2 to the five data cubes at different S/N levels described above. We stack the spectra by galactocentric radius from 0 to 9 kpc in 1 kpc increments as illustrated in Fig. 2. We note that there is very little emission (less than 20% of the pixels in the S/N/1 moment-0 map contain significant emission) outside of 6 kpc.

⁸ The original exercise in Leroy et al. (2021a) actually scales the signal down by factors of 3, 10, 30, 100.

Therefore, we limit most of the discussion to the inner 6 kpc and consider this the typical extent of the molecular gas disc. For the outer radii, an alternative approach could be to average over a larger region, for example binning everything beyond the radius of 6 kpc, in order to potentially recover more of the fainter emission at the cost of spatial information. However, in this case we do not recover more emission due to the steep drop in emission beyond 6 kpc. We use the S/N/1 data (i.e. the simulated data mimicking PHANGS–ALMA CO(2–1) observations) as a prior to account for the varying velocity field across the galaxy and to determine the channels of significant emission to compute the integrated intensities. For each configuration, the respective S/N/1 cube is used as a prior. This means that to stack the 12m+7m+tp cubes, we use the 12m+7m+tp S/N/1 cube as the prior; to stack the 7m+tp data, we use the 7m+tp S/N/1 cube, and so on. This approach is similar to how we typically handle real observational data, where different lines have been observed with the same interferometric set-up. In this case, by construction, the velocity fields of the different line cubes are identical. In reality, we may expect small velocity offsets between different spectral lines leading to slightly broader, and thus potentially less significant stacked lines, though this effect is expected to be small when studying various molecular lines, which should share similar kinematics. The stacked spectra are shown in the right panels of Fig. 2. Since in this case we know the true velocity distribution from the template cube, we repeat the same procedure using the true velocity field (Appendix A).

The resulting radial profiles of the stacked integrated intensities are shown in the bottom left panel of Fig. 2. Overall, we find that the radial trend is well recovered across most of the molecular disc down to the S/N/10 data cubes. In the S/N/30 cube we are still able to recover the radial trend out to 4 kpc, where, in the 3 to 4 kpc bin, the median moment-0 S/N is 0.54. For the noisiest data used here (S/N/100) we obtain only upper limits, which highlights that it is extremely challenging to map molecular discs of nearby galaxies in line emission that is ~ 100 times fainter than CO(2–1) (e.g. the popular Galactic dense gas tracer N_2H^+). PHANGS–ALMA integrated for ~ 1 min per field. This exercise implies that to achieve the S/N ~ 10 required for reliable stacked detections, integrations ~ 100 times longer, ~ 2 h per pointing, would be required. Another approach could be to modify the binning (e.g. by averaging spectra over larger regions). Although this could lose spatial information, and so was not performed here, this approach could potentially recover otherwise undetected emission. Therefore, we recommend adapting the binning parameters to the strength and distribution of the studied line emission. We note that NGC 3059 is a relatively low-luminosity galaxy, and the situation may be more optimistic in somewhat brighter targets.

We highlight the differences between the recovered stacks and the true values in Fig. 3. Based on the computed uncertainties of the stacked integrated intensities, σ_w , we clip at S/N (W/σ_w) levels of 3, 5, and 10. As expected, we find that with stronger σ_w -clipping the stacked line intensities show better agreement with the true values such that for data above 10σ the maximum discrepancy is $<35\%$, and $<15\%$ ($<8\%$) in the inner 6 kpc (4 kpc). We also systematically find values that are too low at larger radii (i.e. apparently significant measurements that do not agree within the uncertainties with the true values for $r_{\text{gal}} > 4$ kpc). This offset might be explained by the low fraction of spectra contributing to the stacks in these bins (see Table A.1). For the outer bins, $r_{\text{gal}} > 4$ kpc, less than half of the spectra inside each bin could be used for stacking, and as a result, we may potentially miss some emission hidden in the noise that we

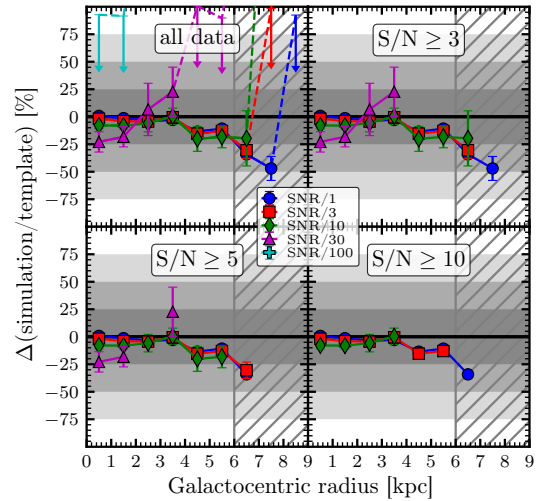


Fig. 3. Agreement between measured and expected radial trends at different sigma-clipping levels. Shown is the relative differences between the measured radial stacks from the simulated 12m+7m+tp cubes and the true stacks, as follows from the bottom left panel of Fig. 2, by subtracting the template trend. The difference between the different panels is that the data of the resulting stacks is clipped at 3, 5, or 10 S/N ($W\sigma_w$). The stacking procedure is always the same. The hatched area denotes the regime, where the prior S/N/1 is detected in less than 20% of the pixels.

are not able to recover. However, we find a very similar discrepancy if the velocity field is perfectly known (Fig. A.2), which suggests that the offset is at least partly arising from the imaging and not the stacking procedure. Nevertheless, we find, over all S/N cubes, an agreement between the significant stacked line intensities and the true values within 23% in bins where the prior is at least moderately ($\geq 36\%$ of the pixels) detected (i.e. within 6 kpc). These results demonstrate that the quality of the stacking results is linked to the significance of the prior used to align the velocity field and the imaging of the interferometric data.

3.1. Uncertainties

For interpreting the results, it is crucial to have a robust measure of the uncertainties and the resulting S/N in order to infer if a data point is significant or not. We measure the uncertainties of the stacked integrated intensities from the standard deviation in the emission-free channels following Eq. (3). Here we check whether this uncertainty matches the uncertainty obtained by propagating the noise measured in the cube.

To do so, we take the S/N/100 cube, which does not contain any significant spectra and consider it as a pure noise cube. We compute the rms in each pixel as the standard deviation across the corresponding pixel. Next, we bin the noise map in radial increments, analogous to radial stacking, and propagate the uncertainty to obtain the expected rms of the stacked spectrum in each bin. The propagated uncertainty is computed as the average rms in each bin corrected for the number of pixels by dividing by the square root of the number of pixels in that bin. Finally, the expected uncertainty is computed analogously to the measured uncertainty (Eq. (3)), but using the cube-propagated rms. We re-scale the cube-propagated rms to the respective noise cubes by multiplying by the respective noise level factors, and plot the measured against the expected uncertainties for all S/N

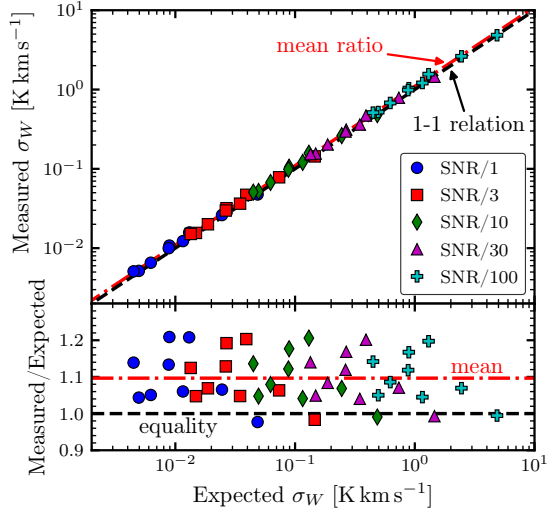


Fig. 4. Measured vs expected uncertainties. *Top:* Comparison between measured (12m+7m+tp) and expected uncertainties of the integrated stacks. The measured uncertainty is obtained from the emission free channel of the stacked spectra following Eq. (3). The expected uncertainty is inferred via Gaussian error propagation from the S/N/100 cube treated as a noise cube. *Bottom:* Ratio of the measured to the expected uncertainties.

cubes (Fig. 4). In the Appendix we also show the resulting S/N of the stacks (i.e. W/σ_W) and compare the measured and expected S/N (Fig. A.1).

We find that the measured uncertainties are strongly correlated with the expected uncertainties, but slightly biased by $\sim 10\%$ on average and little scatter within $\pm 10\%$. The slightly too large measured uncertainties could arise from some emission remaining in the assumed emission-free channels after masking, which contributes to the rms estimation. These results demonstrate that we measure trustworthy statistical uncertainties on the stacked integrated intensities.

3.2. Array configurations

Interferometric observations filter out the extended emission of the source if not combined with single-dish data. Using the simulated observations, we can study how well interferometric data alone can recover line emission in radial bins, and so test whether total power data are needed to obtain accurate stacking results. We repeat the above-described spectral stacking method using data obtained from combining different telescope array configurations: 7m+tp (the ACA including total power data), 12+7 m (the main array and ACA 7 m antennas), 12 m (the main array alone), and 7 m (the ACA 7 m data alone) (see Leroy et al. 2021a, for more information).

Figure 5 presents the radially stacked line intensities from the above-listed configurations relative to the template values. The 12m+7m+tp configuration should recover all spatial scales and can be considered the benchmark for the other configurations. We find that the 7m+tp data performs similarly to the 12m+7m+tp, though with a significantly larger scatter, which is expected due to the lower sensitivity. For the pure interferometric data (i.e. 12+7m, 12 m, and 7 m), we systematically find stacked

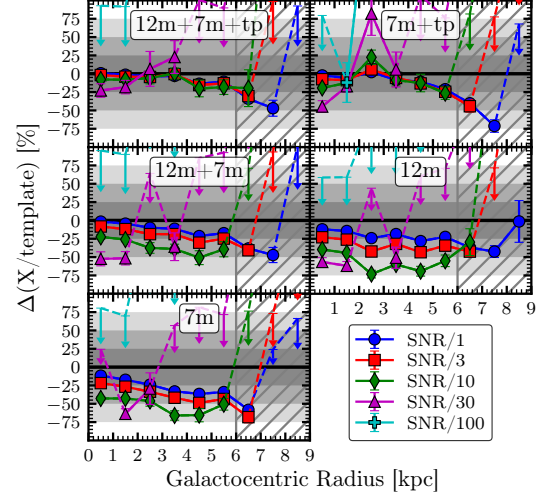


Fig. 5. Flux recovery using different array configurations. Comparison between radial stacking obtained from different array configurations ($X = \{12m + 7m + tp, 7m + tp, 12m + 7m, 12m, 7m\}$), as indicated in the top of each panel. Shown is the ratio between the radial stacks obtained from the simulated data cubes at the given combination of telescope arrays and the true template values against the galactocentric radius. Solid points show data above 3σ and downward pointing arrows denote 3σ upper limits. The hatched area denotes the regime, where the prior, i.e. S/N/1, is detected in less than 20% of the pixels.

line intensities that are too low at all radii, especially when considering 7 m only, where we miss 10–20% across all bins even for the S/N/1 data. Most interestingly, we find a trend with S/N: the lower the S/N of the cube, the larger the bias of the stacks. In the most extreme case (i.e. 7 m S/N/10) the radial profile is detected out to 6 kpc, but yields 30–50% lower line intensities, than obtained with the 12m+7m+tp configuration. These results are in line with the conclusions about the spatial filtering of interferometric data drawn in Leroy et al. (2021a) and enforce the need for total power observations in order to cover the flux information from small spatial scales.

3.3. Weighted stacking

The benefit of the above-described methodology is the potential recovery of faint emission while conserving the flux in each bin. However, the drawback is that we might stack a few highly significant spectra with many noisy spectra, eventually leading to non-detection in the stacked spectra. To overcome this, we can go beyond the ‘equal weight per spectrum’ stacking described above, and weigh the spectra such that we obtain statistically more significant stacked spectra⁹. We compute the weighted stacks by multiplying the spectra ($T_{n,i}(v)$) with the associated weights (w_i) within each bin n . Then, we sum up the weighted spectra and divide them with the sum of the weights:

$$T_{n,\text{stack}}(v) = \frac{\sum_{i=0}^{N_{\text{det}}} T_{n,i}(v) \cdot w_i}{\sum_{i=0}^{N_{\text{det}}} w_i}. \quad (4)$$

⁹ Though keep in mind that this weighted stacking scheme is in general not flux-conserving as opposed to the unweighted stacking introduced before.

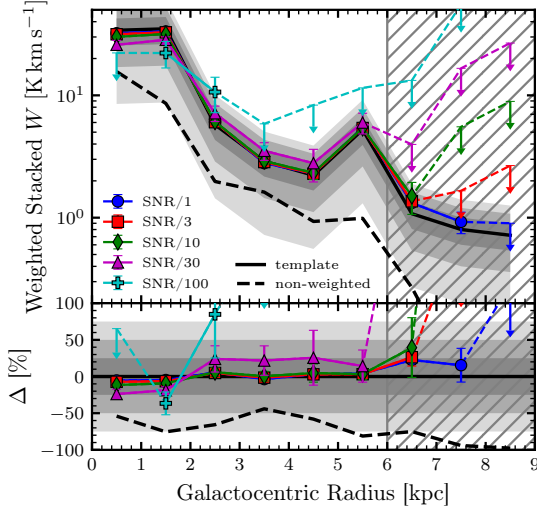


Fig. 6. Intensity-weighted stacking. *Top*: radial stacking similar to Fig. 2, but using the intensity of the prior, i.e. the “S/N/1” integrated intensities, as a weight following Eq. (4). The black solid line shows the template, i.e. the true, radial profile, where the template line intensities are used as the weight. The black dashed line shows the non-weighted radial trend of the template stacking also shown in Fig. 2. *Bottom*: deviation, in per cent, of the stacked radial trend from the template profile. The hatched area denotes the regime, where the prior, i.e. S/N/1, is detected in less than 20% of the pixels.

A useful weighting quantity could be the S/N or the line intensity of the prior. Here we showcase the latter, adopting an intensity-weighted stacking. Thus, we obtain the radial trend of the prior-bright (e.g. CO-bright) regions. We applied the intensity-weighted stacking to the above-introduced simulated observations analogous to the non-weighted stacking. The radial stacking results are presented in Fig. 6. We find that the stacked line intensities of the simulated cubes, excluding S/N/100, are consistent within 20% with the true (weighted) trend. In comparison with the unweighted stacking (Figs. 2 and 3), we find better agreement and no negative bias at low detection fraction of the prior. Thus, weighted stacking can indeed recover faint emission at larger galactocentric radii. However, we note that weighted stacking does not conserve flux and must be interpreted with care, in particular when comparing to stacks derived with another (e.g. non-weighted) method. Moreover, since, by construction, the intensity-weighted stacking used here is computing the weighted average stack over the detected pixels only (i.e. N_{det}), the measured upper limits in the outer bins are much larger than what is obtained in the unweighted case.

3.4. Stacking versus averaging integrated intensities

Instead of averaging stacked spectra, it can be more convenient to average the integrated intensities within the same region or bin. With this approach, typically referred to as binning, the main distinction to the stacking method is that we do not align the velocity field using a prior. Instead, we take advantage of the prior to create velocity masks for each individual spectrum (i.e. for each line of sight), which defines the velocity range over which each spectrum is integrated. The result is an integrated intensity (moment-0) map using a prior inferred velocity (field)

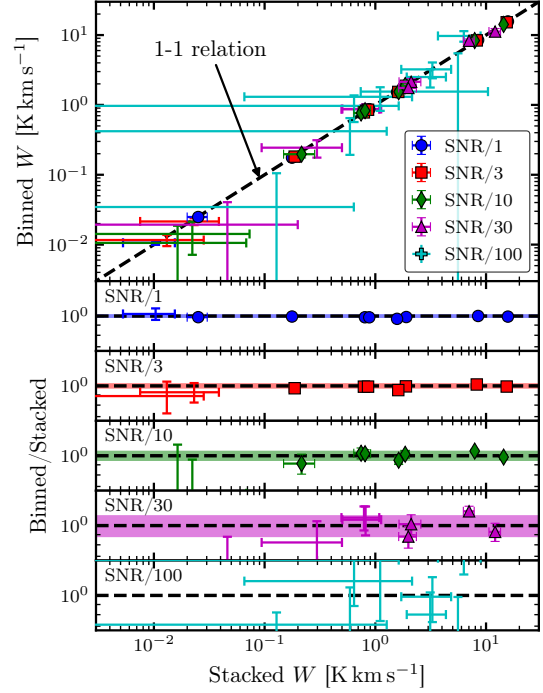


Fig. 7. Binning vs stacking. *Top*: Binned means vs stacked integrated intensities in matched radial bins. The dashed line marks the 1-to-1 relation. Different markers indicate the values recovered from the different S/N cubes. Data above $3\sigma_W$ are shown as markers, else only the error bars are plotted. *Bottom panels*: Ratio of binned mean and stacks to the stacked integrated intensities, separately for each S/N/X cube ($X = 1, 3, 10, 30$). The shaded areas indicate the respective 1σ scatter of the $3\sigma_W$ data.

mask (see e.g. Gallagher et al. 2018b; Bešlić et al. 2021; den Brok et al. 2022; Neumann et al. 2023, for details about the masking process). Afterwards, we average the integrated intensities inside a given bin.

We apply the above averaging approach to the 12m+7m+tp data sets at different noise levels using the same radial bins, and compare the resulting average line intensities with the stacked line intensities computed as in Sect. 2. We find that the two approaches lead to very similar average line intensities inside a given bin, without bias and small scatter of {1, 2, 5, 10}% considering the significant measurements ($S/N \geq 3$) of the S/N/1, 3, 10, and 30 cubes (Fig. 7). In agreement with Gallagher et al. (2018a), we conclude that spectral stacking and averaging masked moment-0 maps yield the same results within 10%. However, we note that spectral stacking still offers the great advantage of also recovering mean line shape, and thus mean kinematic information, which cannot be obtained from the averaged integrated intensities.

4. Conclusions

We performed spectral stacking of simulated interferometric data of the galaxy NGC 3059 as a function of galactocentric radius at different noise levels and combining different telescope arrays. Our main results are the following:

1. Spectral stacking is able to recover the integrated intensities across most of the molecular disc where the prior is predominantly detected. In the most extreme case we detect a stacked spectrum, even in bins where the integrated intensities of the moment-0 map have a median S/N of 0.54. For this specific galaxy, all data above 3σ and 10σ agrees within 23% and 15%, respectively, with the expected values if the prior is detected in at least 36% of the spectra contributing to the stack (i.e. within the inner 6 kpc).
2. Using interferometric data only (i.e. without total power information) can filter out up to 30% of the emission even at the typical PHANGS–ALMA sensitivity and even if the prior is predominantly significant. Even more extreme, for lines that are 10 times (e.g. HCN(1–0)), the 12m-only or 7m-only configurations miss $\sim 50\%$ of the emission in the stacked spectra throughout the full molecular gas disc.
3. The critical limitation of the spectral stacking method is connected to the quality of the prior used to align the velocity field and potentially the imaging procedure. If the prior is not detected across most of the bin, we expect to systematically find stacked line intensities that are too low. This might be improved by using low-resolution priors (e.g. H I 21 cm line) or model priors, which provide a completely defined velocity field. However, we show that the discrepancy can also arise from the imaging of the interferometric data (e.g. if the deconvolution is not able to extract faint emission).

This provides a concrete proof of concept that the stacking method works using combined interferometric and total power data on extended sources. A key result of this analysis is that, at the typical PHANGS–ALMA set-up, the spectral stacking method is able to recover the average integrated intensities within $\sim 23\%$ accuracy, if the prior is detected in at least $\sim 36\%$ of the bin's spectra. We also show that the noise estimated from the line-free parts of the stacked spectra captures the uncertainties of the line intensities with little bias (on average 10% biased high) such that 3σ data can confidently be considered significant detection.

Acknowledgements. We would like to thank the anonymous referee for their insightful comments that helped improve the quality of the paper. L.N. acknowledges funding from the Deutsche Forschungsgemeinschaft (DFG, German Research Foundation) – 516405419. AKL gratefully acknowledges support by grants 1653300 and 2205628 from the National Science Foundation, by award JWST-GO-02107.009-A, and by a Humboldt Research Award from the Alexander von Humboldt Foundation. CE acknowledges funding from the Deutsche Forschungsgemeinschaft (DFG) Sachbeihilfe, grant number BI1546/3-1. J.P. acknowledges support from the Programme National “Physique et Chimie du Milieu Interstellaire” (PCMI) of CNRS/INSU with INC/INP co-funded by CEA and CNES. E.R. acknowledges the support of the Natural Sciences and Engineering Research Council of Canada (NSERC), funding reference number RGPIN-2022-03499. E.S. acknowledges funding from the European Research Council (ERC) under the European Union's Horizon 2020 research and innovation programme (grant agreement no. 694343).

References

- Bešlić, I., Barnes, A. T., Bigiel, F., et al. 2021, *MNRAS*, **506**, 963
 Bigiel, F., Leroy, A. K., Jiménez-Donaire, M. J., et al. 2016, *ApJ*, **822**, L26
 Cady, F. M., & Bates, R. H. T. 1980, *Opt. Lett.*, **5**, 438
 Caldu-Primo, A., Schrubba, A., Walter, F., et al. 2013, *AJ*, **146**, 150
 CASA Team (Bean, B., et al.) 2022, *PASP*, **134**, 114501
 Chen, C.-T. J., Hickox, R. C., Albers, S., et al. 2013, *ApJ*, **773**, 3
 Delhaize, J., Meyer, M. J., Staveley-Smith, L., & Boyle, B. J. 2013, *MNRAS*, **433**, 1398
 den Brok, J. S., Chatzigiannakis, D., Bigiel, F., et al. 2021, *MNRAS*, **504**, 3221
 den Brok, J. S., Bigiel, F., Sliwa, K., et al. 2022, *A&A*, **662**, A89
 Gallagher, M. J., Leroy, A. K., Bigiel, F., et al. 2018a, *ApJ*, **868**, L38
 Gallagher, M. J., Leroy, A. K., Bigiel, F., et al. 2018b, *ApJ*, **858**, 90
 Hickox, R. C., Jones, C., Forman, W. R., et al. 2007, *ApJ*, **671**, 1365
 Jiménez-Donaire, M. J., Bigiel, F., Leroy, A. K., et al. 2017, *MNRAS*, **466**, 49
 Jiménez-Donaire, M. J., Bigiel, F., Leroy, A. K., et al. 2019, *ApJ*, **880**, 127
 Jolly, J.-B., Knudsen, K. K., & Stanley, F. 2020, *MNRAS*, **499**, 3992
 Karim, A., Schinnerer, E., Martínez-Sansigre, A., et al. 2011, *ApJ*, **730**, 61
 Knudsen, K. K., van der Werf, P., Franx, M., et al. 2005, *ApJ*, **632**, L9
 Koch, E., Rosolowsky, E., & Leroy, A. K. 2018, *RNAAS*, **2**, 220
 Leroy, A. K., Hughes, A., Liu, D., et al. 2021a, *ApJS*, **255**, 19
 Leroy, A. K., Schinnerer, E., Hughes, A., et al. 2021b, *ApJS*, **257**, 43
 Lindroos, L., Knudsen, K. K., Fan, L., et al. 2016, *MNRAS*, **462**, 1192
 Neumann, L., Gallagher, M. J., Bigiel, F., et al. 2023, *MNRAS*, **521**, 3348
 Schrubba, A., Leroy, A. K., Walter, F., et al. 2011, *AJ*, **142**, 37
 Usero, A., Leroy, A. K., Walter, F., et al. 2015, *AJ*, **150**, 115
 van der Hulst, J. M., Terlouw, J. P., Begeman, K. G., Zwitter, W., & Roelfsema, P. R. 1992, in *Astronomical Data Analysis Software and Systems I*, ed. D. M. Worrall, C. Biemesderfer, & J. Barnes, *Astronomical Society of the Pacific Conference Series*, **25**, 131

Appendix A: Additional material

Table A.1 lists the detection fraction of the prior $F_{\text{det}} = N_{\text{det}}/N_{\text{tot}}$ in each radial bin, where N_{det} is the number of prior-detected pixels and N_{tot} is the total number of pixels in that bin. In Fig. A.1, we compare the S/N measured from the stacked spectra and the expected S/N that is inferred from the S/N/100 cube considered as a pure noise cube as described in Sect. 3.1. In Fig. A.2, we show the spectral stacking as a function of galactocentric radius similar to Sect. 3 but using the template data cube as prior instead of the S/N/1 cube. In this case we have perfect alignment of the velocity field, and are not limited by the significance of the prior. In Fig. A.3, we show the radial trend obtained by taking the average spectrum over the prior-detected spectra only (i.e. by dividing the summed spectra by N_{det} instead of N_{tot} ; Section 2).

Table A.1. Prior detection fraction per radial bin.

r_{gal} [kpc] (1)	N_{tot} (2)	N_{det} (3)	F_{det} [%] (4)
0 – 1	23	22	95.7
1 – 2	72	61	84.7
2 – 3	128	79	61.7
3 – 4	176	131	74.4
4 – 5	230	107	46.5
5 – 6	278	101	36.3
6 – 7	328	54	16.5
7 – 8	372	11	3.0
8 – 9	322	6	1.9

Notes. (1) Radial bins, as illustrated in Fig. 2. (2) Total number of spectra, i.e. pixels in moment-0 map, inside the respective bin. (3) Number of spectra, where the prior, i.e. “S/N/1”, has been detected thus allowing velocity shuffling and spectral stacking. (4) Fraction of spectra used for stacking.

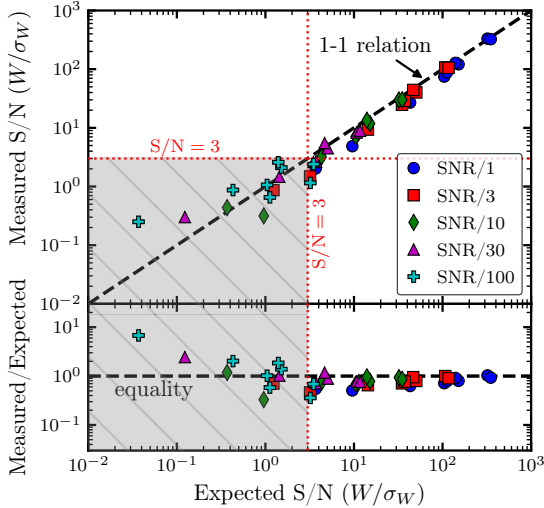


Fig. A.1. Measured vs expected signal-to-noise ratio. *Top:* Comparison between measured (12m+7m+tp) and expected signal-to-noise ratio of the integrated stacks. *Bottom:* Ratio of the measured to the expected S/N against the expected uncertainties.

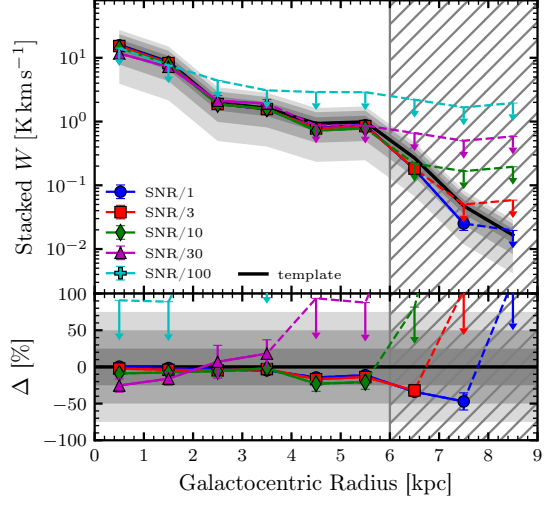


Fig. A.2. Template velocity field. Radial stacking similar to Fig. 2, but using the template (i.e. the true intensity distribution) as prior to aligning the velocity field.

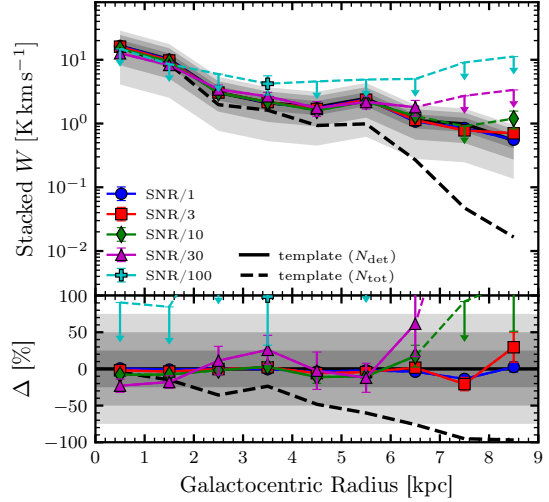


Fig. A.3. Average spectrum over prior-detected pixels. Radial stacking similar to Fig. 2, but computing the average over the prior-detected spectra only, as given by Eq. A.1.

Equation 2 then changes to

$$T_{n,\text{stack}}(v) = \frac{1}{N_{\text{det}}(n)} \sum_{i=0}^{N_{\text{det}}(n)} T_{n,i}(v). \quad (\text{A.1})$$

We find that the recovered stacks, computed from the prior-detected pixels, agree very well and without significant bias with the expected values measured in the prior-detected pixels (indicated by the solid line in Fig. A.3). However, using this method does not recover the true mean radial trend (dashed line), but, by construction, only considers the pixels, where the prior is detected, and is thus biased high, especially at radii where the prior detection fraction is low.

ALMOND paper

The paper Neumann et al. 2023, MNRAS, 521, 3348, 36 pp. (DOI: [10.1093/mnras/stad424](https://doi.org/10.1093/mnras/stad424)) is reproduced below in its original form with permission by the Royal Astronomical Society.

The ALMOND Survey: Molecular cloud properties and gas density tracers across 25 nearby spiral galaxies with ALMA

Lukas Neumann,¹★ Molly J. Gallagher,² Frank Bigiel,¹ Adam K. Leroy,² Ashley T. Barnes,^{1,3} Antonio Usero,⁴ Jakob S. den Brok,^{1,5} Francesco Belfiore,⁶ Ivana Bešlić,¹ Yixian Cao,⁷ Mélanie Chevance,^{8,9} Daniel A. Dale,¹⁰ Cosima Eibensteiner,¹ Simon C. O. Glover,⁸ Kathryn Grasha,^{11,12} Jonathan D. Henshaw,^{13,14} María J. Jiménez-Donaire,^{4,15} Ralf S. Klessen,^{8,16} J. M. Diederik Kruijssen,⁹ Daizhong Liu,⁷ Sharon Meidt,¹⁷ Jérôme Pety,^{18,19} Johannes Puschig,¹ Miguel Querejeta,⁴ Erik Rosolowsky,²⁰ Eva Schinnerer,¹³ Andreas Schruba,⁷ Mattia C. Sormani,⁸ Jiayi Sun,^{2,21,22} Yu-Hsuan Teng,²³ and Thomas G. Williams^{11,24}

¹Argelander-Institut für Astronomie, Universität Bonn, Auf dem Hügel 71, 53121 Bonn, Germany

²Department of Astronomy, The Ohio State University, 4055 McPherson Laboratory, 140 West 18th Ave, Columbus, OH 43210, USA

³European Southern Observatory, Karl-Schwarzschild Straße 2, D-85748 Garching bei München, Germany

⁴Observatorio Astronómico Nacional (IGN), C/Alfonso XII, 3, E-28014 Madrid, Spain

⁵Center for Astrophysics | Harvard & Smithsonian, 60 Garden St., 02138 Cambridge, MA, USA

⁶INAF — Osservatorio Astrofisico di Arcetri, Largo E. Fermi 5, I-50125, Florence, Italy

⁷Max-Planck-Institut für Extraterrestrische Physik (MPE), Giessenbachstr. 1, D-85748 Garching, Germany

⁸Universität Heidelberg, Zentrum für Astronomie, Institut für theoretische Astrophysik, Albert-Ueberle-Straße 2, 69120, Heidelberg, Germany

⁹Cosmic Origins Of Life (COOL) Research DAO, coolresearch.io

¹⁰Department of Physics & Astronomy, University of Wyoming, Laramie, WY, 82071, USA

¹¹Research School of Astronomy and Astrophysics, Australian National University, Canberra, ACT 2611, Australia

¹²ARC Centre of Excellence for All Sky Astrophysics in 3 Dimensions (ASTRO 3D), Australia

¹³Max Planck Institute for Astronomy, Königstuhl 17, D-69117 Heidelberg, Germany

¹⁴Astrophysics Research Institute, Liverpool John Moores University, 146 Brownlow Hill, Liverpool L3 5RF, UK

¹⁵Centro de Desarrollos Tecnológicos, Observatorio de Yebes (IGN), 19141 Yebes, Guadalajara, Spain

¹⁶Universität Heidelberg, Interdisziplinäres Zentrum für Wissenschaftliches Rechnen, Im Neuenheimer Feld 205, 69120 Heidelberg, Germany

¹⁷Sterrenkundig Observatorium, Universiteit Gent, Krijgslaan 281 S9, B-9000 Gent, Belgium

¹⁸Institut de Radioastronomie Millimétrique (IRAM), 300 Rue de la Piscine, F-38406 Saint Martin d'Hères, France

¹⁹LERMA, Observatoire de Paris, PSL Research University, CNRS, Sorbonne Universités, 75014 Paris, France

²⁰Dept. of Physics, University of Alberta, Edmonton, Alberta, Canada T6G 2E1

²¹Department of Physics and Astronomy, McMaster University, 1280 Main Street West, Hamilton, ON L8S 4M1, Canada

²²Canadian Institute for Theoretical Astrophysics (CITA), University of Toronto, 60 St George Street, Toronto, ON M5S 3H8, Canada

²³Center for Astrophysics and Space Sciences, Department of Physics, University of California San Diego, 9500 Gilman Drive, La Jolla, CA 92093, USA

²⁴Sub-department of Astrophysics, Department of Physics, University of Oxford, Keble Road, Oxford OX1 3RH, UK

Accepted XXX. Received YYY; in original form ZZZ

ABSTRACT

We use new HCN(1–0) data from the ALMOND (ACA Large-sample Mapping Of Nearby galaxies in Dense gas) survey to trace the kpc-scale molecular gas density structure and CO(2–1) data from PHANGS-ALMA to trace the bulk molecular gas across 25 nearby, star-forming galaxies. At 2.1 kpc scale, we measure the density-sensitive HCN/CO line ratio and the SFR/HCN ratio to trace the star formation efficiency in the denser molecular medium. At 150 pc scale, we measure structural and dynamical properties of the molecular gas via CO(2–1) line emission, which is linked to the lower resolution data using an intensity-weighted averaging method. We find positive correlations (negative) of HCN/CO (SFR/HCN) with the surface density, the velocity dispersion and the internal turbulent pressure of the molecular gas. These observed correlations agree with expected trends from turbulent models of star formation, which consider a single free-fall time gravitational collapse. Our results show that the kpc-scale HCN/CO line ratio is a powerful tool to trace the 150 pc scale average density distribution of the molecular clouds. Lastly, we find systematic variations of the SFR/HCN ratio with cloud-scale molecular gas properties, which are incompatible with a universal star formation efficiency. Overall, these findings show that mean molecular gas density, molecular cloud properties and star formation are closely linked in a coherent way, and observations of density-sensitive molecular gas tracers are a useful tool to analyse these variations, linking molecular gas physics to stellar output across galaxy discs.

Key words: galaxies:ISM – galaxies:star formation – ISM:clouds – ISM:molecules – ISM:structure – radio lines:ISM

2 *L. Neumann et al.*

1 INTRODUCTION

Star formation is at the heart of many astrophysical processes ranging from planet formation to the evolution of whole galaxies. Yet, the details of the star-forming process are far from being well understood. We know from observations inside the Milky Way (MW) and of other galaxies that the star formation rate (SFR) per unit area is tightly correlated to the gas surface density (e.g. Schmidt 1959; Kennicutt 1998; Bigiel et al. 2008; Schrubba et al. 2011; Leroy et al. 2013). In more detail, observations of Milky Way star-forming regions show that stars form specifically within the densest parts of molecular clouds (MCs) and that the SFR of individual clouds correlates with the mass of dense gas¹ (M_{dense}) as traced by dust emission (e.g. Lada & Lada 2003; Kainulainen et al. 2009; André et al. 2014) or emission of high excitation density lines (e.g. Wu et al. 2005, 2010; Stephens et al. 2016). In a landmark paper, Gao & Solomon (2004) used HCN emission to trace M_{dense} from a large sample of external galaxies and found a linear relation between SFR and M_{dense} . Following up, Wu et al. (2005) studied HCN emission in local molecular clouds confirming the linear SFR- M_{dense} relation which, combining MC and integrated whole galaxy observations, spans 10 dex. These studies suggest that the star formation efficiency of dense gas ($\text{SFE}_{\text{dense}} \equiv \text{SFR}/M_{\text{dense}}$) may be constant across this wide range of scales and environments.

However, the works by Usero et al. (2015), Bigiel et al. (2016), Gallagher et al. (2018a), Jiménez-Donaire et al. (2019) and Bemis & Wilson (2019) on kpc-scale spectroscopic measurements find systematic variations of the HCN/CO line ratio and the SFR/HCN ratio with kpc-scale environmental properties, e.g. the molecular gas surface density or the stellar mass surface density. In addition, observations of the Milky Way's Central Molecular Zone (CMZ) show that the star formation efficiency of dense gas is much lower than is seen in the rest of the Galaxy (see e.g. Longmore et al. 2013; Barnes et al. 2017). This apparent underproduction of stars follows naturally if the critical density of star formation is environmentally dependent, as predicted by turbulent star formation theories (e.g. Kruijssen et al. 2014). One persistent question about these results is how HCN/CO or similar ratios (e.g. HCO⁺/CO, CS/CO) trace density variations quantitatively in different environments when observed in other galaxies. In an attempt to address this, Gallagher et al. (2018b) took a novel step comparing the kpc-scale spectroscopic measurements with the ~ 100 pc-scale molecular gas surface density in their five galaxies sample. They found systematic variations of the HCN/CO line ratio, a proxy for the fraction of dense molecular gas, as a function of the molecular gas surface density. This approach directly connects our two major methods of assessing density and gas properties in extragalactic systems: high resolution spectroscopic CO imaging and multi-species (HCN, HCO⁺, CS) spectroscopy.

Combining multi-species spectroscopy with high resolution imaging has applications beyond only constraining density estimates. Turbulent theories of star formation predict that molecular cloud properties such as mean density, velocity dispersion or magnetic fields influence the density structure of the clouds, which regulates their ability to emit HCN (e.g. Krumholz & McKee 2005; Padoan & Nordlund 2011; Hennebelle & Chabrier 2011; Federrath & Klessen 2012; Padoan et al. 2014). Moreover, these same parameters also regulate the $\text{SFE}_{\text{dense}}$ of the clouds, thus providing a first order explanation

of the observed correlations between the HCN/CO and SFR/HCN ratios and molecular cloud properties.

Until very recently, the exploration of such potential correlations was limited because high-resolution (~ 100 pc) CO imaging of the full molecular gas disc of galaxies has been almost as rare as kpc-scale and full-disc spectroscopy (see e.g. Wong & Blitz 2002; Leroy et al. 2009 for kpc CO mapping, and e.g. Usero et al. 2015; Jiménez-Donaire et al. 2019 for kpc HCN mapping). This situation was recently directly addressed in the Physics at High Angular resolution in Nearby Galaxies project (PHANGS²), which uses the Atacama Large Millimeter/submillimeter Array (ALMA) to observe the molecular gas via the CO(2–1) line at $\sim 1''$ to $2''$ resolution in 90 nearby ($d < 25$ Mpc) galaxies (PHANGS-ALMA; Leroy et al. 2021c). This survey allows access to the molecular gas distribution at ~ 100 pc physical scales, which is close to the size of individual giant molecular clouds (GMCs). By combining PHANGS-ALMA with spectral mapping of dense gas tracers like HCN(1–0), we can explore the molecular cloud properties in the extragalactic regime and compare it to the kpc-scale dense gas spectroscopy. This technique bypasses the lack of extragalactic cloud-scale dense gas observations that are currently only available for a few galaxies (M51, Querejeta et al. 2019 and NGC 3627, Bešlić et al. 2021).

Tracing dense gas associated with star formation is challenging at extragalactic distances because tracers of dense gas that are currently popular in Galactic studies, e.g. N₂H⁺ (see e.g. Pety et al. 2017; Kauffmann et al. 2017; Barnes et al. 2020), are too faint to be mapped at kpc scales across the discs of external galaxies with current instrumentation within reasonable time. Still, we can gain a lot of information about the dense gas by focusing on the brightest higher-critical density lines, i.e. HCN(1–0) or HCO⁺(1–0). The primary method to measure dense gas is based on the observation of various molecular emission lines with a range of effective critical densities (n_{eff} ; see e.g. Leroy et al. 2017a; Gallagher et al. 2018a). To first order, the intensity of a line reflects the total gas mass above n_{eff} , though see discussion in Shirley (2015) and Mangum & Shirley (2015). Therefore, the ratio of two lines with different critical densities reflects the ratio of gas masses above the two critical densities. For example, comparison between CO and HCN line emission yields an approximate gauge of the dense gas fraction (e.g. see Usero et al. 2015; Bigiel et al. 2016 and reference therein), as the latter requires a significantly larger density for excitation.³

Accordingly, in this paper we combine a large new HCN (along with HCO⁺ and CS) data set with PHANGS-ALMA CO observations and use the HCN(1–0)/CO(2–1) ratio to trace the fraction of dense gas. Because the targets were picked to overlap PHANGS-ALMA, we have cloud-scale gas properties, as well as IR- and UV-based SFR estimates across the whole sample. We explore the correlations of several cloud-scale structural and dynamical gas properties with both the HCN/CO ratio, a proxy for the dense gas fraction (f_{dense}), and the SFR/HCN ratio, a proxy for the dense gas star formation efficiency ($\text{SFE}_{\text{dense}}$), across a sample of 25 galaxies. This builds on the study of Gallagher et al. (2018b), who used a subset of these data (five galaxies) and considered only HCN/CO and cloud-scale molecular gas surface density (Σ_{mol}), as well as on the works of Leroy et al. (2017b) and Utomo et al. (2018), who compared CO-based cloud properties to the star formation efficiency in the bulk

¹ Here, the term "dense gas" refers to a density $n_{\text{H}_2} \gtrsim 10^4 \text{ cm}^{-3}$ and is primarily used to distinguish it from the lower-density molecular gas traced by low-J CO.

² <http://phangs.org>

³ $n_{\text{eff}}(\text{HCN}(1-0)) \approx 2 \times 10^4 \text{ cm}^{-3}$ to $2 \times 10^5 \text{ cm}^{-3}$, $n_{\text{eff}}(\text{CO}(2-1)) \approx 1 \times 10^3 \text{ cm}^{-3}$ (Shirley 2015; Mangum & Shirley 2015; Leroy et al. 2017a; Onus et al. 2018).

molecular medium traced by CO emission (SFE_{mol}). We compare the kpc-scale HCN/CO and SFR/HCN to the cloud-scale molecular gas surface density (Σ_{mol}), the velocity dispersion (σ_{mol}), the virial parameter (α_{vir}) and the internal turbulent pressure (P_{turb}) as defined in Section 4.3. We measure Σ_{mol} , σ_{mol} , α_{vir} and P_{turb} using CO(2–1) data from the PHANGS-ALMA survey, and we measure HCN/CO and SFR/HCN using HCN(1–0) data from new ALMA observations, called the ALMOND (ACA Large-sample Mapping Of Nearby galaxies in Dense Gas) survey. ALMOND uses the Morita Atacama Compact Array (ACA) to observe a sub-sample of 25 targets of the PHANGS-ALMA survey in dense molecular gas tracers like HCN(1–0), $\text{HCO}^+(1–0)$ or CS(2–1). Our goal is to characterise the impact of these cloud-scale gas properties on the amount and star-forming ability of the dense gas and its connection with local environment.

This paper is organised as follows. First, we lay out the concept that motivates the studied correlations based on turbulent cloud models in Section 2. Next, we describe our data products and methods in Section 3. In Section 5, we present the main results where we compare the dense gas to cloud-scale molecular gas properties. We further analyse the findings in Section 6 where we separately look at the galaxies’ centres. Finally, we summarise and discuss the results in Section 7.

2 EXPECTATIONS

2.1 Does HCN/CO trace dense gas fraction?

The goal of this section is to set a qualitative, first order expectation of the relations between molecular cloud properties and the $W_{\text{HCN}}/W_{\text{CO}(2-1)}$ ratio (hereafter HCN/CO) as well as the $\Sigma_{\text{SFR}}/W_{\text{HCN}}$ integrated intensity ratio (hereafter SFR/HCN). Using established models of star formation (e.g. Krumholz & McKee 2005, see Section 2.2), we model the probability distribution function (PDF) of the gas density of molecular clouds as a function of several cloud properties, i.e. the mean surface density n_0 , the Mach number \mathcal{M} and the virial parameter α_{vir} (in Section 4.3, we explain our best empirical estimates of these molecular cloud properties). Then, based on the density PDF, we infer qualitative changes of HCN/CO and SFR/HCN as a function of the molecular cloud properties. At the model level, we can infer the gas masses traced above certain density thresholds and thus estimate the dense gas fraction (f_{dense}) and formation efficiency ($\text{SFE}_{\text{dense}}$). Therefore, to infer HCN/CO and SFR/HCN from the models we assume that HCN(1–0) and CO(2–1) emission trace the gas mass above a certain effective critical density using a constant mass-to-light conversion factor. However, Galactic observations, albeit largely limited to selected local clouds or even sub-regions of these, (e.g. Pety et al. 2017; Kauffmann et al. 2017; Barnes et al. 2020; Evans et al. 2020) and simulations (e.g. Shirley 2015; Mangum & Shirley 2015; Leroy et al. 2017a; Onus et al. 2018; Jones et al. 2021) have clearly shown that reality is more complex. Rather than simply tracing gas above some fixed density threshold, HCN always traces a convolution of the density distribution and density-dependent emissivity, with additional complications offered by chemical abundance variations, variations in temperature, and possible excitation by collisions with electrons. Despite these concerns, the preponderance of evidence even in the studies above supports the use of the HCN/CO ratio as a tracer of the density distribution in a cloud, with higher HCN/CO reflecting denser gas.

Given these uncertainties, in our analysis, we focus on the observational quantities, i.e. HCN/CO and SFR/HCN, rather than the

less certain physical quantities, i.e. f_{dense} and $\text{SFE}_{\text{dense}}$. In this section laying out basic theoretical expectations, we adopt the simpler picture that HCN emission has a step-function dependence on density and emits with a fixed mass-to-light ratio, or conversion factor, above that density threshold. The purpose is not to derive quantitative predictions about line emissivities but instead to discuss how currently popular models predict the directions of observed correlations between cloud-scale molecular gas properties and dense gas spectroscopy.

We also note further alternative descriptions of the basic theoretical framework we adopt (e.g. Hennebelle & Chabrier 2011; Federrath & Klessen 2012) and refer the reader to those works for more quantitative discussion of turbulent cloud models.

2.2 Turbulent Cloud Models

In turbulent models of star formation (e.g. Padoan & Nordlund 2002; Krumholz & McKee 2005; Hennebelle & Chabrier 2011; Padoan & Nordlund 2011; Federrath & Klessen 2012, 2013; Padoan et al. 2014) the probability distribution function (PDF; $p(n)$) of the molecular gas number density, n , is to first order described by a log-normal function, which can be written as

$$p(s)ds = \frac{1}{\sqrt{2\pi\sigma_s^2}} \exp\left[-\frac{(s-s_0)^2}{2\sigma_s^2}\right] ds, \quad (1)$$

where $s = \ln(n/n_0)$ is the logarithmic number density in units of the mean number density, n_0 , and $s_0 = -\sigma_s^2/2$ is the centre of the PDF. Note, that gravitational collapse and star formation will introduce a power-law tail at high densities (see, e.g., Girichidis et al. 2014; Burkhardt 2018). This is particularly noticeable in the high-density gas of individual molecular clouds (e.g., Kainulainen et al. 2009; Schneider et al. 2015). However, we expect the contribution of the power-law tail to the overall mass budget of the multi-phase ISM to be negligible at the larger scales of ~ 150 pc and above (e.g. in entire gravitationally bound GMCs; e.g. (Klessen & Glover 2016)).

For isothermal turbulent flows, the width of the log-normal PDF is quantified by the rms Mach number $\mathcal{M} \equiv \sigma_{3D}/c_s$ (σ_{3D} is the three-dimensional velocity dispersion and c_s is the sound speed of the molecular gas), the turbulence driving parameter, b , and the gas to magnetic pressure ratio, β (see e.g. Padoan & Nordlund 2011; Molina et al. 2012):

$$\sigma_s^2 = \ln\left(1 + b^2 \mathcal{M}^2 \frac{\beta}{\beta + 1}\right). \quad (2)$$

The parameter b depends on the ratio of compressive vs. solenoidal modes and on the dimensionality of the flow. For isotropic turbulence in isothermal gas with a natural mix of both modes contributing equally, simple theoretical considerations lead to $b = 3/4$ in two and $b = 2/3$ in three dimensions (Federrath et al. 2008). Numerical simulations indicate somewhat smaller values (Federrath et al. 2010), however, with considerable scatter. We follow Padoan & Nordlund (2002), neglect magnetic fields ($\beta \rightarrow \infty$) and adopt $b \sim 0.5$ such that the width of the PDF becomes

$$\sigma_s^2 = \ln\left(1 + 0.25 \mathcal{M}^2\right). \quad (3)$$

The above formalism implies a link between the distribution of mass above any given density and the mean properties of molecular clouds, i.e. for varying mean density (n_0) or velocity dispersion (σ_{mol}) as is illustrated in Figure 1. Here, we adopt the prescription from Krumholz & McKee (2005) (hereafter KM theory) to compute

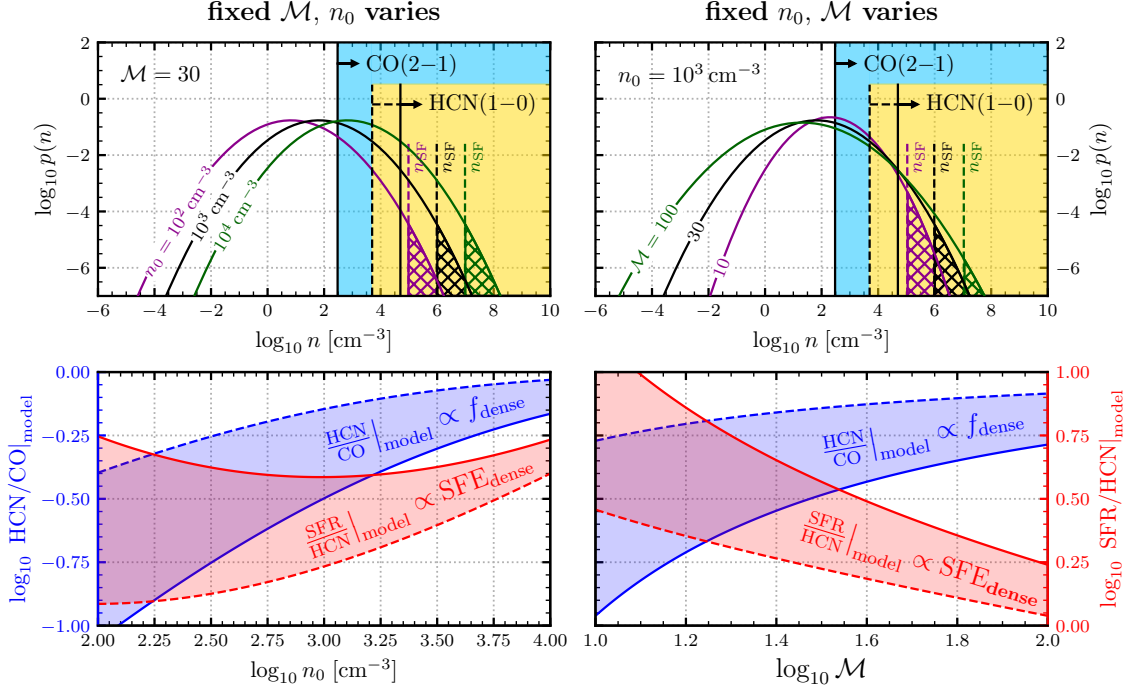
4 *L. Neumann et al.*


Figure 1. *Top:* Volume-weighted probability distribution functions (PDFs) of the molecular cloud gas density, n , for varying mean density (n_0 , left panel) and varying Mach number (\mathcal{M} , right panel). The light blue shaded area indicates the density regime traced by CO(2–1), i.e. all gas above $n_{\text{eff}}(\text{CO}) = 3 \times 10^2 \text{ cm}^{-3}$ (Leroy et al. 2017a). Analogously, the yellow shaded area is the density regime traced by HCN(1–0), where we adopted two effective critical densities such that in one case (solid line) HCN traces all gas above $n_{\text{eff}}(\text{HCN}) = 5 \times 10^4 \text{ cm}^{-3}$ (Leroy et al. 2017a) and in the other case (dashed line) HCN traces gas above $n_{\text{eff}}(\text{HCN}) = 5 \times 10^3 \text{ cm}^{-3}$ (Onus et al. 2018). The dashed lines labelled with n_{SF} show the threshold density above which gas in clouds collapses to form stars. Thus, the hatched areas are a measure of the SFR per free-fall time. *Bottom:* HCN/CO as a proxy for f_{dense} and SFR/HCN as a proxy for $\text{SFE}_{\text{dense}}$ estimated from the PDFs as a function of the mean density (left panel) and the Mach number (right panel) in accordance with the top panel plots. We compute HCN/CO as the ratio of the integrated mass-weighted PDFs within the assumed density regimes (Equation 6). Similarly, SFR/HCN is obtained by integrating the mass-weighted PDF above n_{SF} accounting for the free-fall time at mean density and dividing with the area of the PDF traced by HCN (Equation 7). The solid line and dashed lines are in accordance with the density thresholds in the top panels.

the density threshold n_{SF} above which gas is considered to collapse and form stars within a free-fall time:

$$\frac{n_{\text{SF}}}{n_0} = 0.82 \alpha_{\text{vir}} \mathcal{M}^2. \quad (4)$$

Assuming a fixed virial parameter $\alpha_{\text{vir}} \approx 1.3$ (Krumholz & McKee 2005), the above equation reads: $n_{\text{SF}}/n_0 \approx 1.07 \mathcal{M}^2$. Thus, for fixed virial parameter, the physical interpretation drawn from Equation (4) is that stars form in local overdensities of the molecular clouds determined by the density contrast n_{SF}/n_0 which shifts to higher overdensities if the turbulence (\mathcal{M}) of the molecular gas increases. Variations of the virial parameter are small (~ 0.7 dex; Sun et al. 2020b) compared to variations of the mean density (~ 3.4 dex) or the Mach number (~ 1.7 dex) of molecular clouds which justifies assuming a fixed α_{vir} to first order. However, variations of α_{vir} are still evident and might also manifest in the spectroscopic observations, e.g. by affecting n_{SF} . In this simplified model, α_{vir} does not affect the PDF and thus HCN/CO is unaffected by changes in α_{vir} . On the contrary, based on Equation 4, n_{SF} increases for increasing α_{vir} which would result in a negative correlation between SFR/HCN and α_{vir} . In practice, in this study, we infer the virial parameter from observations by assuming a fixed cloud scale, such that $\alpha_{\text{vir}} \propto \sigma_{\text{mol}}^2/\Sigma_{\text{mol}}$ (see

Section 4.3.3). In this case, α_{vir} is correlated with σ_{mol} (tracing \mathcal{M}) and Σ_{mol} (tracing n_0) making the effect of α_{vir} on HCN/CO and SFR/HCN more complex. Still, we can estimate how $\sigma_{\text{mol}}^2/\Sigma_{\text{mol}}$ tracing α_{vir} affects HCN/CO and SFR/HCN taking into account the distribution and thus the correlation of molecular cloud properties based on observations (see Sections 2.4 and 2.5 and Figure 2).

2.3 Line Emissivity

In an ideal case, we can detect molecular lines, such as HCN(1–0) or CO(2–1), if a substantial fraction of the gas is at densities close to or above the so-called “critical density” for emission. Considering the simplest case of only collisional (de)excitation (e.g. within dense molecular clouds), this critical density can be defined as the density at which the collisional de-excitation rate and spontaneous de-excitation are equal, and hence above this density line emission is enhanced. In general, the critical density of a certain line depends on the optical depth (τ) of the line and the kinetic temperature (T) of the gas (e.g. Tielens 2010; Draine 2011; Mangum & Shirley 2015; Shirley 2015; Klessen & Glover 2016). The concept of a critical density, above which all the line emission is associated with the gas mass above

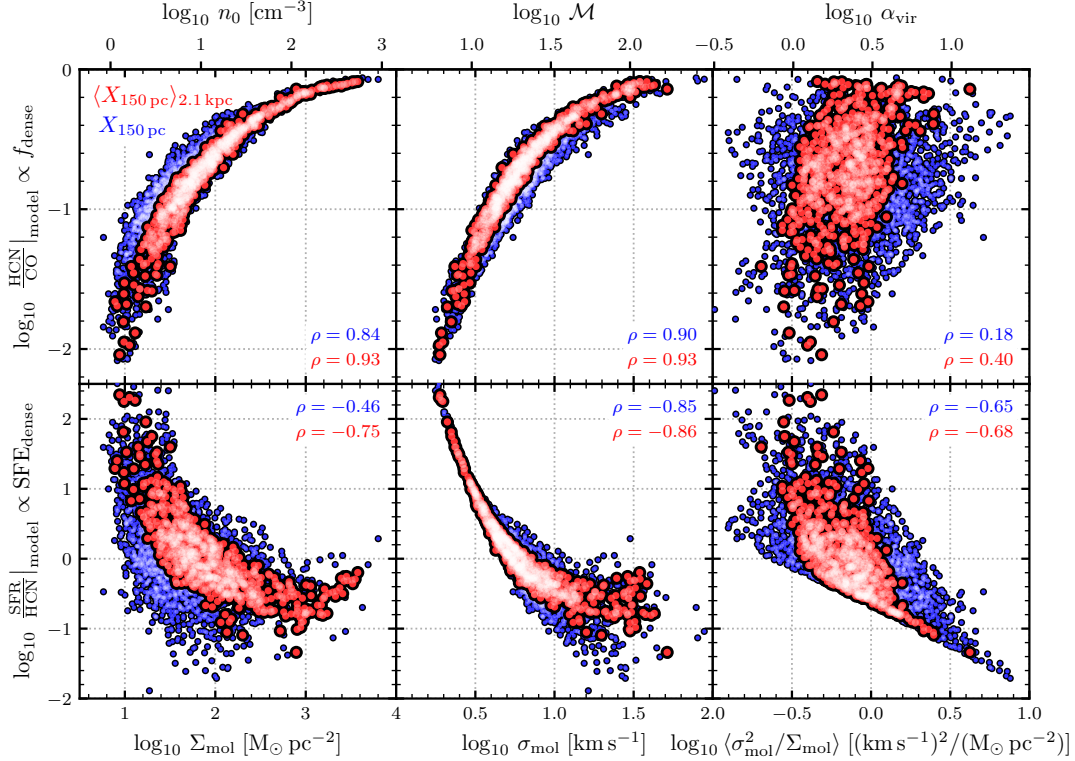


Figure 2. Model predictions of HCN/CO and SFR/HCN against the molecular cloud properties Σ_{mol} , σ_{mol} , α_{vir} (similar to Sun et al. 2018). HCN/CO and SFR/HCN are computed as in Equations 6 and 7 based on a log-normal PDF and assuming $n_{\text{eff}}(\text{HCN}) = 5 \times 10^3 \text{ cm}^{-3}$. The PDF parameters (n_0 , \mathcal{M} , α_{vir}) are inferred from the observed 150 pc molecular gas measurements (Σ_{mol} , σ_{mol} , $\alpha_{\text{vir}} \propto \sigma_{\text{mol}}^2 / \Sigma_{\text{mol}}$). The red data points depict the intensity-weighted averages of the 150 pc measurements (blue) at an averaging scale of 2.1 kpc (see Section 4.4 for more details). We show the Pearson correlation coefficient ρ for both the original data and the weighted averages.

that critical density, is, however, somewhat limited in lower density gas, as sub-thermal excitation effects (e.g. Pety et al. 2017) and additional excitation mechanisms can be significant (e.g. see Goldsmith & Kauffmann 2018). Nonetheless, to first order, we consider all gas above a respective critical density to be traced by the respective molecular line emission. We select the density threshold based on the emissivity-density curves derived by Leroy et al. (2017a) (their Figure 2). We define the threshold where their normalised emissivity (ϵ) exceeds 50 %, i.e. at $n_{\text{eff}}(\text{HCN}) = 5 \times 10^4 \text{ cm}^{-3}$ for HCN(1–0) and $n_{\text{eff}}(\text{CO}) = 3 \times 10^2 \text{ cm}^{-3}$ for CO(2–1) as illustrated in Figure 1 (left panels). The value of n_{eff} for HCN has, however, been the subject of some debate in the recent literature (e.g. Kauffmann et al. 2017; Barnes et al. 2020). For example, numerical simulations from Onus et al. (2018) and Jones et al. (2021) find that HCN(1–0) emission traces gas at densities of $n_{\text{eff}}(\text{HCN}) = 10^3 \text{ cm}^{-3}$ to 10^4 cm^{-3} , which is around an order of magnitude lower than reported by Leroy et al. (2017a). Note however, that Leroy et al. (2017a) uses a different definition of the effective critical density and that both results may be consistent with each other. Nevertheless, to account for some variation of n_{eff} , we adopt a second, lower critical density of

$n_{\text{eff}}(\text{HCN}) = 5 \times 10^3 \text{ cm}^{-3}$ (dashed line in Figure 1).⁴ We then use these density regimes to infer the gas mass traced by HCN(1–0) or CO(2–1) emission via integration of the mass-weighted PDF:

$$I_{\text{line}} \propto \int_{s_{\text{eff}}(\text{line})}^{\infty} \frac{n}{n_0} p(s) ds, \quad (5)$$

where $s_{\text{eff}}(\text{line})$ is the effective critical line density in units of $s = \ln(n/n_0)$ corresponding to $n_{\text{eff}}(\text{line})$. Note that this formalism does not consider radiative transfer modelling and therefore only gives reasonable HCN/CO estimates in terms of comparative analysis.

2.4 HCN/CO correlations

Turbulent cloud models predict the density distribution and star formation rate as a function of the molecular cloud properties. In the following, we adopt the description introduced in Section 2.2 and infer simplified line emissivities (Section 2.3). In Figure 1, we show

⁴ Note that we adopt a single critical density for CO emission, which could suffer from similar effects. Albeit given its already low critical density, which sits close to the density where molecular gas forms ($\sim 10^2 \text{ cm}^{-3}$), this effect should be less pronounced than with HCN.

6 *L. Neumann et al.*

how variations of molecular cloud properties affect the molecular gas density distribution, i.e. the PDF, and consequently the HCN/CO ratio.

At first, we keep the virial parameter fixed at $\alpha_{\text{vir}} = 1.3$ and vary the mean density for fixed Mach number and vice-versa. In Figure 1 (top left panel) we show how the cloud's PDF changes as a function of the mean density (n_0), keeping the Mach number fixed at $\mathcal{M} = 30$ which corresponds to $\sigma_{\text{mol}} \approx 5 \text{ km s}^{-1}$ assuming a sound speed of $c_s = 0.3 \text{ km s}^{-1}$ (at $T \sim 20 \text{ K}$; Krumholz & McKee 2005). We adopt typical molecular cloud densities, varying n_0 from 10^2 cm^{-3} to 10^4 cm^{-3} which results in a shift of the PDF to higher densities without changing the width of the PDF. We estimate the expected HCN/CO line ratio based on a simplified emissivity model and critical densities of HCN(1–0) and CO(2–1) discussed above (Section 2.3) by integrating the PDF over the density ranges of the respective lines:

$$\frac{\text{HCN}}{\text{CO}} \Big|_{\text{model}} = \frac{\int_{s_{\text{eff}}(\text{HCN})}^{\infty} \frac{n}{n_0} p(s) ds}{\int_{s_{\text{eff}}(\text{CO})}^{\infty} \frac{n}{n_0} p(s) ds}, \quad (6)$$

where the respective HCN and CO effective critical densities are $n_{\text{eff}}(\text{HCN}) = 5 \times 10^4 \text{ cm}^{-3}$ (Leroy et al. 2017a) or $n_{\text{eff}}(\text{HCN}) = 5 \times 10^3 \text{ cm}^{-3}$ (Onus et al. 2018) and $n_{\text{eff}}(\text{CO}) = 2 \times 10^3 \text{ cm}^{-3}$. This procedure computes the mass of gas which is traced by the different molecular lines, which serves as a first order estimate of the expected line intensities assuming a constant mass-to-light ratio. Note that equation (6) does not account for the different HCN(1–0) and CO(2–1) mass-to-light conversion factors. Thus we only claim to predict changes in HCN/CO. Moreover, we assume a fixed effective critical density of HCN(1–0) and that the emissivity of the lines below n_{eff} is zero. However, in reality, n_{eff} can vary and the emissivity below n_{eff} is not zero. Therefore, if the dense gas fraction is low, a significant fraction of the HCN emission could come from lower density gas. Thus, our toy model will predict a steeper correlation at low n_0 and low \mathcal{M} .

We find that the HCN/CO line ratio positively correlates with the mean density of the molecular cloud (see top right panel of Figure 1). The physical explanation is that at low mean densities $n_0 \sim 10^2 \text{ cm}^{-3}$ the CO(2–1) line is easily excited while only a small fraction of the cloud's gas is at densities high enough to produce HCN(1–0) emission producing a low HCN/CO line ratio. Increasing n_0 leads to an increasing fraction of gas at the (effective) critical density of HCN(1–0) thus increasing the HCN(1–0) luminosity while the CO(2–1) luminosity is only marginally affected by increasing n_0 due to its low critical density. Thus, increasing the mean density of the cloud results in a higher HCN/CO line ratio. If we assume the CO(2–1) intensity to be a robust tracer of the surface density of the molecular gas at cloud-scales and further assume that the geometry of the clouds is similar such that surface density traces mean density, we expect a positive correlation between the surface density of molecular clouds and the HCN/CO line ratio as a proxy of the dense gas fraction. The connection between cloud-scale Σ_{mol} and HCN/CO has already been tested by Gallagher et al. (2018b), who found a positive correlation, thus supporting the model expectation.

Similarly, we vary the Mach number (and consequently the velocity dispersion) of the molecular cloud adopting typical values of $\mathcal{M} = 10$ to 100 while keeping the mean density fixed at $n_0 = 10^3 \text{ cm}^{-3}$. Comparing with Krumholz & Thompson (2007), the range of Mach numbers describes normal ($\mathcal{M} \sim 30$) over intermediate ($\mathcal{M} \sim 50$) to starburst galaxies ($\mathcal{M} \sim 80$). We find that increasing the turbulence of the molecular cloud widens the PDF without significantly shifting its peak ($s_0 = -\sigma_s^2/2$; see bottom left panel of Figure 1). As a result,

at low velocity dispersion the PDF is narrow and centred around a density of order 10^2 cm^{-3} such that only a small fraction of the gas is at high densities. Therefore, the HCN(1–0) intensity is low while the CO(2–1) intensity is high, hence we expect a small HCN/CO line ratio. Increasing the velocity dispersion leads to a widening of the PDF such that a larger fraction of the gas is at higher densities thus increasing the HCN(1–0) luminosity much more than the CO(2–1) which is less affected by the width of the PDF. Thus, assuming that the velocity dispersion is traced by the CO(2–1) line width, we expect a positive correlation between the line width and the HCN/CO line ratio as shown in the bottom right panel of Figure 1.

As mentioned above, in this simplified model prescription, the actual (theoretical) virial parameter does not affect the PDF thus leaving HCN/CO unchanged. However, the empirical virial parameter, if measured as $\alpha_{\text{vir}} \propto \sigma_{\text{mol}}^2/\Sigma_{\text{mol}}$, might be connected to changes in HCN/CO. Therefore, under the assumption that the virial parameter is proportional to $\sigma_{\text{mol}}^2/\Sigma_{\text{mol}}$ (see Section 4.3.3), we can study changes of HCN/CO with the empirically inferred virial parameter. In Figure 2 (upper row), we show how the model HCN/CO varies with the empirically based molecular cloud properties (see Appendix A for the distribution of the measured cloud-scale gas properties). Each data point corresponds to an aperture in one of our target galaxies. Blue dots indicate measurements at 150 pc, while red dots indicate averages over 2.1 kpc apertures using a mass-weighting scheme (see Section 4.4). We predict HCN/CO as described above adopting the following data-to-model parameter conversions. We convert the observationally inferred Σ_{mol} into n_0 assuming spherical clouds with radius R , such that the depth of the cloud is given by the beam size, e.g. $2R = 150 \text{ pc}$, leading to $n_0/[\text{cm}^{-3}] = 3/(4R\mu m_{\text{H}}) \Sigma_{\text{mol}} = 0.144 \times \Sigma_{\text{mol}}/[\text{M}_{\odot} \text{ pc}^{-2}]$, where $\mu = 2.8$ is the mean particle weight per hydrogen molecule assuming all hydrogen is H_2 (Kauffmann et al. 2008) and m_{H} is the mass of the hydrogen atom. Assuming a sound speed of $c_s = 0.3 \text{ km s}^{-1}$ we obtain $\mathcal{M} = \sqrt{3} \sigma_{\text{mol}}/c_s = 5.8 \times \sigma_{\text{mol}}/[\text{km s}^{-1}]$, where we assume an isotropic velocity dispersion, hence the factor $\sqrt{3}$. In accordance with the model predictions above, we find HCN/CO to positively correlate with n_0 and \mathcal{M} . In addition we observe a weak positive correlation of HCN/CO with the virial parameter (Pearson correlation $\rho = 0.14$ for the 150 pc measurements and $\rho = 0.40$ for the 2.1 kpc scale weighted averages). Physically, the virial parameter is a measure of the gravitational boundedness, where higher α_{vir} means less bound. The derived (weak) positive correlation between HCN/CO and α_{vir} implies that less bound clouds tend to have more dense gas per molecular gas which seems counterintuitive given that one might expect a higher dense gas fraction for more bound clouds. However, high HCN/CO is also connected to highly turbulent clouds as is shown above. Indeed, we observe a steeper correlation of HCN/CO with Mach number than with n_0 , therefore a positive correlation between HCN/CO and α_{vir} is indeed not surprising.

2.5 SFR/HCN correlations

Similar to the HCN/CO correlations above, we can make predictions about the SFR-to-HCN ratio as a function of molecular cloud properties. We model the SFR using Equation (4) where all gas above the threshold density n_{SF} is considered to form stars and n_{SF} is completely determined by the mean density (n_0) and the Mach number (\mathcal{M}), $n_{\text{SF}} \propto n_0 \mathcal{M}^2$ at fixed $\alpha_{\text{vir}} = 1.3$. This allows us to compute n_{SF} for any given tuple (n_0 , \mathcal{M}) or equivalently (Σ_{mol} , σ_{mol}). We add n_{SF} as vertical dashed lines in Figure 1 and consider the cloud's gas above this threshold (hatched area) as the star forming gas. Similar to HCN/CO and following Krumholz & McKee (2005), we estimate

SFR/HCN by integrating the PDF over the relevant density ranges:

$$\frac{\text{SFR}}{\text{HCN}} \Big|_{\text{model}} = \frac{\int_{s_{\text{SF}}}^{\infty} \frac{n}{\sqrt{n_0}} p(s) ds}{\int_{s_{\text{eff}}(\text{HCN})}^{\infty} \frac{n}{\sqrt{n_0}} p(s) ds}, \quad (7)$$

where $n_{\text{eff}}(\text{HCN})$ is defined as in Section 2.4. Equation (7) accounts for the (inverse) dependence of the SFR on the mean free fall time $t_{\text{ff},0} = \sqrt{3\pi/(32G\rho_0)} \propto \rho_0^{-1/2} \propto n_0^{-1/2}$ (e.g. Padoan et al. 2014). Again, we are only interested in relative changes of SFR/HCN so that the units have no physical meaning. We note that the prescription adopted here assumes a single free-fall time, while other pictures (e.g. Federrath & Klessen 2012) adopt a multi-free-fall approach that include an additional density dependent factor (a ratio of free-fall times) inside the integral in the numerator of Equation (7). Multi-free-fall models can predict that $\text{SFE}_{\text{dense}}$ increases with Mach number, i.e. the reverse of single free-fall models predictions and the reverse of the trends found here at low n_0 , \mathcal{M} (Figure 2). Given the sense of observed $\text{SFE}_{\text{dense}}$ trends examined in this work and by others (Querejeta et al. 2015; Leroy et al. 2017a, Utomo et al. in prep.), we proceed with the single free-fall class of models in the following.

We explore the effect of the molecular cloud properties on SFR/HCN within the same parameter space as of HCN/CO. We find that \mathcal{M} negatively correlates with SFR/HCN, as is shown in the bottom right panel of Figure 1. This can be understood in the following way. At low velocity dispersion, HCN is a good tracer of the density regime where the stars are expected to form and thus the SFR/HCN ratio is high. For increasing turbulence the HCN luminosity becomes a less ideal tracer of the local overdensities and traces more of the bulk molecular gas leading to a decreasing SFR/HCN. For changes of SFR/HCN with the mean density the model predicts a decreasing trend at low n_0 and an increasing trend at high n_0 and hence no clear correlation between SFR/HCN and n_0 . We can understand the different dependencies in the following way. At low $n_0 \ll n_{\text{eff}}$ an increase in n_0 leads to HCN tracing more of the bulk molecular gas such that SFR/HCN decreases leading to a negative correlation between SFR/HCN and n_0 similar to \mathcal{M} . Though, if n_0 reaches densities comparable to the critical density of HCN(1–0) the ratio between the gas masses above $n_{\text{eff}}(\text{HCN})$ and n_{SF} is barely affected by changes in n_0 . However, the SFR depends on the mean free-fall time such that a higher gas mass is converted into stars within a shorter time ($t_{\text{ff},0} \propto n_0^{-1/2}$) leading to an increase of SFR/HCN with increasing n_0 . As a result, we expect a negative correlation between SFR/HCN at $n_0 \ll n_{\text{eff}}(\text{HCN})$, n_{SF} and a positive correlation at $n_0 \sim n_{\text{eff}}(\text{HCN})$, n_{SF} .

Analogously to Section 2.4, we additionally infer SFR/HCN for every data based triplet (n_0 , \mathcal{M} , α_{vir}) meaning for each aperture, n_0 and \mathcal{M} are traced via Σ_{mol} and σ_{mol} , respectively, and α_{vir} is proportional to $\sigma_{\text{mol}}^2/\Sigma_{\text{mol}}$. The resulting relations (SFR/HCN against cloud properties) are shown in Figure 2 (lower panels). Remarkably, we find a clear negative correlation between SFR/HCN and n_0 in contrast to the less clear relation shown in Figure 1, where n_0 is varied at fixed \mathcal{M} . There are two reasons that we do not observe the upturn of SFR/HCN at higher n_0 . First, the n_0 values inferred from Σ_{mol} are ~ 1 dex to 2 dex lower than the adopted values in Figure 1 so that n_0 is mostly lower than $n_{\text{eff}}(\text{HCN})$ or n_{SF} and the dependence on the free fall time is less important. Second, the strong negative correlation between SFR/HCN and \mathcal{M} in combination with the positive correlation of n_0 and \mathcal{M} can overcompensate the SFR/HCN upturn at higher n_0 thus leading to a negative correlation between SFR/HCN and n_0 .

In the KM model description, α_{vir} affects n_{SF} without affecting the PDF and thus the line emissivity. This would result in a nega-

tive correlation between SFR/HCN and α_{vir} . However, we measure α_{vir} via $\sigma_{\text{mol}}^2/\Sigma_{\text{mol}}$ assuming a fixed cloud size (see Section 4.3.3). Thus, α_{vir} is constrained by the observational Σ_{mol} and σ_{mol} values and we want to explore variation of the model's SFR/HCN with $\sigma_{\text{mol}}^2/\Sigma_{\text{mol}}$. Analogously to Section 2.4, we infer SFR/HCN for every observationally based triplet (n_0 , \mathcal{M} , α_{vir}) based on the same model description as above but also accounting for variations in α_{vir} . The resulting relations (SFR/HCN against cloud properties) are shown in Figure 2 (lower panels). Consistent with the results above we find very strong negative correlations of SFR/HCN with n_0 and \mathcal{M} . Moreover, we observe a moderate negative correlation of SFR/HCN with the virial parameter (Pearson correlation $\rho = -0.43$ for the 150 pc scale measurement and $\rho = -0.57$ for the weighted averages). The virial parameter quantifies the gravitational boundedness of the cloud. The derived anti-correlation between α_{vir} and SFR/HCN supports the concept that less bound clouds tend to be less efficient in producing stars from the dense gas (lower SFR/HCN).

3 OBSERVATIONS

In this study we link the kpc-scale dense gas spectroscopy with the cloud-scale molecular gas properties across 25 nearby galaxies. To enable this we present a new ALMA survey of high critical density molecular lines, which we call ALMOND (“ACA Large-sample Mapping of Nearby galaxies in Dense gas”). ALMOND aimed to detect emission from high critical density lines, HCN(1–0), HCO⁺(1–0), CS(2–1), from targets of the PHANGS–ALMA survey. Following standard practice for extragalactic work, (e.g. Gao & Solomon 2004; Usero et al. 2015; Bigiel et al. 2016; Gallagher et al. 2018a; Querejeta et al. 2019) ALMOND initially focuses on HCN(1–0) (hereafter HCN), HCO⁺(1–0), and CS(2–1) as our primary tracer of dense molecular gas. We designed ALMOND with the goal of detecting these high critical density tracers, and as a result began by targeting the more massive and actively star-forming PHANGS–ALMA targets. All targets are nearby ($d < 25$ Mpc), relatively massive ($10^{10} M_{\odot} \lesssim M_{\star} \lesssim 10^{11} M_{\odot}$) gas-rich ($10^9 M_{\odot} \lesssim M_{\text{H}_2} \lesssim 10^{10} M_{\odot}$), star-forming ($1 M_{\odot} \text{ yr}^{-1} \lesssim \text{SFR} \lesssim 10 M_{\odot} \text{ yr}^{-1}$) galaxies, selected based on the PHANGS–ALMA CO (2–1) maps and mid-IR emission so that we expected the ACA to be able to achieve significant detections of the high critical density rotational lines near $\nu \approx 85$ –100 GHz, HCN(1–0), HCO⁺(1–0), CS(2–1), at least in the galaxy centres and across spiral arms. At these nearby distances, even the moderate angular resolution of the ACA allows us to resolve key environmental features (centre, bar, spiral arms) in both the bulk and dense molecular gas. Our diverse sample covers a variety of morphology, including 16 barred (9 unbarred) galaxies and 11 galaxies containing (14 without) an active galactic nucleus (AGN). Table 1 lists the galaxy sample along with their physical properties. We summarise the used data products in Table 2.

3.1 New HCN(1–0) observations

ALMOND observed 25 nearby galaxies in dense molecular gas tracers using the Morita Atacama Compact Array (ACA) as part of the ALMA facility. The ACA consists of four 12-m dishes which operate in single dish (“total power”, TP) mode and an array of 14 7-m telescopes. The spectral setup is similar to the one described in Gallagher et al. (2018a), and covers the brightest high critical density lines, HCN(1–0), HCO⁺(1–0) and CS(2–1) as well as a suite of fainter lines. At these frequencies, the ACA has a native resolution of $17''$ to $22''$ which, for our targets, relates to physical scales of \sim

8 *L. Neumann et al.*
Table 1. Galaxy Sample

Galaxy	R.A.	Dec.	d	i	M_{\star}	M_{H_2}	SFR	SFR/ M_{\star}	Bar	AGN
(1)	(J2000) (2)	(J2000) (3)	(Mpc) (4)	($^{\circ}$) (5)	($10^9 M_{\odot}$) (6)	($10^9 M_{\odot}$) (7)	($M_{\odot} \text{ yr}^{-1}$) (8)	(10^{-10} yr^{-1}) (9)	(10)	(11)
NGC 0628	1 ^h 36 ^m 41.7 ^s	15°47′1.1″	9.8	8.9	21.94	2.70	1.75	0.80	N	N
NGC 1097	2 ^h 46 ^m 18.9 ^s	−30°16′28.8″	13.6	48.6	57.48	5.52	4.74	0.83	Y	Y
NGC 1365	3 ^h 33 ^m 36.4 ^s	−36°8′25.5″	19.6	55.4	97.77	18.07	16.90	1.73	Y	Y
NGC 1385	3 ^h 37 ^m 28.6 ^s	−24°30′4.2″	17.2	44.0	9.53	1.68	2.09	2.19	N	N
NGC 1511	3 ^h 59 ^m 36.6 ^s	−67°38′2.1″	15.3	72.7	8.09	1.47	2.27	2.80	N	N
NGC 1546	4 ^h 14 ^m 36.3 ^s	−56°3′39.2″	17.7	70.3	22.39	1.94	0.83	0.37	N	N
NGC 1566	4 ^h 20 ^m 0.4 ^s	−54°56′16.8″	17.7	29.5	60.85	5.05	4.54	0.75	Y	Y
NGC 1672	4 ^h 45 ^m 42.5 ^s	−59°14′50.1″	19.4	42.6	53.61	7.24	7.60	1.42	Y	Y
NGC 1792	5 ^h 5 ^m 14.3 ^s	−37°58′50.0″	16.2	65.1	40.96	6.64	3.70	0.90	N	N
NGC 2566	8 ^h 18 ^m 45.6 ^s	−25°29′58.3″	23.4	48.5	51.21	7.17	8.72	1.70	Y	N
NGC 2903	9 ^h 32 ^m 10.1 ^s	21°30′3.0″	10.0	66.8	43.02	3.74	3.08	0.71	Y	N
NGC 2997	9 ^h 45 ^m 38.8 ^s	−31°11′27.9″	14.1	33.0	54.06	6.79	4.37	0.81	N	N
NGC 3059	9 ^h 50 ^m 8.2 ^s	−73°55′19.9″	20.2	29.4	23.87	2.43	2.38	1.00	Y	N
NGC 3521	11 ^h 5 ^m 48.6 ^s	−0°2′9.4″	13.2	68.8	105.21	5.90	3.72	0.35	N	N
NGC 3621	11 ^h 18 ^m 16.3 ^s	−32°48′45.4″	7.1	65.8	11.38	1.15	0.99	0.87	N	Y
NGC 4303	12 ^h 21 ^m 54.9 ^s	4°28′25.5″	17.0	23.5	33.39	8.12	5.33	1.60	Y	Y
NGC 4321	12 ^h 22 ^m 54.9 ^s	15°49′20.3″	15.2	38.5	55.61	7.77	3.56	0.64	Y	N
NGC 4535	12 ^h 34 ^m 20.3 ^s	8°11′52.7″	15.8	44.7	33.96	3.99	2.16	0.64	Y	N
NGC 4536	12 ^h 34 ^m 27.1 ^s	2°11′17.7″	16.2	66.0	25.07	2.62	3.45	1.37	Y	N
NGC 4569	12 ^h 36 ^m 49.8 ^s	13°9′46.4″	15.8	70.0	64.04	4.55	1.32	0.21	Y	Y
NGC 4826	12 ^h 56 ^m 43.6 ^s	21°40′59.1″	4.4	59.1	17.40	0.41	0.20	0.12	N	Y
NGC 5248	13 ^h 37 ^m 32.0 ^s	8°53′6.7″	14.9	47.4	25.49	4.54	2.29	0.90	Y	N
NGC 5643	14 ^h 32 ^m 40.8 ^s	−44°10′28.6″	12.7	29.9	21.69	2.66	2.59	1.20	Y	Y
NGC 6300	17 ^h 16 ^m 59.5 ^s	−62°49′14.0″	11.6	49.6	29.45	1.90	1.89	0.64	Y	Y
NGC 7496	23 ^h 9 ^m 47.3 ^s	−43°25′40.3″	18.7	35.9	9.92	1.81	2.26	2.28	Y	Y

Notes. (2) Right ascension, (3) declination, (4) distance (Anand et al. 2021), (5) inclination angle (Lang et al. 2020), (6) global stellar mass, (7) global H_2 mass and (8) global star formation rate. Integrated galaxy properties (6–8) are taken from Leroy et al. (2021c). Columns (10) and (11) specify if a galaxy is barred (Y) or unbarred (N) (Querejeta et al. 2021) and if it contains an AGN (Y) or not (N) (Véron-Cetty & Véron 2010).

1 kpc to 2 kpc. In total, ALMOND currently includes 7-m+TP observations of 25 targets (projects 2017.1.00230.S, 2018.1.01171.S, 2019.2.00134.S), which we combine in this analysis with additional 7-m+TP observations of NGC 2903 (project 2021.1.00740.S) and NGC 4321 (project 2017.1.00815.S). The data consist of a homogeneous set of ACA observations of a large sample of 23 galaxies with exceptionally deep observations of NGC 2903 and NGC 4321, for a total of 25 galaxies, which we believe to be the largest or one of the largest-ever mapping surveys targeting these high critical density lines. The data reduction was carried out using the PHANGS–ALMA pipeline (for more details see Leroy et al. 2021b), which uses the standard ALMA data reduction package, CASA (CASA Team et al. 2022).

The resulting PPV (position-position-velocity) cubes have typical spectral resolution of 10 km s^{-1} and typical noise per channel of 1 mK for the deeper observations (NGC 2903 and NGC 4321) and $\sim 3 \text{ mK}$ for the other 23 galaxies. The good sensitivity of the ACA allows us to detect HCN(1–0), $\text{HCO}^+(1-0)$ and CS(2–1) emission in the centres of all targets and in individual locations across the molecular spiral arms in some of the ALMOND galaxies. Across all galaxies, we observe in total 4566 independent sightlines, whereof 242 sightlines show significant HCN emission, i.e. integrated intensities with $\text{S/N} \geq 3$.

Beyond the individual detections, the survey covers a large area and we know the likely location and velocity of the faint HCN(1–0) emission. This allows us to achieve widespread detections of these faint lines via stacking, e.g., constructing sensitive radial profiles. In Appendix B, we show that via spectral stacking HCN can be detected in the central 2 kpc in all galaxies, out to 4 kpc and 6 kpc in 21 and 9 of the 25 galaxies, respectively. In Figure 3, we illustrate this

radial stacking spectra procedure and show the integrated intensities for NGC 4321. These are our deepest observations, and so are not typical, but they nicely illustrate the nature of the ALMOND data and the stacking procedures. For more details on the stacking method see Appendix B. The complete atlas of maps and stacked spectra are presented in Appendix J.

3.1.1 CO(2–1) – Bulk Molecular Gas

We trace the bulk molecular gas via the CO(2–1) emission line as observed by the PHANGS–ALMA survey (Leroy et al. 2021c). ALMA produced CO(2–1) line maps with $1''$ to $2''$ resolution corresponding to physical scales of 25 pc to 180 pc, 2.5 km s^{-1} velocity resolution and 0.2 K to 0.3 K noise per channel. It combines interferometric and single-dish data from the 12-m array and the ACA consisting of the 7-m array and four 12-m dishes observing in total power mode. Thus, it should recover information on all physical scales. In Section 4.3, we infer various dynamical properties of the molecular gas following a series of studies (Sun et al. 2018, 2020a,b) which extensively analysed the molecular gas in PHANGS–ALMA.

3.2 UV + IR – Star Formation Rate

We use star formation rate maps from the “ $z = 0$ Multiwavelength Galaxy Synthesis” study (z0MGS; Leroy et al. 2019) adopting a combination of $22 \mu\text{m}$ (WISE4) and GALEX-FUV 154 nm emission. Leroy et al. (2019) present an atlas of IR and UV images of $\sim 15,750$ local ($d \lesssim 50 \text{ Mpc}$) galaxies at a matched resolution of $7.5''$ and

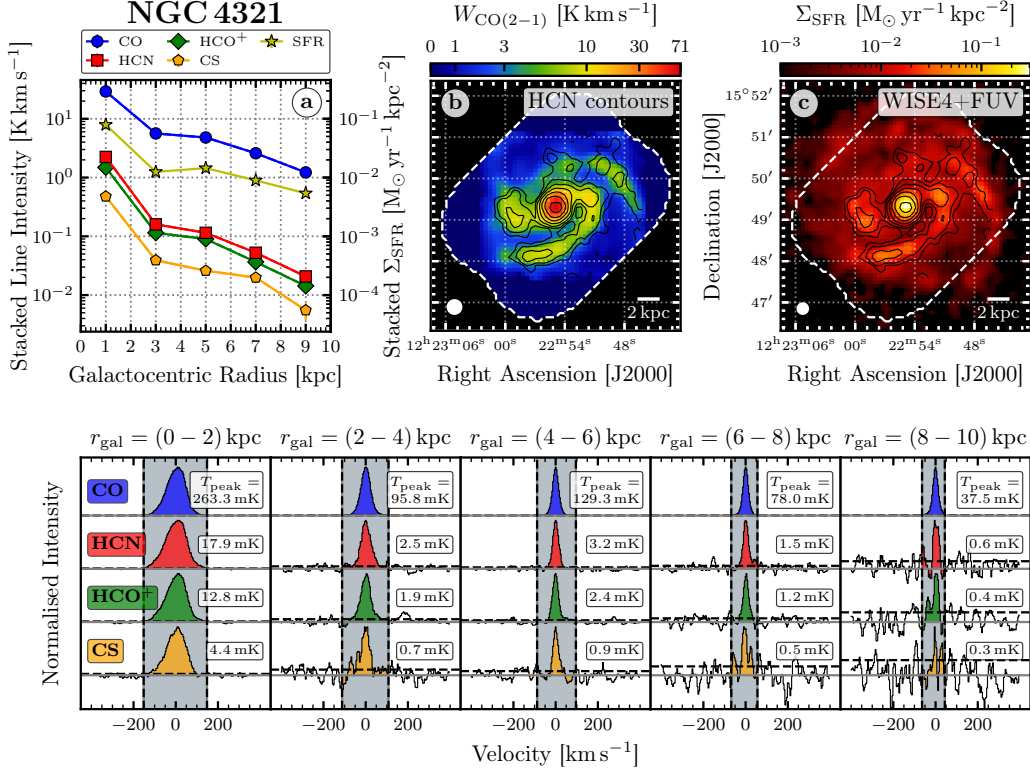


Figure 3. Spectral stacking across NGC 4321. *a*) Integrated intensities of radially stacked spectra in bins of $r_{\text{gal}} = 2$ kpc. Shown are CO(2–1) from PHANGS–ALMA (Leroy et al. 2021c), HCN(1–0), HCO⁺(1–0), CS(2–1) from ALMOND (this work) and SFR surface density from z0MGS (Leroy et al. 2019). Solid points indicate significant data ($S/N > 3$). *b*) CO(2–1) moment-0 map, computed as described in Section 4.1, overlaid with HCN(1–0) contours in S/N levels of 2^n for $n \in \{0, 1, 2, \dots, 7\}$, both at a common spatial resolution of $19.7''$. *c*) SFR map at $15''$ resolution, computed as described in Section 3.2 from a linear combination of the WISE4 IR and GALEX FUV data. *Bottom*: Stacked spectra, obtained as described in Appendix B corresponding to the integrated intensities shown in *a*). The grey shaded area indicates the velocity-integration mask. The spectra are normalised by their peak intensity for each bin and each line individually. The respective peak intensities (measured inside the integration mask) are shown in the box next to each spectra. The horizontal dotted line indicates the rms, i.e. the standard deviation of the spectrum outside the integration mask. We show analogous plots for the other 24 galaxies in Appendix J.

$15''$. Leroy et al. (2019) find a linear combination of WISE4 and FUV to be their most robust tracer of the SFR:

$$\left(\frac{\Sigma_{\text{SFR}}}{\text{M}_{\odot} \text{ yr}^{-1} \text{ kpc}^{-2}} \right) \approx (T_{\text{WISE4}} + T_{\text{FUV}}) \cdot \cos i, \quad (8)$$

where

$$T_{\text{WISE4}} = 3.24 \times 10^{-3} \left(\frac{\log_{10} C_{\text{WISE4}}}{-42.7} \right) \left(\frac{I_{\text{WISE4}}}{\text{MJy sr}^{-1}} \right), \quad (9)$$

and

$$T_{\text{FUV}} = 1.04 \times 10^{-1} \left(\frac{\log_{10} C_{\text{FUV}}}{-43.42} \right) \left(\frac{I_{\text{FUV}}}{\text{MJy sr}^{-1}} \right). \quad (10)$$

We refer to Kennicutt & Evans (2012) for a comparative discussion of SFR tracers. In Equation (8), i is the galaxy’s inclination as listed in Table 1 and the $\cos i$ term corrects for the projection effect due to the galaxy’s inclination. For galaxies without GALEX coverage Leroy et al. (2019) also prescribe formulas using only WISE4. Table 2 lists the available SFR tracers for our sample. The coefficients $\log_{10} C_{\text{WISE4}}$ depend on the galaxy and were benchmarked to Salim

et al. (2016) and Salim et al. (2018) (see Leroy et al. (2019) for details). We downloaded the SFR maps for our galaxy sample at a resolution of $15''$ from the public z0MGS repository⁵. These maps are then convolved to the spatial resolution of the ACA maps (2.1 kpc $\sim 20''$).

4 METHODS

The aim of this work is to compare the kpc-scale dense gas and SFR observations with the cloud-scale molecular gas properties. To do so we need to determine the integrated intensities of each line (Section 4.1). We then estimate the cloud-scale properties from the 150 pc scale CO(2–1) data (Section 4.3), and the dense gas quantities from the coarser HCN(1–0) and SFR data at 2.1 kpc scale (Section 4.2). Next, we explain the weighted averaging method, which is used to compare these two scales (Section 4.4), and the data binning that is

⁵ irsa.ipac.caltech.edu/data/WISE/z0MGS

10 *L. Neumann et al.*
Table 2. Data/Observations

Galaxy	CO observations			HCN observations			SFR tracers
	Survey	Res. (")	Res. (pc)	Survey	Res. (")	Res. (kpc)	
(1)	(2)	(3)	(4)	(5)	(6)	(7)	(8)
NGC 0628	PHANGS–ALMA	1.12	53	ALMOND	18.6	0.89	WISE4, FUV
NGC 1097	PHANGS–ALMA	1.70	112	ALMOND	19.4	1.28	WISE4, FUV
NGC 1365	PHANGS–ALMA	1.38	131	ALMOND	20.6	1.96	WISE4, FUV
NGC 1385	PHANGS–ALMA	1.27	106	ALMOND	19.9	1.67	WISE4, FUV
NGC 1511	PHANGS–ALMA	1.45	107	ALMOND	17.6	1.30	WISE4, FUV
NGC 1546	PHANGS–ALMA	1.28	110	ALMOND	19.0	1.63	WISE4, FUV
NGC 1566	PHANGS–ALMA	1.25	108	ALMOND	19.8	1.69	WISE4, FUV
NGC 1672	PHANGS–ALMA	1.93	182	ALMOND	17.7	1.67	WISE4, FUV
NGC 1792	PHANGS–ALMA	1.92	151	ALMOND	18.8	1.47	WISE4, FUV
NGC 2566	PHANGS–ALMA	1.28	145	ALMOND	18.6	2.11	WISE4
NGC 2903	PHANGS–ALMA	1.45	71	ALMOND	18.4	0.89	WISE4, FUV
NGC 2997	PHANGS–ALMA	1.77	121	ALMOND	20.4	1.39	WISE4, FUV
NGC 3059	PHANGS–ALMA	1.22	120	ALMOND	16.8	1.64	WISE4
NGC 3521	PHANGS–ALMA	1.33	85	ALMOND	21.2	1.36	WISE4
NGC 3621	PHANGS–ALMA	1.82	62	ALMOND	18.9	0.65	WISE4, FUV
NGC 4303	PHANGS–ALMA	1.81	149	ALMOND	20.3	1.67	WISE4, FUV
NGC 4321	PHANGS–ALMA	1.67	123	ALMOND	19.7	1.45	WISE4, FUV
NGC 4535	PHANGS–ALMA	1.56	119	ALMOND	22.9	1.75	WISE4, FUV
NGC 4536	PHANGS–ALMA	1.48	116	ALMOND	21.6	1.70	WISE4, FUV
NGC 4569	PHANGS–ALMA	1.69	129	ALMOND	19.3	1.47	WISE4, FUV
NGC 4826	PHANGS–ALMA	1.26	27	ALMOND	18.8	0.40	WISE4, FUV
NGC 5248	PHANGS–ALMA	1.29	93	ALMOND	19.9	1.44	WISE4, FUV
NGC 5643	PHANGS–ALMA	1.30	80	ALMOND	18.1	1.11	WISE4
NGC 6300	PHANGS–ALMA	1.08	60	ALMOND	17.7	1.00	WISE4
NGC 7496	PHANGS–ALMA	1.68	152	ALMOND	17.9	1.63	WISE4, FUV

Notes. (2–4) CO(2–1) data from PHANGS–ALMA (Leroy et al. 2021c) along with their native resolutions (full-width half-maximum) in arcseconds and parsecs, (5–7) analog for the HCN(1–0) data taken from ALMOND (this work), (8) applied star formation rate tracers from WISE (Wright et al. 2010) and GALEX (Martin et al. 2005). The data has been spatially homogenised. The CO observations from PHANGS–ALMA have been convolved to a physical resolution of 150 pc and the HCN observations from ALMOND as well as the SFR maps have been convolved to 2.1 kpc.

used to improve signal-to-noise (Section 4.5). Finally, we introduce the fitting scheme, which is used to constrain a first order relation between the kpc- and cloud-scale quantities.

4.1 Integrated Intensity Maps

We produce integrated intensity maps from the original CO(2–1), HCN(1–0) (analogously with HCO⁺(1–0), CS(2–1)) PPV cubes for all galaxies. At first, we convolve the data cubes to the target resolution using the respective cloud-scale resolution for the CO(2–1) data and the kpc-scale resolution for the CO(2–1) and HCN(1–0) (HCO⁺(1–0), CS(2–1)) cubes. Then, we put the voxels on hexagonal grids, using one sample per beam (FWHM) for the kpc-scale maps, and two samples per beam (FWHM) for the cloud-scale maps. We use a higher sampling rate (satisfying the Nyquist–Shannon sampling theorem) for the cloud-scale maps in order to avoid losing information in computing the weighted averages (see Section 4.4). After conducting the weighted averages, we resample to match the kpc-resolution maps which are sampled at the beam size to get statistically independent data points for further processing.

We use the CO(2–1) data to create position-position-velocity masks, where we apply customised scripts that have been utilised in previous large program studies (e.g. EMPIRE, Jiménez-Donaire et al. 2019) and is based on the methodology introduced by Rosolowsky & Leroy (2006). We first identify pixels with high signal-to-noise ratio (S/N ; $S/N \geq 4$) in at least three adjacent velocity channels. In

addition we build a low S/N mask requiring at least three adjacent velocity channels with $S/N \geq 2$. Then we iteratively grow the identified high S/N regions to include adjoining regions with moderate S/N as defined by the low S/N mask. In doing so, we recover the more extended 2-sigma detection belonging to a 4-sigma core and thus recover regions of bright CO emission that one would also identify by eye. Finally, we collapse the masked data cubes along the velocity axis by summing the mask-selected channels (in K) multiplied by the channel width (in km s^{-1}) to produce integrated intensity maps (in K km s^{-1}).

We extract the HCN (analogously with HCO⁺ and CS) emission via the CO-based position-position-velocity masks and produce the integrated intensity maps as described above. CO(2–1) is easy to excite and the brightest line observed here, being detected with a much higher S/N compared to the faint dense gas tracers, e.g. HCN. As such, CO emission unveils the regions of molecular gas where we also expect to find emission of the dense molecular gas as traced by HCN(1–0) (or HCO⁺(1–0), CS(2–1)).

For each line of sight, we compute the statistical uncertainties in the integrated intensity σ_I from the rms in the emission-free (not selected by the mask) channels via:

$$\left(\frac{\sigma_I}{\text{K km s}^{-1}} \right) = \left(\frac{\text{rms}}{\text{K}} \right) \times \left(\frac{\Delta v_{\text{channel}}}{\text{km s}^{-1}} \right) \times \sqrt{N} \quad (11)$$

where $\Delta v_{\text{channel}}$ is the channel width and N is the number of mask-selected voxels along the line of sight.

4.2 kpc-Scale Dense Gas Properties

4.2.1 Dense Gas Fraction

In Sections 5 and 6, we focus on the observed ratio $W_{\text{HCN}}/W_{\text{CO}(2-1)}$, which we expect to be sensitive to density with some additional dependence on physical parameters like abundances, temperature, and opacities. In the discussion section we also comment on implications for the actual dense gas fraction (f_{dense}), which is a simple recasting of this ratio using common mass-to-light ratios for both lines. We compute f_{dense} as the ratio of the dense gas surface density (Σ_{dense}) and the molecular gas surface density (Σ_{mol}) which is traced by $W_{\text{HCN}}/W_{\text{CO}(2-1)}$:

$$f_{\text{dense}} = \frac{\Sigma_{\text{dense}}}{\Sigma_{\text{mol}}} = \frac{\alpha_{\text{HCN}} W_{\text{HCN}}}{\alpha_{\text{CO}} R_{21}^{-1} W_{\text{CO}(2-1)}} \approx 2.1 \frac{W_{\text{HCN}}}{W_{\text{CO}(2-1)}}. \quad (12)$$

The kpc-scale integrated intensity maps are obtained as described in Section 4.1. Σ_{mol} is measured via $W_{\text{CO}(2-1)}$ assuming a constant mass-to-light ratio $\alpha_{\text{CO}} = 4.3 \text{ M}_{\odot} \text{ pc}^{-2} (\text{K km s}^{-1})^{-1}$ (Bolatto et al. 2013) and a CO(2–1)-to-CO(1–0) line ratio of $R_{21} = 0.64$ (den Brok et al. 2021; Leroy et al. 2021a). For more details on α_{CO} and R_{21} , see Section 4.3.1. Similarly, Σ_{dense} is obtained via W_{HCN} adopting a more uncertain $\alpha_{\text{HCN}} \approx 14 \text{ M}_{\odot} \text{ pc}^{-2} (\text{K km s}^{-1})^{-1}$ (uncertain by at least ~ 0.3 dex) tracing gas above $n_{\text{H}_2} \approx 5 \times 10^3 \text{ cm}^{-3}$ (Onus et al. 2018). For comparison, but not used in this work, previous studies assumed a lower value of $\alpha_{\text{HCN}} \approx 10 \text{ M}_{\odot} \text{ pc}^{-2} (\text{K km s}^{-1})^{-1}$ and that HCN traces gas above a higher density of $3 \times 10^4 \text{ cm}^{-3}$ (following Gao & Solomon 2004, also see Jones et al. 2021).

4.2.2 Dense Gas Star Formation Efficiency

We compute the star formation efficiency of the dense gas via the ratio of star formation rate surface density and dense gas surface density:

$$\text{SFE}_{\text{dense}} = \frac{\Sigma_{\text{SFR}}}{\Sigma_{\text{dense}}} = \alpha_{\text{HCN}}^{-1} \frac{\Sigma_{\text{SFR}}}{W_{\text{HCN}}}. \quad (13)$$

Note that here Σ_{mol} , Σ_{SFR} and Σ_{dense} are not corrected for the galaxies' inclinations because we are only interested in the ratio of surface densities such that the deprojection term $\cos i$ cancels out. For typical units and by adopting $\alpha_{\text{HCN}} \approx 14 \text{ M}_{\odot} \text{ pc}^{-2} (\text{K km s}^{-1})^{-1}$ like in Section 4.2.2, above Equation (13) becomes:

$$\left(\frac{\text{SFE}_{\text{dense}}}{\text{Myr}^{-1}} \right) = 7.1 \times 10^{-1} \left(\frac{\Sigma_{\text{SFR}}}{\text{M}_{\odot} \text{ yr}^{-1} \text{ kpc}^{-2}} \right) \left(\frac{W_{\text{HCN}}}{\text{K km s}^{-1}} \right)^{-1}. \quad (14)$$

4.3 Cloud-Scale Molecular Gas Properties

We compute the four cloud-scale properties molecular gas surface density (Σ_{mol}), velocity dispersion (σ_{mol}), virial parameter (α_{vir}) and internal turbulent pressure (P_{turb}) using PHANGS–ALMA CO(2–1) data (see Section 3.1.1) following Sun et al. (2018). We measure the cloud-scale properties at beam sizes of 150 pc using pixel-by-pixel values instead of identifying individual molecular clouds. Based on comparisons of the two approaches by Sun et al. (2020b) and Rosolowsky et al. (2021), statistically we expect similar results for the molecular gas properties as measured at cloud-scale compared to cloud properties as obtained for individually identified clouds. In Appendix F we also discuss sub-samples, where we have access to higher resolutions, i.e. 75 pc for five galaxies and 120 pc for twelve galaxies, respectively. We confirm that the results do not significantly depend on the resolution at which the cloud-scale properties are measured.

4.3.1 Molecular Gas Surface Density

We trace Σ_{mol} at 150 pc resolution via $W_{\text{CO}(2-1)}$ using a constant mass-to-light ratio conversion factor:

$$\Sigma_{\text{mol}} = \alpha_{\text{CO}} R_{21}^{-1} W_{\text{CO}(2-1)}. \quad (15)$$

We adopt a constant, Milky Way-like CO-to-H₂ conversion factor of $\alpha_{\text{CO}} = 4.3 \text{ M}_{\odot} \text{ pc}^{-2} (\text{K km s}^{-1})^{-1}$ (uncertainty of ± 0.1 dex) as suggested by Bolatto et al. (2013) and a constant CO(2–1)-to-CO(1–0) line ratio of $R_{21} = 0.64$ (uncertainty of ± 0.06 dex) as recently constrained by den Brok et al. (2021) and for a larger sample including many of these targets by Leroy et al. (2021a), which yields:

$$\left(\frac{\Sigma_{\text{mol}}}{\text{M}_{\odot} \text{ pc}^{-2}} \right) = 6.7 \times 10^2 \left(\frac{W_{\text{CO}(2-1)}}{10^2 \text{ K km s}^{-1}} \right). \quad (16)$$

Note that some of the α_{CO} and R_{21} uncertainty can be attributed to variations as a function of the galactocentric radius, where α_{CO} is found to be lower in the centres of galaxies (Sandstrom et al. 2013), while R_{21} is higher towards galaxy centres (den Brok et al. 2021). To account for systematic variations of α_{CO} with metallicity Z' , recent studies (as in Sun et al. 2020b) adopt a metallicity-dependent $\alpha_{\text{CO}} \propto Z'^{-1.6}$, which leads to lower α_{CO} in the central region of galaxies. However, metallicity variations can only partly explain the low α_{CO} in centres. Sandstrom et al. (2013) conclude that the physical conditions in the centres of galaxies (ISM pressure, gas temperature) are responsible for lowering α_{CO} by roughly a factor of two. Thus, by adopting a constant α_{CO} , we may overestimate Σ_{mol} in the central regions of galaxies and underestimate Σ_{mol} at larger galactocentric radii. We still adopt a constant α_{CO} in analogy to previous studies (e.g. Gallagher et al. 2018a,b; Sun et al. 2018) and discuss in Section 6.1 how lowering α_{CO} by a factor of two in the centres of galaxies affects the studied relations.

4.3.2 Velocity Dispersion

We characterise the line width using the "effective width" according to the prescription of Heyer et al. (2001), calculated via:

$$\sigma_{\text{measured}} = \frac{W_{\text{CO}(2-1)}}{\sqrt{2\pi} T_{\text{peak}}}, \quad (17)$$

where T_{peak} (in units of K) is obtained as the maximum intensity of the cubes' spectra for each line of sight. Then, for a Gaussian line profile with peak intensity T_{peak} the effective width is equal to the rms velocity dispersion of the line (σ_{mol}). In order to correct for the line broadening caused by the instrument (finite channel width, spectral response curve width) we subtract the contribution of the instrument's response following Rosolowsky & Leroy (2006) and Sun et al. (2018):

$$\sigma_{\text{mol}} = \sqrt{\sigma_{\text{measured}}^2 - \sigma_{\text{response}}^2}. \quad (18)$$

Here, σ_{response} is estimated from the channel width and the channel-to-channel correlation coefficient, following Leroy et al. (2016) and Sun et al. (2018).

4.3.3 Virial Parameter

The virial parameter of GMCs is typically defined as $\alpha_{\text{vir}} \equiv 2K/U_g$, where K is the kinetic energy and U_g is its self-gravitational potential

⁶ Z' is the metallicity normalised to the solar metallicity [$12 + \log_{10}(\text{O}/\text{H}) = 8.69$] (Allende Prieto et al. 2001)

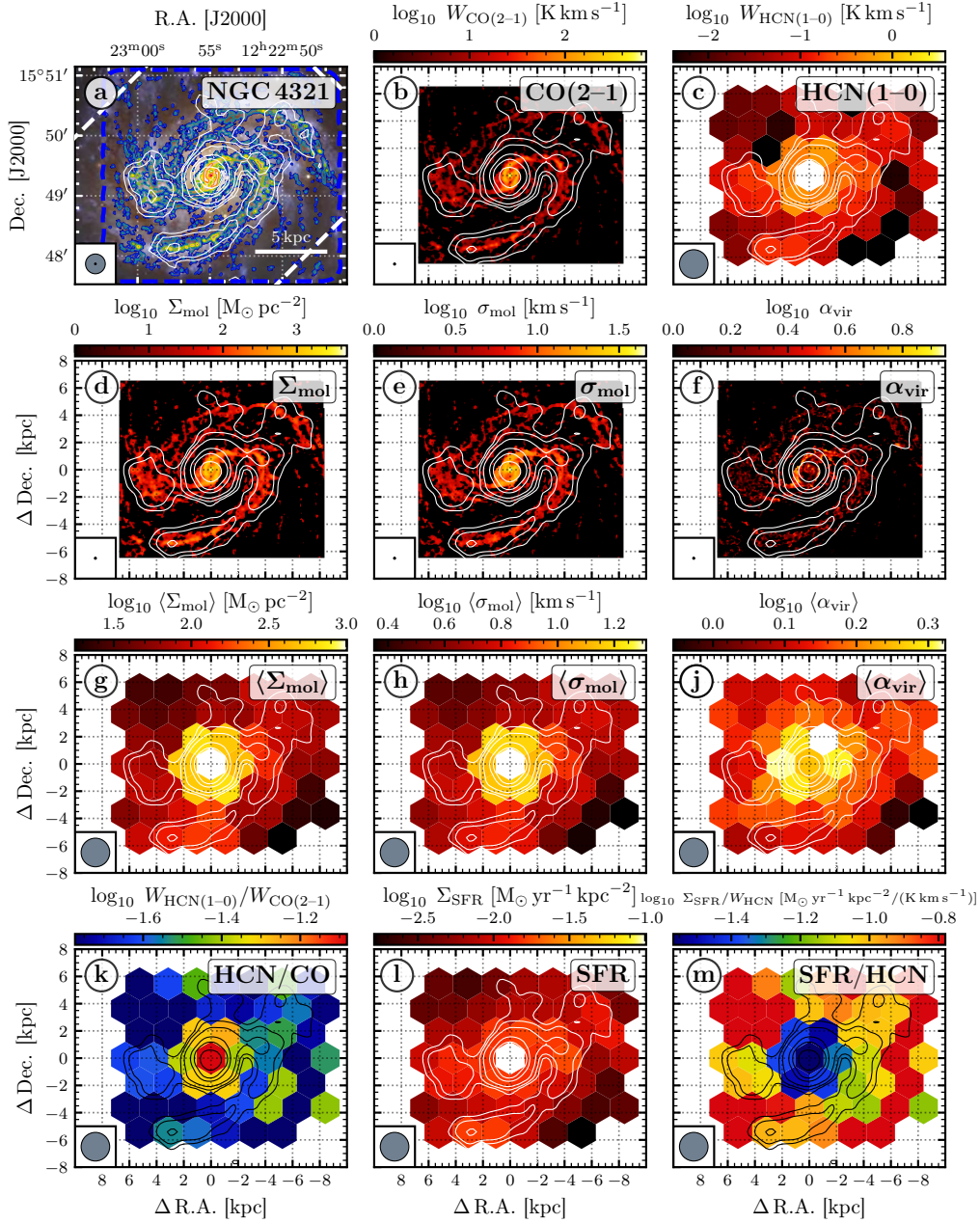
12 *L. Neumann et al.*


Figure 4. Data products compilation of NGC 4321 (one of the deepest observations) at cloud- and kpc-scale resolutions 150 pc and 2.1 kpc respectively: *a)* ESO three colour image composed of 648 nm (red), 544 nm (green), and 433 nm (blue) wideband emission (Image credit: ESO/IDA/Danish 1.5 m/R. Gendler, J.-E. Ovaldsen, C. C. Thöne and C. Féron). Overlaid are colored CO(2–1) contours and white HCN(1–0) contours, respectively in S/N levels of 3, 5, 10, 30, 50, 100, 300 (the same HCN contours are used throughout the other maps). The white and blue dashed contour indicates the ALMOND and PHANGS–ALMA FOV, respectively. *b)* Integrated CO(2–1) intensity at 150 pc resolution from PHANGS–ALMA and *b)* integrated HCN(1–0) intensity at 2.1 kpc resolution from ALMOND as obtained from the data cubes according to Section 4.1. *d)–f)* Cloud-scale properties of the molecular gas (molecular gas surface density Σ_{mol} , velocity dispersion σ_{mol} and virial parameter α_{vir}) computed from CO(2–1) as described in Section 4.3. *g)–i)* CO(2–1) intensity weighted averages ($\langle \Sigma_{\text{mol}} \rangle$, $\langle \sigma_{\text{mol}} \rangle$, $\langle \alpha_{\text{vir}} \rangle$) of the above cloud-scale properties based on the formalism described in Section 4.4. *k)* HCN/CO tracing f_{dense} . *l)* SFR surface density from FUV (GALEX), *m)* IR (WISE) and SFR/HCN tracing $\text{SFE}_{\text{dense}}$ following Section 4.2.

energy of the cloud such that α_{vir} quantifies deviations from virial equilibrium. Virialised clouds have $\alpha_{\text{vir}} = 1$, if surface pressure or magnetic support can be neglected. For unbound clouds α_{vir} moves to higher values.

Following Bertoldi & McKee (1992), under the assumption of spherical clouds, the virial parameter can be expressed as:⁷

$$\alpha_{\text{vir}} \equiv \frac{2K}{U_g} = \frac{5\sigma_{\text{mol}}^2 R}{fGM}, \quad (19)$$

where M , R and σ_{mol} are the cloud's mass, radius and velocity dispersion, G is the gravitational constant and f is a geometrical factor specifying the density profile of the cloud. We adopt $f = 10/9$ which assumes a density profile of the form $\rho \propto r^{-1}$ (e.g. following Rosolowsky & Leroy 2006). Given that the cloud-scale resolutions are at the scale of GMCs we take the beam size as the relevant size scale ($R = D_{\text{beam}}/2$), such that equation (19) implies:

$$\alpha_{\text{vir}} = \frac{5}{2fG} \frac{\sigma_{\text{mol}}^2 D_{\text{beam}}}{\Sigma_{\text{mol}} A_{\text{beam}}} = \frac{10 \ln 2}{\pi fG} \frac{\sigma_{\text{mol}}^2}{\Sigma_{\text{mol}} D_{\text{beam}}} \quad (20)$$

Here, Σ_{mol} is the molecular gas surface density, computed in Section 4.3.1, σ_{mol} is the velocity dispersion (see Section 4.3.2) and D_{beam} is the FWHM of the beam, i.e. 150 pc. Normalising by typical numbers, we obtain:

$$\alpha_{\text{vir}} = 3.1 \left(\frac{\Sigma_{\text{mol}}}{10^2 \text{ M}_{\odot} \text{ pc}^{-2}} \right)^{-1} \left(\frac{\sigma_{\text{mol}}}{10 \text{ km s}^{-1}} \right)^2 \left(\frac{D_{\text{beam}}}{150 \text{ pc}} \right)^{-1} \quad (21)$$

Note, that above formalism is likely to produce uncertainties in α_{vir} reaching factors of a few. However, following the approach of e.g. Sun et al. (2018, 2020b), we are interested in measuring $\sigma_{\text{mol}}^2/\Sigma_{\text{mol}}$ for comparative analysis and consider it as a tracer of α_{vir} , where the conversion factor is uncertain by a factor of a few. In other words, we measure α_{vir} in units of $\sigma_{\text{mol}}^2/\Sigma_{\text{mol}}$ for fixed physical scale.

4.3.4 Internal Turbulent Pressure

We infer the internal turbulent pressure, P_{turb} , from the CO(2–1) observations. Following Sun et al. (2018), the internal pressure in molecular gas with line-of-sight depth $\sim 2R$ can be expressed as:

$$P_{\text{turb}} \approx \rho_{\text{mol}} \sigma_{\text{mol}}^2 \approx \frac{1}{2R} \Sigma_{\text{mol}} \sigma_{\text{mol}}^2. \quad (22)$$

Similar to the virial parameter computation in Section 4.3.3, we aim to measure the quantity $\Sigma_{\text{mol}} \sigma_{\text{mol}}^2$ in order to trace P_{turb} at a scale of $R = D_{\text{beam}}/2$ with the purpose of comparative analysis. P_{turb} is linked to $\Sigma_{\text{mol}} \sigma_{\text{mol}}^2$ via a proportionality factor:

$$\left(\frac{P_{\text{turb}}}{\text{K B cm}^{-3}} \right) \approx 3.3 \times 10^5 \left(\frac{\Sigma_{\text{mol}}}{10^2 \text{ M}_{\odot} \text{ pc}^{-2}} \right) \times \left(\frac{\sigma_{\text{mol}}}{10 \text{ km s}^{-1}} \right)^2 \left(\frac{D_{\text{beam}}}{150 \text{ pc}} \right)^{-1}, \quad (23)$$

where Σ_{mol} and σ_{mol} are taken from Sections 4.3.1 and 4.3.2, respectively.

⁷ Note that this approach neglects contributions from the magnetic energy density or the cosmic ray flux. Moreover, it ignores any surface terms (see e.g. McKee & Zweibel 1992; Ballesteros-Paredes 2006)

4.4 Weighted Averages

In order to connect the cloud-scale - Σ_{mol} , σ_{mol} , α_{vir} , P_{turb} - measurements to the kpc-scale - f_{dense} , $\text{SFE}_{\text{dense}}$ - measurements, we calculate the intensity-weighted averages of Σ_{mol} , σ_{mol} , α_{vir} , P_{turb} inside each kpc-scale beam. These weighted averages - $\langle \Sigma_{\text{mol}} \rangle$, $\langle \sigma_{\text{mol}} \rangle$, $\langle \alpha_{\text{vir}} \rangle$, $\langle P_{\text{turb}} \rangle$ - measure the cloud-scale Σ_{mol} , σ_{mol} , α_{vir} , P_{turb} , respectively, from which the average CO photon emerges within the kpc-scale resolution beam. In practice we compute (following Leroy et al. 2016):

$$\langle X \rangle = \frac{(X \cdot W_{\text{CO}(2-1)}) * \Omega}{W_{\text{CO}(2-1)} * \Omega}. \quad (24)$$

Here, $W_{\text{CO}(2-1)}$ is the CO(2–1) integrated intensity and X is the quantity to be averaged, both at cloud-scale resolution (in this work, 150 pc). X is weighted with $W_{\text{CO}(2-1)}$ (via multiplication) and convolved to the kpc-scale resolution (here, 2.1 kpc) indicated by the asterisk using a Gaussian kernel Ω . Finally, the weighted average, $\langle X \rangle$, is obtained by division with the convolved weights. Consequently, $\langle X \rangle$ is at kpc-scale resolution and can easily be compared to the kpc-scale f_{dense} and $\text{SFE}_{\text{dense}}$ measurements pixel-by-pixel.

The above formalism was introduced by Leroy et al. (2016) and is designed to connect high resolution to low resolution measurements such as conducted in this study, having the advantage of preserving the high resolution information and down-weighting empty regions. As such it was utilised by e.g. Gallagher et al. (2018b) who performed a similar comparison as the one presented in this work. Sun et al. (2020a) computed the weighted averages in terms of Equation (24) applying a top-hat kernel to the cloud-scale data and then computed the weighted averages in each of these apertures. Here, we follow the Gaussian convolution approach using Equation (24) in order to make the weighted averages similarly comparable to the kpc-scale observations. We highlight the difference between the two approaches in the Appendix C.

We estimate the propagated uncertainties in the weighted averages via Monte Carlo computations. We start with the Σ_{mol} , σ_{mol} , α_{vir} , P_{turb} maps, add random Gaussian noise with amplitudes taken from the cloud-scale maps. Then we run the noise-added maps through the weighted averages procedure and repeat this process 100 times. Finally, we take the standard deviation in $\langle \Sigma_{\text{mol}} \rangle$, $\langle \sigma_{\text{mol}} \rangle$, $\langle \alpha_{\text{vir}} \rangle$, $\langle P_{\text{turb}} \rangle$ over all realisations as the uncertainty estimate.

4.5 Data Binning

We detect integrated HCN intensity (analogously for HCO⁺ and CS) with S/N ≥ 3 only in the brightest regions of the galaxies. In order to recover the low S/N information hidden in the data we bin the HCN data by $\langle \Sigma_{\text{mol}} \rangle$, or equivalently $\langle W_{\text{CO}(2-1)} \rangle$ (following Gallagher et al. 2018a). $\langle \Sigma_{\text{mol}} \rangle$ is detected at high significance across much of the galaxy discs in all 25 targets.

We bin each galaxy's data individually, choosing a fixed number of 20 bins, equally spaced in $\langle \Sigma_{\text{mol}} \rangle$, over the full data range of each galaxy. Adapting the binning to each galaxy individually allows us to recover more of the low S/N signal. We choose the number of 20 bins because it increases the number of HCN detections at low $\langle \Sigma_{\text{mol}} \rangle$ without averaging over too large intervals thus maximising the dynamic range in the x -axis variable ($\langle \Sigma_{\text{mol}} \rangle$). In each bin, we compute the binned ratio - $W_{\text{HCN}}/W_{\text{CO}(2-1)}$ or $\Sigma_{\text{SFR}}/W_{\text{HCN}}$ - as the mean of the nominator's data in that bin divided by the mean of the denominator's data in that bin (as in Schrubba et al. 2011 and

14 *L. Neumann et al.*

(Jiménez-Donaire et al. 2017):

$$\frac{W_{\text{HCN}}}{W_{\text{CO}(2-1)}} \Big|_{\text{bin}} = \frac{\text{mean}(W_{\text{HCN}})|_{\text{bin}}}{\text{mean}(W_{\text{CO}(2-1)})|_{\text{bin}}} \quad (25)$$

$$\frac{\Sigma_{\text{SFR}}}{W_{\text{HCN}}} \Big|_{\text{bin}} = \frac{\text{mean}(\Sigma_{\text{SFR}})|_{\text{bin}}}{\text{mean}(W_{\text{HCN}})|_{\text{bin}}} \quad (26)$$

This means that for each bin we take the ratio of the bin means and not the bin mean of the ratios. The binning process extends the dynamic range of significant HCN data and has the advantage of reducing the linear regression bias which is naturally induced by converting from linear to logarithmic scale (for more details see Appendix D).

We propagate the measurement uncertainties from the individual integrated intensity (and SFR) data points which enter the binning using Gaussian error propagation. As we sample the integrated intensities at the beam size (one sample per beam FWHM), we do not need to account for oversampling in the error propagation. In doing so, for each bin the propagated uncertainty roughly decreases as $1/\sqrt{N}$, where N is the number of points in the bin. However, the binned measurements can often still have low S/N. Considering binned data detected if the signal-to-noise ratio ≥ 3 and censored (non-detected) if $S/N < 3$, we can define upper and lower limits on the binned data. The binned integrated CO(2–1) intensities and SFR surface densities are significant ($S/N \geq 3$) across the whole galactic disc for the full sample of galaxies. Thus, the S/N is purely dominated by the HCN data. Therefore, we define upper limits (UL) in the binned HCN/CO(2–1) data via:

$$\text{UL}|_{\text{bin}} = \frac{3 \cdot I_{\text{HCN,unc}}|_{\text{bin}}}{W_{\text{CO}(2-1)}|_{\text{bin}}}, \quad (27)$$

where $I_{\text{HCN,unc}}$ is the (propagated) uncertainty of the integrated HCN intensity in each bin. For SFR/HCN we compute lower limits (LL) via:

$$\text{LL}|_{\text{bin}} = \frac{\Sigma_{\text{SFR}}|_{\text{bin}}}{3 \cdot I_{\text{HCN,unc}}|_{\text{bin}}}. \quad (28)$$

Although UL and LL are regarded (by definition) non-significant, they are still an important part of the data distribution and we use them in our linear regression analysis (Section 4.6).

4.6 Linear Regression and Correlation

To investigate the correlations we fit a linear regression model to the log-scale binned data, resulting from the data processing described above (Section 3). We perform the linear regression by making use of the `LinMix` package⁸ which is based on the Bayesian approach to linear regression proposed by Kelly (2007). In this approach, a likelihood function of the linear regression model is built and MCMC simulations are run using a Gibbs sampler exploring the posterior distribution of the regression parameters. Here, we force the MCMC simulation to take at least 10 000 steps after convergence was reached, i.e. close to the global maximum of the posterior distribution where every iteration can be considered a random draw from the posterior. The model accounts for heteroscedastic uncertainties in the data on both coordinates, intrinsic scatter and censored data, i.e. upper (or lower) limits in the independent variable.⁹ Due to its statistical nature

in exploring the parameter space, it naturally provides trustworthy uncertainty estimates and credibility intervals of the regression parameters. Moreover, it computes the Pearson correlation coefficient ρ (and the p -value) using both detected and censored data. We choose this linear regression method because it accounts for non-detections, determines meaningful fit uncertainties and leads to less biased regression parameter estimates (see Appendix D).

We perform the linear regression by fitting the following linear function to the data in log-log scale:

$$\log_{10} Y = b_{y,x} + m_{y,x} [\log_{10} \langle X \rangle - x_{\text{off},x}], \quad (29)$$

where Y are the kpc-scale measurements (HCN/CO or SFR/HCN) and $\langle X \rangle$ are the weighted averages of the cloud-scale molecular gas properties (Σ_{mol} , σ_{mol} , P_{turb})¹⁰ in their respective units. $b_{y,x}$ and $m_{y,x}$ are the intercept and slope of the fit line, where $y = \{f, S\}$, $x = \{\Sigma, \sigma, P\}$ indicate the corresponding kpc-scale (HCN/CO, SFR/HCN) and cloud-scale quantities (Σ_{mol} , σ_{mol} , P_{turb}). We recenter the distribution in the x -axis coordinate to minimise the covariance between the slope and intercept, applying $x_{\text{off},x} \equiv \{2.5, 1.1, 6.5\}$ for $x = \{\Sigma, \sigma, P\}$ which is near the middle of the data range. Note, that this has no effect on the fitting scheme. In addition, we compute the scatter of the data about the best fit line as the standard deviation of the fit residuals, i.e. the standard deviation in the y -axis data after the fit line has been removed. Here, we only consider significant data ($\text{SNR} \geq 3$) and give the scatter in units of dex.

5 RESULTS

We analyse the dependence of the ratios $W_{\text{HCN}}/W_{\text{CO}(2-1)}$ (hereafter HCN/CO) and $\Sigma_{\text{SFR}}/W_{\text{HCN}}$ (hereafter SFR/HCN) as a function of the cloud-scale molecular gas properties Σ_{mol} , σ_{mol} , α_{vir} and P_{turb} . HCN/CO is used as a proxy for the dense gas fraction (f_{dense}) and SFR/HCN as a proxy for the star formation efficiency of the dense gas ($\text{SFE}_{\text{dense}} = \text{SFR}/M_{\text{dense}}$), both at 2.1 kpc physical scale, albeit with some important caveats (see Sections 2.3 and 4.2.1). The cloud-scale properties are inferred from the CO(2–1) measurements at a fixed physical scale of 150 pc. We use the CO(2–1) intensity to trace Σ_{mol} and the CO(2–1) line width to trace σ_{mol} . We trace α_{vir} and P_{turb} via $\sigma_{\text{mol}}^2/\Sigma_{\text{mol}}$ and $\sigma_{\text{mol}}^2/\Sigma_{\text{mol}}$, respectively (Section 4.3). Figure 6 shows the observed relationships. The upper panels show the HCN/CO correlations with the three molecular cloud properties (Σ_{mol} , σ_{mol} , α_{vir}) from left to right, which are discussed in Section 5.2. Similarly, the lower panels display the SFR/HCN correlations discussed in Section 5.3. For each relation we perform linear regression fitting to the data in logarithmic scale as described in Section 4.6. Moreover, we determine the Pearson correlation and corresponding p -value and compute the scatter in the fit residuals.

In addition, we examine the impact of resolution in Appendix F and find consistent results across all adopted resolutions, i.e. varying cloud-scale and kpc-scale from 75 pc to 150 pc and 1.0 kpc to 2.1 kpc, respectively. Moreover, we show the same relationships taking $\text{HCO}^+(1-0)$ or $\text{CS}(2-1)$ as a tracer of the denser molecular gas (see Appendix G and H).

CO(2–1) measurements. However, the HCN/CO uncertainties are completely dominated by the HCN(1–0) measurement uncertainties. Therefore, the uncertainties between the axes show no significant correlation and we neglect the covariance term in the fitting scheme.

¹⁰ We skip α_{vir} here, because we do not find any significant correlation with α_{vir} and thus do not perform the linear regression.

⁸ <https://linmix.readthedocs.io/en/latest/index.html>

⁹ Note that `LinMix` can also account for the covariance between uncertainties in the x - and y -axis coordinates. You may expect that the uncertainties of HCN/CO and $\langle \Sigma_{\text{mol}} \rangle$ are correlated since both axis depend on the

Table 3. HCN/CO and SFR/HCN Correlations

Cloud-scale Property	Environment	HCN/CO				SFR/HCN			
		Slope (unc.)	Interc. (unc.) ¹	Corr. ρ (p)	Scatter	Slope (unc.)	Interc. (unc.) ¹	Corr. ρ (p)	Scatter
$\langle \Sigma_{\text{mol}} \rangle$	centres + discs	0.35 (0.02)	-1.49 (0.01)	0.88 (0.0)	0.11	-0.33 (0.04)	-0.84 (0.02)	-0.63 (0.0)	0.23
	centres	0.33 (0.05)	-1.42 (0.03)	0.82 (0.0)	0.11	-0.20 (0.14)	-0.90 (0.08)	-0.31 (0.136)	0.30
	discs	0.32 (0.02)	-1.50 (0.01)	0.86 (0.0)	0.14	-0.35 (0.04)	-0.85 (0.02)	-0.66 (0.0)	0.21
$\langle \sigma_{\text{mol}} \rangle$	centres + discs	0.66 (0.04)	-1.5 (0.01)	0.85 (0.0)	0.12	-0.63 (0.07)	-0.83 (0.02)	-0.60 (0.0)	0.23
	centres	0.51 (0.13)	-1.43 (0.04)	0.69 (0.0)	0.14	-0.31 (0.27)	-0.89 (0.09)	-0.26 (0.203)	0.31
	discs	0.64 (0.05)	-1.50 (0.01)	0.83 (0.0)	0.14	-0.74 (0.08)	-0.86 (0.02)	-0.65 (0.0)	0.20
$\langle \alpha_{\text{vir}} \rangle$	centres + discs	0.21 (0.028)	-0.11 (0.226)	...
	centres	-0.12 (0.572)	0.19 (0.363)	...
	discs	0.25 (0.011)	-0.23 (0.019)	...
$\langle P_{\text{turb}} \rangle$	centres + discs	0.17 (0.01)	-1.49 (0.01)	0.88 (0.0)	0.11	-0.15 (0.02)	-0.83 (0.02)	-0.62 (0.0)	0.22
	centres	0.15 (0.03)	-1.41 (0.03)	0.75 (0.0)	0.12	-0.09 (0.07)	-0.90 (0.08)	-0.29 (0.160)	0.31
	discs	0.16 (0.01)	-1.50 (0.01)	0.89 (0.0)	0.14	-0.17 (0.02)	-0.84 (0.02)	-0.67 (0.0)	0.20

Notes. Fit parameters resulting from the linear regression of HCN/CO (tracing f_{dense}) and SFR/HCN (tracing $\text{SFE}_{\text{dense}}$) both at 2.1 kpc scale vs. molecular cloud properties (Σ_{mol} , σ_{mol} , α_{vir} , P_{turb}) at 150 pc scale. Column 2 indicates the environment considered for the fit, where centre + disc means the whole galaxy as in Figure 6. Centre and disc are defined as introduced in Section 6.1 and are shown in Figure 7. Columns 3 and 4 list the slope and intercept with corresponding uncertainty estimates as determined by the linear regression tool. Column 5 shows the Pearson correlation coefficient ρ and its corresponding p -value. Column 6 displays the y-axis scatter of the data about the best fit line measured in units of dex. Due to lack of correlation between HCN/CO, SFR/HCN and the virial parameter, we do not show linear regression results for $\langle \alpha_{\text{vir}} \rangle$, but only list the correlation coefficients and p -values based on the significant data points. Note, that for the other cloud-scale properties, the correlations coefficient (and the p -value) are determined using both the censored and the significant data.

¹ Note that the intercept is measured at ca. the median of the respective cloud-scale property as described in Section 4.6.

5.1 Dense Gas Star Formation Relation

In Figure 5, we show the relation between HCN luminosity and total infrared luminosity, measured at the native resolution of the HCN observations, as has been reported in many previous works (e.g. Lada & Lada 2003; Gao & Solomon 2004; Jiménez-Donaire et al. 2019). We inferred the total IR (TIR) luminosity from the SFR maps using the following equation (Murphy et al. 2011):

$$\frac{\Sigma_{\text{SFR}}}{\text{M}_{\odot} \text{ yr}^{-1} \text{ kpc}^{-2}} = 1.48 \times 10^{-10} \frac{\Sigma_{\text{TIR}}}{\text{L}_{\odot} \text{ kpc}^{-2}} \quad (30)$$

Overall, our HCN and SFR measurements are in agreement with previous works confirming the, to zeroth order, linear relation between HCN inferred dense gas mass and IR inferred SFR. Certainly, our data are on average 0.07 dex lower than the mean value of $\text{SFE}_{\text{dense}} = 776 \text{ L}_{\odot} (\text{K km s}^{-1})^{-1} \text{ pc}^{-2}$ reported by Jiménez-Donaire et al. (2019) and in fact consistent with the low $\text{SFE}_{\text{dense}}$ found in the Milky Way central molecular zone (CMZ).

5.2 HCN/CO vs. Molecular Cloud Properties

5.2.1 HCN/CO vs. Molecular Gas Surface Mass Density

Assuming that cloud-scale surface density traces mean volume density, we expect a positive correlation between the surface density of the molecular cloud (Σ_{mol}) and the HCN/CO line ratio as laid out in Section 2.4. The upper left panel of Figure 6 shows the observed relationship between HCN/CO and $\langle \Sigma_{\text{mol}} \rangle$ (significant data points and upper limits). The underlying red shaded region shows the model expectations which are in good agreement with the data if shifted by -1.0 dex in HCN/CO. At lower $\langle \Sigma_{\text{mol}} \rangle$, the model produces a steeper relation than the data. This discrepancy is expected and can be attributed to the simplified model, which does not account for systematic variations of the HCN emission as a function of the cloud density (see Section 2.4). Our model does not take into account the CO(2–1) or HCN(1–0) light-to-mass conversion factors $\alpha_{\text{CO}(2-1)}$

and α_{HCN} , respectively. Hence, the employed shift would imply a ratio between the conversion factors of $\alpha_{\text{HCN}}/\alpha_{\text{CO}(2-1)} \sim 10$. In agreement with the model expectations and expanding the results by Gallagher et al. (2018b), we find a strong positive correlation between HCN/CO and $\langle \Sigma_{\text{mol}} \rangle$ (see Figure 6) with Pearson correlation coefficient $\rho = 0.88$ (p -values smaller than 10^{-5}) and a linear regression slope of $m_{f,\Sigma} = 0.35 \pm 0.02$. We find small scatter of 0.11 dex about the fit line pointing towards a tight correlation.

For sub-samples of galaxies, where higher resolutions (i.e. 120 pc, 75 pc cloud-scale and 1.5 kpc, 1.0 kpc averaging-scale) can be accessed, we find comparable correlations with $\rho = 0.88$ to 0.97, $m_{f,\Sigma} = 0.35$ to 0.49 (see Appendix F1). In general, we find that the derived relationship can change significantly depending on which galaxies are included in the sample. However, for a fixed sample of galaxies the correlations are consistent for different resolutions, where smaller scales seem to show steeper slopes (a more detailed discussion is found in Appendix F1).

5.2.2 HCN/CO vs. Velocity Dispersion

Similar to the HCN/CO vs. Σ_{mol} correlation, turbulent cloud models predict a positive correlation between HCN/CO and σ_{mol} assuming the effective line width traces the turbulent Mach number (see Section 2.4). Consistent with the model expectations, we report a positive correlation between HCN/CO and $\langle \sigma_{\text{mol}} \rangle$ with Pearson correlation coefficient $\rho = 0.85$ and small p -value $< 10^{-5}$. The regression slope is $m_{f,\sigma} = 0.66 \pm 0.04$ and we find small scatter of 0.12 dex indicating a strong and tight correlation. Variations in the correlation at different resolutions (see Appendix F1) are consistent for the same sample of galaxies and follow similar systematics as seen for HCN/CO vs. $\langle \Sigma_{\text{mol}} \rangle$ which is expected due to the strong correlation between Σ_{mol} and σ_{mol} (see e.g. Sun et al. 2020b; Rosolowsky et al. 2021).

Tracing the velocity dispersion via the line width is appropriate for the discs of galaxies but may lead to biased estimates in the galactic centres (e.g. Henshaw et al. 2016). In Section 6.1, we additionally

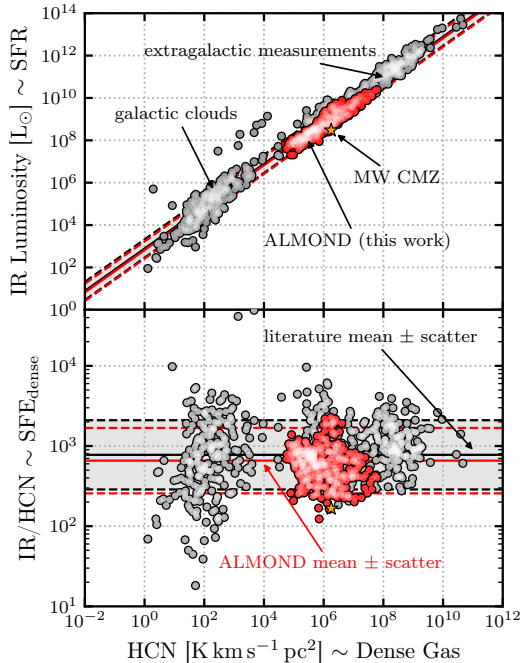
16 *L. Neumann et al.*


Figure 5. Relation between (total) infrared luminosity, tracing SFR, and HCN(1–0) luminosity, tracing dense gas mass. We show our new ALMOND data, where $S/N \geq 5$ along with MW clouds (Wu et al. 2010; Stephens et al. 2016), the CMZ, GMCs in the SMC, LMC and other low metallicity environments (Chin et al. 1997, 1998; Braine et al. 2017) as well as GMCs in other galaxies (Brouillet et al. 2005; Buchbender et al. 2013; Chen et al. 2017). Furthermore, we add other extragalactic observations, i.e. resolved nearby galaxy discs (Kewley et al. 2014; Bigiel et al. 2015; Chen et al. 2015; Usero et al. 2015; Gallagher et al. 2018a) and whole galaxies (Gao & Solomon 2004; Gao et al. 2007; Graciá-Carpio et al. 2008; Krips et al. 2008; Juneau et al. 2009; García-Burillo et al. 2012; Privon et al. 2015). The solid black line indicates the mean SFR/HCN of $10^{2.89} L_{\odot} (K km s^{-1})^{-1} pc^{-2}$ from Jiménez-Donaire et al. (2019) over their literature compilation, with the dashed lines showing the scatter of ± 0.37 dex. In addition, we show the mean ($10^{2.82} L_{\odot} (K km s^{-1})^{-1} pc^{-2}$) and scatter (± 0.41 dex) computed from the significant ($S/N \geq 5$) ALMOND data.

inspect the correlations for the central regions (defined as the central pixel of each galaxy, i.e. the inner ~ 2.1 kpc) and the discs separately (the fit parameters are listed in Table 3). We find that the correlations as obtained from the central regions are slightly offset by < 0.1 dex from the correlations associated to the discs suggesting that the kpc-scale centres are not statistically distinct to the discs.

5.2.3 HCN/CO vs. Virial Parameter

As discussed in Section 2.4, the connection between HCN/CO and the virial parameter is complex. In the simple KM theory, α_{vir} does not affect the PDF and thus keeps HCN/CO unchanged. However, the empirical α_{vir} (Equation (19)), which assumes a fixed cloud size, correlates with σ_{mol} and anti-correlates with Σ_{mol} such that, given the observed cloud-scale properties, variations in $\alpha_{vir} \propto \sigma_{mol}^2 / \Sigma_{mol}$ might be correlated with HCN/CO as shown in Figure 2.

In accordance with the model picture, we find a weak positive ($\rho =$

0.21, $p = 0.028$), but no significant correlation between HCN/CO and $\sigma_{mol}^2 / \Sigma_{mol}$ tracing the virial parameter. Here, the correlation coefficient was computed using only the significant data points (i.e., where $SNR \geq 3$, hence not including censored data as for Σ_{mol} or σ_{mol}), because the fitting algorithm does not converge.

We consistently find positive correlation coefficients, spanning $\rho = 0.21$ to 0.77 , at different resolutions which supports a positive correlation between HCN/CO and $\sigma_{mol}^2 / \Sigma_{mol}$, especially for individual galaxies (e.g. NGC 2903 or NGC 4321, which are also the ones with the highest S/N) and at smaller scales (75 pc cloud-scale and 1.0 kpc averaging-scale). However, including the complete sample of 25 galaxies, our data do not confidently suggest any correlation between HCN/CO and $\sigma_{mol}^2 / \Sigma_{mol} \propto \alpha_{vir}$.

5.2.4 HCN/CO vs. Internal Turbulent Pressure

The internal turbulent pressure, or equivalently the kinetic energy density, measures the turbulence of the gas, σ_{mol}^2 , weighted by the amount of molecular gas, Σ_{mol} , so that $P_{turb} \propto \Sigma_{mol} \sigma_{mol}^2$ (see Equation (22)). We have shown in Sections 5.2.1 and 5.2.2 that HCN/CO positively correlates with $\langle \Sigma_{mol} \rangle$ and $\langle \sigma_{mol} \rangle$. Thus, also agreeing with model predictions, we expect a positive correlation between HCN/CO and $\langle P_{turb} \rangle$. The HCN/CO vs P_{turb} relation plot is not shown in Figure 6 because it directly follows from and is almost identical to the Σ_{mol} and σ_{mol} relations. Though, the linear regression results are listed in Table 11 and the plot is shown in the Appendix F1.

As expected, we find a strong positive correlation between HCN/CO and $\langle P_{turb} \rangle$ with correlation coefficient $\rho = 0.88$ and $p < 10^{-5}$ which are very similar to the correlation coefficients found for $\langle \Sigma_{mol} \rangle$ ($\rho = 0.88$) and $\langle \sigma_{mol} \rangle$ ($\rho = 0.85$). Though, the regression slope is small ($m_{f,p} = 0.17 \pm 0.01$ due to the huge dynamic range in $\langle P_{turb} \rangle$ spanning five orders of magnitude. The scatter in the correlation is small (0.11 dex) indicating a tight correlation. Variations in the correlations as a function of resolution configurations show similar trends as for $\langle \Sigma_{mol} \rangle$ (Section 5.2.1) and $\langle \sigma_{mol} \rangle$ (Section 5.2.2).

5.3 SFR/HCN vs. Molecular Cloud Properties

5.3.1 SFR/HCN vs. Molecular Gas Surface Mass Density

Based on simple turbulent models of star formation (e.g. KM theory; Section 2.2) we expect a negative correlation between SFR/HCN and $\langle \Sigma_{mol} \rangle$. The main driver of the negative correlation is that with increasing mean density of the cloud, HCN traces more of the bulk molecular gas thus decreasing SFR/HCN (Section 2.5). The lower left panel of Figure 6 shows the relationship between SFR/HCN and $\langle \Sigma_{mol} \rangle$. The underlying model predictions (red area) is in good agreement with the data if shifted by 0.6 dex in SFR/HCN. In accordance with the model expectations, we find a negative correlation between SFR/HCN and $\langle \Sigma_{mol} \rangle$ with Pearson correlation coefficient $\rho = -0.63$ and p -value smaller than 10^{-3} . The regression slope is $m_{S,\Sigma} = -0.33 \pm 0.04$ indicating a sub-linear anti-correlation, where the scatter is 0.23 dex. Note, however, that the scatter is larger at higher $\langle \Sigma_{mol} \rangle$ and can be up to ~ 0.5 dex at $\langle \Sigma_{mol} \rangle \sim 10^3 M_{\odot} pc^{-2}$. In comparison with the HCN/CO correlations (Section 5.2.1) the SFR/HCN correlation with $\langle \Sigma_{mol} \rangle$ is weaker, but still significant. Furthermore, the scatter is roughly twice as large compared to the HCN/CO relation as also indicated by the model. The stronger scatter can be explained by the non-monotonic relation between SFR/HCN and n_0 . We find consistent results among different resolutions (for fixed galaxy sample) with the same trend of steeper correlation at smaller scales (see Appendix F2 for more details).

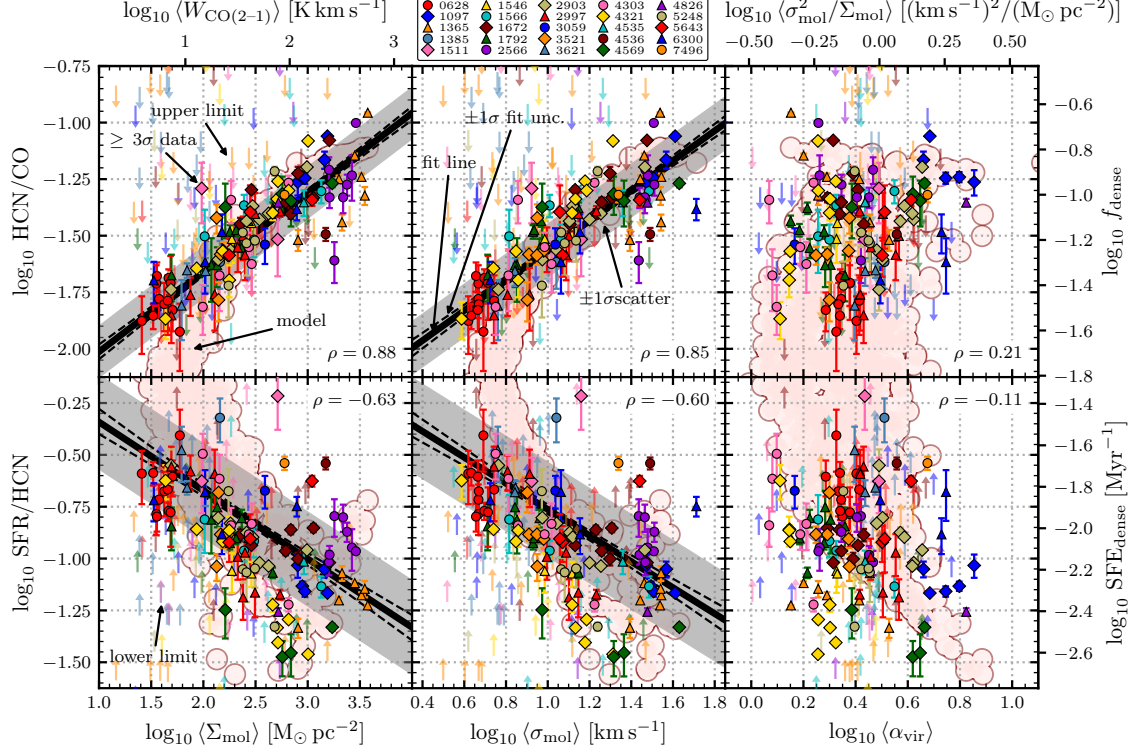


Figure 6. HCN/CO vs. $\langle X \rangle$ and SFR/HCN vs. $\langle X \rangle$ (cloud-scale = 150 pc, kpc-scale = 2.1 kpc) *Top:* HCN/CO as a proxy of dense gas fraction against molecular cloud properties ($\langle \Sigma_{\text{mol}} \rangle$, $\langle \sigma_{\text{mol}} \rangle$, $\langle \alpha_{\text{vir}} \rangle$) as obtained from CO(2–1) data from left to right. The data are binned according to Section 4.5. Filled points specify significant data with $\text{SNR}(\text{HCN}/\text{CO}) \geq 3$ and downward pointing arrows indicate 3σ upper limits on HCN/CO. The thick solid line denotes the best fit linear regression, i.e. the median realisation of the MCMC simulation. The dashed lines indicate the 1σ credibility interval of the MCMC realisations. The grey shaded area shows the scatter of the significant data about the fit line. For $\langle \alpha_{\text{vir}} \rangle$ we do not observe a correlation and thus do not fit a line to the data. *Bottom:* Analogous to the upper panels, SFR/HCN as a proxy of the star formation efficiency of the dense gas vs. molecular cloud properties from left to right. Here, upward pointing arrows denote 3σ lower limits in SFR/HCN. Again, the linear regression to $\langle \alpha_{\text{vir}} \rangle$ was not determined due to lack of correlation. The light red shaded areas show the model prediction, equivalent to the red data in Figure 2, but shifted by -1.0 dex in HCN/CO and -0.6 dex in SFR/HCN to visually overlap with the observational results.

5.3.2 SFR/HCN vs. Velocity Dispersion

As described in Section 2.5, turbulent cloud models can predict a negative correlation between SFR/HCN and the turbulence of the molecular gas due to the widening of the density PDF resulting in a lower SFR/HCN ratio. We find a negative correlation between SFR/HCN and $\langle \sigma_{\text{mol}} \rangle$ with Pearson correlation coefficient $\rho = -0.60$ and p -value smaller than 10^{-3} . We report a regression slope of $m_{S,\sigma} = -0.63 \pm 0.07$ with moderate scatter 0.23 dex. Similar to the $\langle \Sigma_{\text{mol}} \rangle$ relation, the scatter is larger at higher $\langle \sigma_{\text{mol}} \rangle$.

The correlation coefficients are very similar to the ones found for SFR/HCN vs. $\langle \Sigma_{\text{mol}} \rangle$, as expected due to the strong correlation between Σ_{mol} and σ_{mol} . The measured correlations vary with resolution and sample, where the steepness of the correlation tends to increase with the resolution, i.e. with decreasing physical scale (see Appendix F2).

5.3.3 SFR/HCN vs. Virial Parameter

Naively, one could expect that a cloud with lower virial parameter and thus higher gravitational boundedness could form stars more efficiently, suggesting an anti-correlation between SFR/HCN and α_{vir} . Moreover, assuming α_{vir} to have only little effect on the PDF, based on Equation (4), increasing α_{vir} would shift the star formation density threshold (n_{SF}) to higher densities hence decreasing SFR. In this consideration, we would expect an anti-correlation between SFR/HCN and α_{vir} . In the model description adopted here (Section 2), it is less obvious to explore the effect of α_{vir} on the log-normal PDF, the SFR and hence SFR/HCN. Yet, by assuming that α_{vir} traces $\sigma_{\text{mol}}^2/\Sigma_{\text{mol}}$, we explore variations of HCN/CO as a function of empirically based $\sigma_{\text{mol}}^2/\Sigma_{\text{mol}}$ values (red area in Figure 6) and predicted a small positive correlation ($\rho = -0.68$) with significant scatter.

In our data we find no correlation ($\rho = -0.11$, $p = 0.226$) between SFR/HCN and $\langle \sigma_{\text{mol}}^2/\Sigma_{\text{mol}} \rangle$ tracing $\langle \alpha_{\text{vir}} \rangle$, suggesting that SFR/HCN and $\langle \alpha_{\text{vir}} \rangle$ are uncorrelated. However, for the sub-sample that includes the five closest galaxies, we find $\rho = -0.53$ and $p =$

0.003 indicating a moderate negative correlation accordance with the model predictions at least for some galaxies (Appendix F2).

5.3.4 SFR/HCN vs. Internal Turbulent Pressure

Following the same reasoning as in Section 5.2, the effect of the turbulent pressure (P_{turb}) on SFR/HCN can be inferred from the expected correlations of SFR/HCN with Σ_{mol} and σ_{mol} , using $P_{\text{turb}} \propto \Sigma_{\text{mol}} \sigma_{\text{mol}}^2$. Hence, we expect a negative correlation between SFR/HCN and $\langle P_{\text{turb}} \rangle$ due to the negative correlation of SFR/HCN with both $\langle \Sigma_{\text{mol}} \rangle$ and $\langle \sigma_{\text{mol}} \rangle$. We report a negative correlation finding a Pearson correlation coefficient of $\rho = -0.62$ with p -value $< 10^{-3}$. Due to the huge dynamic range of $\langle P_{\text{turb}} \rangle$ the regression slope is shallow ($m_{\text{S,P}} = -0.15 \pm 0.02$). The scatter about the fit line is 0.22 dex very similar to the scatter seen in the $\langle \Sigma_{\text{mol}} \rangle$ and $\langle \sigma_{\text{mol}} \rangle$ relations. Similar to the SFR/HCN vs. $\langle \Sigma_{\text{mol}} \rangle$ and SFR/HCN vs. $\langle \sigma_{\text{mol}} \rangle$ correlations, we find a steeper correlation with increasing resolution, but consistent results among the same sample of galaxies (Appendix F2).

5.4 HCO⁺ and CS

Analogously to HCN(1–0) (Sections 5.2 and 5.3), we perform the same analysis using HCO⁺(1–0) as well as CS(2–1) as a tracer of the denser molecular medium. These molecular lines have expected excitation densities comparable to HCN(1–0). Therefore, we expect to find similar (anti-) correlations. Accordingly, we study how HCO⁺/CO, CS/CO and SFR/HCO⁺, SFR/CS vary with the cloud-scale molecular gas properties. The detailed results are shown in the Appendix G and H.

We find that both HCO⁺/CO and CS/CO positively correlate with $\langle \Sigma_{\text{mol}} \rangle$, $\langle \sigma_{\text{mol}} \rangle$ and $\langle P_{\text{turb}} \rangle$ with Pearson correlation coefficients ~ 0.8 and negligible p -values $< 10^{-5}$. In general, we find very similar slopes for the HCO⁺/CO and CS/CO relations as for the HCN/CO relations showing that HCN, HCO⁺ and CS are likewise sensitive to variations of the cloud-scale molecular gas properties. The scatter in the HCO⁺/CO data is slightly larger which can be explained by the slightly larger HCO⁺ measurement uncertainties. The CS/CO relations are shifted to lower values due to the lower CS brightness compared to HCN or HCO⁺. We also observe larger scatter due to the larger CS measurement uncertainties. These results show, that not only HCN/CO, but also HCO⁺/CO and CS/CO at kpc-scale are good proxies of the average density structure of the molecular gas.

As for SFR/HCN, we find that both SFR/HCO⁺ and SFR/CS anti-correlate with $\langle \Sigma_{\text{mol}} \rangle$, $\langle \sigma_{\text{mol}} \rangle$ and $\langle P_{\text{turb}} \rangle$ with $\rho \sim 0.5$ ($p < 10^{-3}$). This suggests that HCN, HCO⁺ and CS are a similarly tracing the star forming gas and that the ratios with SFR are likewise affected by variations of the cloud-scale molecular gas properties.

6 CORRELATION WITH LOCAL ENVIRONMENT

In the following, we study how the observed correlations may depend on the environment of the galaxies, where we separate the central kpc-scale regions from the discs (Section 6.1). We perform the analysis focusing on the same resolution configuration, i.e. 150 pc cloud-scale and 2.1 kpc kpc-scale, as in Section 5.

6.1 Central Regions vs. Discs

The central regions of galaxies (M51, Querejeta et al. 2019; NGC 253, Jiang et al. 2020; NGC 6946, Eibensteiner et al. 2022) as well

as the galactic CMZ (Longmore et al. 2013; Kruijssen et al. 2014; Barnes et al. 2017) are typically much denser and less efficient at forming stars from the dense gas, making them a particularly interesting environment to study as they form an interesting contrast to the discs. Therefore, we study the same relations as in Section 5 separately for the central regions and the discs. We define the central region (also referred to as "centre" throughout this section) as the single kpc-scale (i.e. 2.1 kpc) pixel at the centre of each galaxy. Note that the physical size of the galaxy centres are typically a factor of ~ 3 smaller (median size of the centre, i.e. small bulge or nucleus of the PHANGS galaxies is ~ 600 pc, Querejeta et al. 2021) compared to the 1 kpc to 2 kpc size adopted here. Therefore, we may underestimate the difference between the centres and the discs in our analysis. Given that we are sampling the maps with one sample per beam, the centre is one single pixel and consequently we do not bin the centres data. For the remaining pixels (i.e. all pixels except the centre) we perform the binning procedure as described in Section 4.5, but use 18 instead of 20 bins which results in similar bin sizes for the discs data compared to the binning of the full data. Finally, we separately fit linear functions to the data for the discs and the centres, analogous to the procedure used in Section 5 (see Figure 7).

In agreement with other studies, we find that, on average, centres appear to have higher HCN/CO by about 0.17 dex (KS p -value¹¹: $p_{\text{KS}} = 0.001$) and lower SFR/HCN by about 0.14 dex ($p_{\text{KS}} = 0.011$) across our sample of 25 nearby galaxies (see Figure 8). Nonetheless, centres also have higher Σ_{mol} and σ_{mol} , and, hence, are found to follow similar HCN/CO and SFR/HCN relations as are observed in the discs; i.e. in agreement with the model expectations and the correlations found in Section 5. This suggests that the physical connection between molecular cloud properties, density distribution and star formation is, to first order and on kpc-scales, valid independent of the local environment.

In detail, the HCN/CO against $\langle \Sigma_{\text{mol}} \rangle$ or $\langle \sigma_{\text{mol}} \rangle$ relations show very similar linear regression slopes for the centres compared to the discs (Figure 7). It is worth noting that we do see a minor offset between HCN/CO vs $\langle \Sigma_{\text{mol}} \rangle$ for centres and discs of about ~ 0.1 dex (measured as the difference in the intercepts of the fit lines at $\Sigma_{\text{mol}} = 10^{2.5} \text{ M}_{\odot} \text{ pc}^{-2}$). On the one hand, this may suggest that there are other physical parameters at play which systematically affect f_{dense} and hence HCN/CO at fixed $\langle \Sigma_{\text{mol}} \rangle$ and $\langle \sigma_{\text{mol}} \rangle$. These parameters could be connected to the galaxy's environment such as the dynamical equilibrium pressure or shear (see e.g. Federrath et al. 2016; Kruijssen et al. 2019). On the other hand, offsets in f_{dense} or Σ_{mol} may be connected to systematic variations of the α_{CO} and α_{HCN} conversion factors (see Section 6.3). Overall, although the centres are slightly (to within $1 - 2 \sigma$) offset to higher HCN/CO values, they follow the same trends with the cloud-scale molecular gas properties. Thus, also in the centres, HCN/CO appears to be a good first-order tracer of mean molecular gas density.

For the SFR/HCN correlations we do not find a significant offset between the centres and the discs as is observed for the HCN/CO correlations. However, we find a flatter slope and significantly larger scatter for the centres (~ 0.3 dex) compared to the discs (~ 0.2 dex), especially at high $\langle \Sigma_{\text{mol}} \rangle$ or $\langle \sigma_{\text{mol}} \rangle$. This increasing scatter is also seen in the model predictions (Figure 2) and is caused by the decrease of the free-fall time at large cloud densities which results in an

¹¹ The two-sample Kolmogorov-Smirnov (KS) test quantifies the significance of the difference between the distributions of two samples (Hodges 1958). Here, we test the probability p_{KS} against the null hypothesis that e.g. centres have lower HCN/CO than discs.

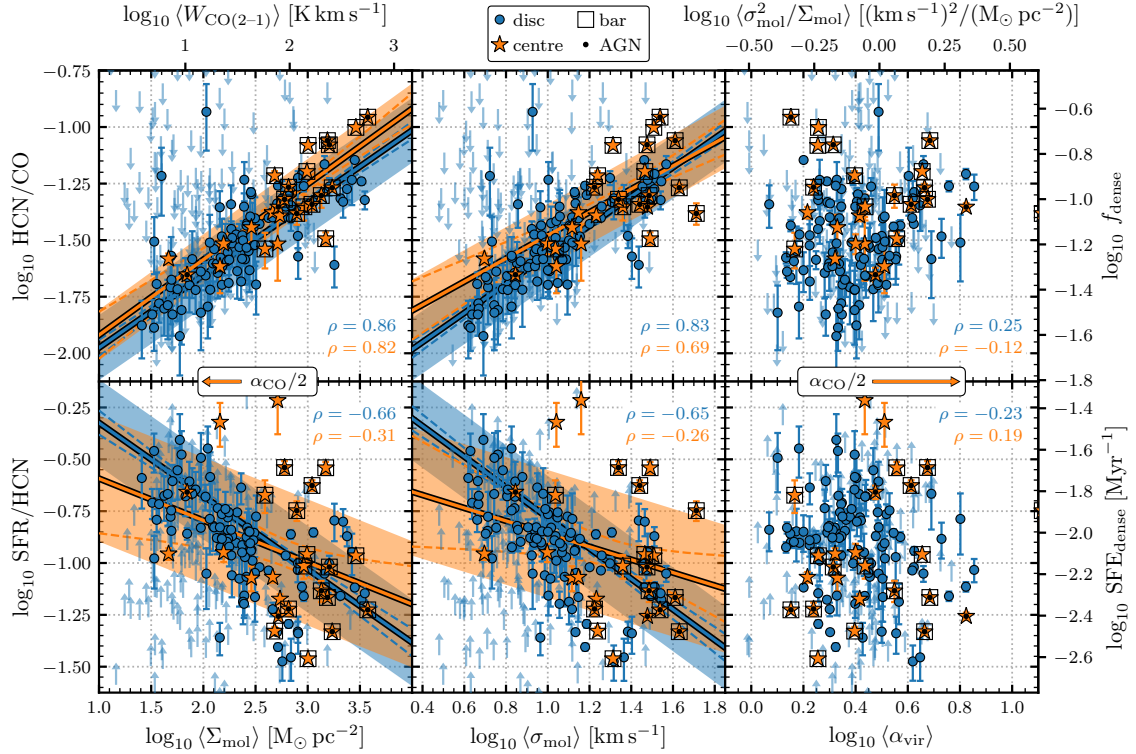


Figure 7. HCN/CO vs. $\langle X \rangle$ and SFR/HCN vs. $\langle X \rangle$ (cloud-scale = 150 pc, kpc-scale = 2.1 kpc) HCN/CO (top) and SFR/HCN (bottom) against molecular cloud properties - $\langle \Sigma_{\text{mol}} \rangle$, $\langle \sigma_{\text{mol}} \rangle$, $\langle \alpha_{\text{vir}} \rangle$ - from left to right, separately fitted for galaxy discs (blue circles) and central regions (orange stars). The shaded areas indicate the scatter and the dotted lines the 1σ credibility areas of the linear regression realisations (see Table 3 for details on the fit results). The central regions are taken as the single pixel at the galaxy centre, i.e. the inner 2.1 kpc. The remaining data points are referred to as “disc” and processed as in Section 4.5. For the central regions we indicate if the galaxies are barred (black squares) and/or contain an AGN (black circle). The length of the orange arrow labelled with $\alpha_{\text{CO}}/2$ indicates the shift of the data points in the Σ_{mol} and α_{vir} plots if α_{CO} would decrease by a factor of two.

increase of SFR/HCN at large Σ_{mol} . Therefore, the KM theory can predict both a lower and a higher SFR/HCN in the centres of galaxies depending on the turbulence of the molecular clouds. Certainly, there are alternative explanations for large variations of SFR and SFE_{dense} in galaxy centres. One idea is that star formation in galaxy centres is episodic due to stellar feedback cycles (e.g. Krumholz & Kruijssen 2015). In addition, the accretion of dense gas to the galaxy centre may vary, leading to SFR fluctuations (Seo et al. 2019; Sormani et al. 2020; Moon et al. 2022).

6.2 Impact of Bars and AGN

In addition to separating the centre from the disc, we want to study the impact of a bar or an AGN on the kpc-scale dense gas quantities in the centres of galaxies (the classifications are listed in Table 1). Sun et al. (2020b) analysed the molecular gas properties at 150 pc-scale in a larger sample of 70 PHANGS galaxies and found that gas in centres of barred galaxies have higher surface density Σ_{mol} and velocity dispersion σ_{mol} compared to gas in centres of unbarred galaxies (as noted above, the defined sizes of the centres in Sun et al. (2020b) are typically smaller than the central regions studied here). In this work, we also find that centres of barred galaxies tend to show

higher HCN/CO by about 0.25 dex ($p_{\text{KS}} = 0.0002$) (see Figures 7 and 8). SFR/HCN is only insignificantly lower ($p_{\text{KS}} = 0.436$) in barred galaxies by about 0.06 dex. Moreover, we find that molecular gas in centres of unbarred galaxies is similar in terms of HCN/CO and SFR/HCN to the values found in discs (a result reported for the molecular cloud properties by Sun et al. (2018)).

Moreover, we examine how an AGN may affect the (dense) molecular gas in the central region of galaxies. Our sample contains eleven AGN galaxies (14 without AGN). Note that there is a significant overlap between AGN and barred galaxies, so we cannot easily discriminate the impact of bars and AGN. On average, the AGN seems to boost HCN/CO in the centres of galaxies. We find 0.12 dex higher median HCN/CO ($p_{\text{KS}} = 0.040$) in the centres of AGN galaxies compared to the centres which do not harbour an AGN. These results suggest that centres of AGN galaxies have higher molecular gas surface densities and turbulence, which, following the correlations found in this work, lead to higher HCN/CO. It is less clear how AGNs affect SFR/HCN, which is only insignificantly ($p_{\text{KS}} = 0.208$) lower by 0.17 dex. Also, in some AGN galaxies, we observe higher SFR/HCN in the central regions. This could be explained by the increase of SFR/HCN at very high Σ_{mol} as seen in models, or point at more complex gas dynamics in centres.

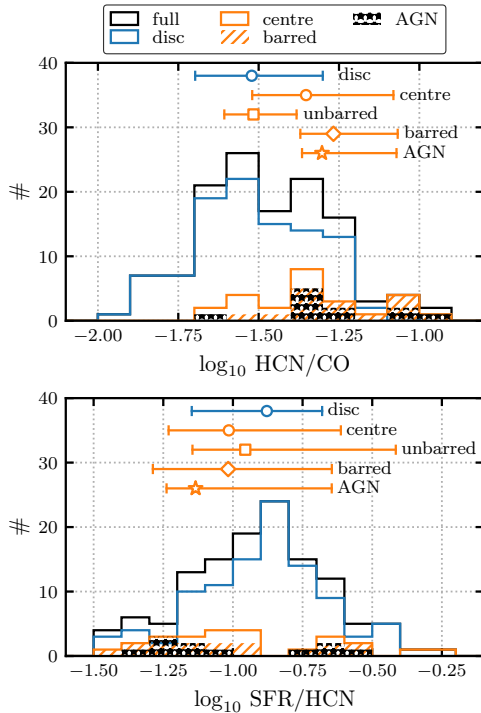
20 *L. Neumann et al.*


Figure 8. Histograms of HCN/CO (*top*) and SFR/HCN (*bottom*) at 2.1 kpc scale in different environments. The full data is shown in black. Centres and discs are colored in orange and blue in analogy with Figure 7. In addition, for the centres, we denote galaxies with a bar (diagonal hatching) or and AGN (starred hatching). The markers and lines above the histogram indicate the median and 16 to 84 percentiles of the respective data.

6.3 Conversion Factors

In Section 4.3.1 we discussed how the CO-to-H₂ conversion factor α_{CO} can vary with local environment. Most notable, α_{CO} has been observed to be lower in the centres of galaxies compared to the disc which is linked to the high surface density, turbulence and temperature yielding a brighter CO emission (see e.g. Watanabe et al. 2011; Shetty et al. 2011a,b; Papadopoulos et al. 2012; Bolatto et al. 2013; Sandstrom et al. 2013; Israel 2020; Teng et al. 2022). We note that α_{CO} can be 3 – 10 times lower in galaxy centres compared to the default MW value that is also adopted here (Israel 2020). Sandstrom et al. (2013) report a factor of ~ 2 lower α_{CO} in the central kpc regions compared to the average disc value in their sample of 26 nearby, star-forming galaxies. Therefore, we indicate how lowering α_{CO} by a factor of two in the central regions of galaxies affects the data points in the correlations studied here. In the first instance, we only consider changes in the cloud-scale properties and leave the y-axis coordinate unchanged. As denoted by the orange arrows in Figure 7), reducing α_{CO} by 0.3 dex decreases Σ_{mol} and increases α_{vir} by 0.3 dex. This has only little effect on the correlations with $\langle \Sigma_{\text{mol}} \rangle$, but would increase the offset in the correlations between the centres and the discs. Though, it would slightly increase the strength of the correlations with $\langle \alpha_{\text{vir}} \rangle$ due to making the clouds in the centres much less bound, such that we would find $\rho = 0.33$ for HCN/CO vs $\langle \alpha_{\text{vir}} \rangle$ and $\rho = -0.12$ for SFR/HCN vs $\langle \alpha_{\text{vir}} \rangle$. However, if we would

account for the power-law extension of the log-normal PDF, bound clouds would always have higher dense gas fraction thus counteracting the shift to higher virial parameter values for the centres. In the end, variations with α_{vir} remain complex and we cannot infer a clear conclusion whether HCN/CO or SFR/HCN varies significantly with α_{vir} .

We investigate how decreasing α_{CO} for the centres may affect the y-axis coordinates if HCN/CO and SFR/HCN are converted to f_{dense} and $\text{SFE}_{\text{dense}}$, respectively. In contrast to α_{CO} , there is very little information on environmental variations of α_{HCN} in the literature. We could assume that α_{HCN} varies similarly as α_{CO} , which might be justified because α_{HCN} becomes optically thick towards centres (see e.g. Jiménez-Donaire et al. 2019) yielding stronger HCN emission. Then, f_{dense} would be unaffected, while $\text{SFE}_{\text{dense}}$ would increase in the centres of galaxies thus decreasing the correlation with the cloud-scale molecular as properties. We could also assume that α_{CO} varies much more than α_{HCN} and thus neglect α_{HCN} variations. In this case, $\text{SFE}_{\text{dense}}$ would be unaffected, while f_{dense} would increase in the centres of galaxies which increases the observed correlation, but also significantly enhances the offset between centres and galaxies. The center-disc offset could only be dissolved if α_{HCN} is lowered even more than α_{CO} in the centres thus yielding a lower f_{dense} .

Overall, variations of α_{CO} and α_{HCN} will eventually change the slope and strength of the correlations, but only at the 0.3 dex level, which is not sufficient to change the direction of the relations. Primarily, the correlations are driven by the discs, which are much less affected by variations of the conversion factors than the centres. We thus, highlight that our findings show significant systematic variations of HCN/CO and SFR/HCN with cloud-scale gas properties. Independent of whether HCN/CO and SFR/HCN can be accurately translated to f_{dense} and $\text{SFE}_{\text{dense}}$, respectively, they are very useful tools to trace the mean density structure of molecular gas.

7 SUMMARY & DISCUSSION

In this work, we investigate the connection of the density-sensitive kpc-scale (2.1 kpc) HCN/CO and SFR/HCN ratios with various structural and dynamical properties (Σ_{mol} , σ_{mol} , α_{vir} , P_{turb}) of the cloud-scale (150 pc) molecular gas across 25 nearby galaxies. In the literature, HCN/CO and SFR/HCN are often synonymous with the dense gas fraction and dense gas star formation efficiency, respectively. This is based on the assumption that CO and HCN emission is originating from molecular gas differing within different (often fixed) density regimes. However, observations (e.g. Pety et al. 2017; Kauffmann et al. 2017; Barnes et al. 2020; Evans et al. 2020) and simulations (e.g. Shirley 2015; Mangum & Shirley 2015; Leroy et al. 2017a; Onus et al. 2018; Jones et al. 2021) highlight that there is still a significant uncertainty in the exact density thresholds and their mass conversion factors. In this study, we focus on the quantities HCN/CO and SFR/HCN and are careful to draw conclusions from the less certain physical quantities, i.e. f_{dense} and $\text{SFE}_{\text{dense}}$.

In Section 2 we lay out qualitative predictions about the direction of the studied correlations based on single free-fall time turbulent cloud models (e.g. the KM theory; Krumholz & McKee 2005). We find that molecular cloud properties affect the density distribution of the molecular gas such that, within this simplified model description, HCN/CO is expected to correlate and SFR/HCN to anti-correlate with molecular cloud properties like the mean density, traced by the surface density, or the Mach number, traced by the velocity dispersion of the molecular gas. The underlying physical mechanisms are that the mean density shifts the density PDF, while the Mach number

affects the width of the PDF which in return affects the line emissivity of molecular lines like CO(2–1) and HCN(1–0) as well as the star formation rate.

We compare the cloud scale properties to the kpc-scale HCN/CO and SFR/HCN via intensity-weighted averaging (Section 4.4). To quantitatively analyse the correlations, we fit a linear regression model to the data in log-log scale in order to determine a first order power-law dependence. We measure the strength of the correlation by computing the Pearson correlation coefficient and the corresponding p -value (Section 5). Moreover, we study the correlation with local environment by separately analysing the central kpc-scale regions to contrast with the discs (Section 6). In the following we summarise and interpret our main findings:

1. We report systematic variations of HCN/CO with cloud-scale molecular gas properties (Figure 6 and Section 5.2). Building up on the works of Gallagher et al. (2018a,b), we find a strong positive correlation ($\rho \approx 0.9$) between HCN/CO and the cloud-scale surface density Σ_{mol} as traced by the CO(2–1) line intensity adopting a fixed line-to-mass conversion factor $\alpha_{\text{CO}} = 4.3 \text{ M}_{\odot} \text{ pc}^{-2} (\text{K km s}^{-1})^{-1}$ (Bolatto et al. 2013) and a fixed CO(2–1)-to-CO(1–0) line ratio $R_{21} = 0.64$ (den Brok et al. 2021). The results are in agreement with the model predictions, where the mean density (assumed to be traced by Σ_{mol}) affects the median of the density PDF without altering its shape such that higher n_0 leads to higher HCN/CO. This is a powerful indication that both HCN/CO and cloud-scale CO trace density. Moreover, we observe a strong positive correlation ($\rho \approx 0.9$) between HCN/CO and the cloud-scale velocity dispersion as traced by the CO(2–1) line width in agreement with our simplified model, in which the Mach number (traced by σ_{mol}) affects the width of the density PDF such that higher \mathcal{M} leads to higher HCN/CO. These correlations also imply that HCN/CO positively correlates with the cloud-scale internal turbulent pressure as traced via $P_{\text{turb}} \propto \Sigma_{\text{mol}} \sigma_{\text{mol}}^2$. Furthermore, we find a weak ($\rho \approx 0.2$, p -value < 0.03) positive correlation between HCN/CO and the virial parameter as measured via $\alpha_{\text{vir}} \propto \sigma_{\text{mol}}^2 / \Sigma_{\text{mol}}$ which is supported by models if n_0 and \mathcal{M} are traced by the cloud-scale CO intensity and line width, respectively.
2. We report that SFR/HCN systematically varies with cloud-scale molecular gas properties (Figure 6 and Section 5.3) finding a negative correlation ($\rho \approx 0.6$) between SFR/HCN and the cloud-scale Σ_{mol} and σ_{mol} . These results are in agreement with turbulent cloud models, in which stars are assumed to form from the dense gas above some threshold density $n_{\text{SF}} \propto n_0 \alpha_{\text{vir}} \mathcal{M}^2$. Our findings show that, although SFR linearly correlates with HCN over several orders of magnitude, SFR/HCN varies systematically as a function of the cloud-scale molecular gas properties, thus disclaiming the constant $\text{SFE}_{\text{dense}}$ hypothesis put forward by Gao & Solomon (2004). Extending the works of Longmore et al. (2013); Kruijssen et al. (2014); Bigiel et al. (2016); Barnes et al. (2017); Gallagher et al. (2018a,b); Jiménez-Donaire et al. (2019); Querejeta et al. (2019); Jiang et al. (2020); Eibensteiner et al. (2022) who showed that the amount of dense gas is not enough to set the star formation rate, we conclude that SFR/HCN is significantly affected by the density distribution of molecular clouds which, based on turbulent cloud models, affects both the emissivity of dense gas tracers like HCN and the star formation rate and hence SFR/HCN. Moreover, we find no universal evidence for a correlation between SFR/HCN and $\sigma_{\text{mol}}^2 / \Sigma_{\text{mol}}$ tracing α_{vir} ($\rho \approx -0.1$, p -value ~ 0.2). For some galaxies (e.g. NGC 2903) we find indications of a negative correlation between SFR/HCN and α_{vir}

($\rho \approx -0.5$, p -value < 0.01) This trend is supported by the model predictions (Figure 2) and would point towards less bound clouds being less efficient in forming stars from a fixed fraction of dense gas.

3. Using HCO^+ or CS as a tracer of the dense molecular gas, we find the same correlations with the cloud-scale molecular gas properties as seen with HCN. This is a powerful indicator that not only HCN, but also other tracers with critical densities in excess of that of low-J CO lines like HCO^+ or CS, observed at kpc-scale, are sensitive to the density structure of the cloud-scale molecular gas.
4. Separating the central $\sim \text{kpc}$ regions from the rest of the galaxy discs. We find that centres have significantly higher HCN/CO and lower SFR/HCN compared to discs (Figure 8 and Section 6.1). Nonetheless, both environments follow similar HCN/CO and SFR/HCN trends against the cloud-scale properties (Figure 7). This suggests that the physical connection between molecular cloud properties, density distribution and star formation is independent of the local environment and extends from low density, less turbulent clouds as predominantly found in the disc to high density and turbulent clouds as found in the centres of galaxies. We also studied the impact of bars and AGN on the central regions of galaxies, finding typically higher HCN/CO and lower SFR/HCN for barred and AGN galaxies compared to their complements (unbarred and without AGN), respectively. This suggest that bars and AGNs boost HCN/CO and lower SFR/HCN in the centres of galaxies. Differences are though small ~ 0.1 dex to 0.2 dex and only significant for HCN/CO. Throughout this work we assumed a constant α_{CO} conversion factor. We study whether these scaling relations change when we assume that centres have systematically lower α_{CO} than discs which has been reported in the literature (Sandstrom et al. 2013). Adopting $\alpha_{\text{CO}}/2$ for the central regions, we find no significant effect on either the HCN/CO or the SFR/HCN relations with the cloud-scale properties.

Our findings demonstrate that density, cloud-scale molecular gas properties and star formation appear interrelated in a coherent way and one that agrees reasonably well with current models. Our results also strongly reinforce the view that HCN/CO and similar line ratios (e.g. HCO^+/CO or CS/CO) are sensitive measures of the density distribution of the molecular gas and thus powerful tools in extragalactic studies. Regardless of physical interpretation, we observe clear correlations between molecular cloud properties and line ratios sampling different physical densities. These should represent significant observational constraints on any theory attempting to relate star formation, gas density, and the ISM in galaxies. Many previous studies (e.g. Chin et al. 1997, 1998; Gao & Solomon 2004; Brouillet et al. 2005; Lada et al. 2010; Wu et al. 2010; Rosolowsky et al. 2011; García-Burillo et al. 2012; Buchbender et al. 2013; Longmore et al. 2013; Kepley et al. 2014; Chen et al. 2015; Usero et al. 2015; Bigiel et al. 2016; Chen et al. 2017; Shimajiri et al. 2017; Gallagher et al. 2018a; Jiménez-Donaire et al. 2019; Bešlić et al. 2021) show that HCN luminosity (tracing dense gas mass) and SFR are strongly correlated probing scales ranging from nearby galactic cloud to entire galaxy spanning ~ 8 orders of magnitude. Therefore, Shimajiri et al. (2017) propose a quasi-universal $\text{SFE}_{\text{dense}}$. Our results support this picture. However, all previous works as well as our results show a ~ 1 dex scatter in $\text{SFE}_{\text{dense}}$. Here, we show that this scatter is not random, but that SFR/HCN correlates with the properties of the molecular gas, i.e. Σ_{mol} and σ_{mol} , at 150 pc scale. It is still much of an open question what drives $\text{SFE}_{\text{dense}}$ in galaxy centres, where we

22 *L. Neumann et al.*

observe typically lower SFE_{dense} but also large scatter. Ultimately, we need high resolution (cloud-scale), high sensitivity spectroscopic mapping of a large sample of galaxies in order to resolve and study the effect of local environment on the dense molecular gas and star formation. This work also motivates to further investigate how spiral arms, bars and AGN may affect the density distribution of molecular gas in galaxy centres.

ACKNOWLEDGEMENTS

We would like to thank the referee for their constructive feedback that helped improve the paper. This work was carried out as part of the PHANGS collaboration. ATB, JP, JdB and FB would like to acknowledge funding from the European Research Council (ERC) under the European Union’s Horizon 2020 research and innovation programme (grant agreement No.726384/Empire). The work of AKL and MJG on the early parts of this work was partially supported by the National Science Foundation under Grants No. 1615105, 1615109, and 1653300. MC gratefully acknowledges funding from the Deutsche Forschungsgemeinschaft (DFG) through an Emmy Noether Research Group (grant number CH2137/1-1). COOL Research DAO is a Decentralized Autonomous Organization supporting research in astrophysics aimed at uncovering our cosmic origins. MC and JMDK gratefully acknowledge funding from the Deutsche Forschungsgemeinschaft (DFG) through an Emmy Noether Research Group (grant number KR4801/1-1) and the DFG Sachbeihilfe (grant number KR4801/2-1), as well as from the European Research Council (ERC) under the European Union’s Horizon 2020 research and innovation programme via the ERC Starting Grant MUSTANG (grant agreement number 714907). CE gratefully acknowledges funding from the Deutsche Forschungsgemeinschaft (DFG) Sachbeihilfe, grant number BI1546/3-1. RSK and SCOG acknowledge support from the Deutsche Forschungsgemeinschaft (DFG) in the Collaborative Research Centre (SFB 881, ID 138713538) “The Milky Way System” (subprojects A1, B1, B2, and B8) and from the Heidelberg Cluster of Excellence (EXC 2181, ID 390900948) “STRUCTURES: A unifying approach to emergent phenomena in the physical world, mathematics, and complex data”, funded by the German Excellence Strategy. RSK also thanks for funding from the European Research Council in the ERC Synergy Grant “ECOGAL – Understanding our Galactic ecosystem: From the disk of the Milky Way to the formation sites of stars and planets” (ID 855130). RSK and SCOG also benefit from computing resources provided by the State of Baden-Württemberg through bwHPC and DFG through grant INST 35/1134-1 FUGG, and from the data storage facility SDS@hd supported through grant INST 35/1314-1 FUGG, and they thank resources provided by the Leibniz Computing Centre (LRZ) for project pr74nu. MQ acknowledges support from the Spanish grant PID2019-106027GA-C44, funded by MCIN/AEI/10.13039/501100011033. ER acknowledges the support of the Natural Sciences and Engineering Research Council of Canada (NSERC), funding reference number RGPIN-2022-03499. The work of JS is partially supported by the Natural Sciences and Engineering Research Council of Canada (NSERC) through the Canadian Institute for Theoretical Astrophysics (CITA) National Fellowship. Y.-H.T. acknowledges funding support from NRAO Student Observing Support Grant SOSPADA-012 and from the National Science Foundation (NSF) under grant No. 2108081. MCS acknowledges financial support from the European Research Council via the ERC Synergy Grant “ECOGAL - Understanding our Galactic ecosystem: from the disk of the Milky Way to the formation sites of stars and planets” (grant 855130). TGW and ES acknowledge funding from the European Re-

search Council (ERC) under the European Union’s Horizon 2020 research and innovation programme (grant agreement No. 694343). AU acknowledges support from the Spanish grants PGC2018-094671-B-I00, funded by MCIN/AEI/10.13039/501100011033 and by “ERDF A way of making Europe”, and PID2019-108765GB-I00, funded by MCIN/AEI/10.13039/501100011033. K.G. is supported by the Australian Research Council through the Discovery Early Career Researcher Award (DECRA) Fellowship DE220100766 funded by the Australian Government. K.G. is supported by the Australian Research Council Centre of Excellence for All Sky Astrophysics in 3 Dimensions (ASTRO 3D), through project number CE170100013. JeP acknowledges support by the French Agence Nationale de la Recherche through the DAOISM grant ANR-21-CE31-0010, and by the Programme National “Physique et Chimie du Milieu Interstellaire” (PCMI) of CNRS/INSU with INC/INP, co-funded by CEA and CNES.

This paper makes use of the following ALMA data, which have been processed as part of the ALMOND and PHANGS–ALMA surveys:

ADS/JAO.ALMA#2012.1.00650.S,
ADS/JAO.ALMA#2013.1.01161.S,
ADS/JAO.ALMA#2015.1.00925.S,
ADS/JAO.ALMA#2015.1.00956.S,
ADS/JAO.ALMA#2017.1.00230.S,
ADS/JAO.ALMA#2017.1.00392.S,
ADS/JAO.ALMA#2017.1.00766.S,
ADS/JAO.ALMA#2017.1.00815.S,
ADS/JAO.ALMA#2017.1.00886.L,
ADS/JAO.ALMA#2018.1.01171.S,
ADS/JAO.ALMA#2018.1.01651.S,
ADS/JAO.ALMA#2018.A.00062.S,
ADS/JAO.ALMA#2019.2.00134.S,
ADS/JAO.ALMA#2021.1.00740.S,

ALMA is a partnership of ESO (representing its member states), NSF (USA), and NINS (Japan), together with NRC (Canada), NSC and ASIAA (Taiwan), and KASI (Republic of Korea), in cooperation with the Republic of Chile. The Joint ALMA Observatory is operated by ESO, AUI/NRAO, and NAOJ. The National Radio Astronomy Observatory (NRAO) is a facility of the National Science Foundation operated under cooperative agreement by Associated Universities, Inc.

This work makes use of data products from the *Wide-field Infrared Survey Explorer (WISE)*, which is a joint project of the University of California, Los Angeles, and the Jet Propulsion Laboratory/California Institute of Technology, funded by NASA.

This work is based in part on observations made with the *Galaxy Evolution Explorer (GALEX)*. GALEX is a NASA Small Explorer, whose mission was developed in cooperation with the Centre National d’Etudes Spatiales (CNES) of France and the Korean Ministry of Science and Technology. GALEX is operated for NASA by the California Institute of Technology under NASA contract NAS5-98034.

Facilities: ALMA, WISE, GALEX

Software: NumPy (Harris et al. 2020), SciPy (Virtanen et al. 2020), Astropy (Astropy Collaboration et al. 2018), pandas (The pandas development team 2021), Matplotlib (Hunter 2007), Colorcet (Kovesi 2015), LinMix (Kelly 2007)

DATA AVAILABILITY

The data used within this paper will be provided on reasonable request to the corresponding author.

REFERENCES

- Allende Prieto C., Lambert D. L., Asplund M., 2001, *ApJ*, **556**, L63
- Anand G. S., et al., 2021, *MNRAS*, **501**, 3621
- André P., Di Francesco J., Ward-Thompson D., Inutsuka S. I., Pudritz R. E., Pineda J. E., 2014, *Protostars and Planets VI*, p. 27
- Astropy Collaboration et al., 2018, *AJ*, **156**, 123
- Ballesteros-Paredes J., 2006, *MNRAS*, **372**, 443
- Barnes A. T., Longmore S. N., Battersby C., Bally J., Kruijssen J. M. D., Henshaw J. D., Walker D. L., 2017, *MNRAS*, **469**, 2263
- Barnes A. T., et al., 2020, *MNRAS*, **497**, 1972
- Bemis A., Wilson C. D., 2019, *AJ*, **157**, 131
- Bertoldi F., McKee C. F., 1992, *ApJ*, **395**, 140
- Bešlić I., et al., 2021, *MNRAS*, **506**, 963
- Bigiel F., Leroy A., Walter F., Brinks E., de Blok W. J. G., Madore B., Thornley M. D., 2008, *AJ*, **136**, 2846
- Bigiel F., Leroy A. K., Blitz L., Bolatto A. D., da Cunha E., Rosolowsky E., Sandstrom K., Usero A., 2015, *ApJ*, **815**, 103
- Bigiel F., et al., 2016, *ApJ*, **822**, L26
- Bolatto A. D., Wolfire M., Leroy A. K., 2013, *ARA&A*, **51**, 207
- Braine J., Shimajiri Y., André P., Bontemps S., Gao Y., Chen H., Kramer C., 2017, *A&A*, **597**, A44
- Brouillet N., Muller S., Herpin F., Braine J., Jacq T., 2005, *A&A*, **429**, 153
- Buchbender C., et al., 2013, *A&A*, **549**, A17
- Burkhart B., 2018, *ApJ*, **863**, 118
- CASA Team et al., 2022, *PASP*, **134**, 114501
- Chen H., Gao Y., Braine J., Gu Q., 2015, *ApJ*, **810**, 140
- Chen H., Braine J., Gao Y., Koda J., Gu Q., 2017, *ApJ*, **836**, 101
- Chin Y. N., Henkel C., Whiteoak J. B., Millar T. J., Hunt M. R., Lemme C., 1997, *A&A*, **317**, 548
- Chin Y. N., Henkel C., Millar T. J., Whiteoak J. B., Marx-Zimmer M., 1998, *A&A*, **330**, 901
- Draine B. T., 2011, *Physics of the Interstellar and Intergalactic Medium*
- Eibensteiner C., et al., 2022, arXiv e-prints, p. arXiv:2201.02209
- Evans Neal J. I., Kim K.-T., Wu J., Chao Z., Heyer M., Liu T., Nguyen-Lu'o'ng Q., Kauffmann J., 2020, *ApJ*, **894**, 103
- Federrath C., Klessen R. S., 2012, *ApJ*, **761**, 156
- Federrath C., Klessen R. S., 2013, *ApJ*, **763**, 51
- Federrath C., Klessen R. S., Schmidt W., 2008, *ApJ*, **688**, L79
- Federrath C., Roman-Duval J., Klessen R. S., Schmidt W., Mac Low M. M., 2010, *A&A*, **512**, A81
- Federrath C., et al., 2016, *ApJ*, **832**, 143
- Gallagher M. J., et al., 2018a, *ApJ*, **858**, 90
- Gallagher M. J., et al., 2018b, *ApJ*, **868**, L38
- Gao Y., Solomon P. M., 2004, *ApJ*, **606**, 271
- Gao Y., Carilli C. L., Solomon P. M., Vanden Bout P. A., 2007, *ApJ*, **660**, L93
- García-Burillo S., Usero A., Alonso-Herrero A., Graciá-Carpio J., Pereira-Santaella M., Colina L., Planesas P., Arribas S., 2012, *A&A*, **539**, A8
- Girichidis P., Konstantin L., Whitworth A. P., Klessen R. S., 2014, *ApJ*, **781**, 91
- Goldsmith P., Kauffmann J., 2018, in *American Astronomical Society Meeting Abstracts #231*, p. 130.06
- Graciá-Carpio J., García-Burillo S., Planesas P., Fuente A., Usero A., 2008, *A&A*, **479**, 703
- Harris C. R., et al., 2020, *Nature*, **585**, 357
- Hennebelle P., Chabrier G., 2011, *ApJ*, **743**, L29
- Henshaw J. D., et al., 2016, *MNRAS*, **457**, 2675
- Heyer M. H., Carpenter J. M., Snell R. L., 2001, *ApJ*, **551**, 852
- Hodges J. L., 1958, *Arkiv for Matematik*, **3**, 469
- Hunter J. D., 2007, *Computing in Science and Engineering*, **9**, 90
- Israel F. P., 2020, *A&A*, **635**, A131
- Jiang X.-J., et al., 2020, *MNRAS*, **494**, 1276
- Jiménez-Donaire M. J., et al., 2017, *MNRAS*, **466**, 49
- Jiménez-Donaire M. J., et al., 2019, *ApJ*, **880**, 127
- Jones G. H., Clark P. C., Glover S. C. O., Hacar A., 2021, arXiv e-prints, p. arXiv:2112.05543
- Juneau S., Narayanan D. T., Moustakas J., Shirley Y. L., Bussmann R. S., Kennicutt R. C. J., Vanden Bout P. A., 2009, *ApJ*, **707**, 1217
- Kainulainen J., Beuther H., Henning T., Plume R., 2009, *A&A*, **508**, L35
- Kauffmann J., Bertoldi F., Bourke T. L., Evans N. J. I., Lee C. W., 2008, *A&A*, **487**, 993
- Kauffmann J., Goldsmith P. F., Melnick G., Tolls V., Guzman A., Menten K. M., 2017, *A&A*, **605**, L5
- Kelly B. C., 2007, *ApJ*, **665**, 1489
- Kennicutt Robert C. J., 1998, *ApJ*, **498**, 541
- Kennicutt R. C., Evans N. J., 2012, *ARA&A*, **50**, 531
- Kepley A. A., Leroy A. K., Frayer D., Usero A., Marvil J., Walter F., 2014, *ApJ*, **780**, L13
- Klessen R. S., Glover S. C. O., 2016, *Saas-Fee Advanced Course*, **43**, 85
- Kovesi P., 2015, arXiv e-prints, p. arXiv:1509.03700
- Krips M., Neri R., García-Burillo S., Martín S., Combes F., Graciá-Carpio J., Eckart A., 2008, *ApJ*, **677**, 262
- Kruijssen J. M. D., Longmore S. N., Elmegreen B. G., Murray N., Bally J., Testi L., Kennicutt R. C., 2014, *MNRAS*, **440**, 3370
- Kruijssen J. M. D., et al., 2019, *MNRAS*, **484**, 5734
- Krumholz M. R., Kruijssen J. M. D., 2015, *MNRAS*, **453**, 739
- Krumholz M. R., McKee C. F., 2005, *ApJ*, **630**, 250
- Krumholz M. R., Thompson T. A., 2007, *ApJ*, **669**, 289
- Lada C. J., Lada E. A., 2003, *ARA&A*, **41**, 57
- Lada C. J., Lombardi M., Alves J. F., 2010, *ApJ*, **724**, 687
- Lang P., et al., 2020, *ApJ*, **897**, 122
- Leroy A. K., et al., 2009, *AJ*, **137**, 4670
- Leroy A. K., et al., 2013, *AJ*, **146**, 19
- Leroy A. K., et al., 2016, *ApJ*, **831**, 16
- Leroy A. K., et al., 2017a, *ApJ*, **835**, 217
- Leroy A. K., et al., 2017b, *ApJ*, **846**, 71
- Leroy A. K., et al., 2019, *ApJS*, **244**, 24
- Leroy A. K., et al., 2021a, arXiv e-prints, p. arXiv:2109.11583
- Leroy A. K., et al., 2021b, *ApJS*, **255**, 19
- Leroy A. K., et al., 2021c, *ApJS*, **257**, 43
- Longmore S. N., et al., 2013, *MNRAS*, **429**, 987
- Mangum J. G., Shirley Y. L., 2015, *PASP*, **127**, 266
- Martin D. C., et al., 2005, *ApJ*, **619**, L1
- McKee C. F., Zweibel E. G., 1992, *ApJ*, **399**, 551
- Molina F. Z., Glover S. C. O., Federrath C., Klessen R. S., 2012, *MNRAS*, **423**, 2680
- Moon S., Kim W.-T., Kim C.-G., Ostriker E. C., 2022, *ApJ*, **925**, 99
- Murphy E. J., et al., 2011, *ApJ*, **737**, 67
- Onus A., Krumholz M. R., Federrath C., 2018, *MNRAS*, **479**, 1702
- Padoan P., Nordlund Å., 2002, *ApJ*, **576**, 870
- Padoan P., Nordlund Å., 2011, *ApJ*, **730**, 40
- Padoan P., Federrath C., Chabrier G., Evans N. J. I., Johnstone D., Jørgensen J. K., McKee C. F., Nordlund Å., 2014, *Protostars and Planets VI*, p. 77
- Papadopoulos P. P., van der Werf P., Xilouris E., Isaak K. G., Gao Y., 2012, *ApJ*, **751**, 10
- Pety J., et al., 2017, *A&A*, **599**, A98
- Privon G. C., et al., 2015, *ApJ*, **814**, 39
- Querejeta M., et al., 2015, *ApJS*, **219**, 5
- Querejeta M., et al., 2019, *A&A*, **625**, A19
- Querejeta M., et al., 2021, *A&A*, **656**, A133
- Rosolowsky E., Leroy A., 2006, *PASP*, **118**, 590
- Rosolowsky E., Pineda J. E., Gao Y., 2011, *MNRAS*, **415**, 1977
- Rosolowsky E., et al., 2021, *MNRAS*, **502**, 1218
- Salim S., et al., 2016, *ApJS*, **227**, 2
- Salim S., Boquien M., Lee J. C., 2018, *ApJ*, **859**, 11
- Sandstrom K. M., et al., 2013, *ApJ*, **777**, 5
- Schmidt M., 1959, *ApJ*, **129**, 243
- Schneider N., et al., 2015, *A&A*, **578**, A29
- Schruba A., et al., 2011, *AJ*, **142**, 37
- Seo W.-Y., Kim W.-T., Kwak S., Hsieh P.-Y., Han C., Hopkins P. F., 2019, *ApJ*, **872**, 5
- Shetty R., Glover S. C., Dullemond C. P., Klessen R. S., 2011a, *MNRAS*, **412**, 1686

24 *L. Neumann et al.*

- Shetty R., Glover S. C., Dullemond C. P., Ostriker E. C., Harris A. I., Klessen R. S., 2011b, *MNRAS*, **415**, 3253
- Shimajiri Y., et al., 2017, *A&A*, **604**, A74
- Shirley Y. L., 2015, *PASP*, **127**, 299
- Sormani M. C., Tress R. G., Glover S. C. O., Klessen R. S., Battersby C. D., Clark P. C., Hatchfield H. P., Smith R. J., 2020, *MNRAS*, **497**, 5024
- Stephens I. W., Jackson J. M., Whitaker J. S., Contreras Y., Guzmán A. E., Sanhueza P., Foster J. B., Rathborne J. M., 2016, *ApJ*, **824**, 29
- Sun J., et al., 2018, *ApJ*, **860**, 172
- Sun J., et al., 2020a, *ApJ*, **892**, 148
- Sun J., et al., 2020b, *ApJ*, **901**, L8
- Teng Y.-H., et al., 2022, *ApJ*, **925**, 72
- The pandas development team 2021, Pandas-Dev/Pandas: Pandas, doi:10.5281/zenodo.5574486
- Tielens A. G. G. M., 2010, The Physics and Chemistry of the Interstellar Medium
- Usero A., et al., 2015, *AJ*, **150**, 115
- Utomo D., et al., 2018, *ApJ*, **861**, L18
- Véron-Cetty M. P., Véron P., 2010, *A&A*, **518**, A10
- Virtanen P., et al., 2020, *Nature Methods*, **17**, 261
- Watanabe Y., Sorai K., Kuno N., Habe A., 2011, *MNRAS*, **411**, 1409
- Wong T., Blitz L., 2002, *ApJ*, **569**, 157
- Wright E. L., et al., 2010, *AJ*, **140**, 1868
- Wu J., Evans Neal J. I., Gao Y., Solomon P. M., Shirley Y. L., Vanden Bout P. A., 2005, *ApJ*, **635**, L173
- Wu J., Evans Neal J. I., Shirley Y. L., Knez C., 2010, *ApJS*, **188**, 313
- den Brok J. S., et al., 2021, *MNRAS*,

APPENDIX A: CLOUD-SCALE MOLECULAR GAS PROPERTIES

Figure A1 displays the velocity dispersion of the molecular gas (σ_{mol}) against its surface density (Σ_{mol}) for all individual sightlines across the full sample of 22 galaxies at 150 pc resolution (blue data points) similar to figure 1 in Sun et al. 2020b. σ_{mol} and Σ_{mol} are inferred from the CO(2-1) observations as described in Sections 4.3.1 and 4.3.2, respectively. The plot also shows loci of constant virial parameter (α_{vir}) and internal turbulent pressure (P_{turb}) as obtained from the CO(2-1) observations as described in Sections 4.3.3 and 4.3.4, respectively, such that $\alpha_{\text{vir}} \propto \sigma_{\text{mol}}^2 / \Sigma_{\text{mol}}$ and $P_{\text{turb}} \propto \Sigma_{\text{mol}} \sigma_{\text{mol}}^2$ at fixed scale (here: 150 pc). Moreover, we indicate the intensity-weighted averages (red points) of the 150 pc measurements at 2.1 kpc averaging scale following Section 4.4. We find that the distribution of the weighted averages in the $\sigma_{\text{mol}} - \Sigma_{\text{mol}}$ plane resembles the distribution of the (original) high resolution measurements very well, providing similar dynamic range in both σ_{mol} and Σ_{mol} . However, the weighted averages show significantly lower dynamic range in α_{vir} . Note that the loci of constant α_{vir} and P_{turb} are not valid for the weighted averages, because we take the weighted averages of the cloud-scale properties individually for each quantity, such that $\langle \alpha_{\text{vir}} \rangle \neq \langle \sigma_{\text{mol}} \rangle^2 / \langle \Sigma_{\text{mol}} \rangle$ and $\langle P_{\text{turb}} \rangle \neq \langle \Sigma_{\text{mol}} \rangle \langle \sigma_{\text{mol}} \rangle^2$.

APPENDIX B: SPECTRAL STACKING

In order to recover more emission, in particular outside of galaxy centers, we perform spectral stacking of the HCN(1-0), HCO⁺(1-0) and CS(2-1) cubes as in Schrubba et al. (2011); Jiménez-Donaire et al. (2017, 2019); Bešlić et al. (2021). The basic idea is that the spectral axis is matched with a known velocity field from a high significance prior, i.e. here CO(2-1). After shuffling the velocities, we average the spectra in bins defined by the galactocentric radius (r_{gal}). We select five bins up to $r_{\text{gal}} = 5$ kpc with bin widths of 2 kpc. In Figure 3, we show the resulting stacked spectra (bottom

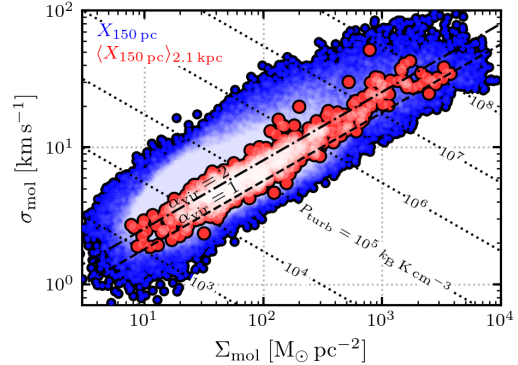


Figure A1. Molecular gas velocity dispersion (σ_{mol}) against surface density (Σ_{mol}) at 150 pc scale across 22 nearby galaxies. The blue points denote the original 150 pc resolution measurements, while the red points are the intensity-weighted averages obtained at 2.1 kpc apertures. The loci of constant virial parameter (α_{vir}) and internal turbulent pressure (P_{turb}) are obtained assuming fixed cloud size, i.e. $\alpha_{\text{vir}} \propto \sigma_{\text{mol}}^2 / \Sigma_{\text{mol}}$ (Equation 19), $P_{\text{turb}} \propto \Sigma_{\text{mol}} \sigma_{\text{mol}}^2$ (Equation 22, and are only valid for the original 150 pc measurements.

Table B1. HCN detection fraction across the 25 ALMOND galaxies

r_{gal} [kpc]	Sightlines		Stacking	
	$N_{\text{det}}/N_{\text{tot}}$	N_{frac} [%]	$N_{\text{det}}/N_{\text{tot}}$	N_{frac} [%]
0 – 2	79/171	46.3	25/25	100
2 – 4	78/473	16.6	21/25	84
4 – 6	49/601	8.1	9/25	36
6 – 8	19/696	2.8	5/25	20
8 – 10	6/705	0.9	2/25	8

Notes. HCN(1-0) detection fraction as a function galactocentric radius. N_{det} is the number of detected spectra for individual lines-of-sight (left), or the radially stacked spectra (right), where the S/N of the integrated intensity $> 3 \sigma$. N_{tot} is the total number of spectra inside the radial bin. $N_{\text{frac}} = N_{\text{det}}/N_{\text{tot}}$ depicts the detection fraction.

panels) and stacked integrated intensities (a). A complete atlas of the remaining 24 ALMOND galaxies is presented in Appendix J. The spectral stacking results demonstrate that, despite the low detection rate at the pixel level across much of the molecular gas discs, we are able to recover significant emission of HCN(1-0) HCO⁺(1-0) and CS(2-1) outside of galaxy centres via stacking at the expense of spatial information. We detect significant HCN emission out to 6 kpc in more than a third (9/25) of the galaxies compared to only 3% for individual sightlines (Table B1), which demonstrates that stacking can successfully unveil HCN emission across most of the molecular gas discs. In particular, these results motivate the binning approach described in Section 4.5, where we average the HCN data in bins of $\langle W_{\text{CO}(2-1)} \rangle$. The two approaches, binning and stacking, yield very similar results within $\sim 10\%$, on average, and without bias (Gallagher et al. 2018b).

APPENDIX C: WEIGHTED AVERAGES

In Section 4.4, we explain the idea of computed intensity-weighted averages from the high-resolution CO data in order to compare with

the coarse-scale dense gas observations using the following equation:

$$\langle X \rangle_{\text{Conv.}} = \frac{(X \cdot W_{\text{CO}(2-1)}) * \Omega}{W_{\text{CO}(2-1)} * \Omega}, \quad (\text{C1})$$

where X is the high-resolution quantity (e.g. Σ_{mol}) and Ω is the convolution kernel to go from the high to the coarse resolution. Sun et al. (2020a) computed the weighted averages inside sharp apertures, such that:

$$\langle X \rangle_{\text{Aper.}} = \frac{\sum_{i \in \text{Aper.}} X_i \cdot I_{\text{CO}(2-1),i}}{\sum_{i \in \text{Aper.}} I_{\text{CO}(2-1),i}}. \quad (\text{C2})$$

We compare the two methods for the galaxy NGC 2903 in Figure C1. While both methods lead to very similar results in the centre or along the bar, there are large discrepancies for the adjacent pixels, where the aperture method produces much lower values. The aperture approach is not affected by any Gaussian kernel dilution and thus useful if the aperture based weighted averages are used to study individually or for comparison with other aperture based weighted averages. However, comparison with observations performed at or convolved to the averaging scale should only be done using the convolution based method, which is symmetrically affected by beam dilution.

APPENDIX D: LINEAR REGRESSION

Linear regression of astronomical data is far from trivial and it is crucial to apply a linear fitting routine which is tailored to the science question and the noise properties of the data appropriately. Here, we ask the question of how the cloud-scale molecular gas properties (x data) affect the dense gas fraction and star formation efficiency (y data). Statistically speaking, the x data can be considered as the independent variable and the y data as the dependent variable, such that we seek to constrain $y(x) = b + m \cdot x$, where $b, m = \text{const.}$ In principle one could also ask the inverted question, i.e. how x depends on y and thus constrain $x(y) = b' + m' \cdot y$ ($b', m' = \text{const.}$). However, based on the formulated science question and given that the x data are detected significantly throughout most of the discs of all galaxies, as opposed to the y data, where about 50% of the data points are censored (here we consider the fully processed, binned data which enters the fitting routine), it is well-grounded to consider x as the independent variable.

We detect HCN significantly ($S/N \geq 3$) only for about 50% of the binned data points. Hence, we have many censored data points, which result in upper limits (HCN/CO) or lower limits (SFR/HCN). Although these data are not significant, it is still valuable information: we know with high certainty (99.7%) that the emission of that data point can not be larger than 3σ thus providing an upper limit. This information should be taken into account in the fitting routine to better constrain the assumed correlation and linear dependence. In addition, conversion to log-log scale can generate a bias in the estimated linear regression if censored data are not taken into account. Moreover, the true correlation most likely does not perfectly follow a linear correlation. Also, there is not necessarily a physical model which predicts a linear dependence (power-law in linear scale) between the x and y data. Thus, we need to account for an intrinsic scatter in the correlation. Even more so, it is important to account for the intrinsic scatter and the data uncertainties separately, in order to get reasonable regression uncertainties (s. Kelly 2007).

Given our science question and the properties of our data, we want to use a linear regression tool which constrains the linear correlation

of the dependent variable y as a function of the independent variable x , while taking into account measurement uncertainties in both variables, intrinsic scatter about the regression and censored y data. All of these requirements are met by the Python regression tool *LinMix* which implements the Bayesian approach to linear regression introduced by Kelly 2007. The tool assumes that the true data distribution is sampled from a superposition of Gaussians in x and y . It performs a Markov chain Monte Carlo (MCMC) simulation using the Gibbs sampler to explore the posterior distribution, i.e. the true distribution of the regression parameters. *LinMix* is capable of computing the Pearson correlation coefficient using both the significant and the censored data. Due to its statistical approach, the tool naturally finds trustworthy constraints on the regression parameters (intercept and slope) and also gives credibility areas, which we use to illustrate the uncertainty of the linear fits.

In astronomy it is very common to determine the power-law of two astronomical quantities by converting the data from linear to logarithmic scale and fitting a line through the data. However, this procedure has some drawbacks. First, conversion to logarithmic scale is only valid for positive data, and negative data (i.e. negative intensities which arise from the data reduction and represent mostly noise) is removed. As a consequence the log-scale data is biased towards positive values and thus biases the linear regression. We can mitigate this bias by using a linear regression tool which can handle censored data and thus takes the insignificant and negative data into account. Next, conversion to logarithmic scale produces asymmetric uncertainties, i.e. if the uncertainties are symmetric in linear scale, they appear shorter in the positive and larger in the negative direction. Again, this will bias the linear regression if the regression tool assumes symmetric uncertainties, because it either overestimates the uncertainties in positive direction or underestimates the uncertainties in negative direction. We note that the fitting routine applied here is affected by this bias. Though, we are not aware of any regression tool which can take into account asymmetric uncertainties in addition to handling censored data. Moreover, we estimated the expected log-scale induced bias with the following simulation: To estimate the bias of the linear regression we start with the measured x -data and produce perfectly correlated y -data in logarithmic scale. Then we convert to linear scale and add Gaussian noise with amplitudes matching the measurement uncertainties. We also add Gaussian intrinsic scatter with amplitude as obtained from the linear regression of the observed data. Finally we convert back to logarithmic scale and run the fitting algorithm. Figure D1 shows the result customized to the HCN/CO vs. $\langle W_{\text{CO}(2-1)} \rangle$ correlation. We find that the determined linear regression slope is in fact biased towards lower values by about $\sim 10\%$. In general, repeating this procedure for the other correlations, we find that the determined slopes are probably $\sim 10\%$ flatter compared to the true correlation, if it were perfectly correlated.

APPENDIX E: LINE-OF-SIGHT CORRELATIONS

In Section 4.5, we explain how we bin the data via $\langle W_{\text{CO}(2-1)} \rangle$ to recover more emission, especially in the low $\langle W_{\text{CO}(2-1)} \rangle$ regime. We show in Appendix B, that averaging data via a high significant prior, i.e. CO(2–1), is effectively unveiling more emission in the CO-emitting regions. As a consequence, the binning method allows us to constrain the relations between HCN/CO, SFR/HCN and the cloud-scale properties with higher significance and with a higher weighting of the significant measurements. However, binning is expected to reduce the scatter in the binned quantities, i.e. HCN/CO and SFR/HCN, thus potentially reducing the scatter and increasing the

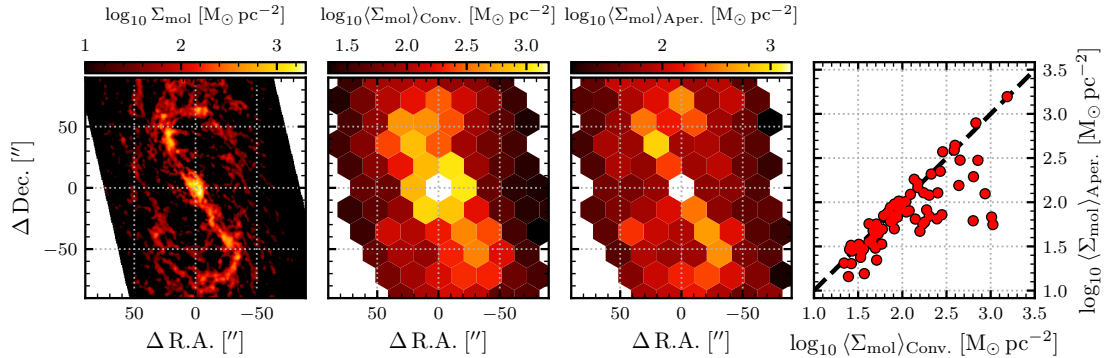
26 *L. Neumann et al.*


Figure C1. Comparison between different approaches of computing intensity-weighted averages. *Left:* Molecular gas surface density (Σ_{mol}) map of NGC 2903 at 75 pc resolution. *Centre left:* Intensity-weighted average Σ_{mol} map at 1 kpc scale based on the Gaussian convolution as defined by Equation 24. This method is employed in this work to compare with the native kpc-scale observations, i.e. the HCN data. *Centre right:* Intensity-weighted averages based on sharp apertures defined as the hexagonal shaped pixels. This method has been applied by e.g. Sun et al. (2020b). *Right:* Pixel-by-pixel comparison between the aperture and convolution based approaches.

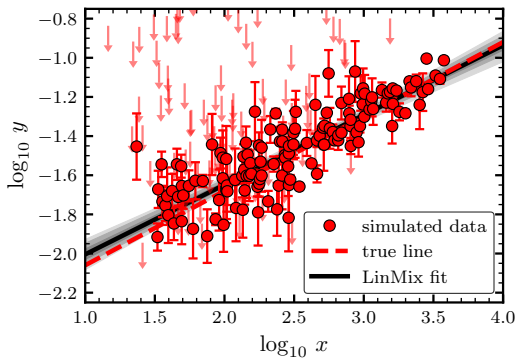


Figure D1. Bias estimation of the linear regression results. Adapted to the HCN/CO (y data) vs. $\langle \Sigma_{\text{mol}} \rangle$ (x data) correlation, we use the $\langle \Sigma_{\text{mol}} \rangle$ data and create perfectly correlated (linear relation) y data, indicated by the red dotted line. Then we add Gaussian noise using the measurement uncertainties in HCN/CO, $\langle \Sigma_{\text{mol}} \rangle$ and also add intrinsic scatter based on the estimated intrinsic scatter of the measured data. Finally, we apply the *LinMix* fitting routine to determine the best fit linear regression (black solid line) and the $\{1, 2, 3\}$ -sigma credibility regions (grey shaded areas).

measured correlation. Therefore, we also present the HCN/CO and SFR/HCN correlations with $\langle \Sigma_{\text{mol}} \rangle$, $\langle \sigma_{\text{mol}} \rangle$, $\langle \alpha_{\text{vir}} \rangle$ using the individual line-of-sight (LOS) measurements (Figure E1). We perform the linear regression on the LOS measurements analogous to Section 5, i.e. taking into account measurement uncertainties, intrinsic scatter and censored data. Qualitatively, we find the same results for the LOS data as for the binned data, i.e. a positive (negative) correlation between HCN/CO (SFR/HCN) with the cloud-scale molecular gas properties. Certainly, we find lower correlations and higher scatter (Table E1). The lower correlation is however partly due to the higher statistical weight of the censored data (higher fraction of censored data taken into account in the fit).

 MNRAS **000**, 1–29 (2023)

APPENDIX F: VARIATION WITH RESOLUTION

We study the HCN/CO and SFR/HCN correlations as a function of the cloud-scale and large-scale resolutions choosing three cloud-scale physical resolutions (75 pc, 120 pc, 150 pc) associated with the CO(2-1) data and three large-scale physical resolutions (1.0 kpc, 1.5 kpc, 2.1 kpc) associated with the HCN data defined as the highest available common resolutions for galaxies inside 11.6 kpc ("highres"; 3 galaxies), 15.3 kpc ("midres"; 9 galaxies), 23.4 kpc ("lowres"; 22 galaxies), respectively. In addition we measure the correlations at the native angular resolutions of the CO(2-1) and HCN observations ("natres"; 22 galaxies). This defines the finest resolution configuration available but accesses different physical scales. The adopted resolution configurations are listed in Table F1.

The resolution configurations introduced above include different galaxy samples. In order to investigate the dependence of the correlations on the adopted resolutions for fixed samples of galaxies we introduce sub-samples of the natres, lowres and midres configurations marked by the suffixed "midtar" and "hightar". Midtar and hightar denote the sub-sample of galaxies which are included in the midres and highres sample, respectively. For instance lowres-hightar denotes the lowres resolution configuration (150 pc cloud-scale, 2.1 kpc large-scale), but only includes the sub-sample of three galaxies which are also included in highres. Figure I1 shows a compilation of the HCN/CO and SFR/HCN correlations for the different resolution configurations. Complementary, Table I1 lists the linear regression results for all adopted resolution configurations.

Overall, we report similar HCN/CO and SFR/HCN correlations with the cloud-scale molecular gas properties across all resolution configurations, where the linear regression parameters are in agreement with each other if the galaxy sample is fixed. For varying samples of galaxies we observe significant deviations in the linear regression slope in some cases indicating galaxy-to-galaxy variations in the HCN/CO and SFR/HCN relations.

F1 HCN/CO vs. Molecular Cloud Properties

For the physically homogenised resolution configurations we consistently find strong positive correlations between HCN/CO and $\langle \Sigma_{\text{mol}} \rangle$,

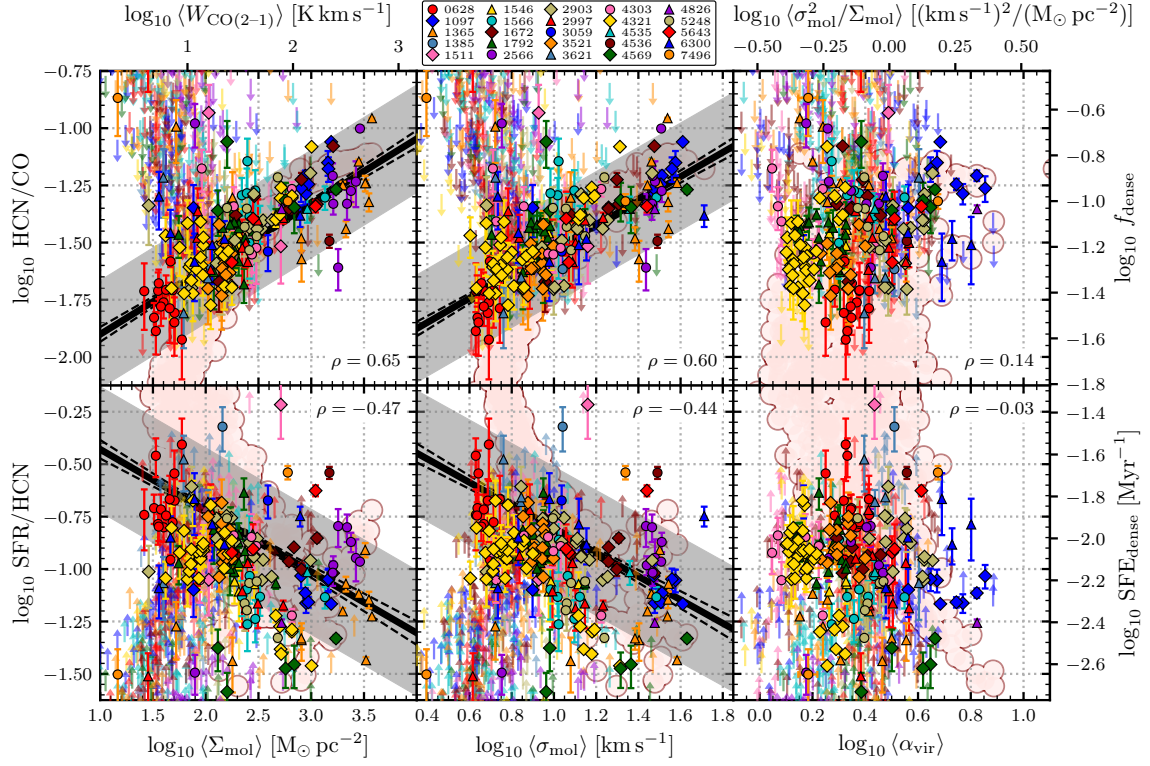


Figure E1. Analogous to Figure 6, but for individual line-of-sight measurements, i.e. without binning the data.

Table E1. HCN/CO and SFR/HCN Correlations

Cloud-scale Property	Data	HCN/CO				SFR/HCN			
		Slope (unc.)	Interc. (unc.) ¹	Corr. ρ (p)	Scatter	Slope (unc.)	Interc. (unc.) ¹	Corr. ρ (p)	Scatter
$\langle \Sigma_{\text{mol}} \rangle$	sightlines	0.28 (0.02)	-1.47 (0.01)	0.65 (0.0)	0.24	-0.29 (0.03)	-0.87 (0.02)	-0.47 (0.0)	0.30
	binned	0.35 (0.02)	-1.49 (0.01)	0.88 (0.0)	0.11	-0.33 (0.04)	-0.84 (0.02)	-0.63 (0.0)	0.23
$\langle \sigma_{\text{mol}} \rangle$	sightlines	0.53 (0.04)	-1.48 (0.01)	0.60 (0.0)	0.23	-0.56 (0.06)	-0.87 (0.02)	-0.44 (0.0)	0.30
	binned	0.66 (0.04)	-1.5 (0.01)	0.85 (0.0)	0.12	-0.63 (0.07)	-0.83 (0.02)	-0.60 (0.0)	0.23
$\langle \alpha_{\text{vir}} \rangle$	sightlines	0.14 (0.059)	-0.03 (0.643)	...
	binned	0.21 (0.028)	-0.11 (0.226)	...
$\langle P_{\text{turb}} \rangle$	sightlines	0.13 (0.01)	-1.48 (0.01)	0.66 (0.0)	0.23	-0.14 (0.02)	-0.86 (0.02)	-0.48 (0.0)	0.30
	binned	0.17 (0.01)	-1.49 (0.01)	0.88 (0.0)	0.11	-0.15 (0.02)	-0.83 (0.02)	-0.62 (0.0)	0.22

Notes. Linear regression parameters analogous to Table II using lowres resolution configuration (HCN/CO, SFR/HCN at 2.1 kpc scale; molecular cloud properties (Σ_{mol} , σ_{mol} , α_{vir} , P_{turb}) at 150 pc scale). The table shows results obtained from individual line-of-sight measurements corresponding to Figure E1, as well as from binned data corresponding to Figure 6.

¹ Note that the intercept is measured at ca. the median of the respective cloud-scale property as described in Section 4.6.

$\langle \sigma_{\text{mol}} \rangle$ and $\langle P_{\text{turb}} \rangle$ (see Figure II (top) and Table II (left)) with Pearson correlation coefficients ranging from $\rho = 0.70$ to 0.82 , 0.61 to 0.79 and 0.60 to 0.79 , respectively, with p-values all smaller than 10^{-5} . For any given correlation (e.g. HCN/CO vs $\langle \Sigma_{\text{mol}} \rangle$), the regression slopes vary among different physical resolution configurations and samples of galaxies, spanning $m_{f,\Sigma} = 0.35$ to 0.54 , $m_{f,\sigma} = 0.51$ to 0.93 and $m_{f,P} = 0.12$ to 0.24 . Though, the linear regression

parameters are in agreement within the 1σ uncertainties for fixed galaxy sample, meaning resolution does not significantly affect the observed relation between HCN/CO and the molecular cloud properties. For instance, for the HCN/CO vs $\langle \Sigma_{\text{mol}} \rangle$ correlation we find $\rho = 0.70, 0.73, 0.81$ and $m_{f,\Sigma} = 0.35 \pm 0.09, 0.37 \pm 0.09, 0.51 \pm 0.10$ for lowres-hightar, midres-hightar and highres, respectively, all in agreement within the 1σ uncertainty limits. In contrast, for fixed res-

28 *L. Neumann et al.*
Table F1. Resolutions

Sample	Galaxies	Resolution			
		lowres (150 pc) _{2.1 kpc}	midres (120 pc) _{1.5 kpc}	highres (75 pc) _{1.0 kpc}	natres ($\sim 1''$) _{$\sim 20''$}
full	NGC 0628, NGC 1097, NGC 1365, NGC 1385, NGC 1511, NGC 1546, NGC 1566, NGC 1672, NGC 1792, NGC 2566, NGC 2903, NGC 2997, NGC 3059, NGC 3521, NGC 3621, NGC 4303, NGC 4321, NGC 4535, NGC 4536, NGC 4569, NGC 4826, NGC 5248, NGC 5643, NGC 6300, NGC 7496	✓	✗	✗	✓
midtar	NGC 0628, NGC 1097, NGC 1511, NGC 2903, NGC 2997, NGC 3521, NGC 3621, NGC 4321, NGC 4826, NGC 5248, NGC 5643, NGC 6300	✓	✓	✗	✓
hightar	NGC 0628, NGC 2903, NGC 3621, NGC 4826, NGC 6300	✓	✓	✓	✓

Notes. Column 2 shows the galaxies included in the respective (sub-) samples resulting from the accessible galaxies at given resolutions. The full sample can reach 150 pc cloud-scale and 2.1 kpc kpc-scale resolution. For the midtar and hightar samples the accessible resolutions are 120 pc cloud-scale, 1.5 kpc kpc-scale and 75 pc cloud-scale, 1.0 kpc kpc-scale, respectively.

olution but varying sample we observe slopes deviating more than 1σ , e.g. midres and midres-hightar lead to $m_{f,\Sigma} = 0.54 \pm 0.06$ and 0.37 ± 0.09 . This points towards a galaxy-to-galaxy variation of the studied HCN/CO relations. However, these variations are not huge, because within the 2σ uncertainty range all resolution configuration are again consistent. In general, we find the trend of increasing correlation and steeper slopes for decreasing scale, i.e. at higher resolution, suggesting a small but systematic resolution dependence of the correlations. For the correlation of HCN/CO with the virial parameter ($\langle\alpha_{\text{vir}}\rangle$) we find much lower correlation coefficients spanning $\rho = 0.17$ to 0.59 and p-values from 10^{-3} to 0.10 suggesting a weak positive correlation between HCN/CO and $\langle\alpha_{\text{vir}}\rangle$. However, the stronger positive correlation seen in the hightar configurations is mainly produced by one galaxy, i.e. NGC 2903, and is not confidently seen in the other targets. Note also that the dynamic range in $\langle\alpha_{\text{vir}}\rangle$ is barely 1 dex so that we might be insensitive to any potentially existing correlation with α_{vir} . In the end, we have no convincing evidence for a correlation between HCN/CO and $\langle\alpha_{\text{vir}}\rangle$.

Above all, studying the HCN/CO correlations with molecular cloud properties at different resolutions leads to consistent results which confidently demonstrates a positive correlation between HCN/CO and $\langle\Sigma_{\text{mol}}\rangle$, $\langle\sigma_{\text{mol}}\rangle$, $\langle P_{\text{turb}}\rangle$, with the trend of increasing correlation with increasing resolution (decreasing scale). The correlation of HCN/CO with $\langle\alpha_{\text{vir}}\rangle$ remains less clear. But consistently positive correlation coefficients point towards weak positive correlation between HCN/CO and $\langle\alpha_{\text{vir}}\rangle$.

F2 SFR/HCN vs. Molecular Cloud Properties

We consistently find negative correlations between SFR/HCN and the cloud-scale properties $\langle\Sigma_{\text{mol}}\rangle$, $\langle\sigma_{\text{mol}}\rangle$, $\langle P_{\text{turb}}\rangle$ across all adopted resolution configurations (see Figure 11 (bottom) and Table 11 (right), where Pearson correlation coefficients range from -0.45 to -0.63 ($\langle\Sigma_{\text{mol}}\rangle$), -0.33 to -0.56 ($\langle\sigma_{\text{mol}}\rangle$) and -0.32 to -0.59 ($\langle P_{\text{turb}}\rangle$) and slopes span $m_{S,\Sigma} = -0.23$ to -0.49 , $m_{S,\sigma} = -0.27$ to -0.78 and $m_{S,p} = -0.06$ to -0.21 for the physically homogenised resolutions. Compared to the HCN/CO correlations, the strength of the SFR/HCN correlation is about 0.2 lower and the intrinsic scatter about the median regression line is 2 – 3 times as large, indicating a weaker correlation and suggesting potentially other physical processes in setting SFR/HCN. Still, we find strong evidence for a negative corre-

lation between SFR/HCN and the aforementioned cloud properties at all resolutions. Moreover, the lack of correlation between SFR/HCN and $\langle\alpha_{\text{vir}}\rangle$ found at the lowest resolution (lowres) is also supported at higher resolution. In fact, the correlation coefficients are $|\rho| < 0.2$ at maximum with p-values as large as 0.98 indicating a very weak negative or no correlation with the virial parameter. The dependence on resolution follows similar systematics as of HCN/CO meaning the correlation increases and the slope steepens for increasing resolution, i.e. decreasing physical scale.

Overall, based on different resolution configurations we find strong evidence for a negative correlation between SFR/HCN tracing $\text{SFE}_{\text{dense}}$ and molecular cloud properties $\langle\Sigma_{\text{mol}}\rangle$, $\langle\sigma_{\text{mol}}\rangle$ and $\langle P_{\text{turb}}\rangle$, where the correlation and steepness of the slope seems to increase with increasing resolution. Furthermore, we find no correlation between SFR/HCN and $\langle\alpha_{\text{vir}}\rangle$. The opposite sign in the correlations compared to HCN/CO points towards an anti-correlation between SFR/HCN and HCN/CO and thus $\text{SFE}_{\text{dense}}$ and $\text{SFE}_{\text{dense}}$.

APPENDIX G: HCO⁺/CO AND SFR/HCO⁺ CORRELATIONS

In analogy to the HCN/CO and the SFR/HCN correlations we show the results of the determined HCO⁺/CO and SFR/HCO⁺ correlations in Figure 12 and in Table 12. First and foremost, we find the same correlations and anti-correlations between the HCO⁺ spectroscopic measurements with the molecular cloud properties as of HCN with similar correlation coefficients, slopes and scatter. Thus, at 1 kpc to 2 kpc resolution, HCN(1-0) and HCO⁺(1-0) are sensitive to the same density variations.

APPENDIX H: CS/CO AND SFR/CS CORRELATIONS

In analogy to the HCN/CO and the SFR/HCN correlations we show the results of the determined CS/CO and SFR/CS correlations in Figure 12 and in Table 12. Despite the much lower signal-to-noise of the CS data we recover the same trends with cloud-scale molecular gas properties as seen for HCN or HCO⁺, though with larger uncertainties.

APPENDIX I: INDIVIDUAL GALAXIES

In Figure 14, we show the same HCN/CO against $\langle \Sigma_{\text{mol}} \rangle$ correlations as in Figure 6 (left panels), but for each galaxy individually.

APPENDIX J: SUPPLEMENTS: ALMOND ATLAS

In Figures J1 to J24, we show supplemental plots analogues to Figure 3 for the remaining 24 galaxies of the ALMOND sample.

This paper has been typeset from a \LaTeX file prepared by the author.

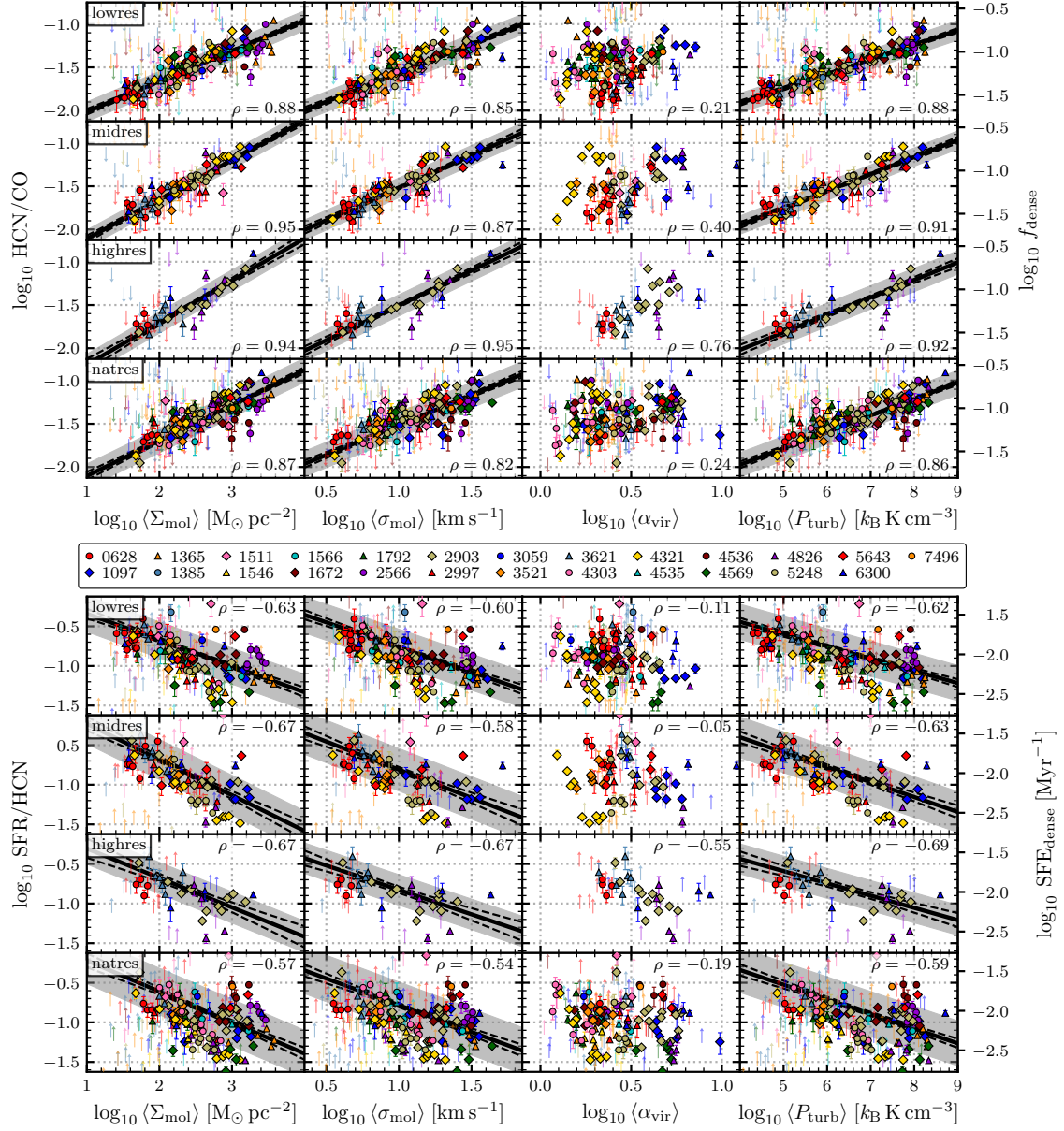
30 *L. Neumann et al.*


Figure 11. HCN/CO (top) vs. $\langle X \rangle$ and SFR/HCN (bottom) vs. $\langle X \rangle$ at different resolutions listed in Table F1. The solid line shows the best fit line where the dotted line is the 1σ uncertainty. The grey shaded area indicates the scatter of the significant data about the fit line.

Table 11. HCN/CO and SFR/HCN Correlations

Cloud-scale Property	Resolution	HCN/CO				SFR/HCN			
		Slope (unc.)	Interc. (unc.)	Corr. ρ (p)	Scatter	Slope (unc.)	Interc. (unc.)	Corr. ρ (p)	Scatter
$\langle \Sigma_{\text{mol}} \rangle$	natres	0.41 (0.03)	-1.49 (0.01)	0.87 (0.0)	0.14	-0.39 (0.05)	-0.81 (0.03)	-0.57 (0.0)	0.29
$\langle \Sigma_{\text{mol}} \rangle$	natres-midtar	0.5 (0.03)	-1.46 (0.01)	0.94 (0.0)	0.12	-0.46 (0.07)	-0.85 (0.03)	-0.60 (0.0)	0.29
$\langle \Sigma_{\text{mol}} \rangle$	natres-hightar	0.5 (0.04)	-1.47 (0.02)	0.95 (0.0)	0.10	-0.44 (0.1)	-0.86 (0.05)	-0.66 (0.0)	0.24
$\langle \Sigma_{\text{mol}} \rangle$	lowres	0.35 (0.02)	-1.49 (0.01)	0.88 (0.0)	0.11	-0.33 (0.04)	-0.84 (0.02)	-0.63 (0.0)	0.23
$\langle \Sigma_{\text{mol}} \rangle$	lowres-midtar	0.43 (0.02)	-1.44 (0.01)	0.95 (0.0)	0.10	-0.42 (0.05)	-0.93 (0.03)	-0.7 (0.0)	0.20
$\langle \Sigma_{\text{mol}} \rangle$	lowres-hightar	0.39 (0.03)	-1.43 (0.02)	0.97 (0.0)	0.07	-0.31 (0.06)	-0.90 (0.04)	-0.73 (0.0)	0.13
$\langle \Sigma_{\text{mol}} \rangle$	midres	0.46 (0.03)	-1.43 (0.01)	0.95 (0.0)	0.10	-0.45 (0.06)	-0.91 (0.03)	-0.67 (0.0)	0.25
$\langle \Sigma_{\text{mol}} \rangle$	midres-hightar	0.41 (0.04)	-1.43 (0.02)	0.92 (0.0)	0.10	-0.37 (0.08)	-0.89 (0.05)	-0.66 (0.0)	0.19
$\langle \Sigma_{\text{mol}} \rangle$	highres	0.49 (0.04)	-1.46 (0.02)	0.94 (0.0)	0.12	-0.37 (0.08)	-0.86 (0.04)	-0.67 (0.0)	0.20
$\langle \sigma_{\text{mol}} \rangle$	natres	0.69 (0.05)	-1.45 (0.01)	0.82 (0.0)	0.15	-0.67 (0.09)	-0.85 (0.03)	-0.54 (0.0)	0.29
$\langle \sigma_{\text{mol}} \rangle$	natres-midtar	0.80 (0.06)	-1.40 (0.02)	0.88 (0.0)	0.14	-0.74 (0.13)	-0.90 (0.04)	-0.56 (0.0)	0.29
$\langle \sigma_{\text{mol}} \rangle$	natres-hightar	0.81 (0.09)	-1.38 (0.02)	0.9 (0.0)	0.13	-0.71 (0.17)	-0.93 (0.05)	-0.61 (0.0)	0.26
$\langle \sigma_{\text{mol}} \rangle$	lowres	0.66 (0.04)	-1.5 (0.01)	0.85 (0.0)	0.12	-0.63 (0.07)	-0.83 (0.02)	-0.60 (0.0)	0.23
$\langle \sigma_{\text{mol}} \rangle$	lowres-midtar	0.69 (0.05)	-1.49 (0.01)	0.88 (0.0)	0.10	-0.65 (0.10)	-0.87 (0.03)	-0.61 (0.0)	0.22
$\langle \sigma_{\text{mol}} \rangle$	lowres-hightar	0.58 (0.07)	-1.52 (0.02)	0.9 (0.0)	0.08	-0.46 (0.1)	-0.83 (0.03)	-0.68 (0.0)	0.13
$\langle \sigma_{\text{mol}} \rangle$	midres	0.75 (0.06)	-1.44 (0.02)	0.87 (0.0)	0.11	-0.71 (0.11)	-0.88 (0.03)	-0.58 (0.0)	0.27
$\langle \sigma_{\text{mol}} \rangle$	midres-hightar	0.63 (0.07)	-1.48 (0.02)	0.89 (0.0)	0.10	-0.56 (0.13)	-0.84 (0.04)	-0.64 (0.0)	0.19
$\langle \sigma_{\text{mol}} \rangle$	highres	0.81 (0.07)	-1.42 (0.02)	0.95 (0.0)	0.12	-0.62 (0.13)	-0.89 (0.04)	-0.67 (0.0)	0.19
$\langle \alpha_{\text{vir}} \rangle$	natres	0.24 (0.01)	-0.19 (0.037)	...
$\langle \alpha_{\text{vir}} \rangle$	natres-midtar	0.41 (0.001)	-0.15 (0.233)	...
$\langle \alpha_{\text{vir}} \rangle$	natres-hightar	0.73 (0.0)	-0.53 (0.003)	...
$\langle \alpha_{\text{vir}} \rangle$	lowres	0.21 (0.028)	-0.11 (0.226)	...
$\langle \alpha_{\text{vir}} \rangle$	lowres-midtar	0.46 (0.0)	-0.12 (0.325)	...
$\langle \alpha_{\text{vir}} \rangle$	lowres-hightar	0.76 (0.0)	-0.53 (0.005)	...
$\langle \alpha_{\text{vir}} \rangle$	midres	0.4 (0.001)	-0.05 (0.666)	...
$\langle \alpha_{\text{vir}} \rangle$	midres-hightar	0.77 (0.0)	-0.54 (0.005)	...
$\langle \alpha_{\text{vir}} \rangle$	highres	0.76 (0.0)	-0.55 (0.002)	...
$\langle P_{\text{turb}} \rangle$	natres	0.19 (0.01)	-1.5 (0.01)	0.86 (0.0)	0.14	-0.19 (0.02)	-0.80 (0.03)	-0.59 (0.0)	0.28
$\langle P_{\text{turb}} \rangle$	natres-midtar	0.22 (0.01)	-1.49 (0.02)	0.92 (0.0)	0.12	-0.2 (0.03)	-0.82 (0.04)	-0.6 (0.0)	0.28
$\langle P_{\text{turb}} \rangle$	natres-hightar	0.22 (0.02)	-1.52 (0.02)	0.95 (0.0)	0.10	-0.19 (0.04)	-0.82 (0.05)	-0.68 (0.0)	0.23
$\langle P_{\text{turb}} \rangle$	lowres	0.17 (0.01)	-1.49 (0.01)	0.88 (0.0)	0.11	-0.15 (0.02)	-0.83 (0.02)	-0.62 (0.0)	0.22
$\langle P_{\text{turb}} \rangle$	lowres-midtar	0.18 (0.01)	-1.47 (0.01)	0.92 (0.0)	0.10	-0.17 (0.02)	-0.88 (0.03)	-0.64 (0.0)	0.21
$\langle P_{\text{turb}} \rangle$	lowres-hightar	0.15 (0.01)	-1.5 (0.02)	0.94 (0.0)	0.08	-0.12 (0.02)	-0.84 (0.03)	-0.71 (0.0)	0.13
$\langle P_{\text{turb}} \rangle$	midres	0.2 (0.01)	-1.46 (0.01)	0.91 (0.0)	0.11	-0.19 (0.03)	-0.87 (0.03)	-0.63 (0.0)	0.26
$\langle P_{\text{turb}} \rangle$	midres-hightar	0.16 (0.02)	-1.49 (0.02)	0.89 (0.0)	0.11	-0.15 (0.03)	-0.84 (0.04)	-0.67 (0.0)	0.19
$\langle P_{\text{turb}} \rangle$	highres	0.20 (0.02)	-1.51 (0.02)	0.92 (0.0)	0.14	-0.15 (0.03)	-0.82 (0.04)	-0.69 (0.0)	0.19

Notes. HCN/CO (tracing f_{dense}) and SFR/HCN (tracing $\text{SFE}_{\text{dense}}$) vs. molecular cloud properties - Σ_{mol} , σ_{mol} , α_{vir} , P_{turb} - correlations for all adopted resolution configurations. Columns 3 and 4 list the slope and intercept with its uncertainty estimates as determined by the linear regression. Column 5 shows the Pearson correlation coefficient ρ and its corresponding p-value. Column 6 displays the scatter, i.e. the standard deviation of the fit residuals of the significant (SNR > 3) data. Due to lack of correlation between HCN/CO or SFR/HCN and the virial parameter, we do not show linear regression results, but only list the correlation coefficient and p-value based on the significant data points. Note, that for the other cloud-scale properties, the correlation coefficient (and the p-value) are determined using both the censored and the significant data.

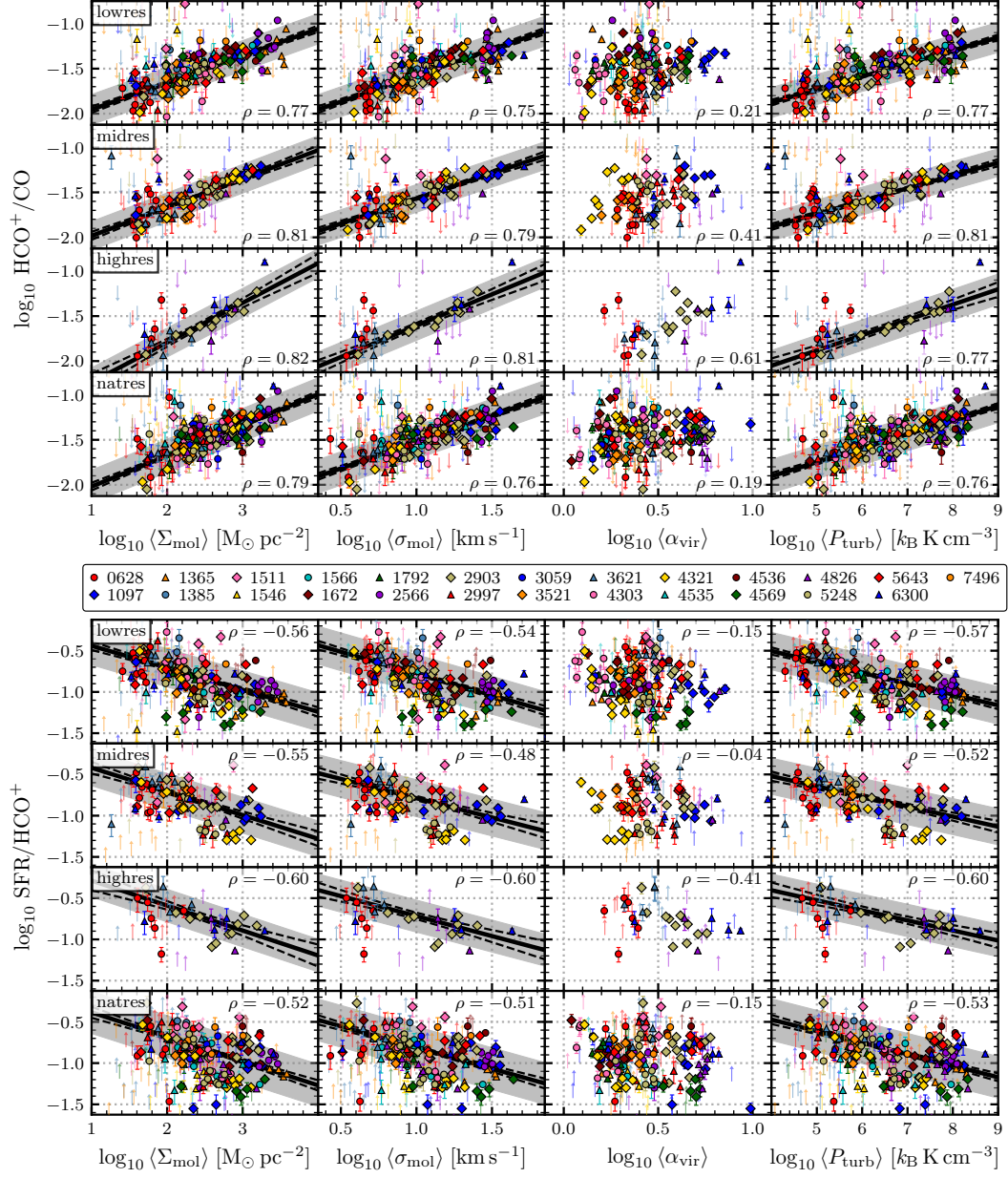
32 *L. Neumann et al.*


Figure 12. HCO^+/CO (top) vs. $\langle X \rangle$ and SFR/HCO^+ (bottom) vs. $\langle X \rangle$ at different resolutions listed in Table F1.

Table 12. HCO⁺/CO and SFR/HCO⁺ Correlations

Cloud-scale Property	Res. Config.	HCO ⁺ /CO				SFR/HCO ⁺			
		Slope (unc.)	Interc. (unc.)	Corr. ρ (p)	Scatter	Slope (unc.)	Interc. (unc.)	Corr. ρ (p)	Scatter
$\langle \Sigma_{\text{mol}} \rangle$	natres	0.34 (0.03)	-1.51 (0.01)	0.79 (0.0)	0.18	-0.3 (0.04)	-0.83 (0.02)	-0.52 (0.0)	0.26
$\langle \Sigma_{\text{mol}} \rangle$	natres-midtar	0.39 (0.04)	-1.52 (0.02)	0.82 (0.0)	0.19	-0.32 (0.06)	-0.83 (0.03)	-0.51 (0.0)	0.26
$\langle \Sigma_{\text{mol}} \rangle$	natres-hightar	0.39 (0.05)	-1.55 (0.03)	0.82 (0.0)	0.17	-0.3 (0.09)	-0.79 (0.04)	-0.53 (0.0)	0.24
$\langle \Sigma_{\text{mol}} \rangle$	lowres	0.3 (0.02)	-1.51 (0.01)	0.77 (0.0)	0.17	-0.27 (0.03)	-0.84 (0.02)	-0.56 (0.0)	0.23
$\langle \Sigma_{\text{mol}} \rangle$	lowres-midtar	0.33 (0.03)	-1.51 (0.02)	0.84 (0.0)	0.15	-0.31 (0.05)	-0.87 (0.03)	-0.6 (0.0)	0.20
$\langle \Sigma_{\text{mol}} \rangle$	lowres-hightar	0.3 (0.05)	-1.53 (0.03)	0.76 (0.0)	0.12	-0.21 (0.06)	-0.80 (0.04)	-0.58 (0.0)	0.14
$\langle \Sigma_{\text{mol}} \rangle$	midres	0.32 (0.03)	-1.51 (0.02)	0.81 (0.0)	0.16	-0.29 (0.05)	-0.85 (0.03)	-0.55 (0.0)	0.22
$\langle \Sigma_{\text{mol}} \rangle$	midres-hightar	0.22 (0.07)	-1.56 (0.05)	0.52 (0.0)	0.20	-0.15 (0.07)	-0.78 (0.05)	-0.39 (0.01)	0.19
$\langle \Sigma_{\text{mol}} \rangle$	highres	0.44 (0.06)	-1.57 (0.03)	0.82 (0.0)	0.16	-0.30 (0.08)	-0.74 (0.04)	-0.60 (0.0)	0.20
$\langle \sigma_{\text{mol}} \rangle$	natres	0.59 (0.05)	-1.47 (0.01)	0.76 (0.0)	0.19	-0.51 (0.07)	-0.86 (0.02)	-0.51 (0.0)	0.25
$\langle \sigma_{\text{mol}} \rangle$	natres-midtar	0.63 (0.06)	-1.47 (0.02)	0.79 (0.0)	0.20	-0.51 (0.10)	-0.86 (0.03)	-0.48 (0.0)	0.26
$\langle \sigma_{\text{mol}} \rangle$	natres-hightar	0.6 (0.1)	-1.49 (0.03)	0.76 (0.0)	0.18	-0.43 (0.14)	-0.84 (0.05)	-0.46 (0.0)	0.25
$\langle \sigma_{\text{mol}} \rangle$	lowres	0.58 (0.05)	-1.52 (0.01)	0.75 (0.0)	0.17	-0.53 (0.07)	-0.83 (0.02)	-0.54 (0.0)	0.23
$\langle \sigma_{\text{mol}} \rangle$	lowres-midtar	0.58 (0.05)	-1.55 (0.01)	0.83 (0.0)	0.15	-0.50 (0.09)	-0.83 (0.03)	-0.54 (0.0)	0.20
$\langle \sigma_{\text{mol}} \rangle$	lowres-hightar	0.48 (0.08)	-1.6 (0.02)	0.79 (0.0)	0.11	-0.35 (0.09)	-0.76 (0.03)	-0.62 (0.0)	0.13
$\langle \sigma_{\text{mol}} \rangle$	midres	0.56 (0.05)	-1.51 (0.02)	0.79 (0.0)	0.15	-0.47 (0.1)	-0.84 (0.03)	-0.48 (0.0)	0.22
$\langle \sigma_{\text{mol}} \rangle$	midres-hightar	0.42 (0.10)	-1.57 (0.04)	0.62 (0.0)	0.19	-0.27 (0.11)	-0.76 (0.04)	-0.42 (0.006)	0.18
$\langle \sigma_{\text{mol}} \rangle$	highres	0.7 (0.10)	-1.54 (0.03)	0.81 (0.0)	0.16	-0.48 (0.12)	-0.77 (0.04)	-0.60 (0.0)	0.19
$\langle \alpha_{\text{vir}} \rangle$	natres	0.19 (0.023)	-0.15 (0.069)	...
$\langle \alpha_{\text{vir}} \rangle$	natres-midtar	0.36 (0.001)	-0.17 (0.115)	...
$\langle \alpha_{\text{vir}} \rangle$	natres-hightar	0.34 (0.044)	-0.26 (0.134)	...
$\langle \alpha_{\text{vir}} \rangle$	lowres	0.21 (0.013)	-0.15 (0.069)	...
$\langle \alpha_{\text{vir}} \rangle$	lowres-midtar	0.44 (0.0)	-0.14 (0.22)	...
$\langle \alpha_{\text{vir}} \rangle$	lowres-hightar	0.78 (0.0)	-0.53 (0.003)	...
$\langle \alpha_{\text{vir}} \rangle$	midres	0.41 (0.0)	-0.04 (0.738)	...
$\langle \alpha_{\text{vir}} \rangle$	midres-hightar	0.61 (0.001)	-0.3 (0.122)	...
$\langle \alpha_{\text{vir}} \rangle$	highres	0.61 (0.001)	-0.41 (0.034)	...
$\langle P_{\text{turb}} \rangle$	natres	0.16 (0.01)	-1.51 (0.01)	0.76 (0.0)	0.19	-0.14 (0.02)	-0.82 (0.02)	-0.53 (0.0)	0.25
$\langle P_{\text{turb}} \rangle$	natres-midtar	0.17 (0.02)	-1.54 (0.02)	0.8 (0.0)	0.19	-0.14 (0.03)	-0.81 (0.03)	-0.51 (0.0)	0.26
$\langle P_{\text{turb}} \rangle$	natres-hightar	0.16 (0.03)	-1.59 (0.03)	0.78 (0.0)	0.18	-0.13 (0.04)	-0.77 (0.04)	-0.54 (0.0)	0.24
$\langle P_{\text{turb}} \rangle$	lowres	0.14 (0.01)	-1.51 (0.01)	0.77 (0.0)	0.17	-0.13 (0.02)	-0.83 (0.02)	-0.57 (0.0)	0.23
$\langle P_{\text{turb}} \rangle$	lowres-midtar	0.15 (0.01)	-1.54 (0.01)	0.84 (0.0)	0.15	-0.13 (0.02)	-0.84 (0.02)	-0.59 (0.0)	0.20
$\langle P_{\text{turb}} \rangle$	lowres-hightar	0.13 (0.02)	-1.58 (0.02)	0.83 (0.0)	0.10	-0.09 (0.02)	-0.77 (0.03)	-0.67 (0.0)	0.13
$\langle P_{\text{turb}} \rangle$	midres	0.14 (0.01)	-1.53 (0.02)	0.81 (0.0)	0.15	-0.12 (0.02)	-0.83 (0.03)	-0.52 (0.0)	0.22
$\langle P_{\text{turb}} \rangle$	midres-hightar	0.1 (0.03)	-1.59 (0.04)	0.58 (0.0)	0.19	-0.07 (0.03)	-0.76 (0.04)	-0.44 (0.004)	0.18
$\langle P_{\text{turb}} \rangle$	highres	0.17 (0.03)	-1.63 (0.04)	0.77 (0.0)	0.17	-0.12 (0.03)	-0.71 (0.04)	-0.6 (0.0)	0.20

Notes. Analog to Table 11 but for HCO⁺(1–0).

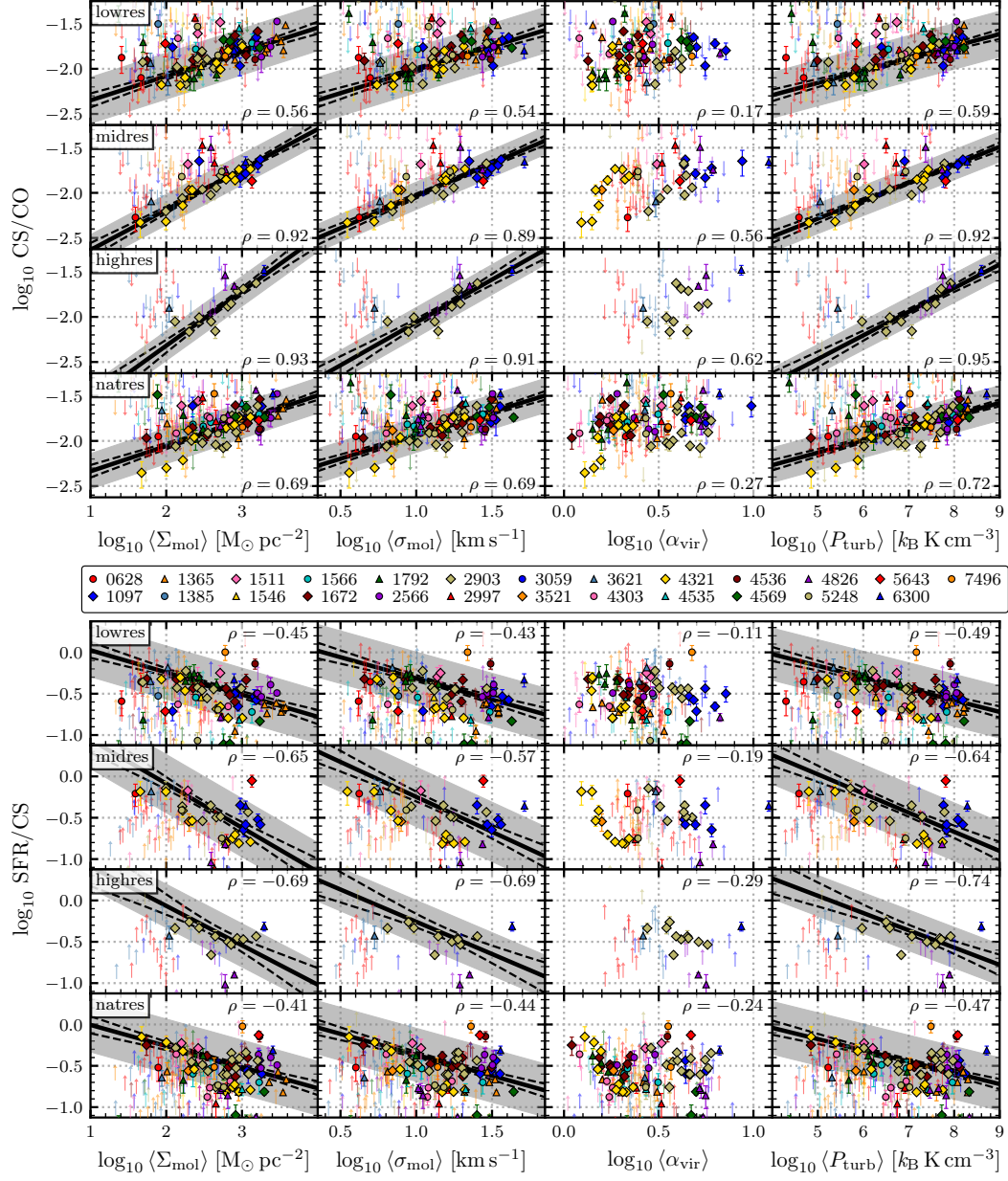
34 *L. Neumann et al.*


Figure 13. CS/CO (*top*) vs. $\langle X \rangle$ and SFR/CS (*bottom*) vs. $\langle X \rangle$ at different resolutions listed in Table F1.

Table 13. CS/CO and SFR/CS Correlations

MC Prop.	Res. Config.	CS/CO				SFR/CS			
		Slope (unc.)	Interc. (unc.)	Corr. ρ (p)	Scatter	Slope (unc.)	Interc. (unc.)	Corr. ρ (p)	Scatter
$\langle \Sigma_{\text{mol}} \rangle$	natres	0.28 (0.04)	-1.92 (0.02)	0.69 (0.0)	0.20	-0.26 (0.06)	-0.39 (0.03)	-0.41 (0.0)	0.33
$\langle \Sigma_{\text{mol}} \rangle$	natres-midtar	0.42 (0.05)	-1.95 (0.03)	0.82 (0.0)	0.18	-0.4 (0.09)	-0.37 (0.04)	-0.54 (0.0)	0.32
$\langle \Sigma_{\text{mol}} \rangle$	natres-hightar	0.45 (0.08)	-1.96 (0.04)	0.84 (0.0)	0.17	-0.36 (0.12)	-0.38 (0.06)	-0.58 (0.0)	0.26
$\langle \Sigma_{\text{mol}} \rangle$	lowres	0.27 (0.05)	-1.95 (0.03)	0.56 (0.0)	0.26	-0.27 (0.06)	-0.38 (0.03)	-0.45 (0.0)	0.32
$\langle \Sigma_{\text{mol}} \rangle$	lowres-midtar	0.45 (0.1)	-1.96 (0.05)	0.60 (0.0)	0.32	-0.45 (0.11)	-0.41 (0.05)	-0.55 (0.0)	0.35
$\langle \Sigma_{\text{mol}} \rangle$	lowres-hightar	0.36 (0.08)	-1.92 (0.04)	0.81 (0.0)	0.17	-0.32 (0.11)	-0.41 (0.06)	-0.62 (0.0)	0.21
$\langle \Sigma_{\text{mol}} \rangle$	midres	0.45 (0.05)	-1.96 (0.02)	0.92 (0.0)	0.17	-0.53 (0.10)	-0.35 (0.05)	-0.65 (0.0)	0.35
$\langle \Sigma_{\text{mol}} \rangle$	midres-hightar	0.50 (0.07)	-1.95 (0.03)	0.97 (0.0)	0.15	-0.51 (0.16)	-0.37 (0.07)	-0.71 (0.0)	0.26
$\langle \Sigma_{\text{mol}} \rangle$	highres	0.60 (0.09)	-2.02 (0.04)	0.93 (0.0)	0.17	-0.48 (0.16)	-0.30 (0.07)	-0.69 (0.0)	0.26
$\langle \sigma_{\text{mol}} \rangle$	natres	0.52 (0.07)	-1.89 (0.02)	0.69 (0.0)	0.19	-0.51 (0.11)	-0.42 (0.03)	-0.44 (0.0)	0.32
$\langle \sigma_{\text{mol}} \rangle$	natres-midtar	0.71 (0.1)	-1.90 (0.03)	0.79 (0.0)	0.18	-0.67 (0.16)	-0.42 (0.04)	-0.53 (0.0)	0.32
$\langle \sigma_{\text{mol}} \rangle$	natres-hightar	0.71 (0.16)	-1.88 (0.04)	0.76 (0.0)	0.19	-0.52 (0.22)	-0.44 (0.06)	-0.51 (0.0)	0.27
$\langle \sigma_{\text{mol}} \rangle$	lowres	0.52 (0.09)	-1.96 (0.03)	0.54 (0.0)	0.25	-0.51 (0.11)	-0.37 (0.03)	-0.43 (0.0)	0.32
$\langle \sigma_{\text{mol}} \rangle$	lowres-midtar	0.73 (0.16)	-2.02 (0.05)	0.56 (0.0)	0.32	-0.69 (0.19)	-0.35 (0.05)	-0.47 (0.0)	0.36
$\langle \sigma_{\text{mol}} \rangle$	lowres-hightar	0.53 (0.13)	-2. (0.04)	0.76 (0.0)	0.16	-0.46 (0.18)	-0.33 (0.06)	-0.58 (0.0)	0.21
$\langle \sigma_{\text{mol}} \rangle$	midres	0.72 (0.08)	-1.96 (0.02)	0.89 (0.0)	0.15	-0.85 (0.17)	-0.33 (0.05)	-0.57 (0.0)	0.36
$\langle \sigma_{\text{mol}} \rangle$	midres-hightar	0.76 (0.11)	-2.00 (0.03)	0.95 (0.0)	0.13	-0.76 (0.25)	-0.29 (0.08)	-0.68 (0.0)	0.26
$\langle \sigma_{\text{mol}} \rangle$	highres	0.95 (0.15)	-1.97 (0.04)	0.91 (0.0)	0.17	-0.78 (0.25)	-0.34 (0.07)	-0.69 (0.0)	0.26
$\langle \alpha_{\text{vir}} \rangle$	natres	0.27 (0.014)	-0.24 (0.032)	...
$\langle \alpha_{\text{vir}} \rangle$	natres-midtar	0.51 (0.0)	-0.22 (0.155)	...
$\langle \alpha_{\text{vir}} \rangle$	natres-hightar	0.38 (0.087)	-0.16 (0.475)	...
$\langle \alpha_{\text{vir}} \rangle$	lowres	0.17 (0.14)	-0.11 (0.361)	...
$\langle \alpha_{\text{vir}} \rangle$	lowres-midtar	0.26 (0.128)	0.01 (0.936)	...
$\langle \alpha_{\text{vir}} \rangle$	lowres-hightar	0.58 (0.031)	-0.27 (0.354)	...
$\langle \alpha_{\text{vir}} \rangle$	midres	0.56 (0.0)	-0.19 (0.271)	...
$\langle \alpha_{\text{vir}} \rangle$	midres-hightar	0.77 (0.003)	-0.44 (0.155)	...
$\langle \alpha_{\text{vir}} \rangle$	highres	0.62 (0.019)	-0.29 (0.311)	...
$\langle P_{\text{turb}} \rangle$	natres	0.14 (0.02)	-1.92 (0.02)	0.72 (0.0)	0.19	-0.14 (0.03)	-0.38 (0.03)	-0.47 (0.0)	0.32
$\langle P_{\text{turb}} \rangle$	natres-midtar	0.19 (0.02)	-1.98 (0.03)	0.82 (0.0)	0.19	-0.18 (0.04)	-0.35 (0.05)	-0.56 (0.0)	0.32
$\langle P_{\text{turb}} \rangle$	natres-hightar	0.20 (0.04)	-2. (0.04)	0.85 (0.0)	0.17	-0.16 (0.05)	-0.36 (0.06)	-0.63 (0.0)	0.25
$\langle P_{\text{turb}} \rangle$	lowres	0.14 (0.02)	-1.95 (0.03)	0.59 (0.0)	0.25	-0.14 (0.03)	-0.37 (0.03)	-0.49 (0.0)	0.32
$\langle P_{\text{turb}} \rangle$	lowres-midtar	0.2 (0.04)	-2. (0.05)	0.61 (0.0)	0.32	-0.2 (0.05)	-0.37 (0.05)	-0.55 (0.0)	0.35
$\langle P_{\text{turb}} \rangle$	lowres-hightar	0.15 (0.03)	-1.98 (0.03)	0.85 (0.0)	0.16	-0.13 (0.04)	-0.36 (0.05)	-0.66 (0.0)	0.20
$\langle P_{\text{turb}} \rangle$	midres	0.2 (0.02)	-1.99 (0.02)	0.92 (0.0)	0.17	-0.23 (0.05)	-0.32 (0.05)	-0.64 (0.0)	0.35
$\langle P_{\text{turb}} \rangle$	midres-hightar	0.21 (0.03)	-2.02 (0.03)	0.96 (0.0)	0.14	-0.20 (0.06)	-0.3 (0.07)	-0.75 (0.0)	0.24
$\langle P_{\text{turb}} \rangle$	highres	0.26 (0.04)	-2.07 (0.04)	0.95 (0.0)	0.16	-0.21 (0.06)	-0.26 (0.07)	-0.74 (0.0)	0.25

Notes. Analog to Table 11 but for CS(2–1).

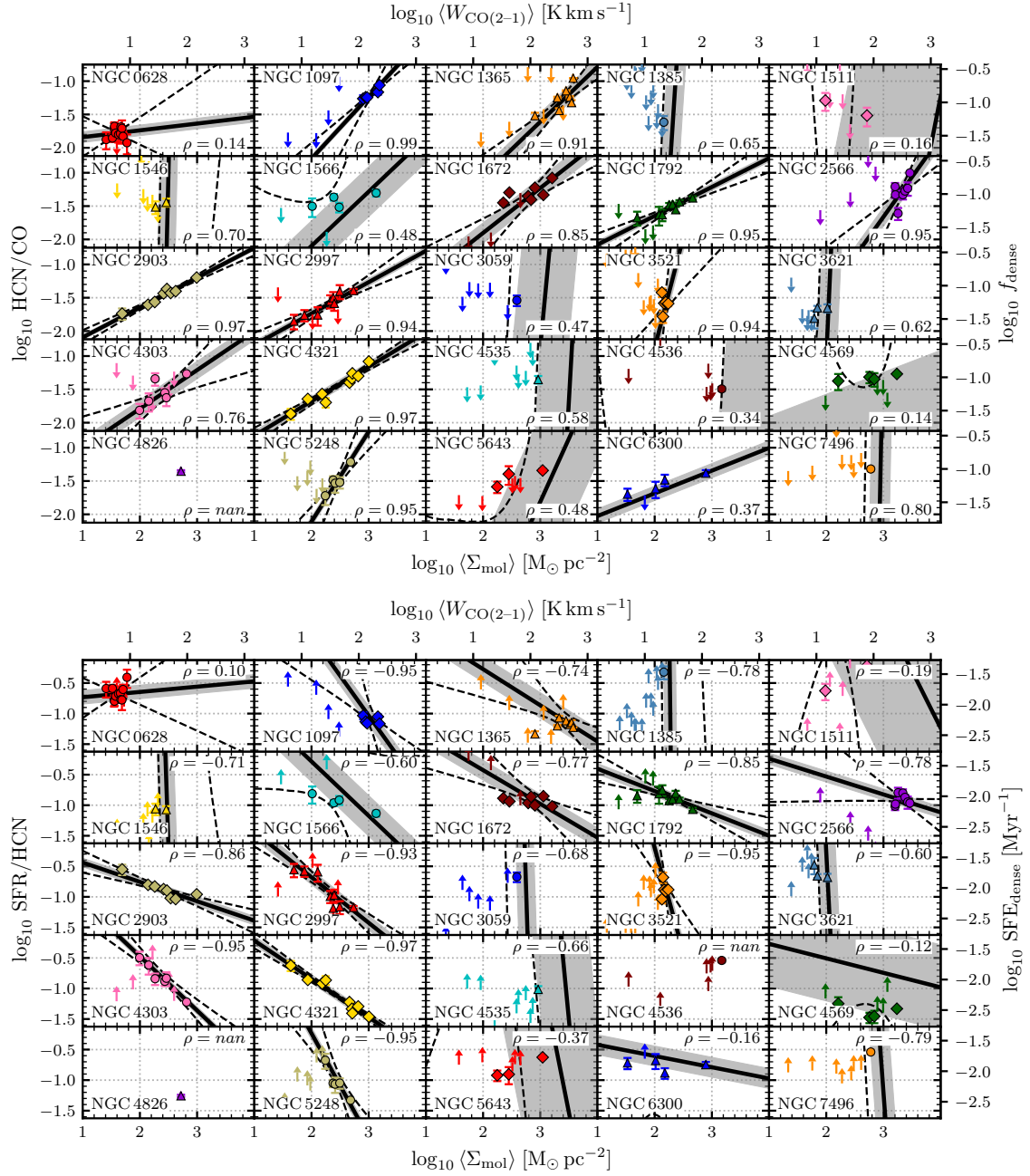
36 *L. Neumann et al.*


Figure 14. HCN/CO (*top*) and SFR/HCN (*bottom*) vs. $\langle \Sigma_{\text{mol}} \rangle$ at 2.1 kpc and 150 pc scales, plotted and fitted individually for each galaxy. The solid line shows the best fit line where the dotted line is the 1σ uncertainty. The grey shaded area indicates the scatter of the significant data about the fit line.

HCN/CO and SFR/HCN vs. cloud-scale gas properties 37

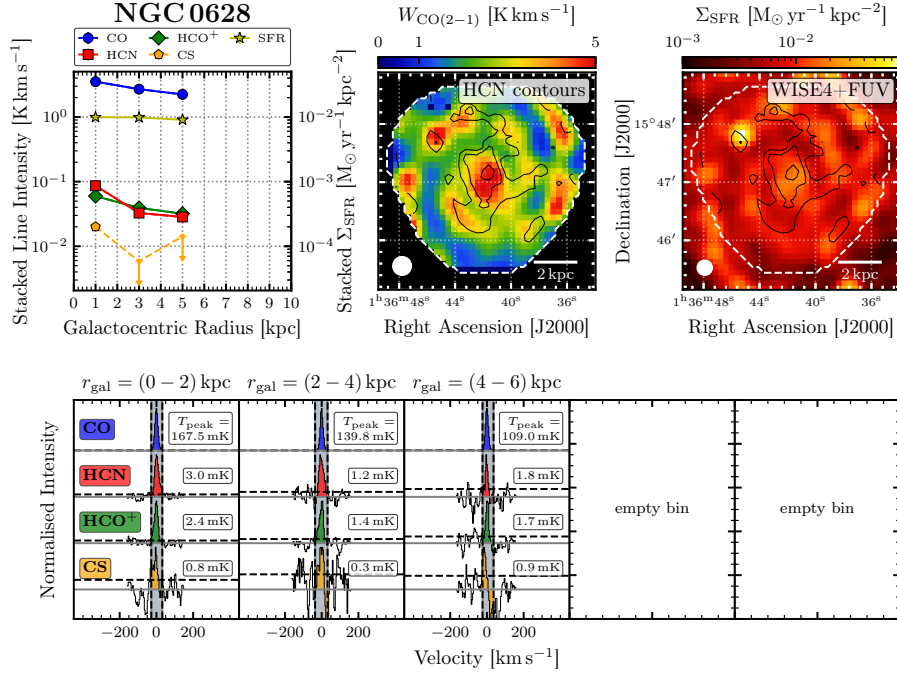


Figure J1. Analogues to Figure 3 for NGC 628.

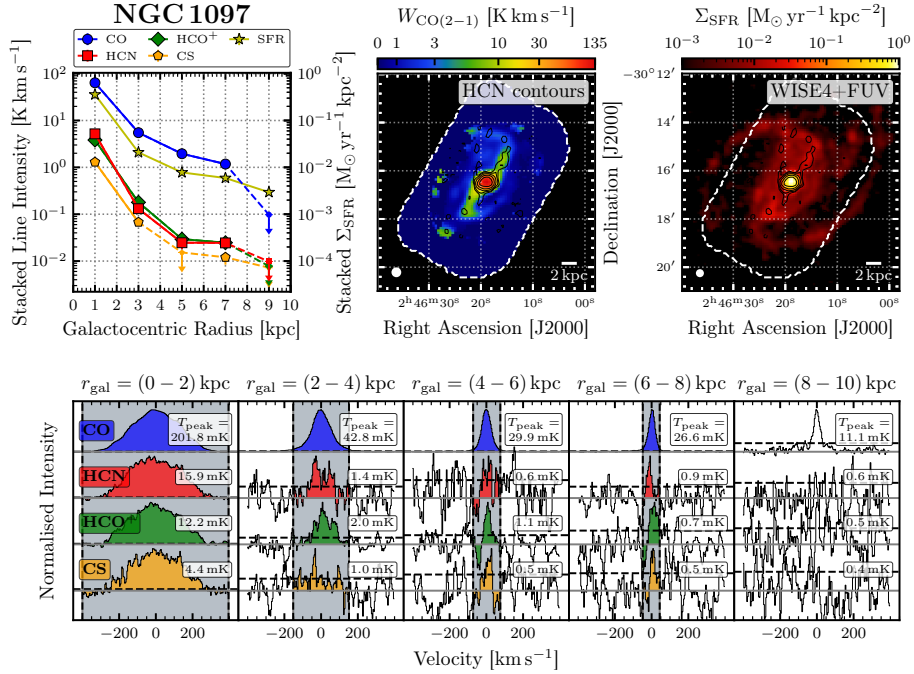


Figure J2. Analogues to Figure 3 for NGC 1097.

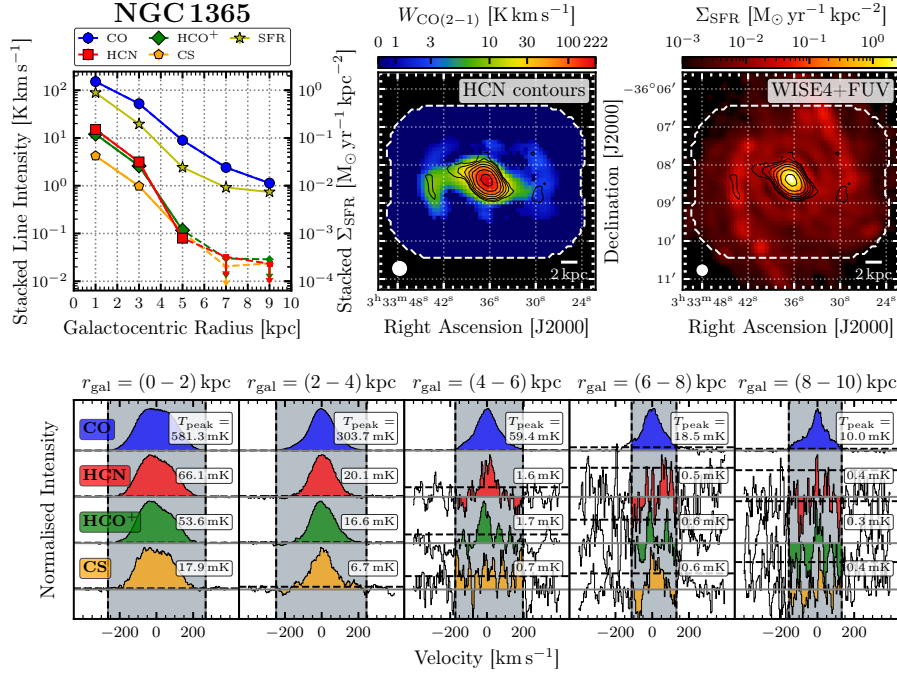
38 *L. Neumann et al.*


Figure J3. Analogues to Figure 3 for NGC 1365.

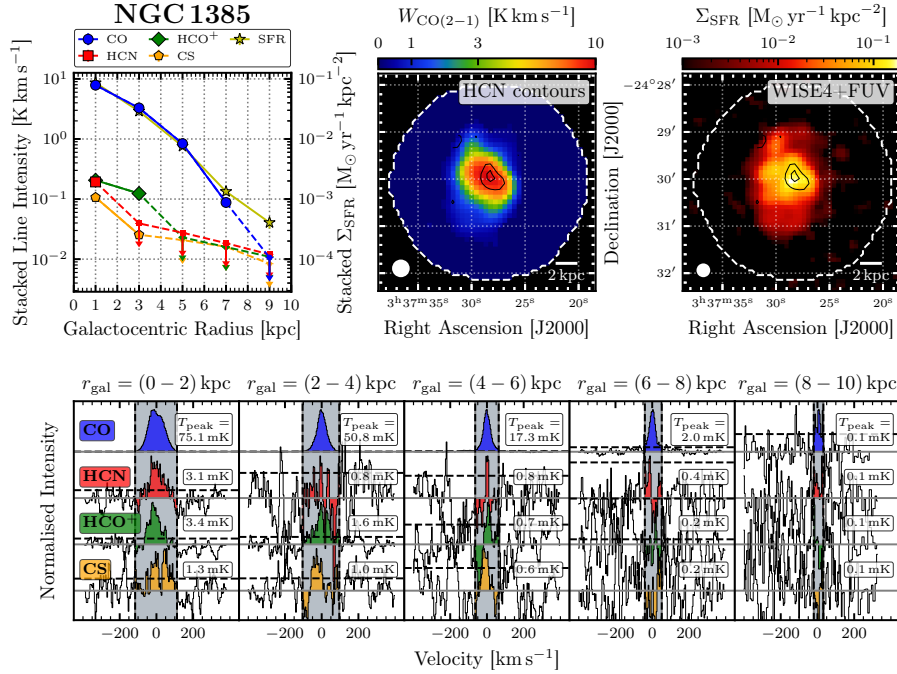


Figure J4. Analogues to Figure 3 for NGC 1385.

HCN/CO and SFR/HCN vs. cloud-scale gas properties 39

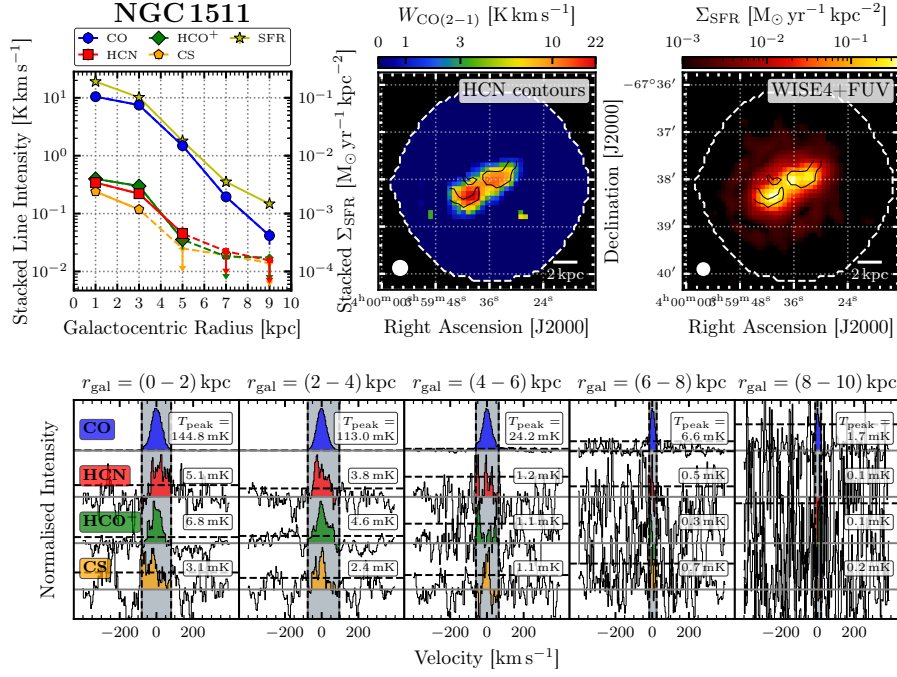


Figure J5. Analogues to Figure 3 for NGC 1511.

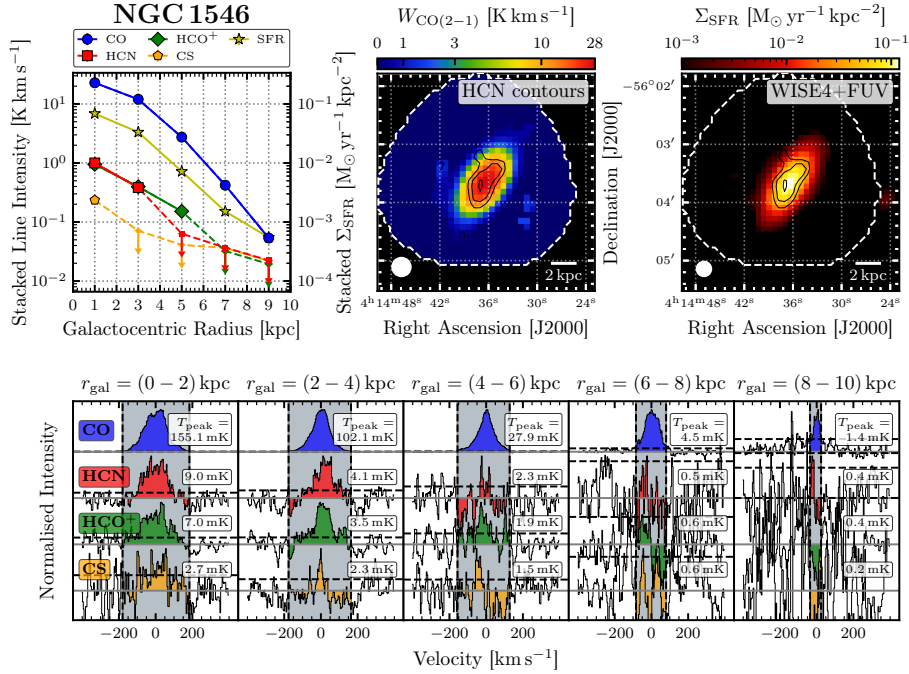
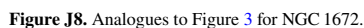
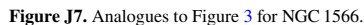


Figure J6. Analogues to Figure 3 for NGC 1546.



HCN/CO and SFR/HCN vs. cloud-scale gas properties 41

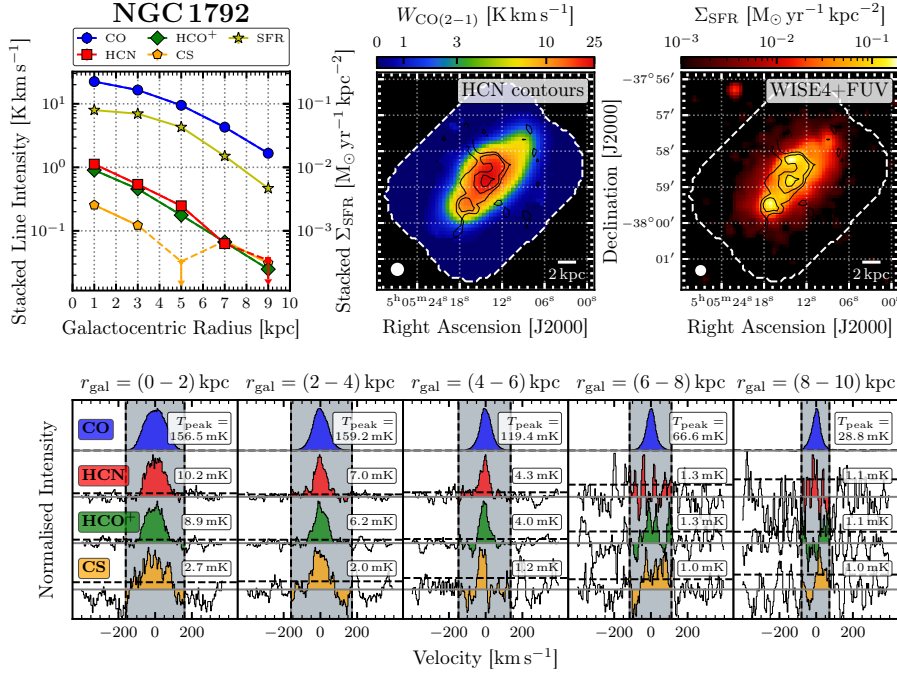


Figure J9. Analogues to Figure 3 for NGC 1792.

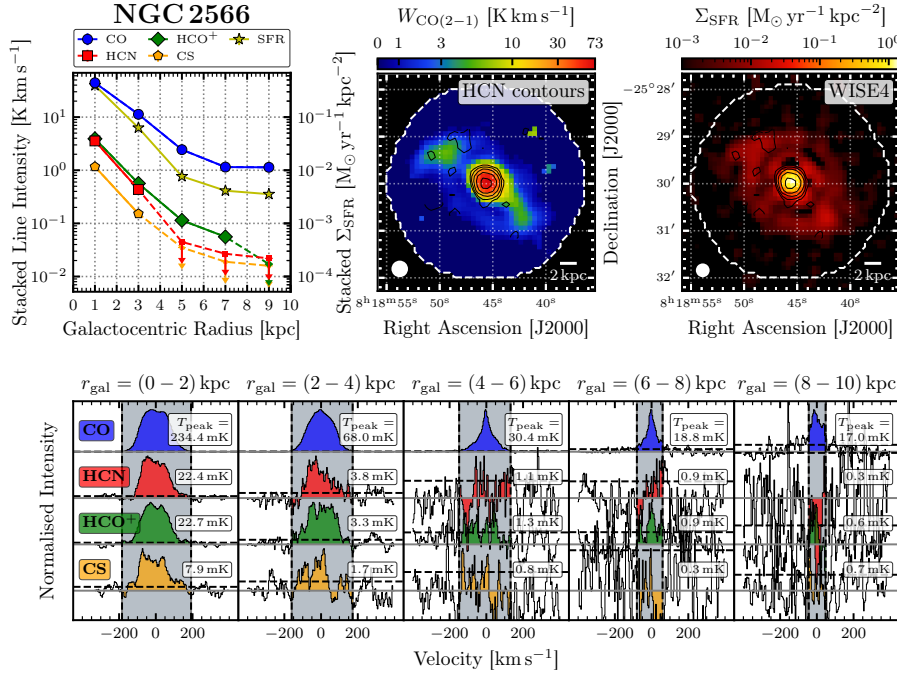


Figure J10. Analogues to Figure 3 for NGC 2566.

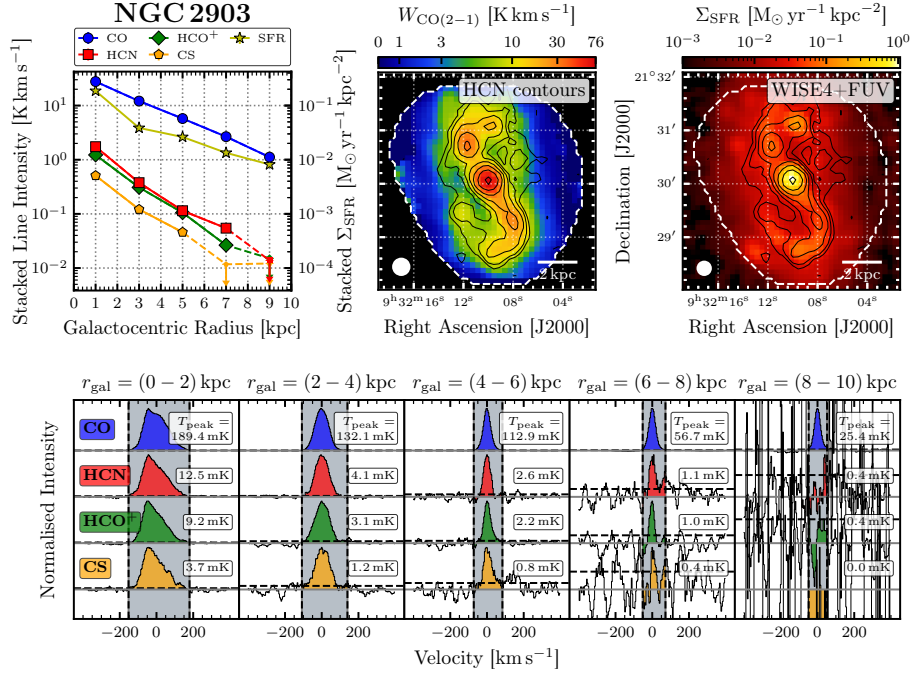
42 *L. Neumann et al.*


Figure J11. Analogues to Figure 3 for NGC 2903.

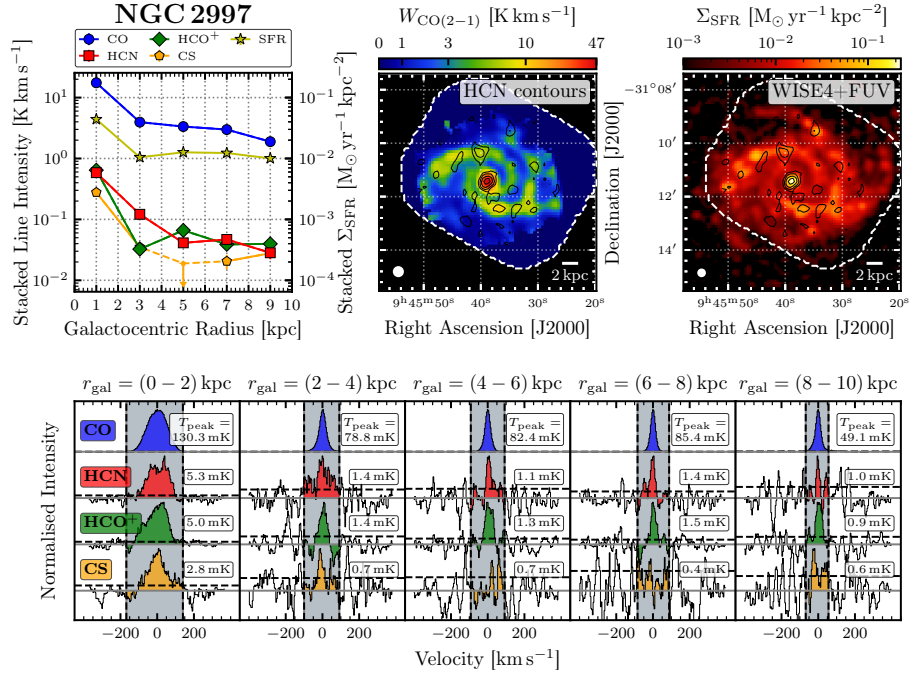


Figure J12. Analogues to Figure 3 for NGC 2997.

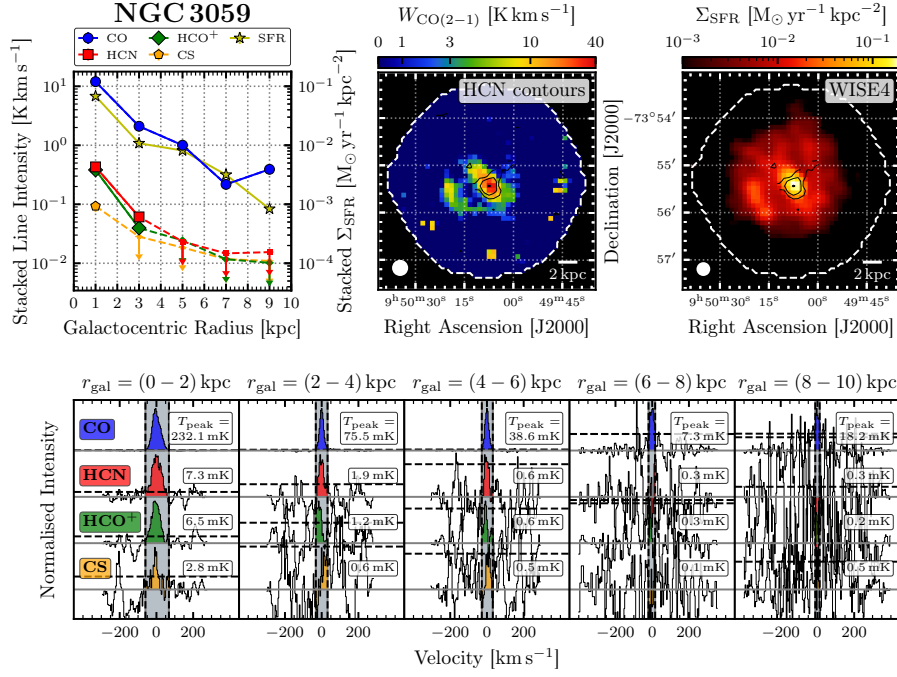


Figure J13. Analogues to Figure 3 for NGC 3059.

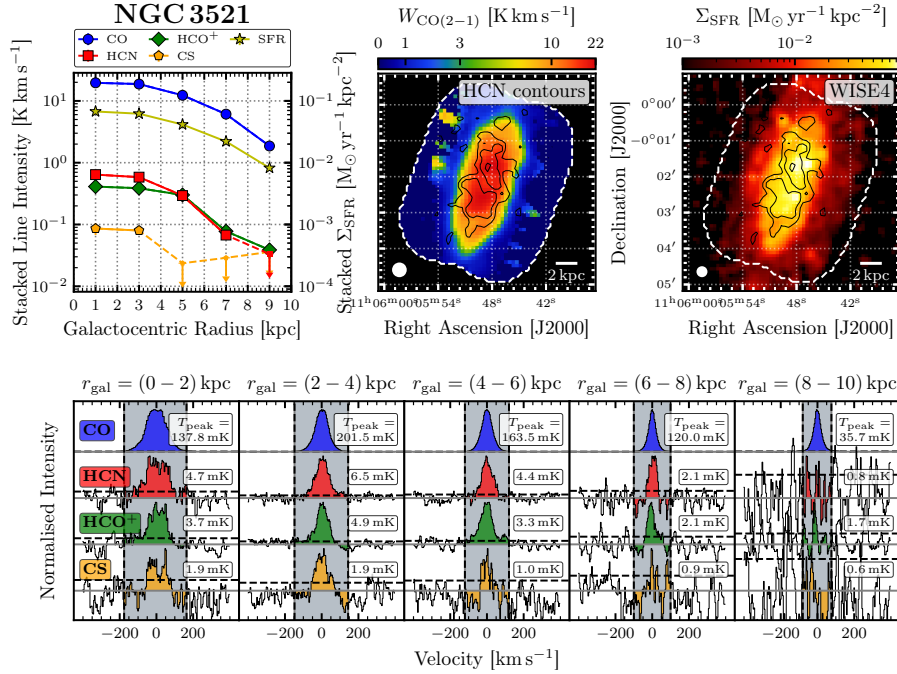


Figure J14. Analogues to Figure 3 for NGC 3521.

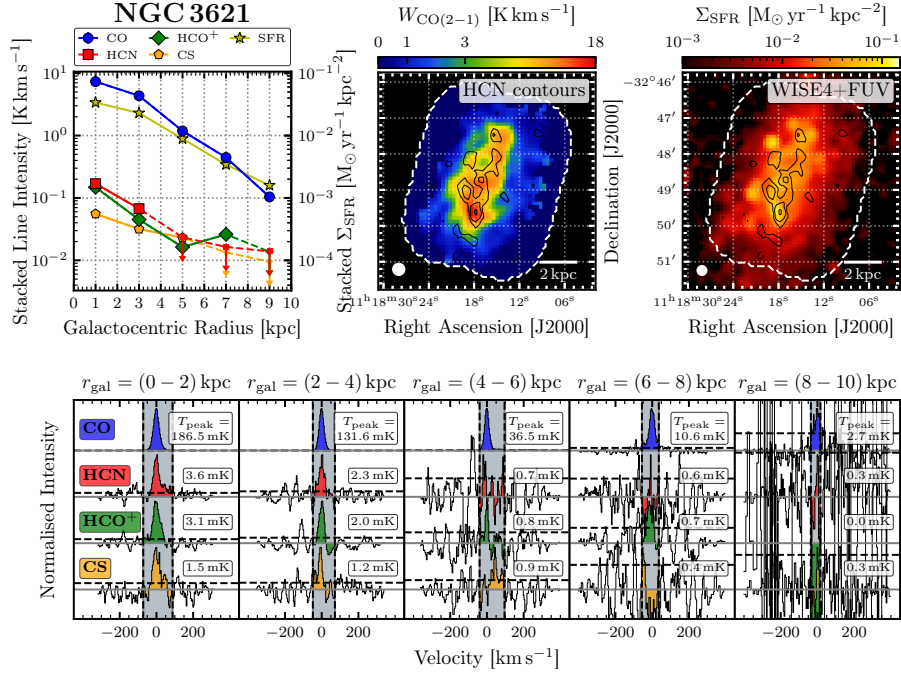
44 *L. Neumann et al.*


Figure J15. Analogues to Figure 3 for NGC 3621.

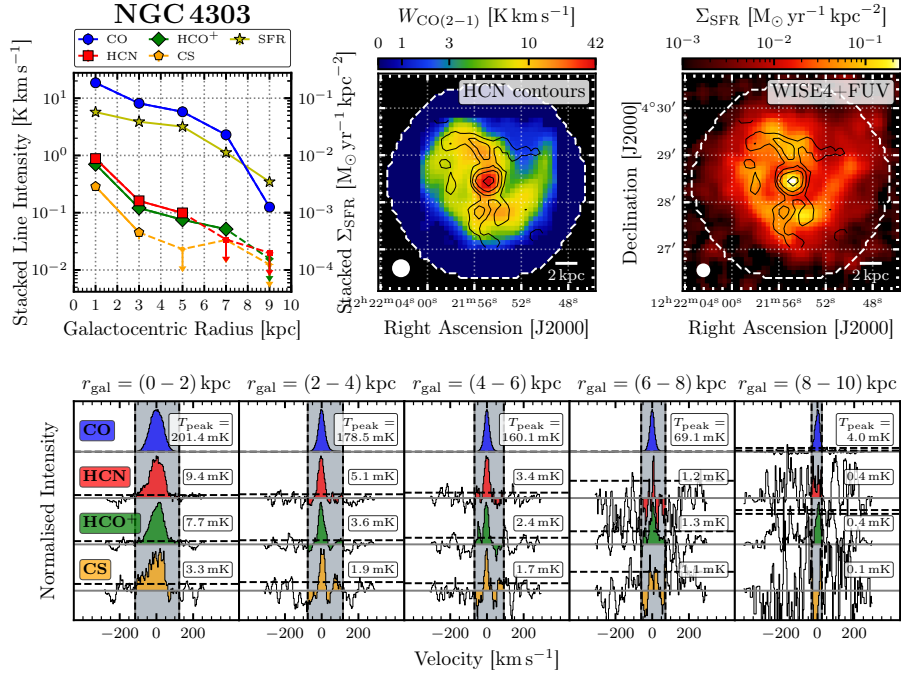


Figure J16. Analogues to Figure 3 for NGC 4303.

HCN/CO and SFR/HCN vs. cloud-scale gas properties 45

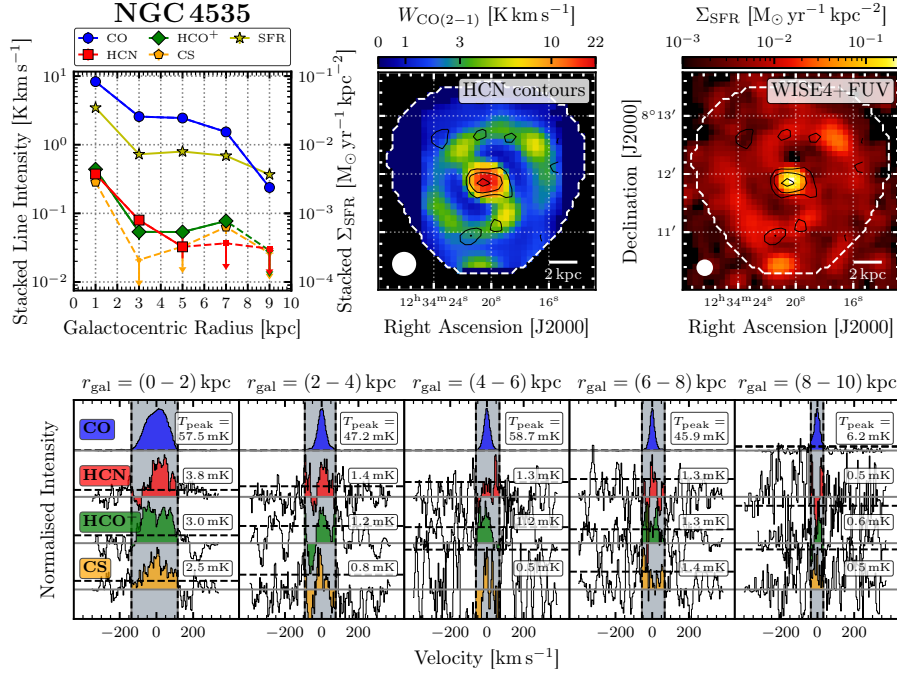


Figure J17. Analogues to Figure 3 for NGC 4535.

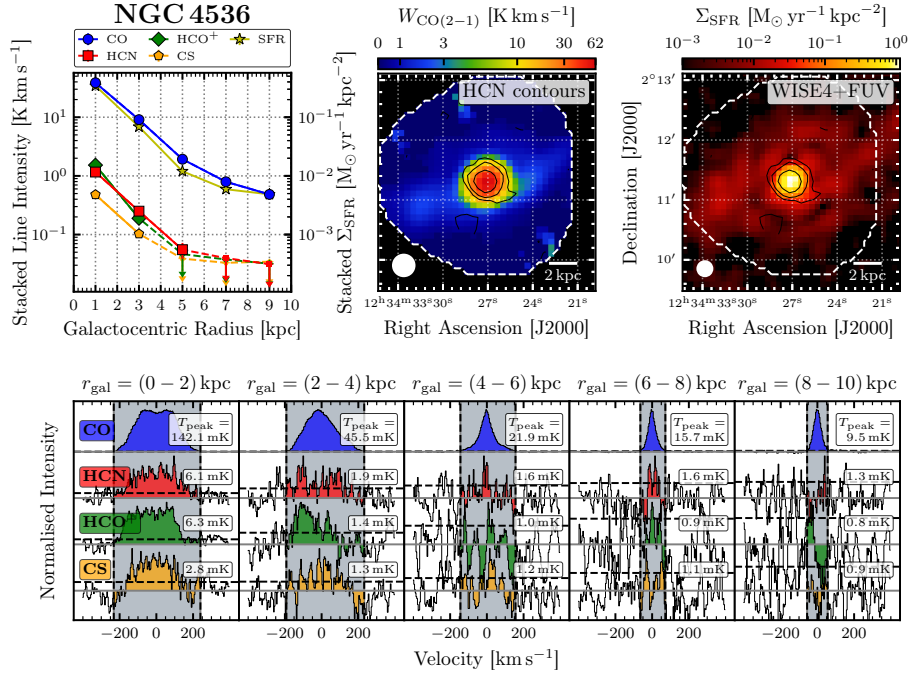


Figure J18. Analogues to Figure 3 for NGC 4536.

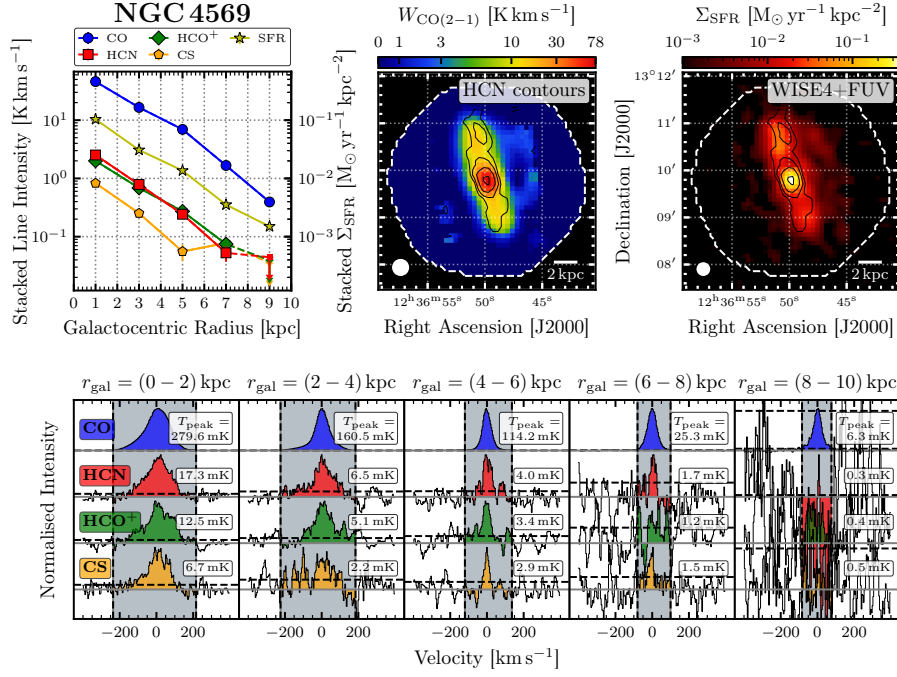
46 *L. Neumann et al.*


Figure J19. Analogues to Figure 3 for NGC 4569.

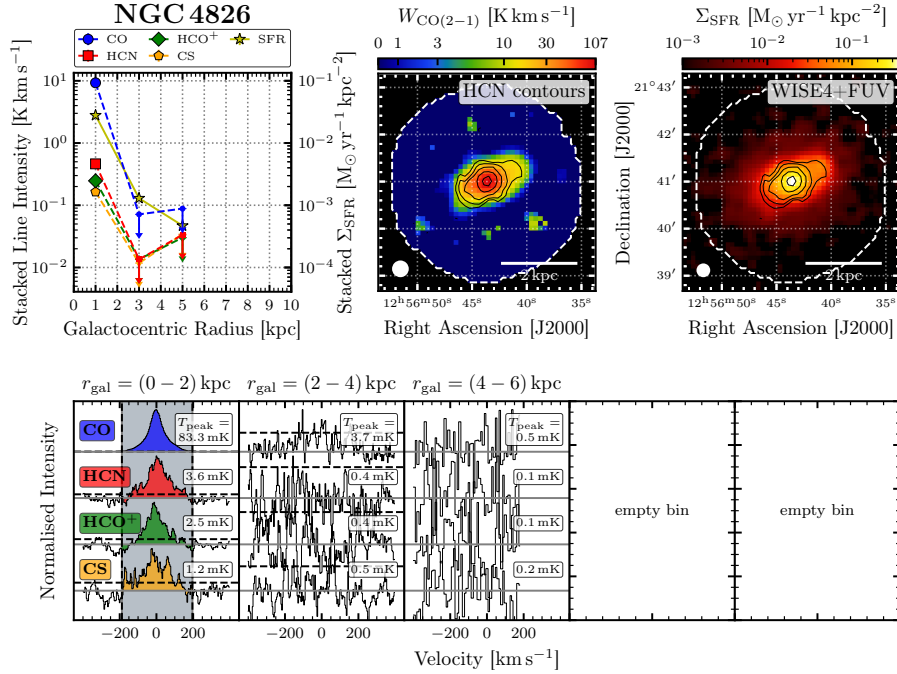


Figure J20. Analogues to Figure 3 for NGC 4826.

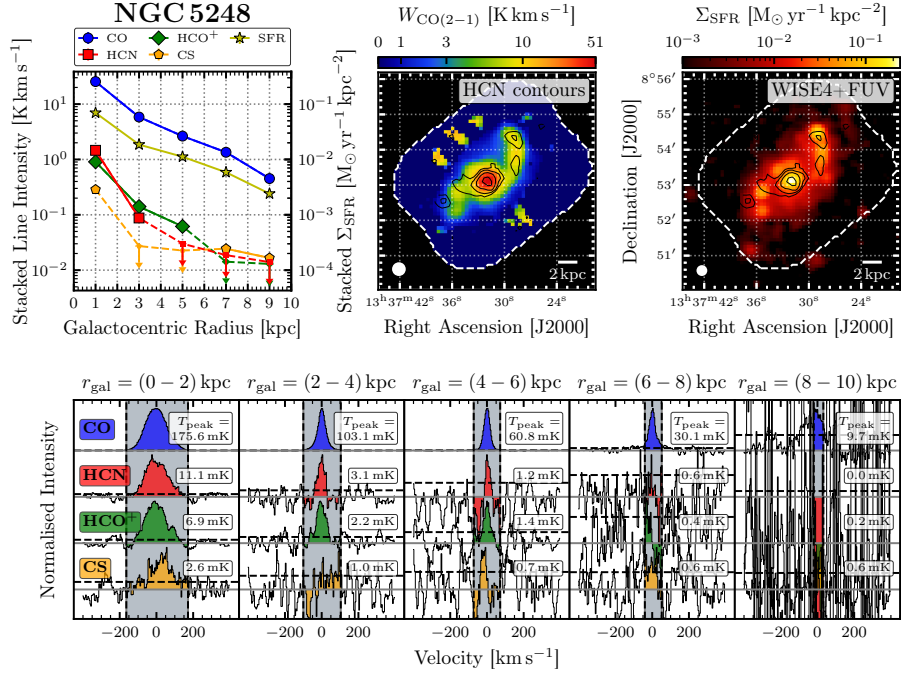


Figure J21. Analogues to Figure 3 for NGC 5248.

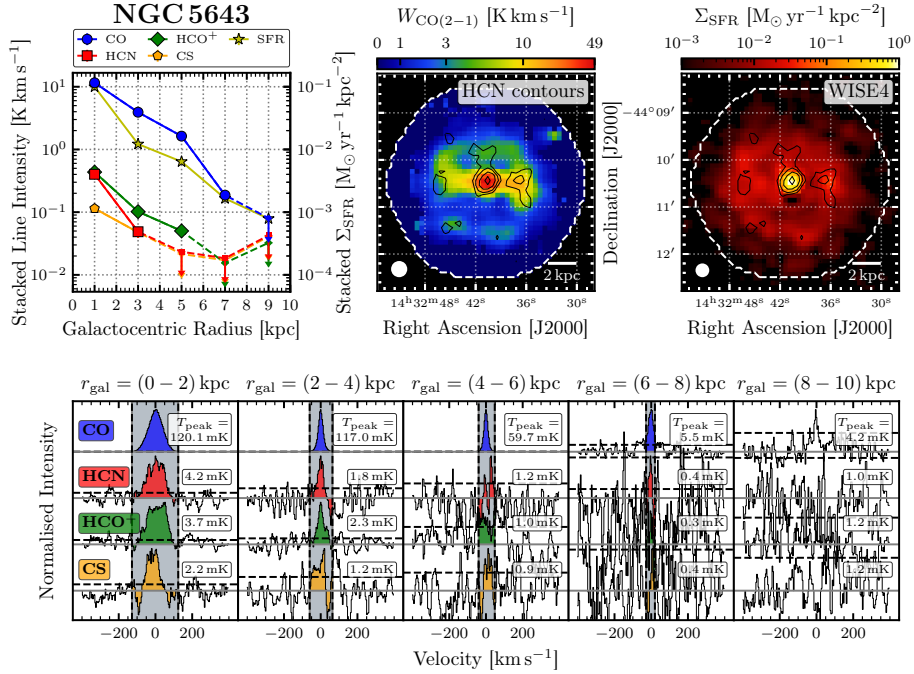


Figure J22. Analogues to Figure 3 for NGC 5643.

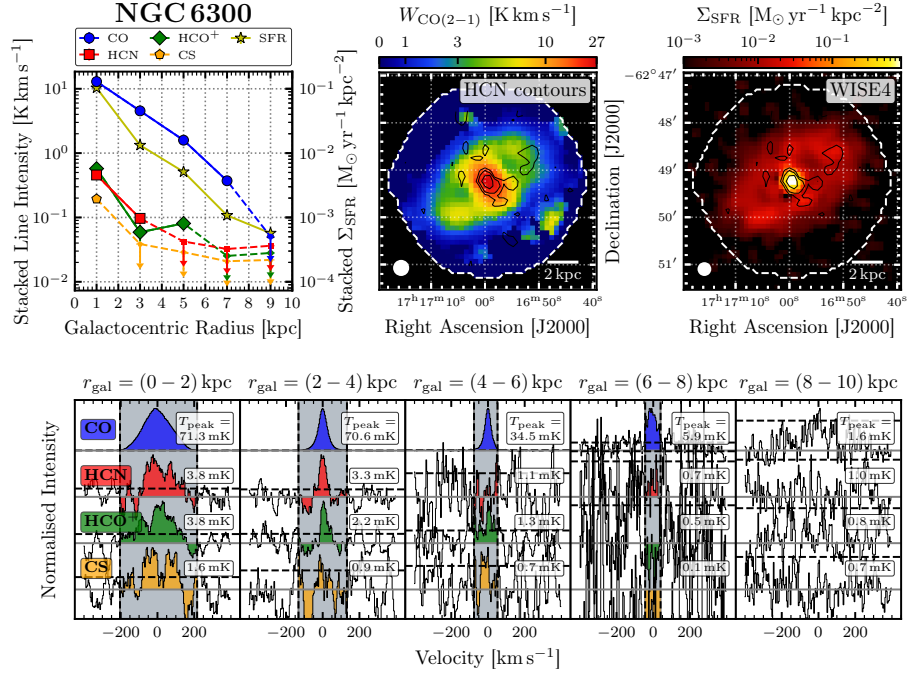
48 *L. Neumann et al.*


Figure J23. Analogues to Figure 3 for NGC 6300.

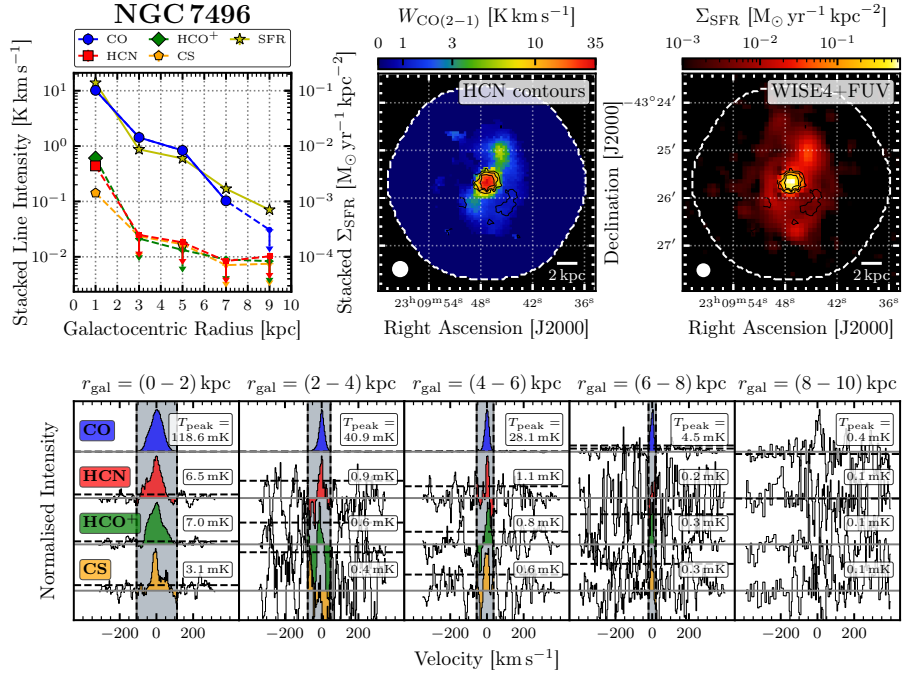


Figure J24. Analogues to Figure 3 for NGC 7496.

APPENDIX C

NGC 4321 paper

The paper Neumann et al. 2024, A&A, in press, 26 pp. (DOI: [10.48550/arXiv.2406.120254](https://doi.org/10.48550/arXiv.2406.120254)) is reproduced below in its original form with permission by ESO.

A 260 pc resolution ALMA map of HCN(1–0) in the galaxy NGC 4321

Lukas Neumann^{1,* **}, Frank Bigiel¹, Ashley T. Barnes², Molly J. Gallagher³, Adam Leroy³,
Antonio Usero⁴, Erik Rosolowsky⁵, Ivana Bešlić⁶, Médéric Boquien⁷, Yixian Cao⁸,
Mélanie Chevance^{9,10}, Dario Colombo¹, Daniel A. Dale¹¹, Cosima Eibensteiner^{1,12},
Kathryn Grasha^{13,14,15}, Jonathan D. Henshaw^{16,17}, María J. Jiménez-Donaire^{4,18}, Sharon Meidt¹⁹,
Shyam H. Menon²⁰, Eric J. Murphy¹², Hsi-An Pan²¹, Miguel Querejeta⁴, Toshiki Saito²²,
Eva Schinnerer¹⁷, Sophia K. Stuber¹⁷, Yu-Hsuan Teng²³, and Thomas G. Williams²⁴

¹ Argelander-Institut für Astronomie, Universität Bonn, Auf dem Hügel 71, 53121 Bonn, Germany² European Southern Observatory, Karl-Schwarzschild Straße 2, D-85748 Garching bei München, Germany³ Department of Astronomy, The Ohio State University, 140 West 18th Ave, Columbus, OH 43210, USA⁴ Observatorio Astronómico Nacional (IGN), C/ Alfonso XII, 3, E-28014 Madrid, Spain⁵ Dept. of Physics, University of Alberta, Edmonton, Alberta, Canada T6G 2E1⁶ LERMA, Observatoire de Paris, PSL Research University, CNRS, Sorbonne Universités, 75014 Paris, France⁷ Universidad de Antofagasta, Centro de Astronomía, Avenida Angamos 601, Antofagasta 1270300, Chile⁸ Max-Planck-Institut für Extraterrestrische Physik (MPE), Giessenbachstr. 1, D-85748 Garching, Germany⁹ Institut für Theoretische Astrophysik, Zentrum für Astronomie der Universität Heidelberg, Albert-Ueberle-Strasse 2, 69120 Heidelberg, Germany¹⁰ Cosmic Origins Of Life (COOL) Research DAO, coolresearch.io¹¹ Department of Physics and Astronomy, University of Wyoming, Laramie, WY 82071, USA¹² National Radio Astronomy Observatory, 520 Edgemont Road, Charlottesville, VA 22903, USA¹³ Research School of Astronomy and Astrophysics, Australian National University, Canberra, ACT 2611, Australia¹⁴ ARC Centre of Excellence for All Sky Astrophysics in 3 Dimensions (ASTRO 3D), Australia¹⁵ Visiting Fellow, Harvard-Smithsonian Center for Astrophysics, 60 Garden Street, Cambridge, MA 02138, USA¹⁶ Astrophysics Research Institute, Liverpool John Moores University, 146 Brownlow Hill, Liverpool L3 5RF, UK¹⁷ Max Planck Institute for Astronomy, Königstuhl 17, 69117 Heidelberg, Germany¹⁸ Centro de Desarrollos Tecnológicos, Observatorio de Yebes (IGN), 19141 Yebes, Guadalajara, Spain¹⁹ Sterrenkundig Observatorium, Universiteit Gent, Krijgslaan 281 S9, B-9000 Gent, Belgium²⁰ Department of Physics and Astronomy, Rutgers University, 136 Frelinghuysen Road, Piscataway, NJ 08854, USA²¹ Department of Physics, Tamkang University, No.151, Yingzhuan Road, Tamsui District, New Taipei City 251301, Taiwan²² National Astronomical Observatory of Japan, 2-21-1 Osawa, Mitaka, Tokyo, 181-8588, Japan²³ Center for Astrophysics and Space Sciences, University of California, San Diego, 9500 Gilman Drive MC0424, La Jolla, CA 92093, USA²⁴ Sub-department of Astrophysics, Department of Physics, University of Oxford, Keble Road, Oxford OX1 3RH, UK

Received February 5, 2024; accepted June 13, 2024

ABSTRACT

The property of star formation rate (SFR) is tightly connected to the amount of dense gas in molecular clouds. However, it is not fully understood how the relationship between dense molecular gas and star formation varies within galaxies and in different morphological environments. Most previous studies have typically been limited to kiloparsec-scale resolution such that different environments could not be resolved. In this work, we present new ALMA observations of HCN(1–0) at 260 pc scale to test how the amount of dense gas and its ability to form stars varies with environmental properties. Combined with existing CO(2–1) observations from ALMA and H α from MUSE, we measured the HCN/CO line ratio, a proxy for the dense gas fraction, and SFR/HCN, a proxy for the star formation efficiency of the dense gas. We find a systematic > 1 dex increase (decreases) of HCN/CO (SFR/HCN) towards the centre of the galaxy, and roughly flat trends of these ratios (average variations < 0.3 dex) throughout the disc. While spiral arms, interarm regions, and bar ends show similar HCN/CO and SFR/HCN, on the bar, there is a significantly lower SFR/HCN at a similar HCN/CO. The strong environmental influence on dense gas and star formation in the centre of NGC 4321, suggests either that clouds couple strongly to the surrounding pressure or that HCN emission traces more of the bulk molecular gas that is less efficiently converted into stars. Across the disc, where the ISM pressure is typically low, SFR/HCN is more constant, indicating a decoupling of the clouds from their surrounding environment. The low SFR/HCN on the bar suggests that gas dynamics (e.g. shear and streaming motions) can have a large effect on the efficiency with which dense gas is converted into stars. In addition, we show that HCN/CO is a good predictor of the mean molecular gas surface density at 260 pc scales across environments and physical conditions.

Key words. ISM: molecules – Galaxies: ISM – Galaxies: star formation – Galaxies: individual: NGC 4321

1. Introduction

Galactic observations of dust in star-forming regions show that stars form in dense substructures, where the inferred star formation rate (SFR) is found to be linearly related to the amount of dense gas (e.g. Heiderman et al. 2010; Lada et al. 2010, 2012; Evans et al. 2014). Gao & Solomon (2004) found that this linear relation also holds for global measurements of galaxies when tracing the SFR with the total infrared (IR) luminosity and the dense gas mass (M_{dense}) via the luminosity of HCN(1–0). Molecular line emission from HCN has an effective critical density of $n_{\text{eff}} \sim 5 \times 10^3 \text{ cm}^{-3}$, which is at least one order of magnitude higher than that of CO ($n_{\text{eff}} \lesssim 10^2 \text{ cm}^{-3}$; Shirley 2015). Over the past two decades, many studies have aimed at mapping HCN across other galaxies (e.g. Usero et al. 2015; Bigiel et al. 2016; Gallagher et al. 2018b; Jiménez-Donaire et al. 2019; Querejeta et al. 2019; Sánchez-García et al. 2022; Neumann et al. 2023b). The observations of star-forming spiral galaxies from these studies as well as numerical works (e.g. Onus et al. 2018) have reported that the IR luminosity tracing embedded SFR is tightly (scatter of ± 0.4 dex) and linearly correlated with the HCN luminosity, tracing M_{dense} and spanning ten orders of magnitude (see e.g. Jiménez-Donaire et al. 2019; Neumann et al. 2023b; Beslic et al. 2024; Schinnerer & Leroy 2024, for literature compilations). efficiency ($\text{SFE}_{\text{dense}} \equiv \text{SFR}/M_{\text{dense}} = \tau_{\text{HCN}}^{-1}$).

Despite the clear relation between the SFR and the dense gas, there is still a total scatter of ≈ 1 dex that cannot solely be explained by the measurement uncertainties, instead indicating that the dense gas star formation efficiency ($\text{SFR}/M_{\text{dense}} \equiv \text{SFE}_{\text{dense}}$) depends on other physical quantities. In the past decade, resolved kiloparsec-scale observations of nearby galaxies (e.g. Usero et al. 2015; Bigiel et al. 2016; Gallagher et al. 2018b,a; Jiménez-Donaire et al. 2019; Querejeta et al. 2019; Sánchez-García et al. 2022; Neumann et al. 2023b) have studied the variation of spectroscopic ratios, such as HCN/CO, a proxy of the dense gas fraction ($f_{\text{dense}} \equiv M_{\text{dense}}/M_{\text{mol}}$, where M_{mol} is the molecular gas mass), and IR/HCN, a proxy of the dense gas star formation efficiency ($\text{SFE}_{\text{dense}}$) with environmental properties, including the stellar mass surface density (Σ_{\star}), the molecular gas surface density (Σ_{mol}), and the hydrostatic pressure in the interstellar medium (ISM) disc (P_{DE}). These studies find that f_{dense} and $\text{SFE}_{\text{dense}}$ vary systematically with the environment. In particular, f_{dense} is significantly enhanced, while $\text{SFE}_{\text{dense}}$ is systematically suppressed in high-surface density, high-pressure regions, indicating a connection between the properties of molecular clouds and their host environment. These results are also supported by studies of the Milky Way central molecular zone (CMZ), where $\text{SFE}_{\text{dense}}$ has been found to be systematically lower than across the Milky Way disc (e.g. Longmore et al. 2013; Kruijssen et al. 2014; Henshaw et al. 2023).

In their pioneering work, Gallagher et al. (2018a) found systematic correlations between the kiloparsec-scale f_{dense} , $\text{SFE}_{\text{dense}}$, and the molecular gas surface density measured at giant molecular cloud (GMC) scales (i.e. ~ 100 pc). Building upon this, Neumann et al. (2023b) used HCN observations of 25 nearby galaxies from the ACA Large-sample Mapping Of Nearby galaxies in Dense gas (ALMOND) survey in order to compare the kiloparsec-scale spectroscopic line ratios with the properties of the molecular gas as traced by CO(2–1) on ~ 100 pc scales from the Physics at High Angular resolution

Galaxies–Atacama Large Millimetre Array (PHANGS–ALMA) survey (Leroy et al. 2021b). They showed that f_{dense} increases and $\text{SFE}_{\text{dense}}$ decreases with increasing surface density (Σ_{mol}) and velocity dispersion (σ_{mol}) of the molecular gas measured at GMC scales. These results are also in agreement with predictions from models describing the star formation in turbulent clouds (e.g. Padoan & Nordlund 2002; Krumholz & McKee 2005; Krumholz & Thompson 2007) and the ISM disc structure (e.g. Ostriker et al. 2010), hence yielding a coherent picture between dense gas, star formation, and turbulent cloud models. In particular, these results have shown that $\text{SFE}_{\text{dense}}$ is not universal but depends on the environment and that density-sensitive line ratios such as HCN/CO are powerful extragalactic tools for tracing the underlying density structure at ~ 100 pc scale even if measured at kiloparsec-scales.

Previous studies of the relationship between dense gas, star formation, and environment (e.g. Usero et al. 2015; Gallagher et al. 2018b,a; Jiménez-Donaire et al. 2019; Neumann et al. 2023b) were thus limited to mapping dense gas at kiloparsec-scales. There are only a few ~ 100 pc resolution maps of HCN or other dense gas tracers (Kepley et al. 2014, M82, 200 pc; Chen et al. 2017, outer spiral arm of M51, 150 pc; Harada et al. 2018, NGC 3256, 200 pc; Viaene et al. 2018, GMCs in M31; 100 pc; Kepley et al. 2018, IC10, 34 pc; Querejeta et al. 2019, M51, 100 pc; Harada et al. 2019, circumnuclear ring of M83, 60 pc; Bešlić et al. 2021, NGC 3627, 100 pc; Martín et al. 2021, NGC 253, 250 pc with the potential of resolutions < 50 pc; Eibensteiner et al. 2022, central 2 kpc of NGC 6946, 150 pc; Sánchez-García et al. 2022, NGC 1068, 60 pc; Stuber et al. 2023, M51, 125 pc; Beslic et al. 2024, NGC 253, 300 pc). However, these are typically less sensitive, and they target certain regions but not the full disc, in contrast to the observations presented here. Many of these works that mapped the whole molecular gas disc did not detect much emission in individual sight lines outside of galaxy centres, and hence the authors had to average over larger regions (e.g. via spectral stacking; Schrubba et al. 2011; Caldú-Primo et al. 2013; Jiménez-Donaire et al. 2017, 2019; Neumann et al. 2023a) at the cost of spatial information. Apart from a few exceptions (M51, NGC 253; see references above), there are no deep wide-field studies of these dense gas ratios at sub-kiloparsec scales, which detect individual sight lines in different morphological environments across the whole molecular gas disc out to 10 kpc in galactocentric radius. Such a study is, however, needed in order to investigate the sub-kiloparsec structured ISM without blending many regions together that may have substantially different environmental and dynamical conditions for the formation of dense gas and its conversion to stars. A $\lesssim 500$ pc scale resolution is needed in order to resolve environments such as the centre (size of ~ 1 kpc), spiral arms (width of ~ 1 kpc), and bar ends (size of $\sim 0.5 - 1$ kpc).

In this work, we present new ALMA observations of dense molecular gas tracers, including HCN(1–0), HCO⁺(1–0), and CS(2–1), across the nearby spiral galaxy NGC 4321 at $3.5'' \sim 260$ pc resolution covering the full disc (i.e. out to $1.1 r_{25}$). These data are paired with CO(2–1) observations from PHANGS–ALMA (Leroy et al. 2021b), tracing the bulk molecular gas; extinction-corrected H α from PHANGS–MUSE (Emmellem et al. 2022); 21 μm observations from PHANGS–JWST (Lee et al. 2023); and 33 GHz observations from VLA (Linden et al. 2020), which are used to trace the SFR. These observations give us one of the best high-resolution, high-sensitivity data sets combining interferometric and total power observations of high critical-density molecular line emission accompanied by

* e-mail: lukas.neumann.astro@gmail.com

** Member of the International Max Planck Research School (IMPRS) for Astronomy and Astrophysics at the Universities of Bonn and Cologne.

the most robust tracers of SFR across the full disc of a nearby star-forming galaxy.

The paper is structured as follows. In Sect. 2, we present the observations and ancillary data of NGC 4321 used in this work, including new ALMA HCN observations. In Sect. 3, we describe the methods to derive the physical quantities from the observations, including the dense gas content, SFR, and ISM pressure. Then, in Sect. 4, we show the results, and we analyse the dense gas spectroscopic line ratios and their variation with environment, which are discussed in Sect. 5. Finally, we conclude and summarise the key findings in Sect. 6.

2. Observations

2.1. The target – NGC 4321

We selected NGC 4321 for this study as previous ALMA/IRAM mapping showed clear HCN detections, supporting data covers almost all aspects of the ISM and galactic structure, and its favourable distance to obtain a wide area map while still resolving, for example, the galactic centre, bar, arms, and other regions. NGC 4321 (main properties listed in Table 1) is a well-studied, spiral, barred (Querejeta et al. 2021) galaxy (Hubble classification: SABbc) that contains a large reservoir of molecular gas ($M_{\text{H}_2} = 7.77 \times 10^9 M_\odot$; Leroy et al. 2021b), is actively forming stars (SFR = $3.56 M_\odot \text{ yr}^{-1}$; Leroy et al. 2019) and can be observed relatively face-on ($i = 38.5^\circ$; Lang et al. 2020). Fig. 1 shows a James Webb Space Telescope (JWST) three-colour image overlaid with HCN contours from this work that highlight the spiral arm structure of the galaxy, seen in dust, gas and star formation. At a distance of $d = 15.2 \text{ Mpc}$ (Anand et al. 2021) it is relatively nearby, allowing access to GMC scales ($< 100 \text{ pc}$) at $\sim 1''$ angular resolution. Moreover, NGC 4321 is a spiral galaxy with similar stellar mass ($M_\star = 5.6 \times 10^{10} M_\odot$) to our Galaxy ($M_\star = 6.1 \times 10^{10} M_\odot$, Licquia & Newman 2015), making it an interesting object to compare with Galactic studies. NGC 4321 has been extensively studied as part of large observing campaigns like PHANGS–ALMA (Leroy et al. 2021b), mapping CO(2–1) across the full disc of the galaxy at $\sim 1'' \sim 100 \text{ pc}$ resolution, as well as the Eight Mixing Receiver (EMIR) Multiline Probe of the ISM Regulating Galaxy Evolution (EMPIRE; Jiménez-Donaire et al. 2019) and ALMOND (Neumann et al. 2023b) surveys, mapping various dense gas tracers including HCN and HCO^+ with the IRAM 30-m telescope and the Atacama Compact Array (ACA), respectively, at kiloparsec scales. Furthermore, NGC 4321 was part of the ALMA science verification CO(1–0) observations (Pan & Kuno 2017) and has high-quality maps of H I (HERACLES; Leroy et al. 2009), stellar structure (S^4G ; Sheth et al. 2010), star formation tracers ($\text{H}\alpha$ from MUSE; Emsellem et al. 2022), as well as near and mid-infrared maps from the JWST (Lee et al. 2023). We show a compilation of the key observations used in this work in Figure 2.

2.2. New ALMA maps of HCN

In this work, we present ALMA Band-3 observations (2017.1.00815.S; PI.: Molly Gallagher) that mapped HCN(1–0) (along with $\text{HCO}^+(1–0)$ and CS(2–1)) across the full disc of the galaxy NGC 4321 at a high angular resolution of $3.5''$ using 216.7 h of ALMA telescope time. The observations combine interferometric observations from the 12-m array (18.1 h observing time) with the ACA consisting of the 7-m array (73.4 h) and the 12-m dishes observing in total power (TP) mode (125.2 h). The mapped area on the sky is $200'' \times 120''$ large created

Table 1. Properties of NGC 4321.

Property	Value
Alternative Name	M100
Right Ascension (J2000) ^(a)	12 ^h 21 ^m 54.9 ^s
Declination (J2000) ^(a)	4 ^h 28 ^m 25.5 ^s
Inclination, $i^{(b)}$	$(38.5 \pm 2.4)^\circ$
Position Angle ^(b)	$(156.2 \pm 1.7)^\circ$
Radius, $r_{25}^{(d)}$	$(182.9 \pm 47.3)''$
Systemic Velocity, $V_{\text{LSR}}^{(b)}$	$(1572 \pm 5) \text{ km s}^{-1}$
Distance, $d^{(a)}$	$(15.21 \pm 0.49) \text{ Mpc}$
Linear Scale	73.5 pc $''^{-1}$
Matched Beam Size	3.5 $'' \sim 260 \text{ pc}$
Morphology ^(c)	SAB(s)bc
SFR ^(c)	$(3.56 \pm 0.92) M_\odot \text{ yr}^{-1}$
$\log_{10}(M_\star/M_\odot)^{(c)}$	10.75 ± 0.11

Notes:

- (a) Anand et al. (2021);
- (b) Lang et al. (2020);
- (c) Leroy et al. (2019);
- (d) HyperLeda database (Makarov et al. 2014);
- (e) NASA Extragalactic Database (NED).

via a mosaic consisting of 27 Nyquist-spaced pointings with the 12-m array. The spectral setup encompasses four spectral windows, each with a bandwidth of 1875 MHz and a channel width of 976 kHz. The first window, centred at 88.5 GHz targets HCN(1–0) (88.6 GHz) and $\text{HCO}^+(1–0)$ (89.2 GHz). The second window at 87.0 GHz covers SiO(2–1) (86.9 GHz) and isotopologues of HCN and HCO^+ , that is, $\text{H}^{13}\text{CN}(1–0)$, $\text{H}^{13}\text{CO}^+(1–0)$. The third spectral window at 98.5 GHz comprises CS(2–1) (97.9809533 GHz). The fourth spectral window at 100 GHz is used to detect continuum emission. The channel width of $\approx 3 \text{ km s}^{-1}$ is sufficient to resolve the spectral lines across the whole disc of the galaxy, and the bandwidth of $\approx 6000 \text{ km s}^{-1}$ allows for mapping of all the lines over the full velocity extent.

The data reduction was performed using the PHANGS–ALMA pipeline (details can be found in Leroy et al. 2021a), which utilises the standard ALMA data reduction package CASA (CASA Team et al. 2022). In this first study, we focus on HCN(1–0) (hereafter HCN) as the brightest proxy for dense molecular gas. The resulting HCN position-position-velocity cube has $\sim 8 \text{ mK}$ noise per 5 km s^{-1} channel. The high resolution, which corresponds to 260 pc physical scales, allowed us to resolve individual environmental regions, including the centre, bar, bar ends, spiral arms, and interarm regions (Fig. 3, right panel), yielding detection of 302 independent lines of sight in HCN emission (see Sect. 3.1 for details on masking and derivation of moment-zero maps).

2.3. Ancillary data

In addition to the new HCN data, tracing dense molecular gas, we use CO observations to trace the bulk molecular gas (Sect. 3.2) and $\text{H}\alpha$ observations to trace SFR (Sect. 3.4). Furthermore, we include H I 21-cm observations (Sect. A.2) and $3.6 \mu\text{m}$ infrared maps (Sect. A.3) to trace the atomic gas and the stellar mass content, respectively. In the Appendix, we further present additional tracers of the SFR, that is, F2100W hot dust observations from JWST (Sect. C.1) and 33 GHz free-free emission

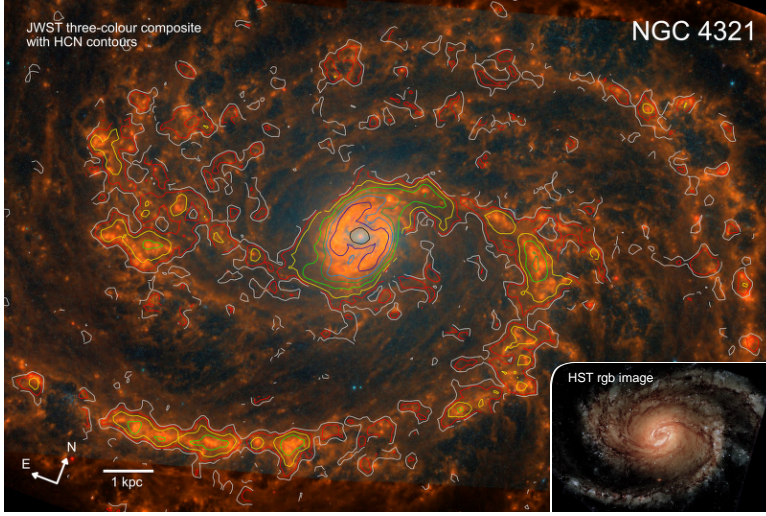


Fig. 1. JWST three-colour image of NGC 4321 overlaid with HCN contours. The background image is a three-colour composite using the MIRI and NIRCAM instruments observations (red = F770W + F1000W + F1130W + F2100W, green = F360M + F770W, and blue = F300M + F335M) taken from the PHANGS–JWST treasury survey (Lee et al. 2023). Overlaid HCN(1–0) contours (new data presented in this work), tracing the dense molecular gas are drawn at S/N levels of (2, 3, 5, 10, 20, 30, 50, 100). The sites of star formation (reddish hues) appear spatially well correlated with the dense gas traced by HCN. This image is rotated by 21° with respect to the right ascension-declination plane as indicated by the north (N)–east (E) coordinate axes in the bottom left. The bottom right image shows a rgb image (red = F814W, green = F555W, blue = F438W + F336W + F275W) from PHANGS–HST (Lee et al. 2022).

from the VLA (Sect. C.2), supporting the use of $H\alpha$ as the primary SFR tracer in this work.

3. Methods

3.1. Integrated intensity maps

We produce integrated intensity maps (moment-zero maps) from the CO and HCN position-position-velocity (PPV) cubes following Neumann et al. (2023b). The methodology goes back to Schrubba et al. (2011) and was utilised in several studies such as EMPIRE (Jiménez-Donaire et al. 2019), CO isotopologue Line Atlas within the Whirlpool galaxy Survey (CLAWS; den Brok et al. 2022) and ALMOND (Neumann et al. 2023b). First, we homogenise the data by convolving the CO data to the HCN resolution (using `convolution.convolve` from `astropy`). Then, we adopt a hexagonal spaxel grid with a beam-size spaxel separation and sample all data to the same spaxel grid and spectral axis. This means that every hexagonal pixel is an independent line-of-sight (LOS) measurement. Then, we create velocity masks based on the CO on a pixel-by-pixel basis to select the velocity range where we also expect to find HCN emission. This is done by building a 4σ mask that is expanded into channels above 2σ in order to recover broader emission belonging to a 4σ core (see e.g. Neumann et al. 2023b, for more details about the masking). By applying the CO-based mask to our data, we compute the integrated intensity of CO (W_{CO}) and HCN (W_{HCN}) by integrating the line’s brightness temperatures (T_{line} , where $\text{line} = \{\text{CO}, \text{HCN}\}$) over the velocity range selected by the mask

$$\left(\frac{W_{\text{line}}}{\text{K km s}^{-1}} \right) = \sum_{n=1}^{N_{\text{mask}}} \left(\frac{T_{\text{line},n}}{\text{K}} \right) \times \left(\frac{\Delta v_{\text{channel}}}{\text{km s}^{-1}} \right). \quad (1)$$

The uncertainties of the integrated intensities ($\sigma_{W_{\text{line}}}$) are then given by

$$\left(\frac{\sigma_{W_{\text{line}}}}{\text{K km s}^{-1}} \right) = \left(\frac{\sigma_{T_{\text{line}}}}{\text{K}} \right) \times \left(\frac{\Delta v_{\text{channel}}}{\text{km s}^{-1}} \right) \times \sqrt{N_{\text{mask}}}, \quad (2)$$

where $\sigma_{T_{\text{line}}}$ is the standard deviation in the emission-free channels (i.e. channels not selected by the mask), $\Delta v_{\text{channel}}$ is the channel width of 5 km s^{-1} and N_{mask} is the number of channels selected by the mask for each LOS.

We note that we also homogenised the two-dimensional maps, for example, the MUSE $H\alpha$ and JWST $21 \mu\text{m}$ maps, with the produced moment-zero maps. This means, we convolve the maps to the 260 pc HCN resolution and reproject them onto the same beam-size hexagonal pixel grid. A summary of the data products is presented in Fig. E.3. We describe the derivation of the physical quantities in the following subsections.

3.2. Molecular gas surface density – CO

We use CO(2–1) (hereafter CO) line observations from PHANGS–ALMA (Leroy et al. 2021b) to trace the bulk molecular gas. For NGC 4321, the CO data are at $1.67''$ resolution, which corresponds to 120 pc physical scale at the distance of the galaxy.¹ We infer the molecular gas surface density (Σ_{mol}) from the CO(2–1) line intensity ($W_{\text{CO}(2-1)}$) using the CO(2–1)-to-CO(1–0) line ratio (R_{21}) and the CO-to- H_2 conversion factor (α_{CO}), which includes the mass contribution from helium:

$$\Sigma_{\text{mol}} = \alpha_{\text{CO}} R_{21}^{-1} W_{\text{CO}(2-1)} \cos(i). \quad (3)$$

$\cos(i)$ corrects for the inclination $i = 38.5^\circ$ of the galaxy. Throughout this work, we adopt two methods (see Appendix A.1 for more details): 1) using constant α_{CO} and R_{21} conversion factors (Sect. A.1.1) that enter the estimation of the dense gas fraction as traced by the HCN-to-CO line ratio (Sect. 3.3). We use a constant α_{CO} for the HCN-to-CO line ratio due to the poor knowledge about variations of the HCN-to-dense gas conversion factor thus keeping f_{dense} proportional to HCN/CO. 2) using spatially varying α_{CO} and R_{21} (Sect. A.1.1) for computing Σ_{mol} and the dynamical equilibrium pressure (Sect 3.6).

3.3. Dense gas fraction – HCN/CO

In this study, we present new HCN observations (Sect. 2.2) and use the HCN line intensity (W_{HCN}) as a proxy for the amount of dense gas. For the main part of this work, we focus on studying the observational HCN-to-CO line ratio, that is,

¹ We do not use the archival CO(1–0) observations as a tracer of molecular gas because of their poorer angular resolution ($4''$, corresponding to $\sim 300 \text{ pc}$), but we do use them to inform our conversion of CO(2–1) intensity to molecular gas surface density, as described later in Sect. 3.2.

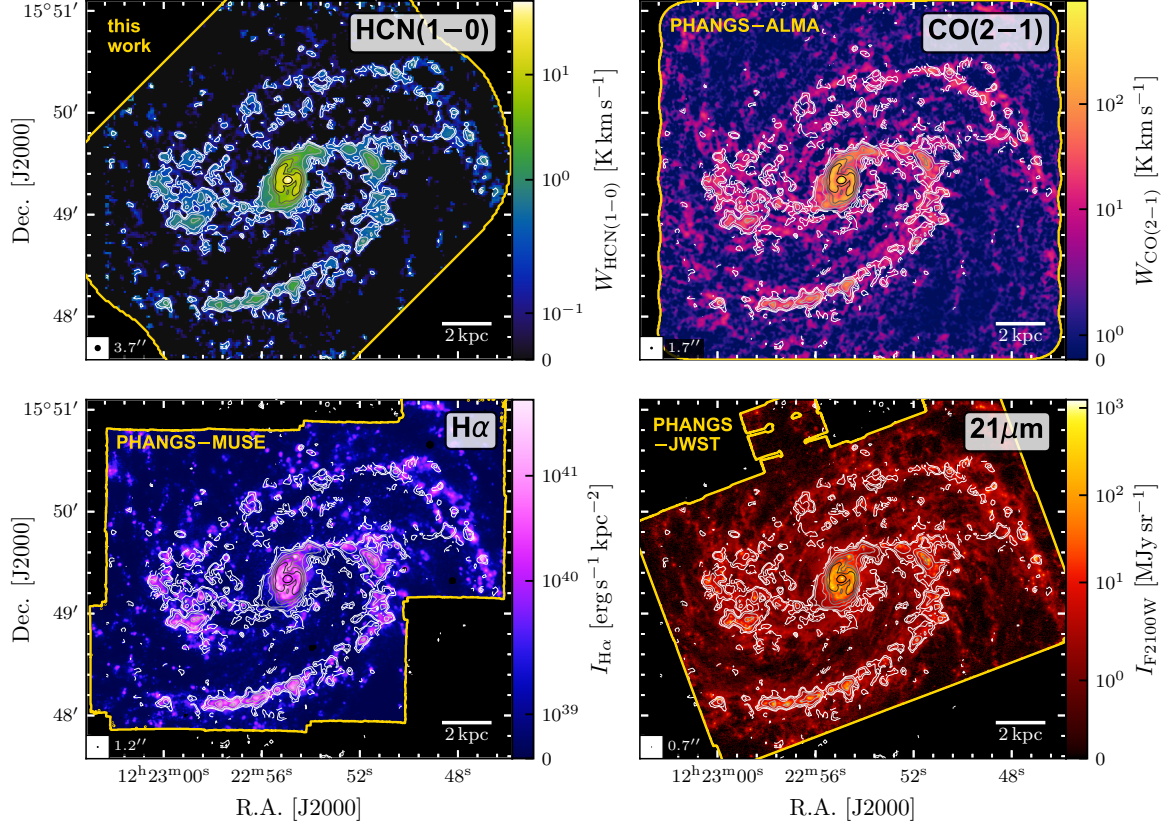


Fig. 2. NGC 4321 data used in this study, each at the native resolution of the respective observations indicated in the bottom left of each panel. *Top left:* HCN(1–0) moment-zero map presented in this work. *Top right:* CO(2–1) moment-zero map from PHANGS–ALMA (Leroy et al. 2021b). *Bottom left:* Extinction-corrected H α flux density from PHANGS–MUSE (Emsellem et al. 2022). *Bottom right:* 21 μ m flux density from MIRI–F2100W (PHANGS–JWST; Lee et al. 2023). In each panel, white-to-black-gradient contours show HCN moment-zero signal-to-noise ratio levels of (2, 3, 5, 10, 20, 30, 50, 100) as in Fig. 1. The yellow-coloured outline shows the FOV of the respective observations.

$W_{\text{HCN}}/W_{\text{CO}(2-1)}$ (hereafter HCN/CO(2–1) or simply HCN/CO) as a density-sensitive line ratio. Gallagher et al. (2018a) and Neumann et al. (2023b) have shown that HCN/CO is indeed tracing the ~ 100 pc-scale mean gas density and it has been reported to scale with the gas surface density within galactic clouds (Tafalla et al. 2023) as expected by molecular line modelling (Leroy et al. 2017). In addition, the reported linear relation between the HCN/CO and $\text{N}_2\text{H}^+/\text{CO}$ line ratios across galactic and extragalactic studies underlines the credibility of HCN/CO as a proxy for the dense gas fraction (Jiménez-Donaire et al. 2023; Stuber et al. 2023). Throughout the discussion (Sect. 5), we comment on the implications of the dense gas fraction (f_{dense}) as a physical quantity proportional to HCN/CO with some uncertainties linked to abundance, temperature and opacity.

Following many previous works (e.g. Usero et al. 2015; Bigiel et al. 2016; Gallagher et al. 2018b,a; Jiménez-Donaire et al. 2019; Bemis & Wilson 2019; Neumann et al. 2023b), the dense gas fraction is defined as the ratio of the dense gas to bulk molecular gas surface density ($f_{\text{dense}} = \Sigma_{\text{dense}}/\Sigma_{\text{mol}}$):

$$f_{\text{dense}} = \frac{\Sigma_{\text{dense}}}{\Sigma_{\text{mol}}} = \frac{\alpha_{\text{HCN}} W_{\text{HCN}}}{\alpha_{\text{CO}} R_{21}^{-1} W_{\text{CO}(2-1)}} \approx 2.1 \frac{W_{\text{HCN}}}{W_{\text{CO}(2-1)}}. \quad (4)$$

The above conversion adopts constant mass-to-light ratios $\alpha_{\text{CO}} = 4.35 \text{ M}_{\odot} \text{ pc}^{-2} (\text{K km s}^{-1})^{-1}$ (Bolatto et al. 2013) and $\alpha_{\text{HCN}} = 14 \text{ M}_{\odot} \text{ pc}^{-2} (\text{K km s}^{-1})^{-1}$ (Onus et al. 2018) for CO and HCN, respectively, and a fiducial CO(2–1)-to-CO(1–0) line ratio of $R_{21} = 0.65$ (den Brok et al. 2022; Leroy et al. 2022). Here, we use the above conversion to infer f_{dense} as an alternative axis in the HCN/CO relations.

The adopted constant HCN-to-dense gas mass conversion factor is expected to trace gas above $n_{\text{H}_2} \approx 5 \times 10^3 \text{ cm}^{-3}$ (Onus et al. 2018)². In contrast to α_{CO} , systematic variations of α_{HCN} are poorly understood and estimated values range from 0.3 to $300 \text{ M}_{\odot} \text{ pc}^{-2} (\text{K km s}^{-1})^{-1}$, spanning three orders of magnitude (García-Burillo et al. 2012; Kauffmann et al. 2017; Nguyen-Luong et al. 2017; Shimajiri et al. 2017; Evans et al. 2020; Barnes et al. 2020; Tafalla et al. 2023), where extragalactic studies, capturing larger physical areas and thus more diffuse emission typically yield values around $10 \text{ M}_{\odot} \text{ pc}^{-2}$ to $20 \text{ M}_{\odot} \text{ pc}^{-2} (\text{K km s}^{-1})^{-1}$. The α_{HCN} conversion

² We note that many previous works (e.g. Gao & Solomon 2004) used a slightly smaller value of $\alpha_{\text{HCN}} = 10 \text{ M}_{\odot} \text{ pc}^{-2} (\text{K km s}^{-1})^{-1}$ tracing gas above $n_{\text{H}_2} \approx 3 \times 10^4 \text{ cm}^{-3}$. However, choosing a different (constant) α_{HCN} has no qualitative effect on our results.

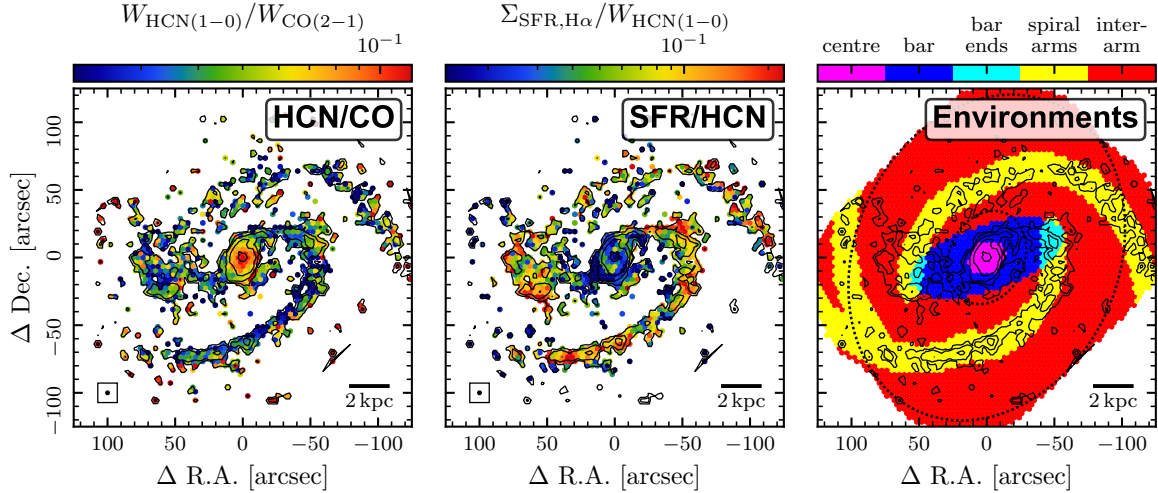


Fig. 3. NGC 4321 maps sampled at beam size. *Left:* HCN/CO line ratio map, as a proxy of the dense gas fraction (f_{dense}). The CO(2–1) data are taken from the PHANGS-ALMA survey (Leroy et al. 2021b). *Middle:* SFR surface density-to-HCN line intensity ratio, as a proxy of the dense gas star formation efficiency ($\text{SFE}_{\text{dense}}$). The SFR surface densities are obtained from the Balmer decrement-corrected H α flux computed from PHANGS-MUSE data (Emsellem et al. 2022; Belfiore et al. 2023). Black contours show HCN S/N levels of 3, 10, 30, 100, and 300, in each of the panels. In the left and middle plots, only pixels above 1-sigma are shown. The colour scale goes from the 10th to the 95th percentile of pixels above 1-sigma noise level. *Right:* Environmental region mask from Querejeta et al. (2021), which is created based on the Spitzer 3.6 μm maps tracing the stellar mass content. Here, we select the regions centre, bar, bar ends, spiral arms and interarm, where the interarm includes the interbar region. The dotted ellipses show loci of constant galactocentric radius (r_{gal}), drawn at $r_{\text{gal}} = 2.6$ kpc and $r_{\text{gal}} = 9.17$ kpc, where the latter indicates the largest radius completely covered by the HCN field of view.

factor might vary similarly to α_{CO} due to its dependence on optical depth, which is a key driver of α_{CO} variations (Teng et al. 2023), though HCN and CO optical depth variations are not expected to be identical. In that case, we could even induce systematic trends by adopting a more accurate, spatially varying α_{CO} , but keeping α_{HCN} constant. Therefore, the best current approach is to study the observational HCN/CO line ratio.

As laid out in this section, we adopt the classical view of utilising HCN/CO as a proxy of f_{dense} . However, we want to point out that the conversion factors are subject to large uncertainties (especially α_{HCN}) such that our f_{dense} estimates are expected to be uncertain by a factor of a few. Therefore, recent works (e.g. Gallagher et al. 2018b,a; Jiménez-Donaire et al. 2019; Neumann et al. 2023b; Tafalla et al. 2023), which study HCN/CO as a function of the molecular gas surface density suggest to interpret HCN/CO as a predictor of the cloud-scale (~ 100 pc) average gas density based on the robust relation between HCN/CO and Σ_{mol} (see also Sect. 4.5). This means, HCN/CO is expected to track $\langle \Sigma_{\text{mol}} \rangle$ more robustly than f_{dense} . We note, that in turbulent cloud models (Krumholz & McKee 2005), an increase of HCN/CO would indicate an increase in f_{dense} as well as $\langle \Sigma_{\text{mol}} \rangle$. Therefore, both interpretations (i.e. HCN/CO traces f_{dense} and HCN/CO traces $\langle \Sigma_{\text{mol}} \rangle$) are reasonable. Throughout this work, we base our results on the observable HCN/CO line ratio, and provide a secondary f_{dense} -axis in Figures 6 to 10, so that, taking into considering aforementioned caveats, HCN/CO can be interpreted as the dense gas fraction via a proportional conversion or alternatively as an indicator of the mean gas density.

3.4. Star formation rate – H α

We use H α recombination line emission taken by the Multi Unit Spectroscopic Explorer (MUSE) of the Very Large Telescope (VLT) as part of the PHANGS-MUSE survey (Emsellem et al. 2022) to trace the SFR. In Appendix C, we discuss using alternative SFR tracers including 21 μm (F2100W) hot dust emission from JWST (Lee et al. 2023) and 33 GHz free-free emission from the VLA (Linden et al. 2020), which can differ significantly (up to one order of magnitude) in the central few kiloparsecs of galaxies. Here, we find that SFR values inferred from the 33 GHz emission confirm the extinction-corrected H α inferred values in the centre of NGC 4321. Moreover, 21 μm emission also yields similar SFR values (within 0.2 dex) when adopting a linear conversion (for more details see App. C.3). Therefore, throughout this work we adopt H α emission as a robust tracer of SFR validated by free-free data in the centre.

We used the Balmer decrement-corrected H α maps to measure the SFR surface density (Σ_{SFR}). Those rely on the extinction curve from O’Donnell (1994) as described in Pessa et al. (2022) and Belfiore et al. (2023). The attenuation corrected H α flux ($L_{\text{H}\alpha, \text{corr}}$) is converted into SFR via $\text{SFR}/(\text{M}_{\odot} \text{ yr}^{-1}) = C_{\text{H}\alpha} \times L_{\text{H}\alpha, \text{corr}}/(\text{erg s}^{-1})$ using the conversion factor $C_{\text{H}\alpha} = 5.3 \times 10^{-42}$ from Calzetti et al. (2007). This conversion assumes a constant star formation history, age of 100 Myr, solar metallicity, and a Kroupa (2001) initial mass function (IMF) (for more detail on the SFR calibration, see Belfiore et al. 2023). In surface density units the above formalism translates to

$$\left(\frac{\Sigma_{\text{SFR}, \text{H}\alpha}}{\text{M}_{\odot} \text{ yr}^{-1} \text{ kpc}^{-2}} \right) = 6.3 \times 10^2 \left(\frac{I_{\text{H}\alpha, \text{corr}}}{\text{erg s}^{-1} \text{ cm}^{-2} \text{ sr}^{-1}} \right) \cos(i). \quad (5)$$

3.5. Dense gas star formation efficiency – SFR/HCN

We took the ratio of the SFR surface density (Σ_{SFR}) to the HCN line intensity (W_{HCN}), that is, $\Sigma_{\text{SFR}}/W_{\text{HCN}}$ (hereafter SFR/HCN), as a proxy of the star formation efficiency of the dense gas ($\text{SFE}_{\text{dense}}$). Similar to HCN/CO tracing f_{dense} , we also focus on the more observationally based SFR/HCN in our analysis and discuss implications on the inferred $\text{SFE}_{\text{dense}}$ connected to uncertainties in the conversion factor (α_{HCN}). $\text{SFE}_{\text{dense}}$ is defined as the ratio of SFR surface density to dense gas mass surface density ($\text{SFE}_{\text{dense}} = \Sigma_{\text{SFR}}/\Sigma_{\text{dense}}$) as in previous works (listed in Sect. 3.3):

$$\text{SFE}_{\text{dense}} = \frac{\Sigma_{\text{SFR}}}{\Sigma_{\text{dense}}} = \alpha_{\text{HCN}}^{-1} \frac{\Sigma_{\text{SFR}}}{W_{\text{HCN}}}. \quad (6)$$

The above equation yields

$$\left(\frac{\text{SFE}_{\text{dense}}}{\text{Myr}^{-1}} \right) = 0.071 \left(\frac{\Sigma_{\text{SFR}}}{\text{M}_{\odot} \text{ yr}^{-1} \text{ kpc}^{-2}} \right) \left(\frac{W_{\text{HCN}}}{\text{K km s}^{-1}} \right)^{-1}. \quad (7)$$

when using the same, constant HCN-to-dense gas mass conversion ($\alpha_{\text{HCN}} = 14 \text{ M}_{\odot} \text{ pc}^{-2} (\text{K km s}^{-1})^{-1}$, Onus et al. 2018) as for f_{dense} (Sect. 3.3).

3.6. Dynamical equilibrium pressure

We compute the dynamical equilibrium pressure, or ISM pressure (P_{DE}) at 260 pc scale following the prescription by Sun et al. (2020). In this prescription the dynamical equilibrium pressure is composed of a pressure term created by the ISM due to the self-gravity of the ISM disc and a term due to the gravity of the stars (see e.g. Spitzer 1942), such that

$$P_{\text{DE}} = \frac{\pi G}{2} \Sigma_{\text{gas}}^2 + \Sigma_{\text{gas}} \sqrt{2G\rho_{\star}} \sigma_{\text{gas},z}, \quad (8)$$

where we assumed a smooth, single-fluid gas disc and that all gas shares a similar velocity dispersion so that $\Sigma_{\text{gas}} = \Sigma_{\text{mol}} + \Sigma_{\text{atom}}$ is the total gas surface density, composed of a molecular (Σ_{mol}) and an atomic (Σ_{atom}) gas component. ρ_{\star} is the stellar mass volume density (App. A.3) near the disc mid-plane and $\sigma_{\text{gas},z}$ is the velocity dispersion of the gas perpendicular to the disc.

In many previous extragalactic studies (e.g. Spitzer 1942; Elmegreen 1989; Elmegreen & Parravano 1994; Wong & Blitz 2002; Blitz & Rosolowsky 2004, 2006; Leroy et al. 2008; Koyama & Ostriker 2009; Ostriker et al. 2010; Ostriker & Shetty 2011; Kim et al. 2011; Shetty & Ostriker 2012; Kim et al. 2013; Kim & Ostriker 2015; Benincasa et al. 2016; Herrera-Camus et al. 2017; Gallagher et al. 2018a; Fisher et al. 2019; Schrub et al. 2019; Jiménez-Donaire et al. 2019) P_{DE} was typically estimated using Equ. (8) with homogenised Σ_{gas} , ρ_{\star} , $\sigma_{\text{gas},z}$ at kiloparsec scales. Recently, Sun et al. 2020 came up with a new formalism that makes use of the high resolution ~ 100 pc scale CO(2–1) data from PHANGS–ALMA. Most importantly, it takes into account the self-gravity of the (molecular) gas at high resolution. In this study we adopt their formalism and combine the 120 pc scale molecular gas term ($\langle P_{\text{cloud}} \rangle$); converted to the lower resolution via a Σ_{mol} -weighted average) with the 260 pc scale atomic gas term (P_{atom}):

$$\langle P_{\text{DE}} \rangle = \langle P_{\text{cloud}} \rangle + P_{\text{atom}}. \quad (9)$$

$\langle P_{\text{cloud}} \rangle$ consists of three terms accounting for the self-gravity of the molecular gas, the gravity of larger molecular structures and the gravity of stars. P_{atom} includes the self-gravity of the atomic gas and the gravitational interaction of the atomic gas with the 260 pc scale molecular gas and the stars (see App. A.4 for more details).

3.7. Morphological environmental masks

We adopt the environmental masks presented in Querejeta et al. (2021), which identify morphological environmental regions based on the appearance of the stellar mass content traced by the *Spitzer* 3.6 μm emission from S⁴G (Sheth et al. 2010). We use the “simple” mask, where each pixel is uniquely assigned to a dominant environment. We define the bar ends as the overlap of the spiral arms with the bar footprint. For simplicity, we combine interbar, interarm into one region, referred to as interarm. We end up with five environments – centre, bar, bar ends, spiral arms, interarm, which are re-sampled onto the same hexagonal grid as the other data defined by the HCN map (Sect. 3.1). We show the adopted environments in the right panel of Fig. 3.

3.8. Stacking and linear regression

To study the average trends, we stack the data (HCN, CO, SFR) in equally spaced bins in linear scale (r_{gal}) or logarithmic scale (P_{DE}). The spectral stacking is done using the python package PyStacker,³ which yields average CO and HCN spectra in each respective bin (the stacked spectra are presented in Fig. 4 and in App. B). Those average spectra are used to compute the average integrated intensities in each bin. For SFR, we simply compute the mean of the SFR values in the respective bin. The bin ratios are then computed as the ratios of the stacked measurements. To first order, HCN and CO lines show similar kinematics across most of the galaxy, so the line ratio, which we discuss in this first paper, encodes most of the relevant information.

We fit the stacked data in order to probe the underlying global relation without “population” biases and to not be dominated by non-detections in constraining the best-fit line. We note, however, that we have also fitted the individual sightline measurements using LinMix,⁴ resulting in similar fit relations in agreement within 1-sigma uncertainties with the fits reported here for the binned data. We use these sightline fits to quantify the uncertainty of the regression slopes since the piecewise fitting routine (see below) does not yield uncertainties.

We then apply a multivariate adaptive regression spline (MARS; Friedman 1991) model to the binned data in order to find the best piecewise linear regression function that describes the data (see Sect. 4.2 and 4.3). MARS is a generalisation of a recursive partitioning algorithm, which iteratively splits the data into separate x -axis regimes and optimises the split point with respect to the piecewise linear regression in each regime via minimising the χ^2 value of the data to the model. The algorithm is adapted to only add another split point if a further component significantly improves the fit, meaning that the χ^2 value is improved by more than 0.01. In this way, we employ a statistically robust and objective method to find the threshold at which the trends change significantly thus identifying physically different regimes in the relations. To perform the MARS model we utilise the R-package *earth*.⁵ Here, we force the model to only consist of up to two linear functions, that is, it can either find one or two regimes depending on if a second regime improves the fit significantly.

³ <https://github.com/PhangsTeam/PyStacker>

⁴ <https://linmix.readthedocs.io/en/latest/index.html>; LinMix is a Bayesian inference tool to linear regression, which can take into account upper limits and infers the posterior distribution of the fit line parameters via MCMC simulation (Kelly 2007).

⁵ <https://cran.r-project.org/package=earth>

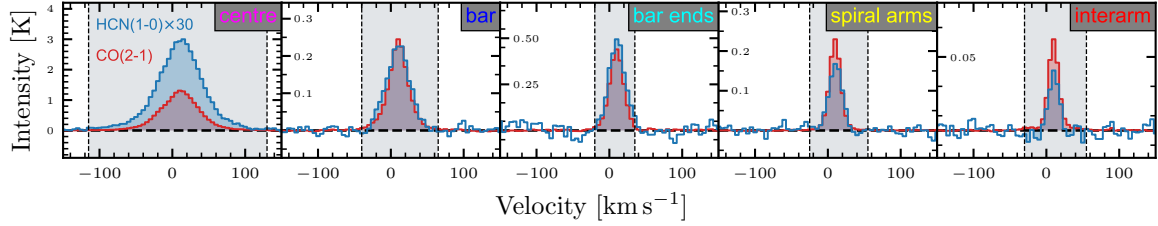


Fig. 4. Stacked spectra by environment. The CO(2–1) line (red) is used to correct for the effect of the velocity field. In every panel, the HCN(1–0) intensities are multiplied by a factor of 30 for better comparison with the CO intensities. The grey-shaded area indicates the velocity window over which the integrated intensities are computed.

Table 2. Line intensities and luminosities by environment.

Environment	$W_{\text{CO}(2-1)}$ [mK km s ⁻¹]	$L_{\text{CO}(2-1)}$ [K km s ⁻¹ kpc ²]	$f_{\text{CO}(2-1)}$	$W_{\text{HCN}(1-0)}$ [mK km s ⁻¹]	$L_{\text{HCN}(1-0)}$ [K km s ⁻¹ kpc ²]	$f_{\text{HCN}(1-0)}$
full galaxy	3861 ± 10	822.2 ± 2.1	1471/3489 (42.2 %)	168 ± 4	35.8 ± 0.8	275/3489 (7.9 %)
centre	82790 ± 76	217.3 ± 0.2	42/43 (97.7 %)	7462 ± 36	19.6 ± 0.1	42/43 (97.7 %)
bar	8233 ± 35	147.2 ± 0.6	227/293 (77.5 %)	303 ± 8	5.4 ± 0.1	70/293 (23.9 %)
bar ends	10875 ± 56	33.9 ± 0.2	50/51 (98.0 %)	464 ± 15	1.4 ± 0.0	26/51 (51.0 %)
spiral arms	4577 ± 13	264.8 ± 0.8	594/948 (62.7 %)	129 ± 6	7.5 ± 0.4	97/948 (10.2 %)
interarm	1178 ± 11	154.9 ± 1.4	558/2154 (25.9 %)	18 ± 4	2.4 ± 0.5	40/2154 (1.9 %)

Notes: Columns 2 and 5 list the stacked integrated intensities of CO(2–1) and HCN(1–0) for the full galaxy (first row) and respective morphological environments. The stacked spectra are shown in Fig. 4. The corresponding CO(2–1) and HCN(1–0) line luminosities are shown in columns 3 and 6. Columns 4 and 7 present the detection fractions of CO(2–1) and HCN(1–0), respectively, by environment. Shown are the number of detected ($S/N \geq 3$) independent sight lines w.r.t. the total number of sight lines in the respective region and the corresponding detection fraction in percent in brackets.

4. Results

4.1. Dense gas spectroscopic ratios across the full disc of NGC 4321 at 260 pc scale

The new high-resolution deep wide-field HCN observations presented in this work allowed us for the first time to study variations of HCN/CO, a proxy of f_{dense} , and SFR/HCN, a proxy of $\text{SFE}_{\text{dense}}$, across the full disc of a Milky Way-like galaxy at unprecedented resolution (260 pc) such that morphological environments could be well separated. These data represent one of the rare deep wide-field HCN maps of a nearby galaxy that allows analysis of 275 detected sight lines even outside of the galaxy centre, as illustrated by Fig. 2 (top left panel). By environment, we detected 42 HCN sight lines in the centre, 70 in the bar, 26 in the bar ends, 97 in the spiral arms, and 40 in the interarm regions (we list the values along with stacked integrated intensities and luminosities in Tab. 2). Figure 2 shows that where CO was detected; HCN is also often detected, though we found HCN to be more concentrated in the centre, bar, bar ends, and spiral arms. To first order, $H\alpha$ and 21 μm emission, tracers of SFR, are spatially correlated with both CO and HCN. The 260 pc scale resolved observations of NGC 4321 confirm the well-established linear correlation between HCN luminosity and SFR.

In Figure 3, we show maps of HCN/CO and SFR/HCN. The variability of these ratios provides information about how HCN correlates with CO and SFR, as discussed below. In the following, we distinguish between five environmental regions (centre, bar, bar ends, spiral arms, interarm) introduced in Sect. 3.7. The right panel of Figure 3 shows the applied environments sampled onto the same coordinate grid and overlaid with HCN contours.

Overall, the HCN emission follows the stellar mass morphology such that outside of the centre, most of the HCN emission is associated with the stellar spiral arms, whereas less HCN is found in the interarm regions. However, there is also large amounts of (dense) molecular gas when following the bar eastward beyond the bar ends. These regions, here depicted as interarm regions, could be interpreted as minor spiral arms or spurs between the spiral arms that harbour large amounts of molecular gas (similar to the spurs observed in M51; Schinnerer et al. 2017). Though not explored here and considered part of the interarm environment, it could be interesting to study these spurs in more detail in further studies.

4.1.1. HCN/CO variations

Figure 5 (left panel) shows the distribution of HCN/CO values in different environments, stacked in increments of 0.1 dex. We also show the mean and scatter of the detected data of the respective distributions. Since S/N clipping systematically selects luminous HCN regions, these values will be biased towards high HCN/CO and low SFR/HCN, with the significance of the bias depending on the completeness of detections in the respective environments. Therefore, we also show the stacked means of all sight lines across each environment (squares in Fig. 5). The values are listed in Tab. 3.

We find that HCN/CO spans roughly 0.6 dex when considering only detected lines of sight ($S/N \geq 3$). In agreement with previous studies (e.g. Usero et al. 2015; Bigiel et al. 2016; Gallagher et al. 2018b; Jiménez-Donaire et al. 2019; Querejeta et al. 2019; Neumann et al. 2023b; Beslic et al. 2024), HCN/CO increases towards the centre of the galaxy, where it reaches val-

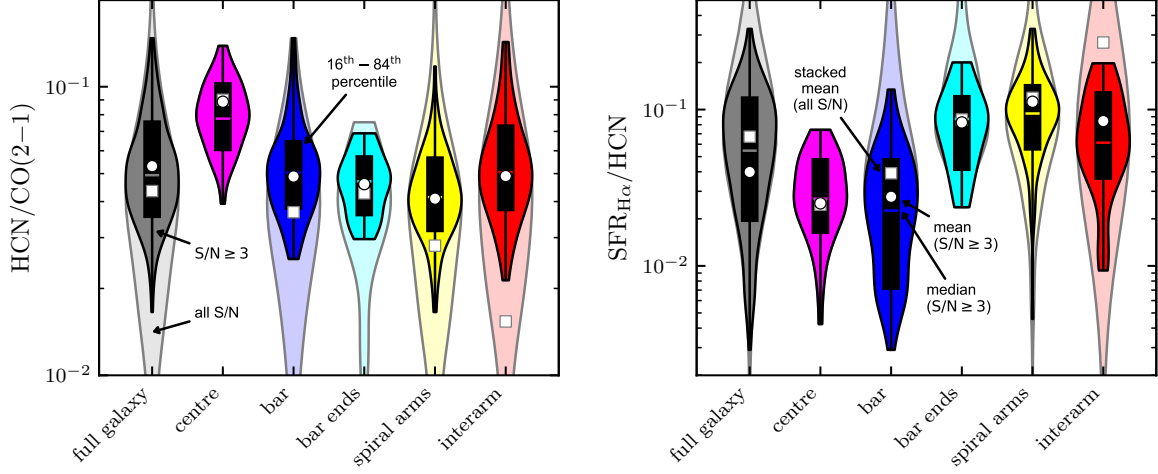


Fig. 5. Violin plots of dense gas spectroscopic ratios separated by environmental regions. *Left:* HCN/CO line ratio, a proxy of the dense gas fraction, f_{dense} . *Right:* $\text{SFR}_{\text{HCN}}/\text{HCN}$, a proxy of the dense gas star formation efficiency, $\text{SFE}_{\text{dense}}$, in units of $(M_{\odot} \text{ yr}^{-1} \text{ kpc}^{-2})/(\text{K km s}^{-1})$. The darker coloured violin areas are created from significant data ($S/N \geq 3$). The lighter coloured areas represent the distribution of all S/N, this means including non-detections. The black bar indicates the 16th to 84th percentile range of the significant data and the coloured vertical line within the bars denotes the median. Circles show the means (sum of the ratio's numerator divided by the sum of the ratio's denominator) of the significant data. Squares show the stacked means, which take into account all data detected in CO within the respective environment. The values are listed in Tab. 3

Table 3. HCN/CO and SFR/HCN statistics by environment.

Ratio	Environment	(16 th , 84 th) perc. S/N ≥ 3	mean S/N ≥ 3	stacks all S/N
HCN CO(2-1)	full galaxy	(0.035, 0.076)	0.067	0.043 ± 0.001
	centre	(0.060, 0.104)	0.089	0.090 ± 0.001
	bar	(0.037, 0.065)	0.049	0.037 ± 0.001
	bar ends	(0.036, 0.058)	0.046	0.043 ± 0.001
	spiral arms	(0.031, 0.057)	0.041	0.028 ± 0.001
	interarm	(0.037, 0.074)	0.049	0.015 ± 0.003
SFR _{HCN} HCN	full galaxy	(0.019, 0.122)	0.040	0.069 ± 0.002
	centre	(0.016, 0.049)	0.025	0.025 ± 0.001
	bar	(0.007, 0.049)	0.028	0.039 ± 0.001
	bar ends	(0.040, 0.124)	0.083	0.086 ± 0.003
	spiral arms	(0.055, 0.146)	0.112	0.125 ± 0.006
	interarm	(0.036, 0.131)	0.084	0.274 ± 0.057

Notes: Statistics of spectroscopic ratios across the different environments (right panel of Fig. 3) corresponding to the distributions shown in Fig. 5. The third column shows the 16th and 84th percentiles of the detected measurements ($S/N \geq 3$). The fourth column lists the mean of the detected data, which is computed as the sum of the numerator data over the sum of the denominator data of the spectroscopic ratio. The fifth column shows the stacks mean over all S/N along with measurement uncertainties (in dex) in the respective environment. The measurement uncertainties are computed from the rms of the emission-free channels of the stacks (Equ. 2) and do not include any calibration or systematic uncertainties.

ues around 0.1 (mean of 0.089 ± 0.0003), indicating an increase of the dense gas fraction or average gas density in centres of galaxy or/and a change in excitation conditions, for example, optical depth, gas temperature, or abundance (e.g. Jiménez-Donaire et al. 2017; Eibensteiner et al. 2022).

Throughout the disc of the galaxy (spiral arms and interarm region), HCN/CO is lower by a factors of two (mean of ≤ 0.049 across detections, with 1-sigma scatter of ± 0.15 dex) compared to the centre (mean of 0.89) and does not show trends with radius or environment (further discussed in Sect. 4.2). This suggests, assuming that HCN/CO is a robust tracer of density (Neumann et al. 2023b), that the density distribution of the molecular gas, which is detected in HCN, is very similar across the disc of NGC 4321. However, we note that when taking into account censored data, the average HCN/CO is lower by almost a factor of two in the interarm region (mean of 0.015 ± 0.003) than in the spiral arms (mean of 0.028 ± 0.001).

Compared to the disc of the galaxy and taking into account non-detections, we observed enhanced HCN/CO in the bar ends (mean of 0.043 ± 0.001) pointing towards the piling up of dense molecular gas, for example, via gas streams from the spiral arms and the bar towards the bar ends (predicted by simulations e.g. Renaud et al. 2015 and observed in NGC 3627 Bešlić et al. 2021). Moreover, we observe indications of a mild gradient of HCN/CO with angular offset from the spiral arm across the southern spiral arm (Fig. 3). If taken at face value, the found HCN/CO gradient could imply a systematic density variation across the spiral arm, changing the physical conditions of the emitting gas.

4.1.2. SFR/HCN variations

Analogously to HCN/CO, we show violin plots along with mean scatter bars of SFR/HCN, a proxy of $\text{SFE}_{\text{dense}}$, in the right panel of Figure 5. In total, the SFR/HCN values span about 2 dex across the detected LOSs indicating a large scatter in SFR/HCN, consistent with the cloud-to-cloud variation found in galactic studies (e.g. Moore et al. 2012; Eden et al. 2012; Csengeri et al. 2016; Urquhart et al. 2021). Certainly, some of the scatter can be attributed to systematic variations with molecular gas conditions

(e.g. Neumann et al. 2023b) and environment (discussed in this work).

In the inner ~ 4 kpc of NGC 4321, SFR/HCN appears to be spatially anti-correlated with HCN/CO (Fig. 3), confirming kiloparsec-scale measurements of previous studies, for example, Usero et al. 2015; Gallagher et al. 2018b; Jiménez-Donaire et al. 2019. As has been reported in several previous studies (e.g. Chen et al. 2015; Bešlić et al. 2021; Neumann et al. 2023b), SFR/HCN decreases towards the centre of the galaxy (mean of 0.025 ± 0.0001 in units of $(M_{\odot} \text{ yr}^{-1} \text{ kpc}^{-2}) / (\text{K km s}^{-1})$) supporting the picture that HCN traces more of the bulk material in dense environments. In addition to the centre, we find SFR/HCN to be particularly low in the bar of the galaxy (mean of 0.039 ± 0.001) (further discussed in Sect. 5.3), while it is higher by a factor of two to seven across the disc (i.e. bar ends, spiral arms and interarm regions, have means between 0.086 ± 0.003 and 0.274 ± 0.057).

The low SFR/HCN in the centre and bar environments can be explained in several ways. On the one hand, the low SFR/HCN can be caused by an increase in HCN emissivity. On the other hand, it could indicate a decrease in SFR at fixed HCN emission, that is, an actually reduced star formation efficiency of dense gas. Another alternative explanation put forward in previous works (e.g. Gallagher et al. 2018b; Jiménez-Donaire et al. 2019; Neumann et al. 2023b) is that, in these high-density, high-pressure environments, HCN is not tracing the actual overdensities anymore, but become more of a bulk molecular gas tracer. The former can be caused by radiative trapping (Shirley 2015; Jiménez-Donaire et al. 2017), lowering the effective critical density of HCN and yielding subthermally excited HCN emission (Leroy et al. 2017; Jones et al. 2023; García-Rodríguez et al. 2023) or electron excitation (Goldsmith & Kauffmann 2017) boosting the HCN emission. The reduced $\text{SFE}_{\text{dense}}$ could be the result of a strong influence of gas dynamics on the star-formation process (bar), for example, shear, hampering the formation of stars despite the availability of dense gas (Sect. 5.3). We note that centres are much more affected by variations in conversion factors (α_{CO} and α_{HCN}) than discs, and the SFR estimator (extinction-corrected $\text{H}\alpha$) is potentially less accurate due to increasing dust attenuation towards centres and the effects of AGN-driven $\text{H}\alpha$ emission (although this galaxy has no AGN according to Véron-Cetty & Véron 2010). Most probably, the low SFR/HCN in the centre is a combination of an increase in gas turbulence driving HCN emission and a lower HCN-to-dense gas conversion factor.

Spiral arms, interarm regions and bar ends share a similar SFR/HCN distribution suggesting they are similarly efficiently converting dense gas into stars. This is contradictory to the hypothesis that bar ends are the sites of increased star formation efficiency, for example, via cloud-cloud collision that might boost the star formation efficiency (Watanabe et al. 2011; Maeda et al. 2021). However, we note that the aforementioned works investigate the star formation efficiency of the bulk molecular gas, traced via SFR/CO. Therefore, their implications are likely not applying to our study of SFR/HCN, since high SFR/CO does not imply high SFR/HCN.

Overall, spiral arms and interarm regions show comparable HCN/CO and SFR/HCN distributions and means across the detected sight lines (HCN/CO of 0.041 and 0.049, SFR/HCN of 0.112 and 0.084, respectively in spiral arms and interarm regions), which demonstrates that although spiral arms appear to show higher gas pressure and accumulate gas, they do not contain higher density clouds nor are more efficiently converting the dense gas to stars. This result agrees with findings from Milky Way clouds (e.g. Dib et al. 2012; Moore et al. 2012; Eden et al.

2012, 2013, 2015; Ragan et al. 2016, 2018; Rigby et al. 2019; Urquhart et al. 2021) as well as supported by high-resolution simulations of galactic-scale star formation (e.g. Tress et al. 2020).

4.2. Radial trends

Figure 6 (left) shows the variation of HCN/CO and SFR/HCN with galactocentric radius. To show the average trend (red markers), we stack the data in radial bins of 0.5 kpc width, that is, at twice the beam size. We then fit a piecewise linear regression model (MARS), using the R-package *earth* as described in Sect. 3.8. The resulting piecewise linear regression parameters are listed in Tab. 4. The MARS model finds two regimes in each of the radial correlations, which separates the relations into a central region (≤ 2.0 kpc for HCN/CO and ≤ 2.8 kpc SFR/HCN) and a disc region (outside of the aforementioned thresholds). The central region covers about half of the bar length, which extends out to 4 kpc.

We note that the apparent offset between the significant data ($\text{S/N} \geq 3$; dark blue markers) and the stacked average trends is expected in the presence of low HCN detection fraction, which is the case for most data at high r_{gal} or low $\langle P_{\text{DE}} \rangle$. While the stacks take into account the non-detections thus recovering the true, unbiased average value, the 3-sigma clipped data are (on average) biased towards higher HCN/CO because the low HCN/CO sight-line measurements tend to fall below the 3-sigma threshold, but are included in the stacked measurement.

4.2.1. HCN/CO versus galactocentric radius

In the inner 2.0 kpc, we measure a very strong (slope $m = -0.38 \pm 0.02$, Pearson correlation coefficient $\rho = -0.86$, $p = 1.73 \times 10^{-51}$), tight (scatter of 0.14 dex) relation between HCN/CO and r_{gal} . HCN/CO increases towards the centre of the galaxy where it is almost one order of magnitude higher than on average at larger r_{gal} agreeing with the spatial variations discussed in Section 4.1. Assuming HCN/CO traces density, this suggests that the fraction of dense gas is higher in the centre, consistent with resolved observations of galaxies (e.g. Bigiel et al. 2016; Gallagher et al. 2018b; Jiménez-Donaire et al. 2019; Bešlić et al. 2021; Neumann et al. 2023b).

Across the disc ($r_{\text{gal}} > 2.0$ kpc), HCN/CO remains constant on average ($m = 0.0 \pm 0.01$, $\rho = -0.14$, $p = 0.306$) suggesting a more constant cloud mean density outside of galaxy centres. However, we observe a large scatter (0.23 dex) about the fit line, indicating substantial variations in HCN/CO depending on the exact location in the galaxy. Overall, this means that outside of the centre of NGC 4321 r_{gal} is not a good predictor of HCN/CO at 260 pc resolution.

4.2.2. SFR/HCN versus galactocentric radius

Similar to HCN/CO, in the central 2.8 kpc, SFR/HCN varies systematically with radius ($m = 0.34 \pm 0.02$, $\rho = 0.32$, $p = 1.64 \times 10^{-5}$), though with the opposite sign ($m = 0.08 \pm 0.01$, $\rho = 0.41$, $p = 1.64 \times 10^{-5}$). SFR/HCN drops towards the centre (SFR/HCN $\sim 1 \times 10^{-2}$) by roughly one order of magnitude with respect to the disc average value (SFR/HCN $\sim 1 \times 10^{-1}$), which taken at face value, points towards galaxy centres being less efficient in converting dense gas to stars in line with many previous works studying dense gas via HCN (e.g. Usero et al. 2015; Bigiel et al. 2016; Gallagher et al. 2018b; Jiménez-Donaire et al. 2019;

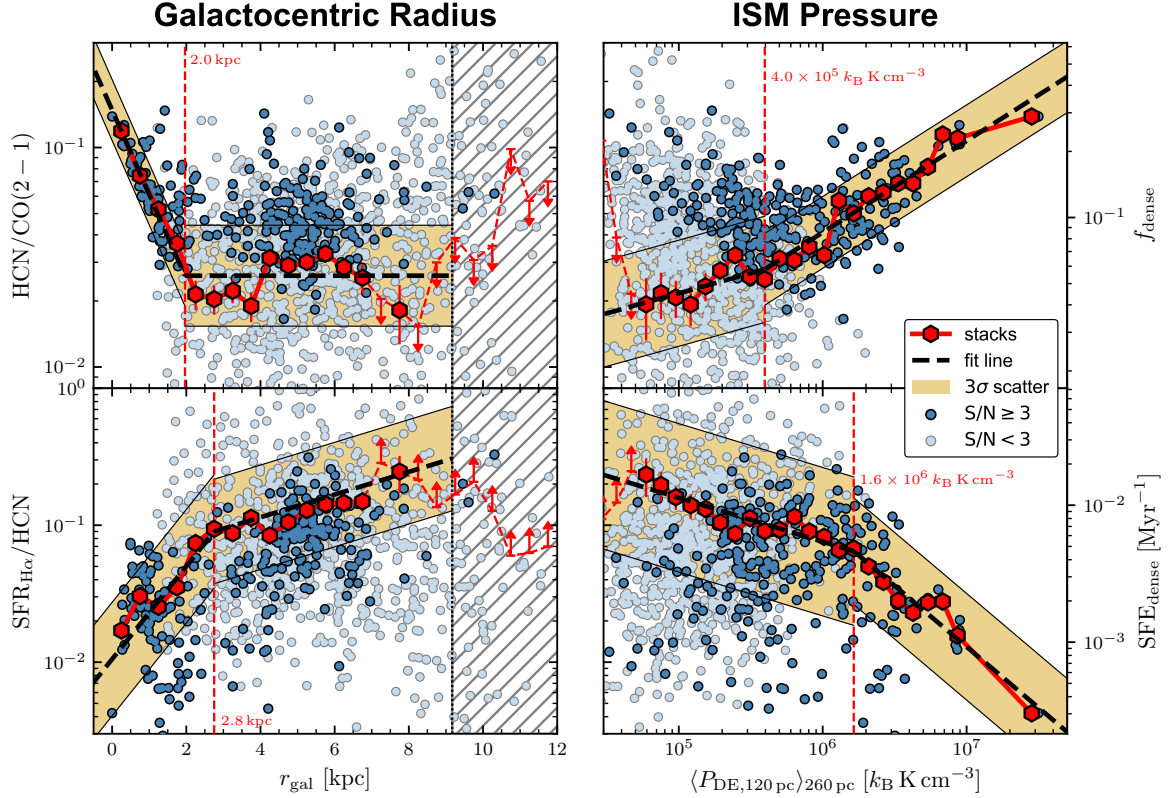


Fig. 6. Dense gas spectroscopic ratios as a function of galactocentric radius and environmental pressure. *Top:* HCN/CO, a proxy of the dense gas fraction, f_{dense} , as a function of r_{gal} and $\langle P_{\text{DE}} \rangle$. *Bottom:* SFR/HCN, a proxy of the dense gas star formation efficiency, $\text{SFE}_{\text{dense}}$, against r_{gal} and $\langle P_{\text{DE}} \rangle$. Significant data, that is, $S/N \geq 3$, are shown as blue markers. Low significance data ($S/N < 3$) are shown in light blue. The red hexagon markers denote significant spectral stacks taken over all data, with the bars showing the uncertainties obtained from the stacked spectra. The red arrows indicate 3σ upper limits of the HCN stacks resulting in HCN/CO upper limits and SFR/HCN lower limits. In the left panels, the hatched region ($r_{\text{gal}} > 9.17$ kpc) indicates the range where the map is not complete (compare with Fig. 3). The vertical red dashed lines indicate the x -axis values separating two regions with different linear regression behaviour based on the MARS model. The dashed black lines indicate the best-fit lines resulting from the MARS model (Tab. 4). The gold-shaded area shows the 3-sigma scatter of the detected sightlines about the fit line.

Table 4. HCN/CO(2 – 1) and SFR/HCN correlations.

x-axis	y-axis	Regime	Slope (stacks)	Slope (los)	Corr. (p)	Scatter
r_{gal}	HCN/CO(2 – 1)	≤ 2.0 kpc	-0.38	-0.26 (0.02)	-0.86 (0.0)	0.14
		> 2.0 kpc	0.00	0.00 (0.01)	-0.03 (0.306)	0.23
	SFR _{Hα} /HCN	≤ 2.8 kpc	0.34	0.22 (0.06)	0.32 (0.0)	0.41
		> 2.8 kpc	0.08	0.08 (0.01)	0.41 (0.0)	0.38
$\langle P_{\text{DE}} \rangle$	HCN/CO(2 – 1)	$\leq 4.0 \times 10^5$ k_B K cm^{-3}	0.18	0.23 (0.02)	0.47 (0.0)	0.24
		$> 4.0 \times 10^5$ k_B K cm^{-3}	0.42	0.40 (0.03)	0.64 (0.0)	0.16
	SFR _{Hα} /HCN	$\leq 1.6 \times 10^6$ k_B K cm^{-3}	-0.32	-0.53 (0.04)	-0.47 (0.0)	0.54
		$> 1.6 \times 10^6$ k_B K cm^{-3}	-0.89	-0.70 (0.22)	-0.39 (0.003)	0.39

Notes – Linear regression parameters for the respective relations and x -axis regimes presented in Fig. 6. The fourth column is showing the slopes obtained from the multivariate adaptive regression spline (MARS) method, producing a continuous piece-wise linear regression. Columns five to seven show the linear regression parameters obtained from the individual sight-line measurements, taking into account all data in the respective regime, using the linear regression tool LinMix. ‘Corr.’ is the Pearson correlation coefficient of sight-line data and ‘ p ’ is the associated p -value. The scatter denotes the 3σ standard deviation of the detected sight-line data about the fit line. The cloud-scale pressure thresholds correspond to 260 pc-scale beam-matched values of $P_{\text{DE}} \approx 1.5 \times 10^5$ k_B K cm^{-3} and $P_{\text{DE}} = 6.3 \times 10^5$ k_B K cm^{-3} , respectively.

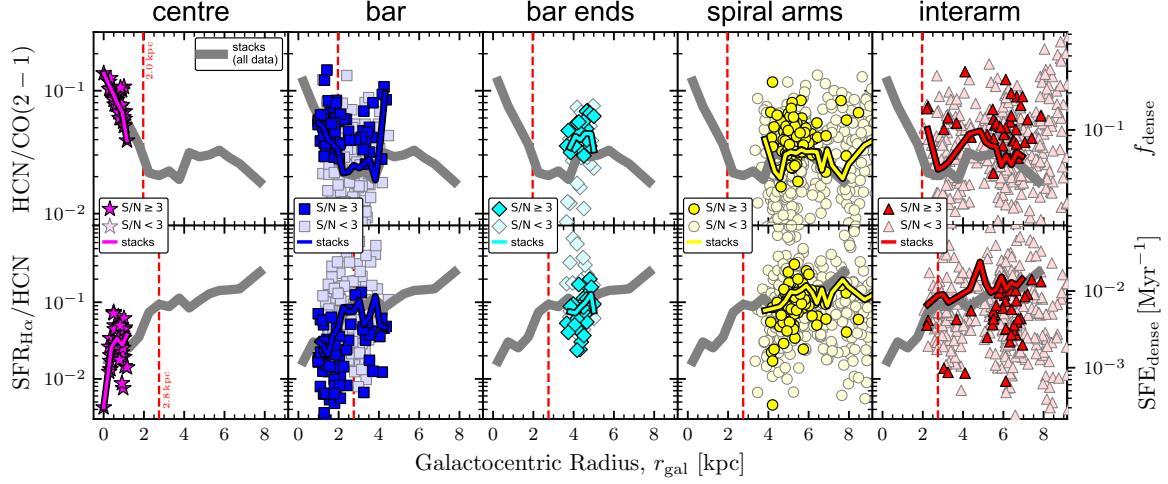


Fig. 7. Dense gas spectroscopic ratios versus radius in different morphological environments. Similar to Fig. 6 (left panels), but separately for each environment (compare with right map in Fig. 3). The lighter markers denote low-significant ($S/N < 3$) data. The grey solid line shows the trend of the spectral stacks as in Fig. 6 (red markers). The coloured lines indicate the stacked measurements of the respective environments taken over all CO detected data (i.e. including HCN non-detections) in the respective environment.

Querejeta et al. 2019; Bešlić et al. 2021; Neumann et al. 2023b; Beslic et al. 2024). However, we note that both HCN (due to optical depth and excitation effects) and $H\alpha$ (due to increased extinction, though here supported by additional SFR tracers; see App. C for a discussion about SFR tracers in the galaxy centre) are expected to become less robust tracers of dense gas mass and SFR in galaxy centres thus mitigating any conclusions about SFE_{dense} in these regions.

4.3. ISM pressure relations

Similar to the radial trends (Sect. 4.2), we employ the MARS tool to the stacked data in order to find regimes with different linear behaviour. The fit results are listed in Tab. 4 and shown in the right-hand panels of Fig. 6. We find a pressure threshold in both relations (HCN/CO and SFR/HCN) at $\langle P_{\text{DE}} \rangle \approx 4 \times 10^5 k_B K cm^{-3}$ and $\langle P_{\text{DE}} \rangle \approx 1 \times 10^6 k_B K cm^{-3}$ computed via Equ. 9 (the threshold value is shown as a contour overlaid on the galaxy map in the Appendix, Fig. E.1; the corresponding pressure values using the alternative Equ. 8 are $P_{\text{DE}} \approx 4 \times 10^5 k_B K cm^{-3}$ (HCN/CO) and $P_{\text{DE}} \approx 1 \times 10^5 k_B K cm^{-3}$ (SFR/HCN)). We note that our cloud-scale $\langle P_{\text{DE}} \rangle$ measurements yield a factor of two to three larger values than the beam-matched 260 pc-scale pressure measurements. For better comparison with previous studies that have no access to ~ 100 pc-scale molecular gas measurements, we quote the corresponding threshold pressure values of $P_{\text{DE}} \approx 1.5 \times 10^5 k_B K cm^{-3}$ to $6.3 \times 10^5 k_B K cm^{-3}$, which consider the CO data convolved to 260 pc-scale (opposed to the weighted average of the 120 pc-scale CO measurements).

4.3.1. HCN/CO versus pressure

We find a strong positive correlation between the ($\langle P_{\text{DE}} \rangle$ -average) HCN/CO and the ISM pressure, $\langle P_{\text{DE}} \rangle$, in both the high ($\rho = 0.64$, $p = 2.84 \times 10^{-34}$) and low-pressure regime ($\rho = 0.79$). The correlation is steeper in the high-pressure ($m = 0.42 \pm 0.03$) regime compared to the low-pressure regime

($m = 0.18 \pm 0.03$). However, the relation could also be well fitted with a single linear function with $m = 0.35 \pm 0.02$. Thus, the average HCN/CO increases in a roughly uniform way from $\langle P_{\text{DE}} \rangle \approx 5 \times 10^4 k_B K cm^{-3}$ to $3 \times 10^7 k_B K cm^{-3}$ suggesting that the ISM pressure is well correlated with the average HCN/CO ($\rho = 0.75$) over almost three orders of magnitude in pressure.

4.3.2. SFR/HCN versus pressure

In the high-pressure regime we find a moderate negative correlation ($\rho = -0.39$, $p = 0.003$, $m = -0.89 \pm 0.22$) between the ($\langle P_{\text{DE}} \rangle$ -average) SFR/HCN and ISM pressure extending over two order of magnitude in x - and y -axis. In the low-pressure regime the relation is significantly flatter ($m = -0.32 \pm 0.04$) than in the high-pressure regime showing that across the disc, where the ISM pressure is low, SFR/HCN seems to partly decouple from the environmental pressure. However, in both regimes, there is a significant scatter (0.39 dex to 0.54 dex) about the average relation indicating that SFR/HCN is likely affected by other physical conditions than just the pressure or cloud properties (see App. D.1), for example, star-formation timescales or gas dynamics, where the latter could play a major role in galaxy centres and bars.

4.4. Morphological environments

In the next step, we analyse the individual morphological environments (centre, bar, bar ends, spiral arms, and interarm, as in Sect. 4.1) in the above-discussed scaling relations. The radial relations (Fig. 7) show that the centre and bar are well separated from the other environments as a function of galactocentric radius, completely dominating the strong negative (HCN/CO) and positive (SFR/HCN) trends with r_{gal} . At larger radii, that is, $r_{\text{gal}} \gtrsim 2.5$ kpc, we found several overlapping environments (bar, bar ends, spiral arms, and interarm) as a function of radius. The mean trends of the HCN/CO and SFR/HCN versus r_{gal} relation for each environment show an identical behaviour as the

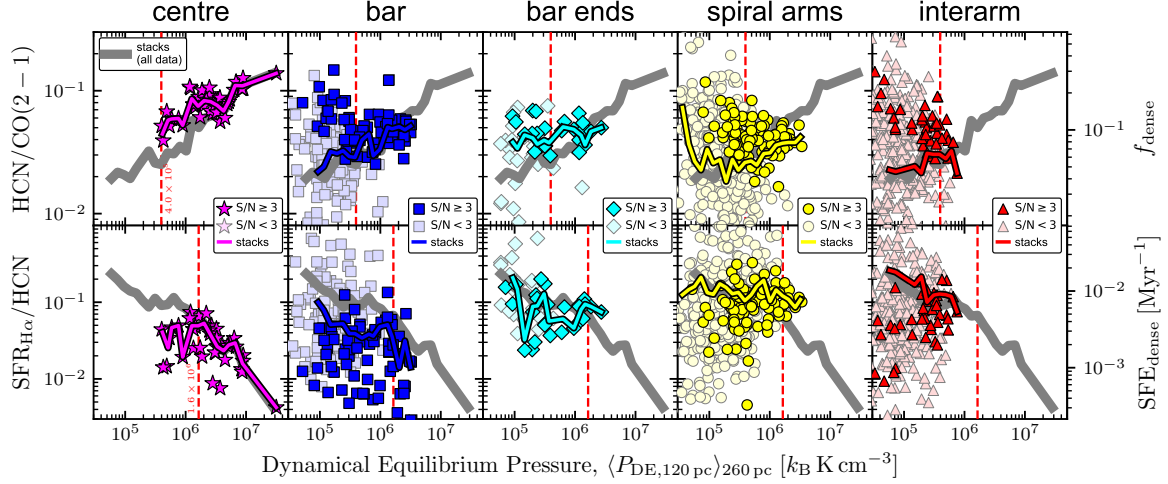


Fig. 8. Dense gas spectroscopic ratios versus pressure in different morphological environments. Similar to Fig. 7, but as a function of the dynamical equilibrium pressure.

global relation shown in Sect. 4.4 and we do not find a difference between these environments.

In the HCN/CO versus $\langle P_{DE} \rangle$ relation (top row of Fig. 8), we observe parallel trends among all environments, with the bar ends and the centre being shifted to higher HCN/CO values (following the mean trends presented as coloured lines). Spiral arms and interarm regions show similar HCN/CO versus pressure relations suggesting that in these environments the molecular clouds have a similar mean density.

In the SFR/HCN versus $\langle P_{DE} \rangle$ relations (bottom row of Fig. 8) the strong trend in the high-pressure regime is again dominated by the centre where SFR/HCN drops by one order of magnitude with increasing ISM pressure. Comparing spiral arms and interarm regions, we find very similar, almost flat trends showing that spiral arms and interarm regions have similar SFR/HCN across 1 dex to 2 dex of ISM pressure and that across the disc SFR/HCN is less dependent on the ISM pressure. In the bar ends we also find a flat trend as a function of pressure but shifted to lower SFR/HCN compared to the disc. The bar, despite having an HCN/CO similar to the disc, shows a much lower SFR/HCN across the whole range of the ISM pressure, which is more consistent with the values found in the centre. This shows that the bar region is a peculiar environment regarding its star-formation properties (see Sect. 5.3 for further discussion).

4.5. HCN/CO as a density tracer

Extragalactic studies of nearby galaxies at kiloparsec-scales (e.g. Gallagher et al. 2018b; Jiménez-Donaire et al. 2019), report a positive correlation of the HCN/CO line ratio with the kiloparsec-scale molecular gas surface density (Σ_{mol}) as traced by the CO line intensity over more than two orders of magnitude. These observational results are supported by theoretical works that show that HCN/CO is expected to positively correlate with the dense gas fraction and the mean gas density (Leroy et al. 2017). The physical interpretation put forward for explaining the strong relation between HCN/CO and Σ_{mol} is that HCN/CO is expected to trace the density distribution of molecular clouds within the beam. This interpretation is strongly supported by

recent works (Gallagher et al. 2018a; Neumann et al. 2023a) that compared the kiloparsec-scale HCN/CO with the cloud-scale Σ_{mol} finding a strong positive correlation. Recently, Tafalla et al. (2023) measured the HCN/CO versus H_2 column density relation in three solar neighbourhood clouds, finding a similar, strong positive correlation, at least qualitatively in agreement with the extragalactic results.

With the new 260 pc-scale HCN observations of NGC 4321, we can now take the next step and study the relation between HCN/CO and Σ_{mol} at sub-kiloparsec scales, making these results more comparable to galactic works. In Fig. 9, we present the relation between the HCN(1–0)-to-CO(1–0) line ratio and Σ_{mol} , measured at 260 pc resolution. Here, Σ_{mol} is inferred from the CO(2–1) line intensity using the lower-resolution R_{21} map and the surface density-metallicity based α_{CO} prescription as described in Sect. 3.2. We note, that here we use the HCN/CO(1–0), inferred from the CO(2–1) using the estimated R_{21} , instead of the HCN/CO(2–1) line ratio in order to better compare with literature relations. The resulting dense gas fraction, f_{dense} , shown as a secondary y-axis, is computed using a MW-based, constant $\alpha_{CO} = 4.35 M_{\odot} pc^{-2} (K km s^{-1})^{-1}$ and a constant $\alpha_{HCN} = 14 M_{\odot} pc^{-2} (K km s^{-1})^{-1}$. Hence f_{dense} is assumed to be proportional to HCN/CO(1–0) (App. A.1).

Analogous to previous sections and following Sect. 3.8, we stacked and fit the data to obtain the mean relation:

$$\log_{10} \left(\frac{HCN}{CO(1-0)} \right) = -2.64 + 0.61 \log_{10} \left(\frac{\Sigma_{mol}}{M_{\odot} pc^{-2}} \right). \quad (10)$$

We list the relation parameters along with uncertainties and relations from the literature in Tab. 5. We note that we exclude data below $\Sigma_{mol} < 10 M_{\odot} pc^{-2}$ (shaded region in Fig. 9) from the fit, because at lower surface densities the trend does not seem to continue in the same manner. This could indicate that at low surface densities, HCN/CO does not increase with Σ_{mol} anymore. Santa-Maria et al. (2023) argued that this could be due to HCN being excited in hot, low-surface density regions. However, due to a lack of sensitivity below $\Sigma_{mol} = 10 M_{\odot} pc^{-2}$, we could not test this hypothesis with our data. We stress that such a trend can be the result of low completeness thus reflect-

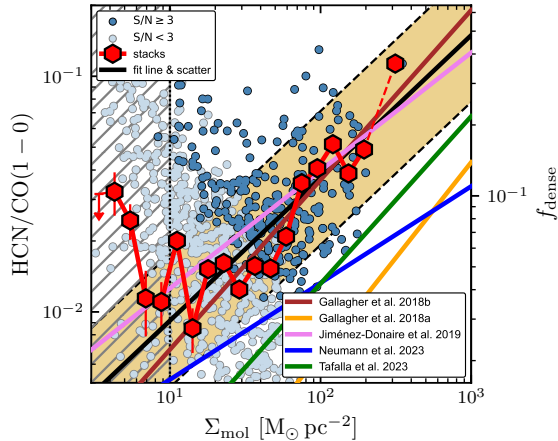


Fig. 9. HCN/CO versus Σ_{mol} relation. Here, we converted the CO(2–1) intensities into CO(1–0) intensities using the R_{21} map introduced in App. A.1. Markers show 260 pc sightline measurements from NGC 4321, with dark blue markers denoting significant ($S/N \geq 3$) data. The fit line was obtained by linear regression using LinMix to the stacked measurements (red hexagons) excluding data below $\Sigma_{\text{mol}} = 10 \text{ M}_{\odot} \text{ pc}^{-2}$. The gold-shaded region shows the 1-sigma scatter of the detected sightlines about the fit line. In addition, we show best-fit relations from literature, covering kiloparsec-scale measurements of nearby galaxies (Gallagher et al. 2018a,b; Jiménez-Donaire et al. 2019; Neumann et al. 2023b), where Gallagher et al. (2018a) and Neumann et al. (2023b) use cloud-scale CO to measure cloud-scale Σ_{mol} and sub-parsec-scale galactic measurements of three nearby clouds (Tafalla et al. 2023).

ing the biased-high average HCN/CO if either HCN and CO are clipped ($S/N \geq 3$) or if the x -axis is not complete. First and foremost, at $\Sigma_{\text{mol}} > 10 \text{ M}_{\odot} \text{ pc}^{-2}$, we find a strong positive correlation between HCN/CO and Σ_{mol} , which agrees well with much of the prior literature. Though, the scatter in the individual 260 pc sightline measurements is twice as large (0.28 dex) as the scatter at kiloparsec-scales (0.14 dex). The larger scatter at smaller scales indicates strong cloud-to-cloud variations in qualitative agreement with galactic studies finding large f_{dense} variations (e.g. Moore et al. 2012; Eden et al. 2012; Csengeri et al. 2016; Urquhart et al. 2021; Tafalla et al. 2023). One explanation for the increased scatter at smaller scales can be cloud evolution effects, leading to changes in the HCN/CO line ratio over the life cycle of molecular clouds, which can only be resolved at smaller scales (e.g. Kruijssen & Longmore 2014). Tafalla et al. (2023) suggest that some of the variations are caused by gas temperature variations between clouds, affecting the HCN excitation. In addition, HCN (and CO) emissivity can be affected by optical depth (Shirley 2015; Leroy et al. 2017; Jiménez-Donaire et al. 2017; Jones et al. 2023; García-Rodríguez et al. 2023) and electron excitation (Goldsmith & Kauffmann 2017), further driving the scatter about the relation. Certainly, in-depth investigations of HCN at higher resolution in nearby galaxies are needed to understand what is driving HCN/CO at fixed surface density.

Comparing with previous literature findings, the exact relations vary significantly between different studies. The reported slopes span values from 0.41 over 0.61 (this work) to 0.81. Neumann, Jiménez-Donaire et al. in prep. combine measurements from EMPIRE (Jiménez-Donaire et al. 2019) and ALMOND (Neumann et al. 2023b) and match methodologies to obtain an

updated, more robust constraint on the HCN/CO versus Σ_{mol} relation at kiloparsec-scales, yielding a slope of 0.59 consistent with the slope found for NGC 4321 in this work. Some of the differences between studies can at least partially be attributed to different methodologies. For instance, the adopted α_{CO} prescription significantly affects the measured relation. For NGC 4321, using a constant α_{CO} yields a shallower relation (slope of 0.48) compared to 0.61 with a varying α_{CO} using the prescription described by Equ. A.2. Moreover, the physical scales observed can significantly affect slopes (Gallagher et al. 2018a found a slope of 0.41 at 2.8 kpc-scale opposed to 0.81 at 650 pc-scale). In addition, using CO(2–1) instead of CO(1–0) will affect the slope if a constant R_{21} is used to convert CO(2–1) to CO(1–0), making the slope flatter than a native CO(1–0) measurement, since R_{21} negatively correlates with Σ_{mol} (Leroy et al. 2022). For these reasons, comparisons between different studies have to be taken with care. Nevertheless, we want to stress that, independent of methodologies, HCN/CO, at least qualitatively, robustly traces the average molecular gas density from sub-parsec to kiloparsec scales.

Even if tracers and methods are matched, the resolution is expected to affect the observed relation if the emission is not beam-filling. EMPIRE (Jiménez-Donaire et al. 2019) and ALMOND (Neumann et al. 2023b) both studied kiloparsec-scale HCN/CO as a function of Σ_{mol} . However, ALMOND used (intensity-weighted) cloud-scale (150 pc) Σ_{mol} , while EMPIRE used matched-resolution kiloparsec-scale Σ_{mol} . Comparing the HCN/CO versus Σ_{mol} from EMPIRE and ALMOND, we find a ~ 1 dex shift of the relation towards higher Σ_{mol} at smaller scales. These results suggest that the CO filling factor is lower by a factor of ~ 10 at ~ 1 kpc compared to ~ 100 pc. Furthermore, increasing the resolution of the HCN measurements, that is, going to smaller-scale HCN/CO measurements, appears to make the relations steeper (see above) and shifted towards higher HCN/CO, suggesting that HCN is clumpier and/or tracing denser gas than CO.

HCN abundance is expected to vary with metallicity due to the strong decrease of nitrogen-bearing species (e.g. HCN) with decreasing metallicity opposed to oxygen-bearing species (e.g. HCO^+) (e.g. Braine et al. 2017, 2023). However, across NGC 4321 the metallicity varies by only ~ 0.1 dex (see bottom panel of Fig. A.1). Therefore, abundance and optical depth variations connected to metallicity changes are expected to play only a minor role in affecting the HCN emissivity. In the appendix (Fig. E.2), we show how the HCN-to- HCO^+ line ratio varies with metallicity across NGC 4321, finding almost no dependence of HCN/ HCO^+ on metallicity, supporting the aforementioned statement that HCN is yielding similar results as other dense gas tracers. To further support this statement, we investigated the same scaling relations that are shown in Fig. 6, replacing HCN by HCO^+ as a dense gas tracer, yielding the same trends with r_{gal} and $\langle P_{\text{DE}} \rangle$. The average relations agree within 10 % with the HCN results except for the central ~ 1 kpc, where HCN is about 30 % brighter than the average line ratio value of $\text{HCN}/\text{HCO}^+ \approx 1.3$.

We note that the trend expressed by Equ. 10 could be driven by the centre, where we find the strongest systematic variations in HCN/CO. If HCN/CO is interpreted as f_{dense} , we expect the highest centre-to-disc variations in the α_{CO} and α_{HCN} conversion factors in the centre caused, for example, by strong variations in optical depth and excitation temperature, which could additionally affect the correlation between f_{dense} and Σ_{mol} . We checked that both the centre and the disc show a significant positive correlation between HCN/CO and Σ_{mol} with slopes of 0.25 (centre) and

Table 5. HCN/CO(1–0) vs Σ_{mol} relations

m (unc.) (1)	b (unc.) (2)	σ (3)	Σ_{mol} res. (4)	HCN/CO res. (5)	Σ_{mol} method (6)	Reference (7)
0.61 (0.10)	-2.64 (0.21)	0.28	260 pc	260 pc	beam-matched	this work
0.72 (—)	-2.88 (—)	—	300 – 600 pc	300 – 600 kpc	beam-matched	Gallagher et al. (2018b)
0.81 (0.09)	-3.80 (0.21)	—	120 pc	650 pc	CO-weighted average	Gallagher et al. (2018a)
0.50 (0.10)	-2.40 (0.20)	—	~ 2 kpc	~ 2 kpc	beam-matched	Jiménez-Donaire et al. (2019)
0.41 (0.03)	-2.70 (0.08)	0.14	~ 100 pc	1 – 2 kpc	CO-weighted average	Neumann et al. (2023b)
0.71 (0.03)	-3.30 (0.80)	—	~ 0.1 pc	~ 0.1 pc	beam-matched	Tafalla et al. (2023)
0.59 (0.03)	-2.64 (0.04)	0.18	1 – 2 kpc	1 – 2 kpc	beam-matched	Neumann, Jiménez-Donaire et al. in prep.

Notes – Best-fit lines of HCN/CO vs Σ_{mol} of the form shown in Equ. 10, with slope m (column 1), intercept b (column 2) and respective uncertainties. σ (column 3) denotes the 1-sigma scatter of the significant data about the fit line. The lines are plotted in Fig. 9. Columns 4 and 5 list the respective x - (Σ_{mol}) and y -axis (HCN/CO) resolutions. “Beam-matched” (column 6) refers to a matched resolution of the x - and y -axis data, and “CO-weighted average” denotes a CO intensity-weighted average measurement of Σ_{mol} , adopted in Gallagher et al. (2018a) and Neumann et al. (2023b). The differences between the physical scales and methodologies are discussed in the text.

0.35 (disc), which shows that even when the centre is excluded there is a clear dependence of HCN/CO on Σ_{mol} . However, the relations in the individual environments are much flatter compared to the overall trend (slope of 0.61) and offset by about 0.4 dex, which indicates that the overall HCN/CO versus Σ_{mol} trend might be enhanced by a centre-to-disc dichotomy.

5. Discussion

5.1. Pressure threshold for dense gas and star formation

Over the last decade, resolved kiloparsec-scale observations of nearby galaxies have found a systematic correlation between high-critical density tracer ratios (i.e. HCN/CO and SFR/HCN) and the environmental pressure in the ISM disc (e.g. Gallagher et al. 2018b,a; Jiménez-Donaire et al. 2019; Neumann et al. 2023b). These results are qualitatively supported by observations of the Milky Way’s CMZ, where the star formation efficiency of the (dense) molecular gas is low (Longmore et al. 2013; Kruijssen et al. 2014; Henshaw et al. 2023). These results contrast with solar neighbourhood results that tend to find a constant SFR/HCN (e.g. Heiderman et al. 2010; Lada et al. 2010, 2012; Evans et al. 2014). However, these solar neighbourhood observations probe a much lower ISM pressure environment ($P_{\text{DE}} \lesssim 2 \times 10^4 k_B \text{ K cm}^{-3}$) than typical extragalactic works. The apparent tension between the galactic and extragalactic works could, however, be solved if there existed a pressure threshold above which cloud properties and hence the observed spectroscopic ratios depend on pressure. Below this threshold, the clouds would be able to decouple from the environment and show universal behaviour in converting the dense gas to stars, a concept also put forward by theoretical works (e.g. Krumholz & Thompson 2007; Ostriker et al. 2010; Krumholz et al. 2012). Gallagher et al. (2018b) suggests that this pressure threshold could be at $P_{\text{DE}} \approx 2 \times 10^5 k_B \text{ K cm}^{-3}$, which is similar to the internal pressure of a typical GMC with $\Sigma_{\text{mol}} = 100 M_{\odot} \text{ pc}^{-2}$. We note that our formulation of the ISM pressure includes both the environment (gas and stellar mass) as well as cloud-scale molecular gas mass leading to a factor of 2–3 higher P_{DE} values compared to the purely kiloparsec-scale environmental P_{DE} (Sun et al. 2020). Therefore, the exact value of the pressure threshold is likely to vary with the resolution at which the pressure is measured.

With the new wide-field, deep HCN observations of NGC 4321 presented in this work, we can now for the first time

explore the low-pressure environment ($P_{\text{DE}} \approx 1 \times 10^5 k_B \text{ K cm}^{-3}$) at 260 pc scales in a Milky Way-like galaxy and address whether there is a pressure threshold for dense gas and star formation. In Figure 6 (right panels), we determined two pressure regimes in each of the relations based on the change in the behaviour of the mean trends using the methodology described in Sect. 3.8. Focusing on the SFR/HCN versus $\langle P_{\text{DE}} \rangle$ relation, we find a clear negative correlation at high pressures that significantly flattens in the low-pressure regime (especially evident in the mean trends of the individual environments), with the threshold being at $\langle P_{\text{DE}} \rangle_{\text{threshold}} = 1.6 \times 10^6 k_B \text{ K cm}^{-3}$. Thus, our results might support the pressure threshold hypothesis laid out above (slope changes by 30 %), though finding a threshold that is one order of magnitude higher than the value inferred from simple theoretical considerations ($P_{\text{DE}} \approx 2 \times 10^5 k_B \text{ K cm}^{-3}$). We note, however, that the measured pressure estimates depend strongly on the scales at which they are measured. Sun et al. (2020) show that larger physical scales (~ 1 kpc) can lead to lower pressure estimates due to averaging out GMC-scale (~ 100 pc) variations of the molecular gas. Therefore, even higher resolution observations ($\lesssim 100$ pc) are needed to obtain robust quantitative pressure estimates comparable with solar neighbourhood measurements.

In the appendix, we also present the relations between the spectroscopic ratios and the 120 pc-scale molecular gas properties (Fig. D.1) representing the self-gravity term on the ISM pressure as well as the relation with stellar mass surface density (Fig. D.2) representing the environment term. We find that a threshold-like behaviour is only seen in the cloud property relation, where SFR/HCN becomes almost constant in the low- Σ_{mol} , low- σ_{mol} regime. In contrast, SFR/HCN shows a monotonic negative relation with Σ_{\star} suggesting that clouds are always connected to the environmental pressure, but in the low-pressure environment the amount of dense gas is converted into stars in a uniform way independent of the cloud-scale properties.

5.2. Normal star formation efficiency in bar ends

Observations (e.g. Kenney & Lord 1991; Harada et al. 2019; Sormani & Barnes 2019; Yu et al. 2022b,a) and simulations (e.g. Sormani et al. 2018) show that gas inflow from the spiral arms and gas outflow from the bar can feed the bar ends with molecular gas. As a consequence, the bar ends are the principal site for cloud-cloud collisions, which are thought to either boost (e.g. Habe & Ohta 1992; Benjamin et al. 2005; López-Corredoira

et al. 2007; Furukawa et al. 2009; Ohama et al. 2010; Fukui et al. 2014; Renaud et al. 2015; Fukui et al. 2016, 2018; Torii et al. 2017; Sormani et al. 2020) or lower (e.g. Fujimoto et al. 2020) the formation of stars, depending on the relative speed of the colliding clouds (e.g. Takahira et al. 2014). This raises the question as to whether bar ends boost or suppress star formation. In accordance with the picture that bar ends are fed by gas flows, we observe relatively bright HCN and CO emission, implying an accumulation of (dense) molecular gas in the bar ends. However, we do not find an increased $\text{SFE}_{\text{dense}}$, traced by SFR/HCN , compared to the rest of the disc (spiral arms and interarm), suggesting that collisions might enhance density but not necessarily lead to different processes in the dense gas. We discuss the bar environment in the following subsection (Sect. 5.3).

5.3. Star formation suppression in the bar

Galactic bars are the sites of strong shear and gas streaming motions, which can potentially affect the (density) structure of molecular clouds and their ability to form stars (e.g. Athanassoulas 1992; Emsellem et al. 2015; Sormani et al. 2018). Díaz-García et al. (2021) find that bar strength can affect quenching, suggesting that bars are loci of suppressed star formation. However, Fraser-McKelvie et al. (2020) also find evidence for increased star formation along bars. Maeda et al. (2023) propose that the star formation efficiency of molecular gas (SFR/CO ; SFE_{mol}) in nearby spiral galaxies is systematically suppressed in bars. Here, we go a step further and study the denser molecular gas (traced by HCN) that is more tightly related to SFR and its star formation efficiency, $\text{SFE}_{\text{dense}}$. On the one hand, we find very similar HCN/CO, tracing f_{dense} , in the bar as well as throughout the disc. Additionally, we observe the same average trend with ISM pressure as in all other environments suggesting that bars contain clouds with similar mean density than galaxy discs. On the other hand, the agreement with disc trends changes for the dense gas star formation efficiency ($\text{SFE}_{\text{dense}}$ traced by SFR/HCN), which is much lower than in the disc. The systematically lower SFR/HCN in the bar becomes even more evident in the relation with pressure, where the average trend of the bar is ≈ 0.5 dex lower compared to the other environments. This suggests that the bar of NGC 4321 is indeed much less efficient in converting dense molecular gas into stars despite the presence of overdense gas.

One explanation for the low $\text{SFE}_{\text{dense}}$ could be shearing motions inside the bar that are solenoidal in nature, lowering the star formation efficiency (e.g. Federrath et al. 2016) or high-speed cloud-cloud collisions (e.g. Fujimoto et al. 2020). Recent simulations (e.g. Sormani et al. 2018) and observations (Wallace et al. 2022) suggest that gas dynamics in the bar are more dominated by streaming motions from the bar ends towards the galactic centre. These streaming motions can result in deformation and stretching of the molecular clouds in the bar leading to elongated, destructed molecular clouds, which might counteract the gravitational collapse hence quenching star formation.

6. Conclusions

We have presented new deep wide-field HCN(1–0) dense molecular gas observations at scales of 260 pc of the nearby spiral galaxy NGC 4321. By combining recent high-resolution ($\sim 1'' \sim 100$ pc) observations of CO (PHANGS–ALMA; Leroy et al. 2021b) tracing the bulk molecular gas and $\text{H}\alpha$ observations (PHANGS–MUSE; Emsellem et al. 2022) tracing SFR (supported by 21 μm observations from PHANGS–JWST (Lee

et al. 2023)), we were able to study for the first time dense gas spectroscopic ratios (HCN/CO, SFR/HCN) in many individual sight lines and environments expanding into the low-pressure regime that is similar to the solar neighbourhood environment. We used morphological masks based on the stellar mass content (Querejeta et al. 2021) to distinguish between different environmental regions that have different structural and dynamical properties that potentially affect the properties of molecular clouds and their ability to form stars. We have studied how HCN/CO, a proxy of the dense gas fraction (f_{dense}), and SFR/HCN , a proxy of the dense gas star formation efficiency ($\text{SFE}_{\text{dense}}$), vary between different galactic environments and depend on the ISM pressure. Our key findings are as follows:

- The HCN/CO increases and SFR/HCN decreases towards the centre of the galaxy, and they are roughly flat across the galactic disc. This suggests that galaxy centres have denser molecular clouds, but they are less efficiently converted into stars than in the disc. These global trends are consistent with previous results from kiloparsec-scale surveys, but our superior resolution allowed us to analyse the role of the environment in more detail. Distinguishing between environmental regions (centre, bar, bar ends, spiral arms, and interarm), we find HCN/CO to be significantly higher in the centre, while SFR/HCN is lower in both the centre and the bar. This shows that the star-formation process is roughly universal across the disc of NGC 4321. In particular, we found no significant difference of HCN/CO and SFR/HCN between the spiral arms and interarm regions, but star formation from the dense gas is significantly less efficient in the bar and centre. The strong trends towards the centre of NGC 4321 suggest either that clouds couple strongly to the surrounding environment or that HCN traces more of the bulk molecular gas that is less efficiently converted into stars, the latter being in agreement with predictions from gravoturbulent cloud models.
- The mean dense gas spectroscopic trends in the disc ($r_{\text{gal}} \gtrsim 2$ kpc) of NGC 4321 are very similar among different environments (Fig. 7, Fig. 8). However, we observed a significant scatter of 0.14 dex to 0.54 dex in all relations at fixed radius or fixed pressure. This indicates that, although they are on average similar, cloud properties and their environment vary more significantly at smaller scales and are potentially strongly affected by local cloud-scale ($\lesssim 100$ pc) physics and local excitation conditions (e.g. gas temperature, optical depth).
- We identified a pressure threshold for dense gas and star formation at $\langle P_{\text{DE}} \rangle_{\text{threshold}} \approx 1 \times 10^6 \text{ k}_B \text{ K cm}^{-3}$ (Equ. 9; Fig. 6) corresponding to 260 pc-scale $P_{\text{DE}} \approx 4 \times 10^5 \text{ k}_B \text{ K cm}^{-3}$ (Equ. 8). While the relation between pressure and HCN/CO can also be well described by a single relation covering both regimes, the relation with SFR/HCN significantly flattens in the low-pressure regime. This supports the idea that there is a pressure threshold below which the star-formation process in molecular clouds becomes less dependent on the environment, as seen in galactic measurements of molecular clouds. Thus, our findings hint towards resolving the tension between galactic and extragalactic studies of dense gas and star formation.
- The bar of NGC 4321 shows a significantly lower SFR/HCN than the disc and is systematically shifted to lower SFR/HCN in relation to the ISM pressure. This is a strong indication that the star formation in the bar is suppressed by shear or streaming motion that prevents the gravitational collapse and thus star formation.

– We found a strong positive correlation between HCN/CO and Σ_{mol} (Fig. 9) with a slope of 0.61 using a varying α_{CO} to compute Σ_{mol} (for comparison, a constant α_{CO} yields a slope of 0.48). Our 260 pc-scale results are in agreement with many previous studies from sub-parsec (galactic) to kiloparsec-scales (extragalactic) and support the use of HCN/CO as a powerful tracer of molecular cloud average density. We emphasise that the exact relation depends on the methodology and that scatter increases at smaller scales. We found a scale-dependence of the relation likely connected to the beam filling factors of CO and HCN, indicating that HCN emission traces denser gas than CO and originates from smaller than 260 pc-scale regions.

These findings present the next step in connecting extragalactic and galactic studies of dense gas and star formation. Overall, our results indicate the presence of a pressure threshold for dense gas and star formation and highlight the potential to link galactic and extragalactic works. However, we are still not able to resolve individual GMCs ($\lesssim 100$ pc) in galaxies beyond the Local Group and explore conditions similar to the solar neighbourhood ($P_{\text{DE}} \approx 2 \times 10^4 k_{\text{B}} \text{ cm}^{-3}$). Even deeper observations of dense gas tracers are needed to find better constraints on spectroscopic dense gas ratios in the solar neighbourhood-like low-pressure environment. Moreover, we show that across the disc, SFR tracers yield similar results, but towards the centre, they can differ a lot, hence requiring more in-depth studies of galaxy centres to infer robust prescriptions of dense gas and star formation in these extreme environments. Further, this work only investigated a single galaxy. Ultimately, we need similar dense gas studies in a large sample of galaxies (as done in PHANGS) to study, for example, the effect of bar dynamics on the star formation efficiency or the pressure threshold hypothesis in a statistically meaningful sample of galaxies. Besides, the scale-dependence of the HCN/CO versus Σ_{mol} relation requires a more detailed study, particularly to address the CO and HCN filling factors at sub-100 pc scales.

Acknowledgements. We would like to thank the referee Jonathan Braine for his insightful comments and constructive feedback that helped improve the quality of the paper. This work was carried out as part of the PHANGS Collaboration. LN acknowledges funding from the Deutsche Forschungsgemeinschaft (DFG, German Research Foundation) - 516405419. AKL gratefully acknowledges support by grants 1653300 and 2205628 from the National Science Foundation, by award JWST-GO-02107.009-A, and by a Humboldt Research Award from the Alexander von Humboldt Foundation. The work of AKL is partially supported by the National Science Foundation under Grants No. 1615105, 1615109, and 1653300. AU acknowledges support from the Spanish grants PID2019-108765GB-I00, funded by MCIN/AEI/10.13039/501100011033, and PID2022-138560NB-I00, funded by MCIN/AEI/10.13039/501100011033/FEDER, EU. ER acknowledges the support of the Natural Sciences and Engineering Research Council of Canada (NSERC), funding reference number RGPIN-2022-03499. MB gratefully acknowledges support from the ANID BASAL project FB210003 and from the FONDECYT regular grant 1211000. MC gratefully acknowledges funding from the DFG through an Emmy Noether Research Group (grant number CH2137/1-1). COOL Research DAO is a Decentralized Autonomous Organization supporting research in astrophysics aimed at uncovering our cosmic origins. KG is supported by the Australian Research Council through the Discovery Early Career Researcher Award (DECRA) Fellowship (project number DE220100766) funded by the Australian Government. KG is supported by the Australian Research Council Centre of Excellence for All Sky Astrophysics in 3 Dimensions (ASTRO 3D), through project number CE170100013. JDH gratefully acknowledges financial support from the Royal Society (University Research Fellowship; URF/R1/221620). HAP acknowledges support by the National Science and Technology Council of Taiwan under grant 110-2112-M-032-020-MY3. MQ acknowledges support from the Spanish grant PID2019-106027GA-C44, funded by MCIN/AEI/10.13039/501100011033. TS acknowledges funding from the European Research Council (ERC) under the European Union's Horizon 2020 research and innovation programme (grant agreement No. 694343). ES acknowledges funding from the European Research Council (ERC) under the European Union's Horizon 2020 research

and innovation programme (grant agreement No. 694343). SKS acknowledges financial support from the German Research Foundation (DFG) via Sino-German research grant SCHI 536/11-1. Y-HT acknowledges funding support from NRAO Student Observing Support Grant SOSPADA-012 and from the National Science Foundation (NSF) under grant No. 2108081. TGW acknowledges funding from the European Research Council (ERC) under the European Union's Horizon 2020 research and innovation programme (grant agreement No. 694343). This paper makes use of the following ALMA data ADS/JAO.ALMA#2011.0.00004.SV, ADS/JAO.ALMA#2015.1.00956.S, ADS/JAO.ALMA#2017.1.00815.S.

ALMA is a partnership of ESO (representing its member states), NSF (USA), and NINS (Japan), together with NRC (Canada), NSC and ASIAA (Taiwan), and KASI (Republic of Korea), in cooperation with the Republic of Chile. The Joint ALMA Observatory is operated by ESO, AUI/NRAO, and NAOJ. The National Radio Astronomy Observatory (NRAO) is a facility of the National Science Foundation operated under cooperative agreement by Associated Universities, Inc.

Data availability

The new data cubes (HCN(1–0) and HCO⁺(1–0)) used within this paper are publicly available via the Strasbourg astronomical Data Center (CDS).

References

- Anand, G. S., Lee, J. C., Van Dyk, S. D., et al. 2021, *MNRAS*, 501, 3621
 Athanassoula, E. 1992, *MNRAS*, 259, 345
 Barnes, A. T., Kauffmann, J., Bigiel, F., et al. 2020, *MNRAS*, 497, 1972
 Belfiore, F., Leroy, A. K., Sun, J., et al. 2023, *A&A*, 670, A67
 Bemis, A. & Wilson, C. D. 2019, *AJ*, 157, 131
 Benincasa, S. M., Wadsley, J., Couchman, H. M. P., & Keller, B. W. 2016, *MNRAS*, 462, 3053
 Benjamin, R. A., Churchwell, E., Babler, B. L., et al. 2005, *ApJ*, 630, L149
 Beslic, I., Barnes, A. T., Bigiel, F., et al. 2024, arXiv e-prints, arXiv:2403.13751
 Bešlić, I., Barnes, A. T., Bigiel, F., et al. 2021, *MNRAS*, 506, 963
 Bigiel, F., Leroy, A. K., Jiménez-Donaire, M. J., et al. 2016, *ApJ*, 822, L26
 Blitz, L. & Rosolowsky, E. 2004, *ApJ*, 612, L29
 Blitz, L. & Rosolowsky, E. 2006, *ApJ*, 650, 933
 Bolatto, A. D., Wolfire, M., & Leroy, A. K. 2013, *ARA&A*, 51, 207
 Braine, J., Shimajiri, Y., André, P., et al. 2017, *A&A*, 597, A44
 Braine, J., Sun, Y., Shimajiri, Y., et al. 2023, *A&A*, 676, A27
 Caldú-Primo, A., Schruha, A., Walter, F., et al. 2013, *AJ*, 146, 150
 Calzetti, D., Kennicutt, R. C., Engelbracht, C. W., et al. 2007, *ApJ*, 666, 870
 CASA Team, Bean, B., Bhatnagar, S., et al. 2022, *PASP*, 134, 114501
 Chen, H., Braine, J., Gao, Y., Koda, J., & Gu, Q. 2017, *ApJ*, 836, 101
 Chen, H., Gao, Y., Braine, J., & Gu, Q. 2015, *ApJ*, 810, 140
 Csengeri, T., Weiss, A., Wyrowski, F., et al. 2016, *A&A*, 585, A104
 den Brok, J. S., Bigiel, F., Sliwa, K., et al. 2022, *A&A*, 662, A89
 den Brok, J. S., Chatzigiannakis, D., Bigiel, F., et al. 2021, *MNRAS*, 504, 3221
 Díaz-García, S., Lisenfeld, U., Pérez, I., et al. 2021, *A&A*, 654, A135
 Dib, S., Helou, G., Moore, T. J. T., Urquhart, J. S., & Dariush, A. 2012, *ApJ*, 758, 125
 Eden, D. J., Moore, T. J. T., Morgan, L. K., Thompson, M. A., & Urquhart, J. S. 2013, *MNRAS*, 431, 1587
 Eden, D. J., Moore, T. J. T., Plume, R., & Morgan, L. K. 2012, *MNRAS*, 422, 3178
 Eden, D. J., Moore, T. J. T., Urquhart, J. S., et al. 2015, *MNRAS*, 452, 289
 Eibensteiner, C., Barnes, A. T., Bigiel, F., et al. 2022, *A&A*, 659, A173
 Elmegreen, B. G. 1989, *ApJ*, 338, 178
 Elmegreen, B. G. & Parravano, A. 1994, *ApJ*, 435, L121
 Emsellem, E., Renaud, F., Bournaud, F., et al. 2015, *MNRAS*, 446, 2468
 Emsellem, E., Schinnerer, E., Santoro, F., et al. 2022, *A&A*, 659, A191
 Evans, Neal J., I., Heiderman, A., & Vutisalchavakul, N. 2014, *ApJ*, 782, 114
 Evans, Neal J., I., Kim, K.-T., Wu, J., et al. 2020, *ApJ*, 894, 103
 Federrath, C., Rathborne, J. M., Longmore, S. N., et al. 2016, *ApJ*, 832, 143
 Fisher, D. B., Bolatto, A. D., White, H., et al. 2019, *ApJ*, 870, 46
 Fraser-McKelvie, A., Aragón-Salamanca, A., Merrifield, M., et al. 2020, *MNRAS*, 495, 4158
 Friedman, J. H. 1991, *The Annals of Statistics*, 19, 1
 Fujimoto, Y., Maeda, F., Habe, A., & Ohta, K. 2020, *MNRAS*, 494, 2131
 Fukui, Y., Ohama, A., Hanaoka, N., et al. 2014, *ApJ*, 780, 36
 Fukui, Y., Torii, K., Hattori, Y., et al. 2018, *ApJ*, 859, 166
 Fukui, Y., Torii, K., Ohama, A., et al. 2016, *ApJ*, 820, 26
 Furukawa, N., Dawson, J. R., Ohama, A., et al. 2009, *ApJ*, 696, L115

- Gallagher, M. J., Leroy, A. K., Bigiel, F., et al. 2018a, *ApJ*, 868, L38
- Gallagher, M. J., Leroy, A. K., Bigiel, F., et al. 2018b, *ApJ*, 858, 90
- Gao, Y. & Solomon, P. M. 2004, *ApJ*, 606, 271
- García-Burillo, S., Usero, A., Alonso-Herrero, A., et al. 2012, *A&A*, 539, A8
- García-Rodríguez, A., Usero, A., Leroy, A. K., et al. 2023, *A&A*, 672, A96
- Gardner, J. P., Mather, J. C., Abbott, R., et al. 2023, *PASP*, 135, 068001
- Goldsmith, P. F. & Kauffmann, J. 2017, *ApJ*, 841, 25
- Habe, A. & Ohta, K. 1992, *PASJ*, 44, 203
- Harada, N., Sakamoto, K., Martín, S., et al. 2018, *ApJ*, 855, 49
- Harada, N., Sakamoto, K., Martín, S., et al. 2019, *ApJ*, 884, 100
- Hassani, H., Rosolowsky, E., Leroy, A. K., et al. 2023, *ApJ*, 944, L21
- Heiderman, A., Evans, Neal J., Allen, L. E., Huard, T., & Heyer, M. 2010, *ApJ*, 723, 1019
- Henshaw, J. D., Barnes, A. T., Battersby, C., et al. 2023, in *Astronomical Society of the Pacific Conference Series*, Vol. 534, *Protostars and Planets VII*, ed. S. Inutsuka, Y. Aikawa, T. Muto, K. Tomida, & M. Tamura, 83
- Herrera-Camus, R., Bolatto, A., Wolfire, M., et al. 2017, *ApJ*, 835, 201
- Jiménez-Donaire, M. J., Bigiel, F., Leroy, A. K., et al. 2017, *MNRAS*, 466, 49
- Jiménez-Donaire, M. J., Bigiel, F., Leroy, A. K., et al. 2019, *ApJ*, 880, 127
- Jiménez-Donaire, M. J., Usero, A., Bešlić, I., et al. 2023, *A&A*, 676, L11
- Jones, G. H., Clark, P. C., Glover, S. C. O., & Hacar, A. 2023, *MNRAS*, 520, 1005
- Kauffmann, J., Goldsmith, P. F., Melnick, G., et al. 2017, *A&A*, 605, L5
- Kelly, B. C. 2007, *ApJ*, 665, 1489
- Kenney, J. D. P. & Lord, S. D. 1991, *ApJ*, 381, 118
- Kennicutt, R. C. & Evans, N. J. 2012, *ARA&A*, 50, 531
- Kepley, A. A., Bittler, L., Leroy, A. K., et al. 2018, *ApJ*, 862, 120
- Kepley, A. A., Leroy, A. K., Frayer, D., et al. 2014, *ApJ*, 780, L13
- Kim, C.-G., Kim, W.-T., & Ostriker, E. C. 2011, *ApJ*, 743, 25
- Kim, C.-G. & Ostriker, E. C. 2015, *ApJ*, 815, 67
- Kim, C.-G., Ostriker, E. C., & Kim, W.-T. 2013, *ApJ*, 776, 1
- Koyama, H. & Ostriker, E. C. 2009, *ApJ*, 693, 1346
- Kregel, M., van der Kruit, P. C., & de Grijs, R. 2002, *MNRAS*, 334, 646
- Kroupa, P. 2001, *MNRAS*, 322, 231
- Kruijssen, J. M. D. & Longmore, S. N. 2014, *MNRAS*, 439, 3239
- Kruijssen, J. M. D., Longmore, S. N., Elmegreen, B. G., et al. 2014, *MNRAS*, 440, 3370
- Krumholz, M. R., Dekel, A., & McKee, C. F. 2012, *ApJ*, 745, 69
- Krumholz, M. R. & McKee, C. F. 2005, *ApJ*, 630, 250
- Krumholz, M. R. & Thompson, T. A. 2007, *ApJ*, 669, 289
- Lada, C. J., Forbrich, J., Lombardi, M., & Alves, J. F. 2012, *ApJ*, 745, 190
- Lada, C. J., Lombardi, M., & Alves, J. F. 2010, *ApJ*, 724, 687
- Lang, P., Meidt, S. E., Rosolowsky, E., et al. 2020, *ApJ*, 897, 122
- Lee, J. C., Sandstrom, K. M., Leroy, A. K., et al. 2023, *ApJ*, 944, L17
- Lee, J. C., Whitmore, B. C., Thilker, D. A., et al. 2022, *ApJS*, 258, 10
- Leroy, A. K., Hughes, A., Liu, D., et al. 2021a, *ApJS*, 255, 19
- Leroy, A. K., Rosolowsky, E., Usero, A., et al. 2022, *ApJ*, 927, 149
- Leroy, A. K., Sandstrom, K., Rosolowsky, E., et al. 2023, *ApJ*, 944, L9
- Leroy, A. K., Sandstrom, K. M., Lang, D., et al. 2019, *ApJS*, 244, 24
- Leroy, A. K., Schinnerer, E., Hughes, A., et al. 2021b, *ApJS*, 257, 43
- Leroy, A. K., Usero, A., Schrubba, A., et al. 2017, *ApJ*, 835, 217
- Leroy, A. K., Walter, F., Bigiel, F., et al. 2009, *AJ*, 137, 4670
- Leroy, A. K., Walter, F., Brinks, E., et al. 2008, *AJ*, 136, 2782
- Licquia, T. C. & Newman, J. A. 2015, *ApJ*, 806, 96
- Linden, S. T., Murphy, E. J., Dong, D., et al. 2020, *ApJS*, 248, 25
- Longmore, S. N., Bally, J., Testi, L., et al. 2013, *MNRAS*, 429, 987
- López-Corredoira, M., Cabrera-Lavers, A., Mahoney, T. J., et al. 2007, *AJ*, 133, 154
- Maeda, F., Egusa, F., Ohta, K., Fujimoto, Y., & Habe, A. 2023, *ApJ*, 943, 7
- Maeda, F., Ohta, K., Fujimoto, Y., & Habe, A. 2021, *MNRAS*, 502, 2238
- Makarov, D., Prugniel, P., Terekhova, N., Courtois, H., & Vauglin, I. 2014, *A&A*, 570, A13
- Martín, S., Mangum, J. G., Harada, N., et al. 2021, *A&A*, 656, A46
- Meidt, S. E., Schinnerer, E., van de Ven, G., et al. 2014, *ApJ*, 788, 144
- Moore, T. J. T., Urquhart, J. S., Morgan, L. K., & Thompson, M. A. 2012, *MNRAS*, 426, 701
- Murphy, E. J., Bremseth, J., Mason, B. S., et al. 2012, *ApJ*, 761, 97
- Neumann, L., den Brok, J. S., Bigiel, F., et al. 2023a, *A&A*, 675, A104
- Neumann, L., Gallagher, M. J., Bigiel, F., et al. 2023b, *MNRAS*, 521, 3348
- Nguyen-Luong, Q., Anderson, L. D., Motte, F., et al. 2017, *ApJ*, 844, L25
- O'Donnell, J. E. 1994, *ApJ*, 422, 158
- Ohama, A., Dawson, J. R., Furukawa, N., et al. 2010, *ApJ*, 709, 975
- Onus, A., Krumholz, M. R., & Federrath, C. 2018, *MNRAS*, 479, 1702
- Ostriker, E. C., McKee, C. F., & Leroy, A. K. 2010, *ApJ*, 721, 975
- Ostriker, E. C. & Shetty, R. 2011, *ApJ*, 731, 41
- Padoan, P. & Nordlund, Å. 2002, *ApJ*, 576, 870
- Pan, H.-A. & Kuno, N. 2017, *ApJ*, 839, 133
- Pessa, I., Schinnerer, E., Leroy, A. K., et al. 2022, *A&A*, 663, A61
- Querejeta, M., Meidt, S. E., Schinnerer, E., et al. 2015, *ApJS*, 219, 5
- Querejeta, M., Schinnerer, E., Meidt, S., et al. 2021, *A&A*, 656, A133
- Querejeta, M., Schinnerer, E., Schrubba, A., et al. 2019, *A&A*, 625, A19
- Ragan, S. E., Moore, T. J. T., Eden, D. J., et al. 2016, *MNRAS*, 462, 3123
- Ragan, S. E., Moore, T. J. T., Eden, D. J., et al. 2018, *MNRAS*, 479, 2361
- Renaud, F., Bournaud, F., Emsellem, E., et al. 2015, *MNRAS*, 454, 3299
- Rigby, A. J., Moore, T. J. T., Eden, D. J., et al. 2019, *A&A*, 632, A58
- Salo, H., Laurikainen, E., Laine, J., et al. 2015, *ApJS*, 219, 4
- Sánchez-García, M., García-Burillo, S., Pereira-Santaella, M., et al. 2022, *A&A*, 660, A83
- Santa-Maria, M. G., Goicoechea, J. R., Pety, J., et al. 2023, *A&A*, 679, A4
- Schinnerer, E. & Leroy, A. K. 2024, *arXiv e-prints*, arXiv:2403.19843
- Schinnerer, E., Meidt, S. E., Colombo, D., et al. 2017, *ApJ*, 836, 62
- Schruba, A., Kruijssen, J. M. D., & Leroy, A. K. 2019, *ApJ*, 883, 2
- Schruba, A., Leroy, A. K., Walter, F., et al. 2011, *AJ*, 142, 37
- Sheth, K., Regan, M., Hinz, J. L., et al. 2010, *PASP*, 122, 1397
- Shetty, R. & Ostriker, E. C. 2012, *ApJ*, 754, 2
- Shimajiri, Y., André, P., Braine, J., et al. 2017, *A&A*, 604, A74
- Shirley, Y. L. 2015, *PASP*, 127, 299
- Sormani, M. C. & Barnes, A. T. 2019, *MNRAS*, 484, 1213
- Sormani, M. C., Tress, R. G., Glover, S. C. O., et al. 2020, *MNRAS*, 497, 5024
- Sormani, M. C., Treß, R. G., Ridley, M., et al. 2018, *MNRAS*, 475, 2383
- Spitzer, Lyman, J. 1942, *ApJ*, 95, 329
- Stuber, S. K., Pety, J., Schinnerer, E., et al. 2023, *A&A*, 680, L20
- Sun, J., Leroy, A. K., Ostriker, E. C., et al. 2020, *ApJ*, 892, 148
- Sun, J., Leroy, A. K., Rosolowsky, E., et al. 2022, *AJ*, 164, 43
- Sun, J., Leroy, A. K., Schrubba, A., et al. 2018, *ApJ*, 860, 172
- Tafalla, M., Usero, A., & Hacar, A. 2023, *A&A*, 679, A112
- Takahira, K., Tasker, E. J., & Habe, A. 2014, *ApJ*, 792, 63
- Teng, Y.-H., Sandstrom, K. M., Sun, J., et al. 2023, *ApJ*, 950, 119
- Torii, K., Hattori, Y., Hasegawa, K., et al. 2017, *ApJ*, 835, 142
- Tress, R. G., Smith, R. J., Sormani, M. C., et al. 2020, *MNRAS*, 492, 2973
- Urquhart, J. S., Figura, C., Cross, J. R., et al. 2021, *MNRAS*, 500, 3050
- Usero, A., Leroy, A. K., Walter, F., et al. 2015, *AJ*, 150, 115
- van der Kruit, P. C. 1988, *A&A*, 192, 117
- Véron-Cetty, M. P. & Véron, P. 2010, *A&A*, 518, A10
- Viaene, S., Forbrich, J., & Fritz, J. 2018, *MNRAS*, 475, 5550
- Wallace, J., Battersby, C., Mills, E. A. C., et al. 2022, *ApJ*, 939, 58
- Walter, F., Brinks, E., de Blok, W. J. G., et al. 2008, *AJ*, 136, 2563
- Watanabe, Y., Sorai, K., Kuno, N., & Habe, A. 2011, *MNRAS*, 411, 1409
- Williams, T. G., Kreckel, K., Belfiore, F., et al. 2022, *MNRAS*, 509, 1303
- Wong, T. & Blitz, L. 2002, *ApJ*, 569, 157
- Wright, G. S., Rieke, G. H., Glaspe, A., et al. 2023, *PASP*, 135, 048003
- Yu, S.-Y., Kalinova, V., Colombo, D., et al. 2022a, *A&A*, 666, A175
- Yu, S.-Y., Xu, D., Ho, L. C., Wang, J., & Kao, W.-B. 2022b, *A&A*, 661, A98

Appendix A: Ancillary data

Appendix A.1: CO-to-H₂ conversion factor – α_{CO}

In this work, we employ two different conversion factors to convert the CO(2–1) line intensity into a molecular gas surface density as described in Sect. 3.2.

Appendix A.1.1: Constant conversion factor

As a first step, we study variations of the HCN-to-CO line ratio, which is a proxy for the dense gas fraction, adopting constant mass-to-light ratios (Sect. 3.3). We adopt a Milky-Way average CO-to-H₂ conversion factor of $\alpha_{\text{CO}} = 4.35 \text{ M}_{\odot} \text{ pc}^{-2} (\text{K km s}^{-1})^{-1}$ that is uncertain by a factor of two (Bolatto et al. 2013). To convert the CO(2–1) into a CO(1–0) line intensity, we use a CO(2–1)-to-CO(1–0) line ratio of $R_{21} = 0.65 \pm 0.17$ (den Brok et al. 2021; Leroy et al. 2022).

Appendix A.1.2: Spatially varying conversion factor

As a second step, we adopt varying conversion factors to obtain the most accurate estimation of the molecular gas surface density given the current knowledge about spatial variations of α_{CO} and R_{21} in nearby galaxies at $\sim 100 \text{ pc}$ scales. This prescription enters the estimation of the dynamical equilibrium pressure (Sect. 3.6). We convert the CO(2–1) moment-zero ($W_{\text{CO}(2-1)}$) into a molecular gas surface density (Σ_{mol}) in a two-step process: First, we convert the CO(2–1) into a CO(1–0) line intensity by applying a spatially varying CO(2–1)-to-CO(1–0) line ratio (R_{21}) map. This makes use of archival CO(1–0) observations of NGC 4321 with ALMA at $4''$ resolution. Hence we can compute R_{21} at $4'' \sim 300 \text{ pc}$ scale and infer CO(1–0) from the measured CO(2–1) at $1.67'' \sim 120 \text{ pc}$ resolution:

$$W_{\text{CO}(1-0)}^{1.67''} \approx W_{\text{CO}(2-1)}^{4''} / R_{21}^{4''} \quad (\text{A.1})$$

Certainly, we expect small-scale variations of R_{21} at $< 300 \text{ pc}$ scales, but using a 300 pc -smoothed R_{21} still provides more accurate estimates of CO(1–0) and hence Σ_{mol} than adopting a constant R_{21} . Here, we measure a median $R_{21} = 0.54$ and a scatter of 0.16 dex. We show a map of R_{21} in Fig. A.1.

Next, we converted the inferred CO(1–0) moment-zero map ($W_{\text{CO}(1-0)}$) into Σ_{mol} by applying the prescription described by Equation 31 from Bolatto et al. (2013):

$$\left(\frac{\alpha_{\text{CO}(1-0)}}{\text{M}_{\odot} \text{ pc}^{-2} (\text{K km s}^{-1})^{-1}} \right) = 2.9 \exp \left(\frac{0.4}{Z' \Sigma_{\text{GMC}}^{100}} \right) \left(\frac{\Sigma_{\text{total}}}{100 \text{ M}_{\odot} \text{ pc}^{-2}} \right)^{-\gamma} \quad (\text{A.2})$$

following the iterative approach presented in Sun et al. (2022). Z' is the local metallicity in units of Solar metallicities, and γ is 0.5 if $\Sigma_{\text{total}} > 100 \text{ M}_{\odot} \text{ pc}^{-2}$ and 0 otherwise. The local metallicity is estimated from optical line measurements taken by MUSE applying a Gaussian Process Regression (GPR) to model the 2D metallicity distribution (Williams et al. 2022). Here, $\Sigma_{\text{GMC}}^{100}$ is fixed at unity, that is, we adopted a fiducial GMC surface density of $100 \text{ M}_{\odot} \text{ pc}^{-2}$, and the total surface density (Σ_{total}) includes molecular gas (CO), atomic gas (H I, Sect. A.2), and stellar mass ($3.6 \mu\text{m}$, Sect. A.3). Since α_{CO} is implicitly needed to compute Σ_{total} , Equation A.2 must be solved iteratively. We show a map of the adopted α_{CO} map in Fig. A.1. The median α_{CO} value is $3.3 \text{ M}_{\odot} \text{ pc}^{-2} (\text{K km s}^{-1})^{-1}$ and thus by a factor of 1.3 lower than the MW based α_{CO} listed above. For this galaxy, α_{CO} systematically decreases by a factor of ~ 3 from the disc over the spiral

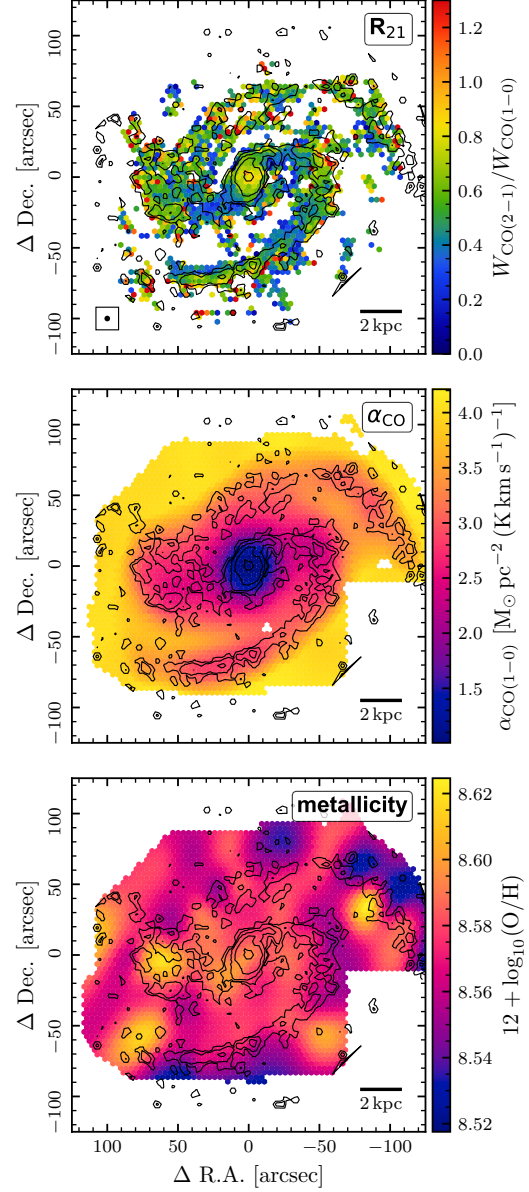


Fig. A.1. Conversion factor maps. *Top:* CO(2–1)-to-CO(1–0) line ratio (R_{21}) map computed from CO(2–1) observations (PHANGS–ALMA) and CO(1–0) observations (ALMA science verification program) at a common $4''$ resolution. *Middle:* CO-to-H₂ conversion factor (α_{CO}) following the prescription from Bolatto et al. (2013) (Equ. A.2) using metallicities (*bottom panel*) from PHANGS–MUSE optical recombination lines observations (Williams et al. 2022).

arms towards the centre of NGC 4321, with a scatter of 0.10 dex. Overall, the inferred total H₂ mass of the varying α_{CO} across the FOV used in this work is $M_{\text{H}_2} = 1.6 \times 10^9 \text{ M}_{\odot}$, which is lower by a factor of 0.57 than the value obtained via a constant MW-based α_{CO} , yielding $M_{\text{H}_2} = 2.8 \times 10^9 \text{ M}_{\odot}$.

We note that [Teng et al. \(2023\)](#) inferred cloud-scale α_{CO} values for the central 2 kpc of NGC 4321 using a multi-line modelling approach based on cloud-scale multi-line, multi-transition CO isotopologues. Despite the existing robust α_{CO} measurement, we employ the surface density-metallicity-based calibration from [Bolatto et al. \(2013\)](#) to obtain continuous α_{CO} values across the full disc of NGC 4321 and note that the measurements from [Teng et al. \(2023\)](#) are on average 0.20 dex smaller than the values used here, but consistent at the 1-sigma level within 0.21 dex.

Appendix A.2: Atomic gas – H I 21-cm

We utilise H I 21-cm line observations to measure the atomic gas surface density. The H I data are from VLA observations associated with HERACLES ([Leroy et al. 2009](#)) mapping several nearby galaxies in H I at $\sim 20''$ resolution. We converted the integrated intensity of H I ($W_{21\text{cm}}$) into atomic gas surface density via ([Walter et al. 2008](#))

$$\left(\frac{\Sigma_{\text{atom}}}{\text{M}_{\odot} \text{pc}^{-2}}\right) = 1.97 \times 10^{-2} \left(\frac{W_{21\text{cm}}}{\text{K km s}^{-1}}\right) \cos(i), \quad (\text{A.3})$$

where $\cos(i)$ is accounting for the inclination of the galaxy ($i = 38.5^\circ$).

Appendix A.3: Stellar mass – 3.6 μm

We use the stellar mass surface density map from [Querejeta et al. \(2015\)](#), who use 3.6 μm observations from the *Spitzer* Survey of Stellar Structure in Galaxies (S⁴G; [Sheth et al. 2010](#)). The 3.6 μm maps are corrected for dust attenuation using an “Independent Component Analysis” (ICA) method that separates stars and dust on a pixel-to-pixel basis (for more details, see [Querejeta et al. 2015](#)). We converted the attenuation-corrected 3.6 μm map into stellar mass surface density, Σ_{\star} , via

$$\left(\frac{\Sigma_{\star}}{\text{M}_{\odot} \text{pc}^{-2}}\right) = 4.22 \times 10^2 \left(\frac{I_{3.6\mu\text{m}}}{\text{MJy sr}^{-1}}\right), \quad (\text{A.4})$$

which assumes a constant mass-to-light ratio of $0.6 \text{ M}_{\odot}/\text{L}_{\odot}$ ([Meidt et al. 2014](#)).

In App. A.4, we use the stellar mass volume density (ρ_{\star}) to compute the dynamical equilibrium pressure of the ISM in the galaxy disc. We estimated ρ_{\star} from the stellar mass surface density, adopting the recipes used in [Blitz & Rosolowsky \(2006\)](#); [Leroy et al. \(2008\)](#); [Ostriker et al. \(2010\)](#); [Sun et al. \(2020\)](#):

$$\rho_{\star} = \frac{\Sigma_{\star}}{4H_{\star}} = \frac{\Sigma_{\star}}{0.54R_{\star}}, \quad (\text{A.5})$$

where H_{\star} and R_{\star} are the scale height and radial scale length of the stellar disc. Above equation assumes an isothermal density profile along the vertical direction ([van der Kruit 1988](#)) and a fixed stellar disc flattening ratio of $R_{\star}/H_{\star} = 7.3$ ([Kregel et al. 2002](#)). We adopt $R_{\star} = 61.1'' \sim 4.5 \text{ kpc}$ from the S⁴G photometric decomposition analysis ([Salo et al. 2015](#)).

Appendix A.4: Dynamical equilibrium pressure

We compute the dynamical equilibrium pressure, or ISM pressure (P_{DE}) following the prescription by [Sun et al. \(2020\)](#). P_{DE} describes the pressure regulated by the mass content in the ISM disc and thus provides an important gauge of the local environment of molecular clouds. The distribution of stars and gas in a

galaxy disc can approximately be described as isothermal fluids in a plane-parallel geometry. In this prescription, the dynamical equilibrium pressure is composed of a pressure term created by the ISM due to the self-gravity of the ISM disc and a term due to the gravity of the stars (see e.g. [Spitzer 1942](#)) such that

$$P_{\text{DE}} = \frac{\pi G}{2} \Sigma_{\text{gas}}^2 + \Sigma_{\text{gas}} \sqrt{2G\rho_{\star}} \sigma_{\text{gas},z}, \quad (\text{A.6})$$

where we assumed a smooth, single-fluid gas disc, and that all gas shares a similar velocity dispersion, so that $\Sigma_{\text{gas}} = \Sigma_{\text{mol}} + \Sigma_{\text{atom}}$ is the total gas surface density, ρ_{\star} is the stellar mass volume density near disc midplane and $\sigma_{\text{gas},z}$ is the velocity dispersion of the gas perpendicular to the disc.

[Sun et al. \(2020\)](#) proposed a new formalism that takes into account the self-gravity of the molecular gas at high resolution (i.e. 100 pc scale). In this work, we adopted their formalism, which is described in the following. To combine the cloud-scale $\Sigma_{\text{mol}, 120 \text{ pc}}$ data with the large-scale Σ_{atom} and ρ_{\star} , we split P_{DE} into two parts: the pressure of the molecular gas at cloud-scale, P_{cloud} , and the pressure of the smooth extended atomic gas due to the gravity of all gas (atomic and molecular) and the stars, P_{atom} . The cloud-scale P_{cloud} consists of three terms accounting for the self-gravity of the molecular gas, the gravity of larger molecular structures, and the gravity of stars:

$$P_{\text{cloud}} = \frac{3\pi}{8} G \Sigma_{\text{mol}, 120 \text{ pc}}^2 + \frac{\pi}{2} G \Sigma_{\text{mol}, 120 \text{ pc}} \Sigma_{\text{mol}, 260 \text{ pc}} + \frac{3\pi}{4} G \rho_{\star} \Sigma_{\text{mol}, 120 \text{ pc}} D_{\text{beam}}, \quad (\text{A.7})$$

where ρ_{\star} is computed as described in App. A.3. In Equ. (A.7), $\Sigma_{\text{mol}, 120 \text{ pc}}$ is given at the cloud-scale resolution (here 120 pc) while $\Sigma_{\text{mol}, 260 \text{ pc}}$ and ρ_{\star} describe the distributions of the molecular gas and the stellar mass density at 260 pc scale. In typical units, Equ. (A.7) reads

$$\begin{aligned} \left(\frac{P_{\text{cloud}}}{k_{\text{B}} \text{ K cm}^{-3}}\right) &= 2.48 \times 10^5 \left(\frac{\Sigma_{\text{mol}, 120 \text{ pc}}}{10^2 \text{ M}_{\odot} \text{ pc}^{-2}}\right)^2 \\ &+ 3.31 \times 10^5 \left(\frac{\Sigma_{\text{mol}, 120 \text{ pc}}}{10^2 \text{ M}_{\odot} \text{ pc}^{-2}}\right) \left(\frac{\Sigma_{\text{mol}, 260 \text{ pc}}}{10^2 \text{ M}_{\odot} \text{ pc}^{-2}}\right) \\ &+ 7.01 \times 10^4 \left(\frac{\Sigma_{\text{mol}, 120 \text{ pc}}}{10^2 \text{ M}_{\odot} \text{ pc}^{-2}}\right) \left(\frac{\rho_{\star}}{10^{-1} \text{ M}_{\odot} \text{ pc}^{-3}}\right) \left(\frac{D_{\text{beam}}}{150 \text{ pc}}\right). \end{aligned} \quad (\text{A.8})$$

The large-scale P_{atom} includes the self-gravity of the atomic gas and the gravitational interaction of the atomic gas with the (large-scale) molecular gas and the stars:

$$P_{\text{atom}} = \frac{\pi G}{2} \Sigma_{\text{atom}}^2 + \pi G \Sigma_{\text{atom}} \Sigma_{\text{mol}, 260 \text{ pc}} + \Sigma_{\text{atom}} \sqrt{2G\rho_{\star}} \sigma_{\text{atom}}, \quad (\text{A.9})$$

where σ_{atom} is the velocity dispersion of the atomic gas, which is fixed at $\sigma_{\text{atom}} = 10 \text{ km s}^{-1}$. In Equ. (A.9), all quantities are convolved to the large-scale resolution. Converting to typical units, we obtained

$$\begin{aligned} \left(\frac{P_{\text{atom}}}{k_{\text{B}} \text{ K cm}^{-3}}\right) &= 3.31 \times 10^5 \left(\frac{\Sigma_{\text{atom}}}{10^2 \text{ M}_{\odot} \text{ pc}^{-2}}\right)^2 \\ &+ 6.62 \times 10^5 \left(\frac{\Sigma_{\text{atom}}}{10^2 \text{ M}_{\odot} \text{ pc}^{-2}}\right) \left(\frac{\Sigma_{\text{mol}, 260 \text{ pc}}}{10^2 \text{ M}_{\odot} \text{ pc}^{-2}}\right) \\ &+ 1.02 \times 10^5 \left(\frac{\Sigma_{\text{atom}}}{10^2 \text{ M}_{\odot} \text{ pc}^{-2}}\right) \left(\frac{\rho_{\star}}{10^{-1} \text{ M}_{\odot} \text{ pc}^{-3}}\right)^{1/2}. \end{aligned} \quad (\text{A.10})$$

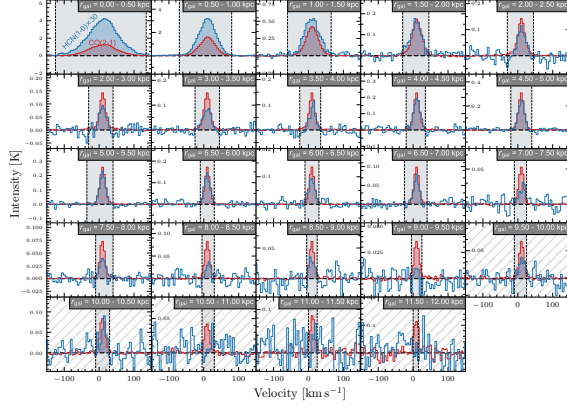


Fig. B.1. Similar to to Fig. 4, but using the galactocentric radius, r_{gal} , as the stacking quantity with 0.5 kpc (twice the beam size) bin widths. The panels with hatched background denote radial bins that are not completely covered by the field-of-view of the observations and thus not considered for the radial fit in Fig. 6.

Finally, we computed the intensity-weighted average, $\langle P_{\text{cloud}, 120 \text{ pc}} \rangle_{260 \text{ pc}}$, at the large-scale to combine the molecular gas weight with the large-scale P_{atom} pixel by pixel:

$$\langle P_{\text{DE}, 120 \text{ pc}} \rangle_{260 \text{ pc}} = \langle P_{\text{cloud}, 120 \text{ pc}} \rangle_{260 \text{ pc}} + P_{\text{atom}}. \quad (\text{A.11})$$

Appendix B: Spectral stacking

We compute spectral stacks using the python package PyStacker⁶ presented in Neumann et al. (2023a). PyStacker uses a high-significance prior (here CO(2–1)) to determine the velocity field of the line emission. It then uses this velocity information to shift the spectra of various line to correct for the Doppler shift, assuming all lines share the same velocity field. Afterwards, we average the shuffled spectra over larger regions usually resulting in higher-significance detections. Here, we stack the emission of CO(2–1) (from PHANGS–ALMA) and HCN(1–0) (this work) via morphological environment (Fig. 4), galactocentric radius, r_{gal} (Fig. B.1), dynamical equilibrium pressure, $\langle P_{\text{DE}} \rangle$ (Fig. B.2), molecular gas surface density (Fig. B.3), Σ_{mol} , stellar mass surface density, Σ_{\star} , and molecular cloud properties, $\langle \Sigma_{\text{mol}} \rangle$, $\langle \sigma_{\text{mol}} \rangle$, $\langle \alpha_{\text{vir}} \rangle$. We use these averaged spectra to compute integrated intensities, where the velocity-integration window is inferred based on the average CO(2–1) spectrum using the same masking method as described in Sect. 3.1. We note that the spectral stacks agree within $\pm 10\%$ with binned integrated intensities computed within the same stacking bins if CO(2–1) is used as a prior to define the velocity-integration mask.

Appendix C: Star formation rate tracers

Appendix C.1: Star formation rate – 21 μm

We use 21 μm (F2100W) emission from recent JWST–MIRI (Gardner et al. 2023; Wright et al. 2023) observations as another probe of SFR, in addition to H α from PHANGS–MUSE (Sect. 3.4) and 33 GHz from VLA (Sect. C.2). These data are part of the “PHANGS–JWST Treasury Program” (Lee et al.

⁶ <https://github.com/PhangsTeam/PyStacker>

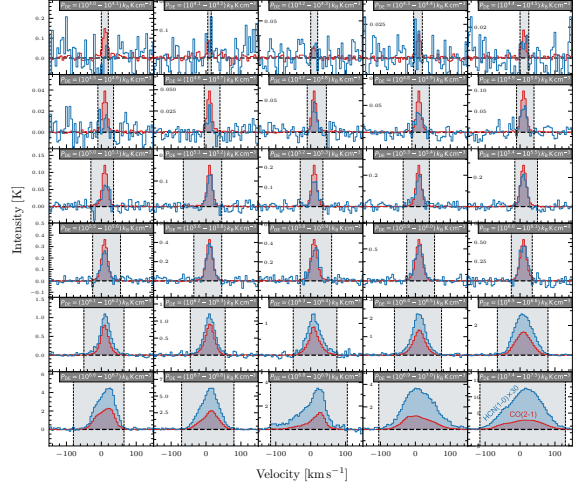


Fig. B.2. Similar to to Fig. 4, but using the dynamical equilibrium pressure, $\langle P_{\text{DE}} \rangle$, as the stacking quantity with 0.1 dex bin widths. Note that the bins from $\langle P_{\text{DE}} \rangle = 10^{7.0}$ to $10^{7.4} \text{ K cm}^{-3}$ do not contain any spectra and are therefore not shown.

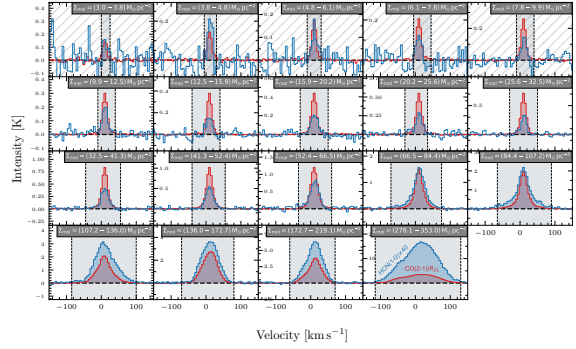


Fig. B.3. Similar to to Fig. 4, but using the molecular gas surface density, Σ_{mol} , as the stacking quantity with 20 bins from $\Sigma_{\text{mol}} = 3 - 353 \text{ M}_{\odot} \text{ pc}^{-2}$. Note that the bin at $\Sigma_{\text{mol}} = 173 - 219 \text{ M}_{\odot} \text{ pc}^{-2}$ does not contain any spectra and is therefore not shown. Bins with $\Sigma_{\text{mol}} < 10 \text{ M}_{\odot} \text{ pc}^{-2}$ are indicated with hatched backgrounds and are not used for the line fit in Fig. 9.

2023) and have been reduced via the PHANGS–JWST data reduction pipeline (Williams et al. in prep.). NGC 4321 was observed by JWST in June 2023 and we use version 0.9 of the PHANGS–JWST data reduction.

Physically, the strong radiation field from young, massive stars heat up the surrounding dust, which re-emits at infrared wavelength probed by F2100W. 21 μm point sources correlate well with H II regions (Hassani et al. 2023) and the F2100W intensity correlates well, though non-linearly, with extinction-corrected H α intensity (Leroy et al. 2023; Belfiore et al. 2023). However, the F2100W also captures stochastically heated emission from small dust grains that can trace the ISM. It may thus be both more robust to extinction than H α and more subject to contamination by diffuse ISM emission.

To infer Σ_{SFR} from F2100, we used the empirical relation from Leroy et al. (2023) (their equation 5), which re-scales the

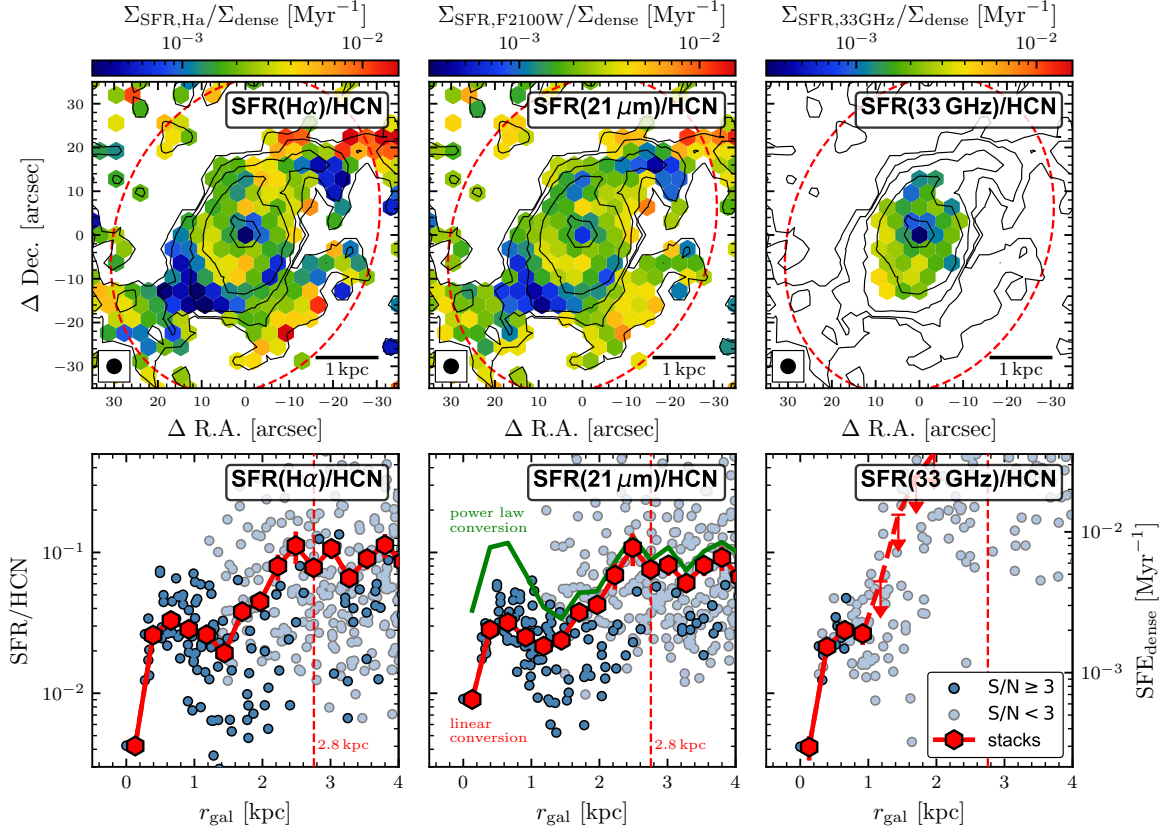


Fig. C.1. Comparison of SFR tracer in dense gas scaling relations in the inner 4 kpc. *Top:* SFR/HCN, tracing dense gas star formation efficiency, using three different SFR tracer from left to right, $H\alpha$ from MUSE, $21\ \mu\text{m}$ from JWST and $33\ \text{GHz}$ from VLA. Contours show HCN intensities as in Fig. 3. The dotted ellipse denotes $r_{\text{gal}} = 2.75\ \text{kpc}$. *Bottom:* SFR/HCN, matching the respective above panels, against galactocentric radius, r_{gal} . Blue points indicate detected ($S/N \geq 3$) and light blue points denote non-significant ($S/N < 3$) data. The red hexagon markers show the spectral stacks taken over all data within the bin. In the middle panel, we show the data obtained from the linear $21\ \mu\text{m}$ -to-SFR conversion (Equ. (C.1)) and additionally indicate the mean trend inferred from a power law conversion, that is, $\text{SFR} \propto L(\text{F2100W})^{1.3}$ (Leroy et al. 2023).

$21\ \mu\text{m}$ flux into a $24\ \mu\text{m}$ flux using $R_{21\ \mu\text{m}/24\ \mu\text{m}} = 0.80$ and then converts to SFR via a linear conversion (e.g. following Kennicutt & Evans 2012) such that the SFR surface density is given by

$$\left(\frac{\Sigma_{\text{SFR}, \text{F2100W}}}{\text{M}_{\odot} \text{yr}^{-1} \text{kpc}^{-2}} \right) = 3.7 \times 10^{-3} \left(\frac{I_{\nu, \text{F2100W}}}{\text{erg s}^{-1} \text{cm}^{-2} \text{sr}^{-1}} \right) \cos(i). \quad (\text{C.1})$$

Thus, we adopted a linear relation between F2100W dust emission and the SFR. We also contrast this prescription with a power-law relation based on Leroy et al. (2023), which leads to up to a factor of three higher values in the central $\sim 2\ \text{kpc}$ of NGC 4321.

Appendix C.2: Star formation rate – 33 GHz

We note that above SFR tracers might lead to significantly discrepant results in galaxy centres, where optical recombination lines can become too extinct to recover robust Balmer decrement corrections and $21\ \mu\text{m}$ emission might be systematically contaminated by stochastically heated dust grain. Therefore, we use free-free $33\ \text{GHz}$ emission from as an additional SFR tracer in the centre of NGC 4321. The data are coming from Very Large

Array (VLA) observations of a large sample of galaxies, including NGC 4321, at $3\ \text{GHz}$ to $33\ \text{GHz}$ at $\sim 2''$ resolution (Linden et al. 2020).

At high radio frequencies the ionising flux of young massive stars is directly proportional to the thermal spectral luminosity. This allowed us to trace the SFR via the thermal part of the $33\ \text{GHz}$ flux measured by the VLA following the prescription in Murphy et al. (2012) (their equation 6):

$$\left(\frac{\Sigma_{\text{SFR}, 33\ \text{GHz}}}{\text{M}_{\odot} \text{yr}^{-1} \text{kpc}^{-2}} \right) = 5.5 \times 10^{16} \left(\frac{T_e}{10^4\ \text{K}} \right)^{-0.45} \left(\frac{\nu}{\text{GHz}} \right)^{0.1} f_{\text{thermal}} \times \left(\frac{I_{\nu, 33\ \text{GHz}}}{\text{erg s}^{-1} \text{cm}^{-2} \text{sr}^{-1}} \right) \cos(i), \quad (\text{C.2})$$

where the thermal fraction (f_{thermal}) values are taken from Linden et al. (2020) (their table 4; $\sim 200\ \text{pc}$ apertures), and we adopted an electron temperature of $T_e = 10^4\ \text{K}$ and $\nu = 33\ \text{GHz}$.

Appendix C.3: Star formation rate tracer comparison

Throughout this work, we have used Balmer decrement-corrected $H\alpha$ emission as a tracer of SFR (Sect. 3.4). Despite

being a robust tracer of SFR overall, when corrected for dust attenuation, in the centres of galaxies, $H\alpha$ might miss some of the SFR-related $H\alpha$ emission due to extremely high attenuation by denser dust thus biasing the SFR estimate high. Also, in extreme environments, like the centre, $H\alpha$ emission might be associated with other processes than young stars and thus bias the SFR high. Therefore, we tested how robust our findings are against the choice of the SFR tracer, which is laid out in the following.

We use JWST F2100W emission to trace SFR via the hot dust emission that is less affected by attenuation effects in the centre of the galaxy as long as these galaxy centres contain sufficient amounts of dust (Sect. C.1). Using the F2100W-inferred SFR (instead of $H\alpha$) leads to similar SFR/HCN values across the disc and in the low-pressure regime for both prescriptions (linear and power-law conversion) adopted here (see Fig. C.1). However, the two calibrations differ by up to a factor of three in the central kiloparsec of the galaxy. The change is so severe that using the power-law calibration yields similar $\text{SFR}_{\text{F2100W}}/\text{HCN}$ values in the centre (median $10^{-1.05}$) as in bar ends (median $10^{-0.96}$), spiral arms (median $10^{-1.06}$) and interarm (median $10^{-1.19}$), and statistically the same $\text{SFR}_{\text{F2100W}}/\text{HCN}$ distribution in the centre compared to the aforementioned environments.

In addition, we compared the two SFR tracers ($H\alpha$ and F2100W) with the 33 GHz-inferred values, as 33 GHz emission is usually considered as the most robust tracer of the SFR in the centres of galaxies (Sect. C.2). We find that $H\alpha$ (decrement-corrected) and 33 GHz yield very consistent results across the whole central 1 kpc probed by 33 GHz emission, agreeing within 20 %. F2100W (linear conversion) leads to a factor of two higher values in the central 260 pc, but otherwise consistent values. Therefore, we conclude that for NGC 4321 Balmer decrement-corrected $H\alpha$ emission is an excellent tracer of the SFR, even in the centre of the galaxy, where increased dust attenuation could have depreciated $H\alpha$ as a robust SFR tracer. Moreover, these results suggest that F2100W is proportional to the SFR across the full disc of NGC 4321.

Appendix D: Scaling relations

Appendix D.1: Molecular cloud relations

In Fig. D.1, we present the relations between HCN/CO and SFR/HCN respectively with the properties of molecular gas at GMC scales (i.e. here at 120 pc). The cloud-scale molecular gas properties are computed following the prescriptions of Sun et al. (2018) and Neumann et al. (2023b), but adopting the varying α_{CO} and R_{21} conversions introduced in Sect. A.1.2. We computed the molecular gas surface density from the CO(2–1) integrated intensity ($W_{\text{CO}(2-1)}$):

$$\Sigma_{\text{mol}} = \alpha_{\text{CO}} R_{21}^{-1} W_{\text{CO}(2-1)}. \quad (\text{D.1})$$

The molecular gas velocity dispersion was obtained from the CO(2–1) equivalent line width and corrected for the velocity channel-to-channel correlation:

$$\sigma_{\text{measured}} = \frac{W_{\text{CO}(2-1)}}{\sqrt{2\pi}T_{\text{peak}}}, \quad (\text{D.2})$$

$$\sigma_{\text{mol}} = \sqrt{\sigma_{\text{measured}}^2 + \sigma_{\text{response}}^2}, \quad (\text{D.3})$$

where σ_{measured} assumes a Gaussian line profile and σ_{response} takes into account the instrument channel width and channel-to-channel correlation. To estimate the virial parameter (α_{vir}), we

assumed spherically symmetric clouds with a given density profile $\rho \propto r^{-1}$ so that α_{vir} could be computed from the CO(2–1) data using Σ_{mol} and σ_{mol} :

$$\alpha_{\text{vir}} = \frac{9 \ln 2}{\pi G} \frac{\sigma_{\text{mol}}^2}{\Sigma_{\text{mol}} D_{\text{beam}}} \propto \frac{\sigma_{\text{mol}}^2}{\Sigma_{\text{mol}}}, \quad (\text{D.4})$$

where G is the gravitational constant. These molecular gas properties are computed at $D_{\text{beam}} = 120$ pc scale and converted to the HCN resolution (i.e. 260 pc) via a Σ_{mol} -weighted average, similar to P_{DE} as described in Sect. 3.6, hence the notation $\langle X_{120\text{pc}} \rangle_{260\text{pc}}$, where X is the quantity to be averaged.

Similar to the relations with radius (Sect. 4.2) and pressure (Sect. 4.3), we apply the MARS linear regression tool (Sect. 3.8) to the cloud property relations shown in Fig. D.1. We find that HCN/CO correlated positively and with Σ_{mol} , σ_{mol} and α_{vir} and is well-described by a single power law over the whole data range that is probed. Similarly, we observe a negative correlation between SFR/HCN and Σ_{mol} , σ_{mol} , α_{vir} . However, for SFR/HCN versus Σ_{mol} and σ_{mol} we find a change in the relation (as determined via MARS) at $\Sigma_{\text{mol}} = 74 \text{ M}_{\odot} \text{ pc}^{-2}$ and $\sigma_{\text{mol}} = 8.3 \text{ km s}^{-1}$, such that SFR/HCN is roughly constant at low Σ_{mol} (σ_{mol}) and strongly decreasing with increasing Σ_{mol} (σ_{mol}) at high Σ_{mol} (σ_{mol}).

Appendix D.2: Stellar mass relations

Figure D.2 shows the HCN/CO and SFR/HCN scaling relation with the stellar mass surface density, Σ_{\star} . We compute Σ_{\star} from the *Spitzer* 3.6 μm image as described in Sect. A.3. Following the same methodology as in Sect. 4.2, 4.3, D.1, we determine the power law behaviour of the mean trend finding strong correlations between HCN/CO (positive correlation) and SFR/HCN (negative correlation) with Σ_{\star} . For HCN/CO versus Σ_{\star} , we observe a tighter relation (0.19 dex scatter) that is consistent over all environments and the whole probed data range, spanning two orders of magnitude in stellar mass surface density ($1 \times 10^2 \text{ M}_{\odot} \text{ pc}^{-2}$ to $1 \times 10^4 \text{ M}_{\odot} \text{ pc}^{-2}$). The found relation shows that Σ_{\star} is a good predictor of HCN/CO over the whole disc of a nearby galaxy at sub-kiloparsec scales, though most of the dynamic range of Σ_{\star} is covered by only two regions, the centre and the bar. The relation between SFR/HCN and Σ_{\star} shows a much higher scatter (0.46 dex), with the bar region being offset to the main relation by 0.2 dex, stressing the strongly suppressed star formation efficiency in the bar (Sect. 5.3). Combined with the results presented in Sect. D.1, the found relations suggest that the threshold behaviour in the SFR/HCN versus P_{DE} relation (Sect. 4.3) is caused by molecular gas cloud-scale physics rather than larger scale environment.

Appendix E: Additional figures

Fig. A.1 shows the CO(2–1)-to-CO(1–0) line ratio (R_{21}) computed from the $4'' \sim 300$ pc resolution CO(1–0) data from Pan & Kuno (2017) and homogenised CO(2–1) observations from PHANGS–ALMA (Leroy et al. 2021b). We use the measured 300 pc-scale R_{21} map to infer the cloud-scale (120 pc) CO(1–0) line intensities from the observed CO(2–1) line intensities, which enter the estimation of the dynamical equilibrium pressure (Sect. 3.6). In Sect. 4.5, we use the R_{21} map to convert the 260 pc-scale $W_{\text{CO}(2-1)}$ into $W_{\text{CO}(1-0)}$ to compare the HCN-to-CO(1–0) versus Σ_{mol} scaling relation with literature findings.

In Fig. E.1, we show a map of the morphological environments overlaid with HCN contours similar to Fig. 3, right panel.

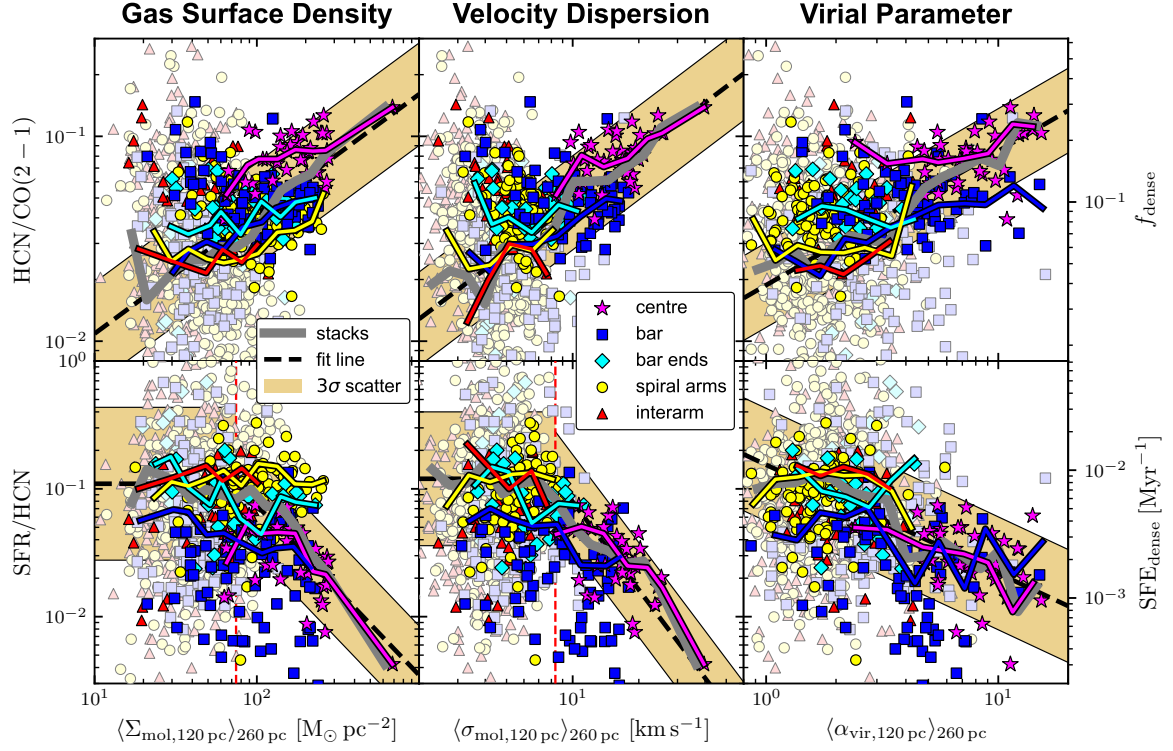


Fig. D.1. HCN spectroscopic ratios against molecular cloud properties. *Top:* HCN/CO and (*bottom*) SFR/HCN measured at 260 pc scale versus cloud-scale molecular gas properties inferred from 120 pc scale CO(2–1) observations. Panels from left to right show molecular cloud surface density (Σ_{mol}), velocity dispersion (σ_{mol}) and virial parameter (α_{vir}) on the x -axis, obtained from PHANGS–ALMA as described in Sect. D.1. Similarly to Fig. 7 and 8, markers indicate the respective environments and line fits as well as linear regression regimes are determined via MARS. The obtained thresholds are $\Sigma_{\text{mol}} = 74 \text{ M}_{\odot} \text{ pc}^{-2}$ for SFR/HCN versus Σ_{mol} and $\sigma_{\text{mol}} = 8.3 \text{ km s}^{-1}$ for SFR/HCN versus σ_{mol} . The linear regression parameters are listed in Tab. D.1.

Table D.1. HCN/CO(2 – 1) and SFR/HCN correlations with Σ_{\star} , $\langle \Sigma_{\text{mol}} \rangle$, $\langle \sigma_{\text{mol}} \rangle$, $\langle \alpha_{\text{vir}} \rangle$.

x-axis	y-axis	Regime	Slope (stacks)	Slope (los)	Corr. (p)	Scatter
$\langle \Sigma_{\text{mol}} \rangle$	HCN/CO(2–1)		0.58	0.40 (0.04)	0.43 (0.0)	0.25
	SFR/HCN	$\leq 74 \text{ M}_{\odot} \text{ pc}^{-2}$	0.00	-0.75 (0.13)	-0.30 (0.0)	0.60
		$> 74 \text{ M}_{\odot} \text{ pc}^{-2}$	-1.33	-2.30 (0.45)	-0.53 (0.0)	0.39
$\langle \sigma_{\text{mol}} \rangle$	HCN/CO(2–1)		0.81	0.51 (0.04)	0.57 (0.0)	0.23
	SFR/HCN	$\leq 8.3 \text{ km s}^{-1}$	0.00	-1.05 (0.26)	-0.27 (0.0)	0.52
		$> 8.3 \text{ km s}^{-1}$	-2.29	-1.58 (0.16)	-0.60 (0.0)	0.37
$\langle \alpha_{\text{vir}} \rangle$	HCN/CO(2–1)		0.65	0.46 (0.03)	0.52 (0.0)	0.21
	SFR/HCN		-0.84	-1.11 (0.07)	-0.55 (0.0)	0.44
Σ_{\star}	HCN/CO(2–1)		0.52	0.44 (0.03)	0.57 (0.0)	0.19
	SFR/HCN		-0.73	-1.02 (0.06)	-0.50 (0.0)	0.46

Notes – Linear regression parameters for the respective relations and x -axis regimes presented in Fig. D.2 and D.1 analogous to Tab. 4. The slopes of the binned relations (column 4) are either determined by MARS if two distinct regimes with different linear regression behaviour have been found, or computed with LinMix if the relation is well described with a single line according to the MARS algorithm.

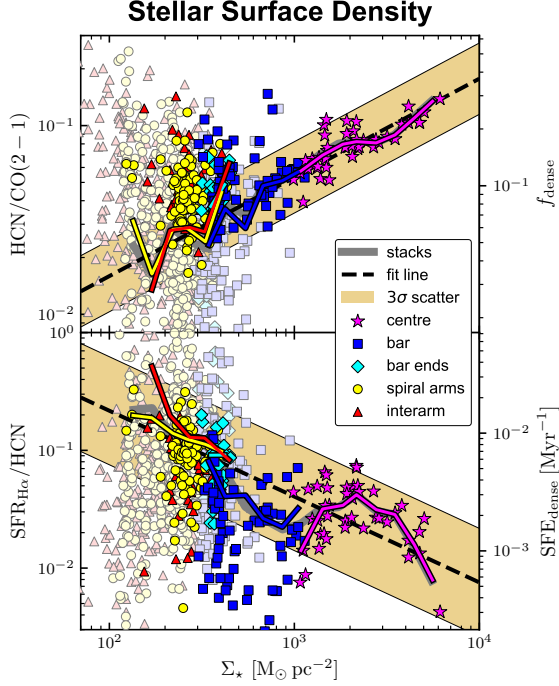


Fig. D.2. HCN spectroscopic ratio versus stellar mass surface density similar to Fig. 7 and 8, but using Σ_* on the x-axis. Stellar mass is traced via the dust-attenuation corrected 3.6 μm emission. The line fit parameters are listed in Tab. D.1.

In addition, we indicate two loci of ISM pressure, P_{DE} , matching the pressure thresholds inferred for the HCN/CO and SFR/HCN versus P_{DE} scaling relations (Sect. 4.3).

Fig. E.2 presents HCN/CO and HCN/HCO⁺ line ratio trends with metallicity. Detected single line measurements of HCN/CO show no correlation with metallicity ($\rho_{\text{Pearson}} = 0.12$). The stacked average HCN/CO increases with metallicity, suggesting that the HCN abundance is more strongly depending on metallicity than CO, which is expected if nitrogen decreases more sharply with metallicity than oxygen (Braine et al. 2017, 2023). In this scenario we would expect a systematic increase of the HCN/HCO⁺ line ratio with metallicity. However, we find only a weak correlation between HCN/HCO⁺ and metallicity ($\rho = 0.35$), indicating that metallicity effect play only a minor role across NGC 4321, potentially due to the small dynamic range in metallicity, spanning less than 0.1 dex (8.54 to 8.62).

In Fig. E.3, we display maps of various data products surface density maps of the atomic gas, (dense) molecular gas and stellar mas, ISM pressure and SFR inferred from H α and 21 μm , respectively. In addition, we show the star formation efficiency of the molecular gas, SFR/CO.

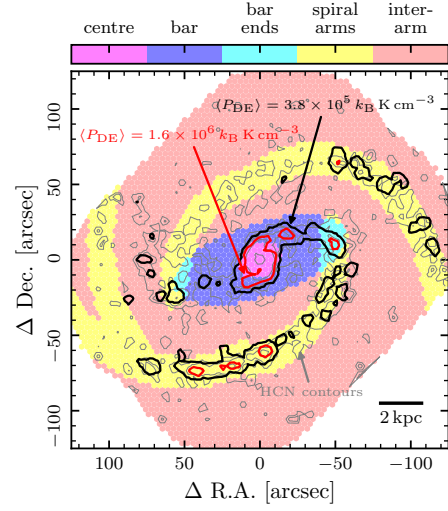


Fig. E.1. Pressure threshold contours. The map shows the same morphological environment masks as in Fig. 3. Overlaid are HCN contours in grey and $\langle P_{\text{DE}} \rangle$ contours at $\langle P_{\text{DE}} \rangle = 3.8 \times 10^5 \text{ K cm}^{-3}$ (black) and at $\langle P_{\text{DE}} \rangle = 1.6 \times 10^6 \text{ K cm}^{-3}$ (red). The pressure contours represent the threshold values in the pressure relations discussed in Sect. 4.3.

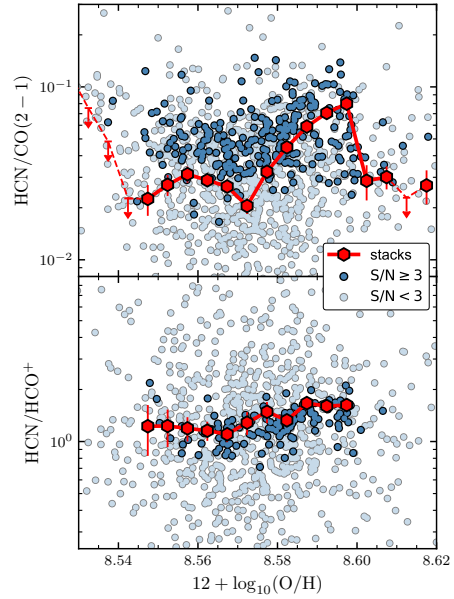


Fig. E.2. Line ratio trends with metallicity. *Top:* HCN/CO(2-1) against metallicity *Bottom:* HCN/HCO⁺ against metallicity. Dark markers indicate significant data ($S/N \geq 3$) and light markers show non-detections ($S/N < 3$). The red hexagon markers show the average trends over all data obtained via spectral stacking. We note that the HCO⁺ data will be separately published and studied in more detail along with other dense gas tracers in Neumann et al. in prep. Here, we only show the HCN/HCO⁺ variation with metallicity to highlight the flat trends hence supporting HCN as a tracer of density across the full molecular gas disc of NGC 4321.

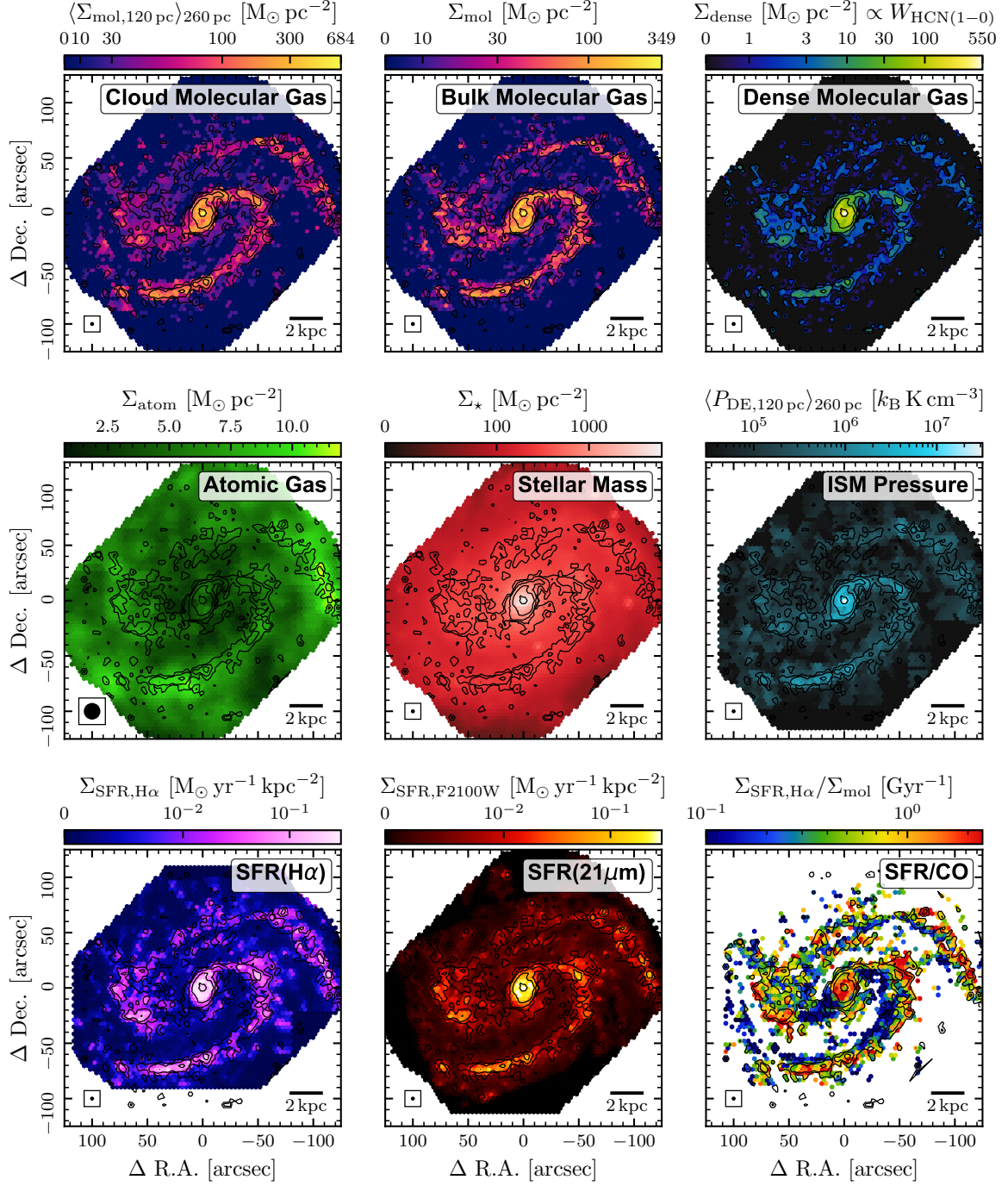


Fig. E.3. Data product maps compilation. All maps are convolved to a common resolution of 260 pc, given by the native resolution of the HCN data, and sampled to a common, hexagonal pixel grid at beam size spacing.

Supplementary material

D.1 ALMOND: additional figures/tables

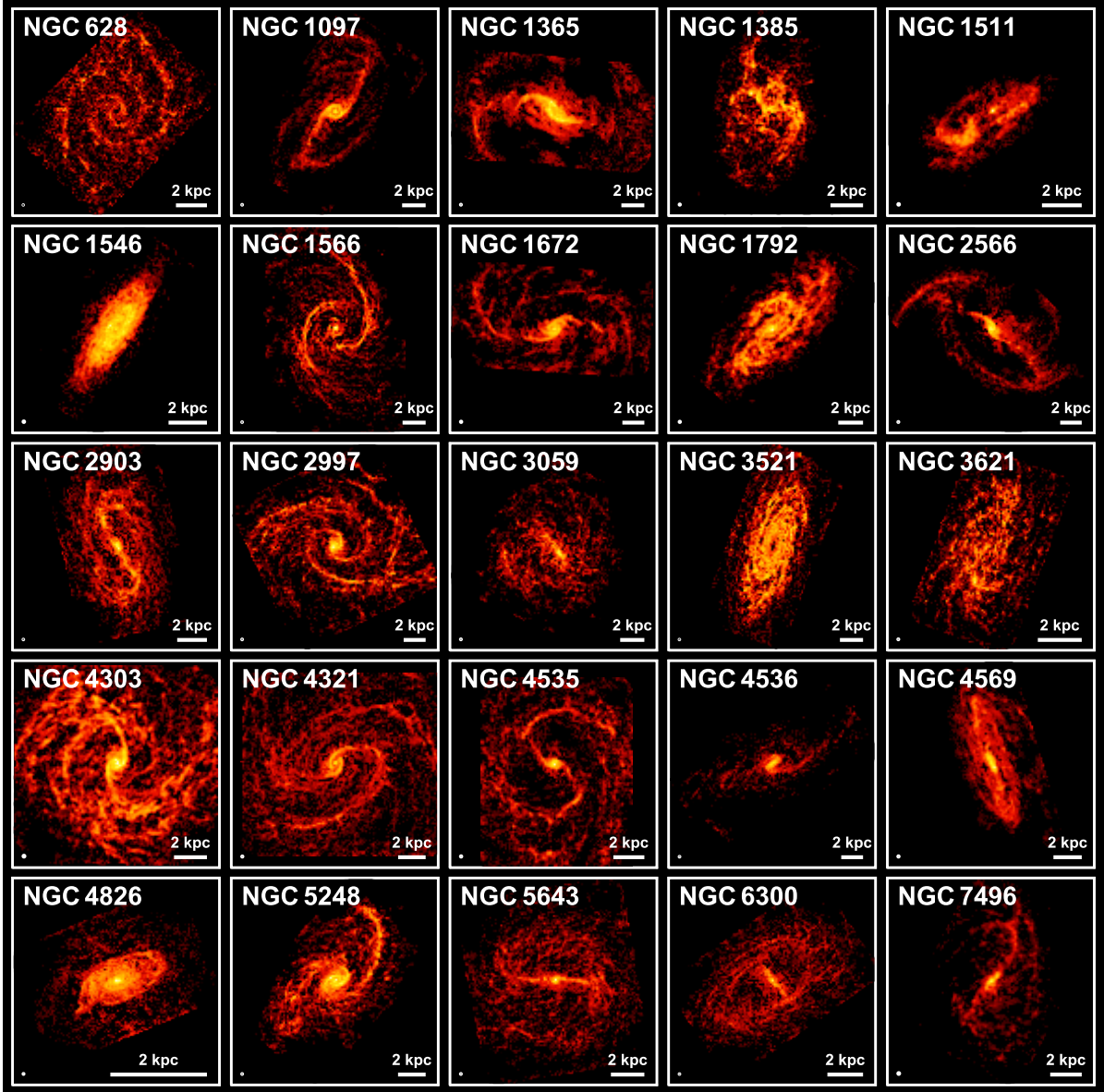


Figure D.1: PHANGS–ALMA CO maps across the ALMOND sample. Similar to Figure 2.5, but for showing the ALMOND galaxy sample.

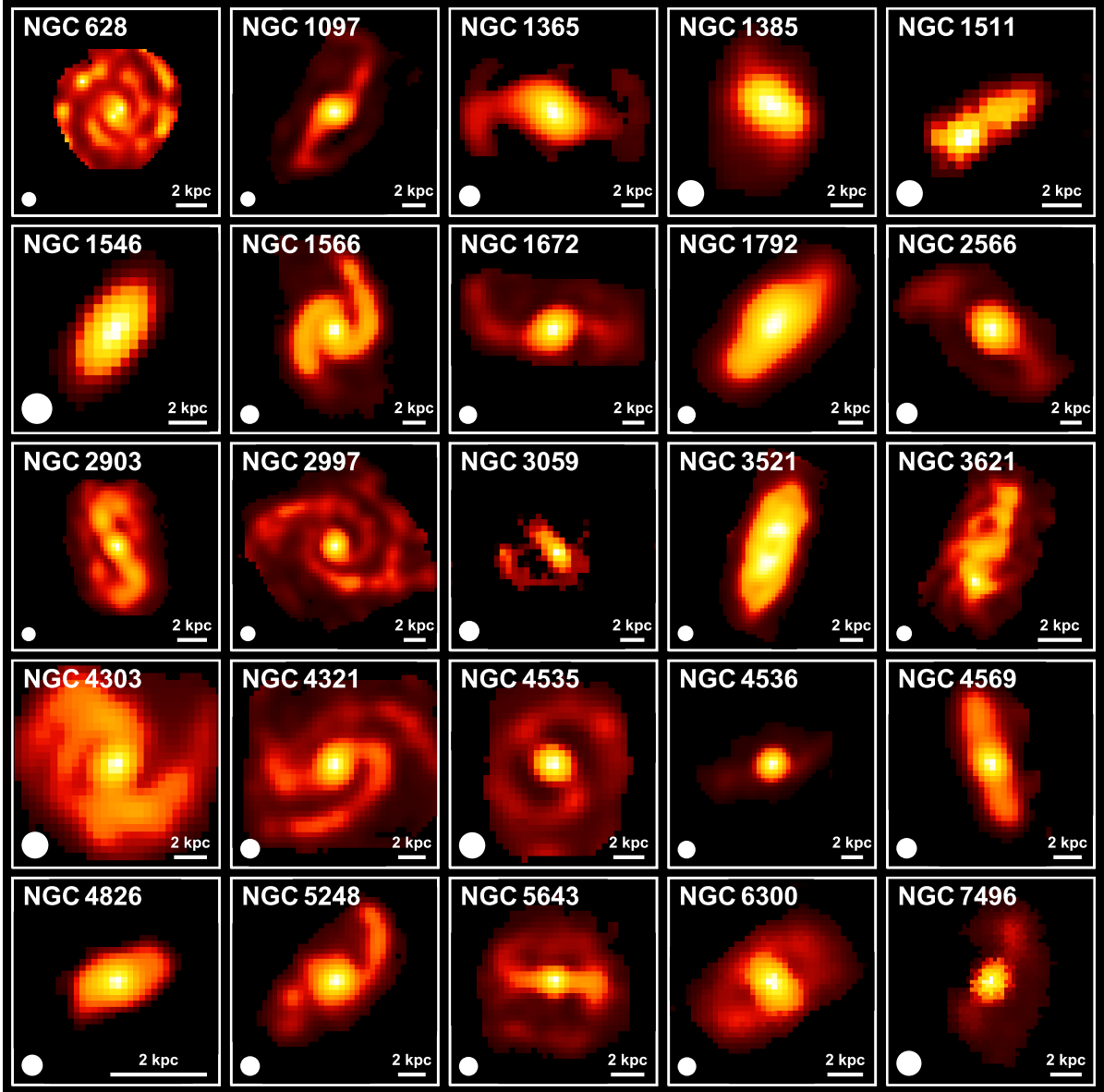


Figure D.2: **Smoothed PHANGS-ALMA CO maps across the ALMOND sample.** Similar to Figure 2.7, but for CO (2 – 1) from PHANGS-ALMA smoothed to the ALMOND resolution.

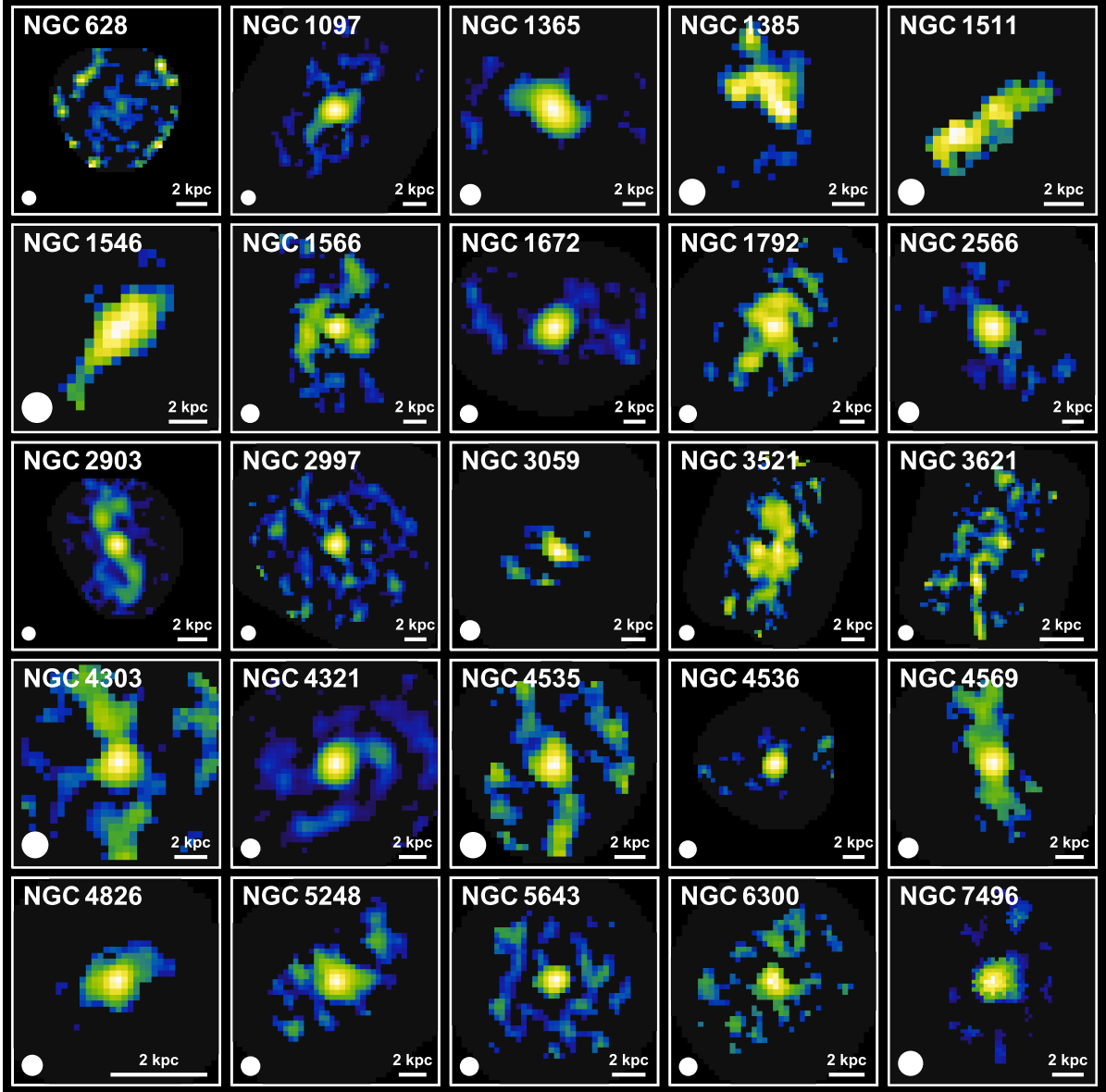


Figure D.3: ALMOND HCO⁺ maps. Similar to Figure 2.7, but for HCO⁺ (1 – 0).

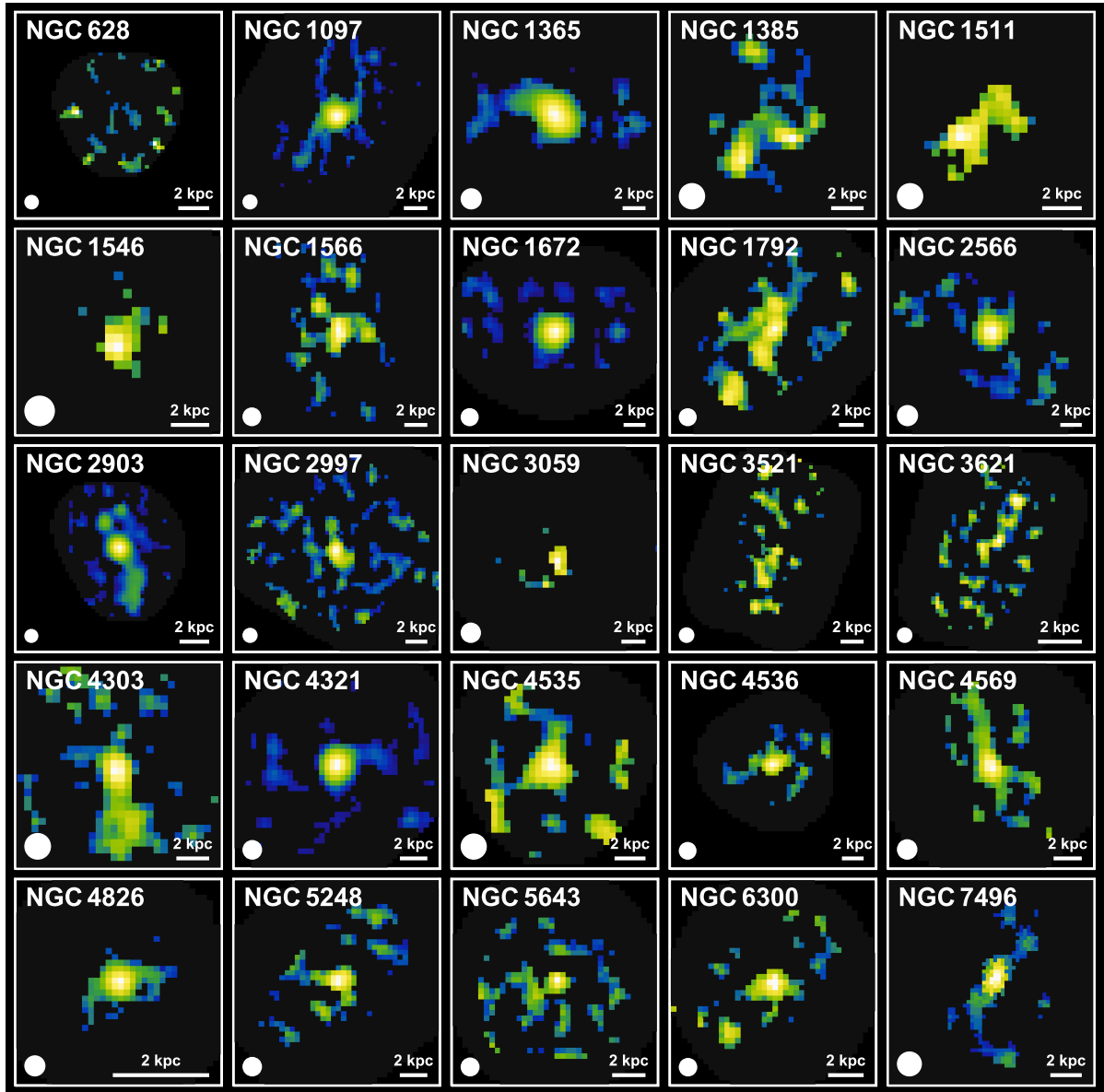


Figure D.4: ALMOND CS maps Similar to Figure 2.7, but for CS ($2 - 1$).

D.2 LEGO: additional figures/tables

Table D.1: LEGO sources

Source	Right Ascension [J2000]	Declination [J2000]	Longitude [deg]	Latitude [deg]	Target Category
OrionSouth	5 ^h 37 ^m 24.560 ^s	−6°46′19.400″	210.57	−19.53	Southern Orion A
IC5146-W	21 ^h 47 ^m 25.340 ^s	47°33′0.000″	93.78	−4.63	IC 5146
W49A	19 ^h 10 ^m 15.376 ^s	9°4′30.922″	43.15	−0.01	High Mass SF
W43	18 ^h 47 ^m 44.502 ^s	−1°51′12.606″	30.86	−0.02	High Mass SF
G45.1+0.1	19 ^h 13 ^m 27.326 ^s	10°53′10.909″	45.12	0.13	High Mass SF
Sh2-208	4 ^h 19 ^m 32.920 ^s	52°58′41.600″	151.29	1.97	Low Metallicity
Sh2-266	6 ^h 18 ^m 36.460 ^s	15°9′23.400″	195.74	−0.20	Low Metallicity
Sh2-284	6 ^h 45 ^m 27.590 ^s	0°17′23.100″	211.99	−1.20	Low Metallicity
G125.6+2.1	1 ^h 15 ^m 53.820 ^s	64°50′5.300″	125.53	2.09	Outer Galaxy
G144.8+0.4	3 ^h 38 ^m 48.360 ^s	55°57′57.600″	144.86	0.39	Outer Galaxy
G147.3-0.2	4 ^h 1 ^m 23.890 ^s	53°20′45.600″	149.04	0.39	Outer Galaxy
G160.2+0.8	4 ^h 51 ^m 33.200 ^s	45°30′8.900″	160.32	0.78	Outer Galaxy
G168.6+1.0	5 ^h 19 ^m 27.770 ^s	39°2′44.600″	168.58	0.99	Outer Galaxy
G170.6-0.3	5 ^h 20 ^m 21.120 ^s	36°35′2.400″	170.70	−0.28	Outer Galaxy

Notes – Columns show the source name, coordinates (right ascension, declination; galactic longitude, latitude), and target category. In this thesis, we focus on the massive star-forming regions (W49A, W43, G45.1+0.1).

Table D.2: Molecular line properties

Species	Transition	Frequency [GHz]	E_u/k_B [K]	A_{ul} [s ⁻¹]	C_{ul} [cm ³ s ⁻¹]	n_{crit} [cm ⁻³]	n_{eff} [cm ⁻³]	Source
CO	$J = 1 - 0$	115.271202	5.53	7.2×10^{-8}	1.3×10^{-10}	5.7×10^2	...	a
¹³ CO	$J = 1 - 0$	110.201354	5.29	6.3×10^{-8}	1.3×10^{-10}	4.8×10^2	...	a
C ¹⁸ O	$J = 1 - 0$	109.782176	5.27	6.3×10^{-8}	1.3×10^{-10}	4.8×10^2	...	a
C ¹⁷ O	$J = 1 - 0, F = 7/2 - 5/2$	112.358988	5.39	6.7×10^{-8}	1.3×10^{-10}	5.2×10^2	...	a
HCN	$J = 1 - 0, F = 2 - 1$	88.6318473	4.25	2.4×10^{-5}	8.1×10^{-11}	3.0×10^5	4.5×10^3	a
HCO ⁺	$J = 1 - 0$	89.188526	5.3×10^2	a
HNC	$J = 1 - 0, F = 2 - 1$	90.663564	4.35	2.7×10^{-5}	2.6×10^{-10}	1.1×10^5	2.3×10^3	a
CN	$N = 1 - 0, J = 1/2 - 1/2, F = 3/2 - 3/2$	113.191317	5.43	1.2×10^{-5}	6.2×10^{-11}	1.9×10^5	...	a
CN	$N = 1 - 0, J = 3/2 - 1/2, F = 5/2 - 3/2$	113.490982	5.45	1.2×10^{-5}	5.0×10^{-11}	2.4×10^5	1.7×10^4	a
CS	$J = 2 - 1$	97.980953	1.2×10^4	a
N ₂ H ⁺	$J = 1 - 0, F_1 = 2 - 1, F = 2 - 1$	93.173777	4.47	3.6×10^{-5}	8.9×10^{-10}	4.1×10^4	5.5×10^3	a
SO	$J_K = 3_2 - 2_1$	99.299905	9.20	1.1×10^{-5}	3.4×10^{-10}	3.3×10^4	...	a
SiO	$J = 2 - 1$	86.846995	b
CCH	$N = 1 - 0, J = 3/2 - 1/2, F = 2 - 1$	87.316925	4.19	1.5×10^{-6}	5.8×10^{-11}	2.7×10^4	...	a
CCH	$N = 1 - 0, J = 1/2 - 1/2, F = 1 - 1$	87.402004	4.20	1.3×10^{-6}	5.9×10^{-11}	2.2×10^4	...	a
C ³⁴ S	$J = 2 - 1$	96.41295	a
CH ₃ OH-E	$J_K = 2_{-1} - 1_{-1}$	96.739363	12.50	2.6×10^{-6}	2.9×10^{-10}	8.7×10^3	...	a
CH ₃ OH-A	$J_K = 2_0 - 1_0$	96.741377	a
H ¹³ CN	$J = 1 - 0, F = 2 - 1$	86.3401764	1.6×10^5	b
H ¹³ CO ⁺	$J = 1 - 0$	86.754288	2.2×10^4	b
HC ₃ N	$J = 12 - 11$	109.173638	34.06	1.0×10^{-4}	6.4×10^{-10}	1.6×10^5	1.1×10^5	c
HNCO	$J_{K_a, K_c} = 5_{0,5} - 4_{0,4}$	109.905753	15.82	1.8×10^{-5}	4.4×10^{-10}	4.1×10^4	...	a
HNCO	$J_{K_a, K_c} = 4_{0,4} - 3_{0,3}$	87.925238	10.55	9.0×10^{-6}	4.3×10^{-10}	2.1×10^4	...	a
HN ¹³ C	$J = 1 - 0, F = 2 - 1$	87.090859	b
H41 α	$N = 42 - 41$	92.034434	d

Notes – Columns show the atomic/molecular species, transition, rest frequency, energy of the upper level, Einstein coefficient for spontaneous emission, collisional deexcitation rate coefficient, critical density, effective excitation density (according to Shirley (2015)), and reference.

(a) Watanabe, Sakai, Sorai et al. (2014)

(b) Pety et al. (2017)

(c) Watanabe, Sakai, López-Sepulcre et al. (2015)

(d) Turner (1989)

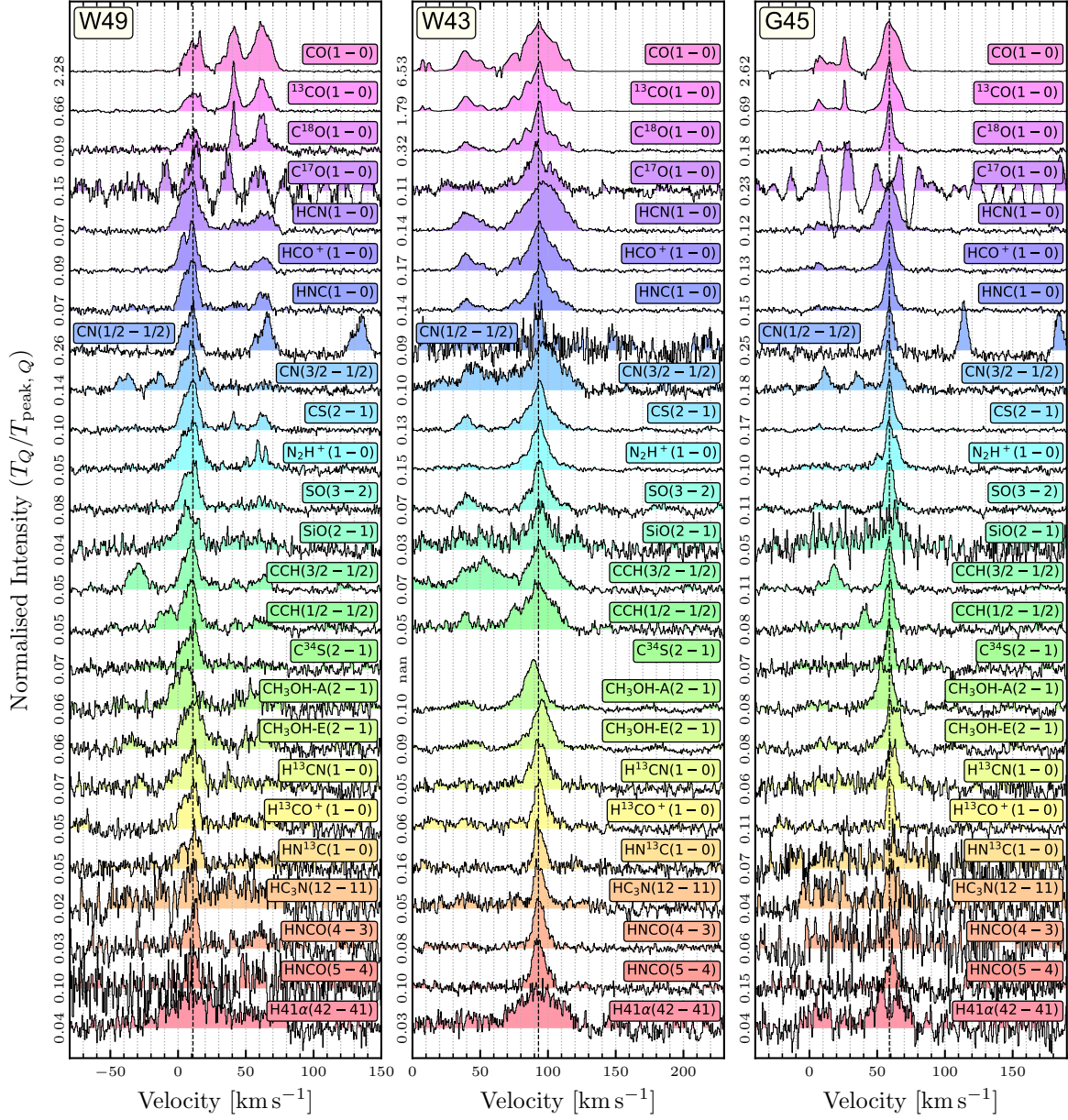


Figure D.5: LEGO cloud-average spectra. Similar to Figure 8.3, but for all molecular lines listed in Table D.2.

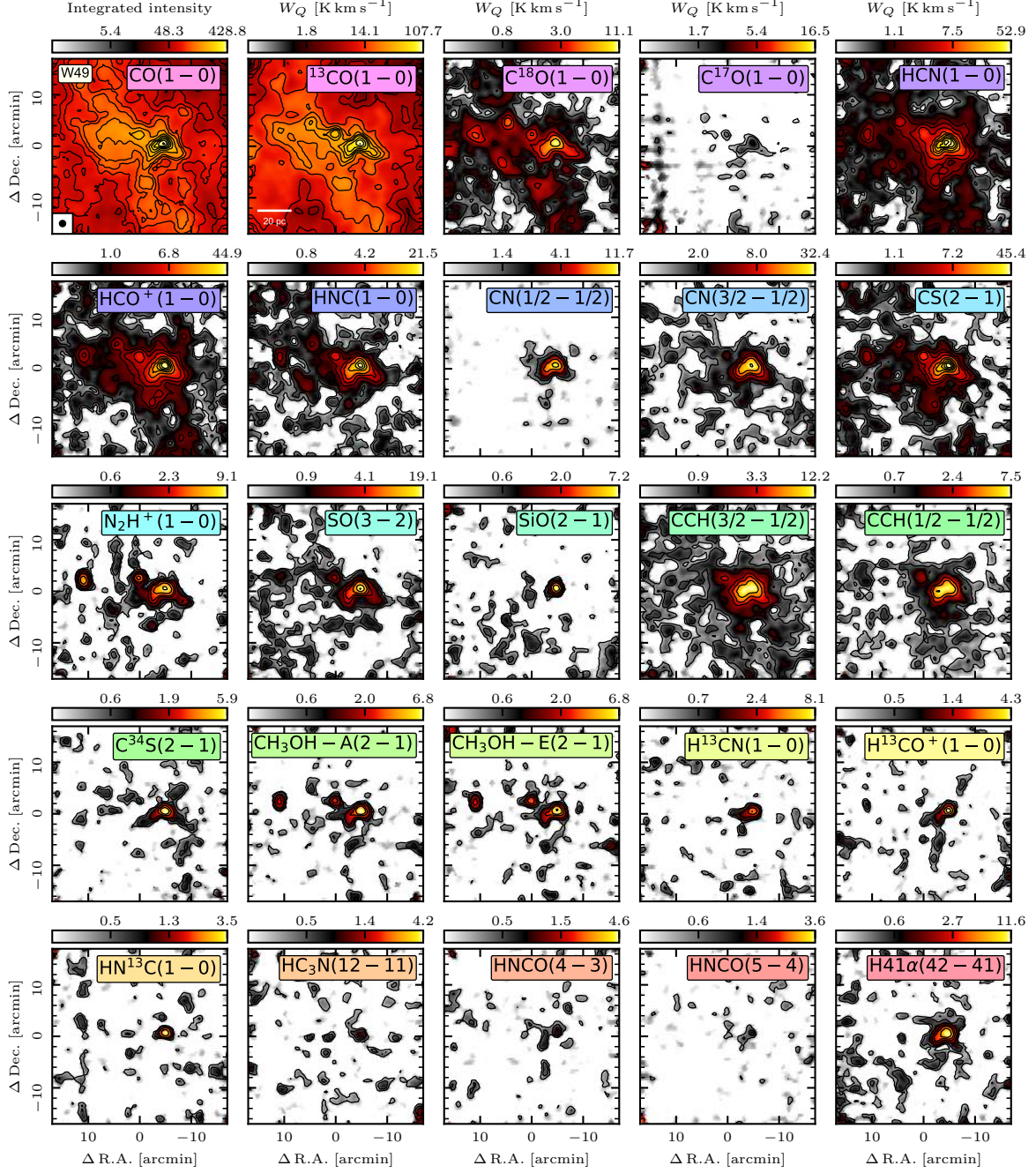


Figure D.6: **Integrated intensity maps of W49.** Similar to Figure 8.4, but for all molecular lines listed in Table D.2 across the W49 cloud region.

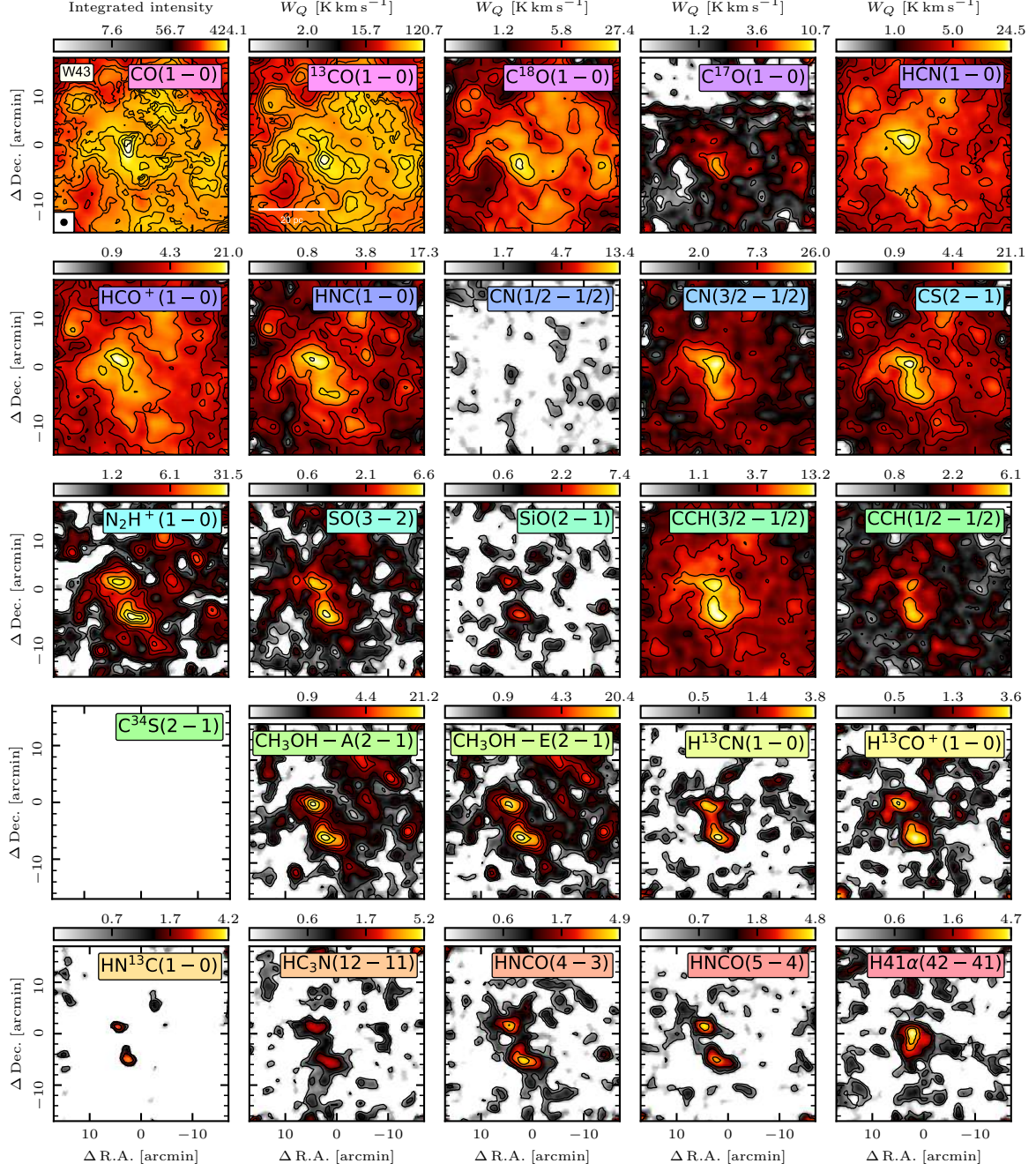


Figure D.7: **Integrated intensity maps of W43.** Similar to Figure 8.4, but for all molecular lines listed in Table D.2 across the W43 cloud region.

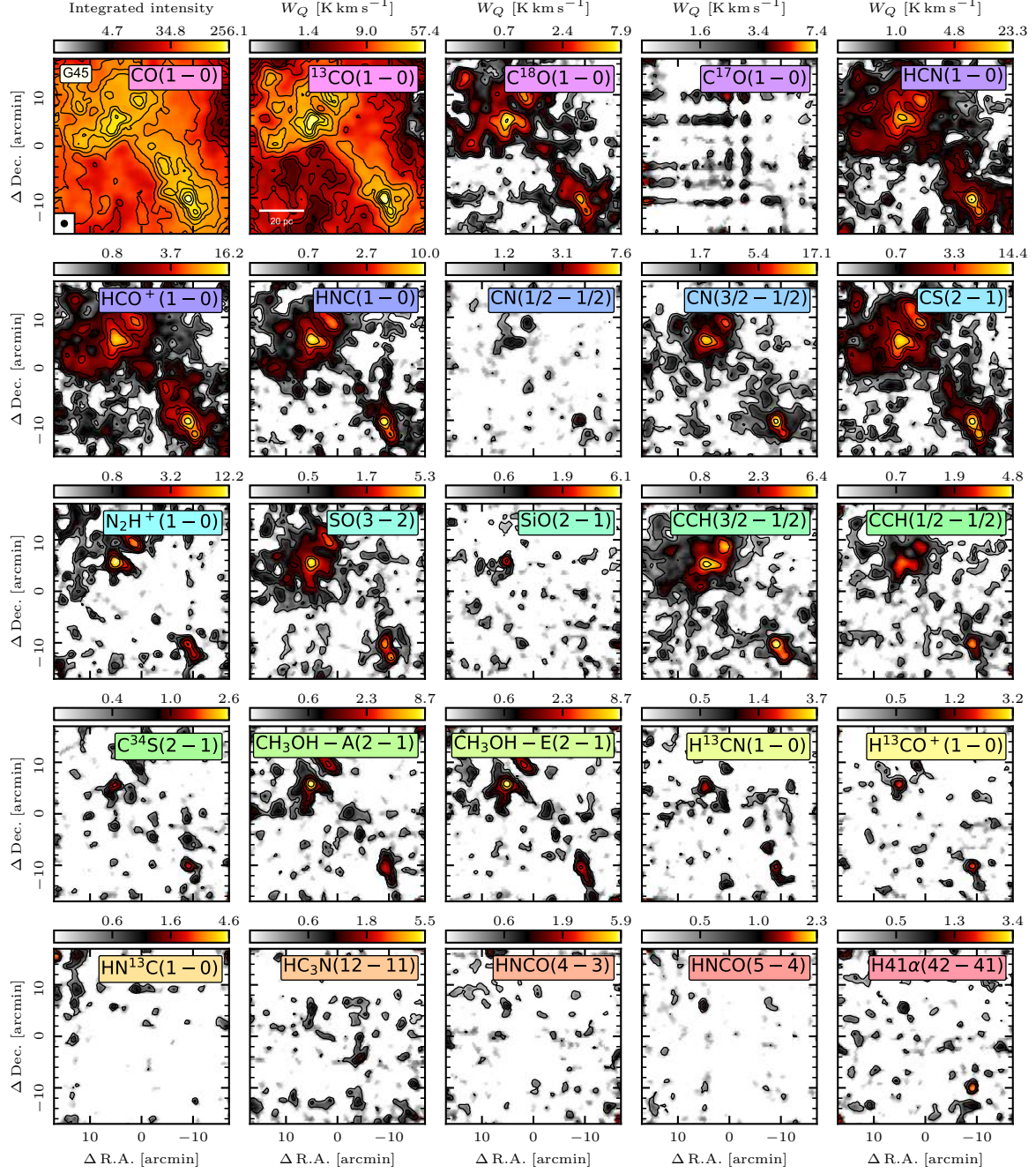


Figure D.8: Integrated intensity maps of G45.1+0.1. Similar to Figure 8.4, but for all molecular lines listed in Table D.2 across the G45.1+0.1 cloud region.

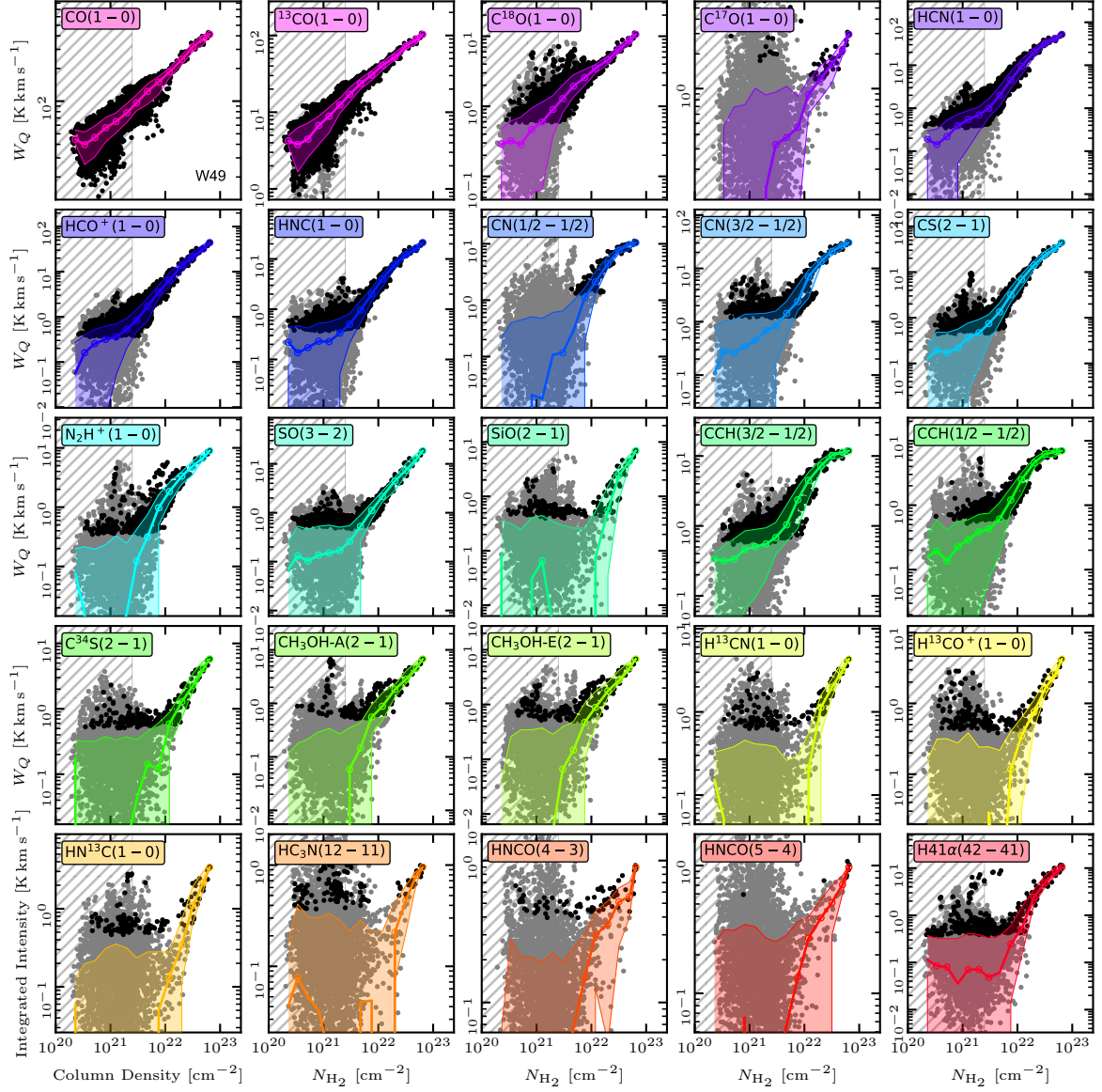


Figure D.9: **Integrated intensity against column density across W49.** Similar to Figure 8.5, but for all molecular lines listed in Table D.2 across the W49 cloud region.

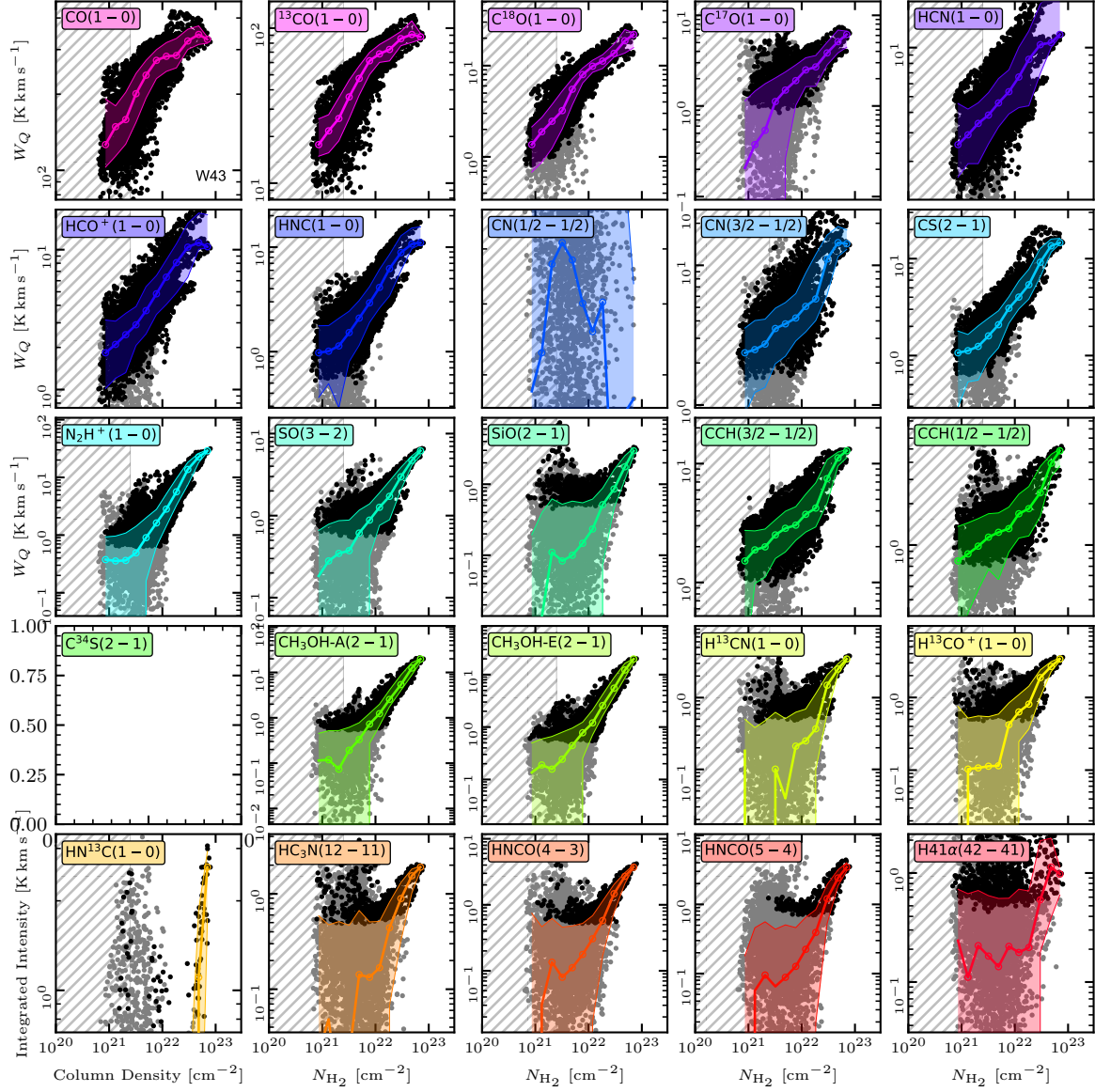


Figure D.10: **Integrated intensity against column density across W43.** Similar to Figure 8.5, but for all molecular lines listed in Table D.2 across the W43 cloud region.

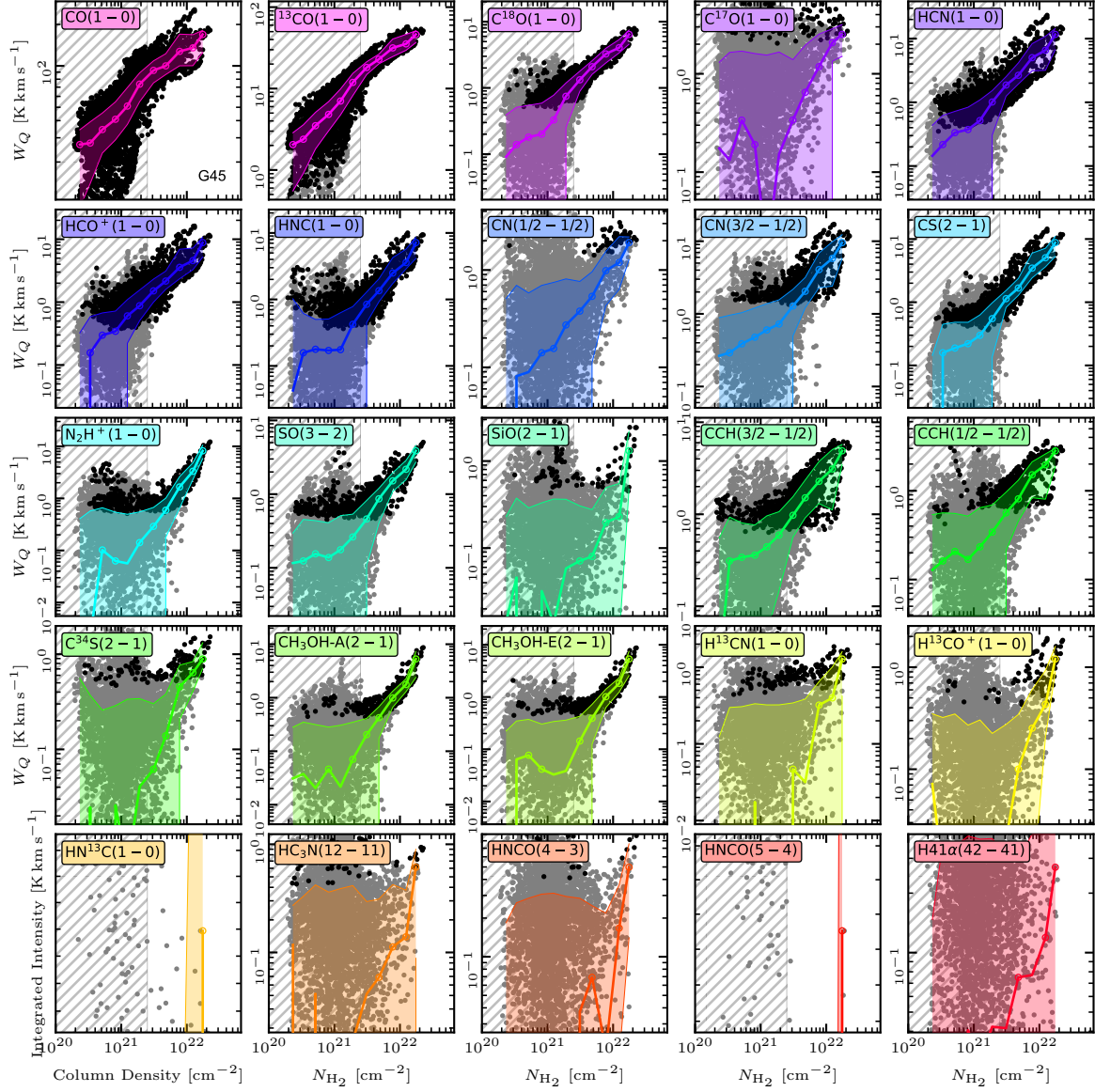


Figure D.11: Integrated intensity against column density across G45.1+0.1. Similar to Figure 8.5, but for all molecular lines listed in Table D.2 across the G45.1+0.1 cloud region.

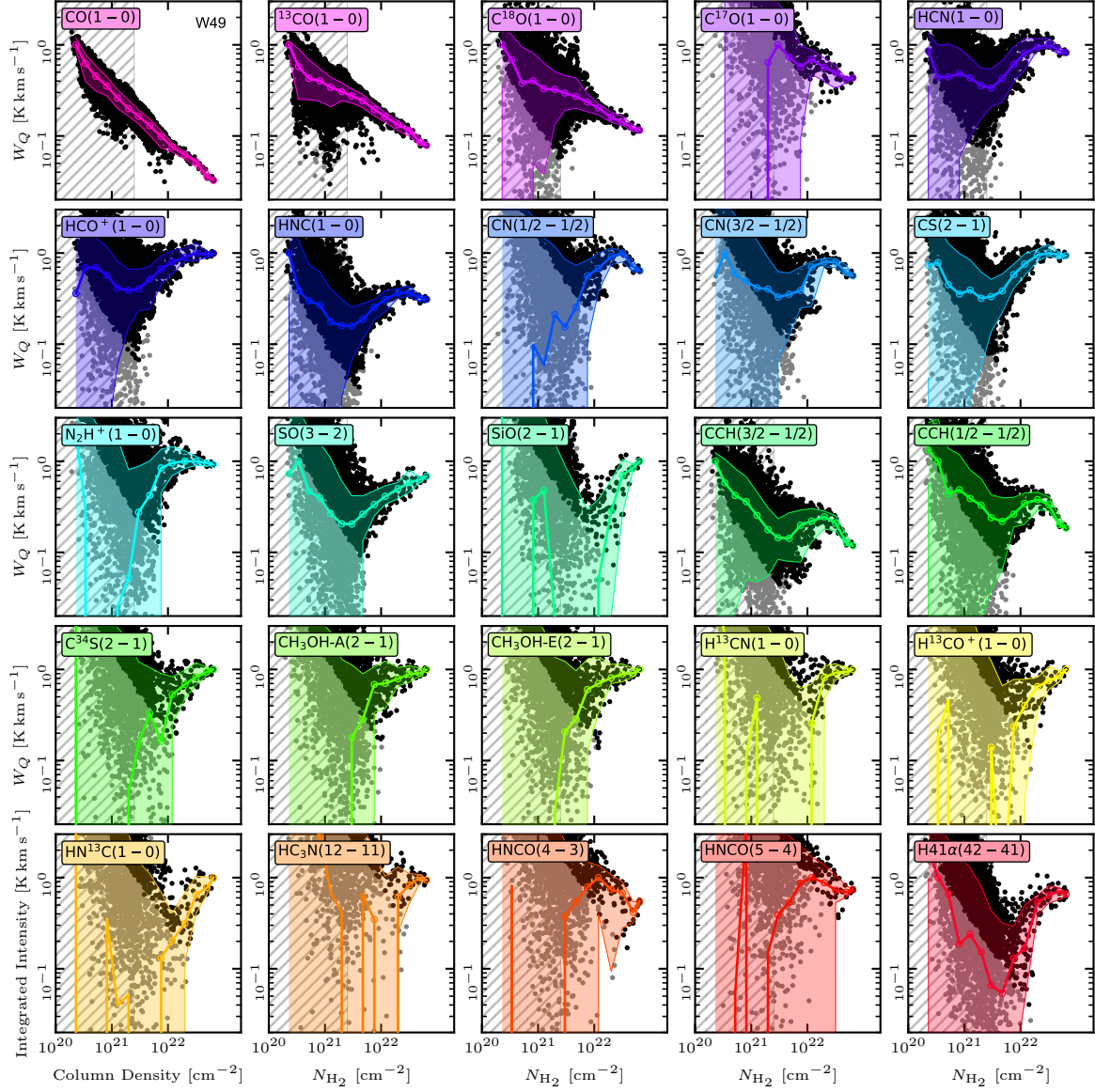


Figure D.12: **Integrated intensity against column density across W49.** Similar to Figure 8.6, but for all molecular lines listed in Table D.2 across the W49 cloud region.

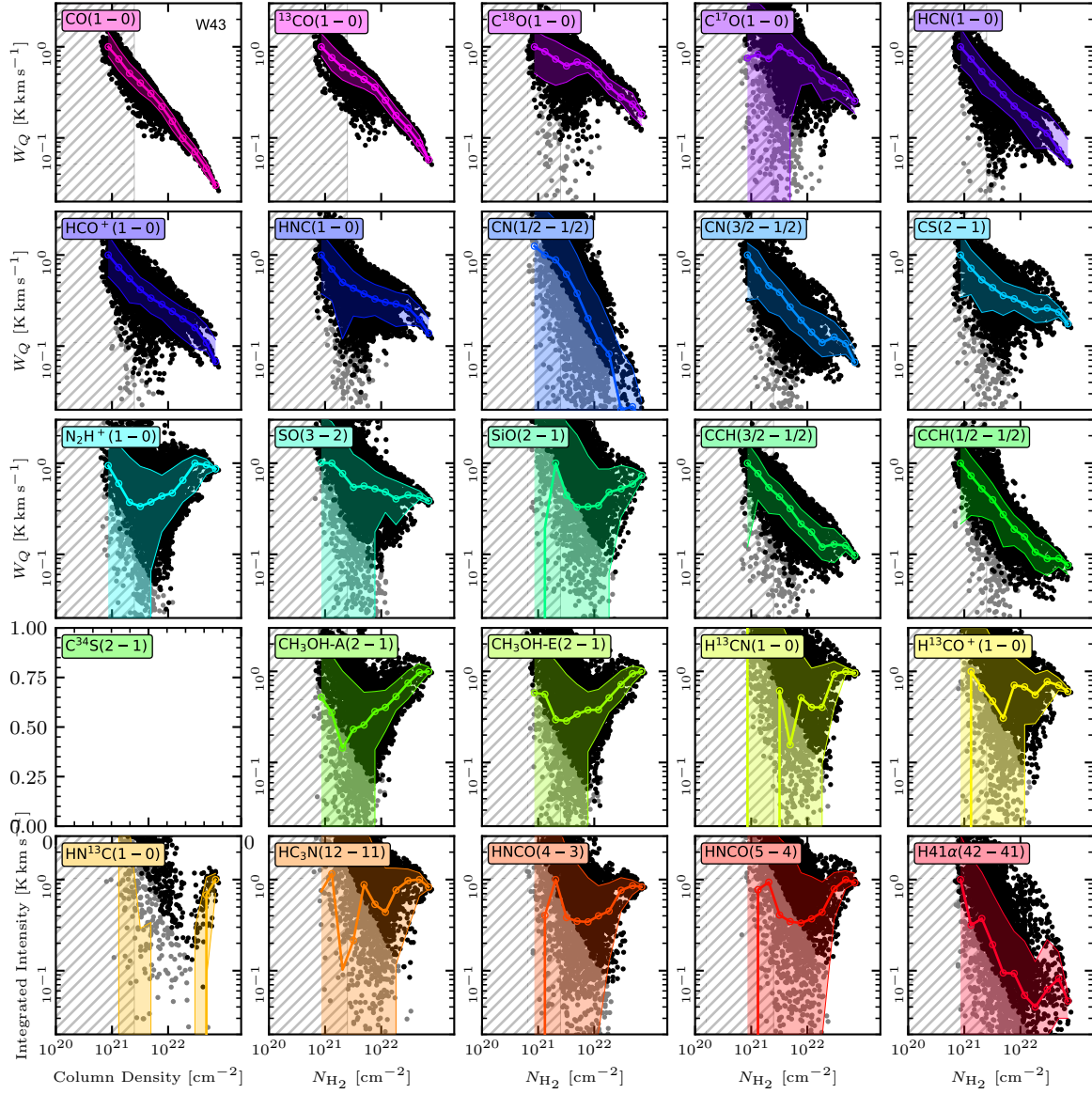


Figure D.13: **Integrated intensity against column density across W43.** Similar to Figure 8.6, but for all molecular lines listed in Table D.2 across the W43 cloud region.

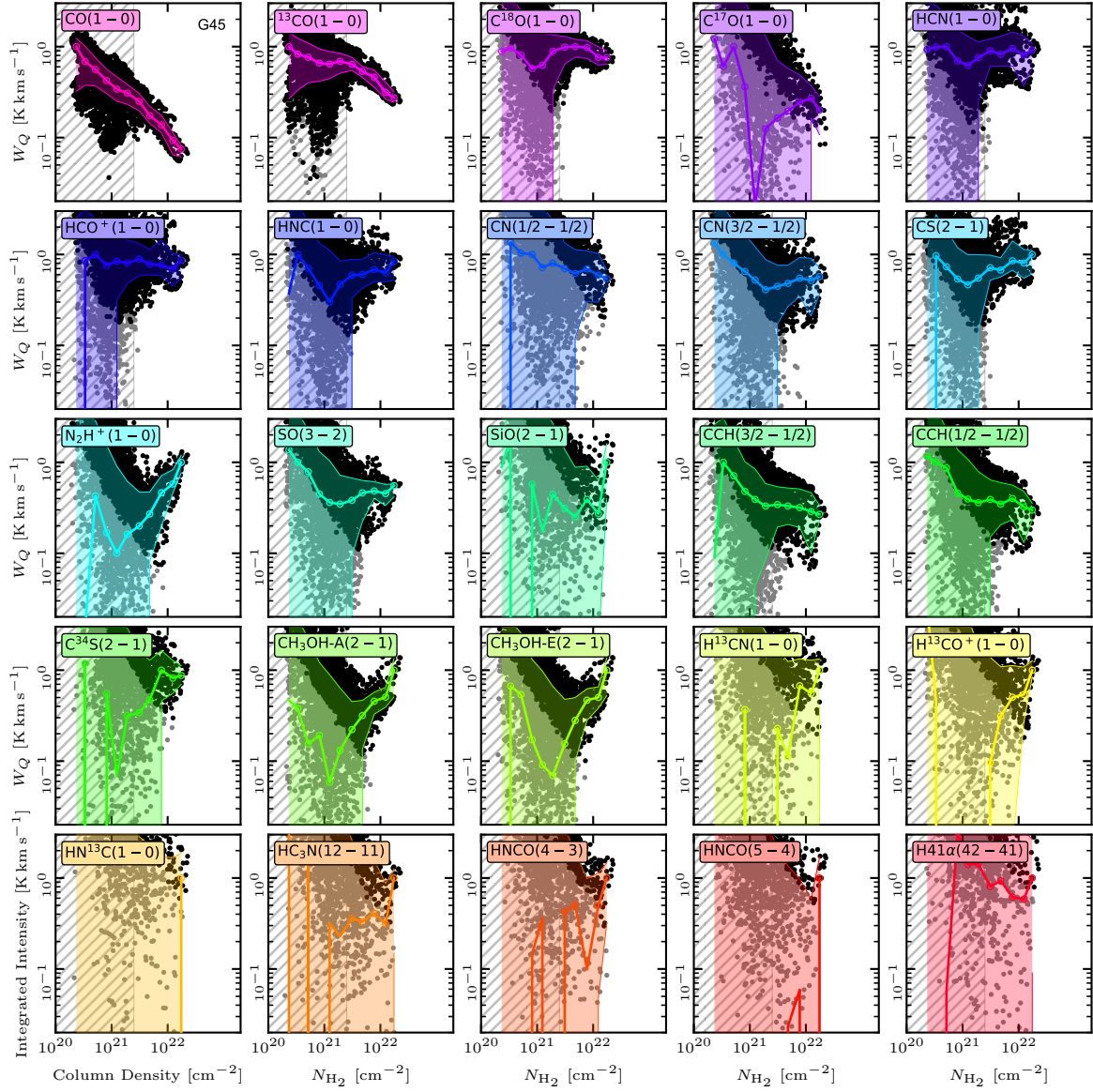


Figure D.14: Integrated intensity against column density across G45.1+0.1. Similar to Figure 8.6, but for all molecular lines listed in Table D.2 across the G45.1+0.1 cloud region.

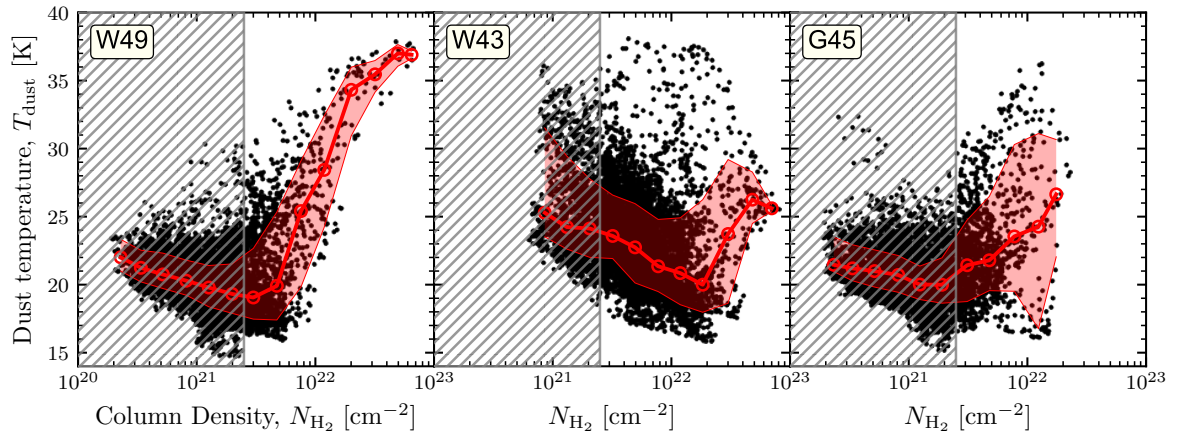


Figure D.15: **Dust temperature against column density across LEGO clouds.** $T_{\text{dust}}-N_{\text{H}_2}$ relation across the three LEGO clouds. The dust temperature and column density are inferred from *Herschel* IR observations via SED fitting assuming a modified blackbody. The black points indicate significant data and the red line shows average trend computed in bins of 0.2 dex increments. The open circle denote significant bin values and the red-shaded region shows the 1-sigma scatter of the data. The hatched region indicates the column density range that is potentially contaminated.

Bibliography

- Akritis, M. G. and M. A. Bershadsky (1996), *Linear Regression for Astronomical Data with Measurement Errors and Intrinsic Scatter*, [Astrophysical Journal](#) **470** 706.
- Anand, G. S. et al. (2021), *Distances to PHANGS galaxies: New tip of the red giant branch measurements and adopted distances*, [Monthly Notices of the Royal Astronomical Society](#) **501** 3621.
- Armillotta, L., M. R. Krumholz, E. M. Di Teodoro and N. M. McClure-Griffiths (2019), *The life cycle of the Central Molecular Zone - I. Inflow, star formation, and winds*, [Monthly Notices of the Royal Astronomical Society](#) **490** 4401.
- Astropy Collaboration, A. M. Price-Whelan, B. M. Sipőcz et al. (2018), *The Astropy Project: Building an Open-science Project and Status of the v2.0 Core Package*, [Astronomical Journal](#) **156**, 123.
- Astropy Collaboration, A. M. Price-Whelan, P. L. Lim et al. (2022), *The Astropy Project: Sustaining and Growing a Community-oriented Open-source Project and the Latest Major Release (v5.0) of the Core Package*, [Astrophysical Journal](#) **935**, 167.
- Astropy Collaboration, T. P. Robitaille et al. (2013), *Astropy: A community Python package for astronomy*, [Astronomy and Astrophysics](#) **558**, A33.
- Barnes, A. T., J. Kauffmann et al. (2020), *LEGO - II. A 3 mm molecular line study covering 100 pc of one of the most actively star-forming portions within the Milky Way disc*, [Monthly Notices of the Royal Astronomical Society](#) **497** 1972.
- Barnes, A. T., S. N. Longmore et al. (2017), *Star formation rates and efficiencies in the Galactic Centre*, [Monthly Notices of the Royal Astronomical Society](#) **469** 2263.
- Belfiore, F., A. K. Leroy, J. Sun et al. (2023), *Calibration of hybrid resolved star formation rate recipes based on PHANGS-MUSE H α and H β maps*, [Astronomy and Astrophysics](#) **670**, A67.
- Belfiore, F., A. K. Leroy, T. G. Williams et al. (2023), *Calibrating mid-infrared emission as a tracer of obscured star formation on H II-region scales in the era of JWST*, [Astronomy and Astrophysics](#) **678**, A129.
- Bešlić, I. et al. (2021), *Dense molecular gas properties on 100 pc scales across the disc of NGC 3627*, [Monthly Notices of the Royal Astronomical Society](#) **506** 963.
- Bigiel, F., A. Leroy et al. (2008), *The Star Formation Law in Nearby Galaxies on Sub-Kpc Scales*, [Astronomical Journal](#) **136** 2846.
- Bigiel, F., A. K. Leroy, L. Blitz et al. (2015), *Dense Gas Fraction and Star-formation Efficiency Variations in the Antennae Galaxies*, [Astrophysical Journal](#) **815**, 103.
- Bigiel, F., A. K. Leroy, M. J. Jiménez-Donaire et al. (2016), *The EMPIRE Survey: Systematic Variations in the Dense Gas Fraction and Star Formation Efficiency from Full-disk Mapping of M51*, [Astrophysical Journal, Letters](#) **822**, L26.

- Böker, T., J. Falcón-Barroso, E. Schinnerer, J. H. Knapen and S. Ryder (2008), *A SINFONI View of Galaxy Centers: Morphology and Kinematics of Five Nuclear Star Formation-Rings*, [Astronomical Journal](#) **135** 479.
- Bolatto, A. D., M. Wolfire and A. K. Leroy (2013), *The CO-to-H₂ Conversion Factor*, [Annual Review of Astronomy and Astrophysics](#) **51** 207.
- Braine, J. et al. (2017), *Dense gas in low-metallicity galaxies*, [Astronomy and Astrophysics](#) **597**, A44.
- Brouillet, N., S. Muller, F. Herpin, J. Braine and T. Jacq (2005), *HCN and HCO⁺ emission in the disk of M31*, [Astronomy and Astrophysics](#) **429** 153.
- Buchbender, C. et al. (2013), *Dense gas in M 33 (HerM33es)*, [Astronomy and Astrophysics](#) **549**, A17.
- Chabrier, G. (2003), *Galactic Stellar and Substellar Initial Mass Function*, [Publications of the ASP](#) **115** 763.
- Chen, H., J. Braine, Y. Gao, J. Koda and Q. Gu (2017), *Dense Gas in the Outer Spiral Arm of M51*, [Astrophysical Journal](#) **836**, 101.
- Chevance, M. et al. (2020), *The lifecycle of molecular clouds in nearby star-forming disc galaxies*, [Monthly Notices of the Royal Astronomical Society](#) **493** 2872.
- Chin, Y. .-, C. Henkel, T. J. Millar, J. B. Whiteoak and M. Marx-Zimmer (1998), *Molecular abundances in the Magellanic Clouds. III. LIRS36, a star-forming region in the Small Magellanic Cloud*, [Astronomy and Astrophysics](#) **330** 901.
- Chin, Y. .-, C. Henkel, J. B. Whiteoak et al. (1997), *Molecular abundances in the Magellanic Clouds. I. A multiline study of five cloud cores.*, [Astronomy and Astrophysics](#) **317** 548.
- Colombo, D., E. Rosolowsky, A. Ginsburg, A. Duarte-Cabral and A. Hughes (2016), *SCIMES: Spectral Clustering for Interstellar Molecular Emission Segmentation*, Astrophysics Source Code Library, record ascl:1609.006.
- Condon, J. J. and S. M. Ransom (2016), *Essential Radio Astronomy*.
- Crocker, A. et al. (2012), *The ATLAS^{3D} project - XI. Dense molecular gas properties of CO-luminous early-type galaxies*, [Monthly Notices of the Royal Astronomical Society](#) **421** 1298.
- Dame, T. M. and C. J. Lada (2023), *A Complete HCN Survey of the Perseus Molecular Cloud*, [Astrophysical Journal](#) **944**, 197.
- de Blok, W. J. G. et al. (2024), *MHONGOOSE – A MeerKAT Nearby Galaxy HI Survey*, [arXiv e-prints](#), [arXiv:2404.01774](#).
- den Brok, J. S., D. Chatzigiannakis et al. (2021), *New constraints on the ¹²CO(2-1)/(1-0) line ratio across nearby disc galaxies*, [Monthly Notices of the Royal Astronomical Society](#) **504** 3221.
- den Brok, J. S., A. K. Leroy et al. (2023), *Resolved low-J ¹²CO excitation at 190 parsec resolution across NGC 2903 and NGC 3627*, [Monthly Notices of the Royal Astronomical Society](#) **526** 6347.
- den Brok, J. S., F. Bigiel, J. Chasten et al. (2023), *Wide-field CO isotopologue emission and the CO-to-H₂ factor across the nearby spiral galaxy M101*, [Astronomy and Astrophysics](#) **676**, A93.
- den Brok, J. S., F. Bigiel, K. Sliwa et al. (2022), *A CO isotopologue Line Atlas within the Whirlpool galaxy Survey (CLAWS)*, [Astronomy and Astrophysics](#) **662**, A89.
- Draine, B. T. et al. (2007), *Dust Masses, PAH Abundances, and Starlight Intensities in the SINGS Galaxy Sample*, [Astrophysical Journal](#) **663** 866.
- Draine, B. T. (2011), *Physics of the Interstellar and Intergalactic Medium*.
- Eibensteiner, C., A. T. Barnes et al. (2022), *A 2-3 mm high-resolution molecular line survey towards the centre of the nearby spiral galaxy NGC 6946*, [Astronomy and Astrophysics](#) **659**, A173.
- Eibensteiner, C., F. Bigiel et al. (2023), *Kinematic analysis of the super-extended H I disk of the nearby spiral galaxy M 83*, [Astronomy and Astrophysics](#) **675**, A37.

- Eibensteiner, C., J. Sun et al. (2024), *PHANGS-MeerKAT and MHONGOOSE HI observations of nearby spiral galaxies: physical drivers of the molecular gas fraction, R_{mol}* , [arXiv e-prints, arXiv:2407.01716](#).
- Elmegreen, B. G. (2018), *On the Appearance of Thresholds in the Dynamical Model of Star Formation*, [Astrophysical Journal](#) **854**, 16.
- Emsellem, E. et al. (2022), *The PHANGS-MUSE survey. Probing the chemo-dynamical evolution of disc galaxies*, [Astronomy and Astrophysics](#) **659**, A191.
- Evans Neal J., I. (1999), *Physical Conditions in Regions of Star Formation*, [Annual Review of Astronomy and Astrophysics](#) **37** 311.
- Evans Neal J., I., A. Heiderman and N. Vutisalchavakul (2014), *Star Formation Relations in Nearby Molecular Clouds*, [Astrophysical Journal](#) **782**, 114.
- Evans Neal J., I., K.-T. Kim et al. (2020), *Star Formation Occurs in Dense Gas, but What Does “Dense” Mean?*, [Astrophysical Journal](#) **894**, 103.
- Fazio, G. G. et al. (2004), *The Infrared Array Camera (IRAC) for the Spitzer Space Telescope*, [Astrophysical Journal, Supplement](#) **154** 10.
- Federrath, C. et al. (2016), *The Link between Turbulence, Magnetic Fields, Filaments, and Star Formation in the Central Molecular Zone Cloud G0.253+0.016*, [Astrophysical Journal](#) **832**, 143.
- Field, G. B., D. W. Goldsmith and H. J. Habing (1969), *Cosmic-Ray Heating of the Interstellar Gas*, [Astrophysical Journal, Letters](#) **155** L149.
- Fujimoto, Y., F. Maeda, A. Habe and K. Ohta (2020), *Fast cloud-cloud collisions in a strongly barred galaxy: suppression of massive star formation*, [Monthly Notices of the Royal Astronomical Society](#) **494** 2131.
- Gallagher, M. J., A. K. Leroy, F. Bigiel, D. Cormier, M. J. Jiménez-Donaire, A. Hughes et al. (2018), *Do Spectroscopic Dense Gas Fractions Track Molecular Cloud Surface Densities?*, [Astrophysical Journal, Letters](#) **868**, L38.
- Gallagher, M. J., A. K. Leroy, F. Bigiel, D. Cormier, M. J. Jiménez-Donaire, E. Ostriker et al. (2018), *Dense Gas, Dynamical Equilibrium Pressure, and Star Formation in Nearby Star-forming Galaxies*, [Astrophysical Journal](#) **858**, 90.
- Gao, Y., C. L. Carilli, P. M. Solomon and P. A. Vanden Bout (2007), *HCN Observations of Dense Star-forming Gas in High-Redshift Galaxies*, [Astrophysical Journal, Letters](#) **660** L93.
- Gao, Y. and P. M. Solomon (2004), *The Star Formation Rate and Dense Molecular Gas in Galaxies*, [Astrophysical Journal](#) **606** 271.
- García-Burillo, S. et al. (2012), *Star-formation laws in luminous infrared galaxies. New observational constraints on models*, [Astronomy and Astrophysics](#) **539**, A8.
- Giannetti, A. et al. (2017), *Galactocentric variation of the gas-to-dust ratio and its relation with metallicity*, [Astronomy and Astrophysics](#) **606**, L12.
- Goicoechea, J. R., F. Lique and M. G. Santa-Maria (2022), *Anomalous HCN emission from warm giant molecular clouds*, [Astronomy and Astrophysics](#) **658**, A28.
- Gong, M., E. C. Ostriker, C.-G. Kim and J.-G. Kim (2020), *The Environmental Dependence of the X_{CO} Conversion Factor*, [Astrophysical Journal](#) **903**, 142.
- Graciá-Carpio, J., S. García-Burillo, P. Planesas, A. Fuente and A. Usero (2008), *Evidence of enhanced star formation efficiency in luminous and ultraluminous infrared galaxies*, [Astronomy and Astrophysics](#) **479** 703.
- Guzmán, A. E. et al. (2015), *Far-infrared Dust Temperatures and Column Densities of the MALT90 Molecular Clump Sample*, [Astrophysical Journal](#) **815**, 130.

- Hannon, S. et al. (2023), *Star cluster classification using deep transfer learning with PHANGS-HST*, *Monthly Notices of the Royal Astronomical Society* **526** 2991.
- Hao, C.-N. et al. (2011), *Dust-corrected Star Formation Rates of Galaxies. II. Combinations of Ultraviolet and Infrared Tracers*, *Astrophysical Journal* **741**, 124.
- Harris, C. R. et al. (2020), *Array programming with NumPy*, *Nature* **585** 357, URL: <https://doi.org/10.1038/s41586-020-2649-2>.
- Hassani, H. et al. (2024), *The PHANGS-AstroSat Atlas of Nearby Star-forming Galaxies*, *Astrophysical Journal, Supplement* **271**, 2.
- Hunter, J. D. (2007), *Matplotlib: A 2D graphics environment*, *Computing in Science & Engineering* **9** 90.
- Hunter, T. R., T. G. Phillips and K. M. Menten (1997), *Active Star Formation toward the Ultracompact H II Regions G45.12+0.13 and G45.07+0.13*, *Astrophysical Journal* **478** 283.
- Jiménez-Donaire, M. J., F. Bigiel, A. K. Leroy, D. Cormier et al. (2017), *Optical depth estimates and effective critical densities of dense gas tracers in the inner parts of nearby galaxy discs*, *Monthly Notices of the Royal Astronomical Society* **466** 49.
- Jiménez-Donaire, M. J., A. Usero et al. (2023), *A constant N_2H^+ (1-0)-to-HCN (1-0) ratio on kiloparsec scales*, *Astronomy and Astrophysics* **676**, L11.
- Jiménez-Donaire, M. J., F. Bigiel, A. K. Leroy, A. Usero et al. (2019), *EMPIRE: The IRAM 30 m Dense Gas Survey of Nearby Galaxies*, *Astrophysical Journal* **880**, 127.
- Jiménez-Donaire, M. J., D. Cormier et al. (2017), *$^{13}CO/C^{18}O$ Gradients across the Disks of Nearby Spiral Galaxies*, *Astrophysical Journal, Letters* **836**, L29.
- Jones, P. A. et al. (2012), *Spectral imaging of the Central Molecular Zone in multiple 3-mm molecular lines*, *Monthly Notices of the Royal Astronomical Society* **419** 2961.
- Juneau, S. et al. (2009), *Enhanced Dense Gas Fraction in Ultraluminous Infrared Galaxies*, *Astrophysical Journal* **707** 1217.
- Kauffmann, J., F. Bertoldi, T. L. Bourke, I. Evans N. J. and C. W. Lee (2008), *MAMBO mapping of Spitzer c2d small clouds and cores*, *Astronomy and Astrophysics* **487** 993.
- Kauffmann, J., P. F. Goldsmith et al. (2017), *Molecular Line Emission as a Tool for Galaxy Observations (LEGO). I. HCN as a tracer of moderate gas densities in molecular clouds and galaxies*, *Astronomy and Astrophysics* **605**, L5.
- Kelly, B. C. (2007), *Some Aspects of Measurement Error in Linear Regression of Astronomical Data*, *Astrophysical Journal* **665** 1489.
- Kennicutt Robert C., J. (1998), *The Global Schmidt Law in Star-forming Galaxies*, *Astrophysical Journal* **498** 541.
- Kennicutt Robert C., J. et al. (2003), *SINGS: The SIRTf Nearby Galaxies Survey*, *Publications of the ASP* **115** 928.
- Kennicutt, R. C., D. Calzetti et al. (2011), *KINGFISH—Key Insights on Nearby Galaxies: A Far-Infrared Survey with Herschel: Survey Description and Image Atlas*, *Publications of the ASP* **123** 1347.
- Kennicutt, R. C. and N. J. Evans (2012), *Star Formation in the Milky Way and Nearby Galaxies*, *Annual Review of Astronomy and Astrophysics* **50** 531.
- Kepley, A. A. et al. (2014), *The Green Bank Telescope Maps the Dense, Star-forming Gas in the Nearby Starburst Galaxy M82*, *Astrophysical Journal, Letters* **780**, L13.
- Kim, J., M. Chevance, J. M. D. Kruijssen, A. K. Leroy et al. (2022), *Environmental dependence of the molecular cloud lifecycle in 54 main-sequence galaxies*, *Monthly Notices of the Royal Astronomical Society* **516** 3006.

- Kim, J., M. Chevance, J. M. D. Kruijssen, A. Schruba et al. (2021), *On the duration of the embedded phase of star formation*, [Monthly Notices of the Royal Astronomical Society](#) **504** 487.
- Kraemer, K. E. et al. (2003), *Five Star-forming Cores in the Galactic Ring Survey: A Mid-Infrared Study*, [Astrophysical Journal](#) **588** 918.
- Krips, M. et al. (2008), *A Multi-Transition HCN and HCO⁺ Study of 12 Nearby Active Galaxies: Active Galactic Nucleus versus Starburst Environments*, [Astrophysical Journal](#) **677** 262.
- Kroupa, P. (2001), *On the variation of the initial mass function*, [Monthly Notices of the Royal Astronomical Society](#) **322** 231.
- Kruijssen, J. M. D. and S. N. Longmore (2014), *An uncertainty principle for star formation - I. Why galactic star formation relations break down below a certain spatial scale*, [Monthly Notices of the Royal Astronomical Society](#) **439** 3239.
- Kruijssen, J. M. D., A. Schruba et al. (2019), *Fast and inefficient star formation due to short-lived molecular clouds and rapid feedback*, [Nature](#) **569** 519.
- Krumholz, M. R. (2015), *Notes on Star Formation*, [arXiv e-prints](#), [arXiv:1511.03457](#).
- Krumholz, M. R. and J. M. D. Kruijssen (2015), *A dynamical model for the formation of gas rings and episodic starbursts near galactic centres*, [Monthly Notices of the Royal Astronomical Society](#) **453** 739.
- Krumholz, M. R., J. M. D. Kruijssen and R. M. Crocker (2017), *A dynamical model for gas flows, star formation and nuclear winds in galactic centres*, [Monthly Notices of the Royal Astronomical Society](#) **466** 1213.
- Krumholz, M. R. and C. F. McKee (2005), *A General Theory of Turbulence-regulated Star Formation, from Spirals to Ultraluminous Infrared Galaxies*, [Astrophysical Journal](#) **630** 250.
- Krumholz, M. R. and T. A. Thompson (2007), *The Relationship between Molecular Gas Tracers and Kennicutt-Schmidt Laws*, [Astrophysical Journal](#) **669** 289.
- Kwan, J. and N. Scoville (1975), *Radiative Trapping and Hyperfine Structure: HCN*, [Astrophysical Journal, Letters](#) **195** L85.
- Lada, C. J., J. Forbrich, M. Lombardi and J. F. Alves (2012), *Star Formation Rates in Molecular Clouds and the Nature of the Extragalactic Scaling Relations*, [Astrophysical Journal](#) **745**, 190.
- Lang, P. et al. (2020), *PHANGS CO Kinematics: Disk Orientations and Rotation Curves at 150 pc Resolution*, [Astrophysical Journal](#) **897**, 122.
- Lee, J. C., K. M. Sandstrom et al. (2023), *The PHANGS-JWST Treasury Survey: Star Formation, Feedback, and Dust Physics at High Angular Resolution in Nearby Galaxies*, [Astrophysical Journal, Letters](#) **944**, L17.
- Lee, J. C., B. C. Whitmore et al. (2022), *The PHANGS-HST Survey: Physics at High Angular Resolution in Nearby Galaxies with the Hubble Space Telescope*, [Astrophysical Journal, Supplement](#) **258**, 10.
- Leitherer, C. et al. (1999), *Starburst99: Synthesis Models for Galaxies with Active Star Formation*, [Astrophysical Journal, Supplement](#) **123** 3.
- Leroy, A. K., A. Hughes et al. (2021), *PHANGS-ALMA Data Processing and Pipeline*, [Astrophysical Journals](#) **255**, 19.
- Leroy, A. K., E. Rosolowsky et al. (2022), *Low-J CO Line Ratios from Single-dish CO Mapping Surveys and PHANGS-ALMA*, [Astrophysical Journal](#) **927**, 149.
- Leroy, A. K., K. M. Sandstrom et al. (2019), *A $z = 0$ Multiwavelength Galaxy Synthesis. I. A WISE and GALEX Atlas of Local Galaxies*, [Astrophysical Journal, Supplement](#) **244**, 24.
- Leroy, A. K., E. Schinnerer et al. (2021), *PHANGS-ALMA: Arcsecond CO(2-1) Imaging of Nearby Star-forming Galaxies*, [Astrophysical Journals](#) **257**, 43.

- Leroy, A. K., A. Usero et al. (2017), *Millimeter-wave Line Ratios and Sub-beam Volume Density Distributions*, [Astrophysical Journal](#) **835**, 217.
- Leroy, A. K., F. Walter et al. (2009), *Heracles: The HERA CO Line Extragalactic Survey*, [Astronomical Journal](#) **137** 4670.
- Loose, H. H., E. Kruegel and A. Tutukov (1982), *Bursts of star formation in the galactic centre*, *Astronomy and Astrophysics* **105** 342.
- Maeda, F., F. Egusa, K. Ohta, Y. Fujimoto and A. Habe (2023), *Statistical Study of the Star Formation Efficiency in Bars: Is Star Formation Suppressed in Gas-rich Bars?*, [Astrophysical Journal](#) **943**, 7.
- Makarov, D., P. Prugniel, N. Terekhova, H. Courtois and I. Vauglin (2014), *HyperLEDA. III. The catalogue of extragalactic distances*, [Astronomy and Astrophysics](#) **570**, A13.
- Martin, C. L. (2005), *Mapping Large-Scale Gaseous Outflows in Ultraluminous Galaxies with Keck II ESI Spectra: Variations in Outflow Velocity with Galactic Mass*, [Astrophysical Journal](#) **621** 227.
- Martín, S. et al. (2021), *ALCHEMI, an ALMA Comprehensive High-resolution Extragalactic Molecular Inventory. Survey presentation and first results from the ACA array*, [Astronomy and Astrophysics](#) **656**, A46.
- McKee, C. F. and E. C. Ostriker (2007), *Theory of Star Formation*, [Annual Review of Astronomy and Astrophysics](#) **45** 565.
- Molinari, S., B. Swinyard, J. Bally, M. Barlow, J. .-. Bernard, P. Martin, T. Moore, A. Noriega-Crespo, R. Plume, L. Testi, A. Zavagno, A. Abergel, B. Ali, L. Anderson et al. (2010), *Clouds, filaments, and protostars: The Herschel Hi-GAL Milky Way*, [Astronomy and Astrophysics](#) **518**, L100.
- Molinari, S., B. Swinyard, J. Bally, M. Barlow, J. .-. Bernard, P. Martin, T. Moore, A. Noriega-Crespo, R. Plume, L. Testi, A. Zavagno, A. Abergel, B. Ali, P. André et al. (2010), *Hi-GAL: The Herschel Infrared Galactic Plane Survey*, [Publications of the ASP](#) **122** 314.
- Moon, S., W.-T. Kim, C.-G. Kim and E. C. Ostriker (2021), *Star Formation in Nuclear Rings with the TIGRESS Framework*, [Astrophysical Journal](#) **914**, 9.
- (2022), *Effects of Varying Mass Inflows on Star Formation in Nuclear Rings of Barred Galaxies*, [Astrophysical Journal](#) **925**, 99.
- (2023), *Effects of Magnetic Fields on Gas Dynamics and Star Formation in Nuclear Rings*, [Astrophysical Journal](#) **946**, 114.
- Murphy, E. J. et al. (2011), *Calibrating Extinction-free Star Formation Rate Diagnostics with 33 GHz Free-free Emission in NGC 6946*, [Astrophysical Journal](#) **737**, 67.
- Neumann, L., F. Bigiel et al. (2024), *A 260 pc resolution ALMA map of HCN(1-0) in the galaxy NGC 4321*, [arXiv e-prints](#), [arXiv:2406.12025](#).
- Neumann, L., J. S. den Brok et al. (2023), *Spectral stacking of radio-interferometric data*, [Astronomy and Astrophysics](#) **675**, A104.
- Neumann, L., M. J. Gallagher et al. (2023), *The ALMOND survey: molecular cloud properties and gas density tracers across 25 nearby spiral galaxies with ALMA*, [Monthly Notices of the Royal Astronomical Society](#) **521** 3348.
- Nguyen Luong, Q. et al. (2011), *W43: the closest molecular complex of the Galactic bar?*, [Astronomy and Astrophysics](#) **529**, A41.
- Nguyen-Luong, Q. et al. (2020), *Large-scale Molecular Gas Distribution in the M17 Cloud Complex: Dense Gas Conditions of Massive Star Formation?*, [Astrophysical Journal](#) **891**, 66.
- Onus, A., M. R. Krumholz and C. Federrath (2018), *Numerical calibration of the HCN-star formation correlation*, [Monthly Notices of the Royal Astronomical Society](#) **479** 1702.

- Panessa, M. et al. (2023), *The evolution of HCO^+ in molecular clouds using a novel chemical post-processing algorithm*, [Monthly Notices of the Royal Astronomical Society](#) **523** 6138.
- Patra, S. et al. (2022), *Tracers of Dense Gas in the Outer Galaxy*, [Astronomical Journal](#) **164**, 129.
- Pety, J. et al. (2017), *The anatomy of the Orion B giant molecular cloud: A local template for studies of nearby galaxies*, [Astronomy and Astrophysics](#) **599**, A98.
- Pilbratt, G. L. et al. (2010), *Herschel Space Observatory. An ESA facility for far-infrared and submillimetre astronomy*, [Astronomy and Astrophysics](#) **518**, L1.
- Privon, G. C. et al. (2015), *Excitation Mechanisms for HCN (1-0) and HCO^+ (1-0) in Galaxies from the Great Observatories All-sky LIRG Survey*, [Astrophysical Journal](#) **814**, 39.
- Querejeta, M. et al. (2019), *Dense gas is not enough: environmental variations in the star formation efficiency of dense molecular gas at 100 pc scales in M 51*, [Astronomy and Astrophysics](#) **625**, A19.
- Reid, M. J. et al. (2009), *Trigonometric Parallaxes of Massive Star-Forming Regions. VI. Galactic Structure, Fundamental Parameters, and Noncircular Motions*, [Astrophysical Journal](#) **700** 137.
- Rieke, G. H. et al. (2004), *The Multiband Imaging Photometer for Spitzer (MIPS)*, [Astrophysical Journal, Supplement](#) **154** 25.
- Rosolowsky, E. and A. Leroy (2006), *Bias-free Measurement of Giant Molecular Cloud Properties*, [Publications of the ASP](#) **118** 590.
- Rybak, M. et al. (2022), *PRUSSIC. I. A JVLA survey of HCN, HCO^+ , and HNC (1-0) emission in $z \sim 3$ dusty galaxies: Low dense-gas fractions in high-redshift star-forming galaxies*, [Astronomy and Astrophysics](#) **667**, A70.
- Salpeter, E. E. (1955), *The Luminosity Function and Stellar Evolution.*, [Astrophysical Journal](#) **121** 161.
- Sánchez-García, M. et al. (2022), *Spatially resolved star-formation relations of dense molecular gas in NGC 1068*, [Astronomy and Astrophysics](#) **660**, A83.
- Santa-Maria, M. G. et al. (2023), *HCN emission from translucent gas and UV-illuminated cloud edges revealed by wide-field IRAM 30 m maps of the Orion B GMC. Revisiting its role as a tracer of the dense gas reservoir for star formation*, [Astronomy and Astrophysics](#) **679**, A4.
- Schinnerer, E. and A. K. Leroy (2024), *Molecular Gas and the Star Formation Process on Cloud Scales in Nearby Galaxies*, [arXiv e-prints](#), [arXiv:2403.19843](#).
- Schinnerer, E., S. E. Meidt et al. (2013), *The PdBI Arcsecond Whirlpool Survey (PAWS). I. A Cloud-scale/Multi-wavelength View of the Interstellar Medium in a Grand-design Spiral Galaxy*, [Astrophysical Journal](#) **779**, 42.
- Schmidt, M. (1959), *The Rate of Star Formation.*, [Astrophysical Journal](#) **129** 243.
- Schöier, F. L., F. F. S. van der Tak, E. F. van Dishoeck and J. H. Black (2005), *An atomic and molecular database for analysis of submillimetre line observations*, [Astronomy and Astrophysics](#) **432** 369.
- Sheth, K. et al. (2010), *The Spitzer Survey of Stellar Structure in Galaxies (S4G)*, [Publications of the ASP](#) **122** 1397.
- Shimajiri, Y. et al. (2017), *Testing the universality of the star-formation efficiency in dense molecular gas*, [Astronomy and Astrophysics](#) **604**, A74.
- Shirley, Y. L. (2015), *The Critical Density and the Effective Excitation Density of Commonly Observed Molecular Dense Gas Tracers*, [Publications of the ASP](#) **127** 299.
- Sormani, M. C., R. G. Treß et al. (2018), *A theoretical explanation for the Central Molecular Zone asymmetry*, [Monthly Notices of the Royal Astronomical Society](#) **475** 2383.
- Sormani, M. C., R. G. Tress et al. (2020), *Simulations of the Milky Way's Central Molecular Zone - II. Star formation*, [Monthly Notices of the Royal Astronomical Society](#) **497** 5024.

- Stephens, I. W. et al. (2016), *Linking Dense Gas from the Milky Way to External Galaxies*, [Astrophysical Journal](#) **824**, 29.
- Stuber, S. K. et al. (2023), *Surveying the Whirlpool at Arcseconds with NOEMA (SWAN). I. Mapping the HCN and N₂H⁺ 3mm lines*, [Astronomy and Astrophysics](#) **680**, L20.
- Sun, J., A. K. Leroy, E. C. Ostriker et al. (2020), *Dynamical Equilibrium in the Molecular ISM in 28 Nearby Star-forming Galaxies*, [Astrophysical Journal](#) **892**, 148.
- Sun, J., A. K. Leroy, E. Schinnerer et al. (2020), *Molecular Gas Properties on Cloud Scales across the Local Star-forming Galaxy Population*, [Astrophysical Journal, Letters](#) **901**, L8.
- Tafalla, M., A. Usero and A. Hacar (2021), *Characterizing the line emission from molecular clouds. Stratified random sampling of the Perseus cloud*, [Astronomy and Astrophysics](#) **646**, A97.
- (2023), *Characterizing the line emission from molecular clouds. II. A comparative study of California, Perseus, and Orion A*, [Astronomy and Astrophysics](#) **679**, A112.
- Takahira, K., E. J. Tasker and A. Habe (2014), *Do Cloud-Cloud Collisions Trigger High-mass Star Formation? I. Small Cloud Collisions*, [Astrophysical Journal](#) **792**, 63.
- Teng, Y.-H., K. M. Sandstrom, J. Sun, M. Gong et al. (2023), *The Physical Drivers and Observational Tracers of CO-to-H₂ Conversion Factor Variations in Nearby Barred Galaxy Centers*, [Astrophysical Journal](#) **950**, 119.
- Teng, Y.-H., K. M. Sandstrom, J. Sun, A. K. Leroy et al. (2022), *Molecular Gas Properties and CO-to-H₂ Conversion Factors in the Central Kiloparsec of NGC 3351*, [Astrophysical Journal](#) **925**, 72.
- Torrey, P. et al. (2017), *An instability of feedback-regulated star formation in galactic nuclei*, [Monthly Notices of the Royal Astronomical Society](#) **467** 2301.
- Tress, R. G. et al. (2020), *Simulations of the Milky Way’s central molecular zone - I. Gas dynamics*, [Monthly Notices of the Royal Astronomical Society](#) **499** 4455.
- Turner, B. E. (1989), *A Molecular Line Survey of Sagittarius B2 and Orion-KL from 70 to 115 GHz. I. The Observational Data*, [Astrophysical Journal, Supplement](#) **70** 539.
- Urquhart, J. S. et al. (2021), *SEDIGISM-ATLASGAL: dense gas fraction and star formation efficiency across the Galactic disc*, [Monthly Notices of the Royal Astronomical Society](#) **500** 3050.
- Usero, A. et al. (2015), *Variations in the Star Formation Efficiency of the Dense Molecular Gas across the Disks of Star-forming Galaxies*, [Astronomical Journal](#) **150**, 115.
- van der Tak, F. F. S., J. H. Black, F. L. Schöier, D. J. Jansen and E. F. van Dishoeck (2007), *A computer program for fast non-LTE analysis of interstellar line spectra. With diagnostic plots to interpret observed line intensity ratios*, [Astronomy and Astrophysics](#) **468** 627.
- Verwilghen, P. et al. (2024), *Simulating nearby disc galaxies on the main star formation sequence. I. Bar formation and the building of the central gas reservoir*, [Astronomy and Astrophysics](#) **687**, A53.
- Virtanen, P. et al. (2020), *SciPy 1.0: Fundamental Algorithms for Scientific Computing in Python*, [Nature Methods](#) **17** 261.
- Walch, S. et al. (2015), *The SILCC (Simulating the LifeCycle of molecular Clouds) project - I. Chemical evolution of the supernova-driven ISM*, [Monthly Notices of the Royal Astronomical Society](#) **454** 238.
- Wallace, J. et al. (2022), *ALMA Uncovers Highly Filamentary Structure toward the Sgr E Region*, [Astrophysical Journal](#) **939**, 58.
- Walter, F. et al. (2008), *THINGS: The H I Nearby Galaxy Survey*, [Astronomical Journal](#) **136** 2563.
- Watanabe, Y., N. Sakai, A. López-Sepulcre et al. (2015), *Spectral Line Survey toward the Young Massive Protostar NGC 2264 CMM3 in the 4 mm, 3 mm, and 0.8 mm Bands*, [Astrophysical Journal](#) **809**, 162.
- Watanabe, Y., N. Sakai, K. Sorai and S. Yamamoto (2014), *Spectral Line Survey toward the Spiral Arm of M51 in the 3 and 2 mm Bands*, [Astrophysical Journal](#) **788**, 4.

- Werner, M. W. et al. (2004), *The Spitzer Space Telescope Mission*, [Astrophysical Journal, Supplement 154 1](#).
- Williams, T. G. et al. (2024), *PHANGS-JWST: Data-processing Pipeline and First Full Public Data Release*, [Astrophysical Journal, Supplement 273, 13](#).
- Wilson, T. L., K. Rohlfs and S. Hüttemeister (2013), *Tools of Radio Astronomy*.
- Wright, E. L. et al. (2010), *The Wide-field Infrared Survey Explorer (WISE): Mission Description and Initial On-orbit Performance*, [Astronomical Journal 140 1868](#).
- Wu, J., I. Evans Neal J., Y. L. Shirley and C. Knez (2010), *The Properties of Massive, Dense Clumps: Mapping Surveys of HCN and CS*, [Astrophysical Journal, Supplement 188 313](#).
- Zhang, B. et al. (2013), *Parallaxes for W49N and G048.60+0.02: Distant Star Forming Regions in the Perseus Spiral Arm*, [Astrophysical Journal 775, 79](#).

List of Figures

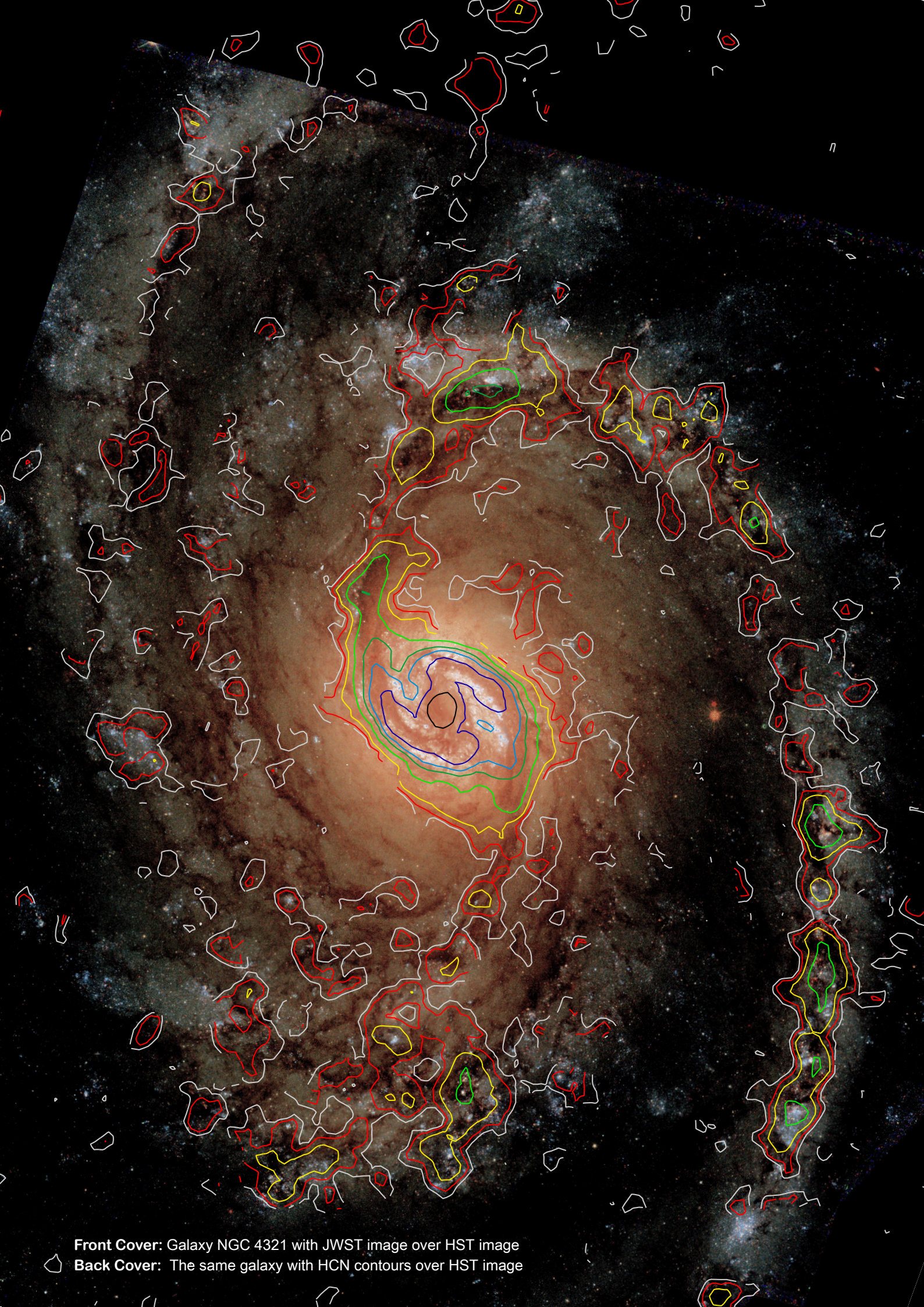
1.1	Hubble tuning fork	2
1.2	Interstellar medium in the Carina nebula	4
1.3	Baryon lifecycle in galaxies	5
1.4	Rotational transition diagram	7
1.5	NGC 628 across the electromagnetic spectrum	15
1.6	Kennicutt-Schmidt relation	17
1.7	Gao-Solomon relation	18
1.8	Dense gas scaling relations	20
1.9	Dense gas-environment-GMC connections	22
2.1	Antenna beam pattern	27
2.2	UV-plane and ALMA LEGO model	30
2.3	IRAM 30 m and ALMA	32
2.4	Atmospheric electromagnetic transmission	35
2.5	The PHANGS–ALMA survey	38
2.6	The PHANGS-MUSE and PHANGS–JWST surveys	40
2.7	The ALMOND survey	41
2.8	LEGO: Massive star-forming region W49	42
3.1	PyStructure workflow	45
3.2	Convolution to a common spatial resolution	47
3.3	Reprojection onto a common, hexagonal spaxel grid	48
3.4	Computation of data products from a ppv data cube	62
3.5	PyStacker workflow	63
3.6	Velocity alignment of CO (2 – 1) spectra across the galaxy NGC 4321	64
3.7	Functioning principle of spectral line stacking	65
3.8	Comparison between line stacking and data binning	66
3.9	Bias of sigma-clipped trends in the presence of incomplete data	66
3.10	Linear regression of simulated data	67
4.1	Peak intensity maps of the template galaxy NGC 3059	69
4.2	Stacked spectra of the NGC 3059-lookalike at different S/N levels	71
4.3	Radial profile of the NGC 3059-lookalike galaxy obtained via spectral stacking	72
4.4	Radial stacks for different antenna configurations	73

List of Figures

5.1	Gao–Solomon relation – a literature compilation	79
5.2	Dense gas fraction scaling relations	82
5.3	Dense gas scaling relations with kpc-scale environment	84
5.4	Gao–Solomon relation – centres vs discs	86
6.1	ALMOND radial stacks across NGC 4321	89
6.2	Expectations from cloud models	91
6.3	Dense gas relations with cloud properties	92
7.1	Infrared and optical images of NGC 4321	95
7.2	Maps of NGC 4321	97
7.3	Dense gas ratios across morphological regions in NGC 4321	98
7.4	Dense gas scaling relations at 260 pc in NGC 4321	99
7.5	SFE _{dense} in the bar of NGC 4321 and HCN/CO as a tracer of molecular gas density	100
8.1	Artistic view of the MW with LEGO cloud locations.	104
8.2	LEGO massive star-forming regions	106
8.3	Cloud-average spectra across massive star-forming regions from LEGO	107
8.4	Integrated intensity maps of selected lines	108
8.5	Line intensity versus column density	109
8.6	Line efficiency scaling relations	110
8.7	Line efficiencies of (dense) molecular gas tracers	111
8.8	Line efficiencies of alternative dense gas tracers	112
8.9	HCN/CO as a density-sensitive line ratio	113
9.1	Schematic of dense gas relations	117
D.1	PHANGS–ALMA CO maps across the ALMOND sample	212
D.2	Smoothed PHANGS–ALMA CO maps across the ALMOND sample	213
D.3	ALMOND HCO ⁺ maps	214
D.4	ALMOND CS maps	215
D.5	LEGO cloud-average spectra	218
D.6	Integrated intensity maps of W49	219
D.7	Integrated intensity maps of W43	220
D.8	Integrated intensity maps of G45.1+0.1	221
D.9	Line intensity against column density across W49	222
D.10	Line intensity against column density across W43	223
D.11	Line intensity against column density across G45.1+0.1	224
D.12	Line emissivity against column density across W49	225
D.13	Line emissivity against column density across W43	226
D.14	Line emissivity against column density across G45.1+0.1	227
D.15	Dust temperature against column density across LEGO clouds	228

List of Tables

1.1	Phases of the interstellar medium	3
3.1	PyStructure products.	52
3.2	Linear Regression Tools	60
5.1	Galaxy sample (EMPIRE + ALMOND)	78
5.2	Gao–Solomon relation	80
5.3	Spectroscopic ratio relations	81
5.4	Dense gas scaling relations with \sim kpc-scale environment	85
7.1	Properties of NGC 4321.	96
8.1	Source properties.	105
D.1	LEGO sources	216
D.2	Molecular line properties	217



Front Cover: Galaxy NGC 4321 with JWST image over HST image

Back Cover: The same galaxy with HCN contours over HST image